UNIVERSITY OF STRATHCLYDE
DEPARTMENT OF THERMODYNAMICS AND FLUID MECHANICS
MECHANICAL ENGINEERING GROUP

FLOODING AND NON-EQUILIBRIUM IN COUNTER-CURRENT FLOWS WITH REFERENCE TO PRESSURISED WATER REACTORS

BY

MOHAMED M.M. MEGAHED

Thesis Presented for the Degree of Doctor of Philosophy in Mechanical Engineering.

DECEMBER 1981

TO MY FATHER

ABSTRACT

During the refill stage of a Loss of Coolant Accident (LOCA) in Pressurised Water Reactor (PWR) the effectiveness with which the emergency coolant penetrates to the lower plenum, and hence to the core, is of paramount importance.

This thesis presents the results of experimental and theoretical work carried out at the University of Strathclyde on two 1/10 scale planar test sections of a PWR downcomer annulus. The experiments involved the countercurrent flows of air and water and the data were compared with existing flooding correlations for tubes. The comparison revealed the inadequacy of the existing correlations.

In the Phase 1 test section arrangement, it was found experimentally that, as the inlet air flowed upwards against two opposing waterfalls, an increase in air flowrate caused the waterfalls to move closer together until a critical air flowrate was reached where the waterfalls collapsed. A theoretical model was also developed to define this collapse condition which was shown to be analogous to the choked flow of air through a nozzle whose cross sectional area varied with pressure. Whilst this phenomenon was not directly related to the PWR refill problem, it was an interesting feature in its own right.

Use was made of previous experimental results for steam-water mixtures on similar test sections, in conjunction with the present air-water data, to study condensation effects. Here the non-equilibrium effects were isolated and correlated against the dependent parameters of inlet water flowrate, inlet subcooling and downcomer wall temperature. A theoretical model for the condensation process was developed which gave good qualitative and quantitative agreement with experiment. Its superiority over a current BCL correlation is demonstrated.

INDEX

		Page
	Abstract	(i)
	Index	(iii)
	Contents	(iv)
	List of Appendices	(ix)
	List of Figures	(xi)
	List of Tables	(xxi)
	Nomenclature	(xxii)
Chapter 1	Introduction	1
Chapter 2	Review of Literature	10
Chapter 3	Apparatus and Instrumentation	128
Chapter 4	Experimental Results	140
Chapter 5	Discussion of Results	166
Chapter 6	Theoretical Analysis	196
Chapter 7	Conclusions and Recommendations	284
	References	289
	Acknowledgements	296
	Appendices	298

CONTENTS

	Page
Abstract	(i)
Index	(iii)
Contents	(iv)
List of Appendices	(ix)
List of Figures	(xi)
List of Tables	(xxi)
Nomeclature	(xxii)
CHAPTER 1 INTRODUCTION	1
1.1 PWR Operation	2
1.2 Loss of Coolant Accident	4
1.3 Current Project	5
CHAPTER 2 REVIEW OF LITERATURE	10
2.1 Theoretical Analysis of Flooding in Vertical Tubes	11
2.1.1 Wave Stability Analysis	12
2.1.1.1 Small Perturbation Models	12
2.1.1.2 Standing Wave Models	18
2.1.2 Film Flow Model	22
2.1.3 Hanging Film Models	25
2.1.4 The Annular Flow Models	30
2.1.5 Entrainment Model	41
2.2 Theoretical Analysis on the Effect of Condensation	43

		Page
2.3	Flooding in PWR Geometries	49
2.4	Previous Work at Strathclyde	68
2.5	Summary and Conclusion	74
CHAPTER 3	APPARATUS AND INSTRUMENTATION	128
3.1	Experimental Apparatus	129
3.1.1	Layout of Test Rig	129
3.1.2	Test Sections	130
3.1.3	Air and Water Supplies	131
3.2	Instrumentation and Measurement	132
3.2.1	Air Flowrates	132
3.2.2	Water (Coolant) Flowrates	133
3.2.3	Outlet Water Flowrates	133
3.2.4	Pressure Measurements	134
3.2.5	Temperature Measurements	134
3.3	Test Programme and Procedures	135
3.3.1	Methods of Testing	135
3.3.2	Experimental Procedures	136
CHAPTER 4	EXPERIMENTAL RESULTS	140
4.1	Descriptions of Flow Patterns	142
4.1.1	Phase 1 Tests	142
4.1.2	Phase 2 Tests	143
4.1.3	Cine Films	144
4.2	Tables of Experimental Data	144
4.3	Graphical Results	145

		Page
4.4	Correlation of Data	147
	4.4.1 Phase 1 Tests	148
	4.4.2 Phase 2 Tests	148
4.5	Auxiliary Tests	149
CHAPTER 5	DISCUSSION OF RESULTS	166
5.1	Water Penetration Characteristics	167
5.2	Comparison of Air First and Water First Tests	169
5.3	Comparison of Phase 1 and Phase 2 Test Data	171
5.4	Comparison with Theoretical Work	173
	5.4.1 Phase 1 Geometry	173
	5.4.2 Phase 2 Geometry	174
	5.4.2.1 Comparison with Schutt (1)	176
	5.4.2.2 Comparison with Grolmes et al (7)	177
	5.4.2.3 Comparison with Imura et al (16)	177
	5.4.2.4 Comparison with Richter and Wallis (33)	178
	5.4.2.5 Comparison with Richter (34)	179
	5.4.3 General Comment on the Comparisons	180
CHAPTER 6	THEORETICAL ANALYSIS	196
6.1	The upward flow of Air between two Waterfalls	197

			Page
	6.1.1	The Trajectories of the Waterfalls	198
	6.1.2	Air Flow	204
	6.1.3	Effect of Air Flow on the Water Trajectories	208
	6.1.4	The condition for the Collapse of the Pair of Waterfalls	212
	6.1.5	Choking Conditions	214
	6.1.6	The Collapse Condition in Terms of J_s^* and J_w^*	217
	6.1.7	Allowance for the Thickness of the Waterfalls	220
6.2		Comparison Between Theory and Experiment	220
	6.2.1	Water Trajectories with Zero Air Flow	220
	6.2.2	Condition for the Collapse of the Pair of Waterfalls	220
6.3		Non-Equilibrium Effects in Director Condensation under Counter-current flow	224
	6.3.1	Isolation of Condensation Effects	226
	6.3.2	Condensation Model	232
	6.3.3	Estimation of the Interfacial Heat Transfer Coefficient	239
	6.3.4	Discussion of the Condensation Model	243

CHAPTER 7 CONCLUSIONS AND RECOMMENDATIONS

Page

7.1 Conclusions 285

7.2 Recommendations 288

References 289

Acknowledgements 296

Appendices 298

LIST OF APPENDICES

APPENDIX	
A	Calibration of Orifice Plate for Air Flowrate Measurements
B	Calibration of Rotameters for Air Flowrate Measurement
C	Calibration of Turbine Flowmeters for Water Flowrate Measurements
D	Experimental Measurements (Unprocessed)
E	Air/Water Data (Phase 1 Tests)
F	Air/water Data (Phase 2 Tests)
G	Penetration Characteristics for Phase 1 Data
H	Penetration Characteristics for Phase 2 Data
I	Comparison between Partial Penetration Data for Phase 1 Tests and Equation (4.4)
J	Comparison of "Water First" with "Air First" Tests Data - (Phase 2 Tests)
K	Comparison of Phase 1 and Phase 2 Test Data
L	Conversion of Theoretical work to Wallis Parameters
M	Measurements of the Waterfall Trajectories
N	Flow over the Brink into the Test Section
O	Position of Waterfalls at bottom of Test Sections for case of Constant ΔP. (Approximate Solutions).
P	Position of Waterfalls at bottom of Test Section for the case of Air following Waterfalls

APPENDIX

Q — Position of Waterfalls at bottom of Test Section for case of Constant ΔP (exact Solution)

R — Position of Waterfalls at bottom of Test Section for the case of Linear Varying Jet - ($\bar{d}_o = d_o$)

S — Evaluation of Air Velocity at Choking Conditions

T — Tables of the Collapse Conditions

U — Allowance for the Thickness of the Waterfalls

LIST OF FIGURES

		Page
Figure 1.1	Diagramatic Arrangement of a PWR	8
Figure 1.2.	Cold Leg Break in a PWR	9
Figure 2.1	Schematic Representation of Bridging - (From Ref (1))	78
Figure 2.2.	Comparison of Theoretical and Experimental Bridging Gas Velocities versus Sucrose Solution (35% WT) Rate-(Schutt (1))	79
Figure 2.3	Comparison of Theoretical and Experimental Bridging Gas Velocities versus water flow rate. - (Schutt (1))	80
Figure 2.4	The Coordinate System used in Ref. (2)	81
Figure 2.5	The Growth Rate αC_1 as a function of the Gas Friction Velocity V_* - (Cetinbudaklar and Jameson (2))	82
Figure 2.6	Comparison of Predicted Flooding Velocities with the Experimental Data of Clift et al (3) - (from ref. (2))	83
Figure 2.7	Axes and Wave Prefiles to Scale - (Shearer Davidson (4))	84
Figure 2.8	Dimensionless Groups for Formation of a Large - Amplitude Wave - (Shearer Davidson (4))	84
Figure 2.9	Analytical Model of Ueda and Suzuki (5)	85
Figure 2.10	Relation between Wave Height and Gas Velocity for Air-Water Flow in an Annulus - (Ueda Suzuki: (5))	85
Figure 2.11	Dimensionless Film Thickness Variation with Dimensionless Interfacial Shear - [Dukler et al (6)]	86

Figure 2.12	Correlation of Gas-Liquid Interface Friction at Flooding Conditions - (Grolmes et al (7)	87
Figure 2.13	Comparison of Flooding Gas Velocity with Eqs.(2.33) & (2.35) - (Grolmes et al (7)	88
Figure 2.14	Hanging Film Model - Wallis Kus (9)	89
Figure 2.15	Several Computer Solutions To (2.37) with Ug = o and $dx^*/dr^* \to \infty$ $r^* \to \infty$ Wallis of Kuo (9)	89
Figure 2.16	Flow Around a Pair of Sources ref (9)	90
Figure 2.17	Annular Flow Model - Wallis (12)	90
Figure 2.18	The Coordinate System Used by Imura et al (16)	91
Figure 2.19	Correlations of Flooding Data Using (2.65) - Imura et al (16)	92
Figure 2.20	The Counter-Current Two-Phase Flow System - Chung (17)	93
Figure 2.21	Flooding results for Different Tube Sizes with Sharp Edge Liquid Inlet and Nozzle Air Supply - Tien et al (18)	94
Figure 2.22	The Wallis Correlation for Flooding - Dukler & Smith (19)	95
Figure 2.23	Subcooled CCFL Correlations - Tien (21)	96
Figure 2.24	Counter-Current Annular Flow Liu et al (22)	97
Figure 2.25	Comparison of Experimental and Calculated Nusselt Number - Liu et al (22)	98
Figure 2.26	Flow Regimes In the Downcomer of PWR - (Wallis et al (24)	99
Figure 2.27	Approximate Flow Region Map - (Wallis et al (24)	100

		Page
Figure 2.28	Some of Crowley's Results (25) for Countercurrent Steam-Water Flow in a Small Scale Model PWR Annulus	101
Figure 2.29	Sketch of the End of Bypass Locus in Steam First Experiments- Crowley et al (25)	102
Figure 2.30	Penetration Data for 70°F Water Based on the Downcomer Width as the Characteristic Dimension - Block & Crowley (26)	103
Figure 2.31	Comparison of the Correlation with Creare Flat Plate Data - Block et al (27)	104
Figure 2.32	Comparison of the Correlation with Creare Cylindrical Vessel Data with Controlled Pressures - Block et al (27)	105
Figure 2.33	Comparison of the Calculated Annulus Condensation Efficiency K_{ne} (at 1/15 - and 1/30 - Scale) with the Prediction of the 1/15 - Scale-Based Correlation Using J* (Equation (2.115)) - Crowley et al (28)	106
Figure 2.34	Comparison of the Measured Penetration Curve Slope m at 1/30 - Scale with the Prediction of the 1/5 - Scale-Based Correlations using J* (Equation (2.114)) - (Crowley et al (28))	106
Figure 2.35	Comparison of the Correlation Based on J* (Eqs. (2.112) to (2.115) with Creare 1/30 - Scale Cylindrical Vessel Data (Uncontrolled Pressure)- Crowley et al (28)	107
Figure 2.36	Comparison of the Correlation Based on K* (Eqs.(2.116)to (2.119) with Creare 1/30 - Scale Cylindrical Vessel Data (Uncontrolled Pressure)- Crowley et al (28)	108

		Page
Figure 2.37	Comparison of BCL and Creare Correlations at various ECC Water Subcoolings for a $J^*_{W_i}$ of 0.5 and a System Pressure of 75 psia - (Cudaik et al (29)	109
Figure 2.38	Behaviour of Factor m Representing Partial Delivery (Rothe and Crowley (30))	110
Figure 2.39	Comparison of *Rothe et al* Correlation with Creare 1/15 - Scale Data for a Vessel Pressure of 65 psia at Various ECC Subcooling - (Rothe and Crowley (30)	110
Figure 2.40	Comparison of the Calculated Froude Number, eq. (2.123) to the experimentally observed value - (ref.(31))	111
Figure 2.41	Comparison of the Calculated Dimensionless Steam Flux, eq. (2.112), to the Experimentally Observed Values - (Alb and Chambr´ (31))	111
Figure 2.42	Nondimensional Gas Flux vs. Water Flux for non-symmetrical Top Flood - (Richter and Murphy (32))	112
Figure 2.43	Water Pentration Data for Air Comparison of Semiscale Data with Dartmouth 1/10 and 2/15 - Scale Data - (Richter and Wallis(33))	113
Figure 2.44	Water Penetration Data for Air and Steam. Comparison of Creare 1/30 - Scale Saturated Steam Data with Dartmouth 1/10 - and 2/15 - scale Air Data - (Ref 33))	114
Figure 2.45	Water Penetration Data for Steam and Air Comparison of Creare 1/15 Scale Low Subcooling Data with Dartmouth 1/10 and 2/15 - Scale Air Data - Ref (33))	115

		Page
Figure 2.46	Water Penetration Data for Air Comparison of Battelle 2/15 - Scale Data and Dartmouth 2/15 Scale Data - (Richter and Wallis(33))	116
Figure 2.47	Slope M of Wallis Correlations as a Function of Scale (Richter and Wallis (33))	117
Figure 2.48	Momentum Balance in a Pipe Counter current Flow - (Richter (34))	118
Figure 2.49	Nondimensional Gas Flux vs. Water Flux for Flooding in a 2/15 - Scale of a Nuclear Reactor Annulus - (Richter (34))	119
Figure 2.50	Line Diagram of Refill Test Rig showing Instrumentation - (Campbell (35))	120
Figure 2.51	Detail of Test Sections - (Campbell (35))	121
Figure 2.52	The Effect of Geometry on Flooding- (Campbell (35))	122
Figure 2.53	The Effect of Inlet Subcooling on Flooding - (Campbell (35))	123
Figure 2.54	Effect of Wall Temperature on Flooding -(Campbell (35))	124
Figure 2.55	Coordinate System for Water Jet Trajectory and Bridge - (Simpson et al (36))	125
Figure 2.56	Approximate Steam Flow Patterns - (Simpson et al (36))	126
Figure 2.57	Dimensionless Plot of Bridging Conditions, Eqs. (2.141) to (2.144) - (Strathclyde)	127
Figure 3.1	Line Diagram of Test Rig Showing Instrumentation Points	137
Figure 3.2	Details of Test Sections	138

		Page
Figure 3.3	General View of Refill Test Rig - Phase 1	139
Figure 4.1	Air-Water Flow Pattern Representation Phase 1	150
Figure 4.2.	Typical Bypass Curves for Air-Water Tests - Phase 1 Tests	151
Figure 4.3	Penetration Characteristics from Air Water Tests - Phase 1	152
Figure 4.4.	Degree of Penetration to Lower Plenum of Inlet Water for Particular Air Flowrates - Phase 1	153
Figure 4.5	Penetration Characteristics from Air- Water Tests - Phase 2	154
Figure 4.6	Degree of Penetration to Lower Plenum of Inlet Water for Particular Air Flowrates - Phase 2	155
Figure 4.7	Bypass Characteristics for Air-Water tests - Phase 1	156
Figure 4.8	Lower Plenum Penetration Characteristics for Air-Water Tests Phase 1	157
Figure 4.9	Dimensionless Plot of All Air-Water Data - Phase 1	158
Figure 4.10	Correlation of Penetration Data for Air-Water Tests - (Phase 1 Test)	159
Figure 4.11	Comparison of Experimental Data with Equation (4.4)	160
Figure 4.12	Dimensionless Plot of All Air-Water Data - Phase 2	161
Figure 4.13	Dimensionless Plot of All Air-Water Data - Phase 2	162
Figure 4.14	Critical Conditions for Liquid Bridging - Phase 2	163
Figure 4.15	Variation of Water Height at the Brink, H_{w_i} with Dimensionless Water Flow, $J^*_{w_i}$ - Phase 1 Tests	164

		Page
Figure 4.16	Variation of Water Height at the Brink, H_{w_i} with Dimensionless Water Flux, $J^*_{w_i}$ - Phase 2 Tests	165
Figure 5.1	Comparison Between Air/Water and Steam/Water Test Data - (Phase 2 Tests - Steam First)	181
Figure 5.2	Comparison between Air/Water and Steam/Water Test Data - (Phase 2 Tests - Steam First)	182
Figure 5.3	Comparison between Air/Water and Steam/Water Test Data - (Phase 2 Tests - Steam First)	183
Figure 5.4	Comparison between Air/Water and Steam/Water Test Data - (Phase 2 Tests - Steam First)	184
Figure 5.5	Bypass Characteristics From Air - Water Test - Phase 1	185
Figure 5.6	Comparison of "Water First" with "Air First" Test Data (Phase 2 Tests)	186
Figure 5.7	Comparison of Phase 1 and Phase 2 Test Data - Water First	187
Figure 5.8	Comparison of Phase 1 and Phase 2 Test Data - Air First	188
Figure 5.9	Comparison between The Bridge Theory and the Experimental Results	189
Figure 5.10	Comparison between Experiment and Schutt's Correlation (1)	190
Figure 5.11	Comparison between Experiment and Grolmes' Correlation (7)	191
Figure 5.12	Comparison between Experiment and Imnra's Correlations (16)	192
Fig Re 5.13	Comparison Between Experiment and Richter and Wallis's Correlation (33)	193

		Page
Figure 5.14	Comparison between Experiment and Richter Correlation (34)	194
Figure 5.15	Comparison of Different Flooding Correlations with Equation (4.6)	195
Figure 6.1	Test section for Phase 1 Tests - Tangential Entry	253
Figure 6.2	Typical Waterfall Trajectories - Zero Air Flow	254
Figure 6.3	Experimental Data for Waterfall Collapse	255
Figure 6.4	Co-ordinate System for Waterfall Analysis	256
Figure 6.5	Possible Air Flow Patterns	257
Figure 6.6	Dimensionless Water Trajectories - Case (i)	258
Figure 6.7	Dimensionless Water Trajectories - Case (ii)	259
Figure 6.8	Position of Waterfalls at bottom of Test Section for the Case of Constant ΔP - (Approximate Solution)	260
Figure 6.9	Position of Waterfalls at bottom of Test section for the case of Air following water walls	261
Figure 6.10	Position of Waterfalls at Bottom of Test Section for the Case of Constant ΔP - (Exact Solution)	262
Figure 6.11	Position of Waterfalls at bottom of Test Section for the case of Linear Varying Air Jet	263
Figure 6.12	Comparison between Theory and Experiment - Collapse Condition for Waterfall Pair	264
Figure 6.13	Sketch of Typical Flooding Behaviour	265
Figure 6.14	Variation of Non-Equilibrium Factor K_{ne}, with Dimensionless Water Flux, J^*_w -(T_{wall} = 20°c)	266

		Page
Figure 6.15	Variation of Non-Equilibrium Factor K_{ne}, with Dimensionless Water Flux, J_w^* -(T_{wall} = 50 °c)	267
Figure 6.16	Variation of Non-Equilibrium Factor K_{ne}, with Dimensionless Water Flux, J_w^* -(T_{wall} = 100 °c)	268
Figure 6.17	Variation of Non-Equilibrium Factor K_{ne}, with Dimensionless Water Flux, J_w^* -(T_{wall} = 150 °c)	269
Figure 6.18	Effect of Wall Temperature on the Non-Equilibrium Factor - ΔT_{sub} = 90 K	270
Figure 6.19	Effect of Wall Temperature on the Non-Equilibrium Factor - ΔT_{sub} = 65 K	271
Figure 6.20	Effect of Wall Temperature on the Non-Equilibrium Factor - ΔT_{sub} = 50 K	272
Figure 6.21	Effect of Wall Temperature on the Non-Equilibrium Factor - ΔT_{sub} = 30 K	273
Figure 6.22	Counter-current Annular Flow	274
Figure 6.23	Correlation of Interfacial Nusselt Number As A Function of Water Prandtl and Reynolds Number	275
Figure 6.24	Correlation of Interfacial Nusselt Number	276
Figure 6.25	Sketch of Typical Non-Equilibrium Behaviour	277
Figure 6.26	Comparison between Calculated and Experimental J_s^* -(T_{wall} = 20 °c)	278
Figure 6.27	Comparison between Calculated and Experimental J_s^* -(T_{wall} = 50 °c)	279
Figure 6.28	Comparison between Calculated and Experimental J_s^* -(T_{wall} = 100 °c)	280

		Page
Figure 6.29	Comparison between Experiment and Predicted Values using BCL Correlations (39) -(T_{wall} = 20 °c)	281
Figure 6.30	Comparison between Experiment and Predicted Values using BCL Correlation (39) -(T_{wall} = 50 °c)	282
Figure 6.31	Comparison between Experiment and Predicted Values using BCL Correlation (39) -(T_{wall} = 100 °c)	283

LIST OF TABLES

Table		Page
2.1	Comparison of Scaled Vessel Dimensions (from Alb and Chambré (31))	63
2.2	Summary of Campbell's Programme	71
6.1	Experimental Values Relating to the Collapse Condition of the Pair of Waterfalls - Water First Tests	199

Other Tables are found in Appendices D, E, F, M, N, O, P, Q, R, and T

NOMENCLATURE

A = Cross sectional area of the test section, m^2

B = Width of the test section, m

B^* = Dimensionless width defined by equation (6.21)

C_w = Wall coefficient of friction

c = Empirical constant in equation (6.75)

c_p = Specific heat at constant pressure

D_e = Film hydraulic diameter defined by equation (6.114) , m

D_H = Hydraulic diameter defined by equation (5.5), m

D_o = Dimensionless outlet hole diameter defined by equation (6.30)

D^* = Bond Number defined by equation (2.56)

d_o = Outlet hole diameter, m

$\bar{d}_o$ = Effective outlet hole diameter$=\sqrt{\frac{\pi}{4}}\, d_o$, m

F = Dimensionless temperature difference defined by equation (6.103)

Fr_{w_b} = Froude number defined by equation (6.58)

Fr_{w_i} = Effective inlet Froud number

Fr_{w_z} = Froude number just before the brink

g = Gravitational acceleration, $m/_s{}^2$

H_w = Thickness of water jet, m

H_{w_i} = Water height at the brink, m

H_{w_m} = Waterfall thickness just before the brink, m

h = Interfacial heat transfer coefficient, kW/m^2K

h_{fg} = Specific latent heat, kJ/kg

h_g = Specific enthalpy of steam, kJ/kg

h_w = Wall heat transfer coefficient, kW/m^2K

Ja = Jacob number defined by equation (6.66)

J_A^* = Dimensionless air flux defined by equation (4.3)

J_s^* = Dimensionless steam flux

J_{sc}^* = Dimensionless condensate flux defined by equation (6.72)

J_w^* = Dimensionless water flux

$J_{w_i}^*$ = Dimensionless inlet water flux, define by equation (4.1)

$J_{w_{LP}}^*$ = Dimensionless water flux penetrating to lower plenum, defined by equation (4.2)

$J_{w_{mod}}^*$ = Modified dimensionless water flux defined by equation (6.74)

j_A = Superficial air velocity, m/s

j_s = Superficial steam velocity, m/s

j_w = Superficial water velocity, m/s

K = Dimensionless parameter defined by equation (6.18)

K_1 = Dimensionless parameter defined by equation (6.37)

K_2 = Dimensionless parameter defined by equation (6.38)

Kg = Gas Kutateladze number

K_L = Liquid Kutateladze number

K_{ne} = Non-equilibrium factor

k = Empirical constant in equation (6.14)

k_w = Thermal conductivity of water, kW/mK

L = Length of the test section, m

M_A = Air flowrate entering the test section, kg/s

M_s = Steam flowrate entering the test section, kg/s

M_{sc} = Mass flowrate of condensed steam, kg/s

$M_{s_{mod}}$ = Modified steam flowrate defined by equation (6.70), kg/s

M_w = Water flowrate, kg/s

M_{w_i} = Inlet water flowrate, kg/s

$M_{w_{LP}}$ = Water penetrating to lower plenum, kg/s

$M_{w_{mod}}$ = Modified water flowrate, defined by equation (6.71)

M_{w_o} = Entrained water flowrate, kg/s

m = Empirical constant in equation (6.75)

N_B = Bond number in equation (5.13)

Nu_i = Interfacial Nusselt number defined by equation (6.118)

Nu_w = Wall Nusselt number defined by equation (6.111)

ΔP = Dimensionless pressure difference defined by equation (6.9)

ΔP_b = Dimensionless pressure difference at the bottom of test section

Pr = Film Prandtl number defined by equation (6.113)

p = Pressure, N/m^2

Δp = Pressure difference across water jet, N/m^2

Q_m = Liquid volume flowrate per unit perimeter

Re = Film Reynolds number defined by equation (6.112)

S = Gap size of test section, m

S^* = Dimensionless length = S/B

T = Temperature

T_b = Bulk temperature

T_s = Saturation temperature

ΔT_{sub} = Water subcooling

T_{wall} = Downcomer wall temperature

T_{w_i} = Inlet water temperature

U_g = Gas velocity, m/s

U_L = Mean liquid velocity, m/s

u = Water velocity in x direction, m/s

u_i = Inlet water velocity, m/s

u_A = Air velocity, m/s

$\bar{v}$ = Absolute water velocity in the jet, m/s

w = Water velocity in y direction, m/s

X = Dimensionless horizontal length defined by equation (6.9)

χ = Dimensionless horizontal length defined by equation (6.22)

Y = Dimensionless parameter defined by equation (6.33)

Z = Dimensionless vertical length defined by equation (6.9)

GREEK SYMBOLS

α = Dimensional group defined by equation (6.99), m^{-1}

α_1 = Dimensional group defined by equation (6.123), m^{-1}

γ = Dimensionless number defined by equation (6.91)

η = Dimensionless parameter defined by equation (6.35)

η_b = Demensionless parameter defined by equation (6.36)

δ = Film thickness, m

λ, λ_1 = Geometrical constants defined by equations (6.39) and (6.47)

μ_w = Dynamic viscosity of water, kg/ms

ϑ = Kinematic viscosity of water, m^2/s

ρ_A = Density of air, kg/m^3

ρ_s = Density of steam, kg/m^3

ρ_w = Density of water, kg/m^3

σ = Surface tension, N/m

ϕ = Dimensionless temperature defined by equation (6.92)

ψ = Dimensional group defined by equation (6.100) kg/m^2s

ABBREVIATIONS

BCL = Battelle Columbus Laboratories

CCFL = Counter Current Flow Limitations

ECC = Emergency Core Coolant

EPRI = Electric Power Research Institute

LOCA = Loss of Coolant Accident

NII = Nuclear Installations Inspectorate

PWR = Pressurised Water Reactor

UK = United Kingdom

CHAPTER 1

INTRODUCTION

CHAPTER 1 : INTRODUCTION

During the past two decades, the share of electric power generated by nuclear reactors has increased dramatically and different types of nuclear reactors are currently operating in different parts of the world.

The basic principle of the nuclear power plant is the removal of energy (heat) generated in the core of the reactor by nuclear fission and its subsequent use to generate steam. The coolant used to remove the heat generated in the core can be either liquid or gas. The present work is related to the safety of Pressurised Water Reactors (PWR), i.e., reactors which use water as the coolant operating at fairly high pressure (~150 bar).

1.1 PWR OPERATION

Figure 1.1 shows a diagrammatic arrangement of a PWR plant under normal operating conditions. Here the pressurised water flows downwards through the annulus surrounding the reactor vessel core barrel and then upwards through the core fuel elements out of the reactor vessel through the hot legs into steam generators where it circulates through tubes, the outer surfaces of which are in contact with a secondary stream of water returning from the turbine condensers. The heat transfer through the tubes causes the water to evaporate, so producing steam to drive the turbines. Since the steam is not obtained directly from the core heating, this

system is called an "indirect cycle system".

After transferring energy in the steam generators, the pressurised water is returned by means of circulating pumps to the reactor vessel via the "cold leg 'piping. There are normally four loops associated with each reactor vessel with each loop having an accumulator vessel connected to the cold leg. The accumulator contains borated water for emergency core cooling purposes in the event of a system leakage and associated depressurisation. The primary system is pressurised by a single pressuriser vessel connected to one of the hot legs as shown in Figure 1.1.

Because of the potential hazards inherent in the operation of a PWR, it is essential that safety features be incorporated into the design. A consideration of prime importance is the loss of coolant accident (LOCA) since this could result in a potential radiological danger to the public in the event of the core cooling being diminished. A postulated LOCA assumes that an instantaneous break or breach occurs in some part of the reactor coolant system, e.g., cold leg piping. The largest pipe break considered is the severance of the largest pipe in the coolant system in such a way that the reactor coolant would discharge unimpeded from both ends - the so-called "double-ended guillotine break". Due to the initially high pressure of the coolant, such a break would result in a rapid expulsion of a large fraction of the reactor coolant into the containment surrounding the reactor, resulting in a rapid depressurisation of the

primary system and consequent flash evaporation of some of the remaining coolant. This is illustrated in Figure 1.2.

1.2 LOSS OF COOLANT ACCIDENT

In the event of a LOCA, due to a double-ended cold leg guillotine break, or other types of breach, the effects within the reactor are postulated to occur as follows :

(i) Blowdown The high pressure (~150 bar), high temperature (~315^{o}C) primary coolant would be rapidly expelled from the primary system. During the later stages of this blowdown, present LOCA calculations predict steam or two-phase flows in the directions shown schematically in Figure 1.2.

(ii) Refill When the vessel pressure decreases to around 41 bar, check valves between the accumulators and the cold leg open and allow emergency coolant to pass into the cold legs. These large volumes of water, maintained at about 41 bar by compressed Nitrogen gas in the accumulator and designated as the Emergency Core Coolant (ECC), enter the downcomer annulus with the expectation of passing downwards by virtue of momentum and gravity. However, the upward steam flow from the core opposes this

desired downward flow of ECC water and can, under some conditions, bypass it around the annulus and straight out the fractured pipe. The refill stage is completed when the lower plenum is filled and the water level reaches the bottom of the core.

(iii) Reflood The reflood period involves the time during which the level of coolant contained in the pressure vessel rises from the bottom to the top of the core, completing the resubmergence of the core and producing safe conditions.

1.3 CURRENT PROJECT

The work presented in this thesis is connected with the safety aspects of PWRs and was supported by H.M. Nuclear Installation Inspectorate (NII), a branch of the Health and Safety Executive of the U.K. Government. The possibility of PWRs being built in the U.K., and the subsequent licensing, requires that NII be fully aware of the merits and demerits of any theoretical correlations, computations or experimental data introduced into the safety case.

In this project, interest is confined to the refill stage of a LOCA; with particular reference to the effectiveness with which the emergency coolant traverses the PWR downcomer and reaches the lower plenum. A review of the literature indicated that conditions can

exist whereby, if the flowrate of counter-current steam generated in the core exceeds certain values, the ECC will not penetrate to the lower plenum but a "liquid bridging" or "flooding" or "bypass effect"* can occur, i.e., the liquid entering the top of the downcomer via an entry pipe flows around the downcomer and out through the break. It was also noted that condensation played an important role in ECC water penetration characteristics. The experimental work carried out at Creare, BCL, and Strathclyde indicated, however, that condensation does not occur under thermal equilibrium, i.e., only a fraction of the steam which could be condensed to raise the temperature of the inlet water to saturation is actually condensed. This non-equilibrium effect was generally accounted for in the literature by introducing a "non-equilibrium factor" or "condensation efficiency" which was determined as a function of the inlet water flow rate by statistical methods and without any theoretical justification. The present work provides a modest attempt at solving the problem of non-equilibrium condensation associated with flooding during the refill stage of a LOCA.

---

* Different names are used in the literature to describe the same effect, viz. the steam holding up the water entering the annulus and causing it to bypass around the annulus and out through the break.

Due to the absence of reliable theoretical models to describe the flooding phenomenon, it was necessary to conduct air/water experiments to complement earlier steam/water experiments carried out at Strathclyde University (refs. 35, 36). An analytical model was also developed, which incorporated the effects of inlet sub-cooling and downcomer wall temperature, to predict the critical steam flux to within $\pm$20%. From observations made during the experimental work, a study of the upward flow of air between two waterfalls was also made with attention being focused on: (i) the prediction of the airflow condition at which the two waterfalls just came together, (ii) a description of the waterfall trajectories. The latter problem was essentially one of choked flow and could be compared with the adiabatic flow of air through a nozzle with flexible walls, the shape of the nozzle being dictated by the air flow. As such, it is a two phase flow problem of particular interest.

This thesis presents (i) the state of the art relevant to the refill problem during a LOCA, (ii) a description of the apparatus and instrumentation which was used for this study, (iii) the experimental data obtained during an air water test programme, (iv) theoretical and analytical models developed in the course of this study.

It is hoped that the information presented will contribute in some way towards a better understanding of the flooding phenomenon involved in the refill stage of a LOCA.

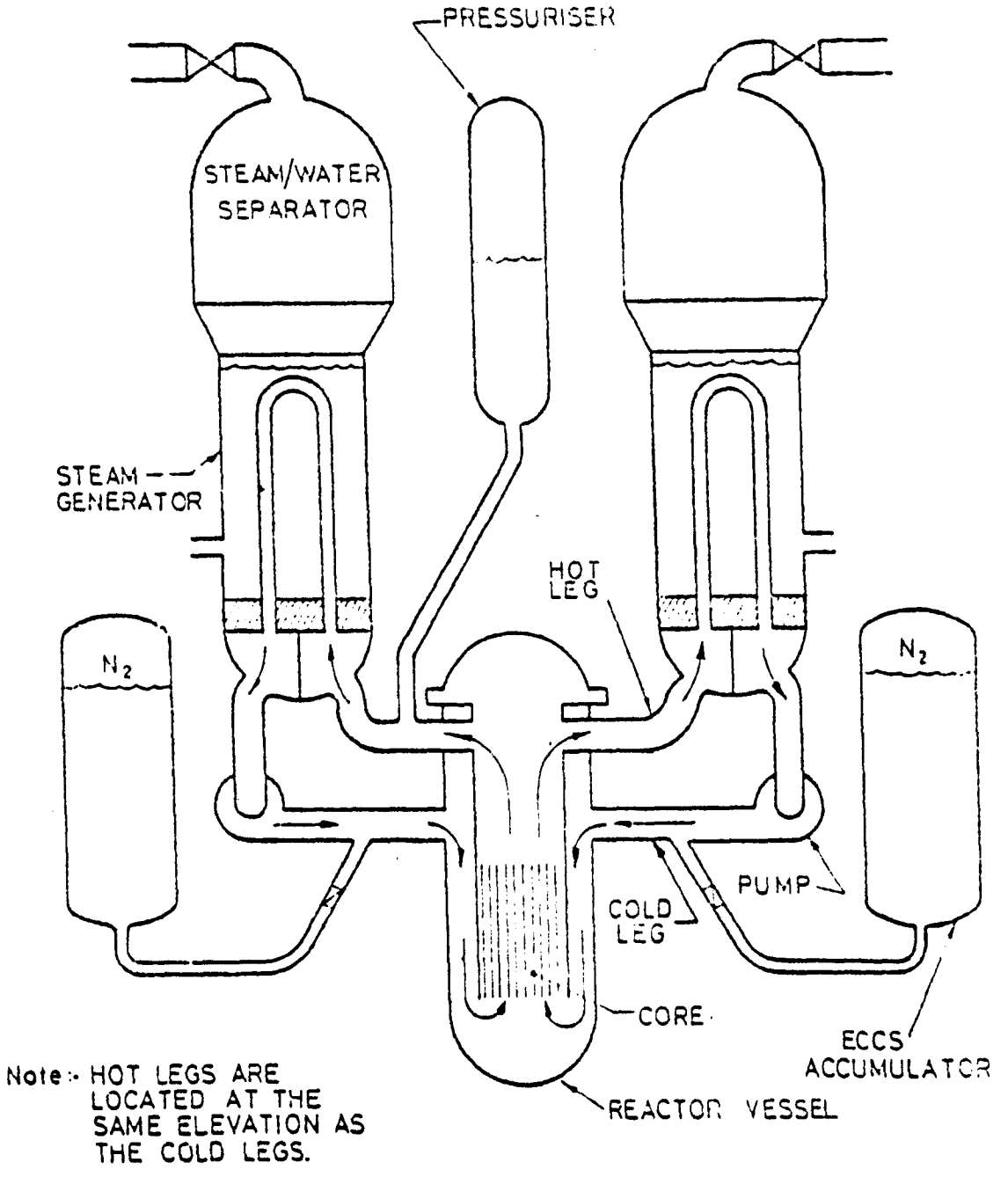

Fig 1.1 DIAGRAMATIC ARRANGEMENT OF A P.W.R.

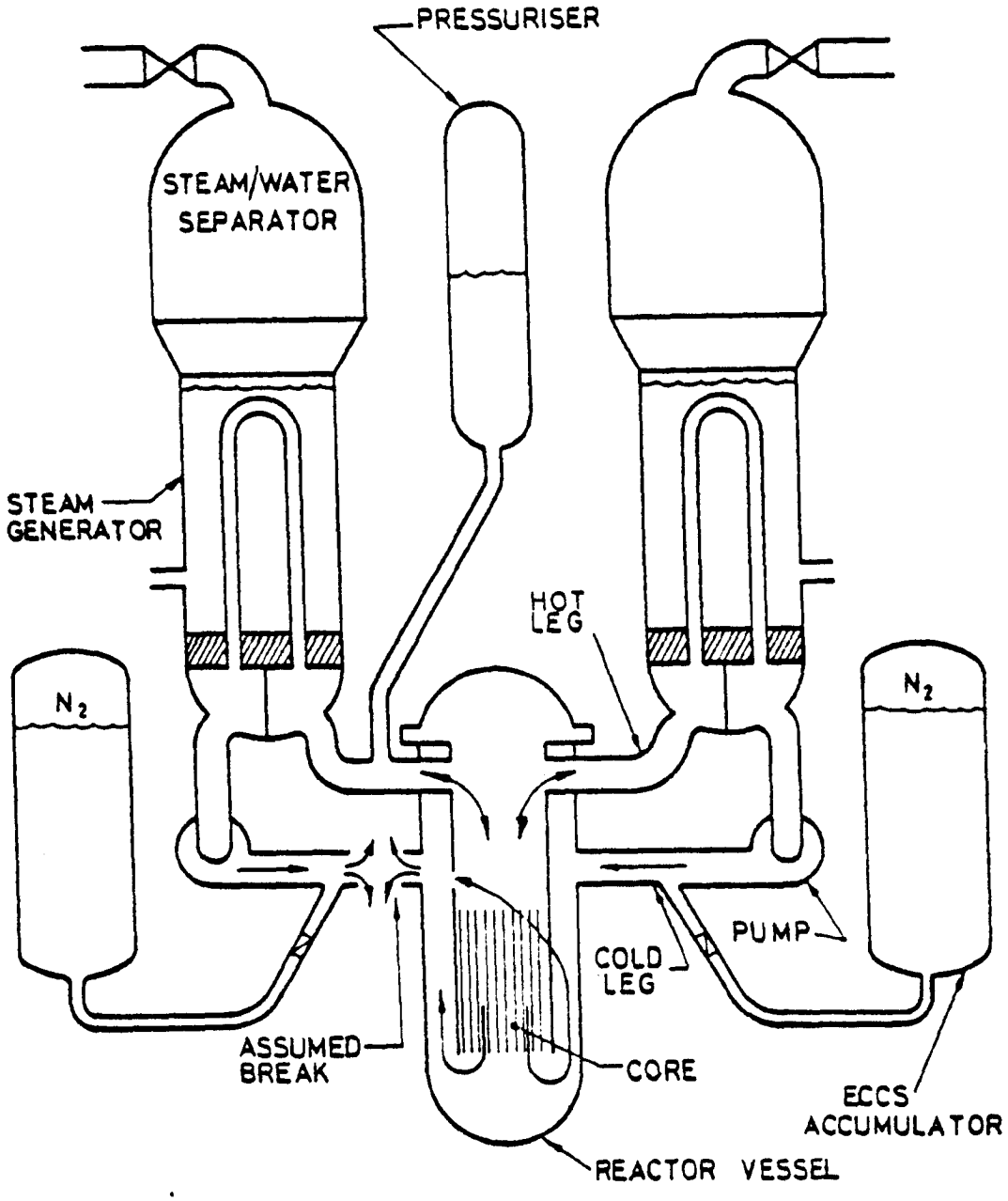

Fig 1.2 COLD LEG BREAK IN A P.W.R.

CHAPTER 2

REVIEW OF LITERATURE

CHAPTER 2 : REVIEW OF LITERATURE

The phenomenon of flooding in vertical counter-current two phase flow systems first received attention from chemical engineers in the design of packed columns. In recent years, however, with the advent of nuclear technology and the growing interest in various heat transfer phenomenon in two phase flows, mechanical and nuclear engineers have also become involved in this phenomenon.

The present review consists of three main sections. In the first section, a critical review is made of the existing theoretical models which lead to the prediction of the critical conditions at the onset of flooding in vertical tubes. These models do not include the effects of heat or mass transfer. In the second section, the limited theoretical work on the effect of condensation is reviewed. The third section presents experimental work on flooding in simulated PWR geometries.

2.1 THEORETICAL ANALYSIS OF FLOODING IN VERTICAL TUBES

The exact mechanism of flooding remains undetermined. Several models have been proposed in the last 15 years or so and these can be divided into the following categories:

(i) Wave stability Analysis

(ii) Film Flow Model

(iii) Hanging Film Models

(iv) Annular Flow Models

(v) Entrainment Model

These models are reviewed in turn.

2.1.1 Wave Stability Analysis

The models presented in this section are promoted by the observation of waves on the gas-liquid interface when flooding conditions are approached. The wave stability analysis speculates that once a finite amplitude wave is formed it continues to grow until it bridges the tube, whereupon the liquid is carried up the tube or duct as a slug or as an entrained phase.

Two approaches have been adopted. The first applies a small perturbation analysis to the interface; the second studies the forces on a single standing wave.

2.1.1.1 Small Perturbation Models

The first theoretical attempt in this direction was carried out by Schutt (1), who endeavoured to find a solution for the Navier-Stokes equations for incompressible, two dimensional isotropic flow. The gas and liquid were assumed to be immiscible with no heat or mass transfer between the phases. The co-ordinate system used is shown in Figure 2.1.

To solve the turbulent Navier-Stokes equation, Schutt assumed the following:

(a) The Navier-Stokes equation can be solved as a two-fold set: one incorporating Reynolds Stress (neglecting

viscosity), and one in linearised form incorporating viscosity (neglecting Reynolds Stresses).

(b) At bridging, the wave equation resulting from double integration of the "viscosity" equation vanishes leaving a more tractable relationship between static and dynamic pressures as an adequate description of the phenomenon.

(c) When used in conjunction with the solution to the "Reynolds Stresses" equation, the large transverse velocity at bridging comes from a "resonance"* condition satisfied by the solution for the transverse velocity.

(d) The longitudinal velocity vanishes at bridging. The details of Schutt's analysis are lengthy, however the resulting bridging equation is given by

$$U_g = \left(\frac{1}{\rho_g} \left[\frac{D}{4} \cdot (I + \rho_L g) - II - III \right] \cdot \frac{2 \tan\varepsilon \cdot \Gamma}{2 \tan\varepsilon \cdot \Gamma - \frac{D/2}{(D/2 - \delta)}} \right)^{\frac{1}{2}} \tag{2.1}$$

where

$$I = \frac{2}{9}(n_{tr} - 1)(|2 + n_{tr}| + 3) \cdot \frac{\rho_L U_L^2}{(D/2 - \delta)} \tag{2.2}$$

$$II = (2 + n_{tr})^2 \cdot \frac{16}{18 Re} \cdot \rho_L U_L^2 \tag{2.3}$$

$$III = (n_{tr} - 1)^2 \cdot \frac{\delta}{9(D/2 - \delta)} \cdot \rho_L U_L^2 \tag{2.4}$$

$$\Gamma = \frac{\left(1 + \exp\left[4\pi\delta/(D/2 - \delta)\right]\right)^2}{1 - \exp\left[4\pi\delta/(D/2 - \delta)\right]} + 1 \tag{2.5}$$

---

* Resonance is defined when a component of a travelling pressure distribution is in phase with and of the same wave length as the free surface wave.

$$\delta = 3.425 \times 10^{-5} \; Re^{0.375} \; m \quad \text{(empirically)} \qquad (2.6)$$

$$Re = \frac{4Q_m}{\nu} \qquad (2.7)$$

$$U_L = \frac{g\rho}{4\mu} \cdot \delta^2 \qquad (2.8)$$

Q_m = volume flowrate per unit perimeter

$\tan \varepsilon$ = arbitrary phase factor which has the empirical value

$$\sqrt{\tan \varepsilon} = 0.1636 - 4.95 \times 10^3 \; \nu \qquad \text{(SI Units)} \qquad (2.9)$$

n_{tr} = profile factor at bridging and should be obtained by trial and error.

For small tube diameters Schutt's results showed reasonable agreement with experimental flooding conditions (Figure 2.2); for larger diameters the theory did not agree well with experiment (Figure 2.3). Despite the complicated mathematical derivation, it was not possible to generate a single flooding correlation from this analysis. However, as the first attempt at a very complicated problem, Schutt's work is to be commended.

Cetinbudklar and Jameson (2) attempted to predict the gas velocity at which the wave became unstable by the use of a stability analysis similar to Schutt's. The problem was formulated in conventional terms so that in each phase the disturbance equation reduced to the Orr-Sommerfield equation. They argued that the standing waves in the liquid surface were in fact moving upwards with respect to the gas next to the surface, which meant the velocity of the liquid at the interface.

The analysis used can be summarised as follows. For

the liquid, all distances were made dimensionless with respect to the undisturbed film thickness δ, all velocities with respect to interfacial velocity u_o, and all other variables with suitable combination of those two. The liquid flow was assumed to be laminar with a parabolic velocity distribution. A sinusoidal disturbance of the form

$$\eta = a \exp (i\alpha(x - Ct) \tag{2.10}$$

was applied to the free surface

where

$C = C_r + iC_i$ was a complex wave velocity. Figure 2.4 shows the co-ordinate system used in the analysis.

A steam function of the form

$$\psi = -F(y)\eta \tag{2.11}$$

was introduced and by substituting this into the Navier-Stokes equation, linearisating and eliminating the pressure, the Orr-Sommerfield equation was obtained thus

$$F'''' - 2\alpha^2 F'' + \alpha^4 F = i\alpha Re \left[(U - C)(F'' - \alpha^2 F) - U'' F \right] \tag{2.12}$$

where

$$Re = \frac{U_o \delta}{\nu} \quad , \quad U_o = \frac{g\delta^2}{2\nu}$$

The boundary conditions were

1) at the wall (y = -1)

$$F(-1) = F'(-1) = 0 \tag{2.13}$$

2) at the interface (y=0)

$$F'(0) = C - U_o \tag{2.14}$$

$$F''(0) = T_s - \alpha^2 (C - U_o) - U_o'' \tag{2.15}$$

(Tangential Stress Continuity)

$$(c-U_0)F'(0) - \frac{i}{\alpha Re}\left(F''(0)-3\alpha^2F'(0)\right) = \alpha^2 W_e - \alpha\frac{P_s}{Re} \quad (2.16)$$

(Normal Stress Continuity)

where

$$We = \frac{\sigma}{\rho_l U_0 \delta}$$

T_s and P_s = dimensionless stresses to be determined from the gas phase.

By arguing that the stability of the film was largely dependent on the conditions near the interface where U' was zero, then $U = U_0$ = constant and U" = 2 and equation (2.12) reduced to a fourth order ordinary differential equation with constant coefficients and solution:

$$F = C_1 \sin\beta_1 y + C_2\cos\beta_1 y + C_3\sin\beta_2 y + C_4\cos\beta_2 y \quad (2.17)$$

where

$$\beta_{1,2} = -\alpha^2 - \frac{i}{2}\alpha Re\,(U_0 - C) \pm \left[2i\alpha Re + \left(\frac{i\alpha Re}{2}(U_0 - C)\right)^2\right]^{1/2} \quad (2.18)$$

$C_{1,2,3,4}$ = constants

The gas was regarded as being in quasi-laminar flow over the liquid and was subjected to small perturbation represented by(2.10) at the gas-liquid interface.

The turbulent fluctuations in the gas were ignored and a mean velocity profile was assumed. The solution of the Orr-Summerfield was assumed to be (ϕ + f) where

$\phi(y)$ is the inviscid solution

$f(y)$ is the viscous solution

The real and imaginary parts of P_s and T_s were calculated as

$$P_{sr} = (1 + 0.644\ K\sqrt{3})\ A_2 \tag{2.19}$$

$$P_{si} = -0.644\ K\ A_2 \tag{2.20}$$

$$T_{sr} = 0.686\ A_1^{2/3}\ (1 + 1.288\ K\sqrt{3}) \tag{2.21}$$

$$T_{si} = 0.686\ A_1^{2/3}\ A_2\ (\sqrt{3} + 1.288\ K) \tag{2.22}$$

where

$$A_1 = \alpha \nu_g / V_\star$$

$$A_2 = \frac{2\alpha^2 V_\star^2 (\rho_g/\rho_L \cdot g)\ I}{1 + 1.288\ K\ (\sqrt{3} + 1.288\ K)}$$

$$K = A_1^{4/3} \alpha\ I$$

$$I = \int_0^\infty V^{+2} \exp(-\alpha y)\, dy$$

V^+ = dimensionless gas velocity $= \dfrac{V}{V_\infty \sqrt{C_f}} = \dfrac{V}{V_\star}$

V_∞ = free stream gas velocity

C_f = friction coefficient

When the solution for F was substituted into the four linear homogenous boundary conditions, a non-trivial solution for the constants C_1, C_2, C_3 and C_4 existed only if the determinant for the coefficients vanished. The two resulting equations were solved for C_i and $V_\star$ given α and Re and with C_r set equal to U_o.

Figure 2.5 illustrates the variation of the wave growth rate (αC_i) with the gas friction velocity $V_\star$ for an air-water system. It was found that each curve passed through a minimum $V_\star$ and it was this value which was taken to be the flooding velocity. Figure 2.6 shows comparison between this theory and the experimental data of Clift et al (3). As can be seen, the agreement is good.

Again the analysis failed to generate a single flooding equation. Also, the results required the assumption of an interfacial friction coefficient and a gas velocity distribution and these are subject to question.

2.1.1.2 Standing Wave Models

Shearer and Davidson (4) produced a theory which assumed that, at the limiting gas flow, a standing wave formed on the liquid surface, with an amplitude several times the mean film thickness. They studied the flow patterns on both the gas and the liquid sides.

On the gas side, the following assumptions were made:

i) The gas flow breaks away from the liquid surface on the leeward side of the wave and hence the gas pressure in this region must be constant.

ii) The shear stress exerted on the liquid surface by the gas can be neglected.

iii) For the variation of gas pressure over the windward surface of the wave, the empirical expression

$$(p - p_g)/\rho_g U_g^2 = (\pi\delta/2\ell)(1 + \pi\delta/4\ell) \qquad (2.23)$$

can be used, where

p = pressure far up wind from the wave

p_g = pressure at any point on its windward surface

δ = film thickness = $\left[\frac{3\mu Q_m}{\rho g}\right]^{1/3}$

ℓ = length from the crest to the trough

U_g = velocity of the gas stream

The co-ordinate system and the wave profile considered are shown in Figure 2.7.

For the liquid side the following assumptions were made :

i) Within the liquid film in the region λ in Figure 2.7, viscous and inertia forces were ignored.

ii) Below the crest, viscous and inertia forces must be included.

iii) Velocity distribution is parabolic.

The resulting differential equation became

$$\sigma \frac{d^3\delta}{dx^3} + \frac{\pi \rho_g U_g}{2\ell}\left(1 + \frac{\pi\delta}{2\ell}\right)\cdot\frac{d\delta}{dx} + \rho_L g + \frac{6}{5}\cdot\frac{\rho_L Q^2}{\delta^3}\cdot\frac{d\delta}{dx} - \frac{3\mu Q}{\delta^3}L = 0 \qquad (2.24)$$

with boundary conditions at $x = 0$

$$\delta = a + \delta_o \qquad \frac{d\delta}{dx} = 0$$

and $$\left(\frac{d^2\delta}{dx^2}\right)_{x=0} = -\left[\frac{3}{2}\, a \cdot (\rho_L g/\sigma)^2\right]^{1/3}$$

(pressure continuity)

where

a = wave amplitude

Q_L = total volume flowrate in the liquid film

From the theory, the authors derived three dimensionless groups, namely,

Weber number, $We_g = (\rho_g U_g^2 \delta_o / \sigma)$

Reynolds number, $Re_L = (4 \rho_L Q_m / \mu_L)$

$Z = [\sigma (\rho_L / \mu_L g)^{1/3} / \mu_L]$

Figure 2.8 shows these dimensionless groups and the comparison with experiments.

The Shearer and Davidson work suggested that a relationship may exist between flooding and standing waves on the interface. An interesting feature of this model was that stability was determined solely as a balance between pressures, viscosity appearing only as a means of determining the undisturbed film thickness and velocity.

However, the agreement between the theory and experiment was not very good and the authors attributed this to the entry conditions, the circularity effect in small tubes and turbulence in the liquid film.

Ueda and Suzuki (5) argued that at bridging, part of the liquid was continuously torn off from the crest of a large amplitude wave and broke up into droplets. Figure 2.9 illustrates a liquid lump of single large amplitude wave formed on the steady liquid film. In this

analysis the following assumptions were made:

i) The location of liquid lump is fixed in space

ii) The shear stress on the gas-liquid interface and the shroud surface are negligible except for those stresses on the liquid lump.

iii) Both gravity force and compressibility of the gas phase were negligible.

From the force balances in the horizontal and vertical directions, the gas velocity U_g and the wave height, Δh, at the onset of flooding was deduced as

$$\left(\frac{\rho_g}{\rho_L} \cdot \frac{U_g^2}{2g}\right)\left(\frac{\rho_g}{\sigma} \cdot \frac{U_g^2}{2}\right)\left(\frac{A_{gl}}{A_{go}}\right)\left[\left(\frac{A_{gl}}{A_{go}}\right)^2 - 1\right] = \eta_c \qquad (2.25)$$

and

$$\pi(D_i + 2\delta)\Delta h = A_{gl} - A_{go} \qquad (2.26)$$

The broken lines in Figure 2.10 show the limit relationship calculated by (2.25) for air-water annuli of shroud diameter D_0, in which the profile factor and the mean film thickness were assumed to be $\eta_c = 1.5$ and $\delta = 0.4$mm respectively.

General Comments on Wave Stability Analysis

1. Some of these theories involve very complicated and lengthy mathematical computations and with empirical factors incorporated, having no theoretical basis. Examples of this are the profile factor n_{tr} and the the phase factor ε introduced by Schutt, the pressure distribution over the windward surface of the wave adopted by Shearer and Davidson, the interfacial friction coefficient introduced by Cetinbudakler and Jameson and the introduction of a

profile factor by Ueda and Suzuki.

2. Despite the lengthy mathematics involved, this type of analysis failed to produce a single flooding equation, and this does not make life easy for the design engineer.

3. All of these theories are based on the presumption that once the growth of waves is initiated, the process will continue until bridging occurs. This presumption must be rejected where flooding takes place in large tubes, or indeed in PWR systems, simply from a consideration of the amount of liquid necessary to fill the tube compared to the small amount of liquid flowing in the film.

2.1.2 Film Flow Models

This model suggests that flooding is caused by a sudden increase in interfacial shear stress due to a wave action which takes place at, or near, the flooding condition. Two similar analyses were proposed, one by Solov'ev et al (43) and the other by Dukler et al (6).

In this model, the liquid is assumed to be Newtonian, steady, laminar and one dimensional, and the interface smooth. This is equivalent to the assumption that the effect of the wave motion on the velocity in the film averages out over the time and position as if the film remained smooth. Thus the Navier-Stokes equation can be approximated to

$$-\frac{\Delta p}{\ell} + \rho_L g = \mu_L \frac{d^2u}{dy^2} \qquad (2.27)$$

Solov'ev et al (43) integrated equation (2.27) and presented the solution in dimensionless form

$$\left(\frac{\rho_L g D^3}{64 \mu_L Q_m}\right) \cdot \left(\frac{X^2}{2} - \frac{X^3}{3}\right) = \frac{(1 - Z)^2}{Z^3} \qquad (2.28 - a)$$

where

$$X = \begin{cases} 1 - \dfrac{\tau_w}{\tau_i} & \text{at } \left(\dfrac{du}{dy}\right)_o < 0 \\ 1 & \text{at } \left(\dfrac{du}{dy}\right)_o = 0 \\ 1 + \dfrac{\tau_w}{\tau_i} & \text{at } \left(\dfrac{du}{dy}\right)_o > 0 \end{cases}$$

$$Z = \frac{\Delta p}{\rho_L g \ell}$$

ℓ = Length of the tube

τ_w = Wall shear stress

τ_i = Interfacial shear stress

The authors argued that the minimum pressure drop corresponded to zero wall shear stress, thus

$$Z_{min} \simeq 4 \sqrt[3]{\frac{6 \mu_L Q_m}{\rho_L g D^3}}$$

Usually $Z \ll 1$, thus equation (2.28 - a) can be written as

$$\bar{Z} = \pm (3X^2 - 2X^3)^{-1/3} \qquad (2.28 - b)$$

where $\bar{Z} = Z/Z_{min}$ and with the plus sign corresponding to cocurrent flow and the minus sign to countercurrent flow.

Equation (2.28 - b) shows that $\bar{Z}$ is a function only of X and does not depend on the physical properites of the liquid or the dimensions of the tube, which implies that equation (2.28 - b) is general. The relationship between X and the dimensionless gas velocity $\bar{U}_q$ was found experimentally to be

$$X = \bar{U}_g^{-2}$$

where

$$U = U_g/U_{min}$$

U_g = gas velocity

U_{min} = gas velocity corresponding to the minimum pressure drop

Thus equation (2.28 - b) can be written as

$$\bar{Z} = \pm \frac{\bar{U}_g^{\,2}}{(3\bar{U}_g - 2)^{1/3}} \qquad (2.28 - c)$$

This is a useful relationship for practical application, however, the main problem concerning flooding (namely the relationship between flooding velocity U_{min}, liquid properties and geometry) is still unknown.

Dukler et al (6) suggested that in most practical cases, the pressure gradient is negligible compared with the term $\rho_L g$, thus when equation (2.27) is integrated with boundary conditions,

$$u = 0 \qquad \text{at } y = 0 \quad \text{(at the wall)}$$

$$\frac{du}{dy} = \frac{\tau_i}{\mu_L} \qquad \text{at } y = \delta \quad \text{(at the interface)}$$

to give the general velocity distribution, u, which is then, in turn integrated over the film thickness δ, it gives

$$R_N^3 - 0.75 \sqrt[3]{4}\, FR_N^2 - 1 = 0 \qquad (2.30)$$

where

R_N = Dimensionless film thickness = $\frac{\delta}{\delta_N}$

δ = Film thickness

δ_N = Nusselt film thickness = $(3Q_m \mu_L / \rho_L g)^{1/3}$

F = Dimensionless shear stress = $\tau_i \,/\, \sqrt[3]{0.5}\, \delta_N \rho_L g$

The solution to equation (2.30) is shown in Figure 2.11. The curve N - 0 is the solution in the case of uniform downflow ($0 \leq F \leq 1$, $u \geq 0$, $Q_L = Q_F$, where Q_F is the feed flowrate). Curve 0 - B is the solution for downflow with circulation in the case of equal amounts of circulating liquid passing up and down ($F \geq 1$, $u \gtrless 0$, $Q_L = Q_F$). Curve D - U - C is the solution in the case of upflow ($F \geq \sqrt[3]{4}$, $u \gtrless 0$, $Q_L = -Q_F$).

Dukler et al did not present any experimental data to support their theoretical work reviewed above.

Furthermore, the information on interfacial shear stress (and hence F) is very limited, a factor which undermines the practical use of their model.

2.1.3 Hanging Film Models

Grolmes et al (7) argued that, below the flooding velocity, the gas has some effect on the waviness of the liquid flow, but does not appreciably affect the velocity profile in the liquid film.

They assumed the liquid to be one dimensional, Newtonian and laminar, and under these conditions the equation for the falling liquid film became

$$\mu_L \frac{d^2 u_L}{dy^2} + \rho_L g = 0 \qquad (2.31)$$

with boundary conditions

$$u_L = 0 \quad \text{at} \quad y = 0 \quad \text{(at the wall)}$$

$$\mu_L \frac{du_L}{dy} = \tau_i \quad \text{at} \quad y = \delta \quad \text{(at the interface)}$$

The interfacial shear stress, τ_i was taken as

$$\tau_i = \frac{1}{2} \rho_g U_g^2 f_{2\phi} \qquad (2.32)$$

where

$f_{2\phi}$ = interfacial friction factor at flooding conditions

Flooding was assumed to take place when the mean film velocity was equal to zero with the critical gas velocity being deduced as

$$U_g = \frac{2}{\sqrt{3}} \cdot \left[\frac{\rho_L}{\rho_g} \cdot \frac{g\delta}{f_{2\phi}} \right]^{\frac{1}{2}} \qquad (2.33)$$

where

$$\delta = \left(\frac{3 \mu_L Q_m}{\rho_L g} \right)^{1/3} \qquad (2.34)$$

Equation (2.33) could thus be used as a relation for flooding velocity provided a satisfactory correlation can be found for $f_{2\phi}$. The authors approached the problem by looking for a correlation between the interface friction factor at the onset of flooding and the liquid film thickness. Their own data and the data of Tobilevich (8) with fluids of higher liquid viscosity were used to establish such a correlation. Figure 2.12 shows the results of this correlation which is expressed as

$$f_{2\phi} = 0.006 + \frac{200\,\delta^{2}}{\left[\frac{\mu}{\mu_R}\right]^{0.44}} \quad (\delta \text{ in cm}) \qquad (2.35)$$

where μ_R = reference viscosity = 1 cp

Figure 2.13 shows a comparison between the flooding velocity predicted using equations (2.33) and (2.35), and experimental data. The limit of applicability of this analysis was recommended to be

$$\delta_{min} = 1.72 \left[\frac{\sigma}{\rho}\right]^{1/5} \left[\frac{\nu}{g}\right]^{2/5} \left[y(\Theta)\right]^{1/5} \qquad (2.36)$$

where δ = film thickness (cm)

μ = viscosity (g/cm.sec)

ρ = density (g/cm^3)

ν = kinematic viscosity (cm^2/sec)

σ = surface tension (dyne/cm)

g = acceleration of gravity (980 cm/sec^2)

$y(\Theta)$ = function of contact angle ~ 1/3 for water on glass

The introduction of the interfacial friction factor, $f_{2\phi}$, is useful from a practical point of view, even if insufficient information about it exists. It is likely that more experiments need to be carried out to confirm its dependence on the different variables. Also, the assumption of the Nusselt film thickness is open to question.

Wallis and Kuo (9) tackled the problem in terms of separated flow as indicated in Figure 2.14, where gas of density ρ_g flows over liquid of density ρ_L. At $x = +\infty$ the gas velocity is uniform and equal to U_g in the negative x direction. The gas flow is considered to be inviscid and irrotational and the liquid is considered stationary.

By considering Bernoulli's equation for the gas and liquid phases, and the interface boundary condition of pressure continuity, these authors obtained the relation:

$$\frac{1}{2}\cdot\frac{\rho_g U_g^2}{\sqrt{\Delta\rho g\sigma}}\left[\left(\frac{d\phi^*}{dx^*}\right)^2+\left(\frac{d\phi^*}{dy^*}\right)^2\right]+\frac{\frac{d^2x^*}{dy^{*2}}}{\left[1+\left(\frac{dx^*}{dy^*}\right)^2\right]^{3/2}}+\frac{\left|\frac{dx^*}{dy^*}\right|}{r^*\left[1+\left(\frac{dx^*}{dy^*}\right)^2\right]^{1/2}}-(x_o^*-x^*)=C \tag{2.37}$$

where C = constant

$$x^* = x\sqrt{\frac{\Delta\rho g}{\sigma}}$$

$$y^* = y\sqrt{\frac{\Delta\rho g}{\sigma}}$$

$$r^* = r\sqrt{\frac{\Delta\rho g}{\sigma}}$$

$$\phi^* = \frac{\phi}{U_g} \sqrt{\frac{\Delta \rho g}{\sigma}}$$

with boundary conditions,

$$\frac{d\phi^*}{dx^*} = 1 \quad , \quad \frac{d\phi^*}{dy^*} = 0 \quad \text{at } x^* = \infty$$

$$\frac{dx^*}{dy^*} = \text{Cot } \beta \quad , \quad r^* = r_o^* \quad \text{at } x^* = x_o^*$$

where β is the contact angle.

A key dimensionless group which emerged from (2.37) was the Kutateladze number, K_g, defined as

$$K_g = \rho_g^{\frac{1}{2}} U_g \left(\Delta \rho g \sigma \right)^{-\frac{1}{4}} \tag{2.38}$$

A dimensionless diameter was introduced as

$$D^* = 2r_o^* = D \cdot \sqrt{\frac{\Delta \rho g}{\sigma}} \tag{2.39}$$

Equation (2.37) indicates various limiting behaviours and these cases were examined by Wallis et al.

Case (1) : Large D*. Kg = 0 $\quad \frac{dx^*}{dr^*} \to 0 \quad$ as $r^* \to \infty$

This corresponded to the case of an extensive sheet of liquid with an interface shape which is uniform in the third dimension, a problem which was solved by Bankoff (10) resulting in

$$y^* = \ln \left[\sqrt{\left(\frac{4}{x^{*2}} - 1 \right)} + \frac{2}{x^*} \right] - 2\sqrt{\left(1 - \frac{x^{*2}}{4} \right)} \tag{2.40}$$

Case (2) : Finite D*, Kg = 0

Equation(2.37) was solved numerically for $U_g = 0$, $\frac{dx^*}{dr^*} \to 0$ as $r^* \to \infty$ and Figure 2.15 shows different solutions which were generated by varying the initial surface slope at large r*. These results describe the spreading of the liquid film over the mouth of a sharp edged hole in a horizontal surface.

Case (3) : Large D*, $Kg \neq 0$, $\beta = 90^\circ$

With the assumption of a small curvature for large D*, the Kutateladze number could also be defined from equation (2.37) as

$$K_g^2 = 2\left(x_o^* + \sin^3\beta \left(\frac{d^2x^*}{dy^{*2}}\right)_{x_o^*} - x^* - \frac{\frac{d^2x^*}{dy^{*2}}}{\left[1 + \left(\frac{dx^*}{dy^*}\right)^2\right]^{3/2}} \right) \left|\frac{dW^*}{dz^*}\right|^2 \qquad (2.41)$$

where W^* = dimensionless complex velocity potential

$$= \frac{W}{U_g}\left(\frac{\Delta\rho g}{\sigma}\right)^{\frac{1}{2}} \qquad (2.42)$$

$$Z^* = Z \cdot \left(\frac{\Delta\rho g}{\sigma}\right)^{\frac{1}{2}} \qquad (2.43)$$

$$z = x + iy \qquad (2.44)$$

A successful choice of an approximate shape of the interface was obtained from the flow around a pair of sources located at $(0, \pm a)$ with strength A, transverse to a uniform flow (Figure 2.16).

The method of solution adopted was to solve for the interface and velocity obtained from the potential

flow theory outlined above and to calculate the curvature terms in equation (2.41) numerically for constant K_g ($\pm$ 10% of mean value). The maximum value of K_g was found to be 1.87, well below the known experimental value of 3.2.

The assumption used in deriving this theory, namely frictionless gas and liquid, seems to be an over simplification of a complicated problem.

2.1.4. The Annular Flow Models

Kutateladze (11) proposed a model having a liquid with a vanishingly small viscosity, thus eliminating its consideration from the problems of the laminar or turbulent nature of the motion and to concentrate attention on the structural changes caused by the presence of the interfaces.

In this very simple statement of the problem, the stability of the stream structure as a whole was determined by the stability of the elements of the phases comprising it, e.g., droplets, bubbles and films. The factors which disturbed these elements were the dynamic heads of the phases in contact with them, whereas a stabilizing factor was the surface tension. Kutateladze proposed the following group as a measure of the ratio of these forces,

$$K_g^2 = \frac{\rho_g U_g^2 \delta}{\sigma} \qquad (2.45)$$

where $\rho_g U_g^2$ was the dynamic head of the gas and δ a characteristic dimension of the liquid.

In formations which arose freely, i.e., when it could be assumed that

$$\delta \sim \sqrt{\frac{\sigma}{g(\rho_f - \rho_g)}} \tag{2.46}$$

the stability criterion defined by equation (2.45) assumed the form

$$K_g = \frac{U_g \rho_g^{1/2}}{\sqrt[4]{g\,(\rho_f - \rho_g)}} \tag{2.47}$$

This factor K_g (known as the Kutateladze Number) has been used by a number of investigators to correlate data.

Experimentally, K_g was found to be 3.2 for the complete bypass of the liquid film.

Wallis (12, 13, 14) considered the separate cylinders model shown in Figure 2.17 and applied a force balance to each "cylinder" with a mixing length theory to obtain the following two equations

$$j_g^* = \frac{r_o}{7\ell_g} \Delta P^{*1/2} \alpha^{7/4} \tag{2.48}$$

$$j_f^* \cong \frac{r_o}{7\ell_f} (1 - \Delta P^*)^{1/2} (1 - \alpha)^{7/4} \tag{2.49}$$

where $$\Delta P^* = -\frac{\left[\frac{dP}{dZ} + \rho_g g\right]}{g\,(\rho_f - \rho_g)} \tag{2.50}$$

$$j_g^* = j_g \left[\frac{\rho_g}{gD\,(\rho_f - \rho_g)}\right]^{1/2} \tag{2.51}-a$$

$$j_f^* = j_f \left[\frac{\rho_f}{gD(\rho_f - \rho_g)}\right]^{1/2} \tag{2.51}-b$$

r_o = tube radius

α = void fraction

ℓ_f, ℓ_g = mixing length of liquid and gas respectively

j_f, j_g = superficial velocity of liquid and gas respectively

Wallis considered two cases for scaling the mixing length. In the first case it was scaled using the dimensions of each cylinder; in the second it was scaled by the overall pipe diameter.

Eliminating the pressure drop between equations (2.48) and (2.49) and using the appropriate relation for the mixing length, then

$$\frac{j_g^{*2}}{\alpha^n} + \frac{j_f^{*2}}{(1-\alpha)^n} = 1 \qquad (2.52)$$

Differentiating (2.52) with respect to α and eliminating α between the resulting equation and (2.52) gave

$$j_g^{*2/(n+1)} + j_f^{*2/(n+1)} = 1 \qquad (2.53)$$

Usually n had the value 3.5 or 2.5 depending on the relationship used to determine the mixing length. If an intermediate value of 3 is taken, equation (2.53) yields to the well known Wallis correlation

$$j_g^{*\frac{1}{2}} + j_f^{*\frac{1}{2}} = 1 \qquad (2.54)$$

or in a more general form

$$j_g^{*\frac{1}{2}} + m j_f^{*\frac{1}{2}} = C \qquad (2.55)$$

The use of average velocities, instead of the local velocities used in the wave stability analysis, simplifies application to design. Indeed, much of the experimental work reported in the literature has been correlated on the basis of equation (2.55).

It should be noted that the parameter j_g^* and the Kutateladze number, K_g, can be related if the diameter, D, in equation (2.51) is replaced by δ, defined by equation (2.46).

Wallis and Makkenchery (15) argued that the Kutateladze number was the correct criterion in large pipes if the liquid film remained thin. In this case the perturbation in the gas flow around the film was confined to a boundary layer and was substantially independent of tube diameter. In very small tubes, on the other hand, surface tension forces could act to pull the liquid film into a bridge across the gas core and, for a finite surface contact angle, the liquid film could be held up against gravity, even with no gas flow at all. The criterion for this condition could be expressed in terms of the Bond number,

$$D^* = D\left[g(\rho_f - \rho_g)/\sigma\right]^{\frac{1}{2}} \qquad (2.56)$$

It should be noted that equations (2.47), (2.51) and (2.56) are related through the equation

$$j_g^* = Kg/\sqrt{D^*} \qquad (2.57)$$

The experimental work of Wallis and Makkenchery suggested that a constant value of j_g^* gave a reasonable fit to the data in the intermediate region. In very small tubes ($D^* \leq 2$) the critical velocity tended to zero.

Imura et al (16) considered the system shown in Figure 2.18, where both the gas and liquid were assumed to be inviscid fluids with regard to stability of the liquid film. The governing equations for both phases in the flow were the Laplace equation for velocity potential

$$\frac{\partial^2 \Phi}{\partial x^2} + \frac{1}{r}\frac{\partial}{\partial r}\left(r\frac{\partial \Phi}{\partial r}\right) = 0 \qquad (2.58)$$

and the Bernoulli equation

$$\frac{P}{\rho} = \frac{\partial \Phi}{\partial t} - \frac{1}{2}\left[\left(\frac{\partial \Phi}{\partial x}\right)^2 + \left(\frac{\partial \Phi}{\partial y}\right)^2\right] - gx + \text{const.} \qquad (2.59)$$

The boundary conditions were

$$\underline{\text{at } r = R}: \quad \frac{\partial \Phi_l}{\partial r} = 0 \quad \text{(at the tube surface)}$$

$$\underline{\text{at } r = 0}: \quad \frac{\partial \Phi_g}{\partial r} = 0$$

$$\underline{\text{at } r = (R - \delta)}: \quad -\frac{\partial \Phi_i}{\partial r} = \frac{\partial \eta}{\partial t} + U_i \cdot \frac{\partial \eta}{\partial x}$$

(at the interface)

$$\text{and} \quad P_l - P_g = \sigma\left[\frac{\partial^2 \eta}{\partial x^2} \Big/ \left[1 + \left(\frac{\partial \eta}{\partial x}\right)^2\right]^{3/2} - \frac{1}{R - \delta - \eta}\right] \qquad (2.60)$$

The wave at time t was assumed to have the following sinusoidal form

$$\eta = \eta_o(t) \sin \alpha(x-ct) \tag{2.61}$$

Equation (2.58) was integrated over both liquid and gas phases with the appropriate boundary conditions and the resulting ϕ_g and ϕ_L values substituted into equation (2.59). With approximations and manipulations the following equation was obtained:

$$U_g + U_L = \left[\frac{\sigma}{\rho_g} \left(\alpha - \frac{1}{R - \delta} \right) \right]^{\frac{1}{2}} \tag{2.62}$$

where U_g = gas velocity

U_L = liquid velocity

σ = surface tension

α = wave number

R = radius of the tube

δ = film thickness

The following empirical relation between the wave length and the liquid film thickness , was assumed

$$\lambda = \xi' \delta \tag{2.63}$$

thus

$$\alpha = \frac{2\pi}{\lambda} = \frac{2\pi}{\xi' \delta} = \frac{\xi}{\delta} \tag{2.64}$$

where

ξ', ξ = dimensionless quantities

Equation (2.62) could be expanded in the dimensionless form

$$\frac{G}{L}\left(1 + \frac{L}{G}\frac{\rho_g}{\rho_L}\frac{S_g}{S_L}\right) = \frac{S_g}{S}\frac{1}{L}\left(\frac{\rho_g \sigma}{\delta}\right)^{1/2}$$

$$\times \left(\xi - \frac{1}{R/\delta - 1}\right)^{1/2} \qquad (2.65)$$

where G = superficial mass velocity of gas

L = superficial mass velocity of liquid

S = cross-sectional area of the tube

S_g = cross-sectional area occupied by gas

The following empirical expression was obtained as the best equation for correlating the data

$$\xi = 0.046 \left(\frac{d^2 \rho_L g}{\sigma}\right)^{0.5} \times \left(\frac{\mu_L}{\mu_g}\right)^{0.12} \qquad (2.66)$$

Figure 2.19 shows the comparison between experimental data and equations (2.65) and (2.66).

Chung (17) neglected the tube curvature effect and represented the flow as a two-dimensional plane shown in Figure 2.20. The counter-current flow was approximated as the immiscible, inviscid streams flowing counter current to each other in an infinitely long channel. By arguing that, in a vertical falling film, gravity was largely balanced by the viscous force, and by applying the small perturbation method, the author reduced the perturbed Bernoulli equation to

$$\frac{P'_L}{\rho_L} = -\frac{\partial \phi'_L}{\partial t} + \bar{v}_L \cdot \frac{\partial \phi'_L}{\partial y} \qquad (2.67)$$

$$\frac{P'_g}{\rho_g} = \frac{\partial \phi'_g}{\partial t} + \bar{V}_g \cdot \frac{\partial \phi'_g}{\partial y} \qquad (2.68)$$

and the Laplace equation to

$$\frac{\partial^2 \phi'_L}{\partial x^2} + \frac{\partial^2 \phi'_L}{\partial y^2} = 0 \qquad (2.69)$$

$$\frac{\partial^2 \phi'_g}{\partial x^2} + \frac{\partial^2 \phi'_g}{\partial y^2} = 0 \qquad (2.70)$$

with boundary conditions

$$\frac{\partial \phi'_L}{\partial x} = 0 \qquad \text{at } x = -h \qquad \text{(at the wall)}$$

$$\frac{\partial \phi'_g}{\partial x} = 0 \qquad \text{at } x = H-h \qquad \text{(at the centre line)}$$

$$\frac{\partial \eta}{\partial t} - \bar{V}_L \frac{\partial \eta}{\partial y} = \left.\frac{\partial \phi'_L}{\partial x}\right|_{\eta = x}$$

(at the interface)

$$\frac{\partial \eta}{\partial t} - \bar{V}_g \frac{\partial \eta}{\partial y} = \left.\frac{\partial \phi'_g}{\partial x}\right|_{\eta = x}$$

and

$$P'_L - P'_g = -\sigma \cdot \frac{\partial^2 \eta}{\partial y^2} + g(\rho_L - \rho_g)\eta$$

(interfacial pressure) (2.71)

where (') and (-) denote the perturbation and time averaged components respectively and

$$\eta = \eta_o \sin\left[\frac{2\pi}{\lambda} \cdot (y - ct)\right] \tag{2.72}$$

Assuming the perturbation ϕ could be expressed as

$$\phi_i = X_i(x) \cdot \cos\left[\frac{2\pi}{\lambda}(y - ct)\right] \quad , \quad i = L, g \tag{2.73}$$

the perturbation terms were found to be:

$$\phi_L = -\eta_o(c+\bar{V}_L) \frac{\cosh\left[\frac{2\pi}{\lambda}(x+h)\right]}{\sinh\left[\frac{2\pi}{\lambda}(h+\eta)\right]} \cos\left[\frac{2\pi}{\lambda}(y-ct)\right] \tag{2.74}$$

and

$$\phi_g = -\eta_o(C-\bar{V}_g) \frac{\cosh\left[\frac{2\pi}{\lambda}(x+h-H)\right]}{\sinh\left[\frac{2\pi}{\lambda}(H-h-\eta)\right]} \cos\left[\frac{2\pi}{\lambda}(y-ct)\right] \tag{2.75}$$

Substituting (2.74) and (2.75) into (2.71) yielded the characteristic equation:

$$\rho_g \coth\left[\frac{2\pi}{\lambda}(H-h-\eta)\right](C-\bar{V}_g)^2 + \rho_L \coth\left[\frac{2\pi}{\lambda}(h+\eta)\right](c+\bar{V}_L)^2 = \frac{\lambda}{2\pi} g \cdot (\rho_L - \rho_g) + \frac{2\pi\sigma}{\lambda} \tag{2.76}$$

Due to the algebraic complexity of the hyperbolic cotangent function, equation (2.76) would not yield a general explicit criterion, so the author proposed the following approximation:

$$\coth\left[\frac{2\pi}{\lambda}(h+\eta)\right] \sim C_1 \frac{\frac{\lambda}{2\pi}}{h+\eta} \tag{2.77}$$

$$\coth\left[\frac{2\pi}{\lambda}(H-h-\eta)\right] \sim C_1 \frac{\frac{\lambda}{2\pi}}{H-h-\eta} \tag{2.78}$$

where C_1 was a constant chosen to best fit the hyperbolic cotangent terms with their approximate expressions. Substituting equations (2.77) and (2.78) into equation (2.76) gave

$$\rho_g \frac{H}{H-h-\eta} (C-\bar{V}_g)^2 + \rho_L \frac{H}{H+\eta} (C+\bar{V}_L)^2 = \frac{1}{C_1}\left[Hg(\rho_L - \rho_g) + (\frac{2\pi}{\lambda})^2 H\sigma\right] \quad (2.79)$$

By arguing that the travelling dynamic waves of longitudinal type were a special case of kinematic waves, the wave velocity for one dimensional flow systems was expressed as

$$C = \bar{V} + K(\frac{\partial V}{\partial K}) \quad (2.80)$$

where $\bar{V}$ was the mean velocity, K the local depth of the fluid, and V the velocity at any axial location of the channel. With some manipulation, equation (2.80) was used to reduce equation (2.79) to:

$$\frac{\rho_g j_g}{\alpha^3} + \frac{\rho_L j_L}{(1-\alpha)^3} = \frac{1}{C_1}\left[Hg(\rho_L - \rho_g) + (\frac{2\pi}{\lambda})^2 H\sigma\right] \quad (2.81)$$

Considering the stability and flow limitation, the envelope for equation (2.81) was obtained and eliminated from the resulting equation and equation (2.81) to give:

$$\left[\rho_g^{\frac{1}{2}} j_g\right]^{\frac{1}{2}} + \left[\rho_L^{\frac{1}{2}} j_L\right]^{\frac{1}{2}} = \frac{1}{C_1}\left[2Hg(\rho_L - \rho_g)\right]^{\frac{1}{4}} \quad (2.82)$$

or in terms of the Kutateladze number:

$$K_g^{\frac{1}{2}} + K_L^{\frac{1}{2}} = C_K \quad (2.83)$$

where C_K was a constant.

In a real situation, inlet disturbances do exist and cause additional heat loss. The efficiency of these inlet disturbances on flooding could only be taken into account through some semi-empirical modification of equation (2.83) to give

$$K_g^{\frac{1}{2}} + mK_L^{\frac{1}{2}} = C_K \qquad (2.84)$$

where m and C_K were constants determined experimentally. The constant C_K depended on the actual disturbances. Since the amount of disturbance was influenced by the inlet circumference then C_K was a function of the inlet circumference, or, in the case of a round tube, the tube diameter.

The author proposed the expression

$$C_K = C_2 \tanh\left[C_3 D^{*\frac{1}{4}}\right] \qquad (2.85)$$

where C_2 and C_3 were experimental constants and D* the Bond number.

Tien et al (18) correlated their experiments with the equation:

$$K_g^{\frac{1}{2}} + mK_L^{\frac{1}{2}} = C_2 \tanh\left[C_3 D^{*\frac{1}{4}}\right] \qquad (2.86)$$

and Figure 2.21 shows the experimental data for the case of nozzle air supply with sharp edge inlet. The data were correlated successfully by the equation

$$K_g^{\frac{1}{2}} + 0.8K_L^{\frac{1}{2}} = 2.1 \tanh\left[0.8D^{*\frac{1}{4}}\right] \qquad (2.87)$$

The significance of equation (2.83) is that it shows clearly that flooding results from interfacial instability and flow limitation and that flooding

correlations of the Wallis-Kutateladze type, as given in equations (2.55) and (2.84), have their origin in the force balance across the interface.

2.1.5 Entrainment Model

This model was presented by Dukler and Smith (19) in 1977. Their measurements demonstrated that the onset of flooding was associated with the onset of entrainment and that wave closure and blocking did not occur. The model considered a balance between the gravity and drag forces acting on a drop of liquid suspended in a gas stream which could be expressed as

$$\frac{1}{2}C_d\left(\frac{\pi}{4}d^2\right)\cdot\rho_g V_g^2 = \left(\frac{\pi}{6}d^3\right)g\left(\rho_L-\rho_g\right) \qquad (2.88)$$

where d = droplet diameter

C_d = drag coefficient around the drip

Hinze (20) showed that the average drop size could be determined by

$$d = \frac{\sigma We}{\rho_g V_g^2} \qquad (2.89)$$

Combining equations (2.88) and (2.89) gave

$$V_g = \left[\frac{4We}{3C_d}\right]^{\frac{1}{4}}\frac{\left[\sigma g\left(\rho_L-\rho_g\right)\right]^{\frac{1}{4}}}{\rho_g^{\frac{1}{2}}} \qquad (2.90)$$

At the very low liquid upward flowrates at which entrainment was initiated, $V_g \simeq j_g$, which reduced (2.90) to

$$K_g = \left[\frac{4We}{3C_d}\right]^{\frac{1}{4}} \qquad (2.91)$$

The critical Weber number took the value of 12 for drops which were suddenly accelerated, such as drops torn

off a slow moving liquid surface; in the turbulent regime, the drag coefficient for spheres had a constant value of 0.44.

Substituting in equation (2.91) with the values of We and C_d of 12 and 0.44 respectively gave

$$K_g = 2.46 \qquad (2.92)$$

This value of the Kutateladze number is less than the reported experimental value of 3.2. The theory reviewed above, whilst not substantiated by the experimental data of the authors themselves, nevertheless could be useful for large diameter tubes, with the same limitation as the Kutateladze model.

Figure 2.22 shows the Dukler data plotted on the basis of the Wallis correlation. The good agreement between the data and the Wallis correlation was attributed by the authors to the fact that the tube size was not very different from the size used by Wallis.

Comments on Parametric Dependence

The parametric dependence of the flooding correlations discussed in section 2.1 is not well established, and an examination of some geometric and fluid properties is made below.

i) The tube entry geometry seems to have a definite effect on flooding. the flooding velocity decreases with the less smooth entry geometries. The work of Chung (17) and Tien et al (18) indicated that gas entry conditions also affect the flooding characteristics.

ii) The effect of viscosity and the liquid film thickness are not clear. Some investigators (13,17) indicated that in general, viscosity has a destabilising effect, while others (2,5) indicated the opposite effect. The interrelationship between the hydraulic diameter and the film thickness makes it very difficult to isolate the effect of the latter.

iii) Surface tension may be important to the flooding characterisation as was shown in some of the work reviewed above (17, 2, 11).

iv) Tube diameter and tube length effects are not yet clear. Some experimental work (2,4,11,17) showed no explicit diameter dependence, whereas the analysis by Imura et al (16) and Wallis and Kue (9) indicated the opposite.

2.2 THEORETICAL ANALYSIS ON THE EFFECT OF CONDENSATION

During the postulated loss of coolant accident, condensation plays an important role and can change considerably the characteristics of flooding. Hence it is important to include the effects of condensation in the flooding correlations. Most of the effort to improve the existing models has been directed towards empirical work without much understanding of the flooding-condensation mechanism. However, some analytical work has been reported lately, aimed at solving this problem.

The most obvious effect of condensation is to reduce the amount of vapour available for hold-up. Hence, it is reasonable to consider the phenomenon of flooding with

heat and mass transfer as a superposition of two events:

i) Condensation under non-equilibrium conditions

ii) Counter-Current Flow Limitation (CCFL)

Tien(21) proposed that the reduction in steam flow should be calculated on the basis that the condensation enthalpy change was balanced by the sensible heat required to raise the temperature of the subcooled water to the saturation temperature. The effective vapour flow, based on the Kutateladze number K_{ge} was given by

$$K_{ge} = K_g - K_{ne}\, J_a \cdot \left(\frac{\rho_L}{\rho_g}\right)^{\frac{1}{2}} \cdot K_L \qquad (2.93)$$

where K_{ne} was an empirical constant to account for non-equilibrium effects and J_a the Jacob number defined as

$$J_a = \frac{C_p \cdot \Delta T_{sub}}{h_{fg}}$$

Substituting K_{ge} from equation (2.93) for K_g in equation (2.83) gave the subcooled CCFL correlation:

$$\left[K_g - K_{ne}\, J_a \left(\frac{\rho_L}{\rho_g}\right)^{\frac{1}{2}} K_L\right]^{\frac{1}{2}} + K_L^{\frac{1}{2}} = C_K \qquad (2.94)$$

or

$$\left[K_g - \phi K_L\right]^{\frac{1}{2}} + K_L^{\frac{1}{2}} = C_K \qquad (2.95)$$

where

$$\phi = K_{ne}\, J_a \left(\frac{\rho_L}{\rho_g}\right)^{\frac{1}{2}}$$

Figure 2.23 illustrates the CCFL correlation at different values of ϕ. Also shown on this figure are the following limited relations:

i) The ordinary CCFL correlation as given by (2.83) which represents the limiting case of $\Delta T_{sub} = 0$ and small K_L.

ii) $K_g = \phi K_L$ (2.96)

which describes the limit at large K_l (i.e., $K_{ge} = 0$)

No experimental data were provided by the author to substantiate the model, nevertheless it does seem logical and the general trend of the subcooled flooding curves calculated from equation (2.95) have the same shape as those reported in the experimental literature reviewed in section 2.3. The above model would be very useful if reliable information about K_{ne} could be obtained.

Liu et al (22) tried to obtain a physical understanding of the non-equilibrium factor K_{ne} by considering the arrangement shown in Figure 2.24. Here the falling liquid film was assumed to be turbulent, the temperature of the falling liquid, T, was assumed to be uniform across the film and only changing in flow direction. The steam was assumed to be saturated and free of non-condensable gases. The shear stress at the vapour liquid interface was neglected and the physical properties of the fluid were constant and uniform.

Tha mass balance for the differential section δx yielded:

$$\frac{dM_s}{dx} = \frac{dM_L}{dx} \qquad (2.97)$$

and the heat transfer rate across the interface

$$\frac{dM_s}{dx} \cdot \delta x \cdot h_{fg} = h \cdot (T_{sat} - T) \cdot \delta x \qquad (2.98)$$

where h was an interfacial heat transfer coefficient per unit length. The energy balance for the same differential section could also be written as

$$\frac{d}{dx}(M_L C_p T)\, \delta x = h_g \frac{dM_s}{dx} \cdot \delta x \qquad (2.99)$$

Solving equations (2.97), (2.98), and (2.99) with some approximation yielded the following expressions for the condensed steam flowrate

$$M_{s_c} = M_{L_i} J_a \left[1 - \exp\left(\frac{-hL}{C_p M_{L_i}}\right)\right] \qquad (2.100)$$

which could be expressed in a dimensionless form compatible with equation (2.93)

$$K_{g_c} = K_L \cdot J_a \cdot \left(\frac{\rho_L}{\rho_g}\right)^{\frac{1}{2}} K_{ne} \qquad (2.101)$$

where $$K_{ne} = \left[1 - \exp\left(\frac{-hL}{C_p M_{L_i}}\right)\right] \qquad (2.102)$$

The authors calculated the average heat transfer coefficient by comparing the steam-water and air-water data obtained in the BCL 1/15 scale glass vessel

facility. The average heat transfer coefficient was correlated using Akers and Rosson (23) expression given by

$$N_u = 0.145\ Pr_L^{1/3}\ Re_q^{0.8} \qquad (2.103)$$

where Re_q is a two-phase equivalent Reynolds number given by

$$Re_q = Re_v\left(\frac{\mu_v}{\mu_L}\right)\left(\frac{\rho_L}{\rho_v}\right)^{\frac{1}{2}} + Re_L \qquad (2.104)$$

Figure 2.25 shows a comparison between experimental and calculated Nusselt numbers.

The authors attributed the non-equilibrium condensation to:

i) conduction-controlled heat transfer at the interface.

ii) condensation induced pressure oscillation

iii) the finite contact time (finite condensation length)

The heat transfer across the interface was due to bubble collapse at the interface which could be treated as an instantaneous heat source at the interface. The temperature at the interface was very high, thus preventing other bubbles collapsing in the short time period until the temperature of the interface was lowered by conduction heat transfer. Pressure oscillations could result in intermittent heat transfer due to the variation in water subcooling.

The work of Liu et al (21) was a step in the right direction, however it is necessary to discuss and

question some of the assumptions and correlations presented in this model. The assumption of a heat transfer coefficient per unit length is unusual and not very meaningful, hence equation (2.98) should perhaps have been written as

$$\frac{dM_s}{dx}\ \delta x\ h_{fg} \quad = \quad hB\ (T_{sat} - T)\ \delta x \qquad (2.98)\text{-a}$$

where B is the width of the falling liquid film. Also, correlating the heat transfer coefficient with an equivalent Reynolds number, which depends on the steam Reynolds number, contradicts the assumption of a constant interfacial heat transfer coefficient, since the local steam Reynolds number varies considerably with x. Another argument against this type of correlation is that conduction controlled condensation is governed mainly by the falling liquid film, thus it might be expected that the interfacial heat transfer coefficient would be a function of the liquid subcooling (or Jacob number) since this will influence the heat conduction. Indeed a close examination of Figure 2.25 reveals a dependence on subcooling in the data. Finally, the assumption that no heat is transferred from/to the walls to/from the liquid film is probably not true since in the experimental work, no precautions were taken to prevent wall-film heat transfer. In the actual PWR, the falling water film will certainly be heated by the hot annulus walls and this effect should have been included in the model.

2.3 FLOODING IN PWR GEOMETRIES

The next logical step, after the theoretical and experimental work on circular cross-sections (tubes), is to consider scaled models of different PWR geometries. Because of the difficulty in understanding the actual mechanism of flooding in a simple geometry, most of the work on complex geometries has been experimental, and with the resulting empirical correlations, and this is reviewed below.

Wallis et al (24) investigated the possible flow regimes which could be present in the downcomer of the PWR during the refill period of a postulated loss of coolant accident. The experiments were carried out with water only, i.e., no counter-current gas or vapour was used. The test section was a scaled model of an "unwrapped" downcomer annulus and the principal experimental variables were

i) cold leg diameter

ii) gap spacing

iii) injection water flowrate

Six possible regimes were identified, as follows :

Regime O

Here the inlet water tube did not "run full" and the water either dribbled out of the end or formed a narrow jet which jumped across the gap and flowed as a rivulet down the far wall.

Regime 1

This regime consisted of a water stream which filled the cross-section of the gap. The stream was broadest a little below the injection point and then contracted as it accelerated under the influence of gravity.

Regime 2

In this regime, the upper part of the water jet filled the gap, as in regime 1, but the lower part separated from the near wall and jumped the gap to form a spreading film on the far wall. This film fell under gravity directly below the injection point.

Regime 3

This regime was an outgrowth from Regime 2 as the flowrate was increased. The jet separated completely from the near wall, impinged on the far wall and spread out in all directions. Most of the liquid stream lines eventually terminated in a"hydraulic jump" where they expanded to fill the gap. The film regime was surrounded by a broad band of liquid, filling the gap to form a continuous arch.

Regime 4

This was the limit for Regime 3 in which the band of liquid was thin enough to be considered as a single streamline rather than a two-dimensional continuum flow.

Regime 5

The jet impinged on the far wall and spread out to form an outer band which did not fill the gap but fell partially away from the wall.

All of the above flow regimes are shown in Figure 2.26. The authors proposed an approximate flow regime map to identify the boundaries between the different flow regime and this is shown in Figure 2.27.

This work provides a very good start in the study of modelling the actual PWR situation. A possible extension of this work could be a study of the film thickness which is included in several models (1,2,3,6, 7 and 17), the heat transfer coefficient between the hot walls and the liquid film or the liquid Reynolds number.

Crowley et al (25) studied the intereaction of counter-current steam and water system in a 1/30 linearly scaled "unwrapped" annulus simulating the downcomer of the PWR. This work was orientated towards geometric changes such as baffles and thermal shields.

Tests were conducted both by setting the water flow and increasing steam to the flooding point (water first) and by setting the steam flow and increasing the water flow to the point where flooding ceased (steam first). The steam entering the test section was saturated or slightly superheated at 102-103^{o}C (215-217^{o}F) and three different levels of sub-cooling were used, corresponding to inlet water temperatures of 13, 38 and 60^{o}C (55, 100 and 140^{o}F) respectively. The results were presented in terms of the Wallis parameters defined in equations (2.51)a and (2.51)b with D replaced by the hydraulic diameter D_H.

These authors observed that the transition from total penetration of the water to the lower plenum, to total expulsion of the water out of the break was sharp and well defined. Figure 2.28 shows a typical set of critical conditions (flooding) obtained at different inlet water cubcoolings. A reference line is shown to indicate the locus where the enthalpy of the steam was just enough to raise the water temperature to saturation, i.e., the line of thermodynamic ratio R_T equals unity where

$$R_T = \frac{M_w C_p \Delta T_{sub}}{M_s h_{fg}} \qquad (2.105)$$

Increasing the water subcooling improved the flooding condition from a LOCA point of view, i.e., a larger value of steam flowrate was required to cause flooding at a particular flowrate.

The effect of thermal shield in reducing bypass or changing the locus was found to be negligible, but a baffled system was able to sustain higher steam flows before flooding occurred.

The authors divided the experimental results into three regions, as sketched in Figure 2.29, and these are discussed below.

Region 1

The behaviour in this region essentially followed the Wallis correlation, this being due to the fact that Region 1 lay to the left of the $R_T = 1$ line. Thus it

was not possible for the water to condense all of the steam at these flows. However, since some water was able to penetrate the annulus, it was possible that an amount of steam could be condensed in the lower plenum. Thus the amount of steam required to cause bypass is slightly above that predicted by the Wallis correlation due to lower plenum condensation.

Region 2

In this region, the data lay above the line $R_T = 1$. The difference between the data points and the line $R_T = 1$ was attributed by the authors to the steam which avoided condensation in the lower plenum.

Region 3

In this region the data had the tendency to level off at higher liquid flowrates. No satisfactory explanation was given for this region.

The data show clearly a non-equilibrium condensation superimposed on the hydrodynamic nature of flooding described in section 2.1, and this is most obvious in Region 2. In those early days, the investigators eagerly trying to find an empirical correlation failed to appreciate the presence of non-equilibrium. However, the work reviewed above gave a good experimental and physical description of flooding.

Block and Crowley (26) conducted steam-water experiments in a 1/15 scale planar model of a PWR downcomer, with multiple cold and hot legs, at between 1 and 2 bar (15-30 psia) system pressure. The

principal variables tested were:

i) inlet water temperature (or sub-coolong)

ii) water flowrate

iii) steam flowrate

iv) downcomer gap spacings

The authors found that the data obtained from different downcomer gaps did not overlay when plotted using the Wallis parameters based on the downcomer hydraulic diameter, i.e., the gap size ($D_H = 2S$). Therefore, they concluded that the downcomer gap was not the governing characteristic dimension. The downcomer width (or circumference) was arbitrarily chosen instead. Thus the new dimensionless variables were defined as

$$J_g^* = j_g \left[\frac{\rho_g}{gW(\rho_L - \rho_g)} \right]^{\frac{1}{2}} \qquad (2.106)$$

$$J_L^* = j_L \left[\frac{\rho_L}{gW(\rho_L - \rho_g)} \right]^{\frac{1}{2}} \qquad (2.107)$$

where W was the downcomer width or circumference. Figure 2.30 shows experimental data based on the downcomer width as the characteristic dimension for different gap sizes.

The experimental data also showed that higher values of counter-current steam were required to bypass the ECC water as the water subcooling or flowrate was increased.

Block et al (27) presented a semi-empirical model

for calculating the rate of delivery of water to the lower plenum as a function of time in the presence of steam upflow and superheated downcomer walls. The following assumptions were made:

(i) The walls were planar, thermally thick" and axial conduction could be neglected.

(ii) The walls were initially at uniform temperature, T_w.

(iii) The upward steam flow from the core was constant and the steam was not superheated.

(iv) The heat transfer coefficient was infinite over the wetted portions of the walls and zero elsewhere.

(v) No lower plenum voiding.

(vi) The liquid in the downcomer was well mixed.

The conservation of mass yielded

$$j_g = j_{gW} + j_{gc} - j_{g,cond} \qquad (2.108)$$

where j_g = net volumetric flux of steam upward in the annulus

j_{gW} = the volume flux of wall-generated steam

j_{gc} = the volumetric steam flux from the core

$j_{g,cond}$ = the volume flux of the core steam that condenses on the water in the vessel

The authors chose the Wallis correlation for the bypass condition

$$J^{*\frac{1}{2}}_{g} + m\, J^{*\frac{1}{2}}_{fd} = C \qquad (2.109)$$

where J^{*}_{g} and J^{*}_{fd} were defined by equations (2.106) and (2.107).

The condensation of steam upflow was expressed as

$$J^{*}_{g,cond} = K_{ne} J^{*}_{f,in} \frac{C_p (T_{sat} - T_L)}{h_{fg}} \sqrt{\frac{\rho_L}{\rho_g}} \qquad (2.110)$$

Using equations (2.106), (2.107), (2.108), and (2.110) into (2.109) yielded:

$$\left[J^{*}_{gW} + J^{*}_{gc} - K_{ne} (T_{sat} - T_L) \frac{C_p}{h_{fg}} \sqrt{\frac{\rho_L}{\rho_g}} \cdot J^{*}_{f,in} \right]^{\frac{1}{2}} + m\, J^{*\frac{1}{2}}_{f,d} = C \qquad (2.111)$$

If J^{*}_{gW} was considered negligible, equation (2.111) became

$$\left[J^{*}_{gc} - K_{ne} (T_{sat} - T_L) \frac{C_p}{h_{fg}} \sqrt{\frac{\rho_L}{\rho_g}}\, J^{*}_{f,in} \right]^{\frac{1}{2}} + m J^{*\frac{1}{2}}_{f,d} = C \qquad (2.112)$$

The authors proposed the following correlations for m, c and K_{ne}

$$c = 0.32 \qquad (2.113)$$

$$m = \exp\left[-5.6\, J^{*0.6}_{f,in} \right] \qquad (2.114)$$

$$K_{ne} = \left(\frac{P_{Lp}}{14.7}\right)^{\frac{1}{4}} \times \left(\frac{1}{1 + bJ^*_{f,in}}\right) \qquad (2.115)$$

where P_{Lp} is in psia

b = 16 for flat plate and 30 for cylinder

Figures 2.31 and 2.32 show comparisons between experimental and predicted values of the dimensionless steam flux for the flat plate and cylindrical geometries. The agreement is very good.

The model presented above has been used as a starting point for much theoretical work (21,22).

Crowley et al (28) conducted counter-current flow tests in a 1/30 scale cylindrical vessel at three different injected water temperatures: 100°C, 65°C and 20°C (212°F, 150°F and 70°F). The data exhibited the same general trends as those of Ref. (27).

Figure 2.33 compares calculated values fo K_{ne} as a function of $J^*_{f,in}$ for 1/15 and 1/30- scale data. It is seen that equation (2.115) provides a fairly good fit to the data at both scales.

Figure 2.34 compares values of m as a function of $J^*_{f,in}$ calculated from the 1/30-scale data and the correlation of equation (2.114). The 1/30-scale data shows a reasonable agreement with the correlation.

A scatter plot for the 1/30-scale data is shown in Figure 2.35, which indicates that the "theory" under-predicts the actual penetration curve. A better agreement was obtained using the Kutateladze number

instead of the Wallis parameters. Equations (2.112)-(2.115) were transformed into:

$$\left[K_{gc} - K_{ne}(T_{sat} - T_L)\left(\frac{C_p}{h_{fg}}\right)\left(\frac{\rho_L}{\rho_g}\right)^{\frac{1}{2}} K_{f,in}\right]^{\frac{1}{2}} + mK_{f,d}^{\frac{1}{2}} = C_2 \tag{2.116}$$

$$C_2 = 1.41 \tag{2.117}$$

$$m = \exp\left[-5.6\left(\frac{K_{f,in}}{19.5}\right)^{0.6}\right] \tag{2.118}$$

$$K_{ne} = \left(\frac{P_L P}{14.7}\right)^{\frac{1}{4}} \times \left(\frac{1}{1 + 1.54K_{f,in}}\right) \tag{2.119}$$

Figure 2.36 presents a scatter plot of the 1/30-scale data compared with the correlations of equations (2.116) through (2.119).

The authors could not recommend strongly either J* or K. Their work was considered, however, as a step forward towards a more realistic modelling of flooding with condensation in PWR.

Cudnik et al (29) of BCL presented experimental studies of ECC penetration behaviour in a 1/15-scale model of a four-loop pressurised water reactor. Data correlation efforts focussed on obtaining a correlation of the 1/15-scale, steel vessel penetration data. The correlation form proposed by BCL was

$$\left[j_g^* - K_{ne}\lambda j_{wi}^*\right]^{\frac{1}{2}} + m\left[F\, j_{wi}^*\right]^{\frac{1}{2}} = \left[K_g / \sqrt{D^*}\right]^{\frac{1}{2}} \qquad (2.120)$$

where $F = \left(j_{w_{LP}}^* / j_{w_i}^*\right)$

$$\lambda = J_a\left[\frac{\rho_L}{\rho_g}\right]^{\frac{1}{2}}$$

K_g = Kutateladze number = 3.2

A linear regression analysis was utilized to find the values of K_{ne} and m which minimised the sum of the squares of the differences between the measured and calculated values of $\left[j_g^* \sqrt{D^*}\right]$. Comparisons of the observed error trends with those obtained using constants for the empirical factors m and K_{ne} suggested that using (2.114) and (2.115) in (2.120) provided a better correlation of the data, probably due to subcooling and j_{wi}^* effects being better represented. Thus the BCL correlation defined by equation (2.120) was modified to:

$$\left[j_g^* - f.K_{ne}\lambda j_{wi}^*\right]^{\frac{1}{2}} + m.m_f\left[F j_{wi}^*\right]^{\frac{1}{2}} = \left[K_g/\sqrt{D^*}\right]^{\frac{1}{2}} \qquad (2.121)$$

where m and K_{ne} are given by equations (2.114) and (2.115) respectively and

$f = 0.90$

$m_f = 2.1252$

The differences between the BCL and the Creare correlations included

(i) The BCL correlation used j*s, based on the

downcomer gap width, whereas the Creare correlation used J^*_s, based on the downcomer circumference.

(ii) The BCL correlation used values for the f and m_f factors of 0.9 and 2.1252 respectively, whereas the Creare correlation used unity coefficients.

(iii) The right hand side of BCL correlation was given by $[K_g/\sqrt{D^*}]^{\frac{1}{2}}$ which was a very weak function of pressure; the right hand side of the Creare correlation was constant.

Figure 2.37 shows a comparison between BCL and Creare correlations. It is clear from the figure that the BCL correlation consistently predicts a steeper penetration curve than is predicted by the Creare correlation, although the deviation is not great.

The above work did not present any physical understanding of ECC penetration. Also, it was not clear why the authors based their correlation on the downcomer gap size, contrary to the findings of Creare that the gap size was not the characteristic dimension for flooding.

Rothe and Crowley (30) focussed their attention on a single ECC injection rate (J^*_{wi} = 0.116) in order to emphasise the effects of pressure and sub-cooling. The Creare correlation defined by equation (2.112) was modified as follows:

i) the coefficient C was taken to be 0.4 instead of 0.32.

ii) the pressure effect was eliminated in K_{ne}. For $J^*_{wi} = 0.116$, K_{ne} was found to be 0.16.

iii) the slope m was considered to be

a) a constant for saturated water and steam as well as for air and water

b) adequately represented by a function of thermodynamic ratio for sub-cooled water. This is shown graphically in Figure 2.38.

In fitting the data, the following approach was followed:

1. The coefficient C was given by $J^{*½}_{gb}$ where J^*_{gb} was the complete bypass point for saturated water.
2. The condensation coefficient was determined from the complete bypass points for water with various sub-coolings.
3. The slope coefficient m was determined from the entire data base with C and K_{ne} fixed.

This approach reflected the view that the complete bypass points were relatively stable operating points and that the partial delivery range was dynamically unstable.

Figure 2.39 shows a comparison of the new Creare correlation with data at various sub-coolings. The agreement is good, but again it is purely experimental without any theoretical justification or physical understanding of non-equilibrium condensation. This work, however, re-affirmed that correcting the supplied

steam flux J_g^* for condensation effect to an "effective" steam flux is an appropriate way to correlate data.

Alb and Chambré (31) applied dimensional analysis to the partial penetration of ECC water in a PWR downcomer annulus and this gave rise to the following functional relation:

$$Fr_g = \phi\left(Fr_{wi},\ F,\ \frac{\rho_L}{\rho_g},\ \frac{S}{W},\ \frac{L}{W},\ \left[\frac{\nu_L^2/g}{W^3}\right]^{1/3},\ J_a,\ E_{vo},\right.$$

$$\left.Pr_L,\ \frac{K.\Delta T_{sub}}{\rho_L(g^3W^5)^{1/2}},\ \frac{\nu_L}{\nu_g},\ \frac{\Delta\rho}{\rho_L}\right) \qquad (2.122)$$

A comparison of the dimensions of the various scale models, presented in Table 2.1, showed that most models tested were not geometrically similar to each other. The authors argued that this could be the reason for the different experimental results obtained in the various experimental models. The 1/15 and 2/15-scale models of BCL were found to be geometrically similar. The penetration data from these two models were correlated to give:

$$Fr_g = 0.011253\ (1+F)^{-0.7206}\ J_a^{0.6169}\ Fr_{wi}^{0.3104}\ \left(\frac{\rho_L}{\rho_g}\right)^{0.2366} \qquad (2.123)$$

The authors did not recommend equation (2.123) to be used to predict the penetration data obtained on non-geometrically scaled models. The Froude number correlation given by equation (2.123) was compared with

TABLE 2.1★

COMPARISON OF SCALED VESSEL DIMENSIONS

Dimension	Creare, scale			Battelle, scale			
	1/30	1/15	1/15	1/15 [a]	1/15	1/15 [b]	2/15 [b]
Cold leg inside diameter, $D_{CL} = D_{BR}$	1.0	2.0	1.875	2.0	2.1	2.1	4.02
Hot leg simulator diameter, D_{HL}	1.5	3.0	3.0	2.5	[c]	[c]	7.84
Gap size, S	0.267	0.625	0.5	0.6	0.6	0.6	1.23
Upper annulus height, L_1	3.0	6.0	6.0	4.37	4.37	4.37	8.74
Downcomer length, L_2	9.0	18.0	19.0	16.13	16.13	16.13	32.26
Lower plenum depth, L_3	24.0	24.0	30.0	14.5	14.5	14.5	29.11
Vessel inner diameter, D_I	6.14	12.0	11.5	12.1	12.1	12.1	24.35
Core barrel outer diameter, D_O	5.6 5.13	10.73	10.5 9.5	10.9	10.9	10.9	21.89
Average annulus circumference, W	18.4 17.7	35.6	34.6 33.0	36.1	36.1	36.1	72.63
Steam distributor	no	no	no	yes	yes	yes	yes
Intact cold legs	3	3	3	3	3	3	3
Hot legs	4	4	4	4	4	2	2

a) Transparent vessel model.
b) 60–120 injection geometry configuration, all other geometries use a 90–90 injection geometry configuration.
c) Geometric dimension not available to us, as of this writing.

★ From Alb and Chambré (31)

the modified Wallis correlation given by equations (2.112) to (2.115) by testing both against the BCL experimental data. The comparisons are shown in Figures 2.40 and 2.41 respectively.

It is clear from these Figures that the Froude number correlation is better than the modified Wallis correlation in predicting the BCL data. However, equation (2.123) is no more "universal" than the modified Wallis correlation; the proper scaling parameters are still far from clear. On the other hand, it is easier to understand the logic behind the modified Wallis correlation thatn equation (2.123).

Richter and Murphy (32) presented the results of experiments performed in an annulus, approximately 2/15 scale of a reactor vessel, at Dartmouth College. In order to study the influence of asymmetry of liquid and gas flow in the annulus on the flooding behaviour, the experiments were performed with symmetrical top flooding, non-symmetrical top flooding and side injection of water.

The authors found that asymmetrical introduction of water into the test section leads to higher water penetration rates for the same gas flowrates. In addition, zero penetration occurs at higher gas flow-rates than for symmetrical top flooding. The work of Richter and Murphy (32) supported the conclusion of Rothe and Crowley (30), that the zero penetration in all scales tested so far can be described approximately

by a constant dimensionless gas flux J_g^* = 0.16. The data obtained for non-symmetrical top flooding and the resulting correlation is shown in Figure 2.42.

In a recent "state of the art" by Richter and Wallis (33), a comparison between the experimental results of Creare, BCL and Dartmouth for different scales has been presented. These are shown in Figures 2.43-2.46.

Richter and Wallis (33) speculated that for saturated water and steam (or air-water) a flooding correlation of the following type would be valid at all scales:

$$J_g^{*1/2} + 0.8\, J_L^{*1/2} = 0.4 \qquad (2.124)$$

where the slope m = 0.8 is a rough approximation from Figure 2.47.

A theoretical attempt to solve the obvious contradiction between the Wallis correlation (2.55) and the Kutateladze prediction for zero penetration has been provided by Richter (34). He considered the arrangement shown in Figure 2.48. The penetration of liquid in a pipe (or annulus) was assumed to occur in the form of a thin wavy film flowing along the walls which was the predominant flow observed in the experiments.

Considering the force balance on the total cross section (Control Volume I) yielded:

$$-\frac{dP}{dz}\frac{\pi D^2}{4} + \tau_w \pi D = \left[\rho_L(1-\alpha) + \rho_g \alpha\right] g \frac{\pi D^2}{4} \qquad (2.125)$$

where α is the void fraction of the gas and τ_w is the wall shear stress. For the Control Volume II, which included the gas phase only,

$$-\frac{dP}{dz}\left(\frac{\pi D^2}{4}\alpha\right) - \tau_i \pi D \sqrt{\alpha} = \rho_g g \left(\frac{\pi D^2}{4}\alpha\right) \qquad (2.126)$$

where τ_i is the interfacial shear stress. Eliminating the pressure drop from (2.125) and (2.126) gave

$$\frac{4\tau_w}{D} + \frac{4\tau_i}{D\sqrt{\alpha}} = (\rho_L - \rho_g)\, g\, (1 - \alpha) \qquad (2.127)$$

With manipulation and approximation, the following correlation was developed for large diameter tubes and very thin films.

$$\frac{C_w}{4} N_B^3 j_g^{*6} j_L^{*2} + C_w N_B j_g^{*4} + 150\, C_w j_g^{*2} = 1 \qquad (2.128)$$

where N_B = Bond number $= D^2\left[\frac{g(\rho_L - \rho_g)}{\sigma}\right]$ (2.129)

and C_w = wall friction factor = 0.008 experimentally

Applying the same approach to the annulus led to

$$C_w N_B'^3 J_g^{*6} S^{*2} J_L^{*2} + C_w N_B' J_g^{*4} + 150\, C_w \frac{J_g^{*2}}{S^*} = 1 \qquad (2.130)$$

where $N_B' = W^2\left[\frac{g(\rho_L - \rho_g)}{\sigma}\right]$ (2.131)

and $S^* = \frac{S}{W}$ (2.132)

The first term in (2.130) represents the pressure drop due to wall friction; the second term is the presure drop due to friction at the interface if the surface is smooth. Finally, the third term describes the pressure drop due to the wavy interface.

For zero penetration, i.e., $J_L^* = 0$, equation (2.130) becomes:

$$J_g^{*2} = \frac{75}{N_B' S^*} \left[1 - \left(1 + \frac{N_B' S^{*2}}{75^2 C_w} \right)^{\frac{1}{2}} \right] \qquad (2.133)$$

Two extremes were examined:

i) $\frac{N_B' S^{*2}}{75 C_w} \ll 1$ (valid for small models)

$$\text{i.e., } \left(1 + \frac{N_B' S^{*2}}{75^2 C_w} \right)^{\frac{1}{2}} \simeq 1 + \frac{1}{2} \frac{N_B' S^{*2}}{75^2 C_w} \qquad (2.134)$$

If the full scale reactor gap width was 0.25m and circumference 14.4m, equations (2.133) and (2.134) would give:

$$J_g^{*\frac{1}{2}} = 0.41 \qquad (2.135)$$

which is in good agreement with the result of Rothe and Crowley (30).

ii) $\left(\frac{N_B' S^{*2}}{75 C_w} \right) \gg 1$ (valid for large models)

$$\text{i.e.} \quad \therefore \left[1 - \left(1 + \frac{N_B'^{\,} S^{*2}}{75^2 C_w}\right)^{\frac{1}{2}}\right] \simeq \left(\frac{N_B'^{\,} S^{*2}}{75^2 C_w}\right)^{\frac{1}{2}} \qquad (2.136)$$

Introducing this into equation (2.133) gave:

$$K_g = J_g^* \cdot N_B'^{*\frac{1}{4}} = \left(\frac{1}{C_w}\right)^{\frac{1}{4}} = 3.3 \qquad (2.137)$$

which is very close to the experimental value of 3.2.

The result in equation (2.137) is very interesting. The Kutateladze number contains gas inertia, buoyancy and surface tension terms, but this shows that it is equivalent to the fourth root of the inverse of the wall friction factor. The correlation presented in equation (2.130) gives the Wallis solution for small scales and the Kutateladze solution for large scales. Figure 2.49 shows a comparison between experimental data and equation (2.130). The agreement is good. It should be noted, however, that the assumption of a uniformly distributed film along the wall might be questionable if, during partial delivery, water penetrated the annulus on one side while steam escaped on the other.

2.4 PREVIOUS WORK AT STRATHCLYDE

The University of Strathclyde has been engaged for a number of years in a research programme covering different aspects of problems associated with the safety of PWR's. The research programme is supported by

H.M. Nuclear Installation Inspectorate, a branch of the Health and Safety Executive of the U.K. Government. The present review will be limited to the work relating to the refill problem during LOCA.

Campbell (35) carried out an experimental and theoretical programme on a 1/10-scale model of PWR downcomer annulus which involved three different test sections, namely Phase 1, Phase 2 and Phase 3 test sections. The Phase 1 test section had a rectangular cross section with a gap size of 25.4mm, a test section width of 69mm and tangential entry coolant ducts which had a rectangular cross section 76mm x 25.4mm. The Phase 2 test section was similar to that of Phase 1 except that the coolant entry ducts were half pipes, 76mm diameter, normal to the plane of test section. Phase 3 was a cylindrical type test section with a gap size of 25.4mm and core diameter of 406mm. All three test sections and adjacent pipe work were manufactured from transparent polycarbonate to allow visual and photographical studies. A layout of the test rig and instrumentation, and diagrammatic arrangements of the test sections, are shown in Figures 2.50 and 2.51.

The working fluids were steam and water, at pressures around atmospheric, with a range of subcooled conditions at coolant entry. The test facility allowed heating of the back plate (or core) to a temperature which was kept constant during each test, thus allowing the effect of hot walls on bypass to be identified. A

summary of Campbell's test programme is shown in Table 2.2.

The data was presented in terms of j* parameters defined by equations (2.51)-a and (2.51)-b which are reproduced below for convenience.

$$j_s^* = j_s \left[\frac{\rho_s}{gD_H(\rho_w - \rho_s)}\right]^{\frac{1}{2}} \qquad (2.51)\text{-a}$$

$$j_w^* = j_w \left[\frac{\rho_w}{gD_H(\rho_w - \rho_s)}\right]^{\frac{1}{2}} \qquad (2.51)\text{-b}$$

where D_H = hydraulic diameter $\simeq 2S$

Figure 2.52 shows the effect of geometry on the end of bypass conditions. The effect of inlet subcooling is shown in Figure 2.53 and the effect of wall temperature is shown in Figure 2.54.

The transition between the start of bypass and complete bypass did not exist. The data exhibited an on/off behaviour, i.e., either all the inlet water penetrated to the lower plenum or none reached the lower plenum. It was also clear from the data that, increasing the inlet subcooling or decreasing the wall temperature, increased the amount of steam required to cause ECC bypass. Non-equilibrium conditions were noticed, but due to a lack of base line data (i.e., no data at zero subcooling), it was not possible to isolate the non-equilibrium factor observed by other investigators.

Simpson et al (36) made use of the experimental observation in the water first Phase 1 tests that the

TABLE 2.2 SUMMARY OF CAMPBELL'S PROGRAMME

	Phase 1 Tests	Phase 2 Tests	Phase 3 Tests
Geometry	Planar	Planar	Cylindrical
Coolant Entry	Tangential	Normal	Normal
Scale	1/10	1/10	1/10
Injection Modes	Water first Steam first	Water first Steam first	Water first Steam first
Range of Water Flowrate	0.0 -0.005m^3/s	0.0-0.005m^3/s	0.0-0.007m^3/s
Range of Steam Flowrate	0.0-0.75m^3/s	0.0-0.75m^3/s	0.0-0.9m^3/s
Pressure in Test Section	1.15 bar	1.15 bar	1.15 bar
Downcomer Wall Temperature i) Water First ii) Steam First	 20,75,125^oc 20,50,100,150^oc	 20,75,125^oc 20,50,100,150^oc	 20,120^oc 20,120^oc
Inlet Water Subcooling (Steam Temp-Water Temp)	90,65,50,30K	90,65,50,30K	80,55,40,20K
Steam Temperature	110^oc	110^oc	100^oc

water flowing into the downcomer was supported by the uprising steam and argued that bridging occurred when the steam input was just sufficient for the water bridge to reach the centre of the outlet hole.

The arrangement considered is shown in Figure 2.55. The equations of motion for an element of water jet, of length δs at the point (x,z) with u and w the velocity components in the x and z directions respectively, were found to be

$$\frac{du}{dt} = -\frac{\Delta p}{\rho_w H_w} \cdot \frac{w}{(u^2 + w^2)^{\frac{1}{2}}} \qquad (2.138)$$

and

$$\frac{dw}{dt} = -\frac{\Delta p}{\rho_w H_w} \cdot \frac{u}{(u^2 + w^2)^{\frac{1}{2}}} \qquad (2.139)$$

From continuity

$$H_w \bar{V} = H_{wi} u_i \qquad (2.140)$$

where $\bar{V} = (u^2 + w^2)^{\frac{1}{2}}$ was the absolute velocity of the element at position (x,z), Δp the pressure difference caused by the rising steam across the element of local thickness H_w and density ρ_w, and the subscript "i" referred to the inlet pipe where the flow was assumed to be horizontal.

The integral equations for the water trajectories were obtained by solving equations (2.138) to (2.140), to give:

For $Z \leqslant Z_T$

$$X = \int_0^Z \frac{dZ}{\left[\frac{1 - Z}{\left(1 - \int_0^Z \Delta P.dZ\right)} - 1\right]^{\frac{1}{2}}} \qquad (2.141)\text{-a}$$

and for $Z > Z_T$

$$X = \int_0^{Z_T} \frac{dZ}{\left[\frac{1 - Z}{\left(1 - \int_0^Z \Delta P.dZ\right)} - 1\right]^{\frac{1}{2}}} - \int_{Z_T}^Z \frac{dZ}{\left[\frac{1 - Z}{\left(1 - \int_0^Z \Delta P.dZ\right)} - 1\right]^{\frac{1}{2}}} \qquad (2.141)\text{-b}$$

where $X = \frac{2g}{u_i^2}.x$, $Z = \frac{2g}{u_i^2}.z$, and $\Delta P = \frac{\Delta p}{2g\,\rho_w H_{Wi}}$

and Z_T = value of Z at the top of the trajectory

The pressure difference across the jet was evaluated by approximating the steam flow to the pattern shown in Figure 2.56-a. The criterion for bridging was considered to be that the water jets should just reach the entry to the outlet pipe (i.e., $Z = 0$ when $X = \frac{W}{2}$) giving

$$\frac{W}{2} = \frac{20}{3} \frac{(2\,\Delta P_m - 1)^{\frac{1}{2}}}{\Delta P_m (1 - \Delta P_m)} \qquad (2.142)$$

and

$$\frac{W}{2} = 2^{2/3} \cdot (J_w^* \cdot F_{rwi})^{-2/3} \qquad (2.143)$$

and

$$\Delta P_m = \frac{2^{2/3}}{16} (J_s^* \cdot Fr_{wi}^{\frac{1}{2}})^2 \cdot (J_w^* \cdot Fr_{wi})^{-2/3} \left(\frac{B}{d_o}\right) \qquad (2.144)$$

where

$$\frac{W}{2} = \frac{gB}{u_i^2}$$

$$J_x^* = j_x \left[\frac{\rho_x}{gB\,(\rho_w - \rho_s)} \right]^{\frac{1}{2}} \qquad (x = w,s)$$

$$Fr_{wi} = \frac{u_i^2}{gH_{wi}}$$

B = Breadth of test section

d_o = Outer hole diameter

ΔP_m = Maximum value of ΔP

Equations (2.142), (2.143 and (2.144) yielded a unique plot of $J_s^* (Fr_{wi})^{\frac{1}{2}}$ versus $J_w^* (Fr_{wi})$, which could be drawn as shown in Figure 2.57. The theory presented above was not compared with any experimental data and its validity was doubtful pending experimental work with saturated water and steam (or air and water).

2.5 SUMMARY AND CONCLUSION

(i) Most of the theoretical approaches to flooding have been carried out with reference to vertical tubes. Different mechanisms have been proposed which do not include the effect of heat or mass transfer. These mechanisms were grouped in the present review into the following categories:

(a) Wave Stability Analysis (1,2,4,5)

(b) Film Flow Model (6)

(c) Hanging Film Models (7.9)

(d) Annular Flow Models (11,12,13,14,15,16,17,18)

(e) Entrainment Model (19)

(ii) Only the annular flow models have prospects of success due to their simplicity and possible back-up by experimental data. It should be remembered, however, that all of the experimental work was carried out in small tubes and required extrapolation to very large tubes or PWR geometries can be dangerous.

(iii) The most popular correlating parameters are those presented by Wallis and Kutateladze defined as

$$J_x^* = j_x \left[\frac{\rho_x}{gD\,(\rho_L - \rho_g)} \right]^{\frac{1}{2}}$$

and

$$K_x = j_x \left[\frac{\rho_x}{g\sigma\sqrt{(\rho_L - \rho_g)}} \right]^{\frac{1}{2}}$$

where x refers to either liquid or gas phase and D is a length dimension which was taken at the beginning as the tube diameter and was replaced later by the tube circumference.

(iv) Both of the above parameters are interdependent because J^* will reduce to K if the length dimension D takes the value of

$$D = \left[\frac{\sigma}{g\,(\rho_L - \rho_g)} \right]^{\frac{1}{2}}$$

(v) The two parameters differed in their prediction of the point of complete bypass. The experimental work of Wallis and Makkenchery (15) showed that K_g is the proper parameter in large tubes and J_g^* is better in small tubes. This has been supported lately by theoretical work by Richter (34).

(vi) Different linear scaled PWR models have been used in the experimental work with the data generally being correlated successfully using

$$J_g^{*\frac{1}{2}} + mJ_L^{*\frac{1}{2}} = C_1$$

or

$$K_g^{\frac{1}{2}} + mK_L^{\frac{1}{2}} = C_2$$

(vii) The gap size (or hydraulic diameter) seems not to be the proper scaling parameter in J^*. Instead, Wallis proposed the mean circumference, but without any theoretical justifications.

(viii) When subcooled water and steam were used in the flooding experiments, the behaviour was very different from that observed in air-water experiments. This was due to condensation which was found to have a stabilising effect on flooding.

(ix) A modified Wallis correlation was proposed to account for the effect of condensation under non-equilibrium conditions in the following form :

$$\left[J_s^* - K_{ne} J_a \left(\frac{\rho_L}{\rho_s} \right)^{\frac{1}{2}} J_{wi}^* \right]^{\frac{1}{2}} + m J_{W_{LP}}^{*\frac{1}{2}} = C$$

(x) Different values for K_{ne}, m and C have been proposed in the literature, but no theoretical justification has been given. The latest experimental work suggests that $C = 0.4$ and this has been supported by Richter (34) in theoretical work. The non-equilibrium factor takes many forms without any physical understanding of the factors affecting non-equilibrium such as geometry, flow patterns, energy transfer, dwell time, wall temperature etc.

(xi) Strathclyde proposed a model which gave some theoretical justification for the use of Wallis parameters but this has not been verified by experimental work.

(xii) The present work acknowledges the contributions made by previous investigators and intends to provide another step in the right direction by addressing the problem of non-equilibrium. It will also test the validity of the different correlations and theories presented in the literature in addition to making a fresh investigation into some of the problems related to a LOCA, such as the choking of the gas phase.

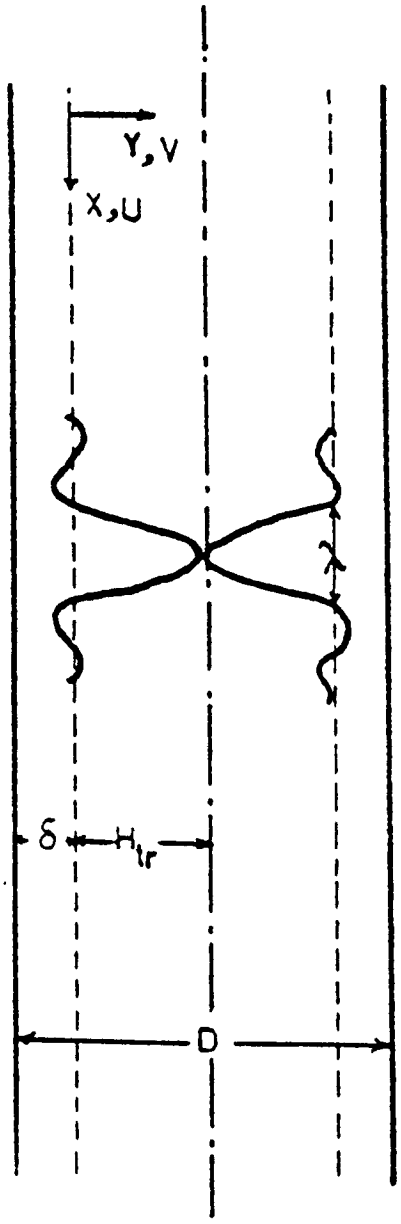

Fig 2.1 SCHEMATIC REPRSENTATION OF BRIDGING [from ref.(1)]

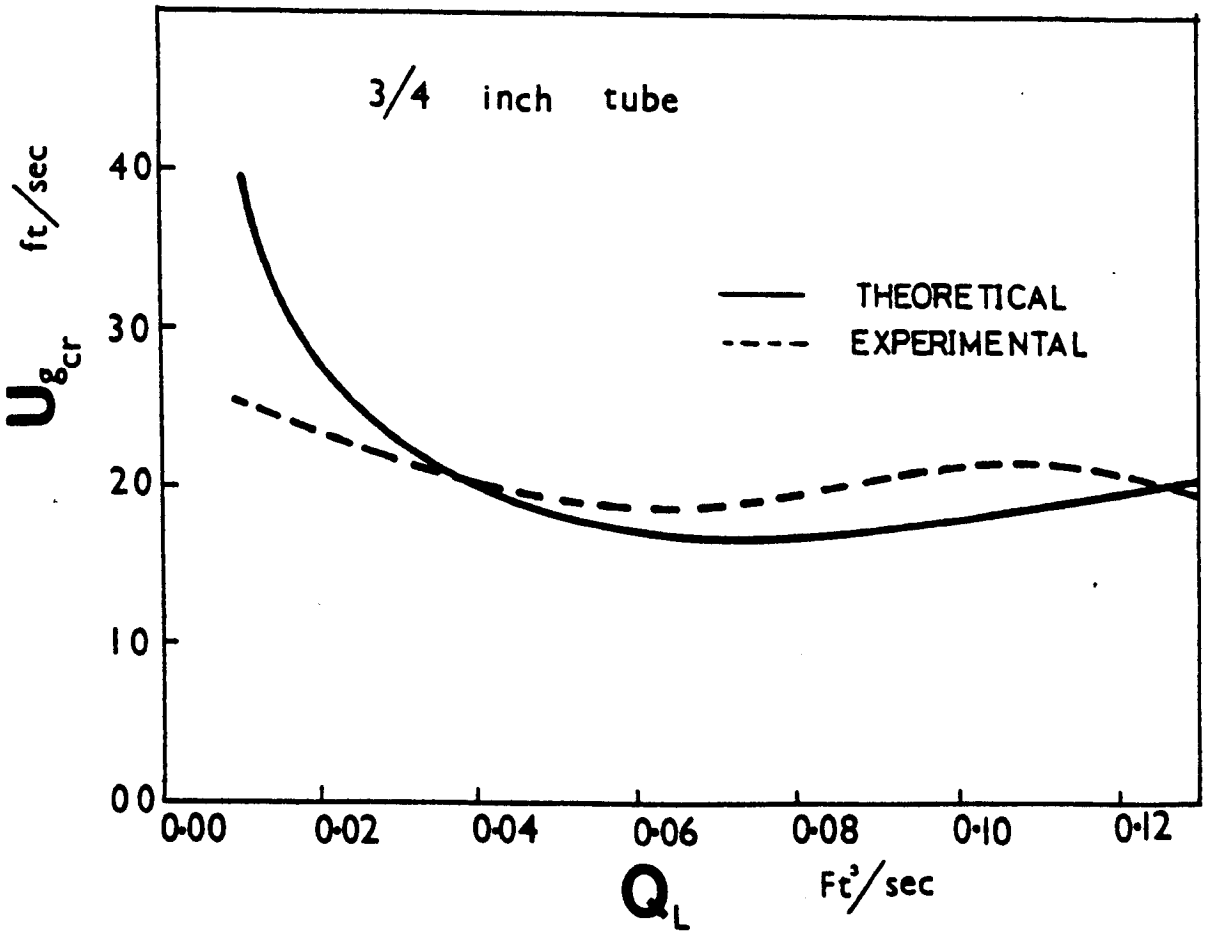

Fig 2·2 COMPARISON OF THEORETICAL AND EXPERIMENTAL BRIDGING GAS VELOCITIES VERSUS SUCROSE SOLUTION (33·5% WT) FLOW RATE, [Schutt(1)]

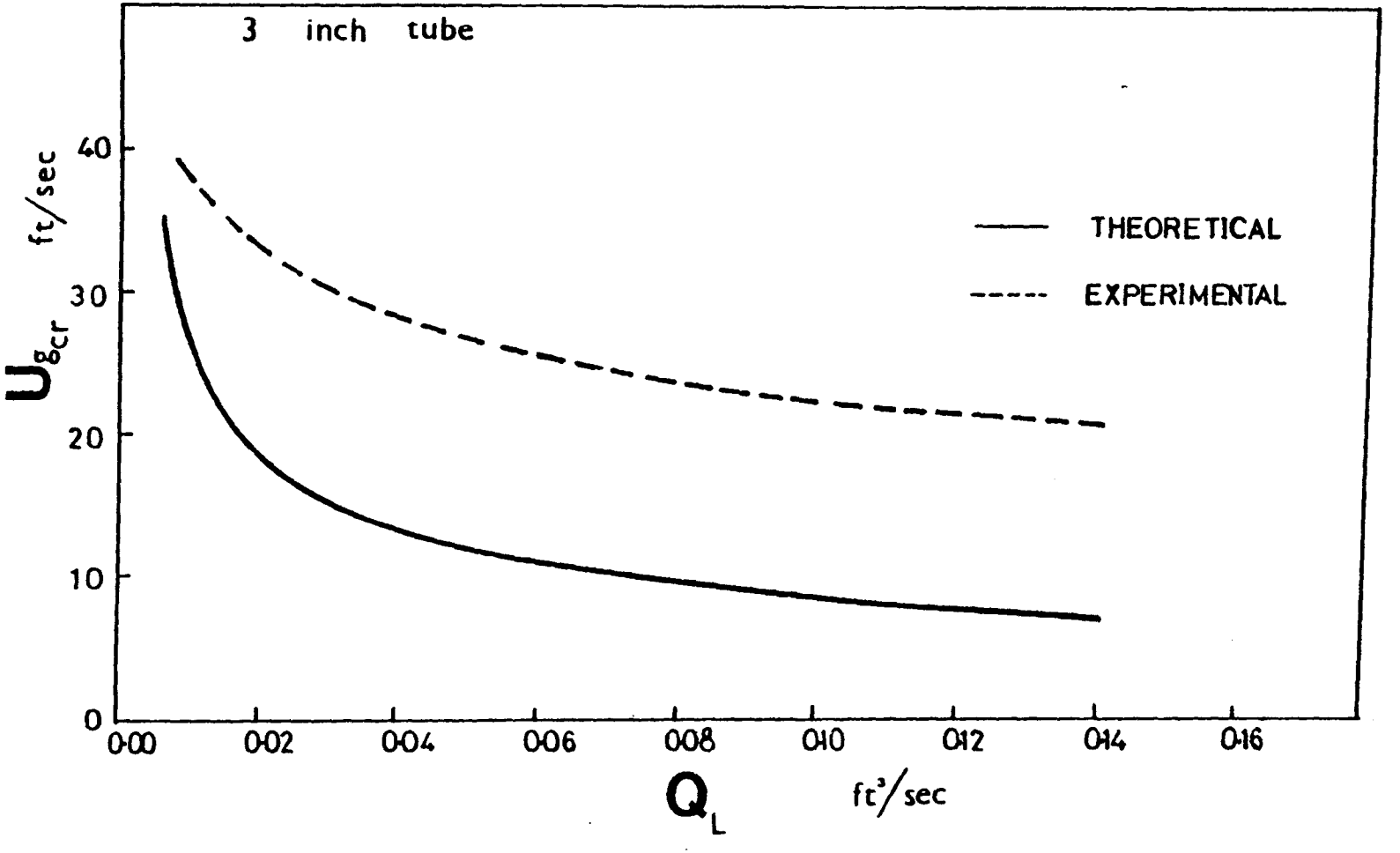

Fig 2·3 COMPARISON OF THEORETICAL AND EXPERIMENTAL BRIDGING GAS VELOCITIES VERSUS WATER FLOW RATE, [Schutt (1)]

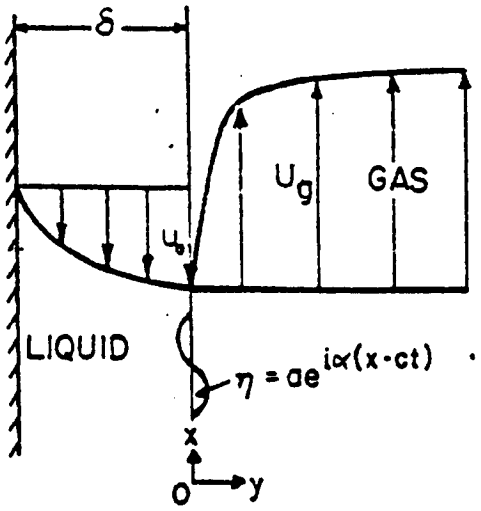

Fig 2·4 THE COORDINATE SYSTEM USED IN REF. [2]

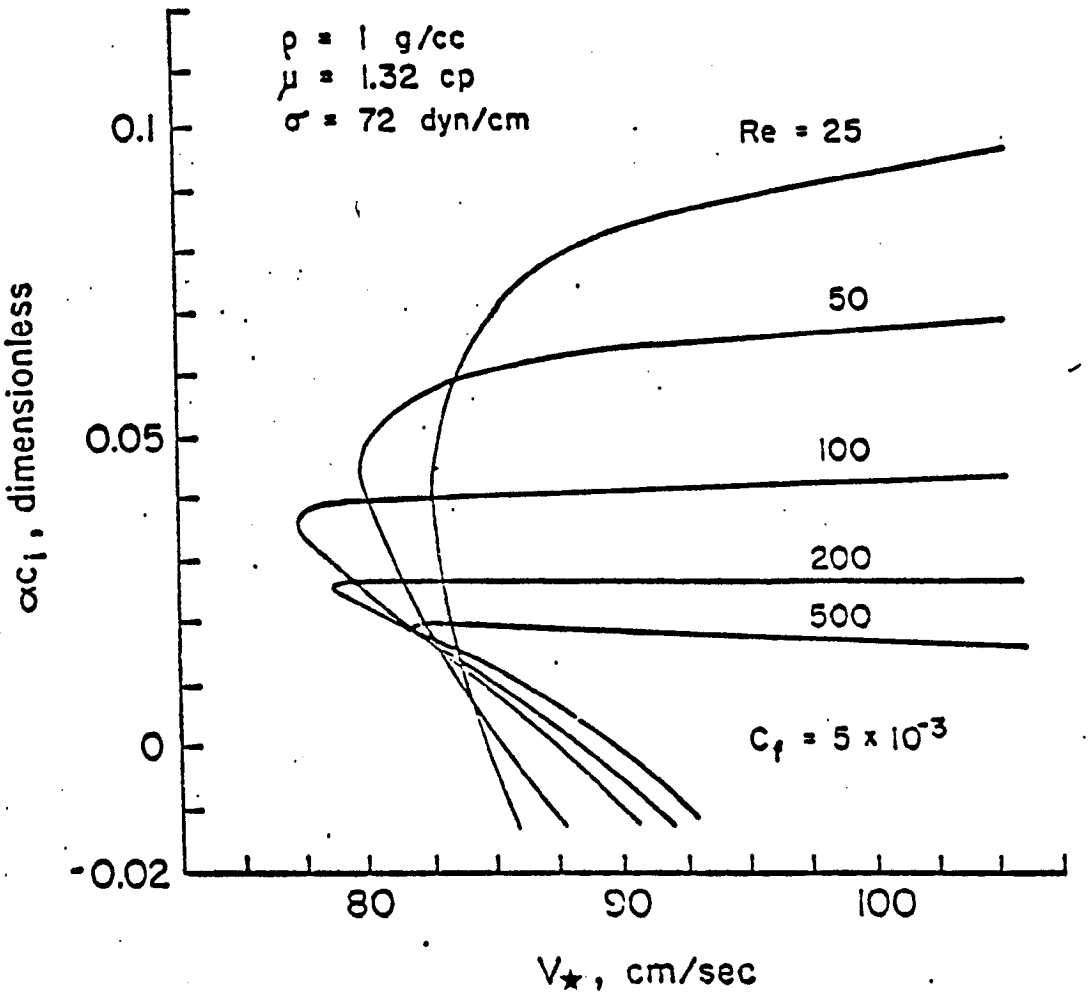

Fig 2-5 THE GROWTH RATE αc_i AS A FUNCTION OF THE GAS FRICTION VELOCITY $V_\star$ (Air/Water) - [Cetinbudaklar & Jameson (2)]

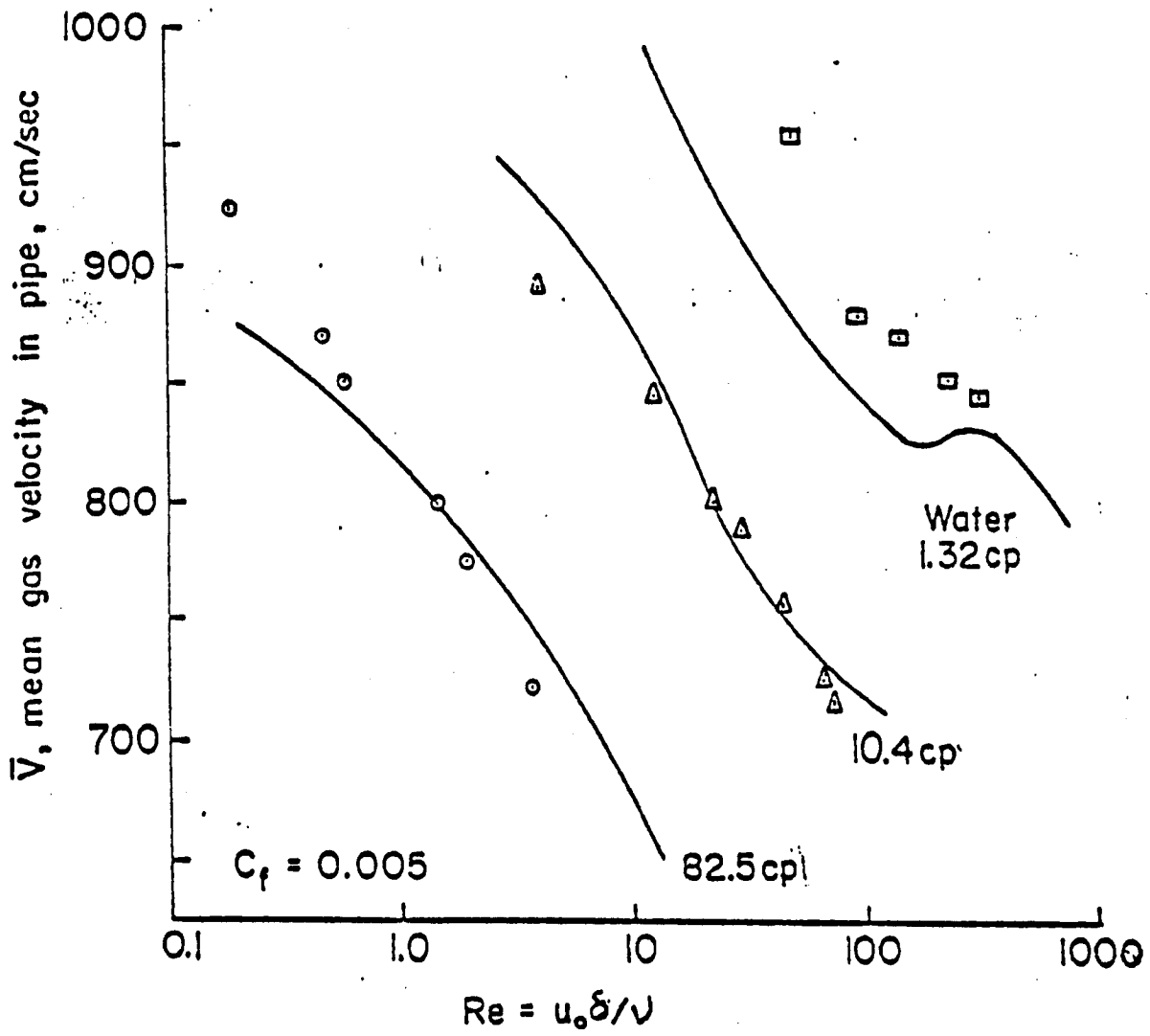

Fig 2.6 COMPARISON OF PREDICTED FLOODING VELOCITIES WITH THE EXPERIMENTAL DATA OF CLIFT et al [3]

[from ref. (2)]

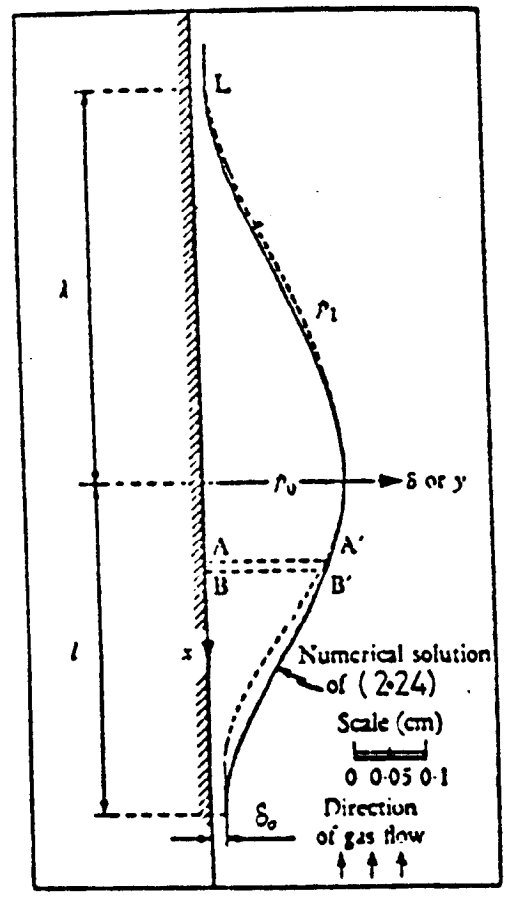

Fig 2·7 Axes and wave profiles to scale. The experimental profile is shown as broken line.
[Shearer & Davidson (4)

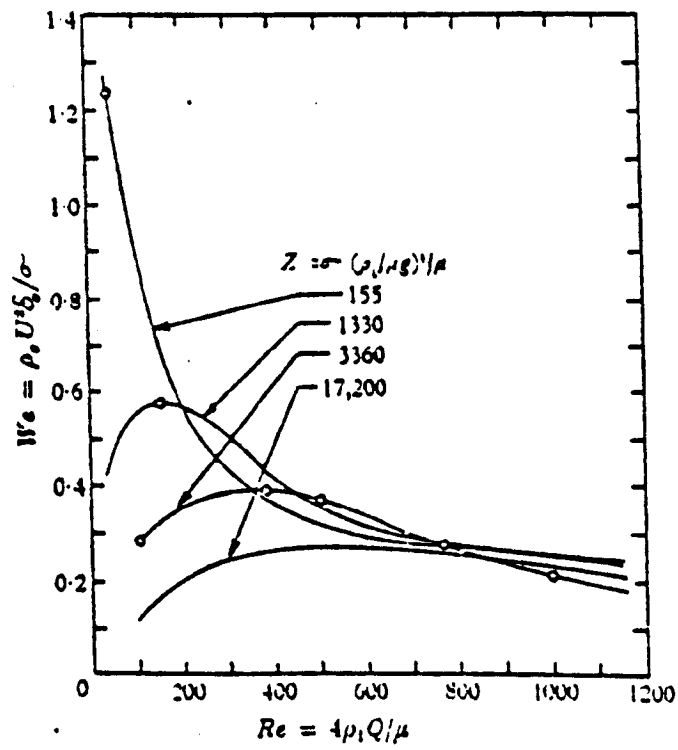

Fig 2·8 Dimensionless groups for formation of a large-amplitude wave. The circled points have been compared with experiment—[Shearer & Davidson (4)]

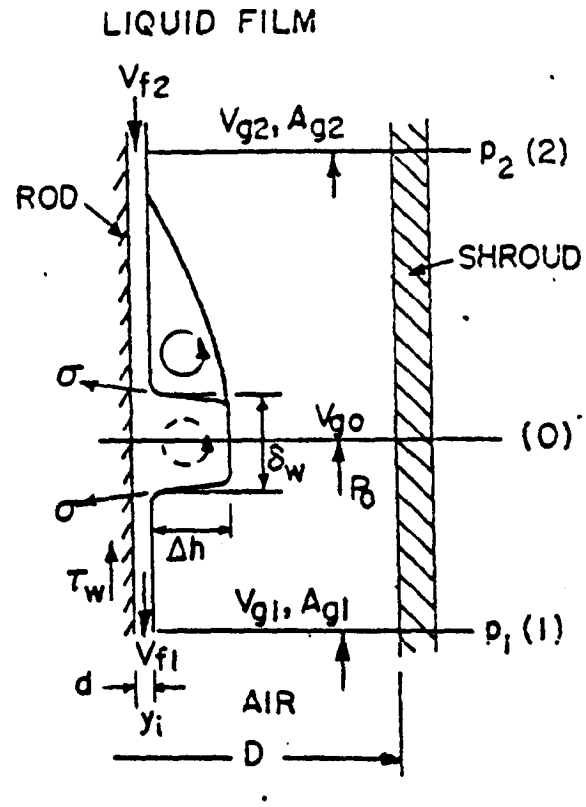

Fig 2·9 Analytical Model Of Ueda & Suzuki (5)

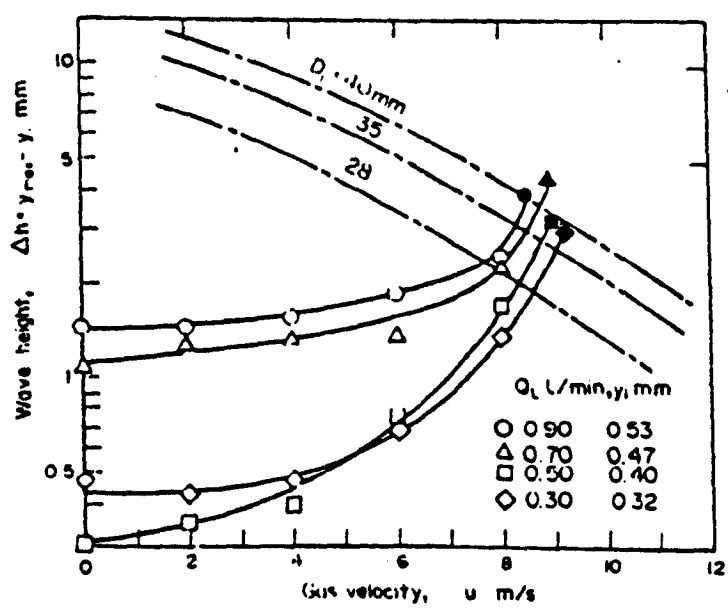

Fig 2·10 Relation between wave height and gas velocity for air-water flow in an annulus. (D_i = 40 mm, Probe position l = 0.90 m).

[Ueda & Suzuki (5)]

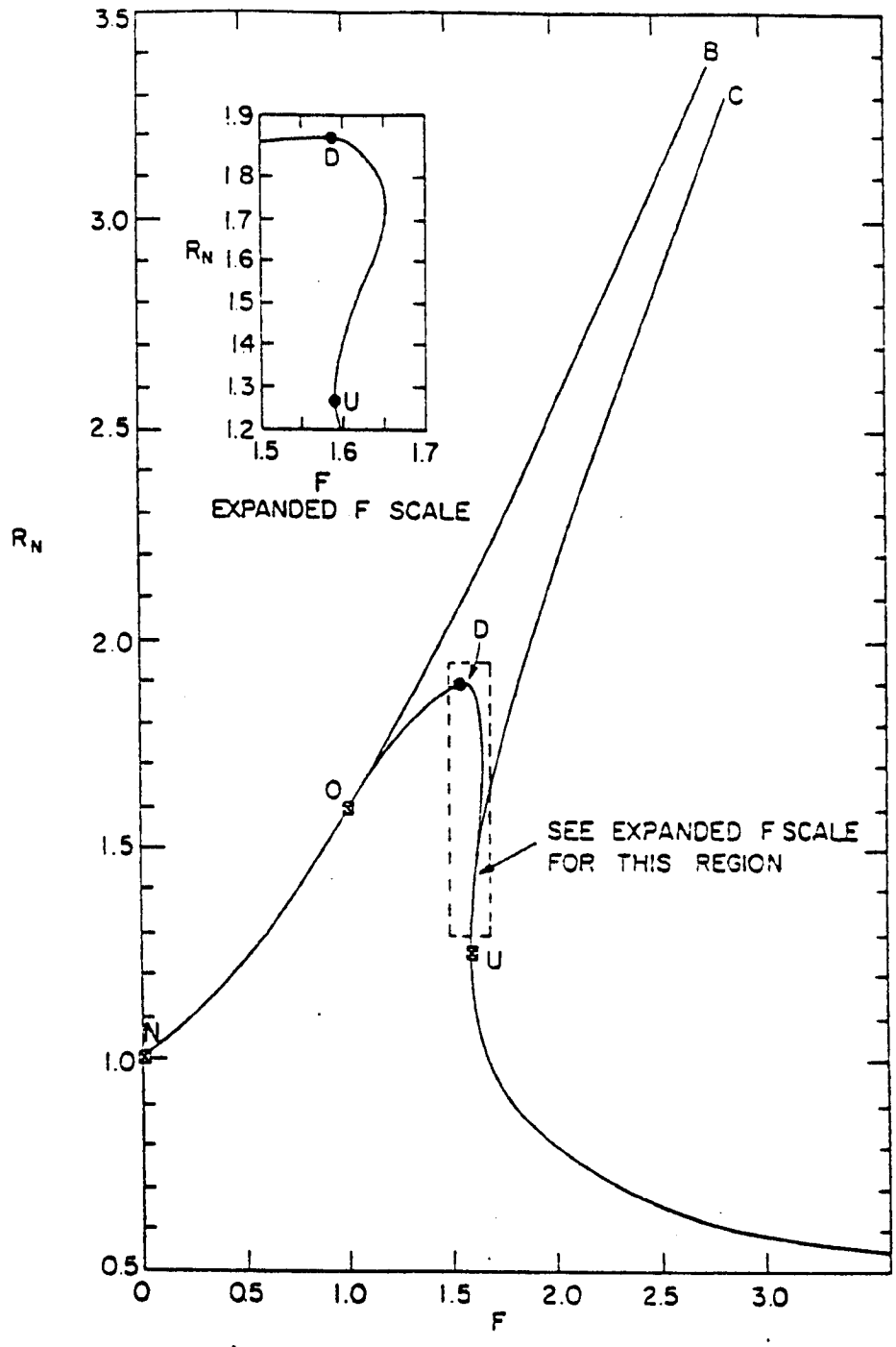

FIG 2·11 DIMENSIONLESS FILM THICKNESS VARIATION WITH DIMENSIONLESS INTERFACIAL SHEAR [Dukler et al (6)]

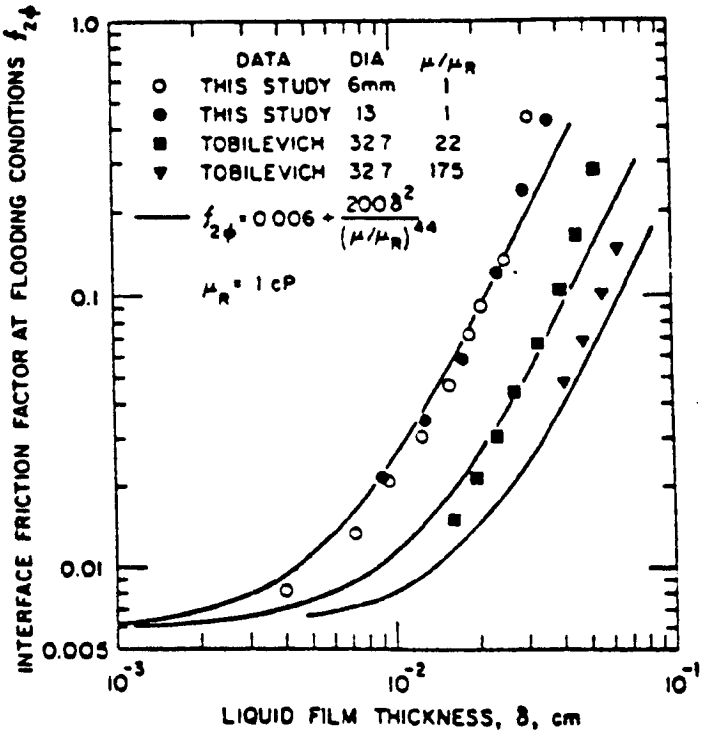

Fig.2.12 Correlation of gas-liquid interface friction factor at flooding conditions. [Grolmes et al (7)]

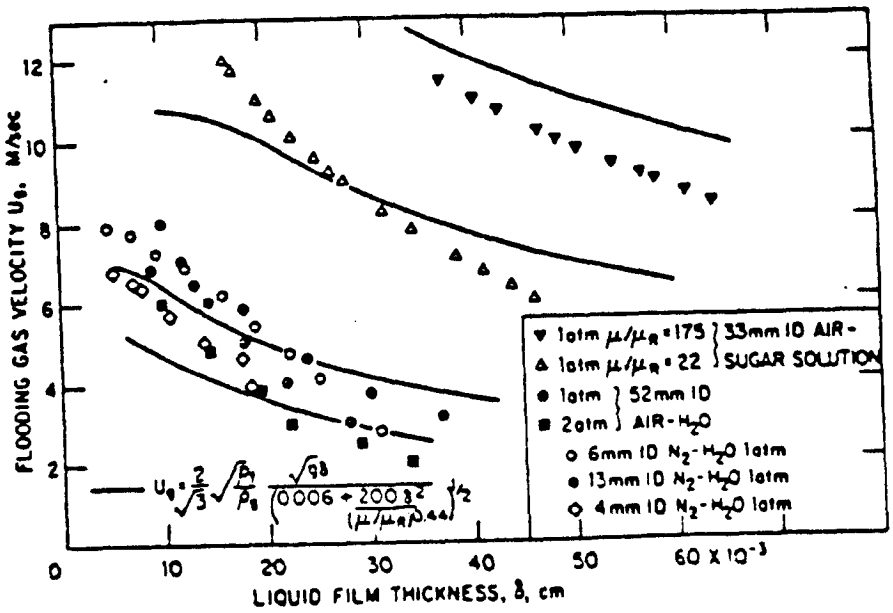

Fig.2.13 · Comparison of flooding gas velocity with Eqs. (2.33) & (2.35) - [Grolmes et al (7)]

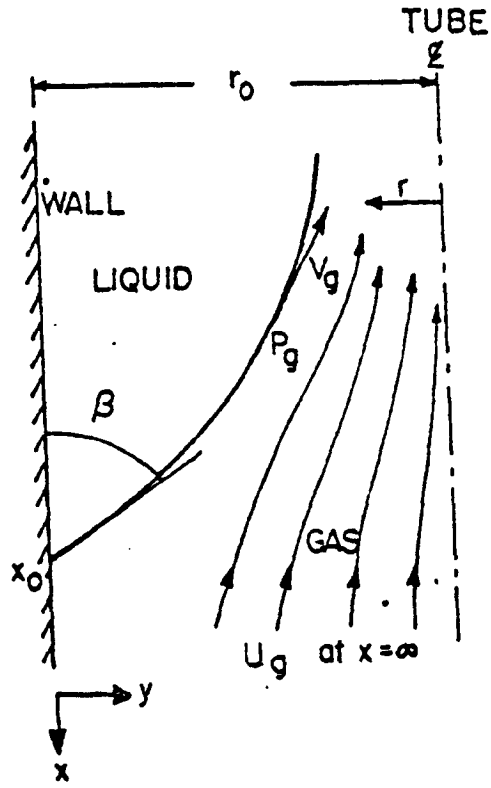

Fig 2.14 Hanging Film Model -[Wallis & Kuo(9)]

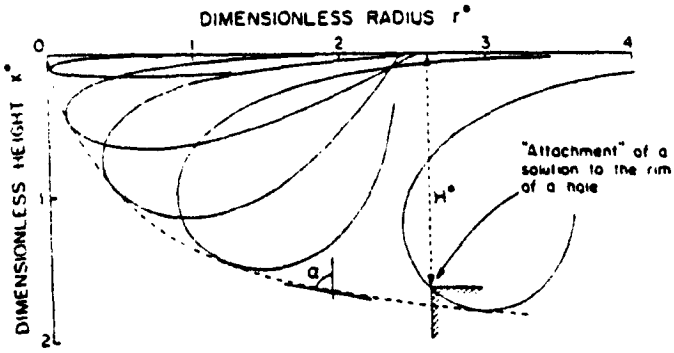

Fig 2.15 Several Computer Solutions To (2.37) With $U_g = 0$ and $dx^*/dr^* \to 0$ as $r^* \to \infty$ [Wallis & Kuo (9)]

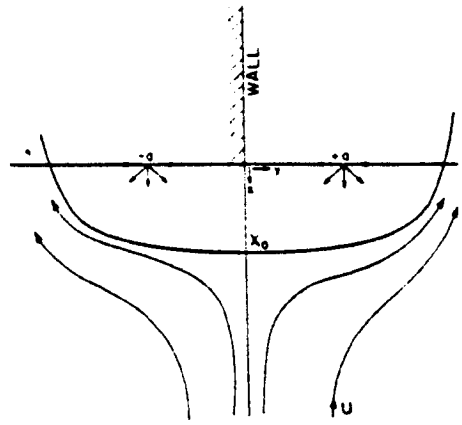

Fig 2.16 Flow around a pair of sources.- [ref. (9)]

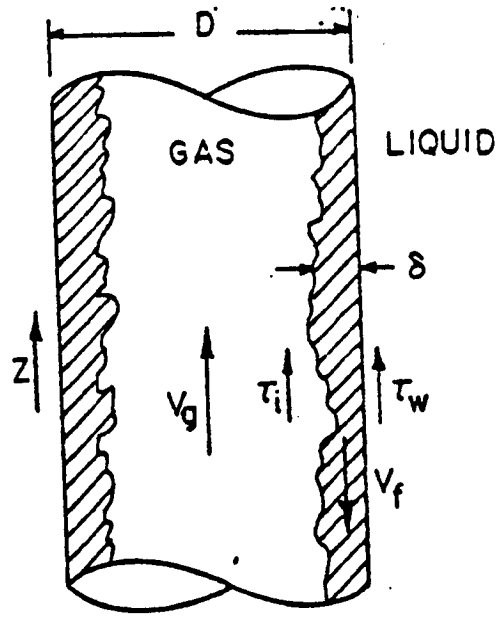

Fig 2.17 Annular Flow Model - [Wallis (12)]

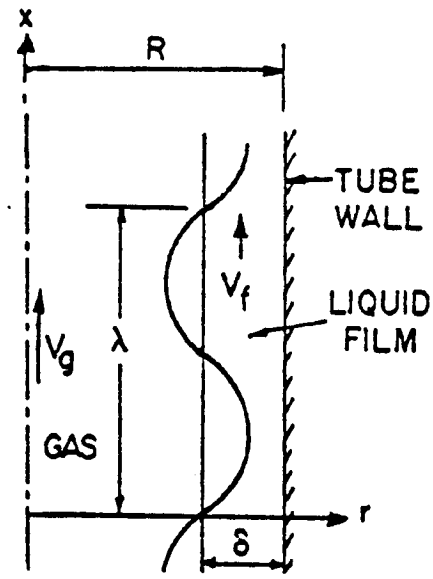

Fig 2·18 The Coordinate System Used by Imura et al (16)

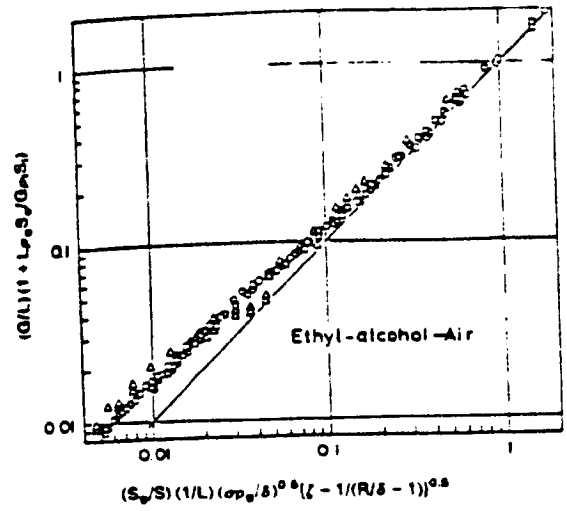

(a)

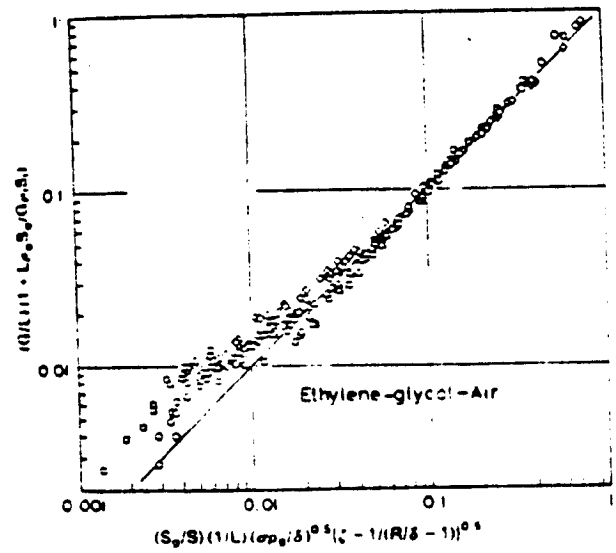

(b)

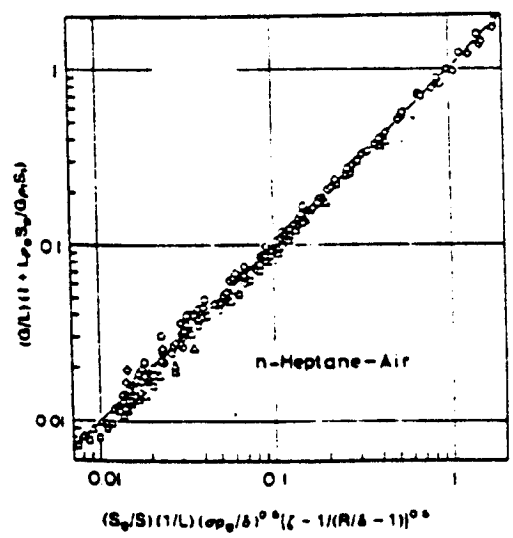

(c)

Fig 2.19 Correlation Of Flooding Data Using (2.65)

[Imura et al (16)]

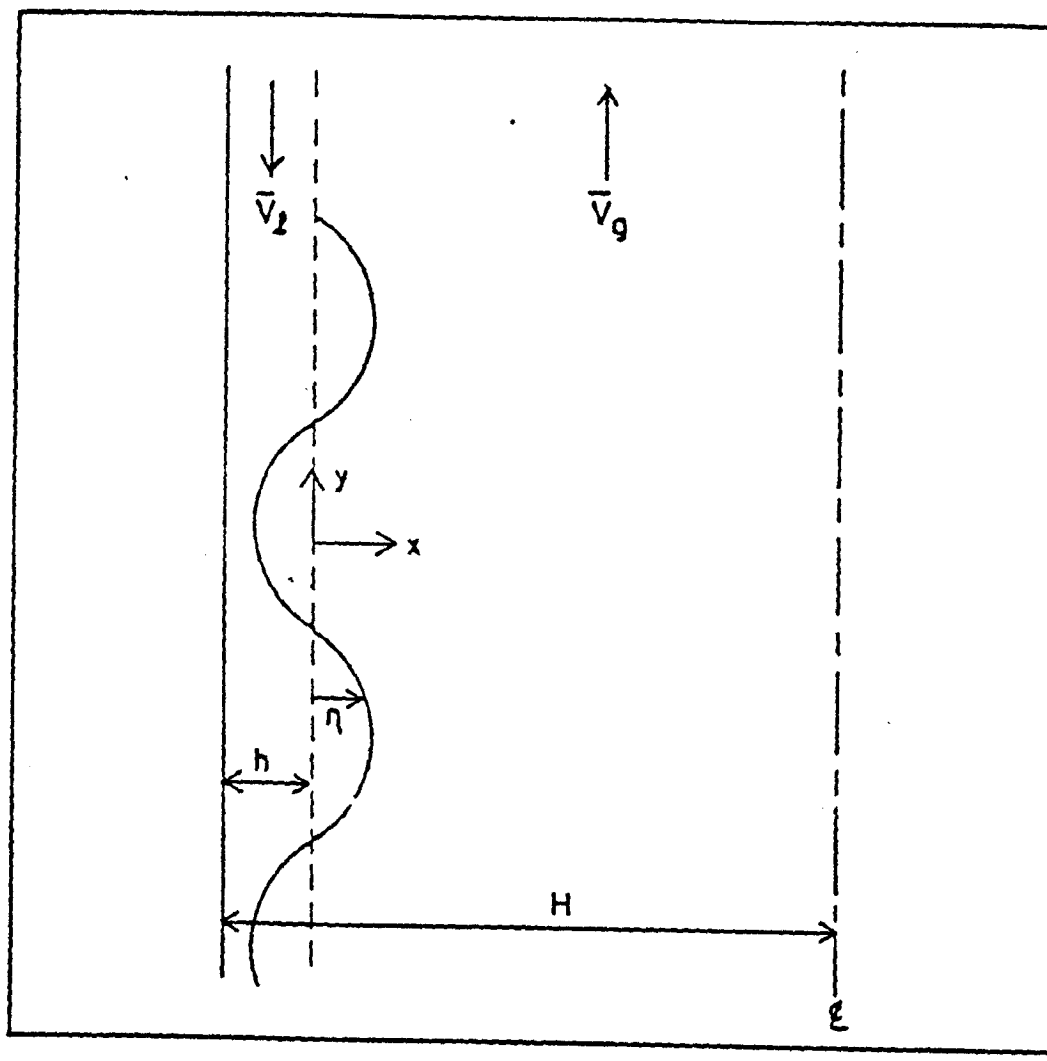

FIG 2·20 The Counter-Current Two-Phase Flow System - [Chung(17)]

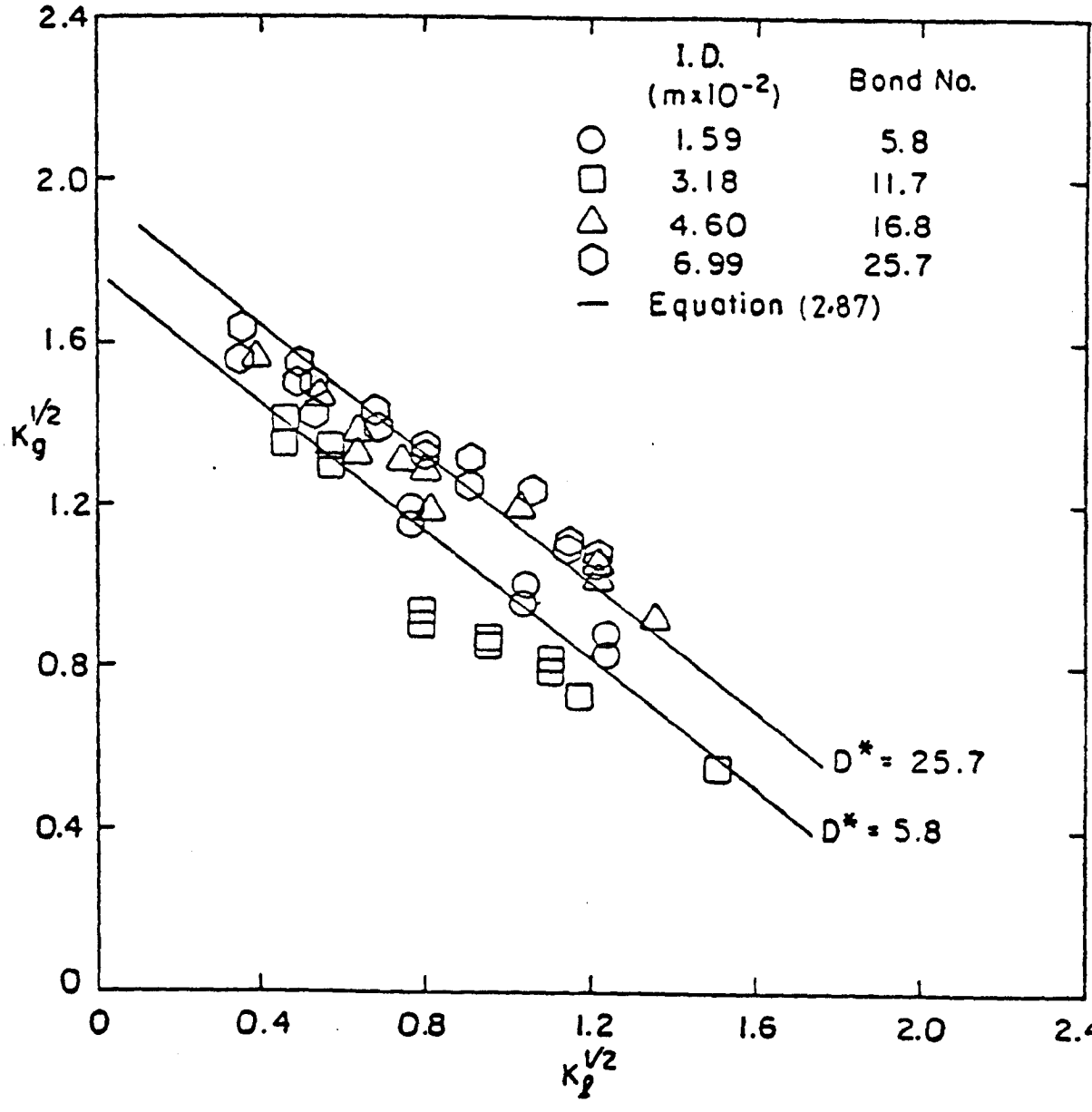

Fig. 2.21 Flooding Results for Different Tube Sizes with Sharp Edge Liquid Inlet and Nozzle Air Supply [Tien et al(18)]

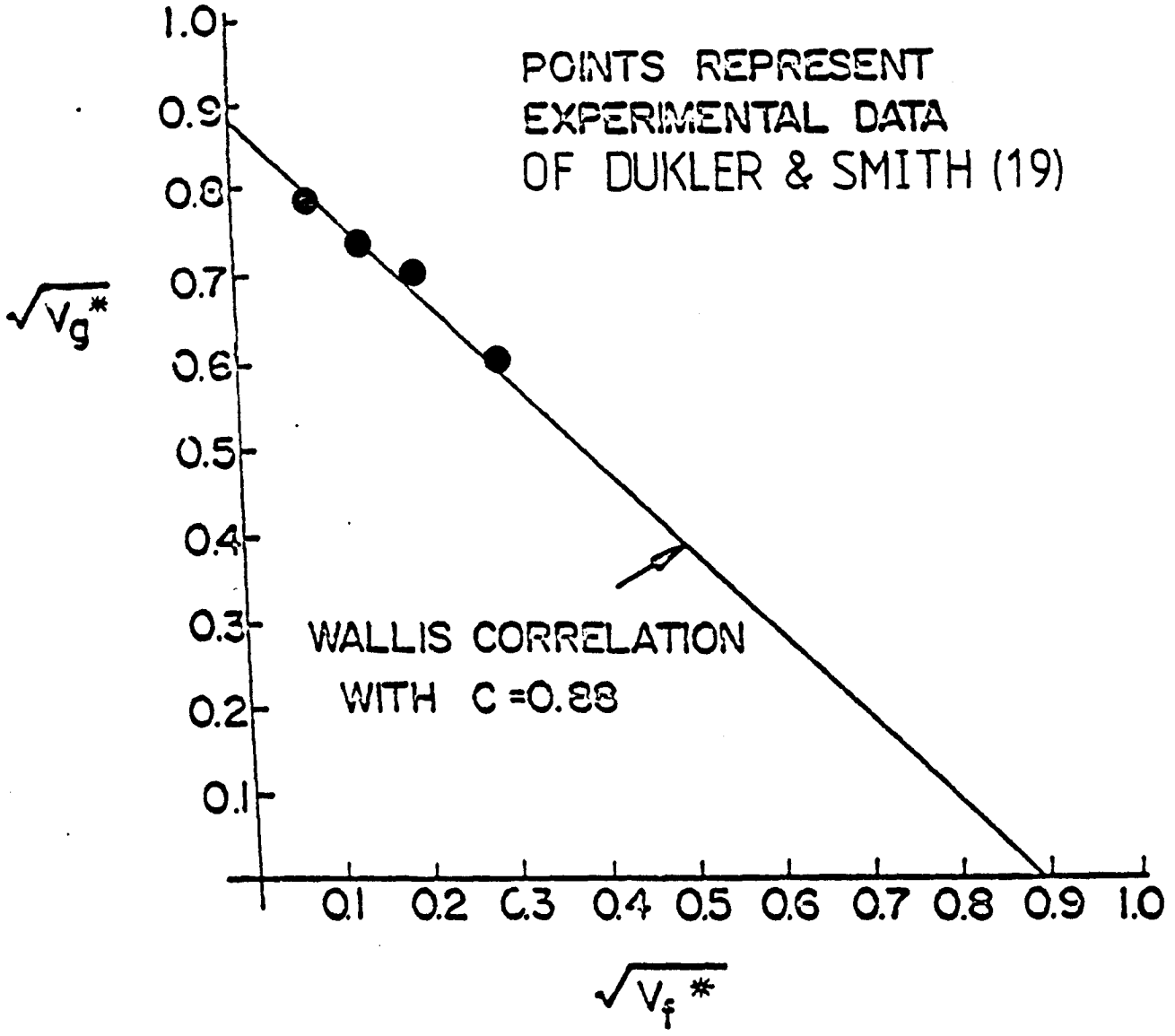

FIG 2.22 THE WALLIS CORRELATION FOR FLOODING

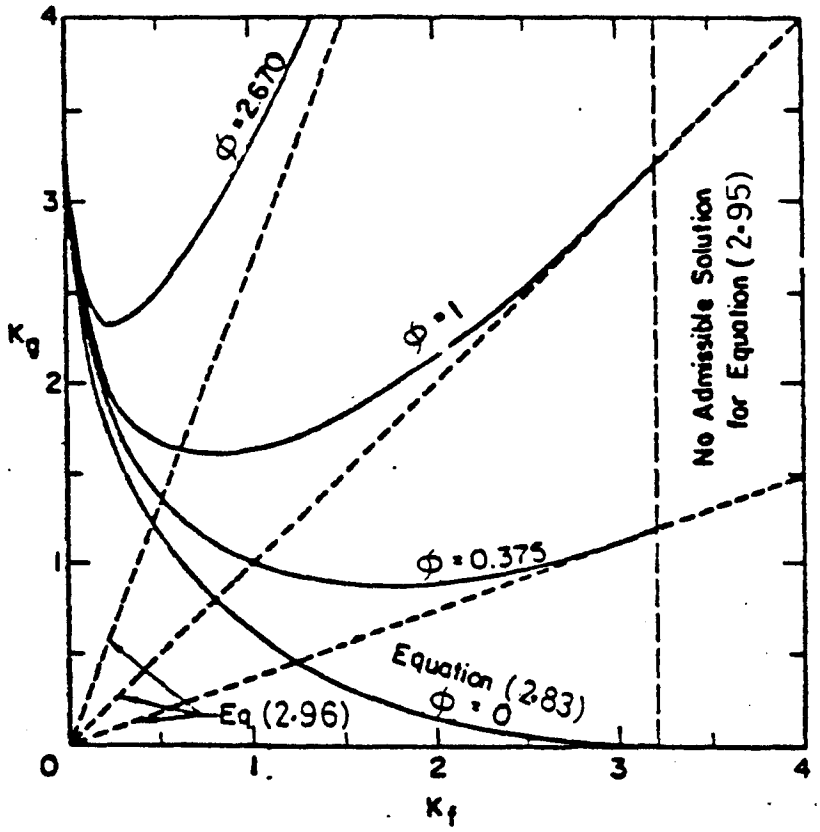

Fig 2.23 Subcooled CCFL Correlation [Tien (21)]

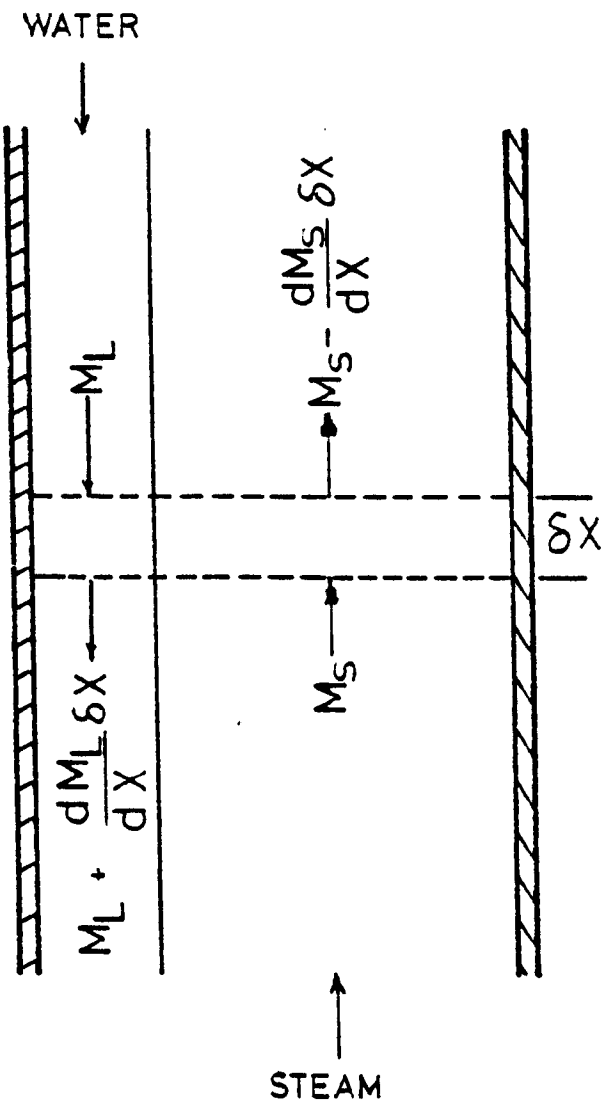

Fig 2·24 Counter-current Annular Flow [Liu et al (22)]

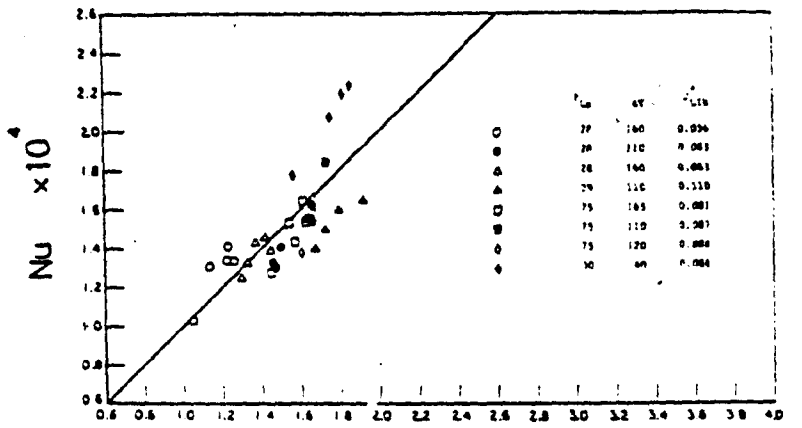

Fig 2·25 Comparison Of Experimental And Calculated Nusselt Number - [Liu et al (22)]

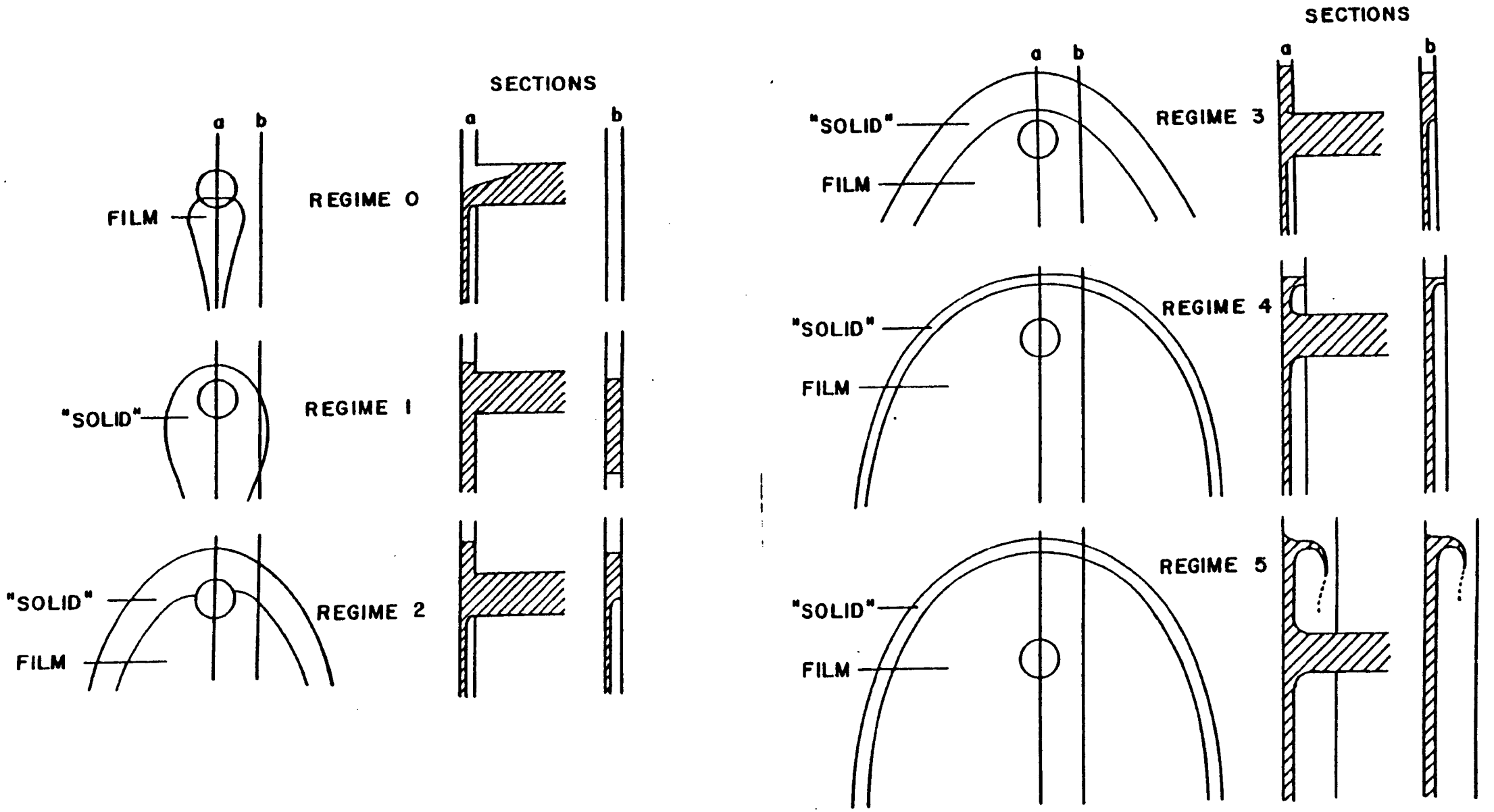

Fig 2.26 Flow Regimes In The Downcomer Of PWR [Wallis et al (24)]

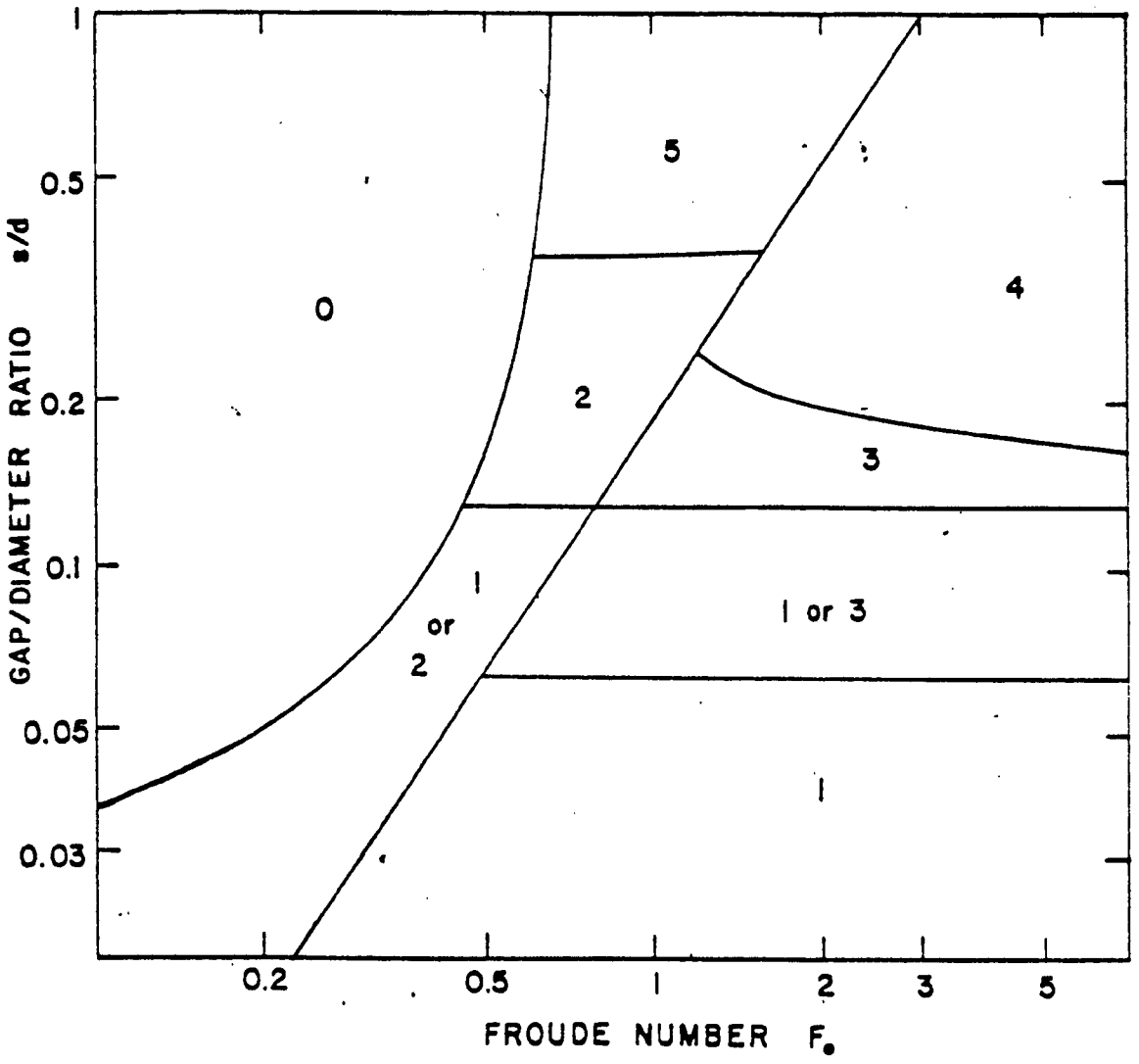

Fig 2·27 Approximate Flow Regime Map

[Wallis et al (24)]

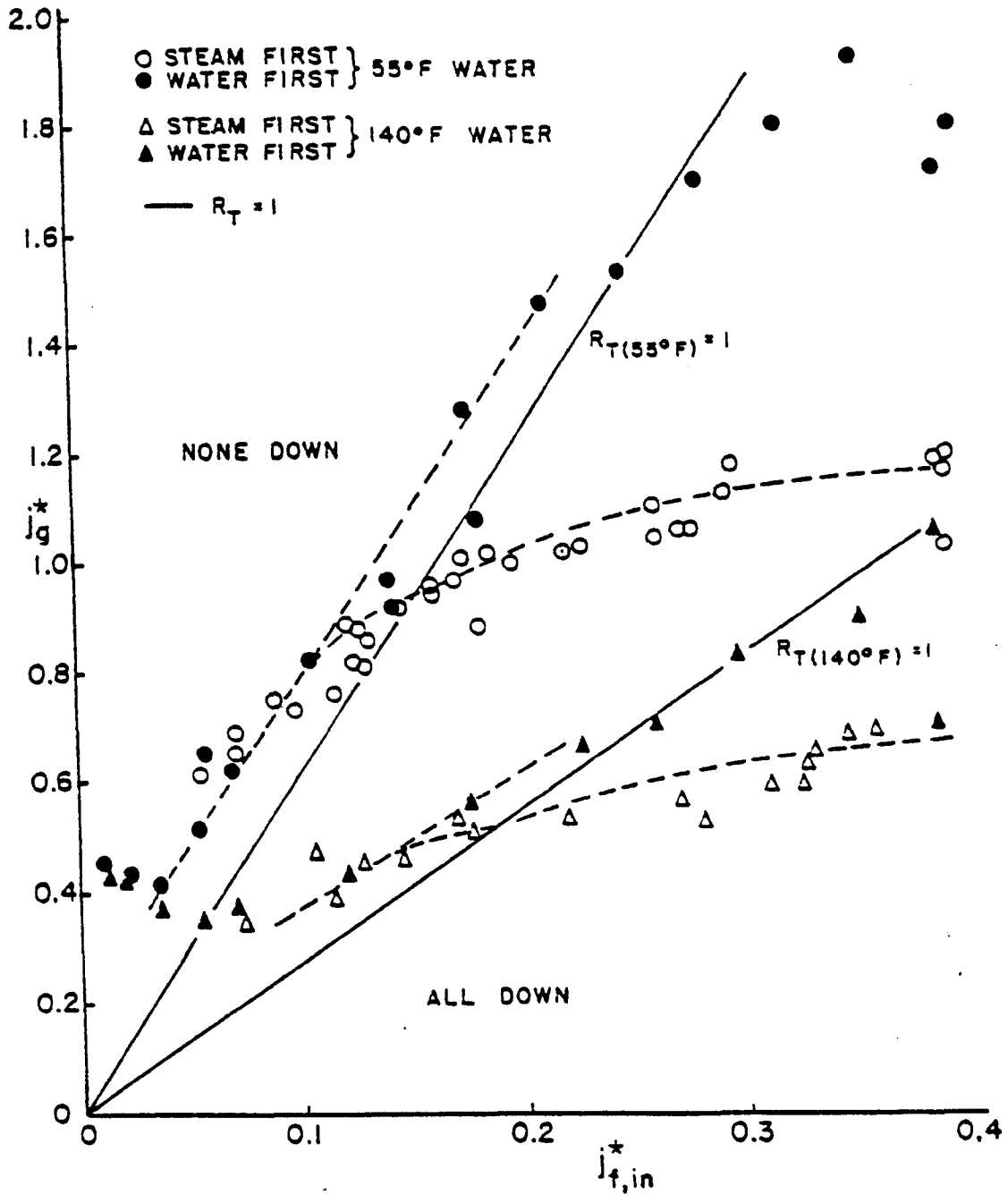

Fig 2-28 Some of Crowley's results(25) for countercurrent steam-water flow in a small scale model PWR annulus. The open points represent the transition from complete bypass (none down) to complete delivery (all down) in a steam-first test as water flow was increased. The solid points represent the reverse transition as steam flow was increased in a water-first test.

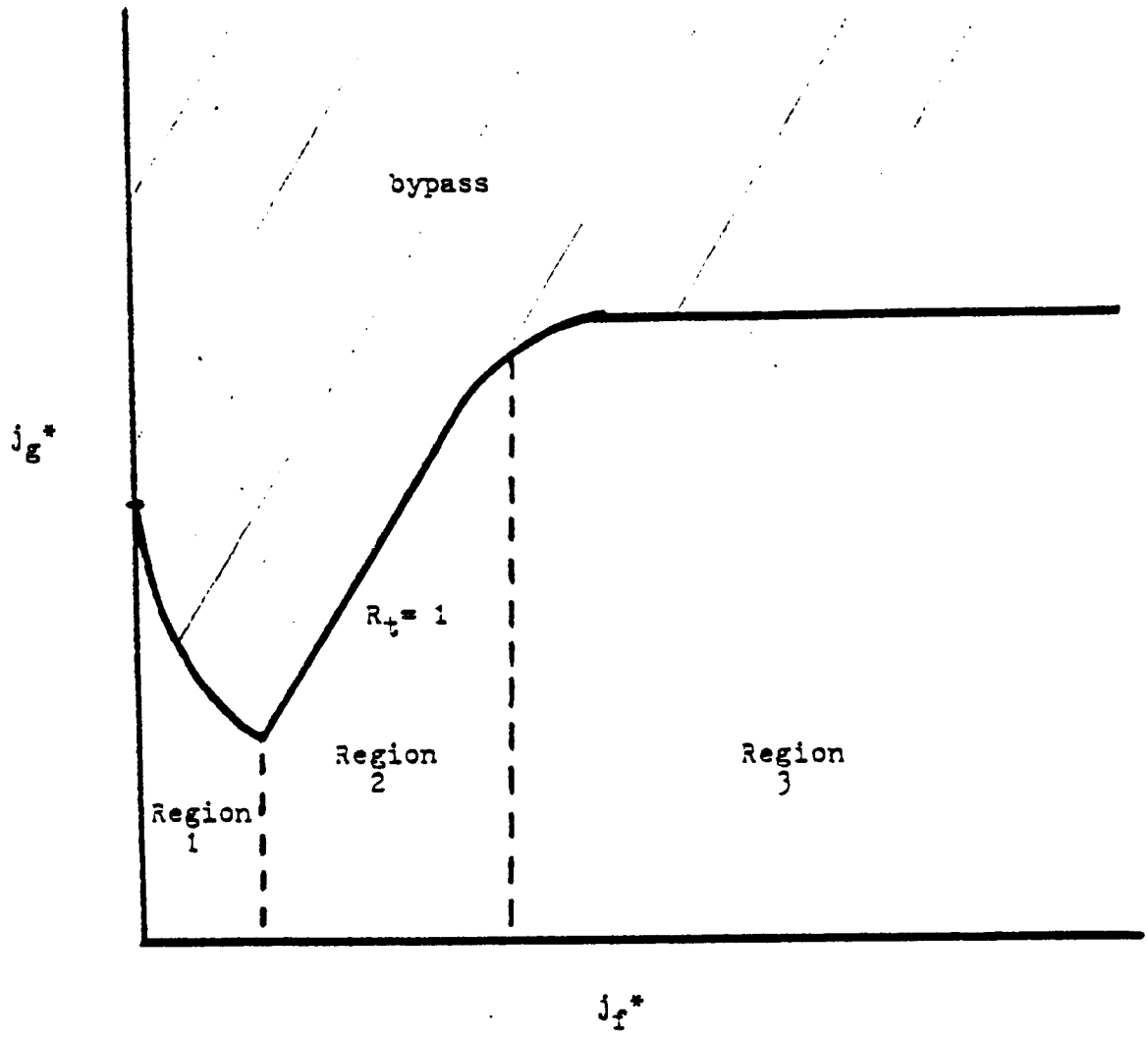

Fig 2·29 Sketch of the end of bypass locus in steam-first experiments -[Crowley et al (25)]

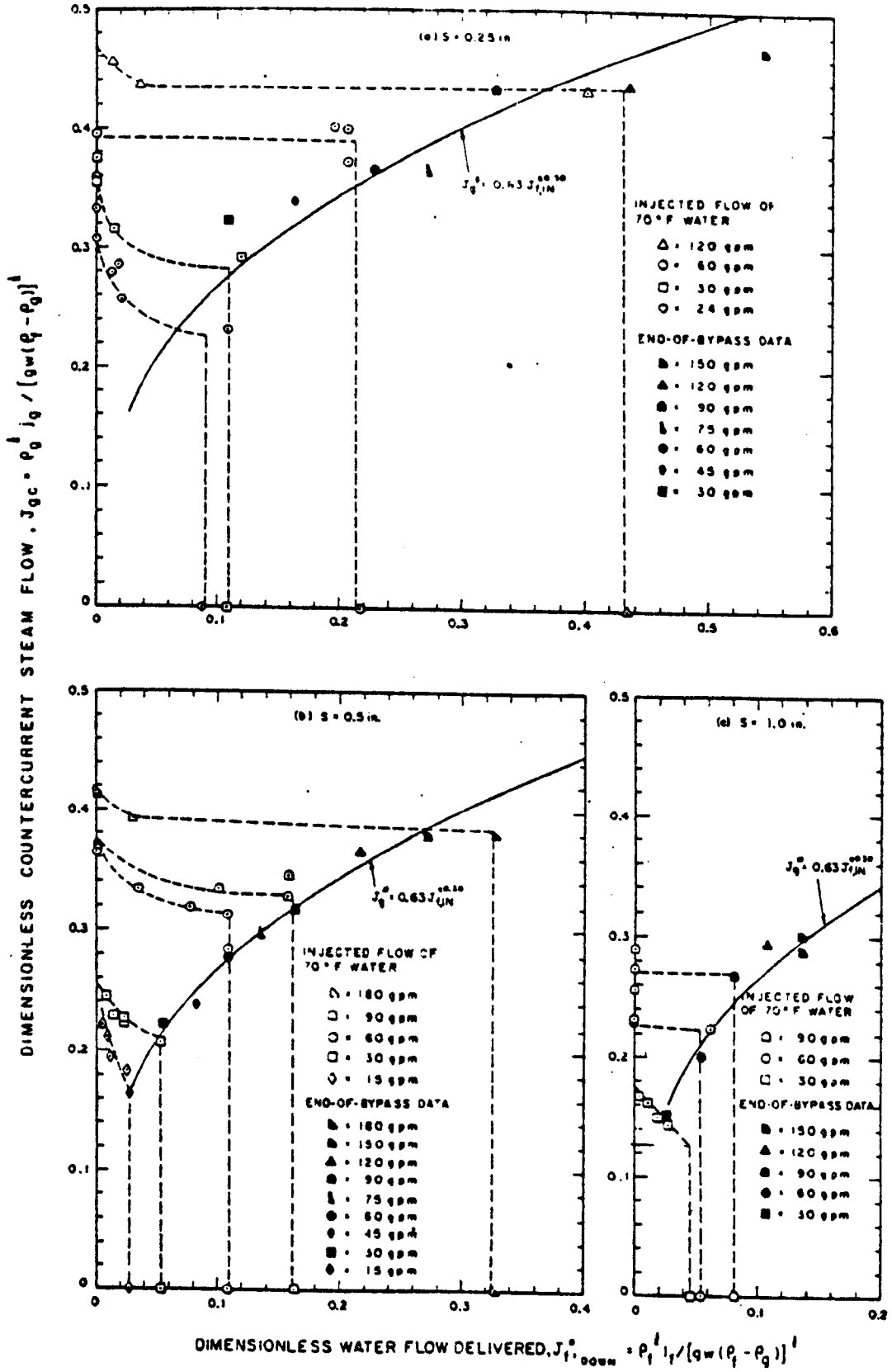

Fig 2-30 PENETRATION DATA FOR 70°F WATER BASED ON THE DOWNCOMER WIDTH AS THE CHARACTERISTIC DIMENSION [BLOCK & CROWLEY (26)]

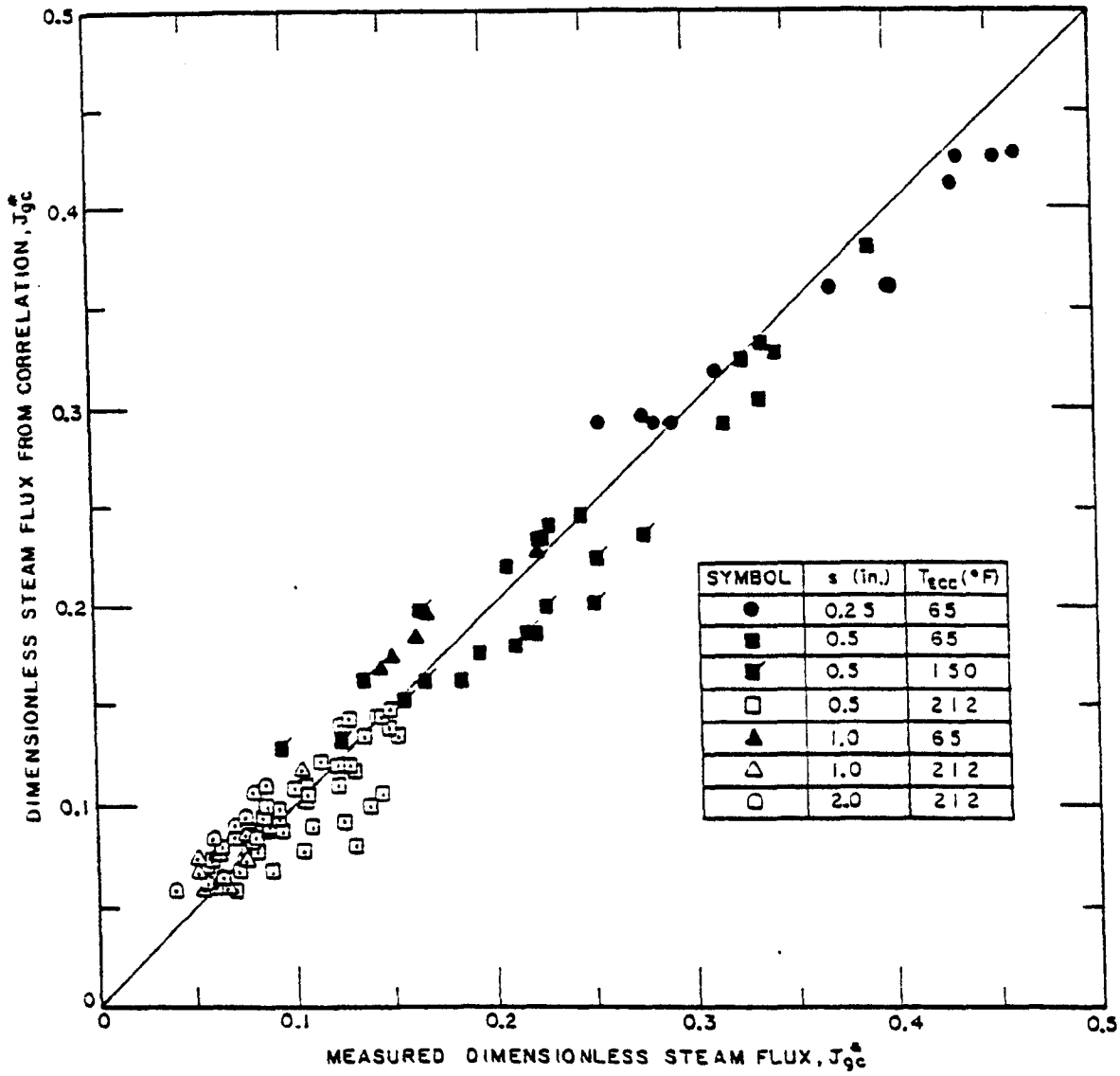

Fig 2.31 COMPARISON OF THE CORRELATION WITH CREARE FLAT PLATE DATA - [BLOCK et al (27)]

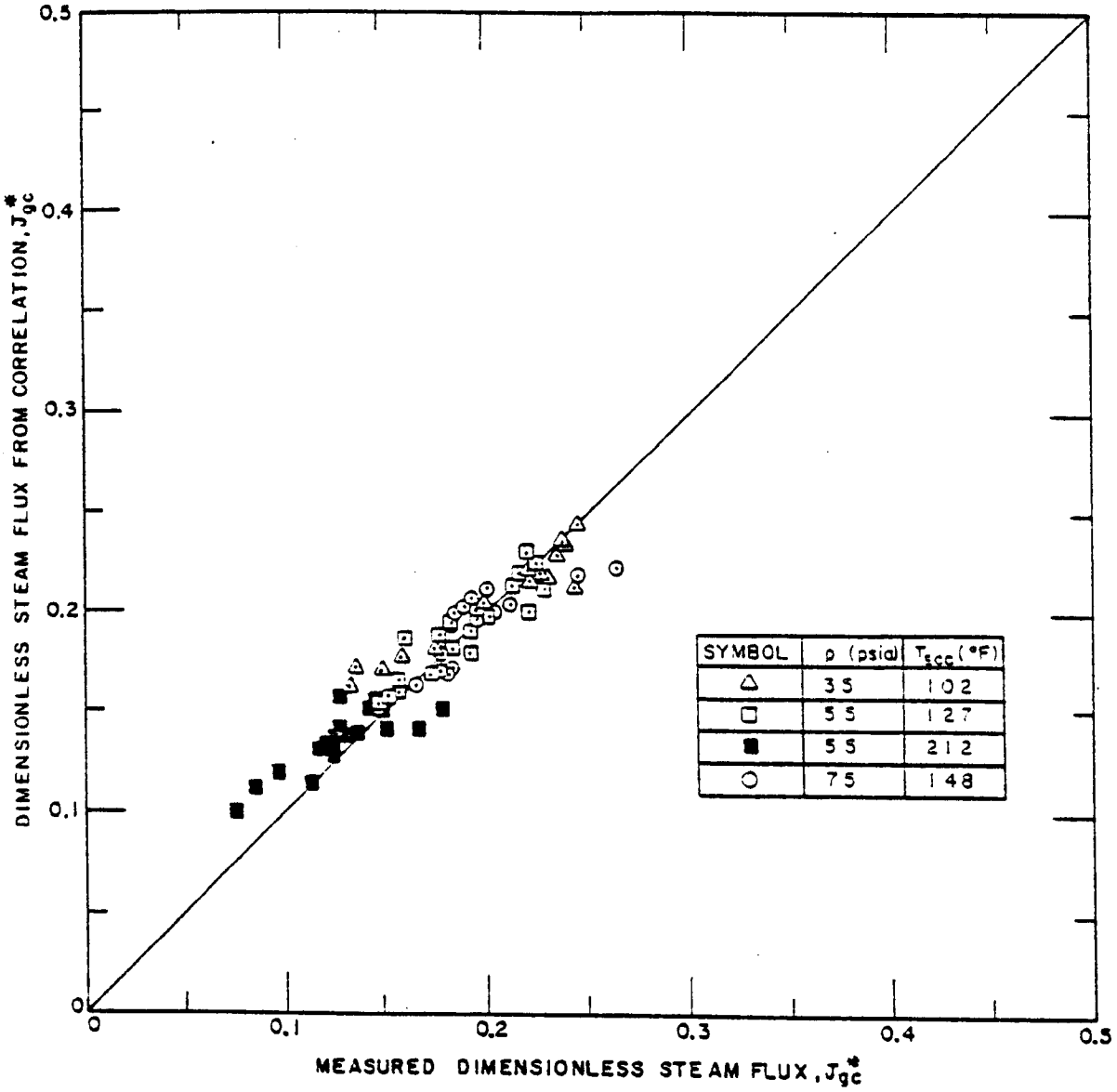

Fig 2.32 COMPARISON OF THE CORRELATION WITH CREARE CYLINDRICAL VESSEL DATA WITH CONTROLLED PRESSURES [BLOCK et al (27)]

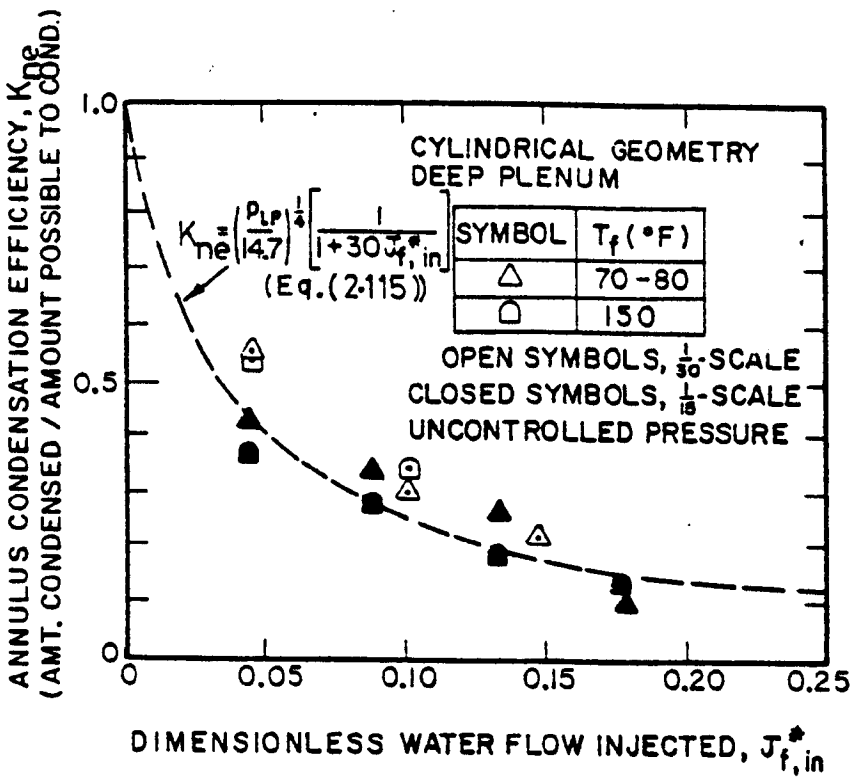

Fig 2.33 COMPARISON OF THE CALCULATED ANNULUS CONDENSATION EFFICIENCY (AT 1/15- AND 1/30-SCALE) WITH THE PREDICTION OF THE 1/15-SCALE-BASED CORRELATION USING J* (EQUATION (2.115)) - [CROWLEY et al (28)]

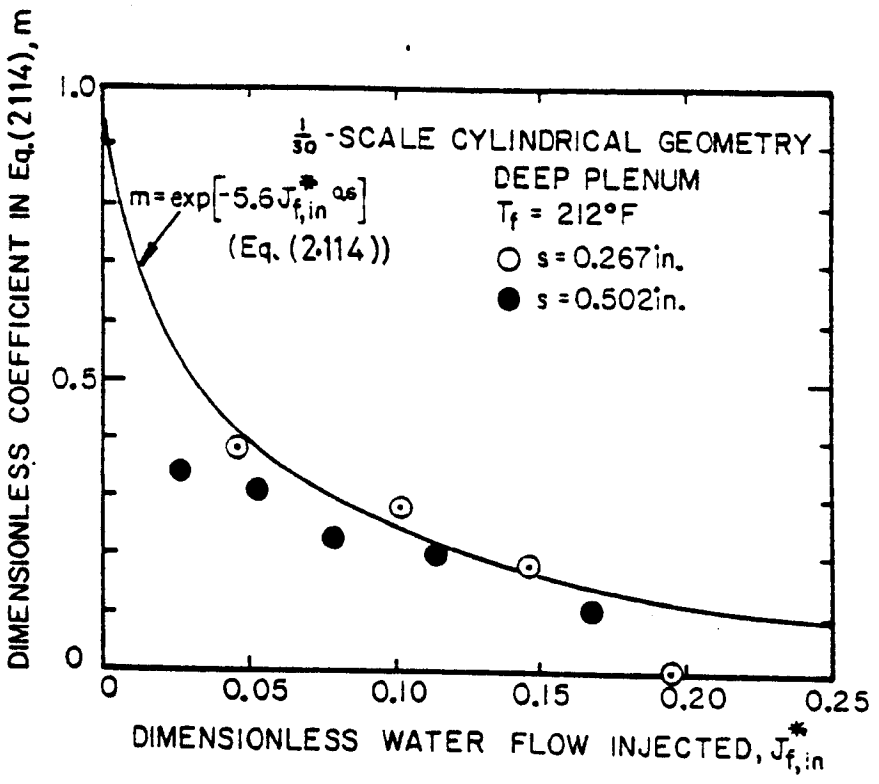

Fig 2.34 COMPARISON OF THE MEASURED PENETRATION CURVE SLOPE m AT 1/30-SCALE WITH THE PREDICTION OF THE 1/15-SCALE-BASED CORRELATION USING J* (EQUATION(2.114)) [CROWLEY et al (28)]

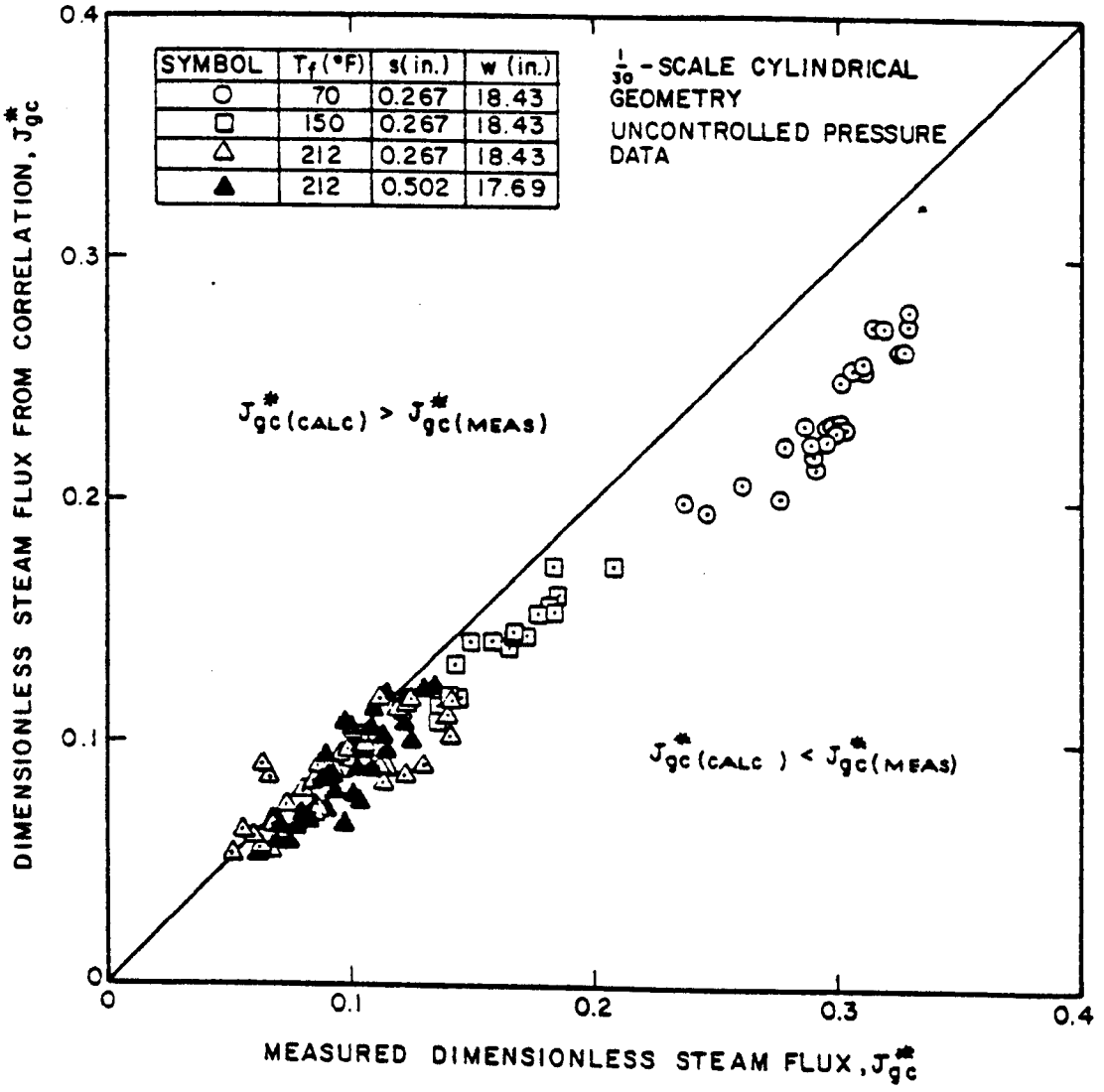

Fig 2.35 COMPARISON OF THE CORRELATION BASED ON J* [EQS.(2.112) TO (2.115)] WITH CREARE 1/30-SCALE CYLINDRICAL VESSEL DATA (UNCONTROLLED PRESSURE) - [CROWLEY et al (28)]

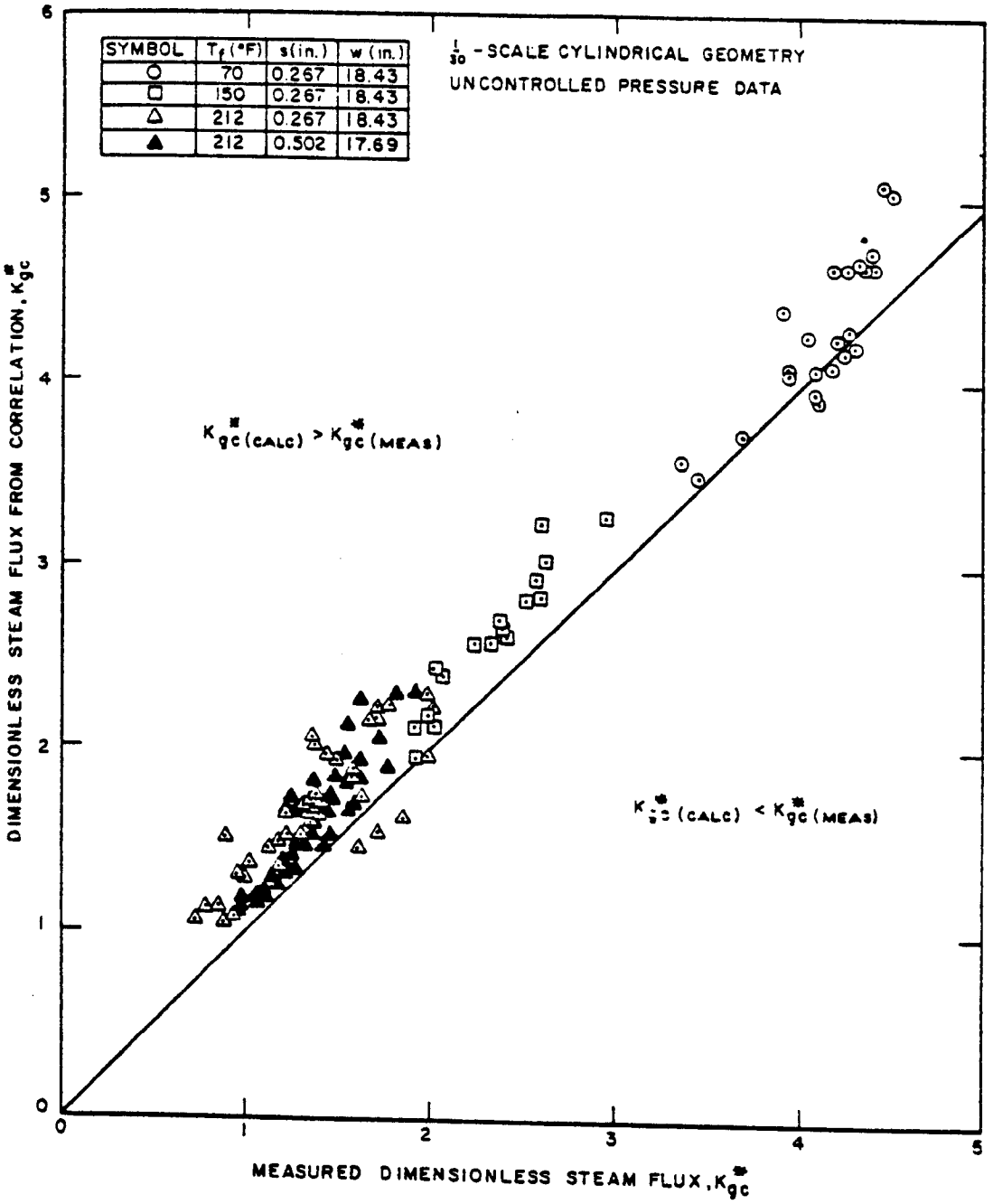

Fig 2.36 COMPARISON OF THE CORRELATION BASED ON K* [EQS. (2.116) TO (2.119)] WITH CREARE 1/30-SCALE CYLINDRICAL VESSEL DATA (UNCONTROLLED PRESSURE) - [CROWLEY et al (28)]

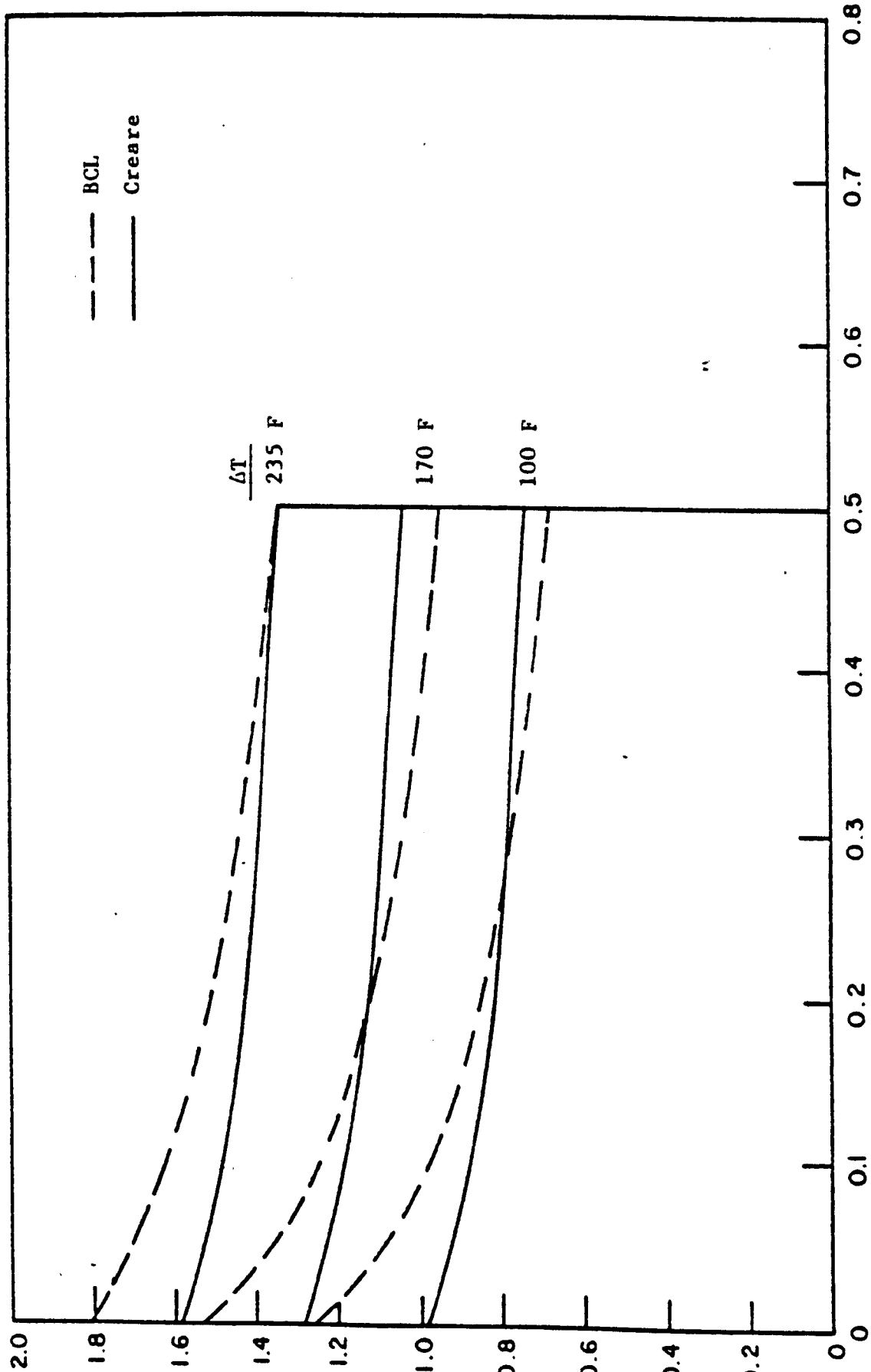

FIG. 2-37 COMPARISON OF BCL AND CREARE CORRELATIONS AT VARIOUS ECC WATER SUBCOOLINGS FOR A $j_{w_i}^*$ OF 0.5 AND A SYSTEM PRESSURE OF 75 PSIA -[CUDNIK et al (29)]

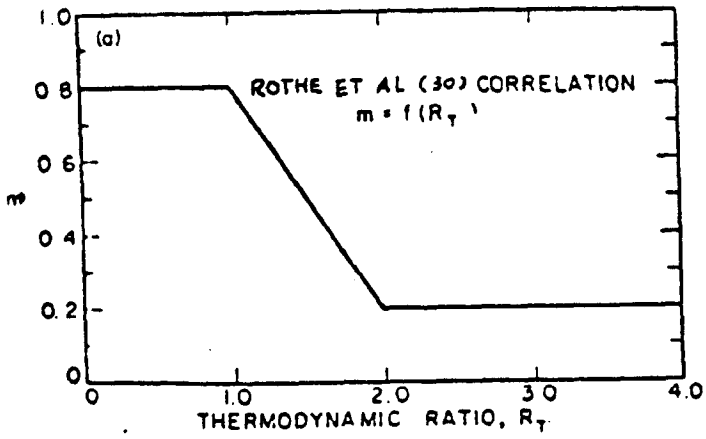

Fig 2.38 Behaviour Of Factor m Representing Partial Delivery

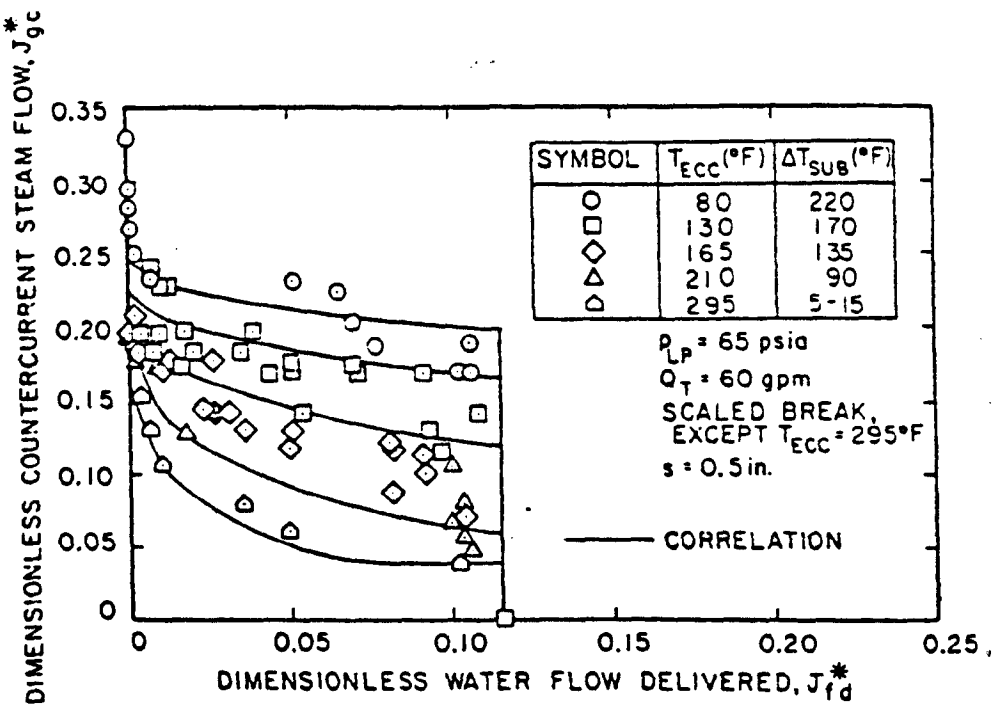

Fig 2.39 Comparison Of Rothe et al (30) Correlation With Creare 1/15-Scale data For A Vessel Pressure Of 65 psia At Various ECC Subcoolings

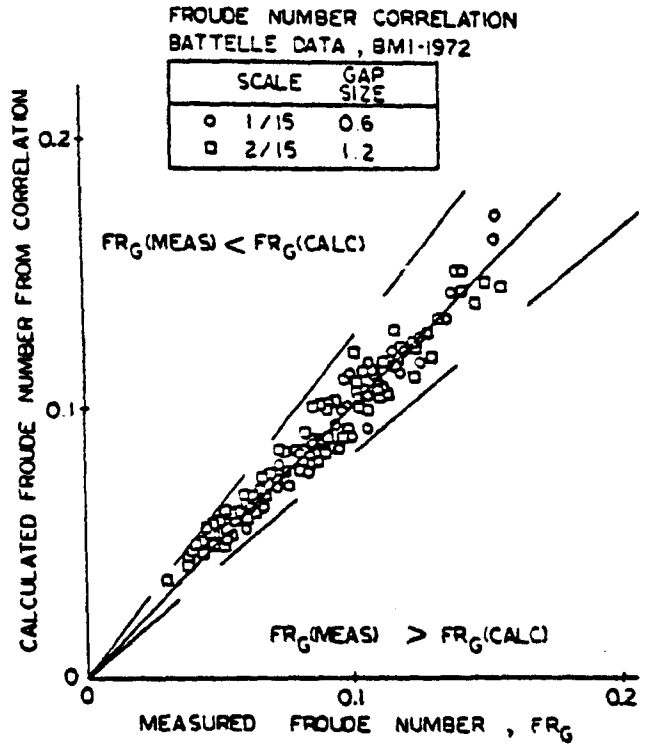

Fig 2.40. Comparison of the calculated Froude number, eq. (2.123) to the experimentally observed value. – [ref. (31)]

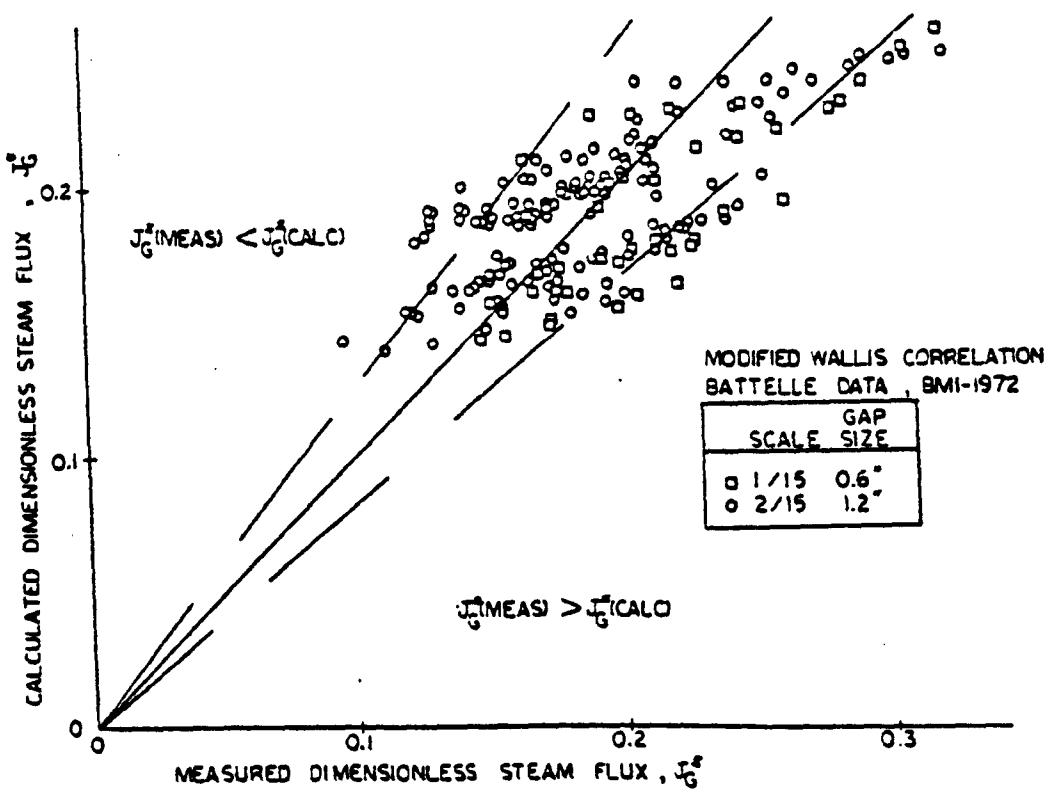

Fig 2.41 Comparison of the calculated dimensionless steam flux, eq (2.112), to the experimentally observed values.

[Alb & Chambré (31)]

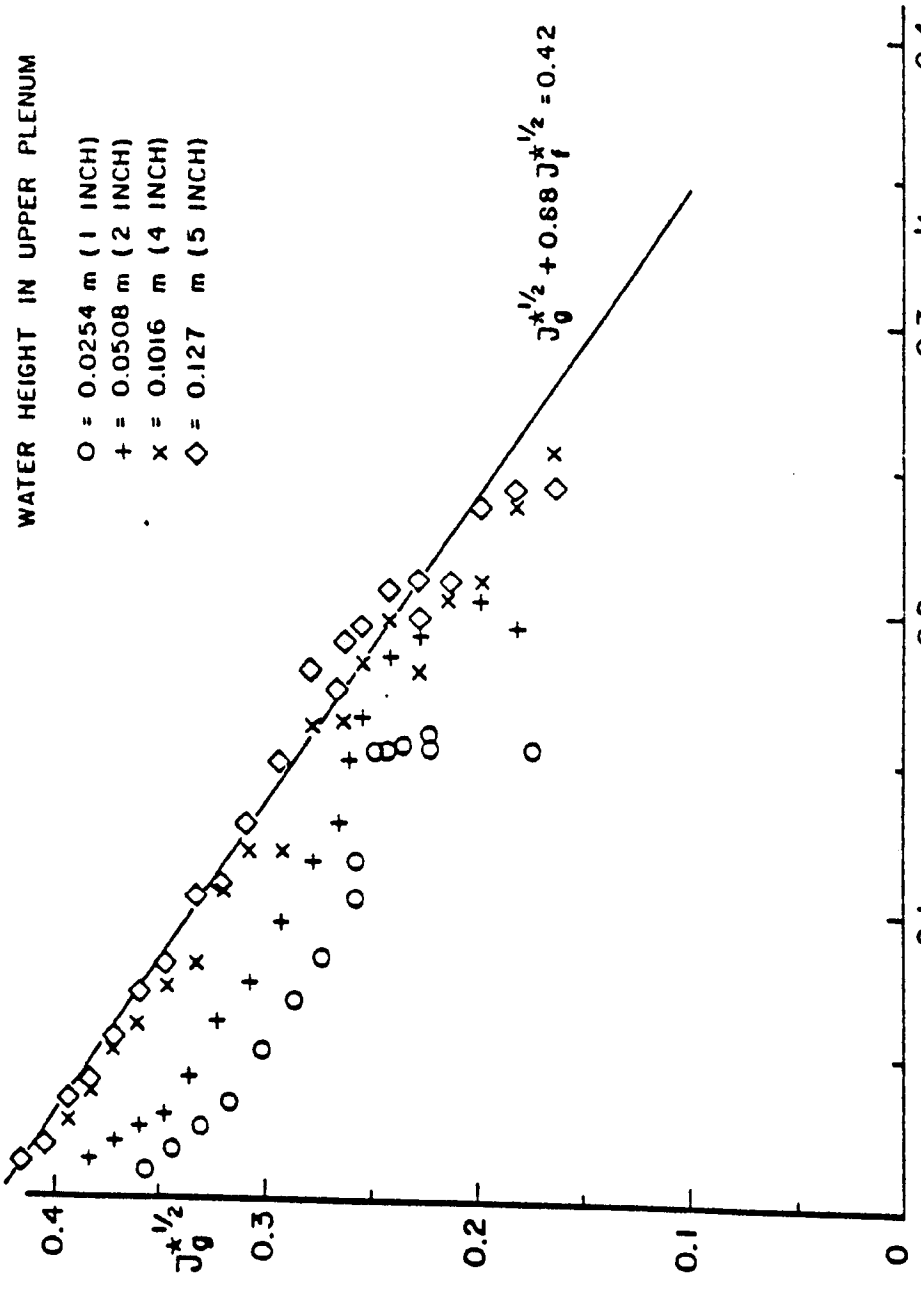

Fig 2.42 Nondimensional Gas Flux vs. Water Flux for Nonsymmetrical Top Flood. Different Water Heights in Upper Plenum – [Richter & Murphy (32)]

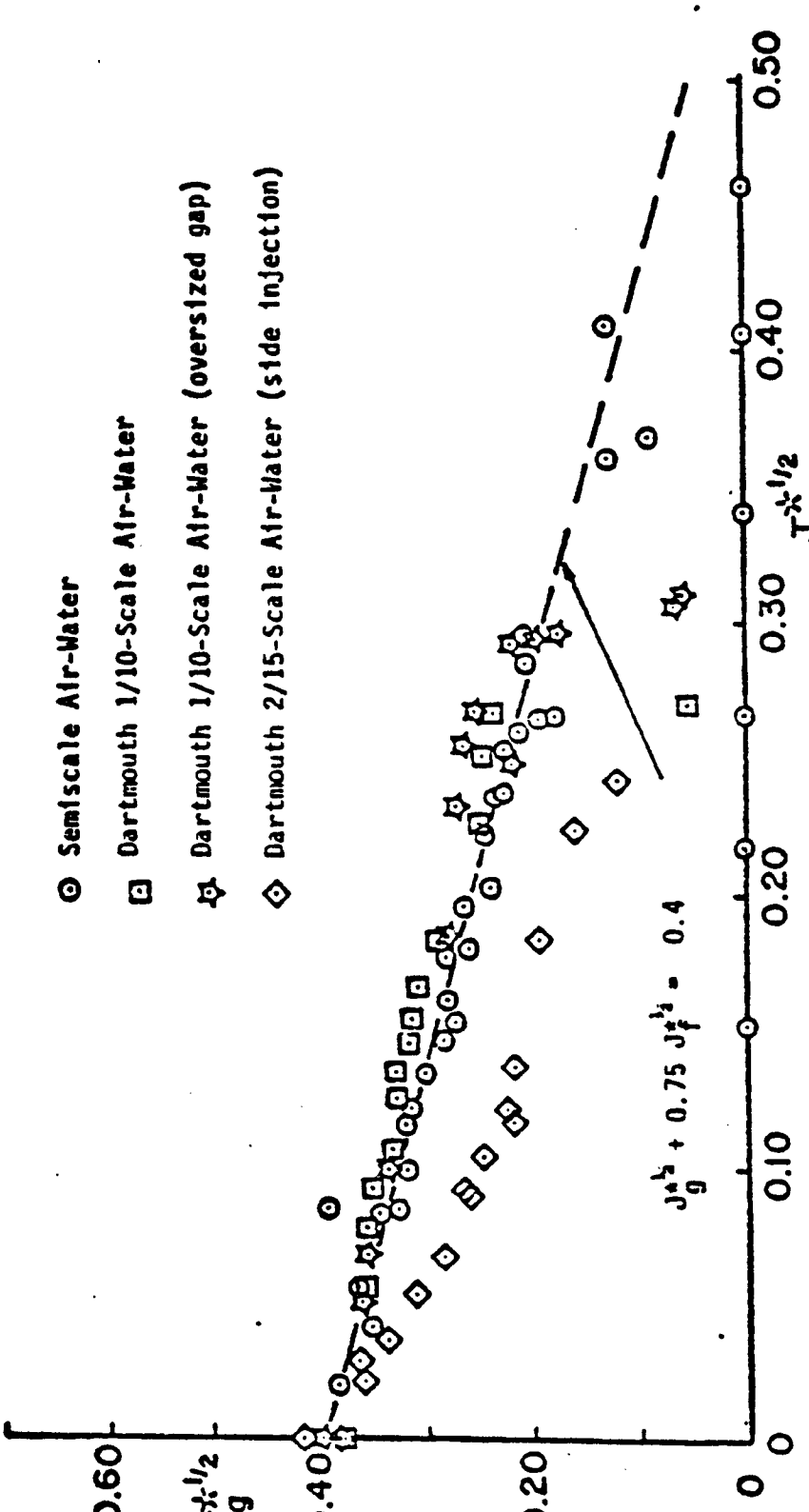

Fig 2.43 Water Penetration Data for Air. Comparison of Semiscale Data with Dartmouth 1/10 and 2/15-Scale Data. - [Richter & Wallis (33)]

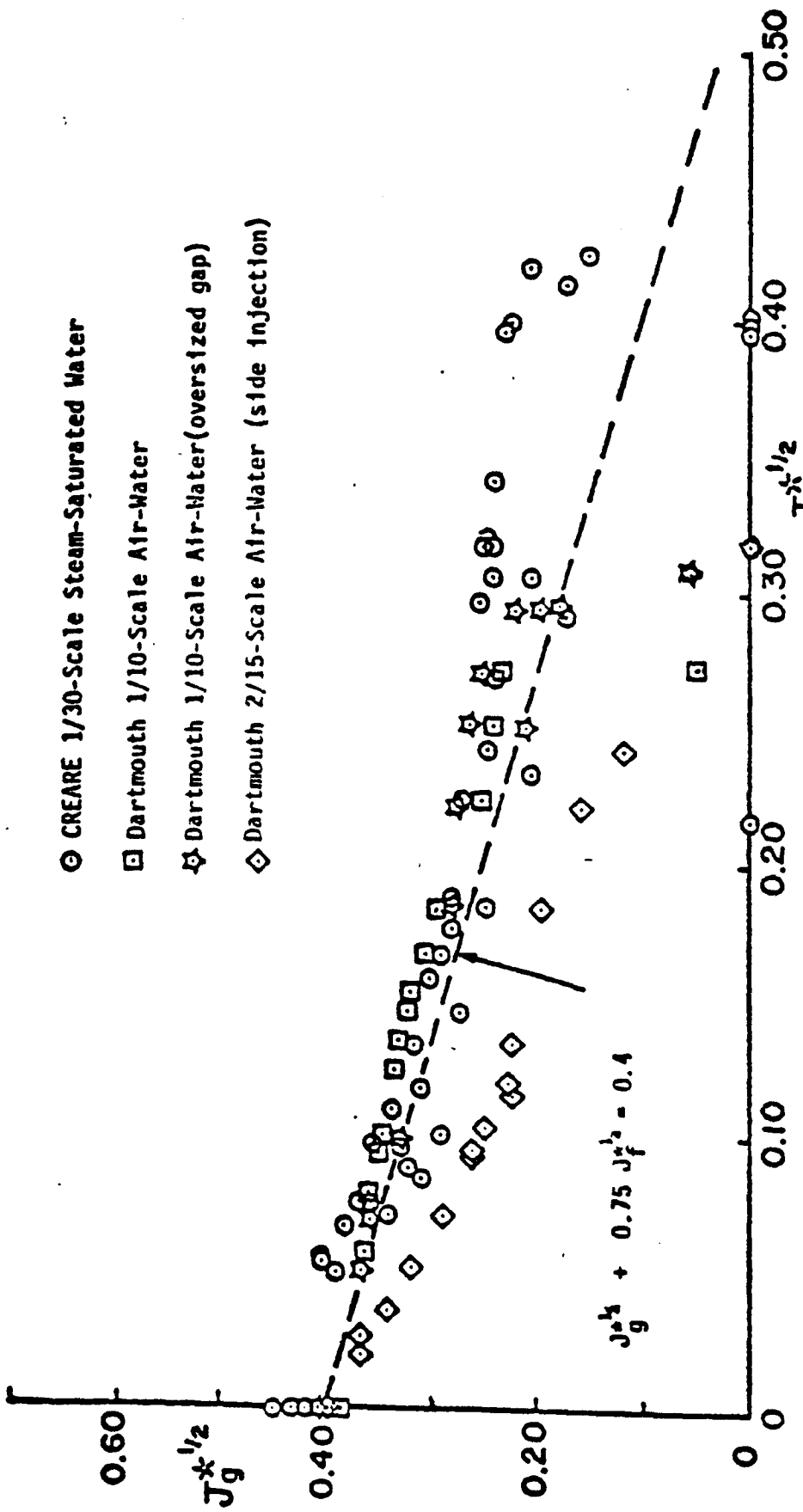

Fig 2.44 Water Penetration Data for Air and Steam. Comparison of CREARE 1/30-Scale Saturated Steam Data with Dartmouth 1/10- and 2/15-Scale Air Data.-[Ref.(33)]

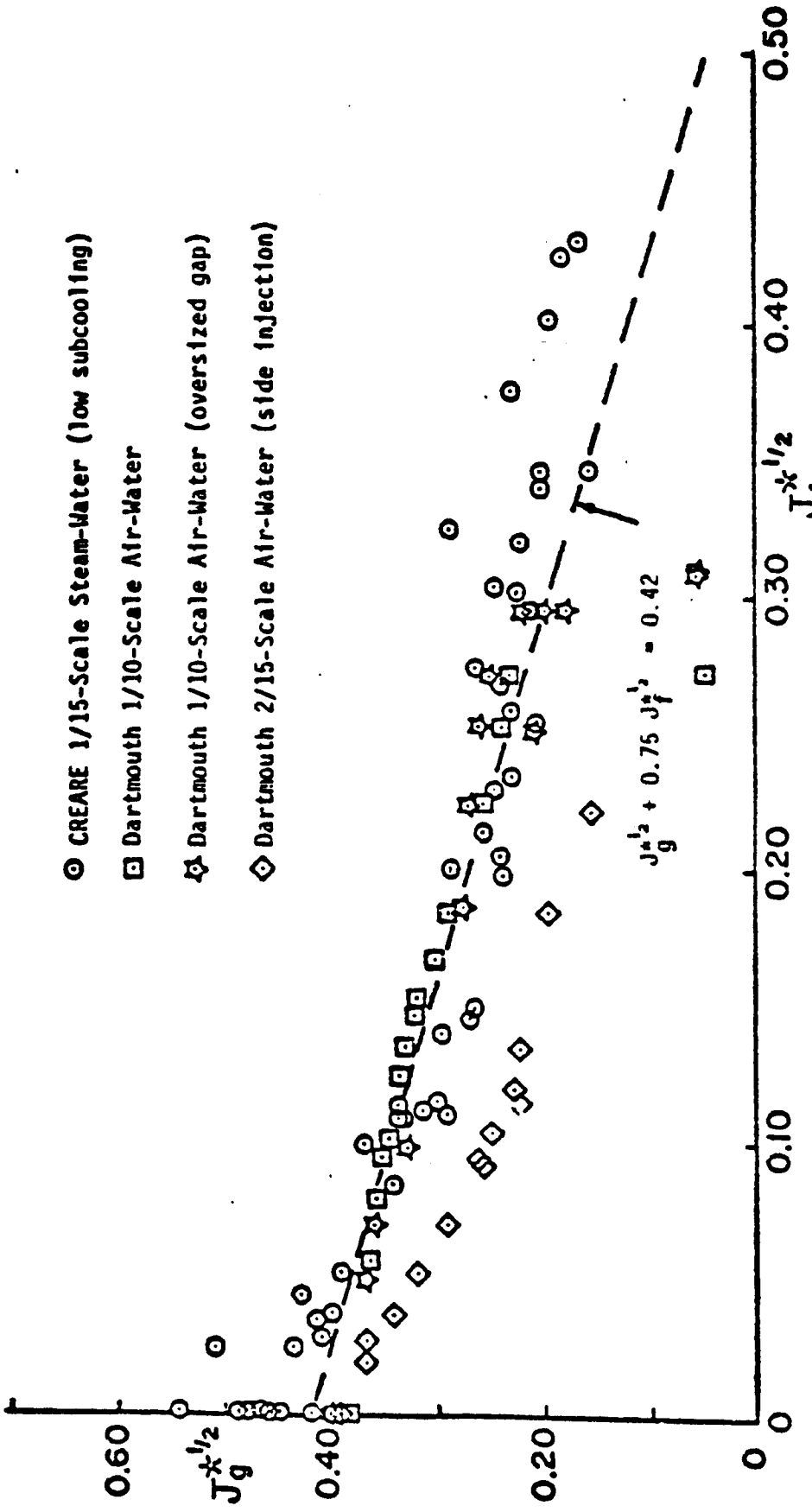

Fig 2.45 Water Penetration Data for Steam and Air. Comparison of CREARE 1/15-Scale Low Subcooling Data with Dartmouth 1/10 and 2/15-Scale Air Data-[Ref.(33)]

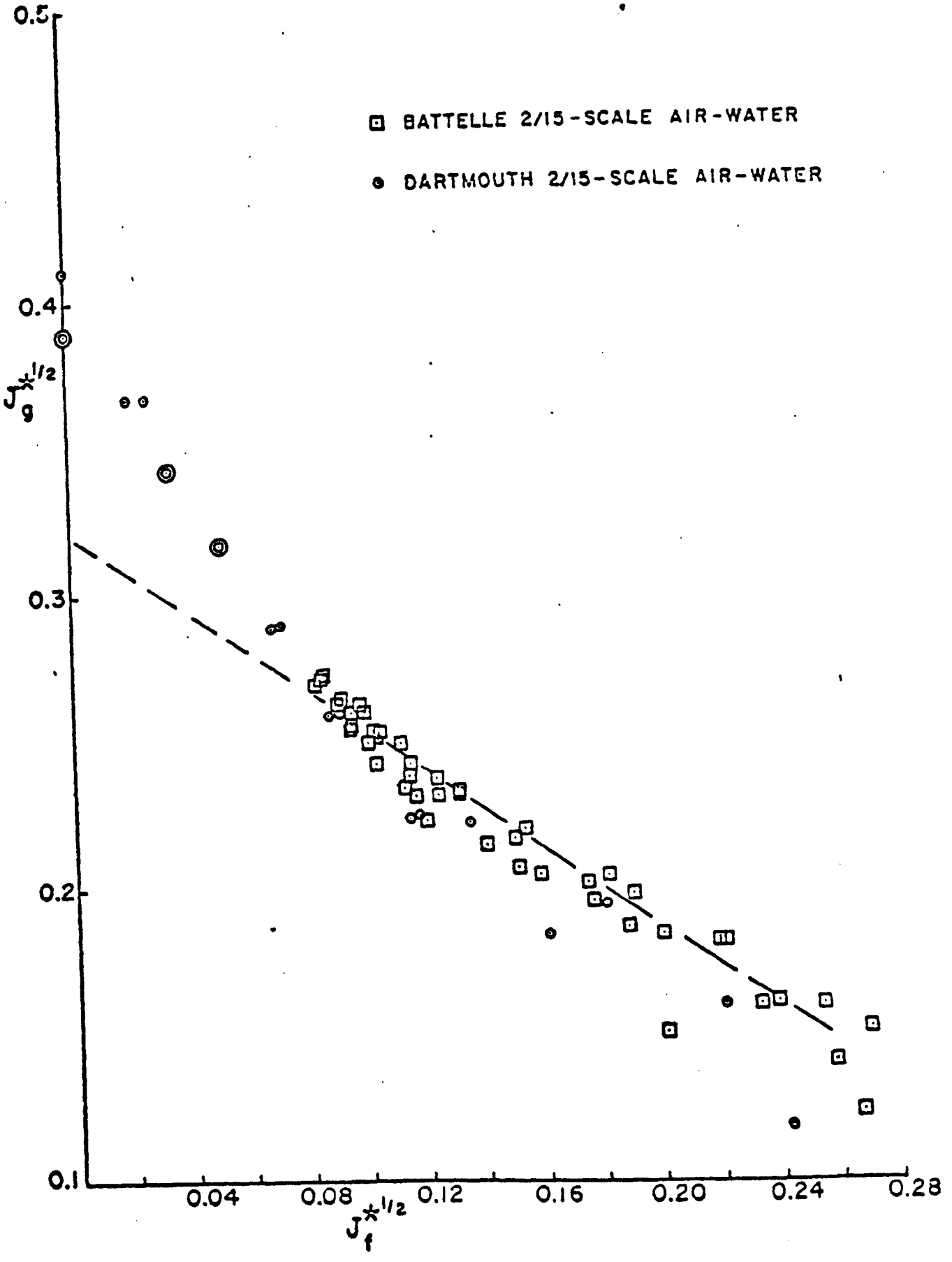

Fig 2.46 Water Penetration Data for Air. Comparison of Battelle 2/15-Scale Data and Dartmouth 2/15-Scale Data-[Richter & Wallis (33)]

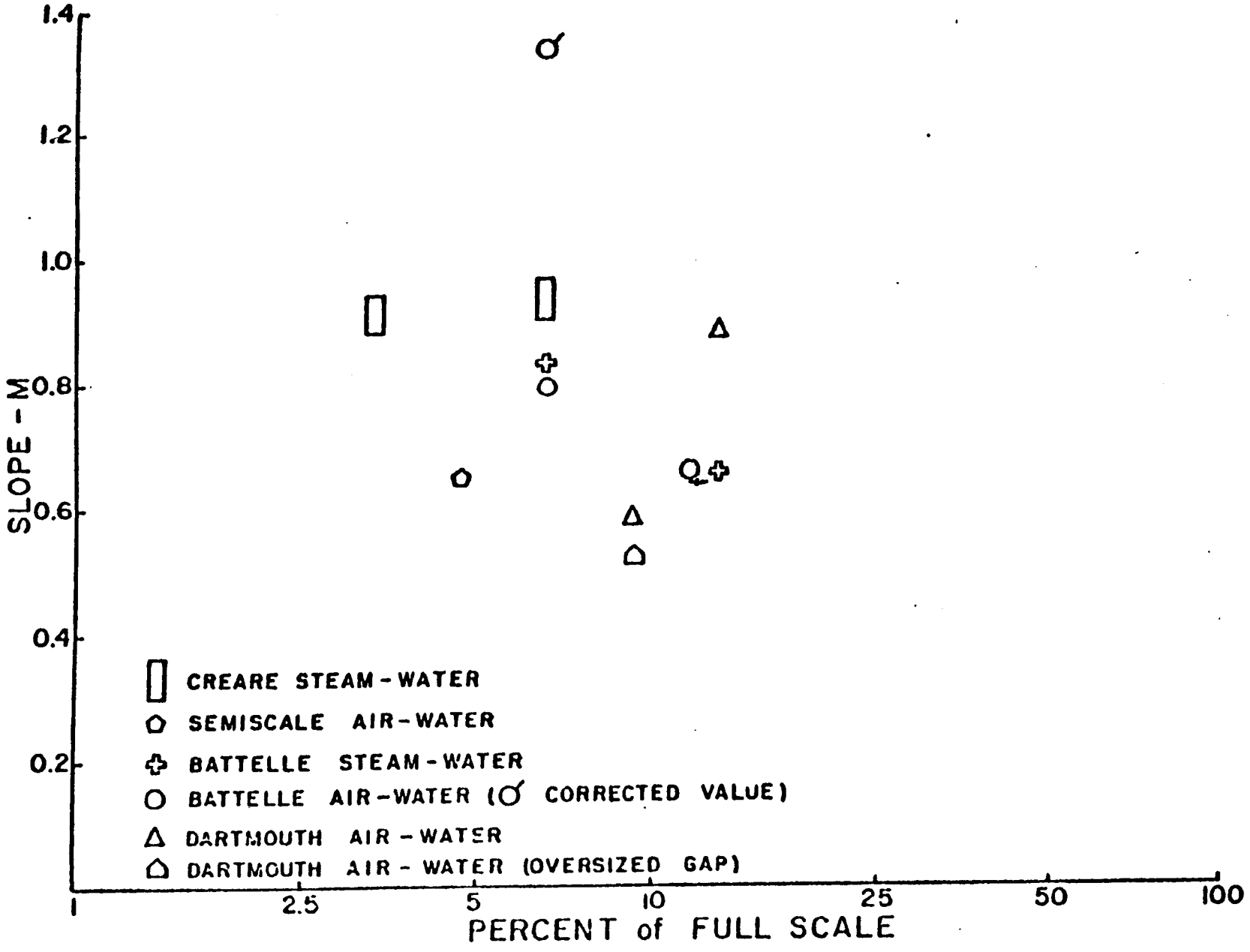

Fig.2-47 Slope M of Wallis Correlation as a Function of Scale - [Ref. (33)]

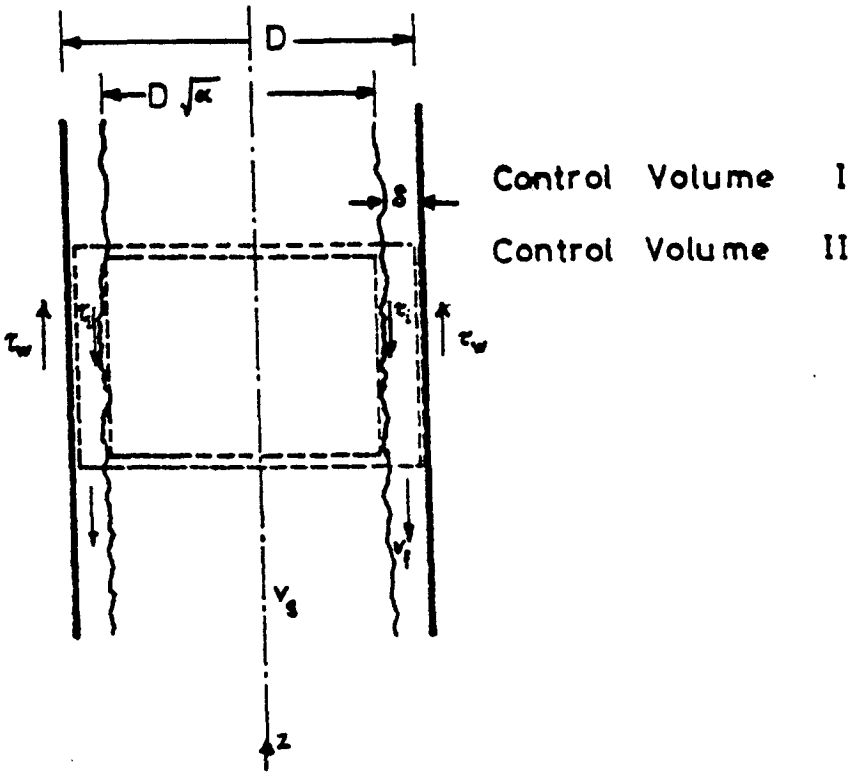

Fig 2·48 Momentum Balance in a Pipe Counter-current Flow-[Richter(34)]

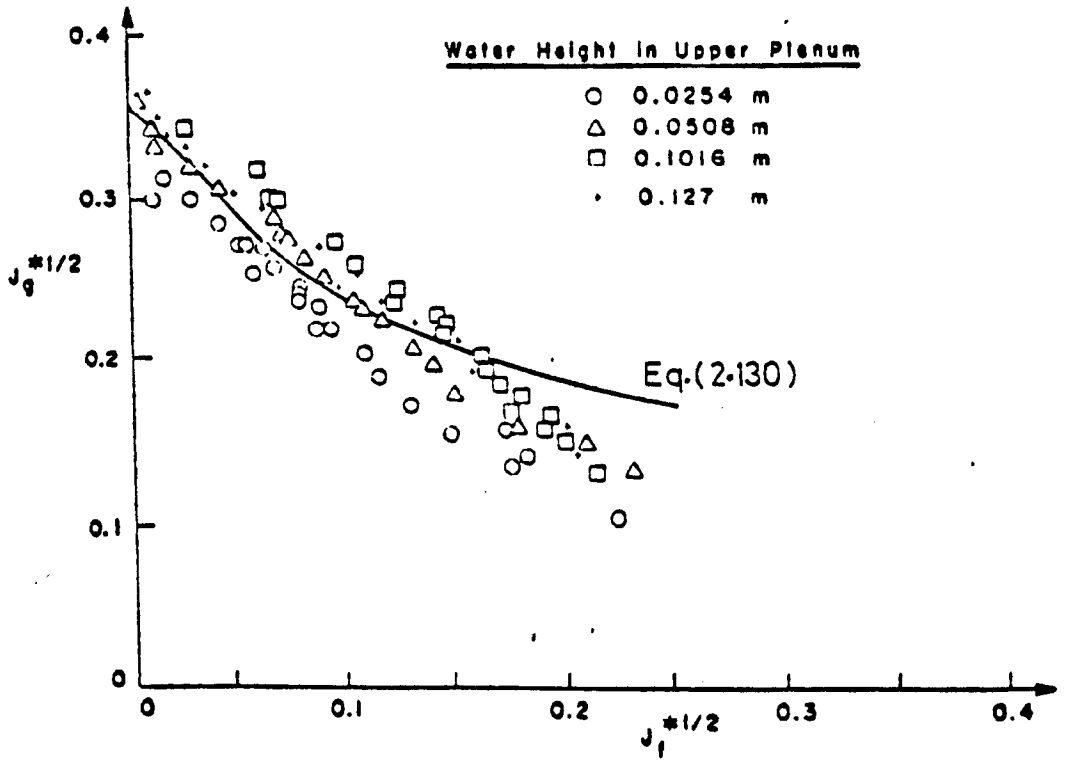

Fig 2.49 Nondimensional gas flux vs water flux for flooding in a 2/15 scale of a nuclear reactor annulus. –[Richter (34)]

P - PRESSURE MEASUREMENT.
T - TEMPERATURE MEASUREMENT
F - FLOWRATE MEASUREMENT

ALL MEASUREMENTS TRANSDUCED AND ELECTRICAL OUTPUTS TAKEN TO TIMING AND MULTIPLEX UNITS.

REACTOR TERMINOLOGY IS SHOWN IN BRACKETS.

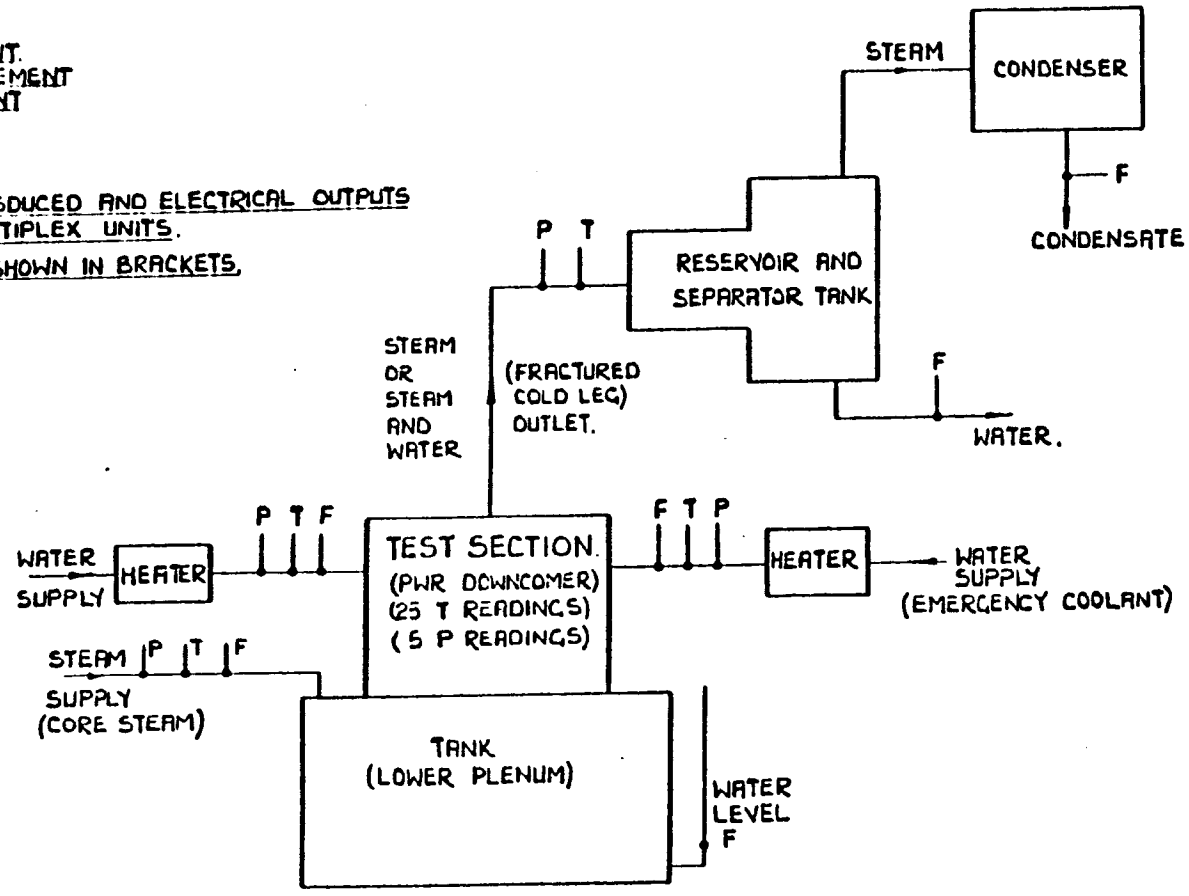

Fig 2·50 LINE DIAGRAM OF REFILL TEST RIG SHOWING INSTRUMENTATION.

[CAMPBELL (35)]

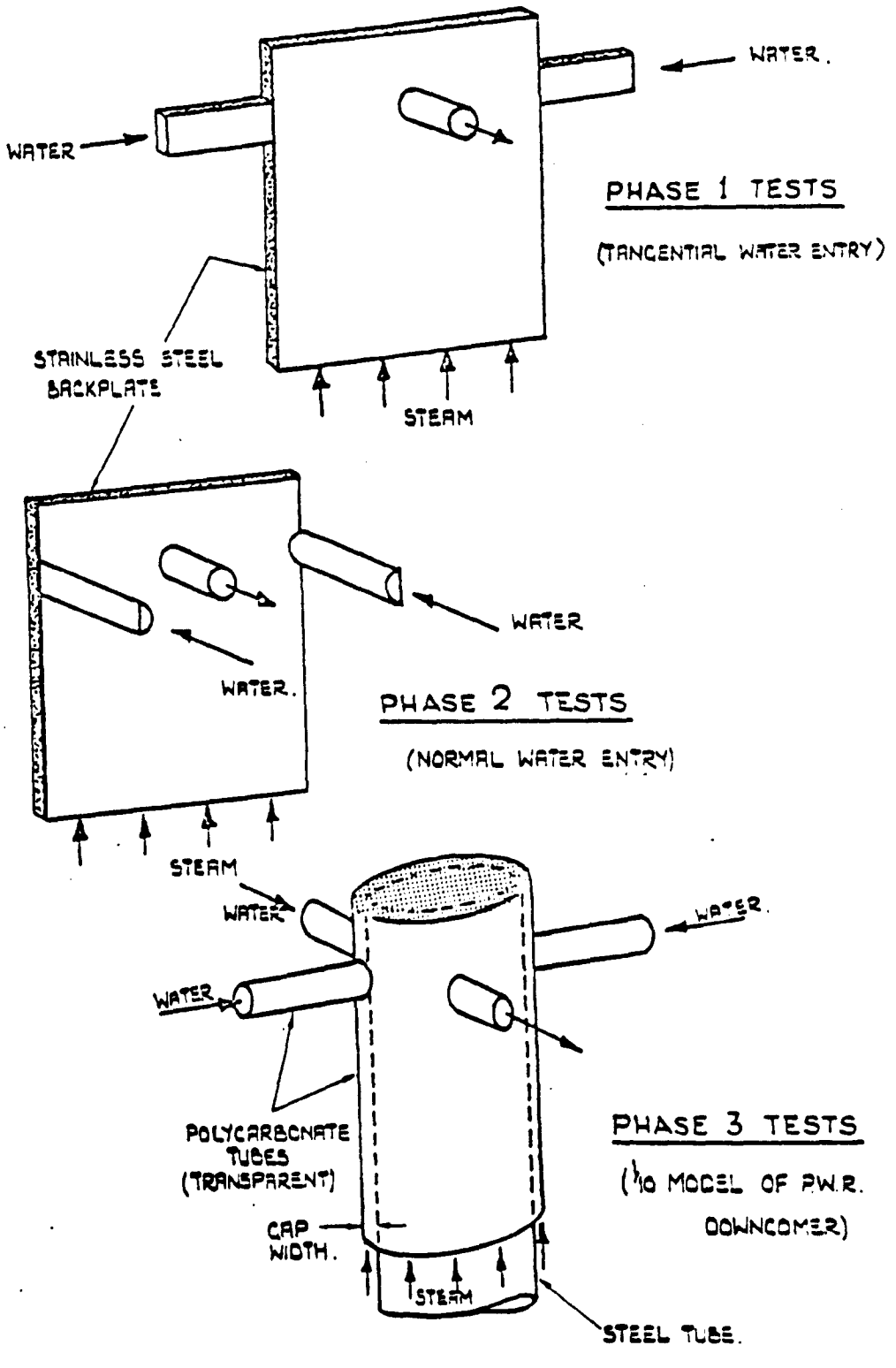

Fig 2·51 DETAILS OF TEST SECTIONS

[CAMPBELL (35)]

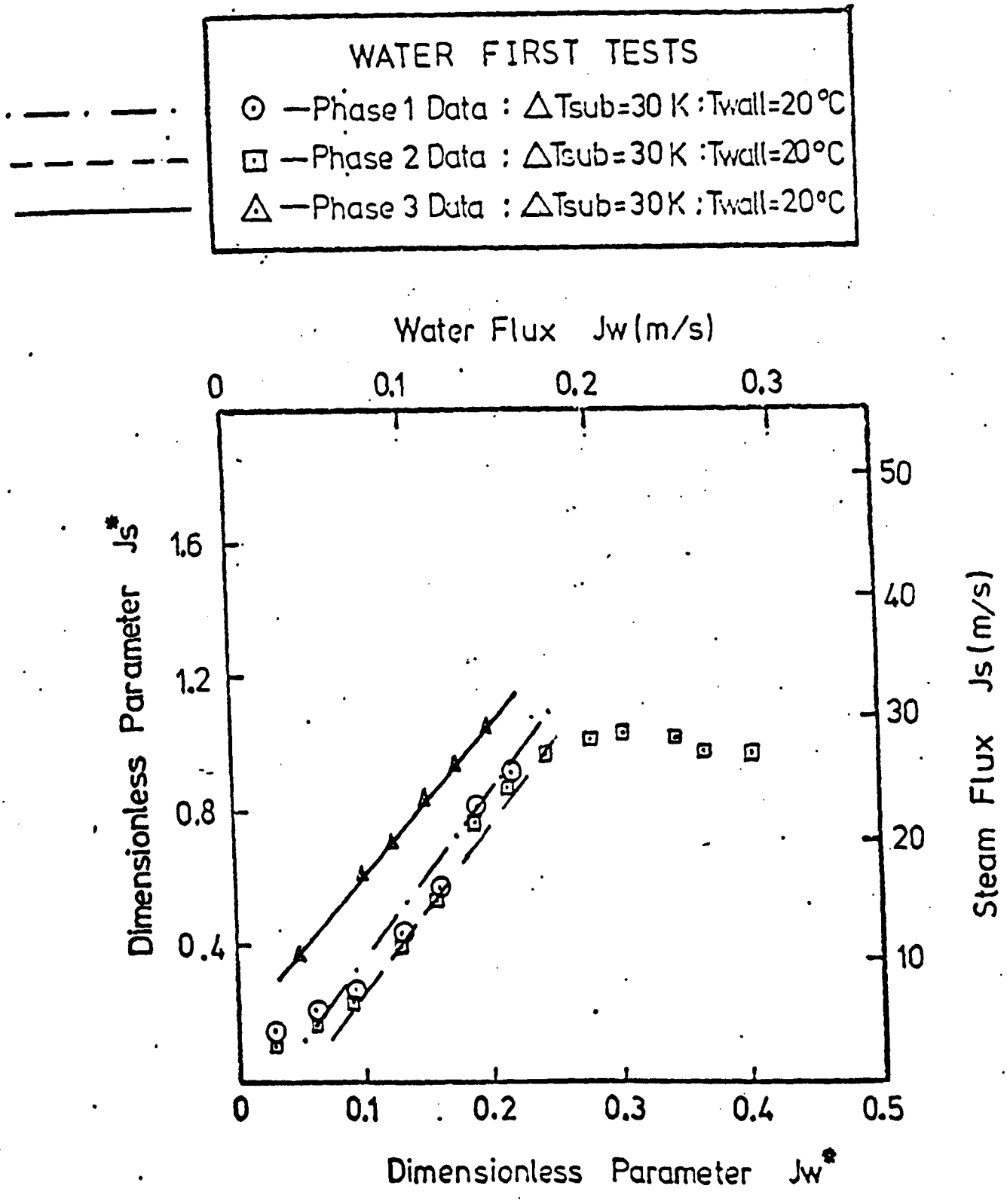

Fig 2·52 THE EFFECT OF GEOMETRY ON FLOODING [CAMPBELL (35)]

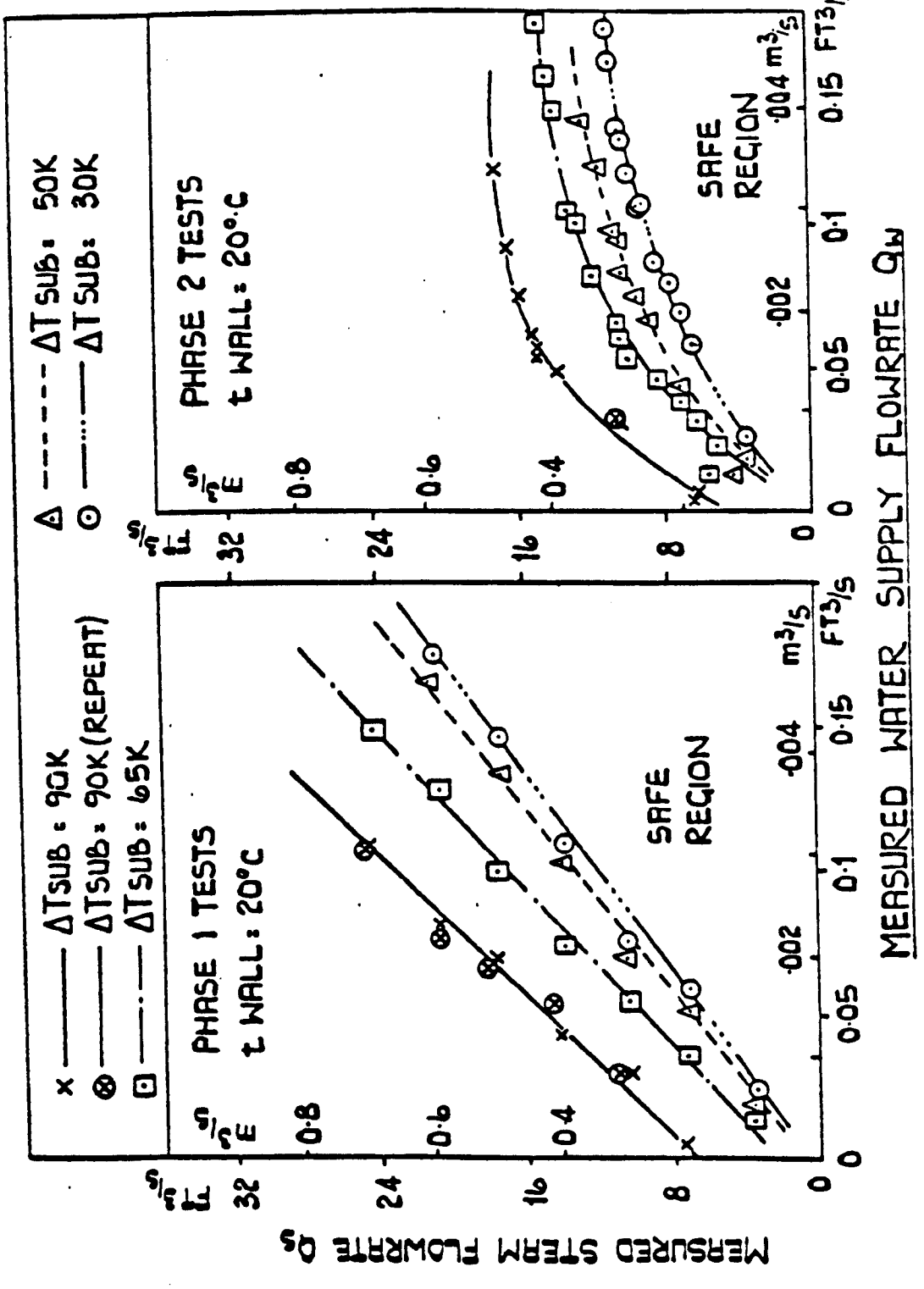

Fig 2.53 The Effect Of Inlet Subcooling On Flooding [Campbell (35)]

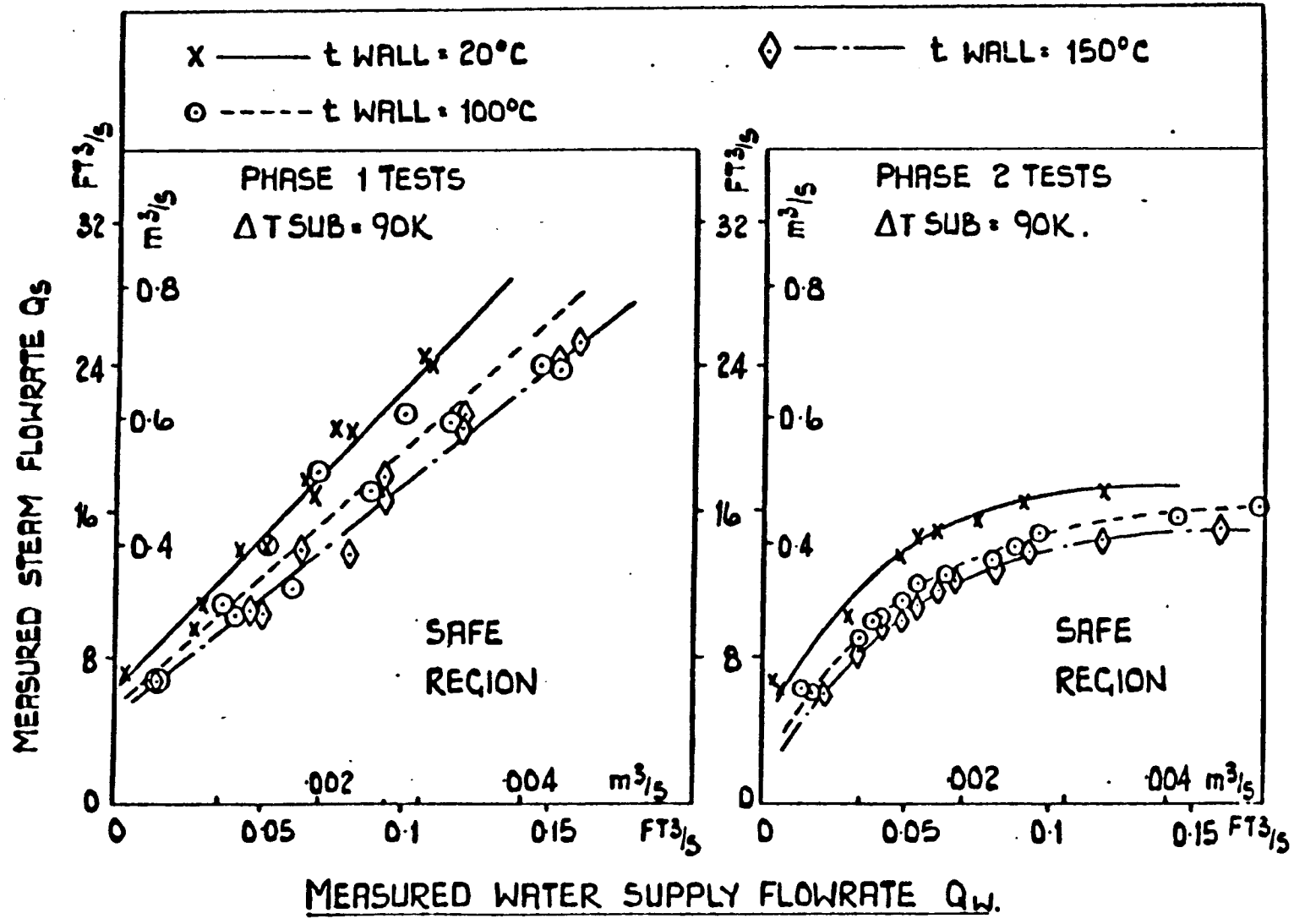

Fig 2.54 Effect Of Wall Temperature On Flooding [Campbell (35)]

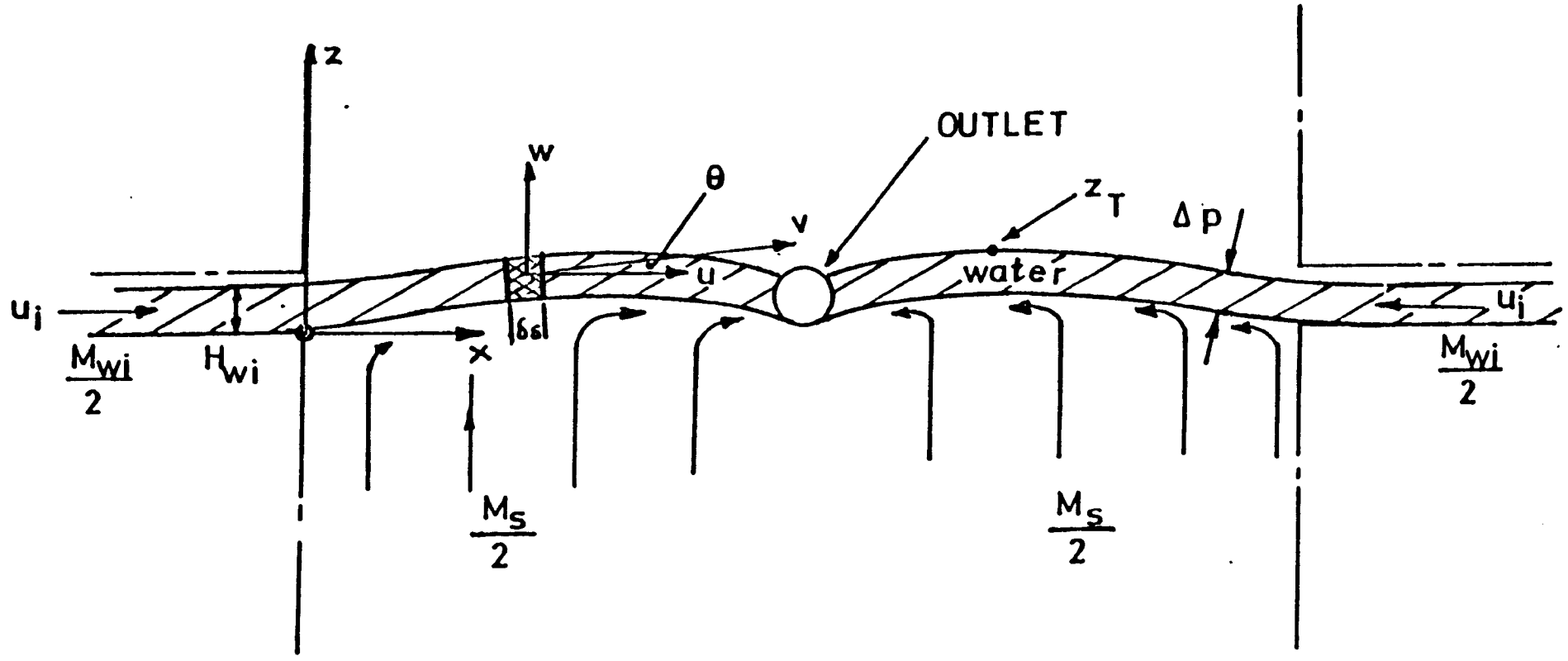

FIG 2.55 COORDINATE SYSTEM FOR WATER JET TRAJECTORY AND BRIDGE.

[SIMPSON et al (36)]

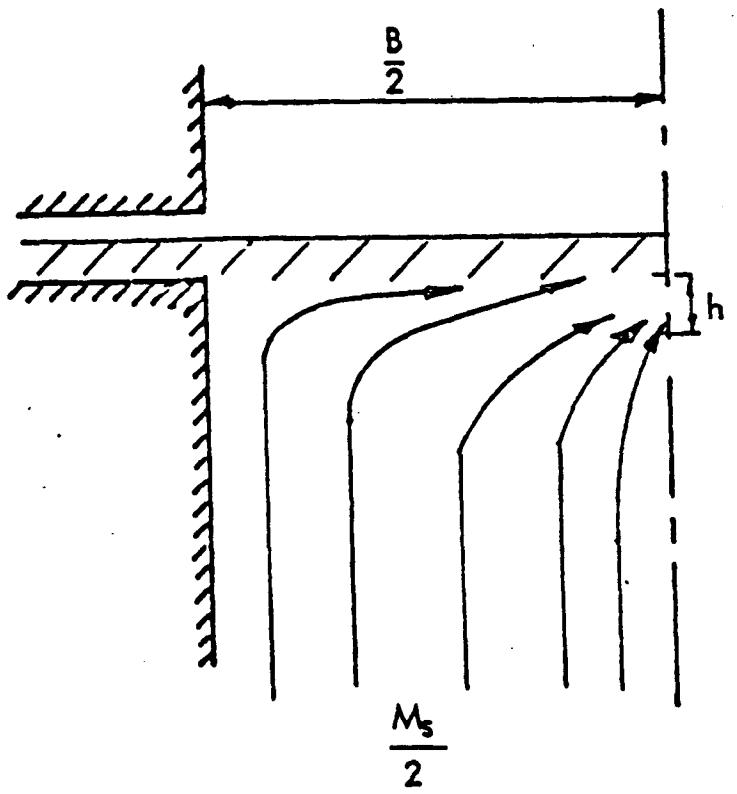

(a) NO INTERACTION BETWEEN STEAM AND WATER

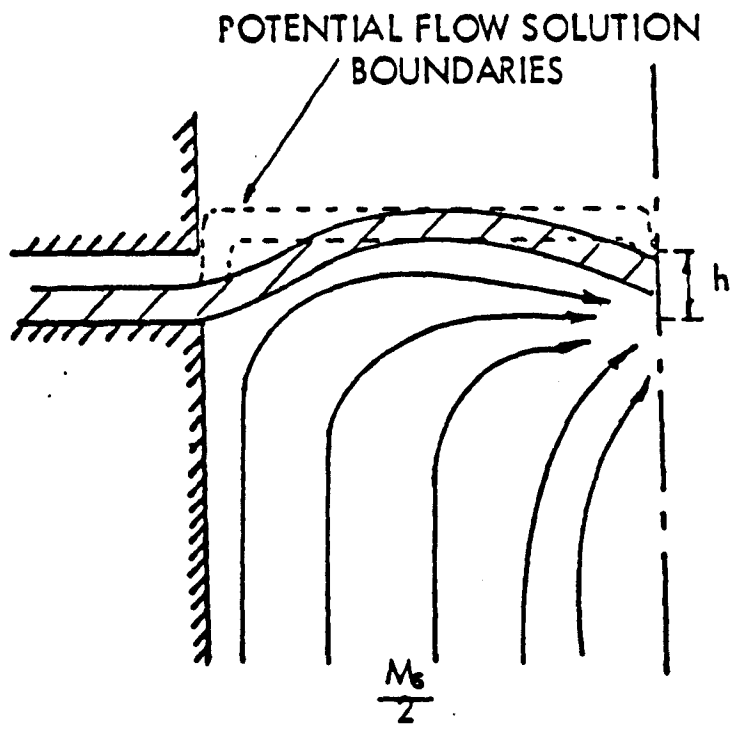

(b) INTERACTION BETWEEN STEAM AND WATER

Fig 2·56 APPROXIMATE STEAM FLOW PATTERNS

[SIMPSON et al (36)]

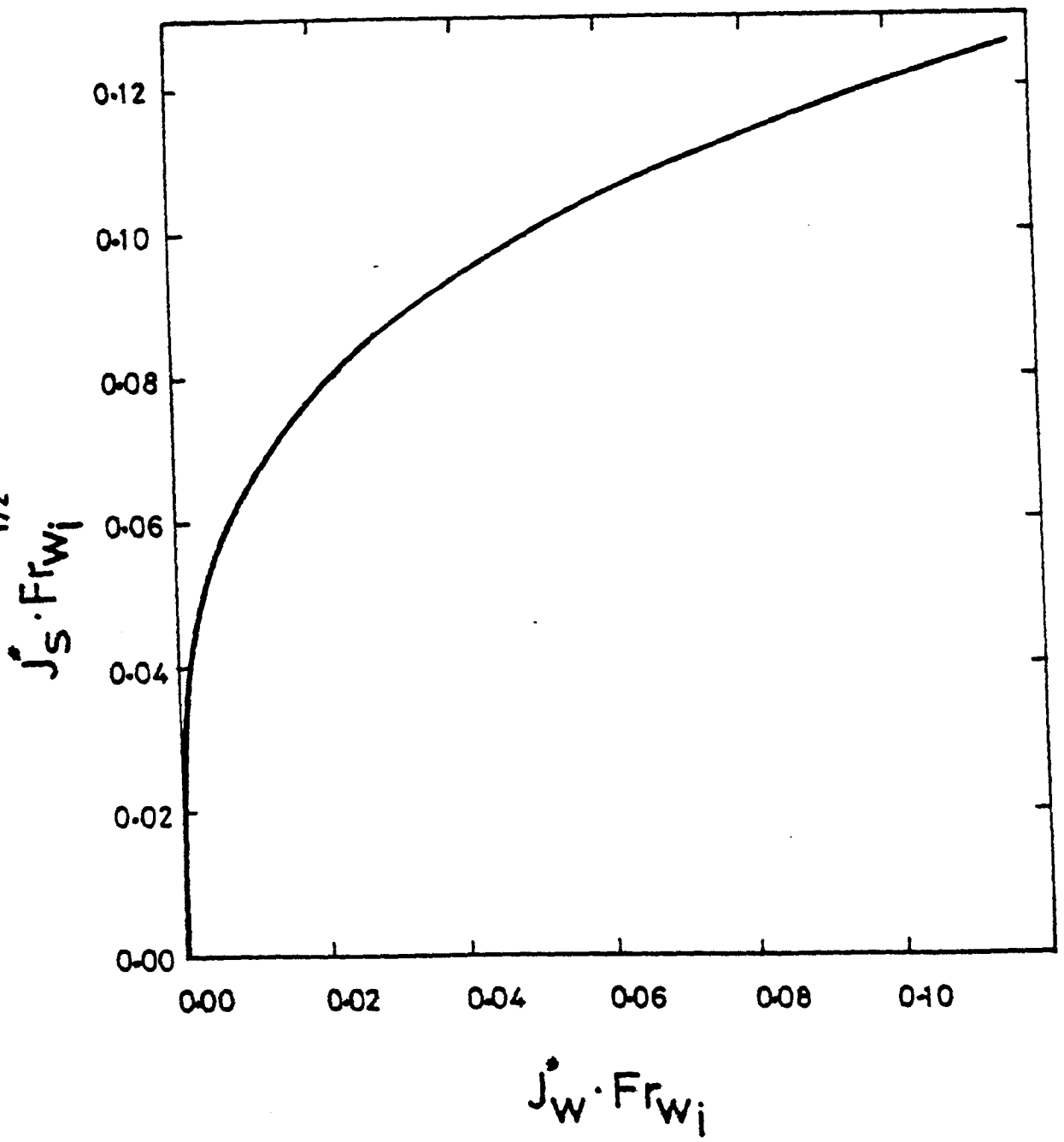

Fig. 2.57 Dimensionless Plot Of Bridging Conditions, Eqs. (2.142) - (2.144)

CHAPTER 3

APPARATUS AND INSTRUMENTATION

CHAPTER 3 : APPARATUS AND INSTRUMENTATION

3.1 EXPERIMENTAL APPARATUS

The experimental apparatus was similar in many respects to that used by Campbell (35) to simulate the conditions existing in the downcomer annulus of a PWR during a LOCA. It was constructed as a 1/10-scale representation of a typical Westinghouse PWR design and involved two different planar test sections which will be detailed later.

In the tests carried out by the author, the working fluids were air and water at pressures close to atmospheric since steam-water data were already available (35). Here the air represented the steam generated during the sudden depressurisation in the initial stages of the LOCA whilst the water represented the emergency core coolant. The air-water combination further represented the conditions whereby the steam and the injected water were at the same temperature so that no mass transfer occurred.

The test sections and adjacent pipe work were manufactured from transparent polycarbonate to allow visual studies of the physical mechanisms leading to bypass.

3.1.1. Layout of the Test Rig

A layout of the test rig and instrumentation is shown in Figure 3.1. Referring to this Figure, low

pressure air was introduced into the lower plenum tank* for passage up the test section and through the outlet pipe. The air flowrate was measured using an orifice plate inserted into the main air supply line and both air pressure and temperature were measured in the lower plenum.

Concurrent with the air entry, water was supplied at twin entry points (these representing the cold leg entry points in the real PWR). When total penetration of the injected water to the lower plenum did not occur, the air-water mixture passed out of the test section via the outlet pipe (representing the broken pipe in a cold leg break LOCA) to a tank mounted on a weighing machine. The temperature and flowrate of the water at each entry point were measured.

Details of the instrumentation used are given in Section 3.2.

3.1.2 Test Sections

Two test sections were used during the experimental programme and diagrammatic arrangements of these are shown in Figure 3.2

Referring to Figure 3.2, both of these test sections represented a 1/10-scale development (or planar model) of the downcomer annulus of a PWR. The width of the test

---

* The lower plenum tank was not a scaled version of the reactor lower plenum but was merely a tank for locating the"steam"entry and collecting the injected water which penetrated the downcomer.

section represented half the circumference of the annulus and was 686mm (27 inches); the gap size was 25.4mm (1 inch). The outlet pipe representing the broken cold leg was 76mm (3 inches) in diameter and was centred on one face of the test section at the same level as the entry pipes or ducts. The front face of the test section was manufactured from transparent polycarbonate and the back from stainless steel. The transparent front face allowed photographic and visual observations of the events inside the test section to be made.

The main difference between the two test sections concerned the water entry ducts. For Phase 1 tests, these were rectangular in cross-section, 76mm x 25.4mm, and were connected to each side of the test section providing a tangential type entry. For Phase 2 tests, the water entry ducts were half pipes of 76mm diameter connected normal to the test section. Each of the inlet ducts was provided with a scale at the junction with the test section to measure the water height at the brink. A photographic view of the test rig with the Phase 1 test section is shown in Figure 3.3.

3.1.3 Air and Water Supplies

The water supply to the test rig was taken from the main service supply in the laboratory, thus allowing a total capacity of 1.36×10^{-2} m^3/s for general use. The water temperature was generally $15^{o}c \pm 5^{o}c$.

The air was supplied by the laboratory compressor at a pressure of 200 psi. In order to reduce and maintain the pressure at 15 psi, a special reducing valve was used upstream of the test section.

3.2 INSTRUMENTATION AND MEASUREMENT

The measurements required during the tests were the air and water flowrates, the outlet water flowrate, various pressures and pressure differences and the temperature at a number of measuring stations.

The data was collected manually and recorded on data sheets.

3.2.1 Air Flowrates

The air flowrate measurements were made using an orifice plate in conjunction with a differential manometer and a digital thermometer. The orifice plate was manufactured and calibrated in accordance with BS1042 and details of the calibration are shown in Appendix A. The pressure tapping points were located at the D and D/2 positions and duplicate temperature measurements were made upstream of the orifice.

For low air flowrates two ROTAMETERS were used, the calibration of these being carried out in accordance with the manufacturer's recommendation. Details of the rotometer calibration are given in Appendix B.

3.2.2 Water (Coolant) Flowrates

Measurements of inlet water flowrates were made at each entry point using turbine flowmeters. These are volume flowrate measuring devices which utilise the speed of rotation of the turbine rotor and its characteristic dimensions, the rotor speed being measured by an electronic pick-up unit and the signal passed to a calibrated meter. The turbine flowmeters were calibrated in situ before and after Phase 1 tests. Before the start of Phase 2 tests, the flowmeters were returned to the manufacturers for general overhauls. On return to the laboratory, another in situ calibration was carried out. Details of these calibrations and graphs representing the characteristics of the turbine flowmeters are shown in Appendix C.

3.2.3 Outlet Water Flowrates

The water passing out through the broken leg was directed to a large tank mounted on a weighing machine that could measure up to 2000lbs mass. The lever on the weighing machine was divided into divisions of ½lb.

The technique for measuring the water flowrate was very simple and straight-forward. The weighing machine was adjusted to indicate a particular reading, when this weight was reached and the lever started to move, a stop-watch was started and then the weighing machine was adjusted to a higher weight. When that weight was reached the stop-watch was stopped. The difference

between the two weights divided by the recorded time gave the outlet water flowrate. The difference in weight and the time taken were large enough to minimise measurement errors.

3.2.4 Pressure Measurements

Two pressure gauges were installed upstream of the orifice plate and the rotameters which could read up to 2.5 bars. The lower plenum pressure was measured using a U-tube. For low pressures, coloured water was used as the manometric fluid in the U-tube. For higher pressures, mercury was used.

The pressure difference across the orifice plate was measured by a differential manometer.

3.2.5 Temperature Measurements

An electronic digital thermometer capable of measuring temperatures with accuracy of $\pm 0.1^{\circ}c$ was used. The digital thermometer had 10 input channels which allowed duplication of all temperature measurements to be made in the interests of accuracy and reliability.

The temperatures measured were:

(i) The air temperature upstream of the orifice plate or rotameters.

(ii) The air temperature in the lower plenum.

(iii) The inlet water temperature upstream of the turbine flowmeters.

(iv) The water temperature in the lower plenum.

(v) The water temperature in the outlet pipe.

3.3 TEST PROGRAMME AND PROCEDURES

The tests were designed to obtain information on the critical conditions required for bridging, in the absence of heat or mass transfer, under different geometries and methods of introducing air and water.

The test programme covered a range of conditions which can be summarised as follows:

1. Air Flowrate : 0 - 0.25 m^3/s
2. Water Flowrate : 0 - 0.005 m^3/s
3. Air Temperature : 10 - 20^{o}c
4. Water Temperature : 10 - 20^{o}c
5. Air Pressure : 0.8 - 1.15 bar

3.3.1 Methods of Testing

Two methods of testing were used. In one, the water was introduced first to the test section and then the air was introduced (i.e., water-first tests). In the other, the air flow was established before the water was introduced (i.e., air-first tests).

In the water-first tests, a steady flowrate was introduced into the test section, evenly distributed between the inlet pipes, and the air flow increased gradually, until liquid bridging occurred. This procedure was repeated over a range of water flowrates for both Phase 1 and Phase 2 tests.

In the air-first tests, a steady air flowrate was established in the test section before the main on/off valve was opened to allow a pre-set amount of water to flow evenly and simultaneously into the test section via the two inlet pipes. For Phase 1 tests, the air-first tests were carried out by introducing a steady air flowrate and increasing the water flowrate in steps and recording the different readings and visual observation. For Phase 2 tests, a different procedure was followed to allow comparison between air-first and water-first. The water flowrate was adjusted and then the main control valve was shut, then air was introduced and when it was established, the main control valve was opened. This procedure was repeated for a range of air flowrates.

3.3.2 Experimental Procedures

Before and after each phase of tests, the turbine flowmeters were calibrated.

Prior to any test the lower plenum was checked to ensure it was empty of water, thus avoiding lower plenum voiding which would give false outlet water flowrate values.

Sufficient time was given to achieve steady state condition before the measurements were recorded. The unprocessed data for Phase 1 and 2 tests are tabulated in Appendix D.

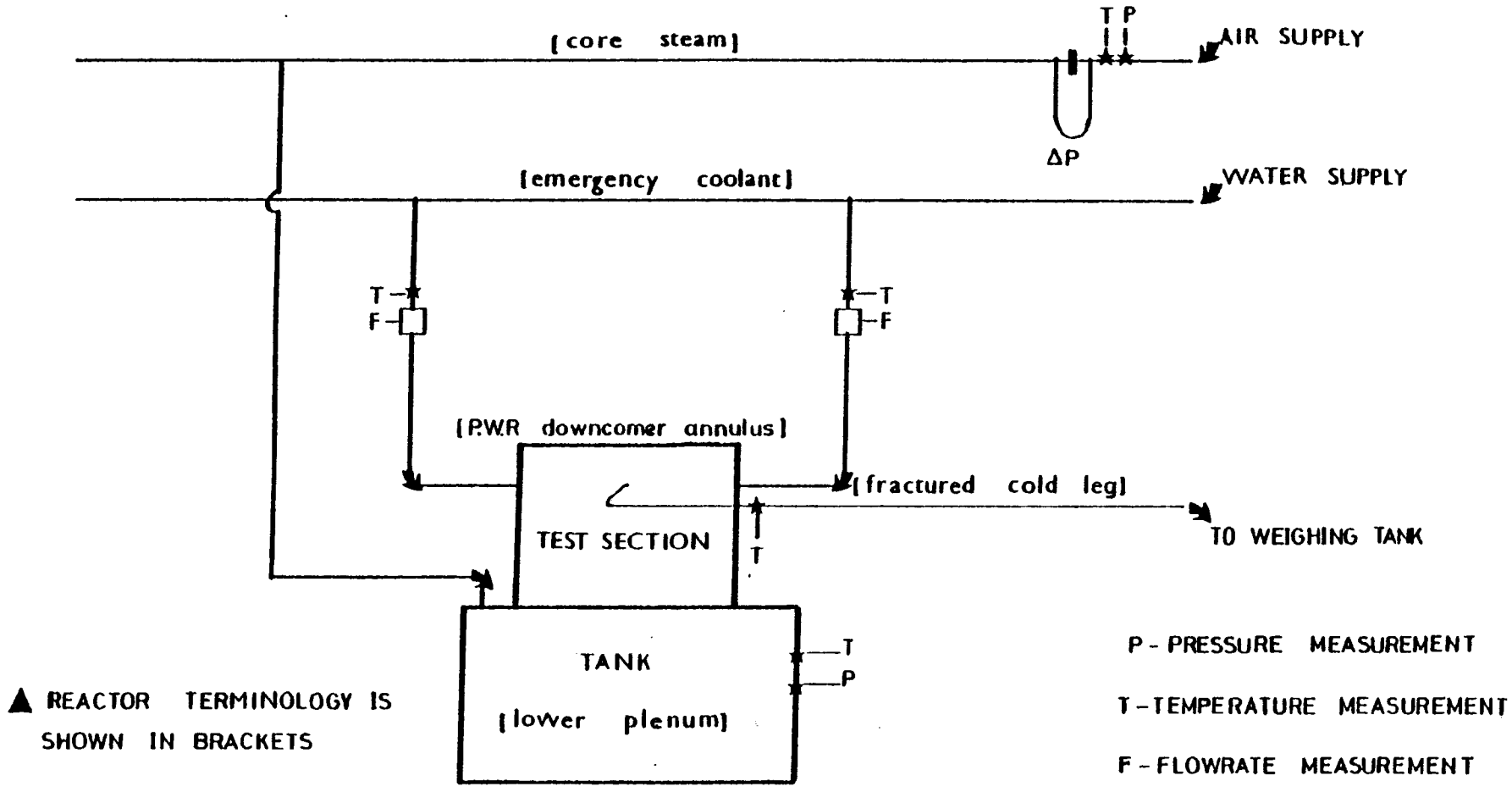

Fig 3.1 Line Diagram Of Test Rig Showing Instrumentation Points

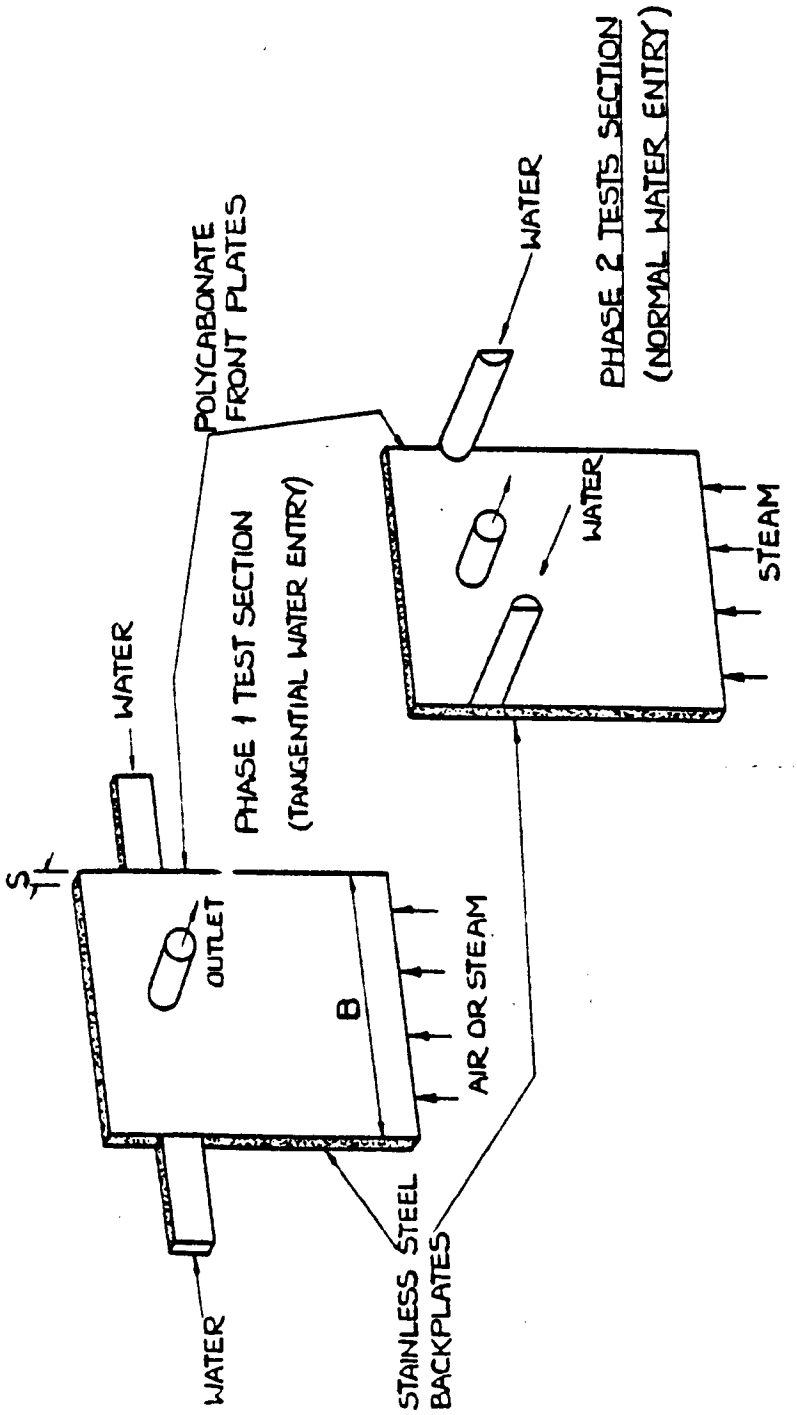

Fig 3.2 DETAILS OF TEST SECTIONS

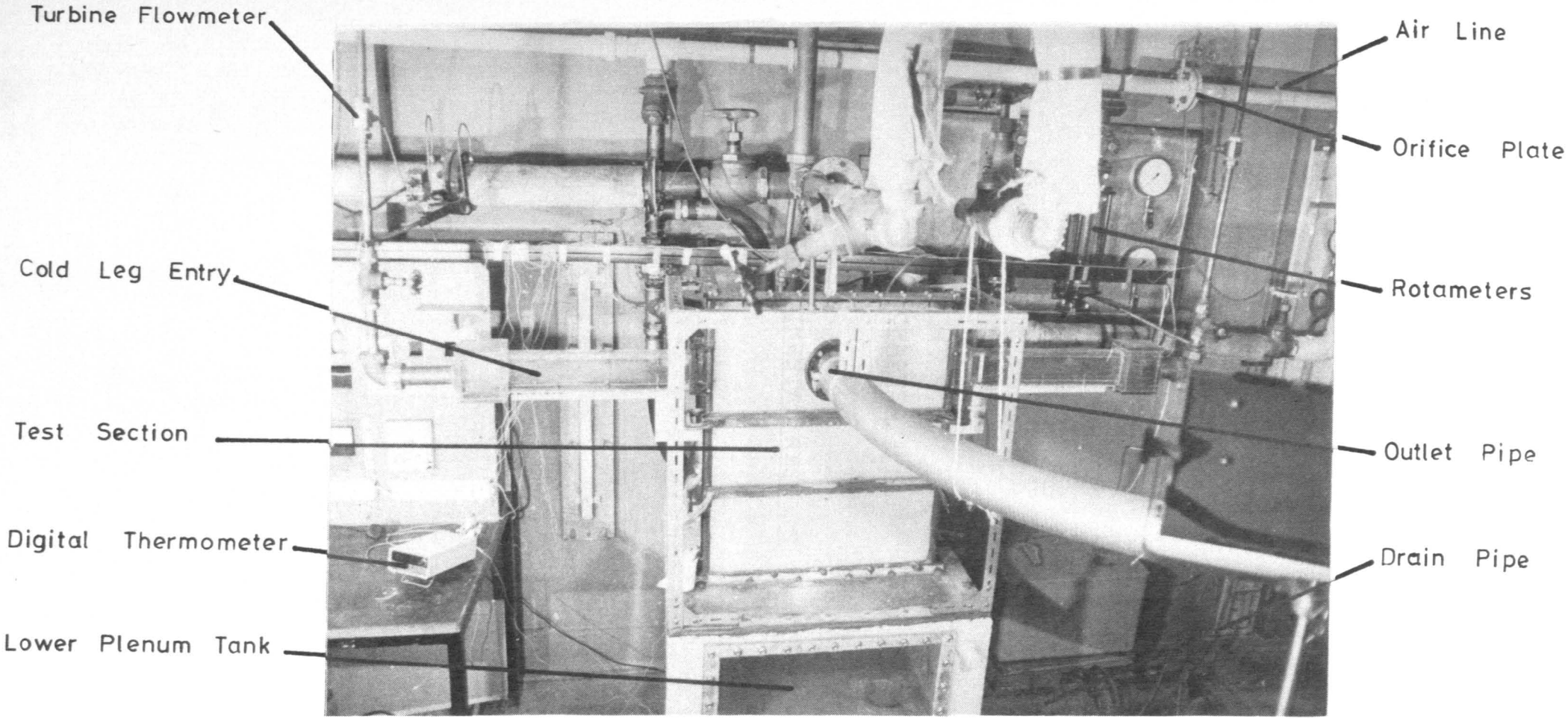

Fig 3-3 General View Of Refill Test Rig - Phase 1

CHAPTER 4

EXPERIMENTAL RESULTS

CHAPTER 4 : EXPERIMENTAL RESULTS

In this Chapter, the air-water data are presented for both the Phase 1 and Phase 2 tests and include :

(i) A complete physical picture of the events leading up to liquid bypass and a description of the various flow patterns observed during the tests.

(ii) Tables of experimental data relating to conditions up to and beyond bypass (or liquid bridging) for a range of air and water flowrates.

(iii) Graphs illustrating the water penetration characteristics and critical conditions for liquid bridging.

(iv) Correlation of experimental data in terms of the Wallis J* dimensionless flux parameters for air and water.

(v) The results from auxilary tests carried out to establish the relationships between water flowrate and liquid level in the inlet water pipes at the brink of the test section.

These are dealt with in turn.

4.1 DESCRIPTION OF FLOW PATTERNS

4.1.1 Phase 1 Tests

Consider the water first type tests, defined in Section 3.3.1, where water was passed in from the sides of the test section, in the form of two waterfalls as shown in Figure 4.1-a, and air introduced into the bottom of the test section. As the air rose between the two waterfalls, the suction caused the two jets to come together, (Figure 4.1-b), forming a barrier to the upward rise of air. It was observed however that the two waterfalls opened along the centre plain of the test section to form a passage for the upward rise of the air moving against the downwards film flow of the water (this is indicated in the side views). An increase in air flow caused the bridging of the two waterfalls to occur further up the test section until ultimately the bridge reached the outlet hole, as shown in Figure 4.1-c, where bypass of water commenced. A further increase in air flow enhanced the water entrainment until the waterfalls lost their identity and the air-water combination became a turbulent two phase mixture in the test section, with practically none of the inlet water flow penetrating to the bottom of the test section (Figure 4.1-d). The conditions for the flow patterns shown in Figure 4.1 are indicated approximately in Figure 4.2.

For the air-first test series, the flow patterns obtained were generally similar to those described above, except that under some particular conditions, an anti-clockwise vortex developed around the outlet hole allowing more water to penetrate to the lower plenum.

4.1.2 Phase 2 Tests

The flow patterns in the Phase 2 test series were predominantly film flows which did not fill the test section. The flow patterns obtained without a counter-current air flow confirmed those predicted by the flow regime map given in reference (24).

In the water first tests, the impinging water jets formed a film on the back plate. At small values of air flow, the water film passed undisturbed to the lower plenum; as the air flow was increased a point was reached where surface waves on the liquid film were evident at the bottom of the test section. With further increase in the air flowrate, the waves appeared to become stationary before moving up the test section and causing liquid bypass to occur shortly afterwards. At higher air flows, as in Phase 1, the air-water combination became a turbulent two-phase mixture in the test section with complete bypass not quite being achieved due to the location of the inlet pipes which allowed a small amount of inlet water to run down the side walls into the lower plenum.

In the air-first tests, the flow patterns were identical to those described above for water-first tests. In contrast to the Phase 1 tests (air-first), vortex motion was not observed.

4.1.3 Cine Films

As part of the test programme, cine films were taken to help in the understanding of the experimental results. All of the flow patterns identified above could be seen and were captured in the cine films, which are stored in the Department of Thermodynamics and Fluid Mechanics, University of Strathclyde.

4.2 TABLES OF EXPERIMENTAL DATA

The test data are tabulated in Appendices E, for Phase 1 tests, and F, for Phase 2 tests. The data are identified in terms of either "air-first" or "water-first" tests with the main data recorded for each type being:

(i) Inlet water flowrate, M_{wi}.

(ii) Entrained water flowrate, M_{WO}.

(iii) Water penetrating to the lower plenum, $M_{W_{LP}}$.

(iv) Air flowrate entering the test section, M_A.

Tables 1 to 18 in Appendices E and F show the experimental data relating to water-first and air-first tests and cover the conditions before inception of bypass, partial penetration and complete (or near complete)

bypass.

4.3 GRAPHICAL RESULTS

The experimental data are presented graphically using the dimensionless parameters J^*_{wi}, $J^*_{w_{LP}}$, J^*_A given by

$$J^*_{wi} = \frac{M_{wi}}{A \rho_w} \left[\frac{\rho_w}{gB(\rho_w - \rho_A)} \right]^{\frac{1}{2}} \quad (4.1)$$

and

$$J^*_{w_{LP}} = \frac{M_{w_{LP}}}{A \rho_w} \left[\frac{\rho_w}{gB(\rho_w - \rho_A)} \right]^{\frac{1}{2}} \quad (4.2)$$

and

$$J^*_A = \frac{M_A}{A \rho_A} \left[\frac{\rho_w}{gB(\rho_w - \rho_A)} \right]^{\frac{1}{2}} \quad (4.3)$$

where

A = Cross sectional area of the test section

B = Width of the test section which was chosen as the characteristic length dimension in J*.

(Note: In this thesis, the symbol J* is used to denote the dimensionless flux based on the width of the test section B to differentiate between it and j*, which is based on the hydraulic diameter or the gap size)

Typical penetration characteristics for Phase 1 tests are shown in Figure 4.3 (water-first) and Figure 4.4 (air-first) and for Phase 2 tests in Figure 4.5 (water-first) and Figure 4.6 (air-first). The lines shown

represent a "best fit" through the data. It should be remembered, however, that the air-first tests for Phase 1 and Phase 2 were carried out in a different way as mentioned previously in Chapter 3. Only the test run plotted in Figure 4.6 was done in a way similar to that of Phase 1 to enable comparison between the two Phases. The complete set of data can be found in Appendices G and and H.

Considering the water-first tests for both Phase 1 and Phase 2, these show that at low air flowrates all the inlet water penetrated to the lower plenum and this is represented by the data following a vertical line in the graphs. As the air flow increased a point is reached whereby part of the liquid is entrained and the water penetrating to the lower plenum is consequently decreased. A further increase in the air flow results in a further decrease in the lower plenum penetration rate until a point is reached where all of the inlet water is bypassed.

Figures 4.4 and 4.6 show an alternative method of presenting the data, particularly for air-first tests. For a fixed air flowrate, at low inlet water flowrates, all of the inlet water penetrates to the lower plenum and this is represented by the 45^{o} line in the graphs. As the inlet water flowrate is increased, a point is reached whereby the rate of lower plenum filling becomes independent of the inlet water flowrate, i.e., in the partial penetration region the lower plenum filling is

a function of the air flowrate only. This point was taken to be the start of bypass. Also shown in Figure 4.4 and other graphs in Appendix G is the"vortex"region which was found to start when $J^*_{wi} \simeq 0.085$.

4.4 CORRELATION OF DATA

4.4.1 Phase 1 Tests

Figure 4.7 shows a dimensionless plot of all water-first test data identified in terms of different inlet water flowrates. These data are replotted as the air mass flowrate M_A versus the water mass flowrate reaching the lower plenum $M_{w_{LP}}$ in Figure 4.8. These graphs suggest that a Wallis type flooding correlation could reasonably correlate the data. Thus the experimental data were replotted in Figures 4.9 and 4.10 in terms of $J^{*\frac{1}{2}}_A$ versus $J^{*\frac{1}{2}}_{w_{LP}}$ and $M_A^{\frac{1}{2}}$ versus $M_{w_{LP}}^{\frac{1}{2}}$ respectively. The resulting straight lines define not only the inception of bypass but also the partial penetration conditions, if it is assumed that the partial penetration curves follow the common envelope curve drawn in Figure 4.7 (or Figure 4.8). The relationship between J^*_A and $J^*_{w_{LP}}$ for the partial penetration can be summarised by the following equation:

$$J^{*\frac{1}{2}}_A + 1.26\, J^{*\frac{1}{2}}_{w_{LP}} = 0.43 \qquad (4.4)$$

or in dimensional form:

$$M_A^{\frac{1}{2}} + 0.237\, M_{W_{LP}}^{\frac{1}{2}} = 0.545 \qquad (4.5)$$

These two equations also describe the inception of bypass if $J^*_{W_{LP}}$ and $M_{W_{LP}}$ were replaced by J^*_{wi} and M_{wi} respectively, since the partial penetration line coincides with the inception of bypass line (as argued previously) and $J^*_{W_{LP}} = J^*_{wi}$ ($M_{W_{LP}} = M_{wi}$) at the start of bypass.

Equation (4.4) is of the same form as that developed by Wallis (12) to describe flooding in tubes except that the coefficient of J^*_{wi} is 1.26 instead of 1.0 and the constant on the right hand side (which is dependent on the choice of the characteristic dimension used in J*) is 0.43.

A comparison between Equation (4.4) and the partial penetration data is shown in Figure 4.11 and others in Appendix I. This will be discussed further in Chapter 5.

4.4.2 Phase 2 Tests

A similar approach was used to correlate the Phase 2 data. Figure 4.12 shows a dimensionless plot of all water-first data identified in terms if different inlet water flowrates. These data exhibit the same general characteristic shape as the Phase 1, but when the data were replotted in Figure 4.13 in terms of $J_A^{*\frac{1}{2}}$ versus $J^*_{W_{LP}}{}^{\frac{1}{2}}$, they did not yield a straight line. The data for the inception of bypass or flooding were extracted from the partial penetration data shown in Appendix H and plotted in terms of $J_A^{*\frac{1}{2}}$ versus $J^*_{wi}{}^{\frac{1}{2}}$ in Figure 4.14. The resulting

flooding equation is:

$$J_A^{*\frac{1}{2}} + 0.484\, J_{wi}^{*\frac{1}{2}} = 0.349 \qquad (4.6)$$

Equation (4.6) is also shown in Figure 4.12 and 4.13, together with the experimental data.

4.5 AUXILIARY TESTS

Strathclyde's initial attempts at formulating a theoretical model for Phase 1 tests highlighted the fact that the height of liquid in the injection pipes could be important. However, measurements of the water height were not taken.

In the present work, the height of the inlet water level at the brink was measured using a cathetometer and telescope. Figure 4.15 shows the variation of this water level with the dimensionless inlet water flux for Phase 1 tests (Note that J_{wi}^* in this plot represents the total inlet water flowrate, i.e., from both sides). A similar plot for the Phase 2 tests is shown in Figure 4.16.

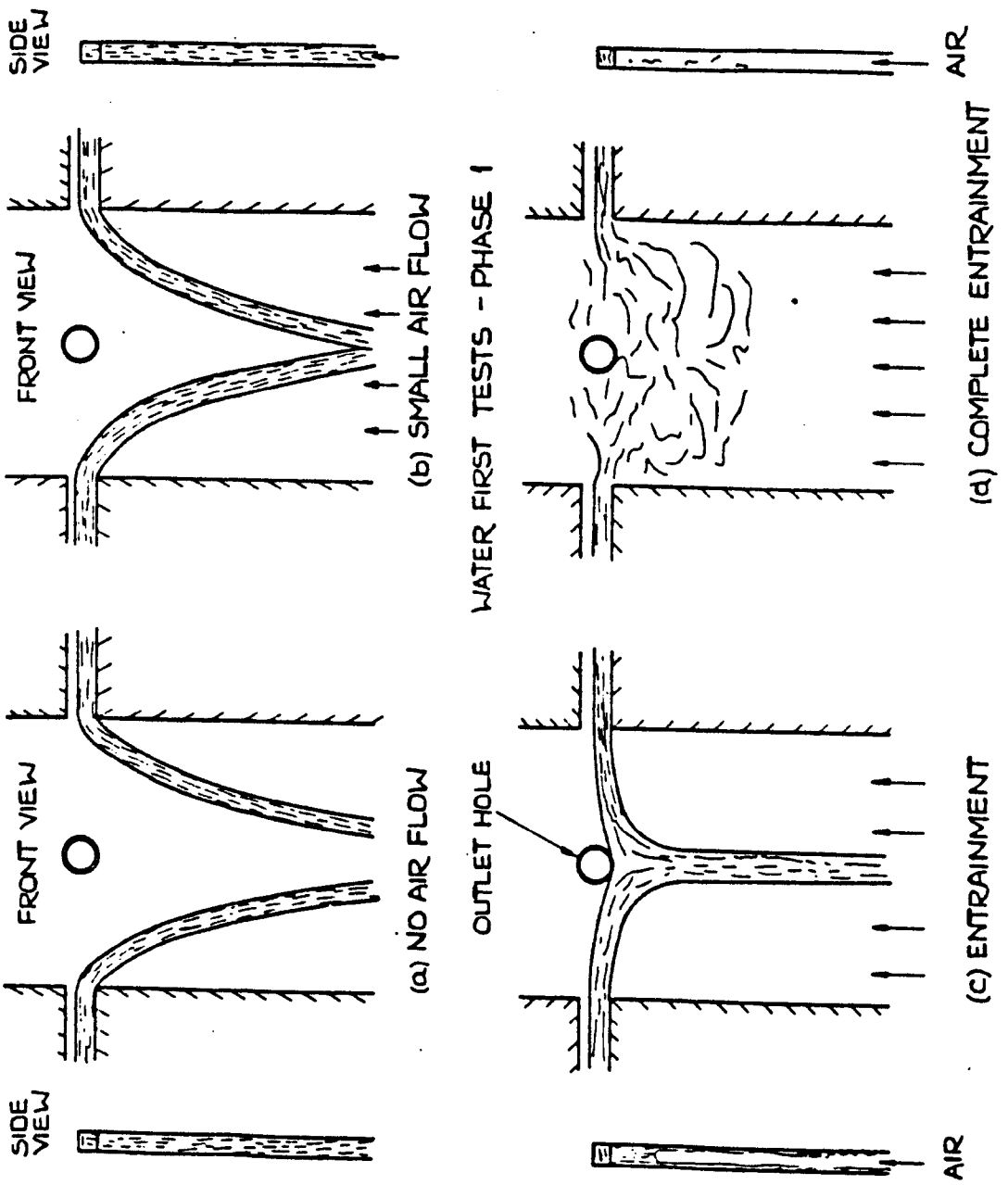

Fig 4.1 AIR-WATER FLOW PATTERN REPRESENTATION.

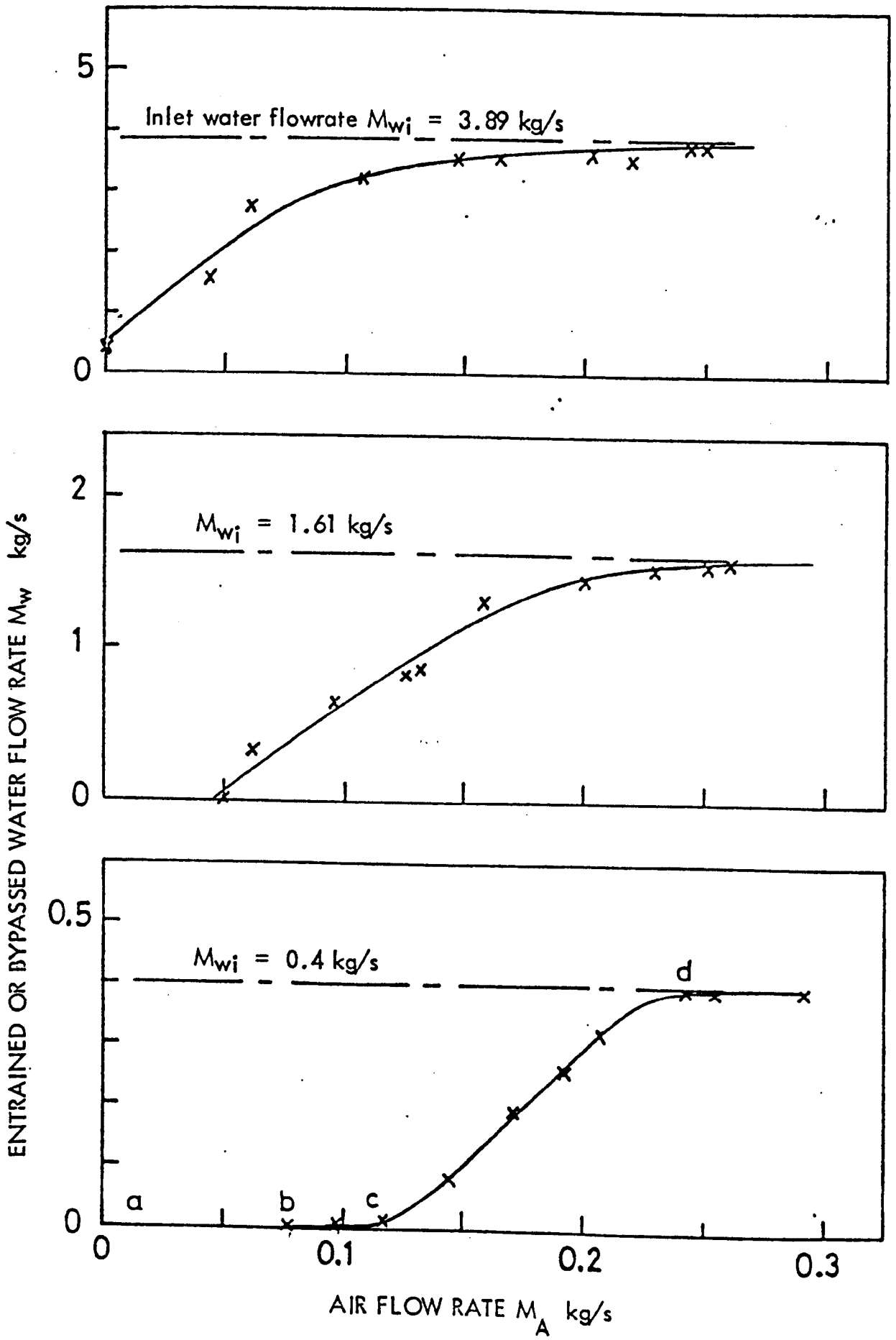

Fig 4.2 TYPICAL BYPASS CURVES FOR AIR-WATER TESTS

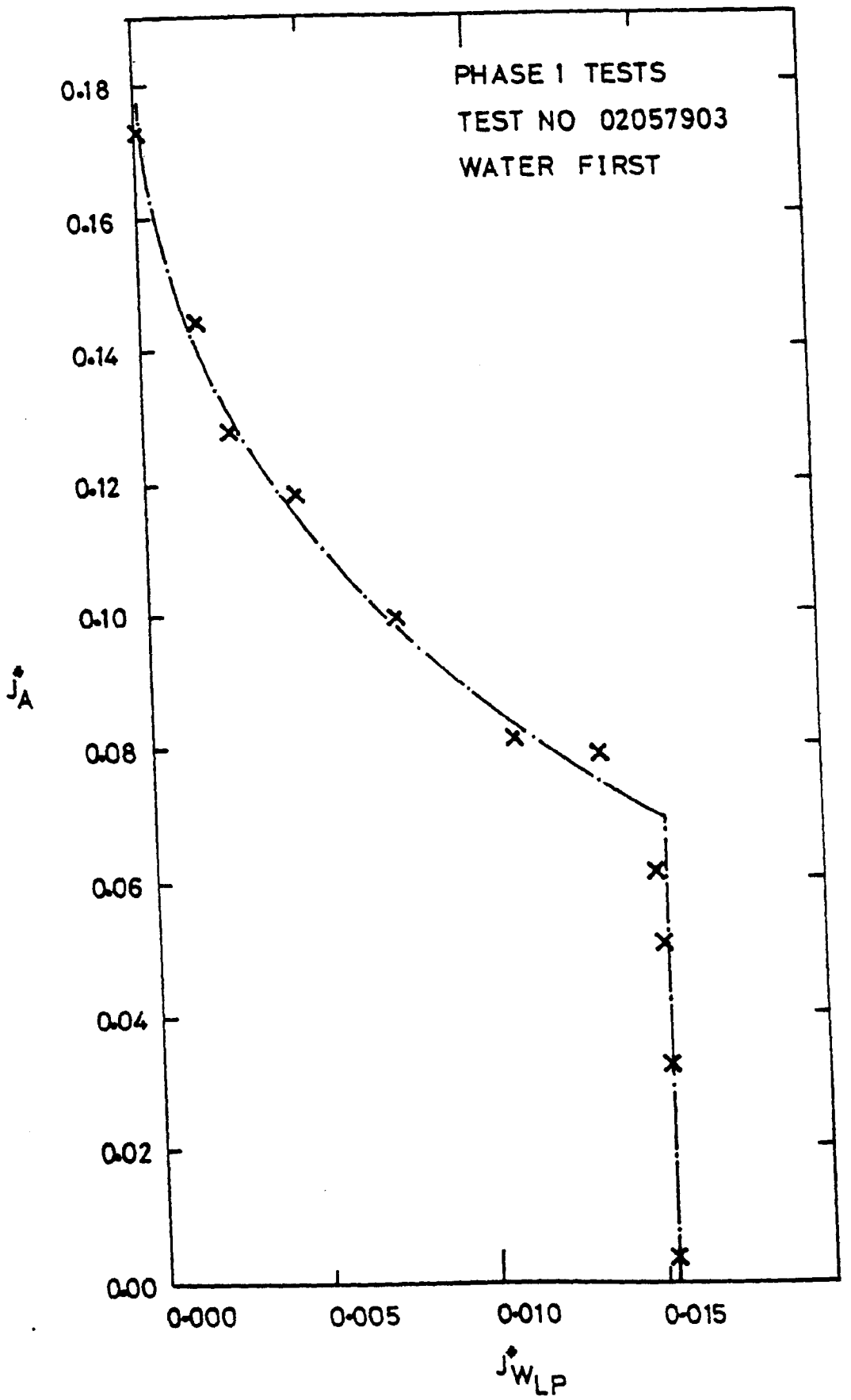

Fig 4.3 Penetration Characteristics From Air-Water Tests

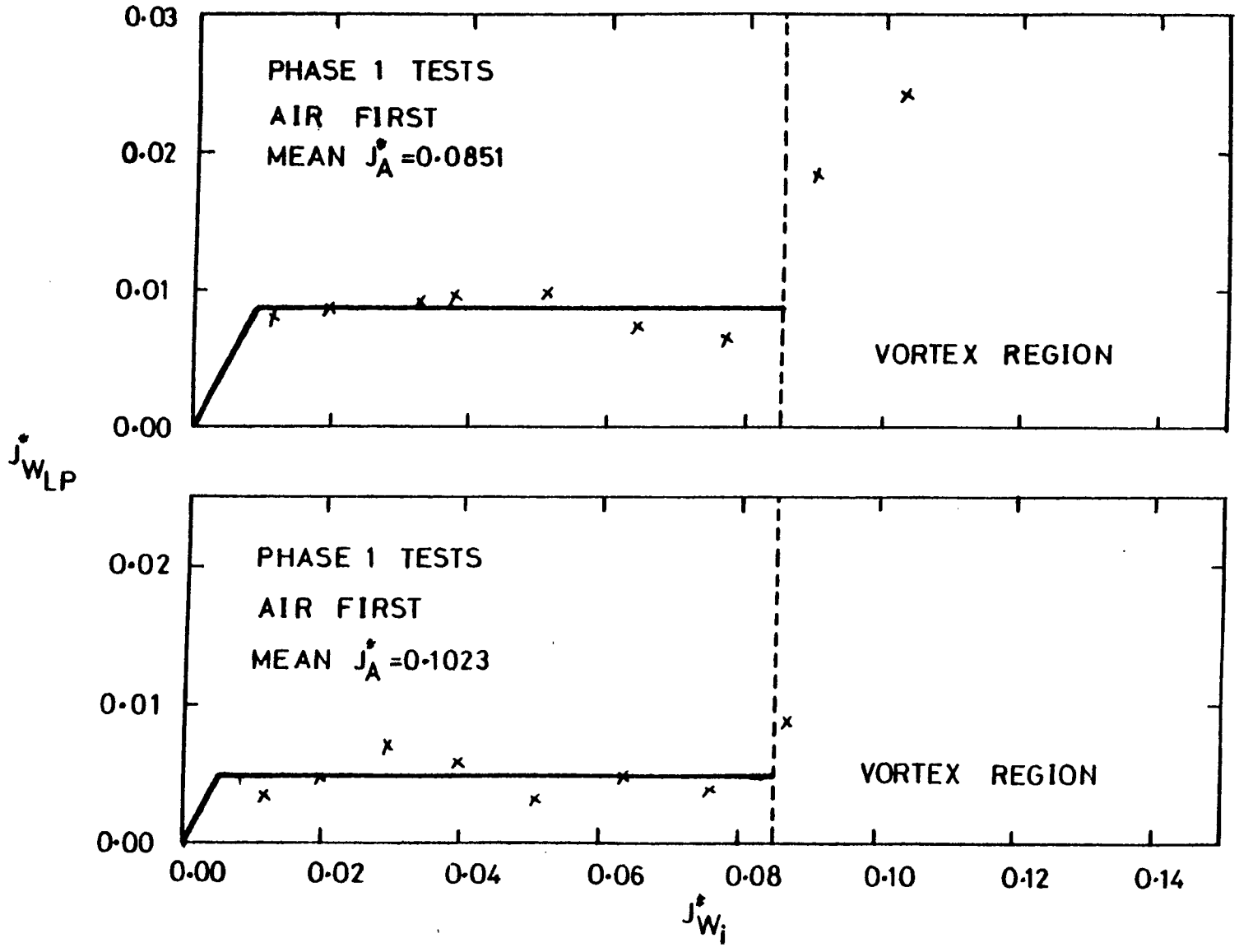

FIG 4.4 Degree of Penetration to Lower Plenum of Inlet Water for Particular Air Flowrates

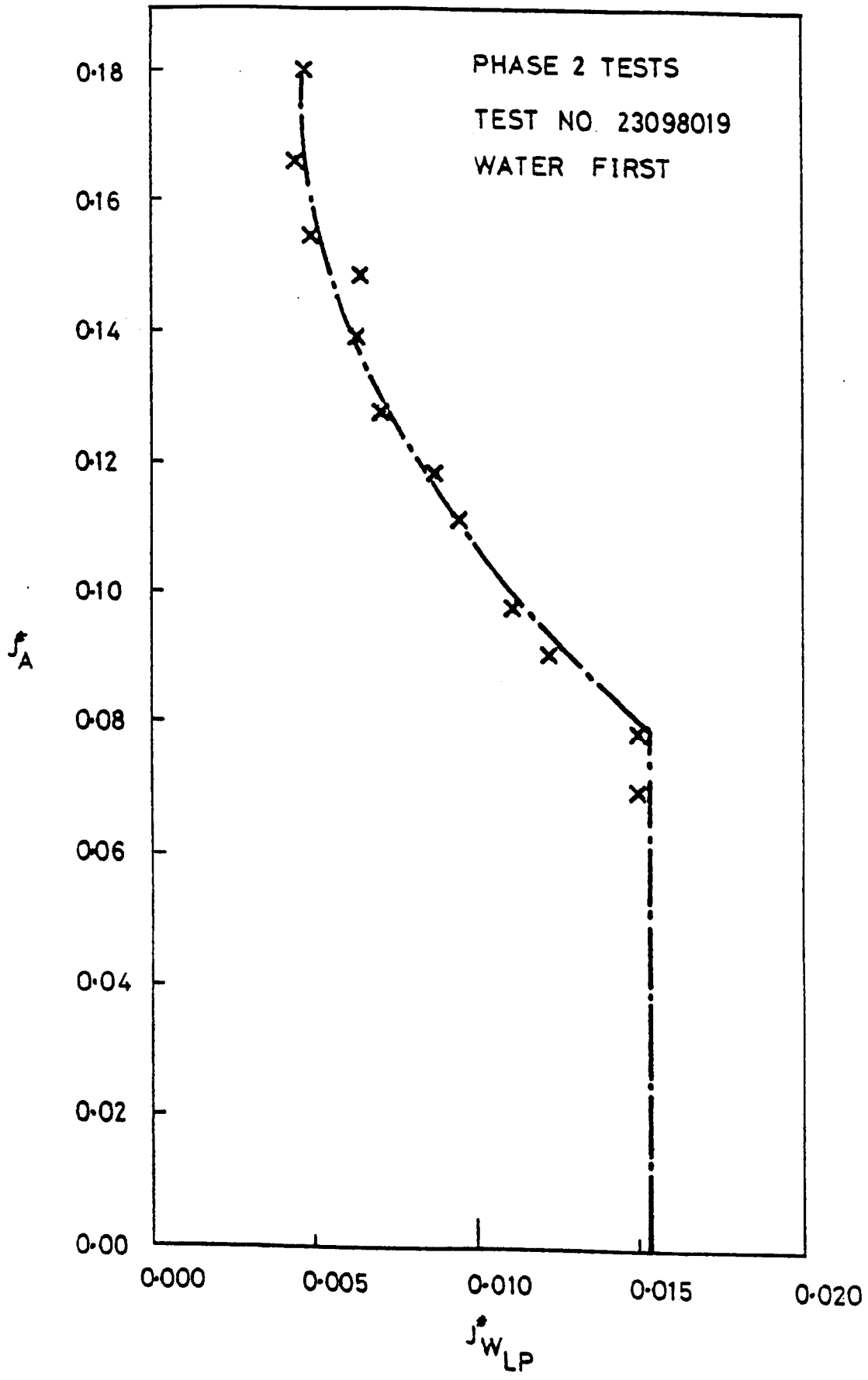

Fig 4·5 Penetration Characteristics from Air Water Tests

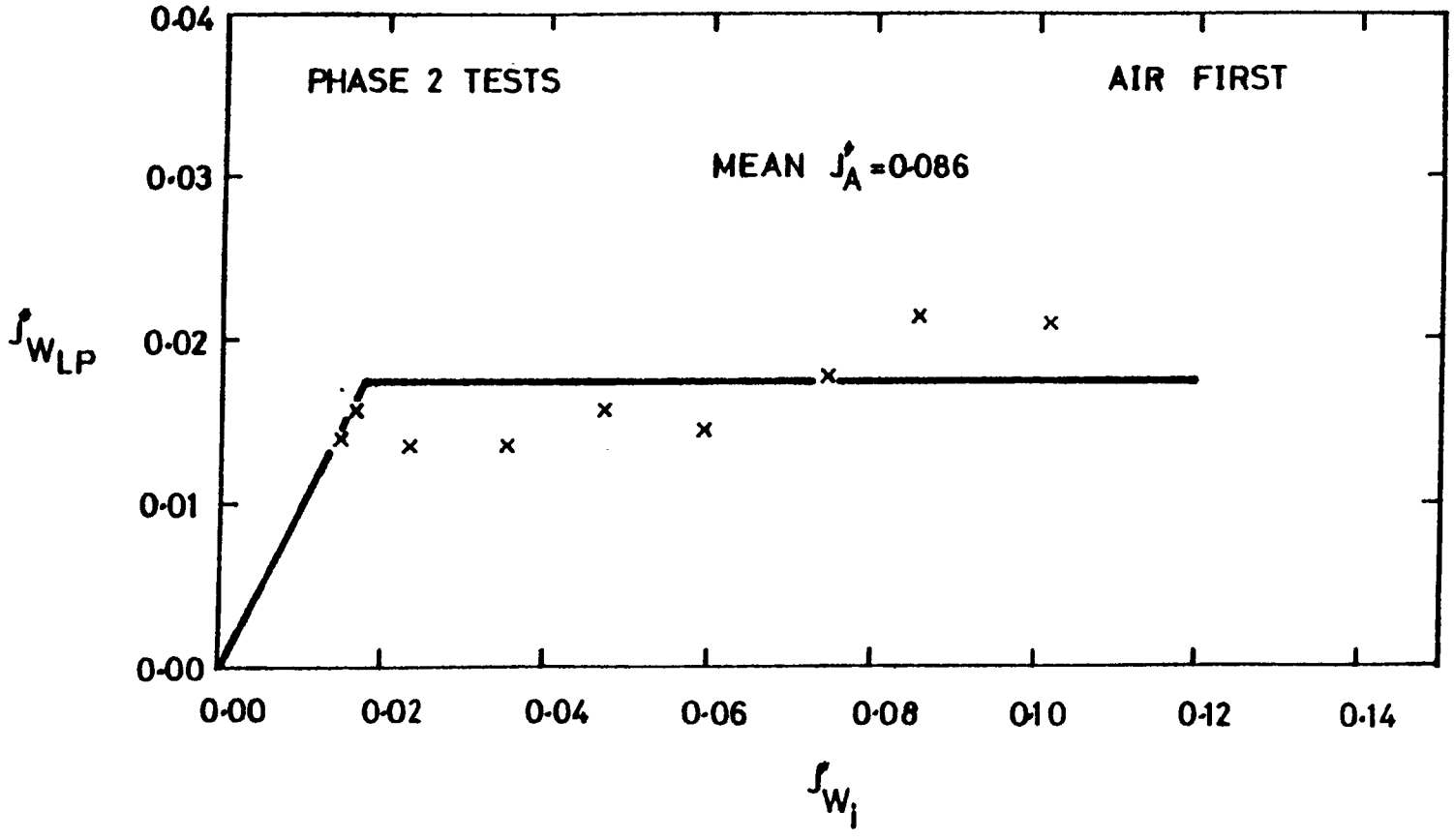

Fig 4·6 Degree Of Penetration To Lower Plenum Of Inlet Water For Particular Air Flowrates

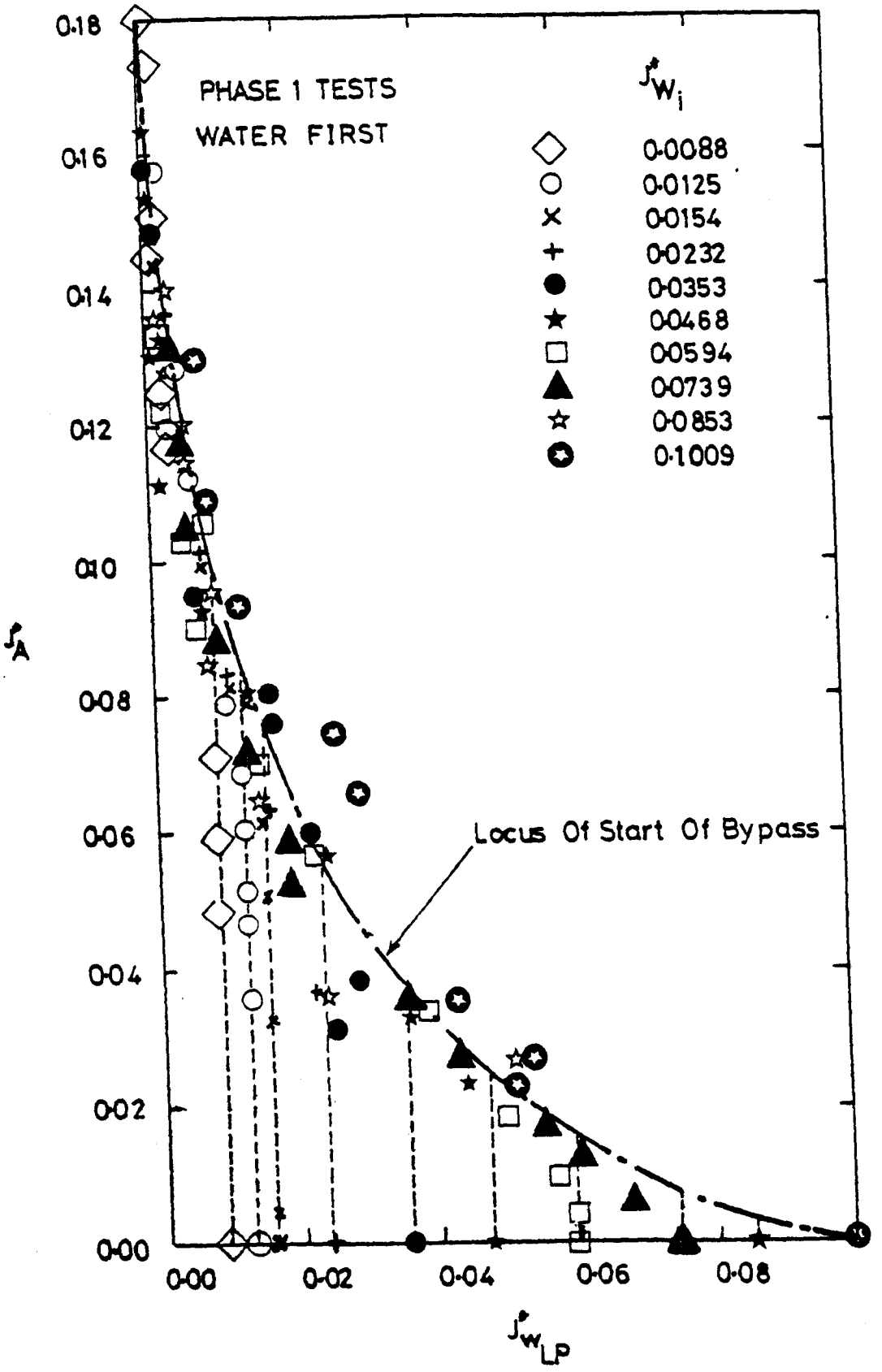

Fig 4.7 Bypass Characteristics from Air Water Tests

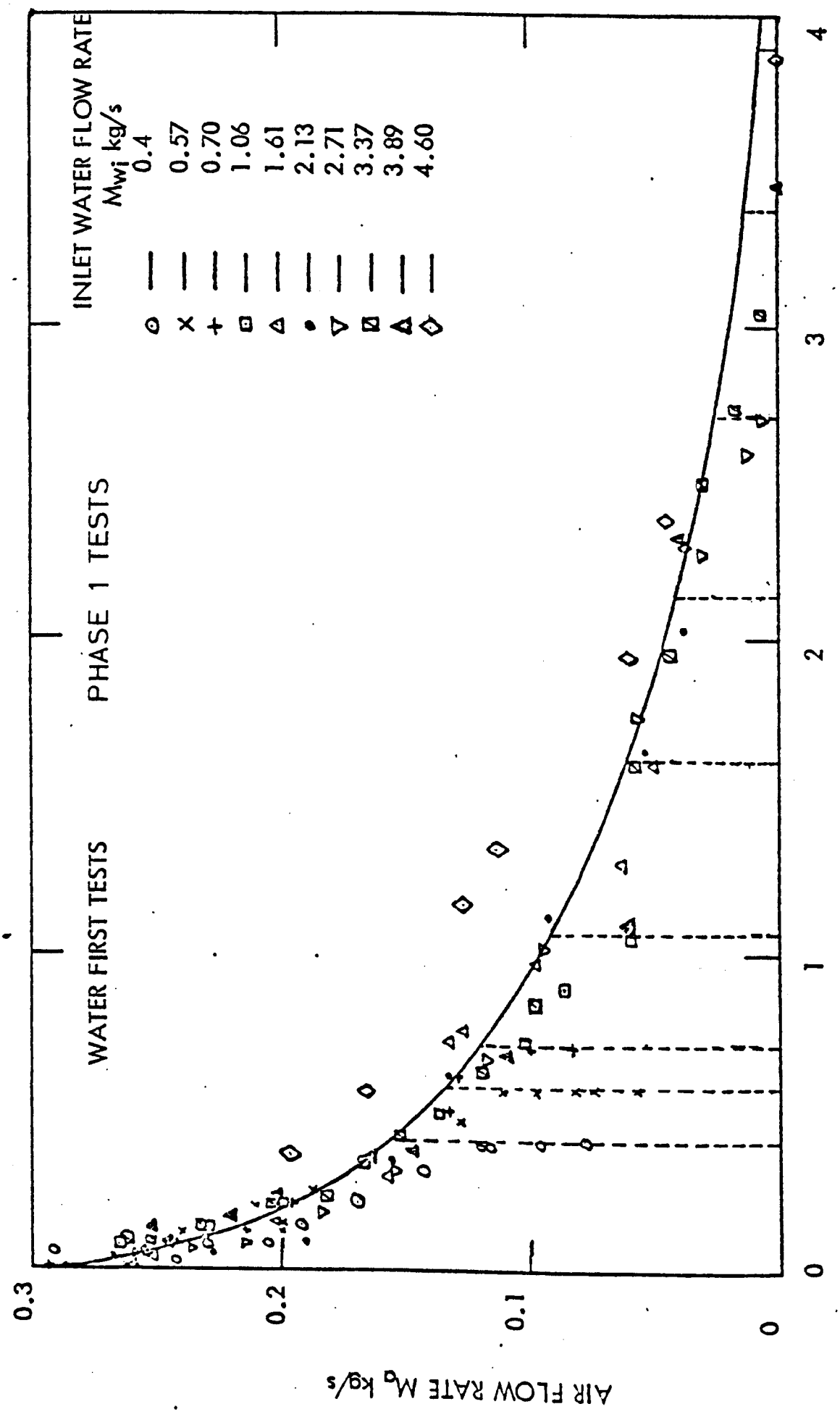

Fig 4.8 LOWER PLENUM PENETRATION CHARACTERISTICS FOR AIR-WATER TESTS

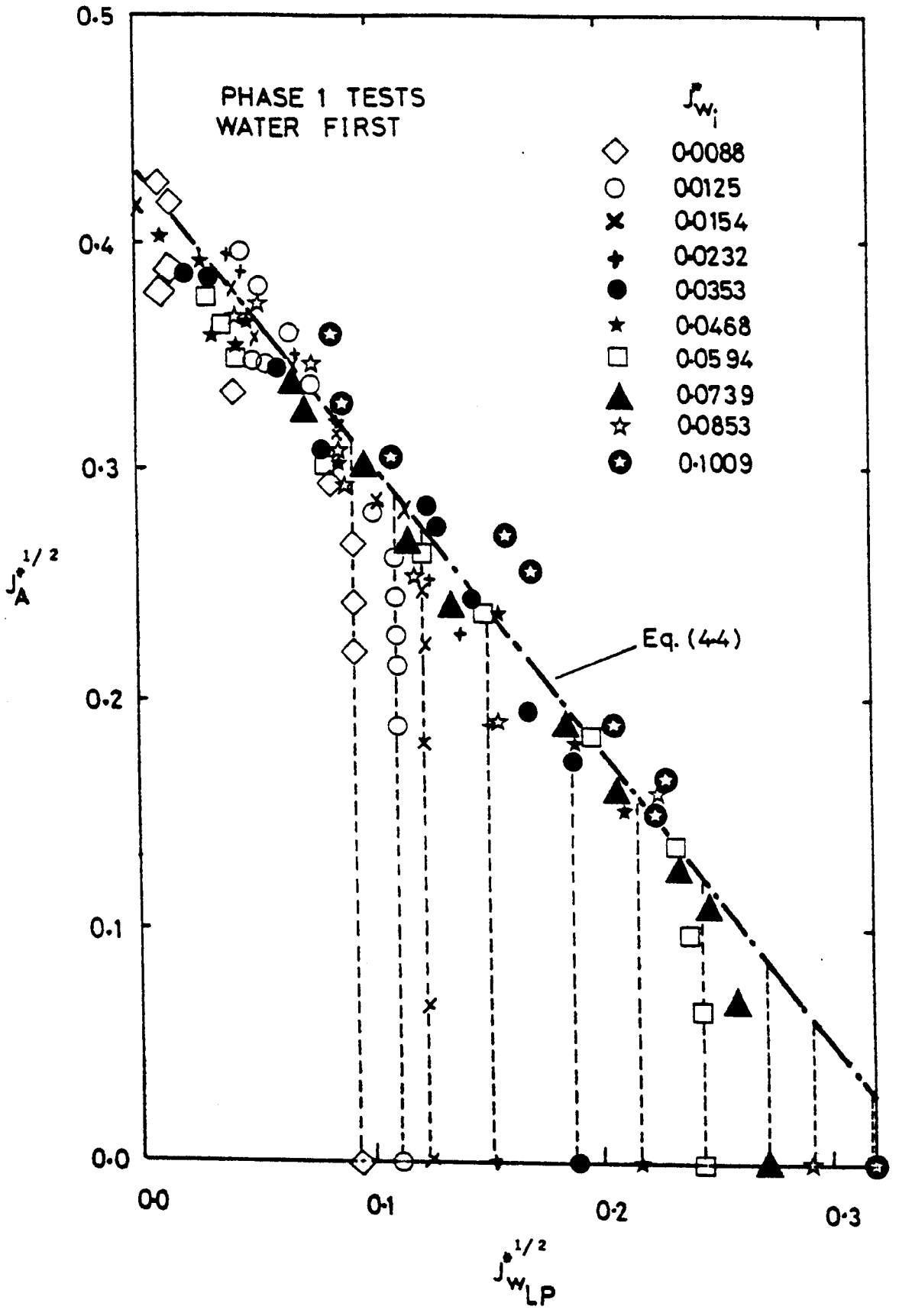

Fig 4.9 DIMENSIONLESS PLOT OF ALL AIR-WATER DATA

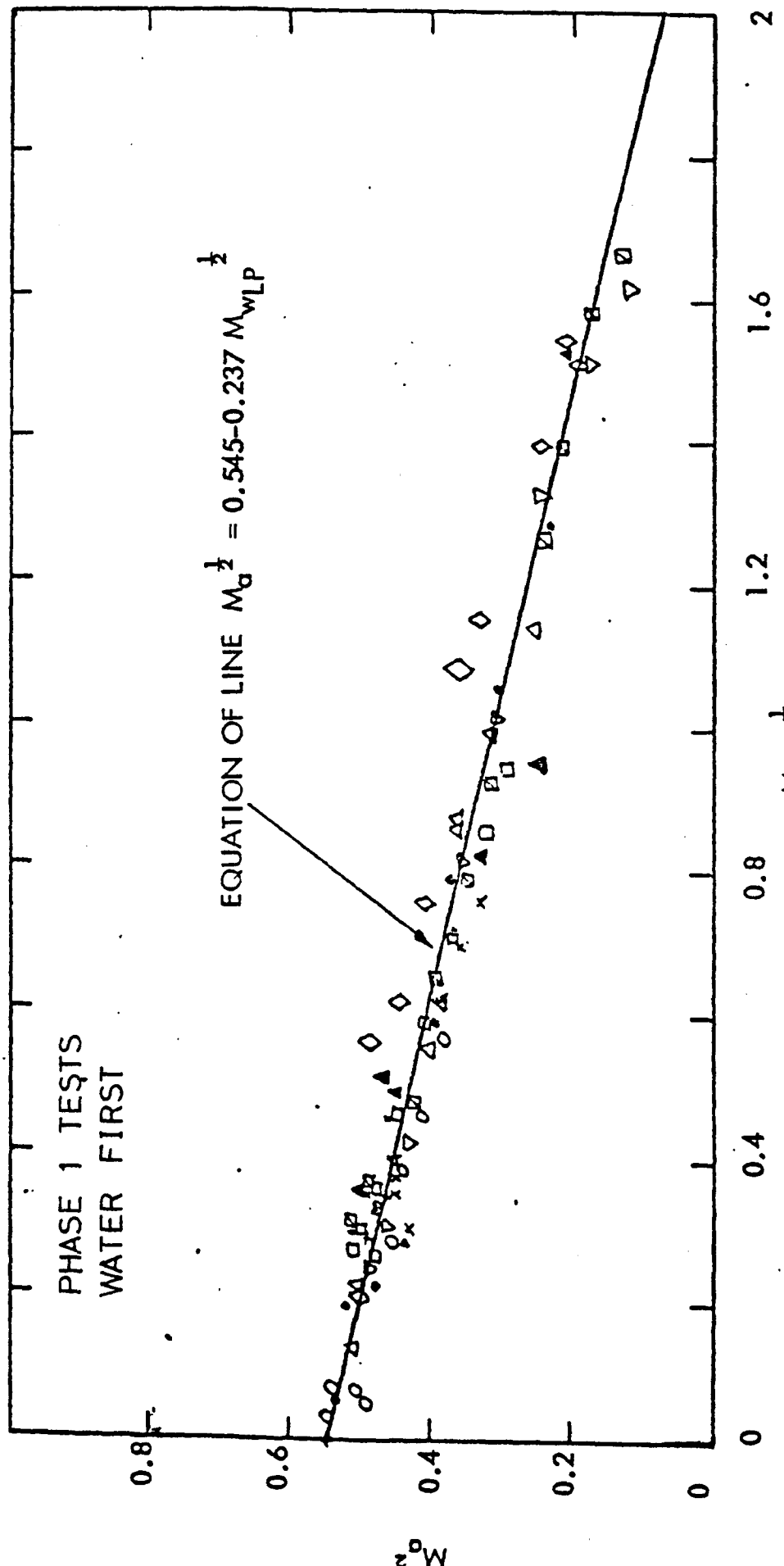

Fig 4.10 CORRELATION OF PENETRATION DATA FOR AIR-WATER TESTS

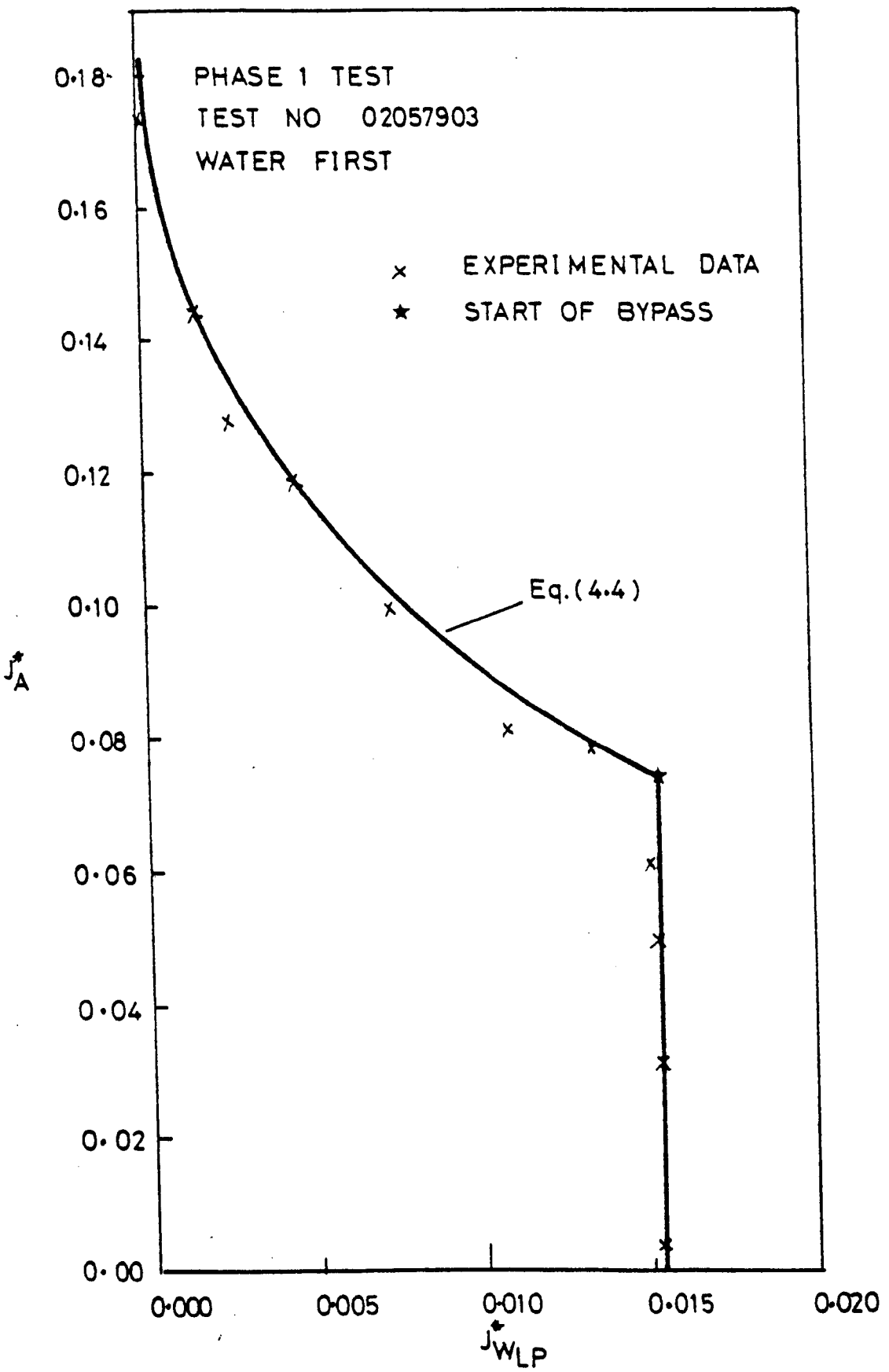

Fig 4.11 Comparison of Experimental Data With Equation (4.4)

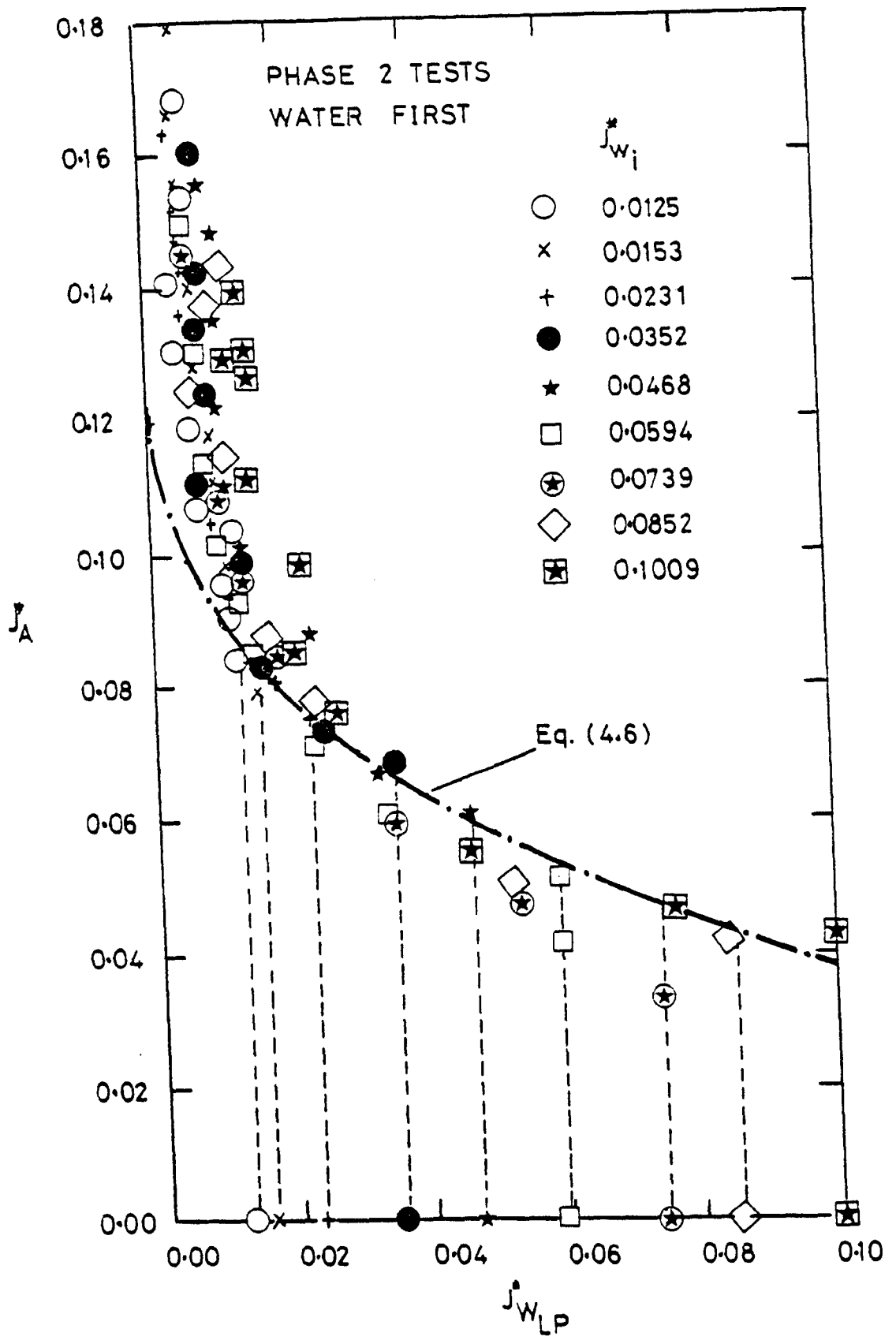

Fig 4.12 DIMENSIONLESS PLOT OF ALL AIR-WATER DATA

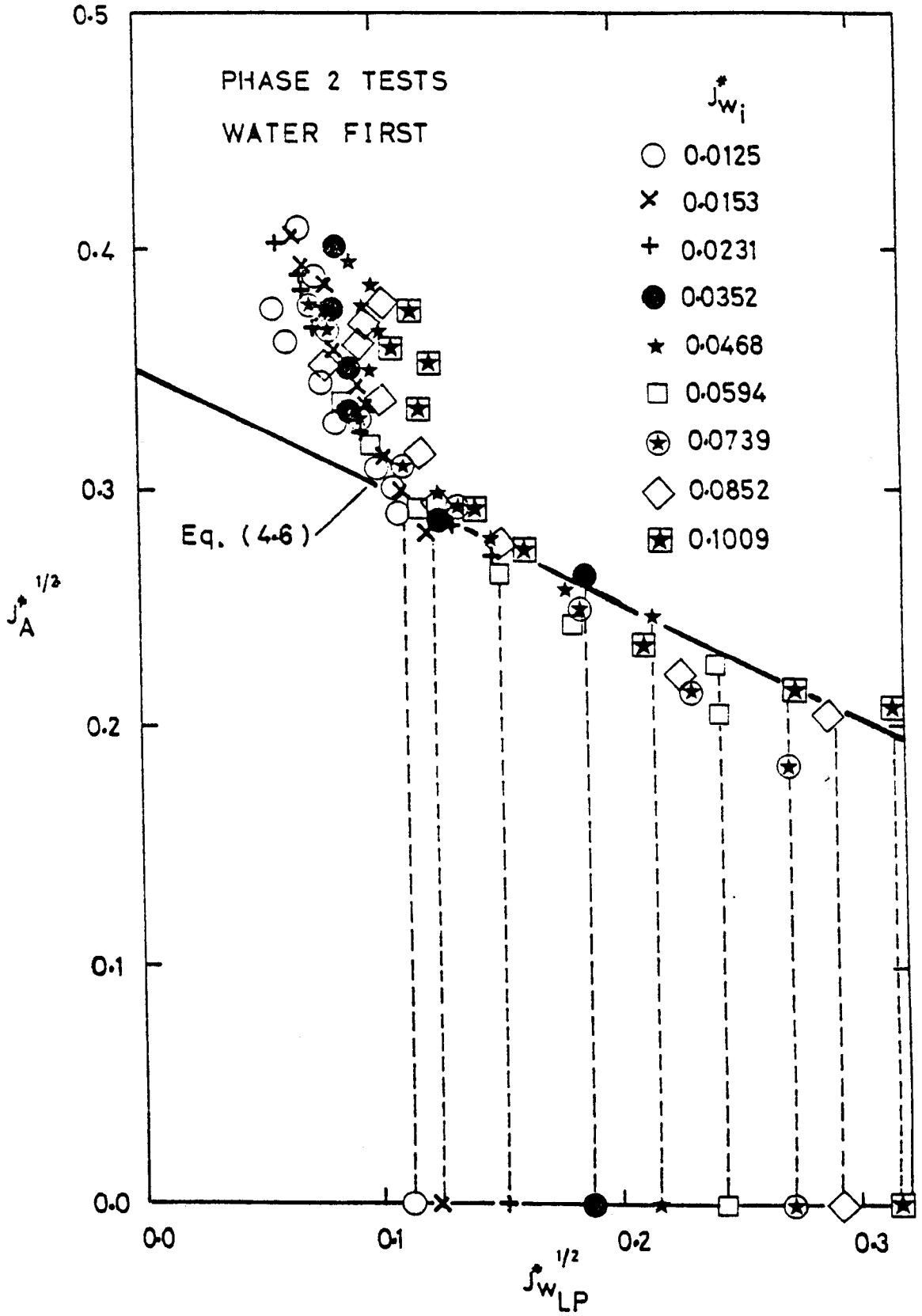

Fig 4·13 DIMENSIONLESS PLOT OF ALL AIR-WATER DATA

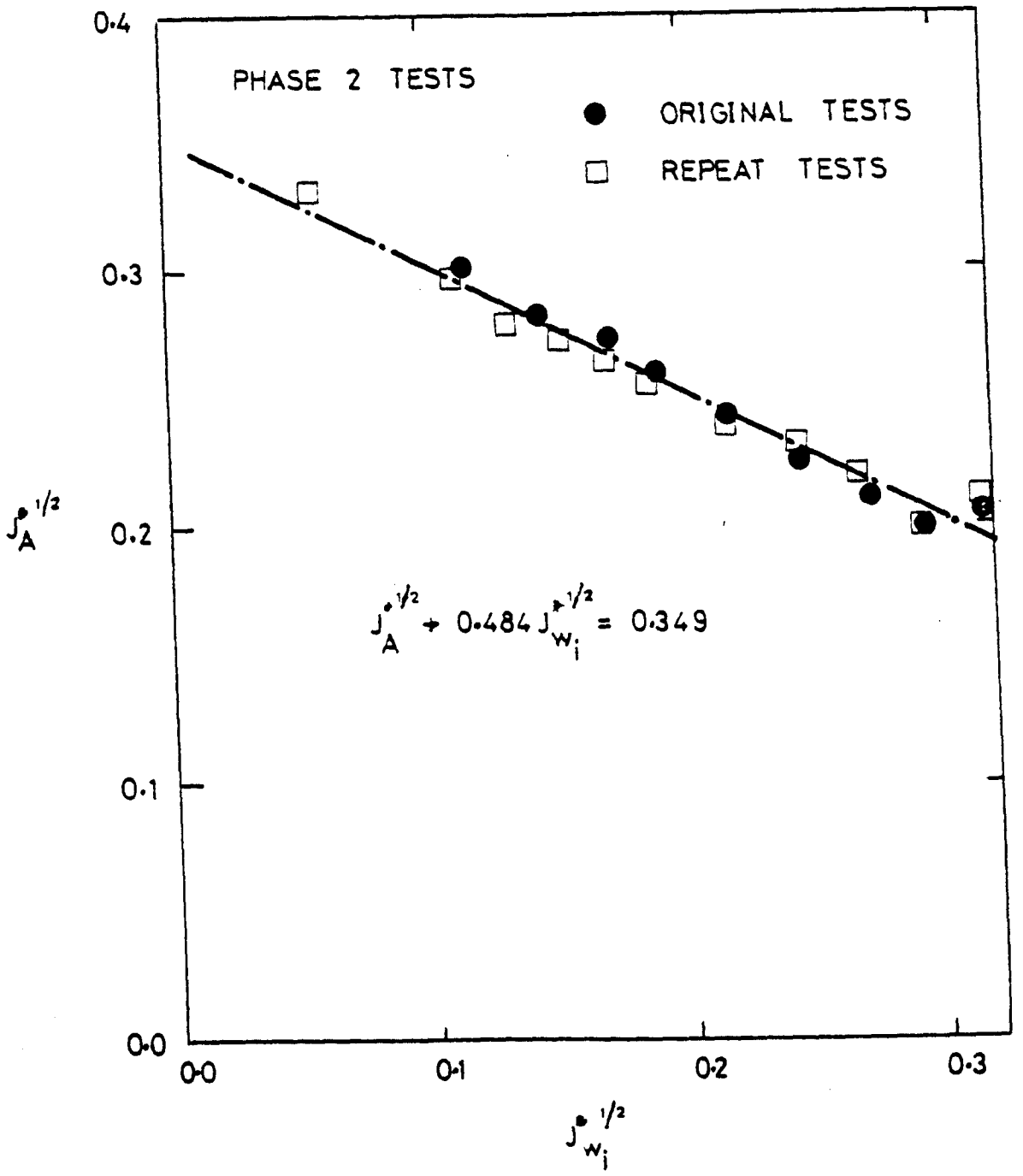

Fig 4.14 Critical Conditions for Liquid Bridging

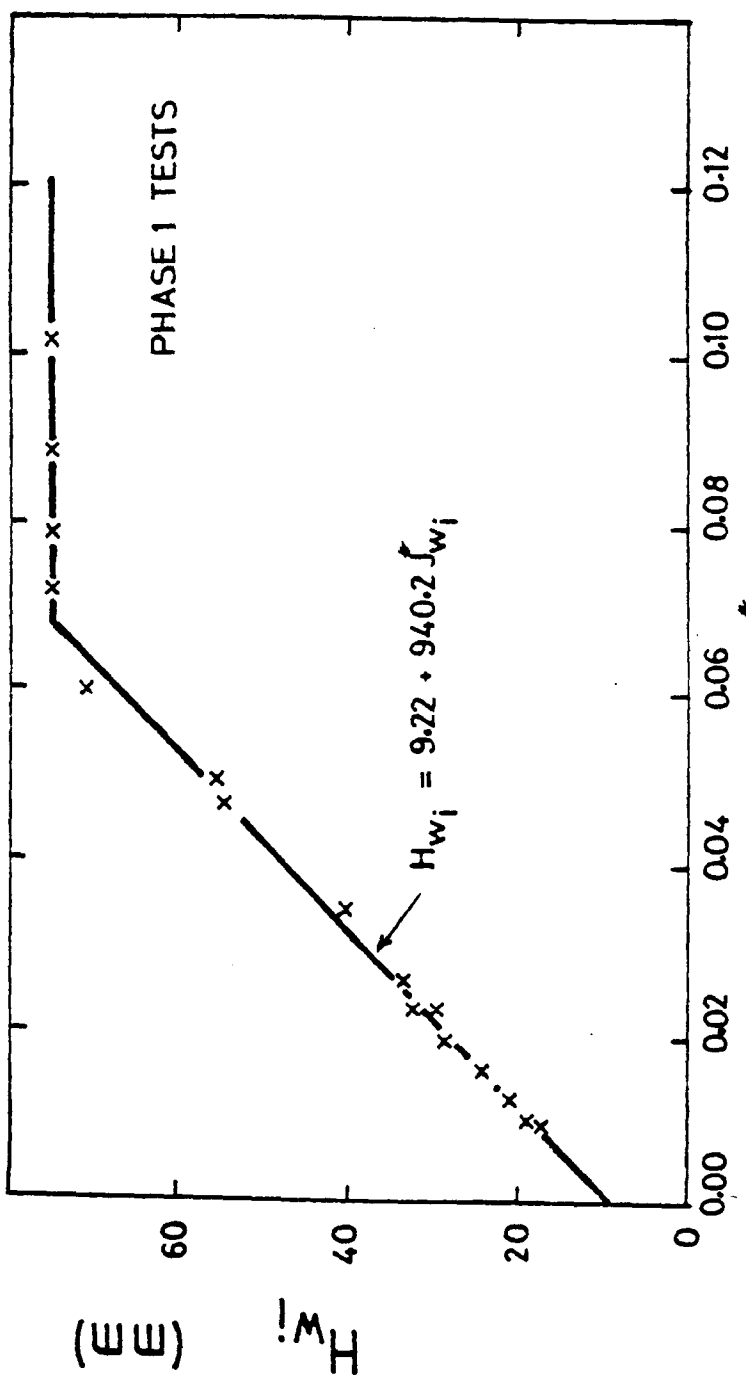

Fig 4.15 Variation Of Water Height At The Brink, H_{w_i} With Dimensionless Water Flux, $f^*_{w_i}$

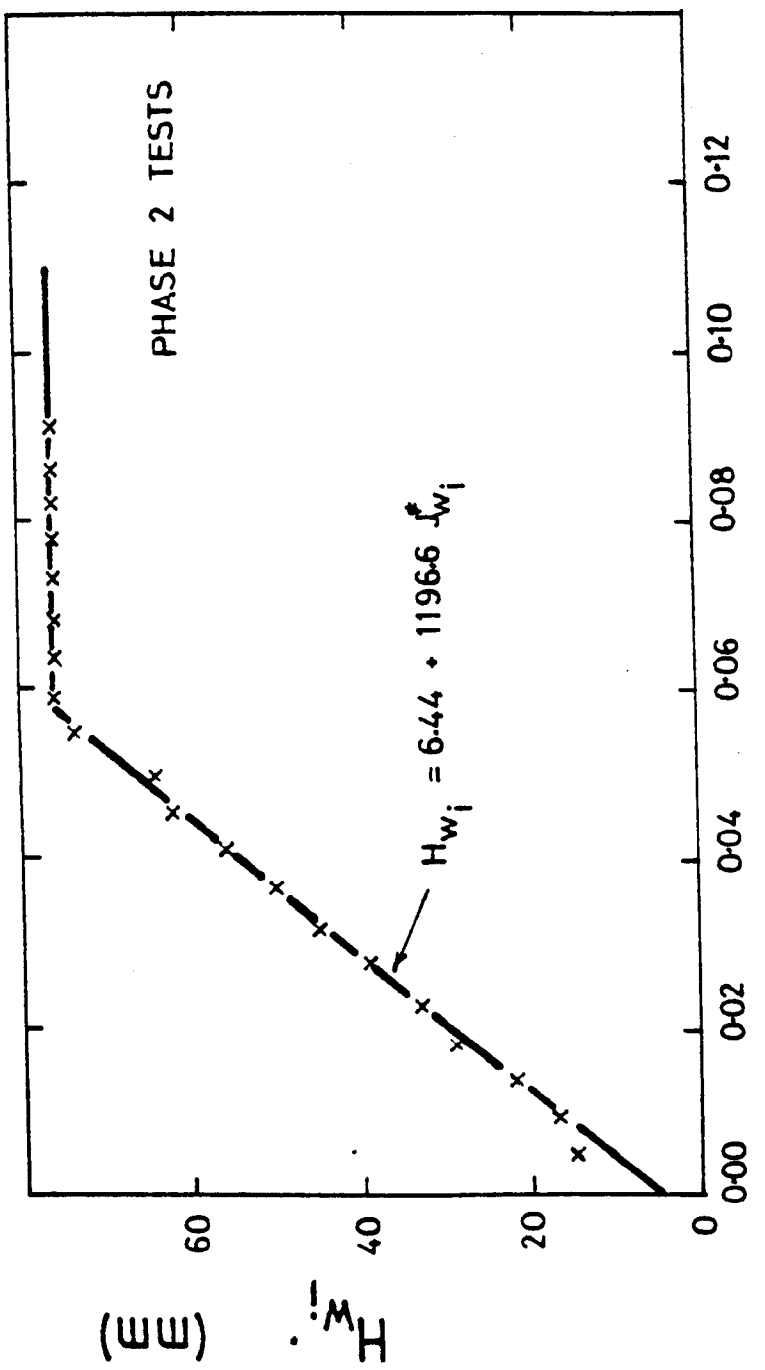

Fig 4.16 Variation Of Water Height At The Brink, H_{w_i}, With Dimensionless Water Flux, $j^*_{w_i}$

CHAPTER 5

DISCUSSION OF RESULTS

CHAPTER 5 : DISCUSSION OF RESULTS

The experimental results presented in Chapter 4 are discussed here with emphasis on the shapes of the penetration and bypass characteristics, and the differences between these characteristics and those of steam/water counter current flow systems. A comparison with some of the theoretical work in the literature is also presented and discussed.

5.1 WATER PENETRATION CHARACTERISTICS

The water penetration characteristics show the ability of the coolant to penetrate to the lower plenum in the presence of counter-current gas (or vapour) flow. In the present test programme, the coolant was water and the gas was air at near atmospheric conditions as mentioned in Chapter 3. This simulates the case of saturated steam and water system, i.e., no mass transfer between the two phases and no temperature difference.

Referring to Figures 4.3 and 4.5 and others in Appendices G and H, it can be seen that at low value of air flowrates, all of the injected water passes unaffected to the lower plenum. As the air flowrate is increased a point is reached where a small part of this water is expelled out of the test section (the start of bypass). Further increase in the air flowrate results in further decrease in the water penetrating to the lower plenum until another critical point is reached,

where all of the injected water is entrained (complete bypass). The transition between the "start of bypass" point and the "complete bypass" point is a gradual change, unlike Campbell's steam water data (35)with high subcooling where the two critical points more or less coincided with each other. This on-off behaviour was probably due to the local pressure reduction caused by condensation which contributed to the rapid growth of surface waves to block the passage of steam.

The dimensionless plot of all of the data for both Phase 1 and Phase 2 tests is shown in Figure 4.7 and 4.12. These Figures, together with Figures 4.4 and 4.6, indicate that the partial penetration region follows a common curve and in this region the amount of water penetrating to the lower plenum is a function of the air flowrate only. This is a very interesting result which indicates that there is a maximum penetration flowrate for any particular air flowrate regardless of the injected water flowrate.

If attention is focussed now on the start of bypass, it is clear from Figures 4.7 and 4.12 that increasing the inlet water flowrate reduces the air flow required to cause the start of bypass. This effect could be attributed to the decrease of the area available for air, hence increasing the pressure in the lower plenum and reducing the distance required to be bridged by surface waves, thus allowing smaller waves to bridge the test section. Again, this behaviour is completely different from Campbell's

steam/water data as shown in Figures 5.1 to 5.4, where increasing the inlet water flowrate resulted in an increased steam flowrate being necessary to cause bridging. This difference could be attributed to condensation, because increasing the mass flowrate of inlet water increased the heat capacity of the water phase thus more steam will be condensed. This suggests that, for steam/water counter-current flows, part of the steam is condensed and may have some effect on flooding (or bypass) but with the remaining part being mainly responsible for the flooding. However, close examination of the steam/water data indicated that non-equilibrium effects exist. This point is investigated theoretically in Chapter 6.

5.2 COMPARISON OF AIR FIRST AND WATER FIRST TESTS

A comparison between "water first" and "air first" test data would indicate the effect of mode of injection and this could be useful in the study of flooding characteristics in the actual PWR. The air first test simulates more accurately the situation during a potential LOCA because it is most likely that after the blowdown period a flow of steam will be established in the downcomer annulus before the ECC water is injected via the cold leg. However, in the experimental work it is easier to control the "water first" type of tests more than "air or steam first" test. This probably explains the reason why most of the experimental work

reported in the literature is of the "water first" type.

Direct comparison between "water first" and "air first" data for Phase 1 test series was not possible due to the differences in the method of testing outlined previously in Chapter 3. However, a comparison between all the air first data and equation (4.4) obtained from "water first" data shows very good agreement, this being shown in Figure 5.5.

The disadvantage in not having a means of direct comparison between "air first" and "water first" data for Phase 1 test series, together with the difficulty in maintaining the air flow rate at a constant value, led to the change in the experimental technique during Phase 2 test, as mentioned in Chapter 3. Figure 5.6 and others in Appendix J show a direct comparison between "water first" and "air first" data for the Phase 2 test series. As can be seen, the two sets of data are almost identical with no obvious effect of changing the mode of injection.

It can also be seen from the above comparison that the correlations for the start of bypass obtained from water first tests are valid for the air first tests also. This result is also different from that obtained by Campbell (35), whose data indicated that the critical conditions for the steam first and water first tests are not coincident. This could be due to lower plenum condensation effects resulting in a reduction of the steam flowrate entering the test section. For this reason,

the author has disregarded Campbell's "water first" data in subsequent analysis. From this point on, "Campbell's data" will refer to steam first tests only.

5.3 COMPARISON OF PHASE 1 AND PHASE 2 TEST DATA

The comparison between Phase 1 and Phase 2 test data gives an indication of the effect of the angle of water injection into the test section, since both Phases involved planar test sections.

This effect is illustrated in Figures 5.7 and 5.8, and in Appendix K. Considering "water first" tests for both Phases, shown in Figure 5.7, it is clear that for a particular inlet water flowrate, the start of bypass for Phase 1 test conditions requires a lower air flowrate than that for Phase 2. If "air first" is considered (shown in Figure 5.8), a similar effect can be seen. The only deviation from this finding occurred when J^*_{wi} (in Phase 1) exceeded the value of 0.085 when a vortex motion was developed around the outlet pipe (broken leg) allowing more water to penetrate to the lower plenum. At first, this vortex motion was thought to be caused by a slight imbalance between the two waterfalls, but close examination of the direction of the vortex motion indicated that it was always anti-clockwise. A possible explanation is that a non-uniform pressure distribution exists along the width of the test section due to the location of the air inlet pipe being on one side of the lower plenum. This

vortex effect, however, did not appear in the "water-first" tests, probably because the water phase was fully established in the test section before introducing the air.

Another obvious effect regarding the point of complete bypass can be seen by examining Figures 4.9, 4.13, 5.7 and others in Appendix K. While complete bypass is achieved for Phase 1 at $J_A^* = 0.185$, a much higher value of air flowrate is needed for complete bypass in Phase 2. This could be attributed to the "end effects" resulting from the location of the water inlet pipes on both sides of the test section, thus allowing a "solid" stream of water to run down the sides to the lower plenum. This explains the deviation of the data points from Equation (4.6) in Figure 4.13 at $J^*_{W_{LP}} \simeq 0.1$. One can speculate whether or not Equation (4.6) would have represented the penetration data better had the water inlet pipe been in the centre of the test section width (as was the case in the Creare and Dartmouth experiments, (refs. 24-28). There may be some support for the speculation from the Phase 1 test data where a single equation (4.4) did represent all of the penetration data and where the tangential water entry could have "pushed" the water away from the sides of the test section.

The behaviour of the air/water test data discussed here is quite different from Campbell's steam/water tests which indicated that the "waterfall type of flow regime present in Phase 1 tests gave a more effective

penetration than the film flow regime of Phase 2". This difference can be attributed to condensation effects since the waterfalls will provide a smaller surface contact area between thesteam and water, for interaction, than will the film flows present in Phase 2.

5.4 COMPARISON WITH THEORETICAL WORK

Several attempts have been made in the last two decades or so to present theoretical and empirical models to predict flooding in tubes and PWR geometries. These were reviewed in detail in Chapter 2. In the remainder of this Chapter, some of the theoretical models will be tested against the present data.

5.4.1 Phase 1 Geometry

As far as is known, no other investigation involved a geometry similar to the Phase 1 test section used by Strathclyde. Simpson et al (36) presented a theoretical bridge type model to predict the flooding or bypass conditions for Phase 1 test which reduced to the equations (2.142) to (2.144). In this model, the Froude number, Fr_{wi}, was taken to be equal to unity; however, accurate measurement of the height of water at the brink of the test section indicated that this was not the case. Referring to Figure 4.15, it was found that the water height at the brink, H_{wi}, in a partially filled pipe could be correlated with the dimensionless water flux, J^*_{wi} to give

$$H_{wi} = 9.22 + 940.2\ J^*_{wi} \qquad (5.1)$$

with H_{wi} in millimetre.

Equation (5.1) was solved together with Equations (2.142) to (2.144) to give J^*_A vs J^*_{wi}. Figure 5.9 shows a comparison between the resulting solution and the start of bypass for the present experimental work given by equation (4.4). Also shown is the graph the condition for complete bypass given by

$$J^{*\frac{1}{2}}_A = 0.43 \qquad (5.2)$$

It is clear from the graph that the bridge theory does not agree with either the locus of the start of bypass (Equation (4.4)) or the complete bypass condition given by Equation (5.2). This could be due to the fact that the bridge theory does not allow for the fact that the two waterfalls opened along the centre plane of the test section to form a passage for the upward rise of air moving against the downwards film flow of the water, as indicated in Section 4.1.1. The theory could be correct, however, for steam/water situations where condensation could cause a blockage of the passage.

5.4.2 Phase 2 Geometry

Phase 2 geometry simulates the actual PWR conditions

better than Phase 1 and several investigators have used planar test sections similar to the Phase 2 test section. However, most of the theoretical work has been carried out to predict flooding in tubes. In this Section, a comparison between different theoretical correlations and the present Phase 2 test data is made.

Before proceeding with the comparison, it is worth re-iterating the system used.

(i) The comparison is carried out in terms of Wallis parameters defined by:

$$J_W^* = \frac{M_W}{\rho_W A}\left[\frac{\rho_W}{gB(\rho_W - \rho_A)}\right]^{\frac{1}{2}} \simeq \frac{M_W}{\rho_W A}\sqrt{\frac{1}{gB}} \qquad (5.3)$$

$$J_A^* = \frac{M_A}{\rho_A A}\left[\frac{\rho_A}{gB(\rho_A - \rho_A)}\right]^{\frac{1}{2}} \simeq \frac{M_A}{\rho_A}\cdot\sqrt{\frac{1}{gB}}\cdot\left(\frac{\rho_A}{\rho_W}\right)^{\frac{1}{2}} \qquad (5.4)$$

(ii) Whenever the tube diameter is involved in an empirical correlation (e.g., the coefficient ξ defined by equation (2.66)), the hydraulic diameter

$$D_H = 2S \qquad (5.5)$$

is used instead of diameter

(iii) The units used throughout are SI units

The Phase 2 test data are compared with the theoretical correlations of Schutt (1), Grolmes et al (7),

Imura et al (16) and Richter (34). The empirical correlation presented by Richter and Wallis (33) to predict flooding in small PWR geometry is also used in the comparison. These correlations are dealt with in turn.

5.4.2.1 Comparison with Schutt (1)

Schutt (1) applied the small perturbation method to the Navier-Stokes equation and produced Equation (2.1) to describe the flooding conditions. The equation is very complicated in its present form; however, it can be approximated under the present test conditions to:

$$J_A^* = 0.063 \left[\left(4.64 J_w^{*0.75} - J_w^{*0.5}\right) \cdot \frac{\Gamma}{\Gamma - 20} \right]^{\frac{1}{2}} \qquad (5.6)$$

where

$$\Gamma = \frac{\left[1 + \exp\left(1.763\ J_w^{*0.375}\right)\right]^2}{1 - \exp\left(1.763\ J_w^{*0.375}\right)} + 1 \qquad (5.7)$$

The details of this approximation are given in Appendix L.

Figure 5.10 shows a comparison between the present experimental data and Equation (5.6). It is clear from the Figure that Schutt's correlation predicts higher values of air flowrate at the start of bypass. Also the qualitative agreement between Schutt (1) and Equation (4.6) is very poor.

5.4.2.2 Comparison with Grolmes et al (7)

Grolmes et al (7) presented a semi-empirical correlation to predict the start of bypass or flooding in vertical tubes. The procedures presented in Appendix L reduced Equation (2.33) to:

$$J_A^* = \frac{0.074 \quad J_W^*}{(0.006 + 15.68 \; J_W^{*2/3})^{\frac{1}{2}}} \qquad (5.8)$$

The comparison between Equation (5.8) and the experimental data is shown in Figure 5.11. It is evident from the comparison presented in Figure 5.11 that both the qualitative and the quantitative agreement between Equations (4.6) and (5.8) is very poor.

5.4.2.3 Comparison with Imura et al (16)

The semi-empirical flooding correlation (Equation (2.65)) was reduced to the following Equations for the test conditions of the present experimental work.

For $J_{Wi}^* \leqslant 0.0067$

$$J_A^* = \frac{0.0733}{J_W^{*1/6}} - 0.3197 \; J_W^{*2/3} \qquad (5.9)$$

For $J_{Wi}^* > 0.0067$

$$J_A^* = \frac{0.0483}{J_W^{*\frac{1}{4}}} - 0.1385 \; J_W^{*\frac{1}{2}} \qquad (5.10)$$

The derivation of Equations (5.9) and (5.10) is shown in Appendix L.

Figure 5.12 shows a comparison between Equation (5.9) and (5.10), and the experimental data. From the Figure it is clear that the qualitative agreement between the data and Imura's flooding equation is good. However, Imura's flooding curve is consistenetly higher than the experimental flooding curve given by Equation (4.6).

5.4.2.4 Comparison with Richter and Wallis (33)

As a result of an extensive review of flooding literature, Richter and Wallis (33) proposed the following empirical equation as a flooding equation suitable for all PWR geometries:

$$J_A^{*\frac{1}{2}} + 0.8J_W^{*\frac{1}{2}} = 0.4 \qquad (5.11)$$

Figure 5.13 shows a comparison between Equation (5.11) and the experimental data. As can be seen, the agreement is much better than the previous correlations. Not a very surprising result, since Equation (5.11) was obtained by approximating the existing flooding data from different scaled PWR geometries. However, this agreement becomes poorer as J_{Wi}^* exceeds 0.04. The present data supports the previous works at Creare and Dartmouth which indicated that at complete bypass ($J_W^* = 0$)

$$J_A^{*\frac{1}{2}} = 0.4 \qquad (5.12)$$

This is probably a reasonable approximation which seems to be insensitive to the geometry or the injection angle (for Phase 1, $J_A^{*\frac{1}{2}}$ was equal to 0.43 at complete bypass).

5.4.2.5 Comparison with Richter (34)

Richter (34) developed a theoretical model to describe the conditions at the start of bypass. This model yielded the following equation:

$$C_w N_B J_g^{*6} S^{*2} J_L^{*2} + C_w N_B J_g^* + 150 C_w \frac{J_g^{*2}}{S^*} = 1 \quad (5.13)$$

where

$$C_w = 0.008$$

$$S^* = \frac{S}{B}$$

$$N_B = B^2 \left[\frac{g(\rho_L - \rho_g)}{\sigma} \right]^{\frac{1}{2}}$$

Equation (5.13) is compared with the experimental data in Figure 5.14. The comparison shows that Richter's theory overpredicts the flooding conditions. However, the data supports the prediction of the point of complete bypass as given by Equation (5.13). The qualitative agreement is good and quantitatively it is not too far from the experimental data.

5.4.3 General Comment on the Comparisons

It is clear from the above comparisons that none of the correlations tested really agree with the expiremental data. Moreover, the general comparison shown in Figure 5.15 indicates that these correlations do not agree with each other. This indicates clearly that the actual mechanism of flooding remains undetermined. A possible reason for the differences is the lack of reliable data for the liquid film thickness under PWR gemoetry conditions. It goes without saying that the film flow resulting from impinging jets is different from that of a falling film. Also it might be expected that turbulence would be more likely to be present in the former than in the latter.

In the present situation none of the above correlations should be used outwith the experimental conditions from which they were derived.

As a result of the above discussion, the author shall use Equation (4.6), obtained from the present air/water tests, as a basis for developing a model for condensation effects. This model is presented in Chapter 6.

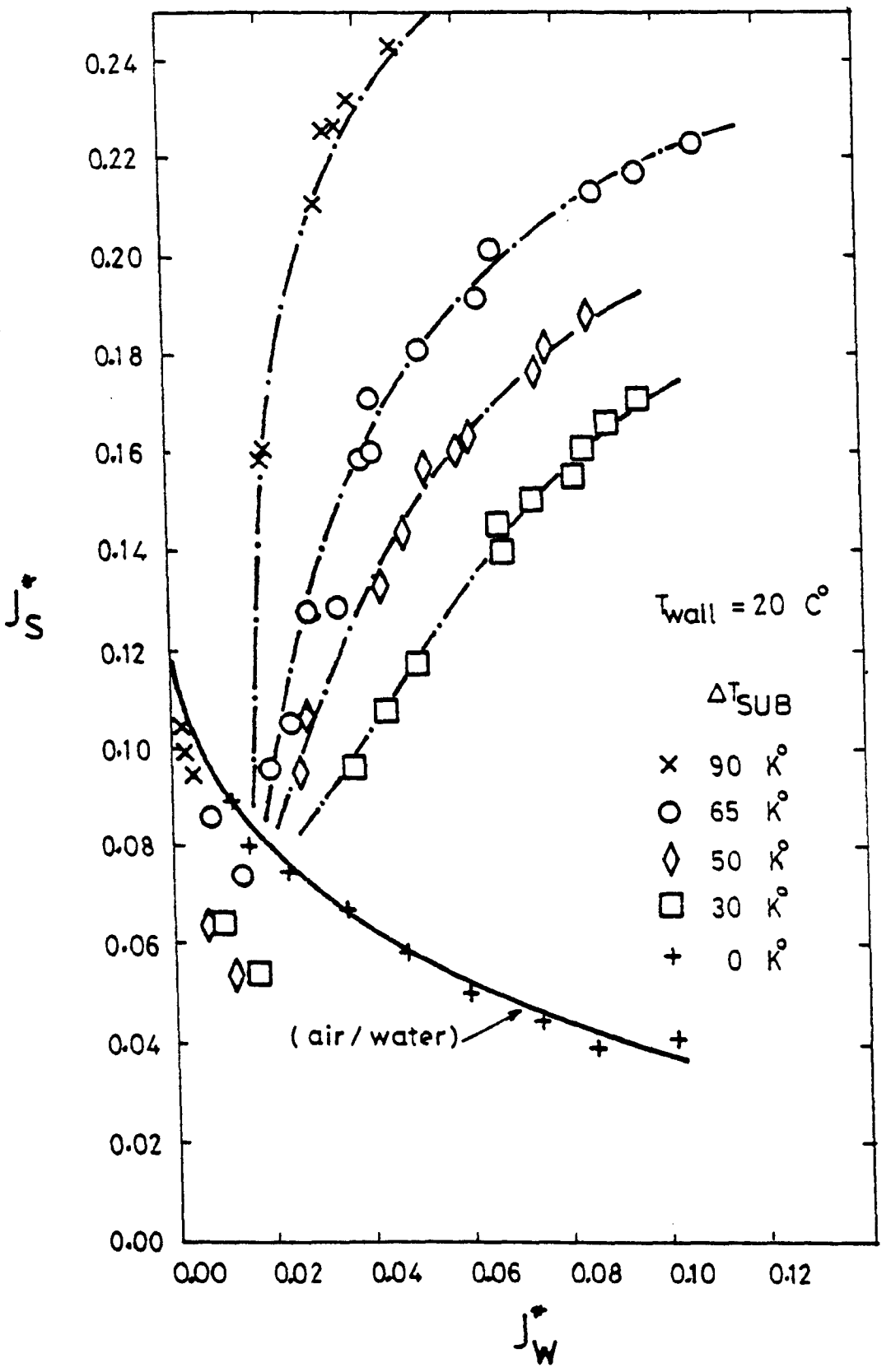

Fig 5.1 COMARISON BETWEEN AIR/WATER AND STEAM/WATER TEST DATA (PHASE 2 TESTS - STEAM FIRST)

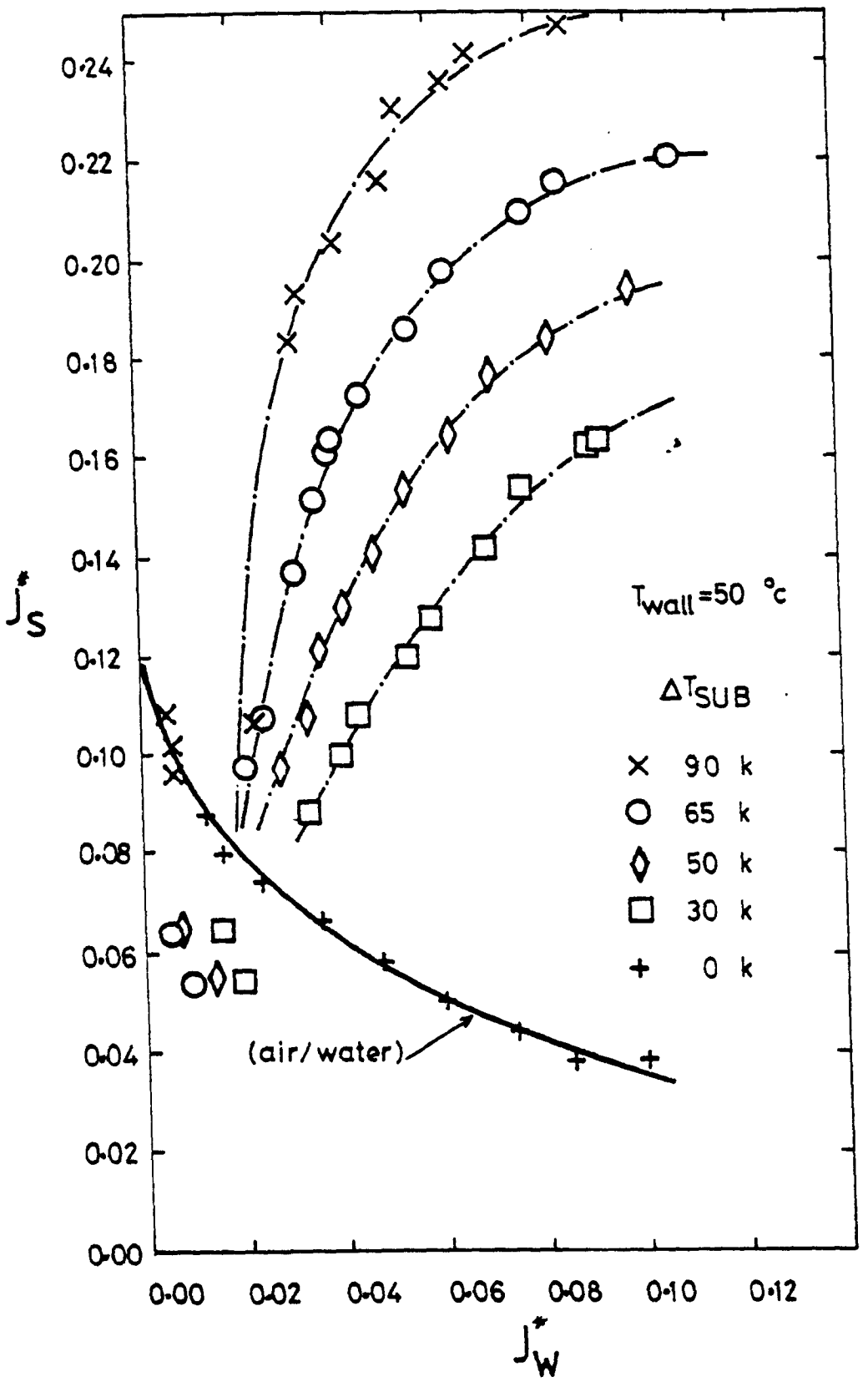

Fig 5.2 COMPARISON BETWEEN AIR / WATER AND STEAM/WATER TEST DATA (PHASE 2 TESTS - STEAM FIRST)

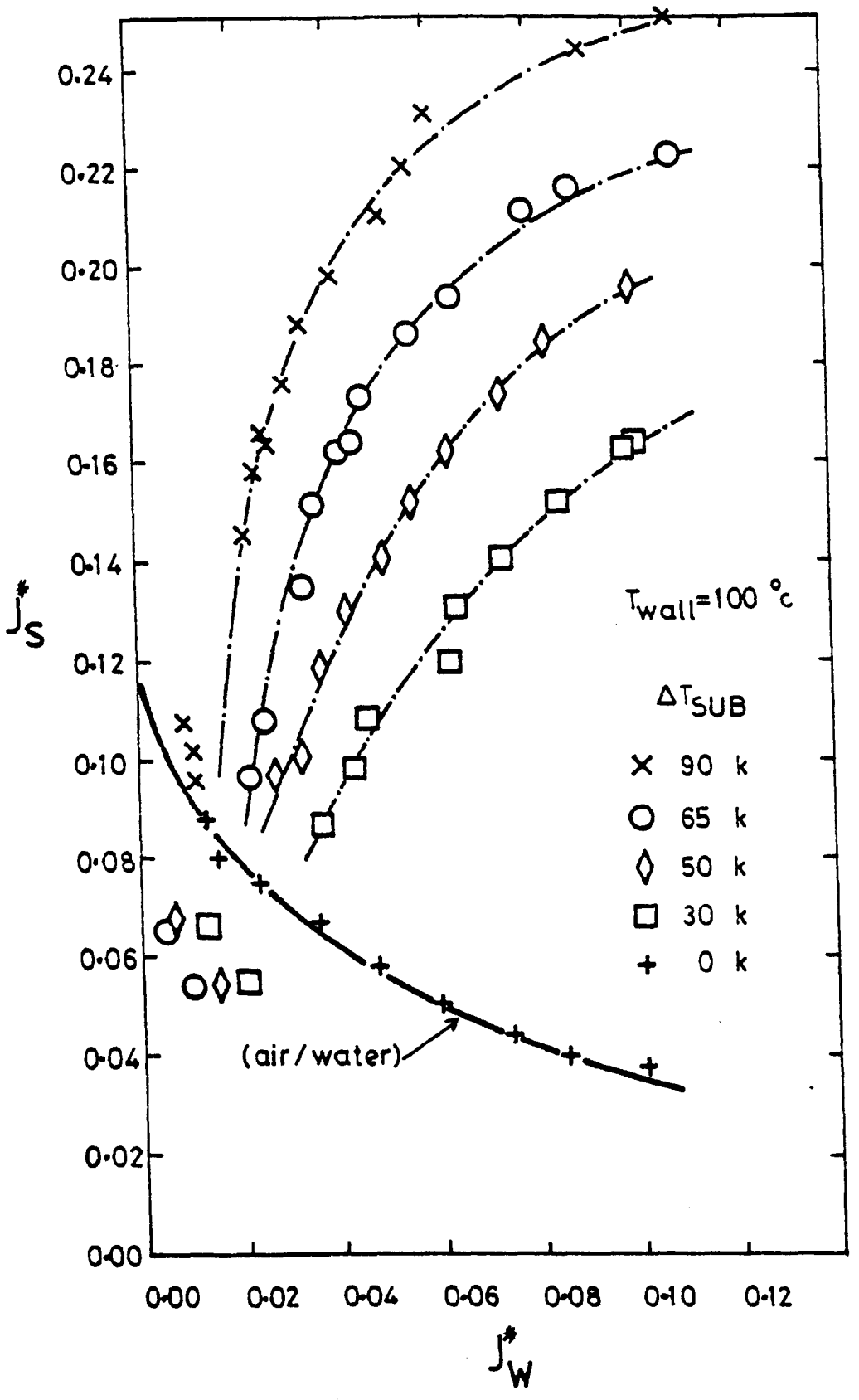

Fig 5.3 COMPARISON BETWEEN AIR/WATER AND STEAM/WATER TEST DATA (PHASE 2 TESTS - STEAM FIRST)

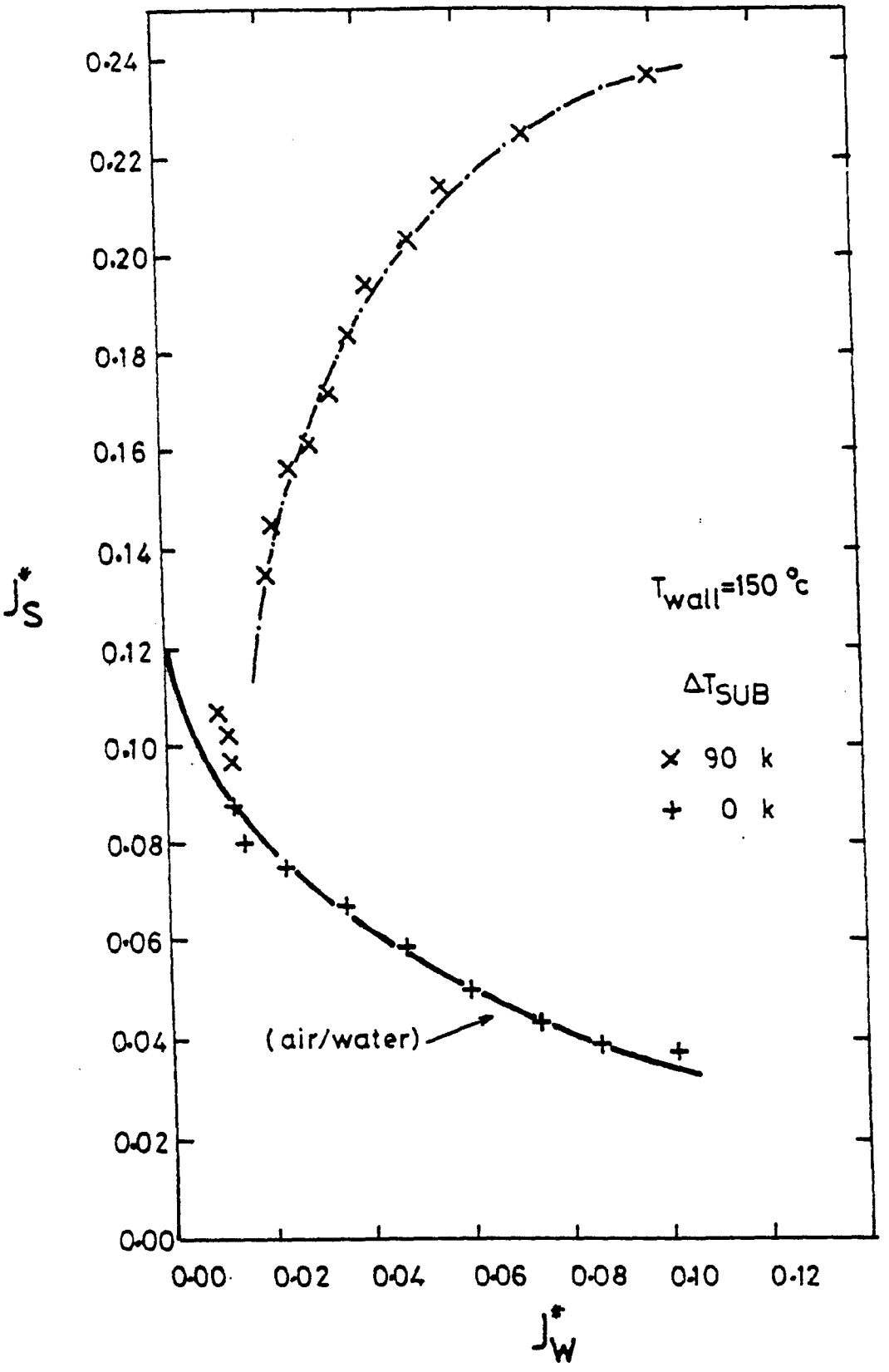

Fig 5·4 COMPARISON BETWEEN AIR / WATER AND STEAM / WATER TEST DATA (PHASE 2 TESTS - STEAM FIRST)

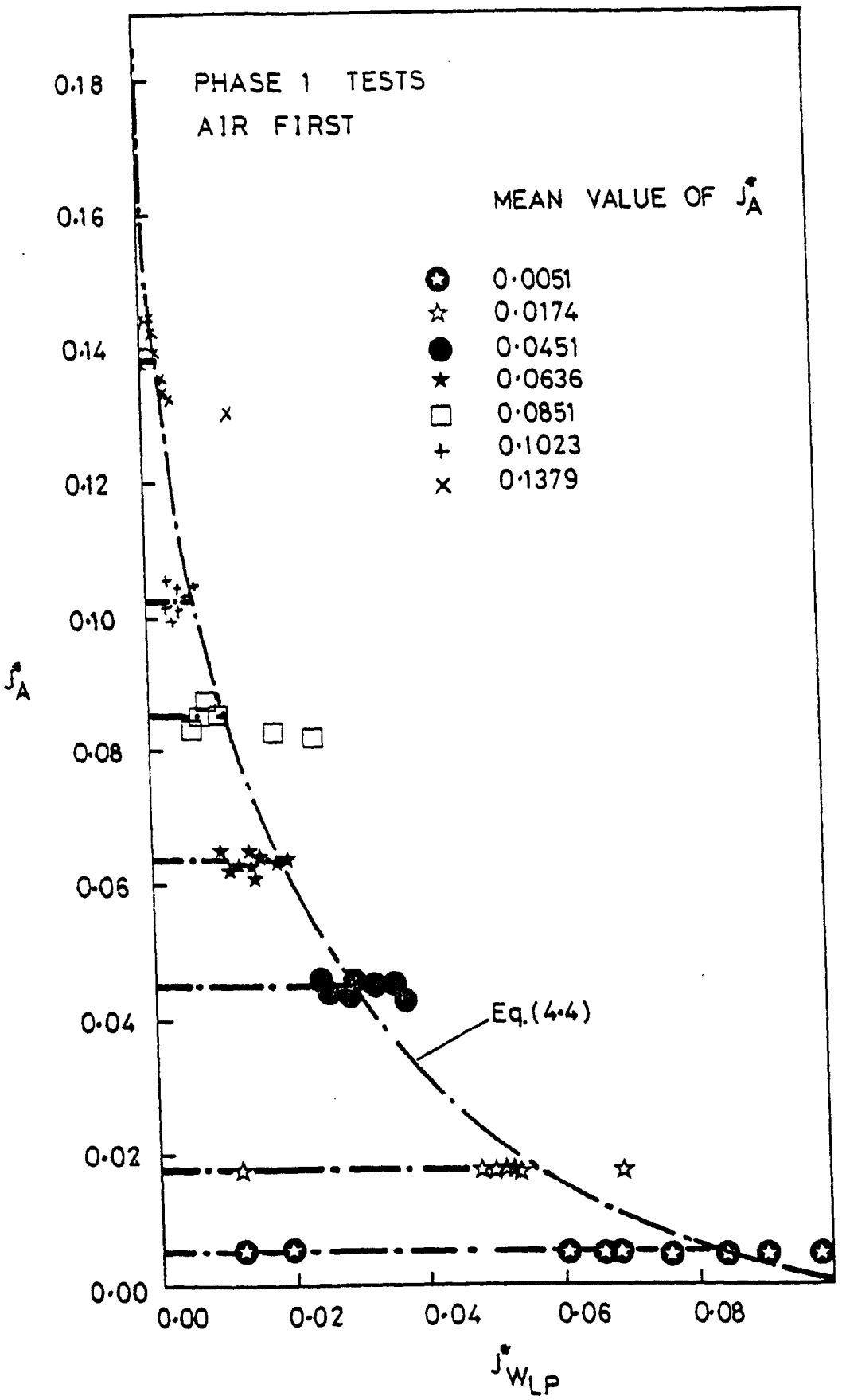

Fig 5.5 Bypass Characteristics from Air Water Tests

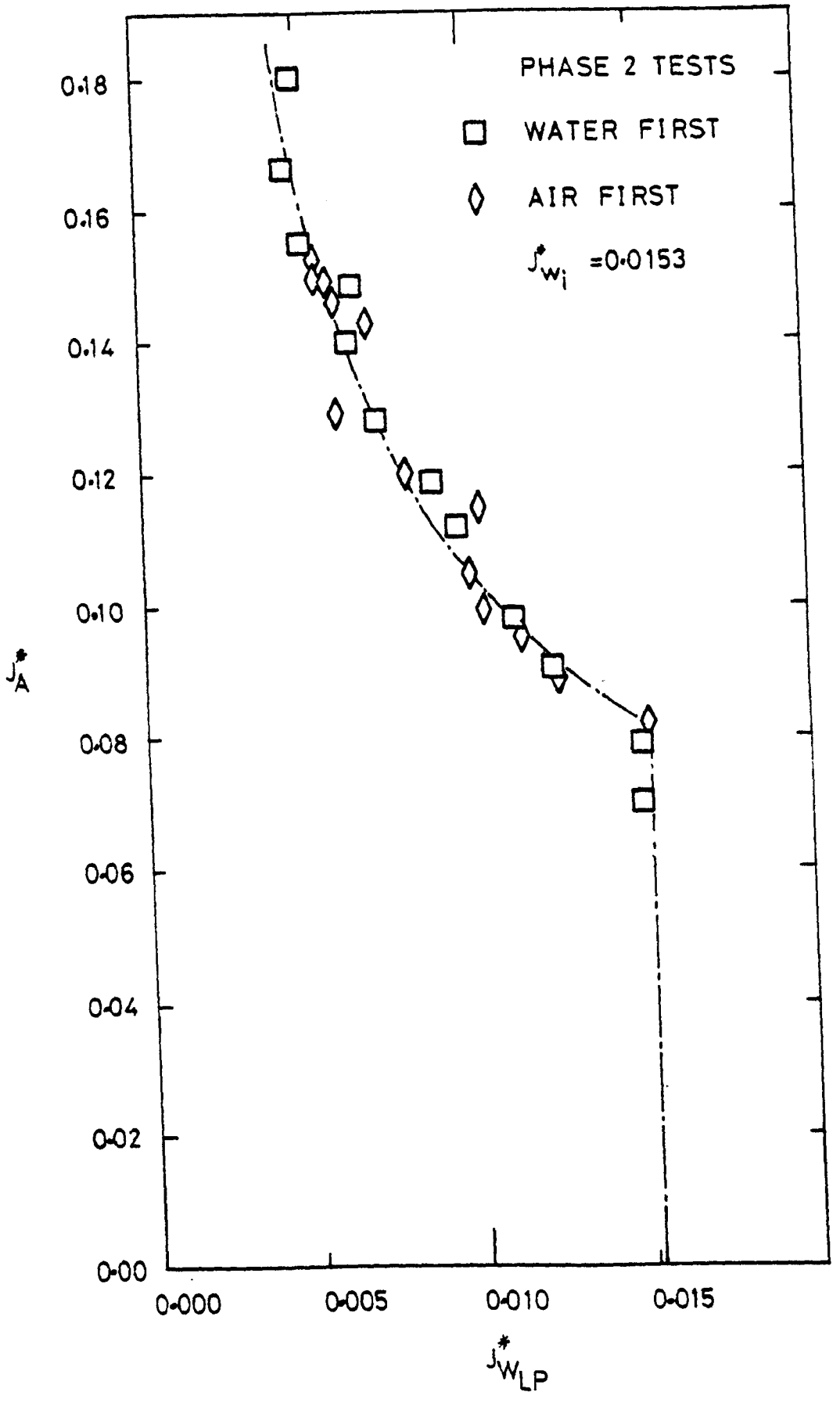

Fig 5.6 Comparison Of "Water First" With "Air First" Test Data

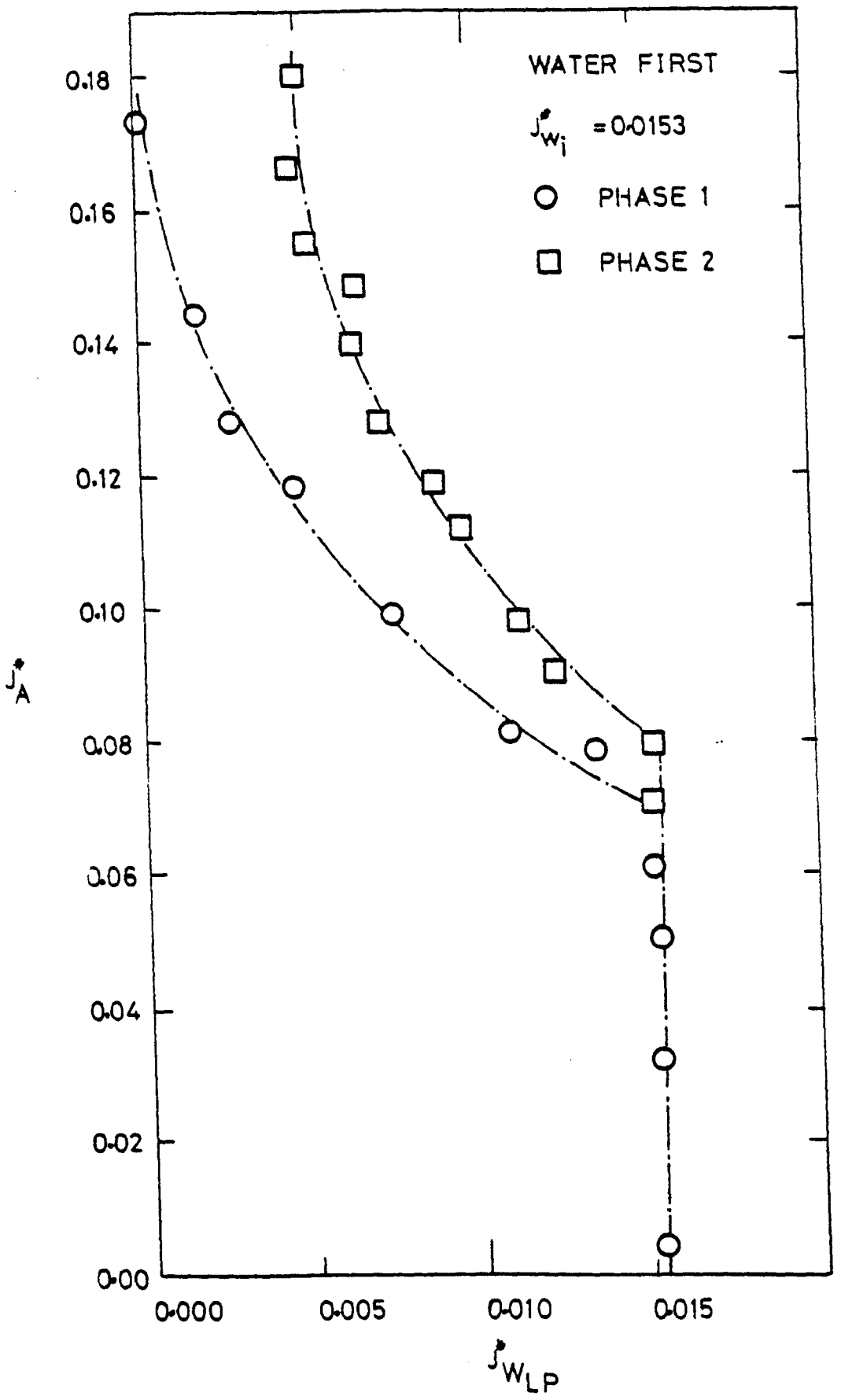

Fig 5·7 Comparison Of Phase 1 & Phase 2 Test Data

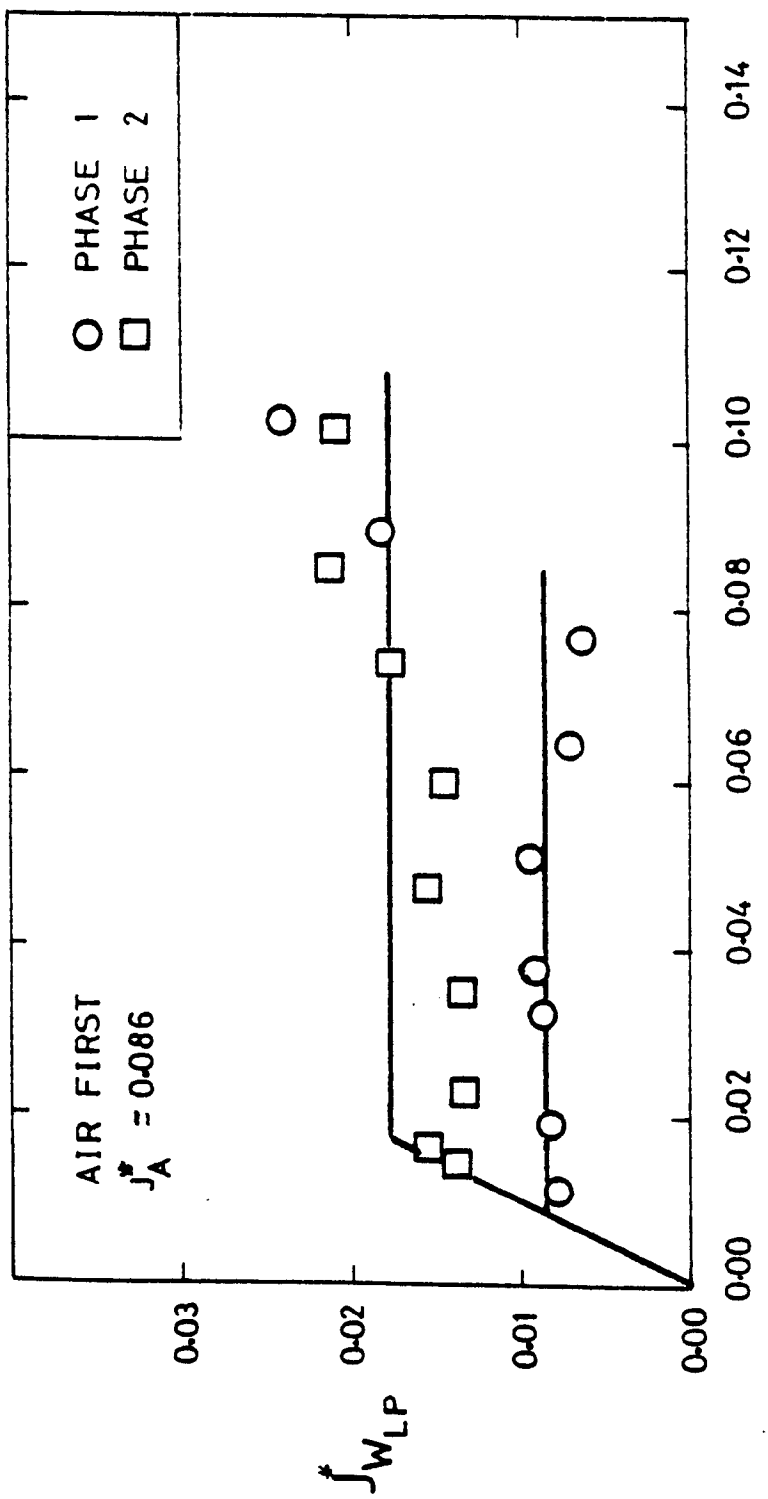

Fig 5.8 Comparison Of Phase 1 & Phase 2 Data

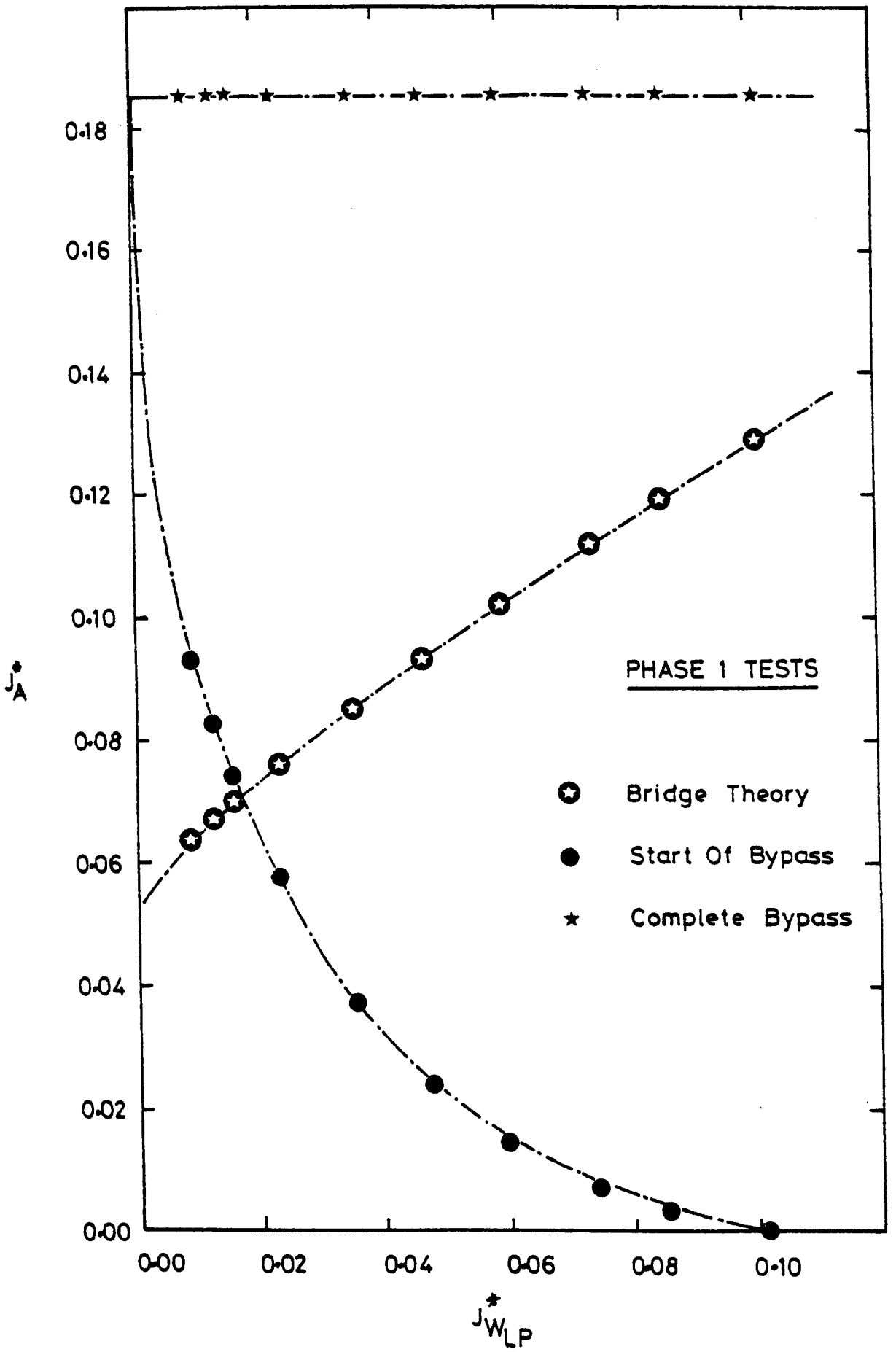

Fig 5·9 Comparison Beteen The Bridge Theory And The Experimental Results

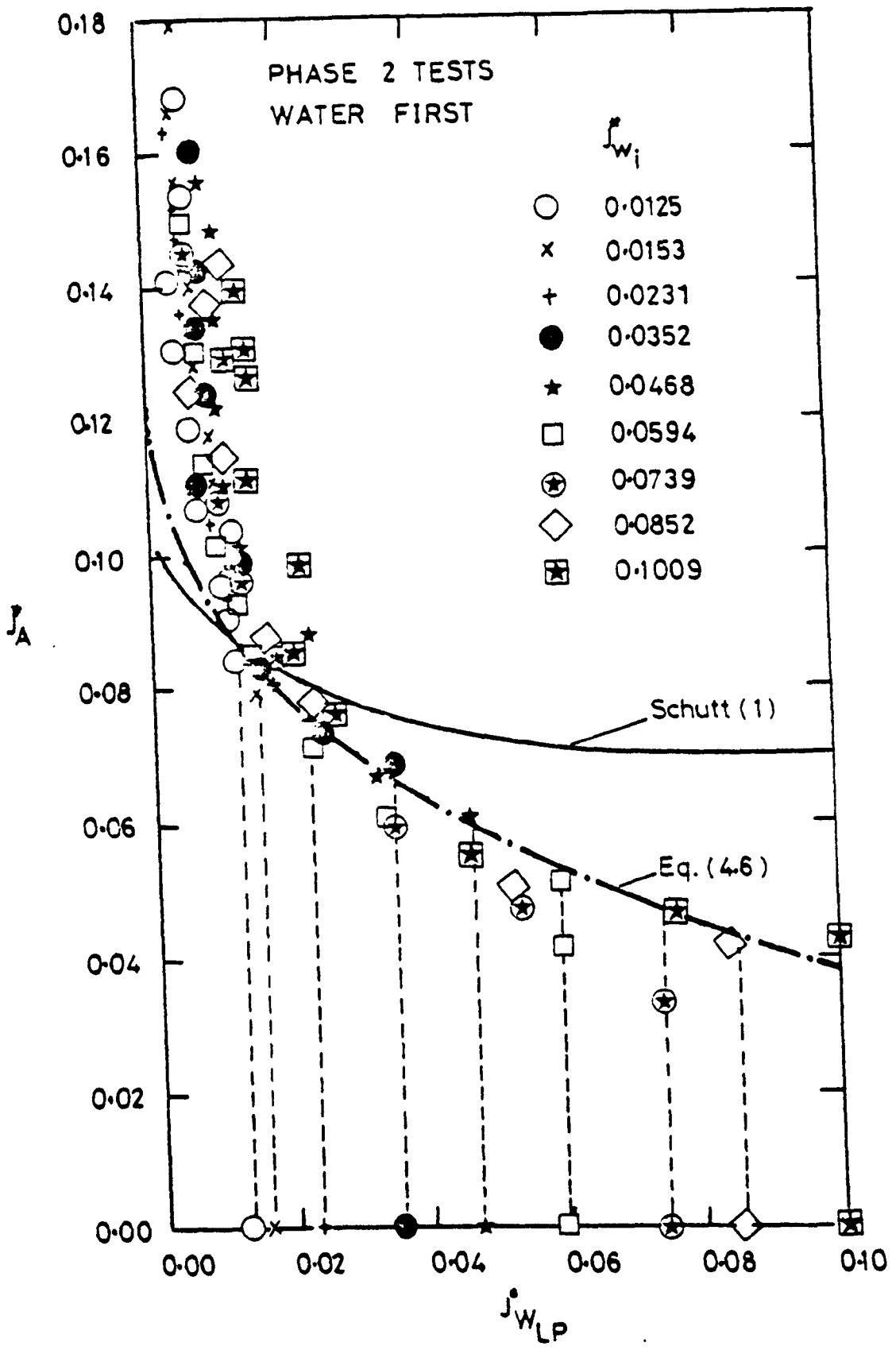

Fig 5.10 DIMENSIONLESS PLOT OF ALL AIR-WATER DATA (COMPARISON BETWEEN EXPERIMENT AND SCHUTT'S CORRELATION (1))

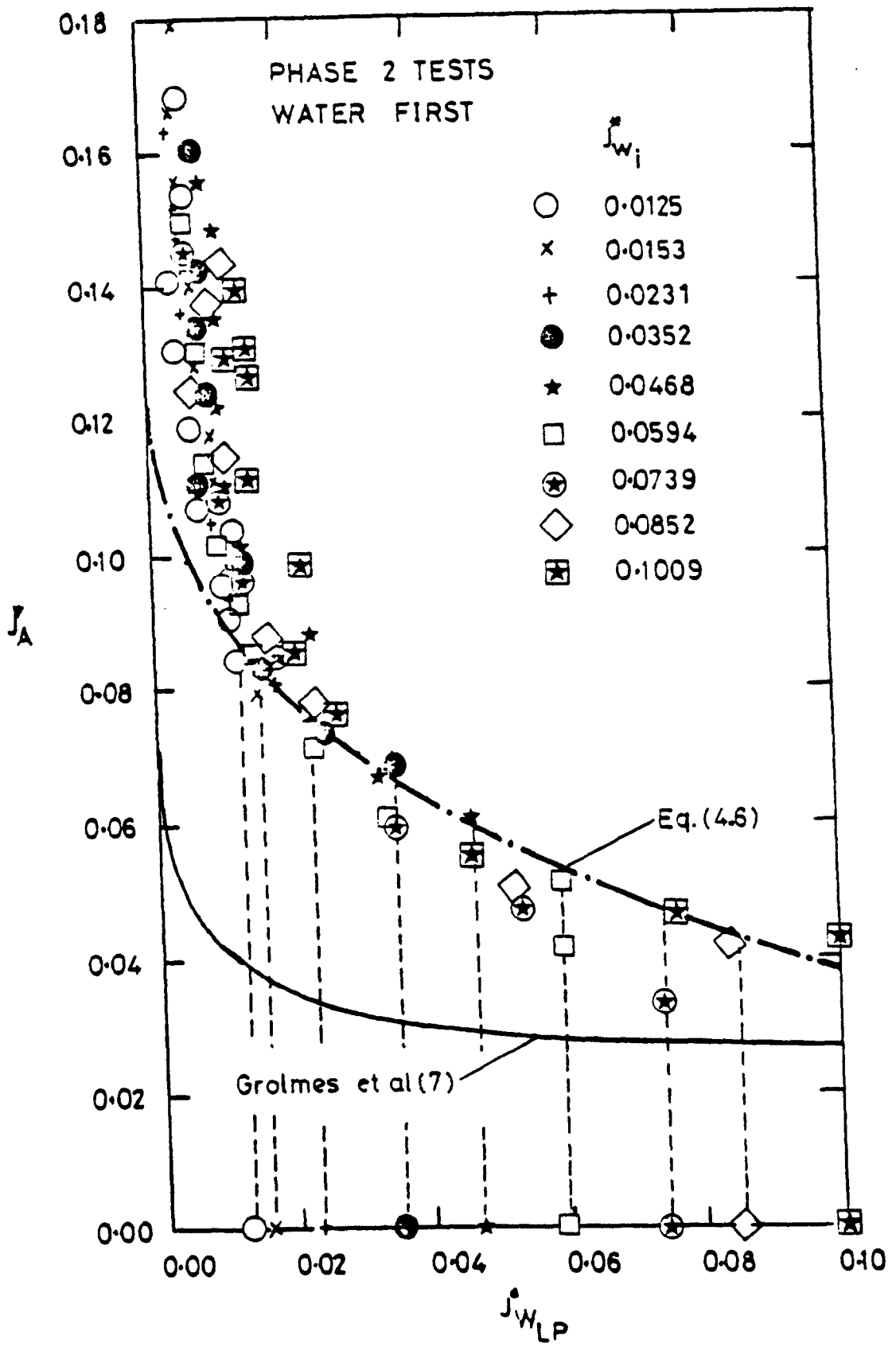

Fig 5.11 DIMENSIONLESS PLOT OF ALL AIR-WATER DATA (COMPARISON BETWEEN EXPERIMENT AND GROLMES' CORRELATION [7])

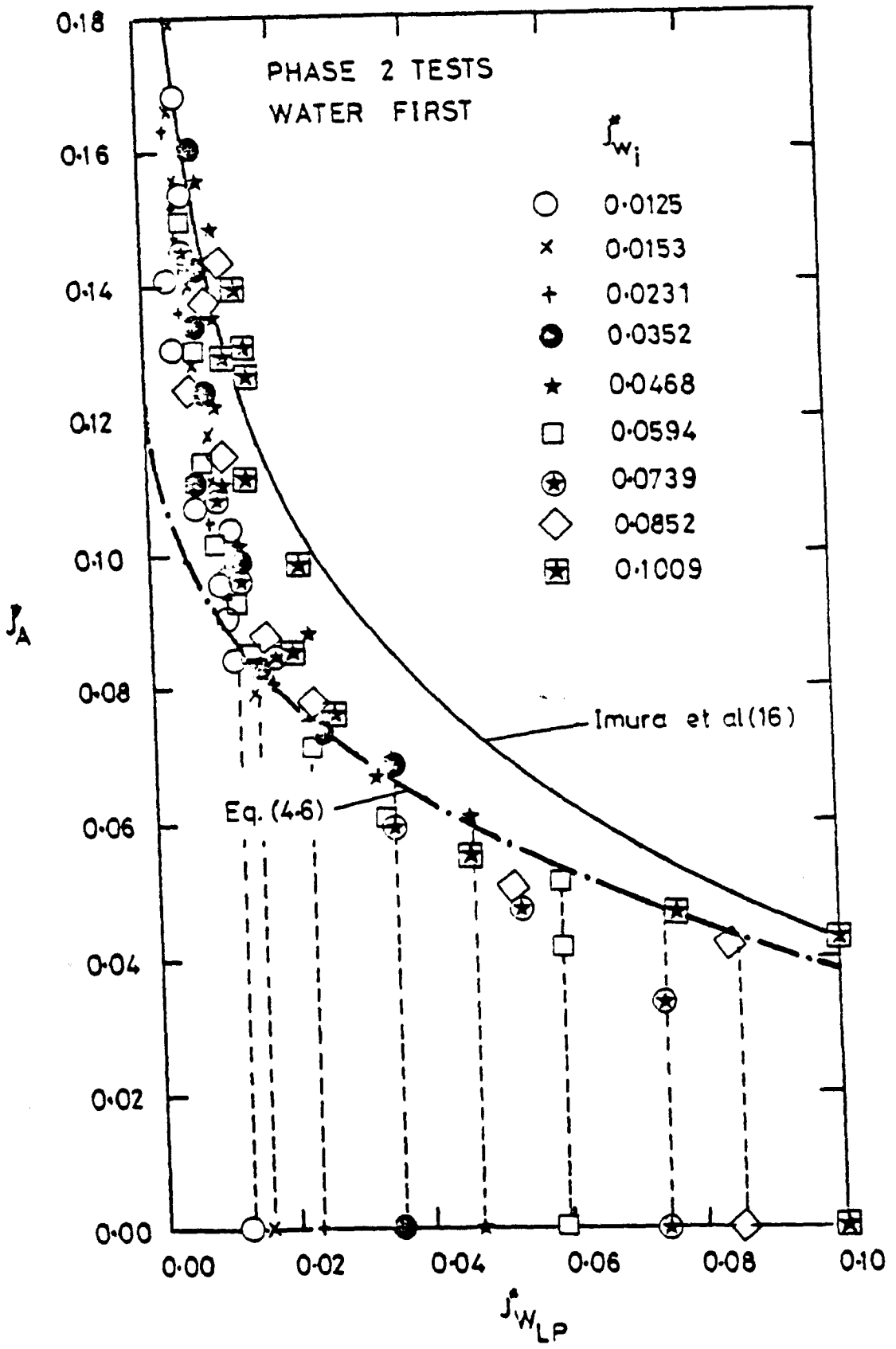

Fig 5·12 DIMENSIONLESS PLOT OF ALL AIR-WATER DATA (COMPARISON BETWEEN EXPERIMENT AND IMURA'S CORRELATION (16))

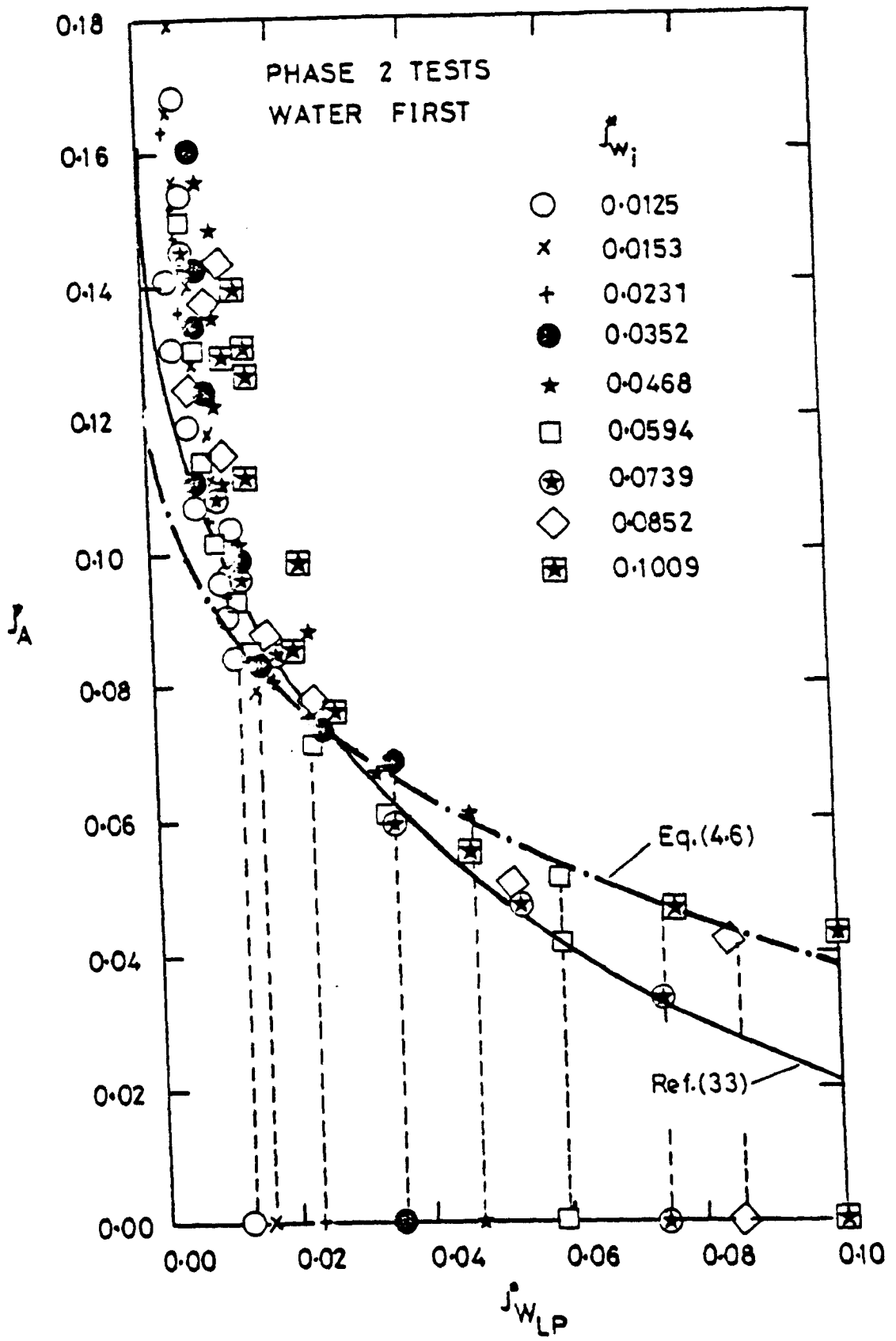

Fig 5.13 DIMENSIONLESS PLOT OF ALL AIR-WATER DATA (COMPARISON BETWEEN EXPERIMENT AND RICHTER & WALLIS'S CORRELATION (33))

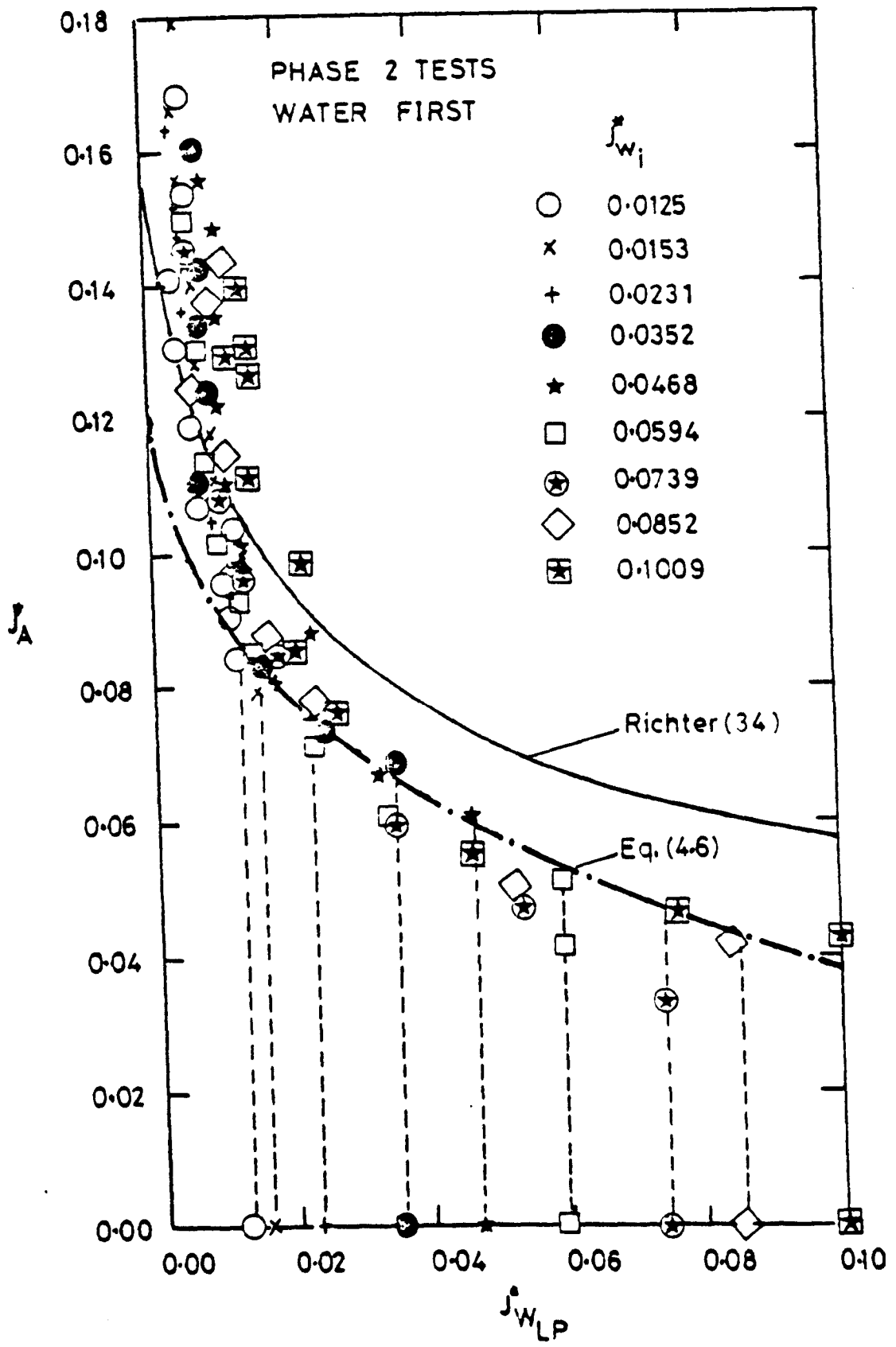

Fig 5.14 DIMENSIONLESS PLOT OF ALL AIR-WATER DATA (COMPARISON BETWEEN EXPERIMENT AND RICHTER CORRELATION (34))

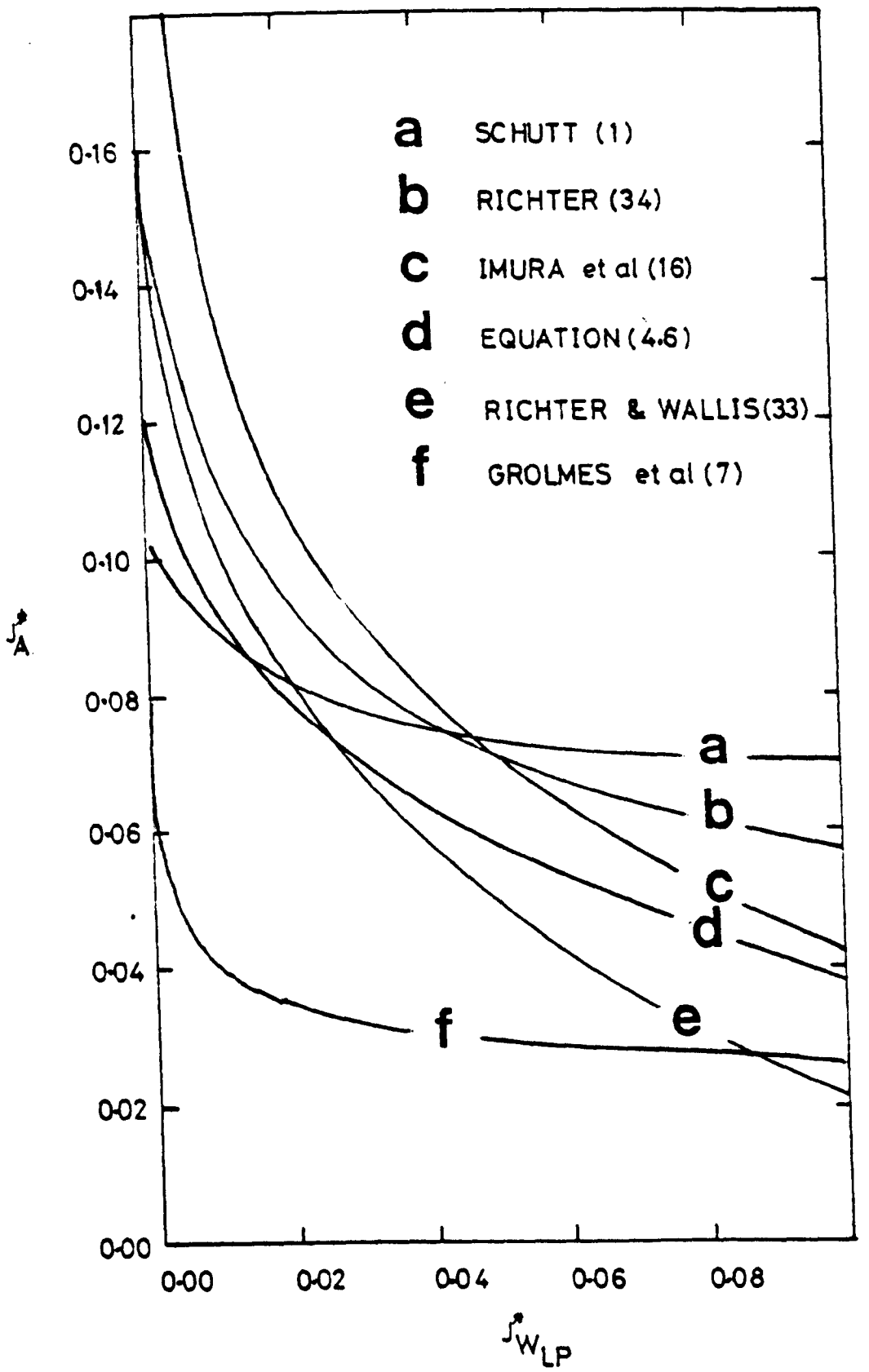

Fig 5.15 COMPARISON OF DIFFERENT FLOODING CORRELATIONS WITH EQUATION (4.6)

CHAPTER 6

THEORETICAL ANALYSIS

CHAPTER 6 : THEORETICAL ANALYSIS

In this Chapter, the experimental work presented is related to theoretical analyses for both the Phase 1 and Phase 2 configurations. For Phase 1, a theoretical investigation into the effect of the air rising between the two opposed waterfalls is presented. For Phase 2 (which is a better simulation of the PWR geometry) a theoretical expression is presented to predict non-equilibrium effects which allow for the effect of geometry, inlet water flowrate, inlet water subcooling and downcomer wall temperature.

These are dealt with in turn.

6.1 THE UPWARD FLOW OF AIR BETWEEN TWO WATERFALLS

This section is concerned with the upward flow of air between the waterfalls with attention being focussed on (i) predicting the airflow conditions at which the two waterfalls just come together and (ii) describing the waterfall trajectories.

The study arose from observations made during the experimental work reported in Chapter 4. During these tests, when the water was introduced through the side entries it flowed down through the test section in the form of twin waterfalls, as indicated in Figure 6.1. It was found that, for any particular inlet water flowrate, varying the air flowrate altered the water trajectories

and eventually produced a condition at which the waterfalls were pulled together (condition b in Figures 4.1 and 4.2).

Waterfall trajectories were measured using a cathetometer and telescope and typical results are shown in Figure 6.2. These measurements are tabulated in Appendix M. The conditions under which the waterfalls were observed to come together at the bottom of the test section (i.e., condition b in Figure 4.1) are plotted in Figure 6.3 in the form of air mass flowrate versus total water mass flowrate (i.e., twice the water mass flowrate per inlet pipe). The curve is drawn as rising from the origin, although experimental data were not obtained at very low values of M_W; a theoretical justification for this is given later. Figure 6.3 does indicate a maximum value of M_A as M_W increases followed by a drop to zero as M_W is further increased. This final condition is due to the horizontal velocity component of the inlet water being sufficiently large as to cause the waterfalls to meet even with zero air flow. The results in Figure 6.3 are also tabulated in Table 6.1.

6.1.1 The Trajectories of the Waterfalls

A simple theory for the trajectories of the waterfalls is presented here in which the drag of the water on the flat surfaces of the test section is neglected and the jet is assumed to be projected horizontally with a uniform velocity u_i and pressure p. Consider an element

TABLE 6.1

M_w kg/s	M_A kg/s	J_w^*	J_A^*	Fr_{wz}	Fr_{wi}	$Fr_{wi}{}^{1/2}J_A^*$	$Fr_{wi}J_w^*$
0.536	0.00756	0.0118	0.0047	1.32	2.26	0.0071	0.0267
0.712	0.000658	0.0156	0.0042	1.28	2.24	0.0063	0.0349
0.884	0.00409	0.0194	0.0026	1.41	2.29	0.0039	0.0444
1.057	0.0013	0.0232	0.0008	1.35	2.27	0.0012	0.0527
0.40	0.0073	0.0088	0.0045	1.35	2.27	0.0068	0.02
0.702	0.0083	0.0154	0.0052	1.35	2.27	0.0078	0.035
1.056	0.0013	0.0232	0.0008	1.35	2.27	0.0012	0.0527
2.23	0	0.0489	0	1.118	2.19	0	0.1071

$$Fr_{wi} = 0.55\, Fr_{wz}\left[1 + \frac{1}{0.67\, Fr_{wz}}\right]^{3/2}$$

EXPERIMENTAL VALUES RELATING TO THE COLLAPSE CONDITION OF THE PAIR OF WATERFALLS.

WATER FIRST TESTS

of the water jet of length ds and thickness H_w at point (x,z) and with velocity components u (in the x direction) and w (in the z direction) as shown in Figure 6.4. Thus, if Δp is the pressure difference across the element ds, the equations of motion for the element of water of density ρ_w and local thickness H_w are

$$\frac{du}{dt} = \left(\frac{\Delta p}{\rho_w H_w}\right) \frac{w}{(w^2 + u^2)^{\frac{1}{2}}} \qquad (6.1)$$

$$\frac{dw}{dt} = g - \left(\frac{\Delta p}{\rho_w H_w}\right) \frac{u}{(w^2 + u^2)^{\frac{1}{2}}} \qquad (6.2)$$

Now from continuity:

$$H_w \bar{v} = H_{wi} u_i \qquad (6.3)$$

where $\bar{v} = (u^2 + w^2)^{\frac{1}{2}}$ is the absolute velocity of the water element and H_{wi} and u_i are the thickness and velocity of the waterfall at the test section entry. It is then possible to solve equations (6.1) to (6.3) to give the velocities u, w, $\bar{v}$ by

$$\bar{V} = (2gz + u_i^2)^{\frac{1}{2}} \qquad (6.4)$$

$$u = u_i + \frac{1}{\rho_w H_{wi} u_i} \int_0^z \Delta p \, dz \qquad (6.5)$$

$$w = u_i \left[\left(1 + \frac{2q}{u_i^2} z \right) - \left(1 + \frac{1}{\rho_w H_{wi} u_i^2} \int_0^z \Delta p \, dz \right)^2 \right]^{\frac{1}{2}} \qquad (6.6)$$

Noting that the position of (x,z) of the water element at any time t is given by the differential equation

$$\frac{dx}{dy} = \frac{u}{w} \qquad (6.7)$$

The equation of the water trajectory is obtained as

$$x = \int_0^z \frac{dz}{\left[\frac{1 + \frac{2q}{u_i^2} z}{\left(1 + \frac{1}{\rho_w H_{wi} u_i^2} \int_0^z \Delta p \, dz \right)^2} - 1 \right]^{\frac{1}{2}}} \qquad (6.8)$$

That can be made dimensionless by defining the variables X and Z which are proportional to the reciprocal of Froude numbers and a dimensionless pressure difference ΔP as:

$$X = \frac{2g}{u_i^2} x \quad ; \quad Z = \frac{2g}{u_i^2} z \quad ; \quad \Delta P = \frac{\Delta p}{2 g \rho_w H_{w_i}}$$

(6.9)

giving

$$X = \int_0^Z \frac{dZ}{\left[\frac{1 + Z}{(1 + \int_0^z \Delta P dZ)^2} - 1 \right]^{\frac{1}{2}}} \qquad (6.10)$$

This is the general equation for the trajectory of each waterfall when subjected to a gravitational force and a pressure difference which can vary from point to point along the trajectory. Equation (6.10) can be written as:

$$X = \int_0^Z \frac{dZ}{\left[\frac{1 + Z}{(1 + F_z)^2} - 1 \right]^{\frac{1}{2}}} \qquad (6.11)$$

where

$$F_z = \int_0^z \Delta P . dZ \qquad (6.12)$$

When $F_z = 0$, Equation (6.11) reduces to the parabolic form:

$$X = 2Z^{\frac{1}{2}} \qquad (6.13)$$

No allowance has been made so far for the effect that just before the end of the water inlet pipe (i.e., the brink), the vertical velocity profile (and the water height) is non-uniform because the pressure of the water at the bottom of the inlet pipe has to decrease from $(p_a + g\,\rho_w H_{wi})$ to p_a, the atmospheric pressure. This is a complex problem and an approximate solution is described in Appendix N, where it is shown that the effective mean inlet velocity u_i and Froude number, Fr_{wi}, are enhanced by the mean hydrostatic head at the inlet pipe to give :

$$u_i = k \left[\frac{M_w/2}{\rho_w H_{w_m} S} \right] \left[1 + \frac{1}{k^2 Fr_{w_z}} \right]^{\frac{1}{2}} \qquad (6.14)a$$

and

$$Fr_{w_i} = k^3 Fr_{w_z} \left[1 + \frac{1}{k^2 Fr_{w_z}} \right]^{3/2} \qquad (6.14)b$$

where Fr_{w_z} and H_{w_m} are the Froude number $\left[\frac{M_w/2}{\rho_w H_{w_m} S}\right]^2 / [gH_{w_m}]$

and the waterfall thickness measured just <u>before</u>

the brink, k, is a constant, experimentally determined later,

and $Fr_{wi} = \frac{u_i^2}{gH_{wi}}$.

6.1.2 Air Flow

As shown in Figure 6.4, the air rises between the two waterfalls as if flowing in a divergent duct with flexible walls, but some will be brought to rest underneath the waterfalls. The resultant pressure difference over the water element will thus correspond to the kinetic head of the air between the waterfalls at position z. If the air flow is assumed to be one dimensional* of local velocity u_A, and if the density ρ_A of the air is assumed to be constant

$$\Delta p = \frac{1}{2} \rho_A u_A^2 \qquad (6.15)$$

The air velocity u_A depends on the path followed by the air jet as it passed between the waterfalls, a complex problem in fluid mechanics.

Equation (6.15) can be written as:

$$\Delta p = \frac{1}{2} \rho_A \left[\frac{M_A}{\rho_A (B - 2x) S} \right]^2 \qquad (6.16)$$

where M_A is the air mass flowrate and B and S are the breadth and depth of the test section, and x is the horizontal distance to the air passage and is a function of z in general.

---

* NOTE: Three dimensional air patterns in the lower plenum tank are neglected in the analysis. The effects of entry losses, shear stress on waterfalls and liquid entrainment in air are also neglected.

The mass flowrate per side can be expressed as :

$$\frac{M_w}{2} = \rho_w U_i H_{wi} S \qquad (6.17)$$

From Equations (6.16) and (6.17), the general dimensionless pressure difference can be expressed as :

$$\Delta P = \left(\frac{M_A}{M_w}\right)^2 \left(\frac{\rho_w}{\rho_A}\right) Fr_{Wi}^{-1} \frac{1}{(B^*/2 - X)^2} \qquad (6.18)$$

or

$$\Delta P = \frac{K}{(B^*/2 - X)^2} \qquad (6.19)$$

where

$$K = \left(\frac{M_A}{M_w}\right)^2 \left(\frac{\rho_w}{\rho_A}\right) Fr_{wi}^{-1} \qquad (6.20)$$

$$B^* = \frac{2g}{u_i^2} B \qquad (6.21)$$

$$X = \frac{2g}{u_i^2} x \qquad (6.22)$$

It should be noticed that, as K increases, so the ratio $\frac{M_A}{M_w}$ increases thus, for the present experiments, trajectory curves for varying K values can be regarded as those relating to diferent upward air flowrates. The shape of the water trajectory depends on X which depends on the mode of air flow between the waterfalls. Three

possible modes of air flow are illustrated in Figure 6.5.

(i) In the first and most conservative case, illustrated in Figure 6.5a, it is assumed that the air follows the curvature of the waterfall, unaffected by the outlet hole of the test section. The curvature can be approximated to

$$x = c z^{\frac{1}{2}} \tag{6.23}$$

where c is a constant and x is measured to the centre of the water jet (jet thickness effects will be considered later .

Now, from the boundary condition $x = x_b$ at $z = z_b$, the value of the constant c can be evaluated as

$$c = \frac{x}{z_b^{\frac{1}{2}}} = \frac{x_b}{z_b^{\frac{1}{2}}} \tag{6.24}$$

Substituting Equation (6.24) into (6.23) gives:

$$x = x_b \left(\frac{z}{z_b} \right)^{\frac{1}{2}} \tag{6.25}$$

OR in dimensionless form:

$$X = x_b \left(\frac{z}{z_b} \right)^{\frac{1}{2}} \tag{6.26}$$

(ii) At the opposite extreme, it is assumed that the air separates from the walls of the waterfalls, as it enters the water channel at its narrowest width $(B - 2x_b)$, at the bottom of the test section with a slow moving circulation pattern between the gas jet and the waterfall giving an approximately uniform pressure. If it is further assumed, as in Figure 6.5b, that the width of the air jet remains constant at the bottom value of $(B - 2x_b)$, i.e., a parallel jet, it follows that:

$$x = x_b \tag{6.27}$$

or in dimensionless form:

$$X = X_b \tag{6.28}$$

(iii) In the third case, it is assumed that the air moves as a jet from the inlet of breadth $(B - 2x_b)$ to the outlet hole of diameter d_o, as shown in Figure 6.5c, so that:

$$x = \left(\frac{B}{2} - \frac{d_o}{2}\right) + \left(\frac{\frac{d_o}{2} - \frac{B}{2} + x_b}{z_b}\right) z \tag{6.29}$$

which can be expressed in dimensionless form as :

$$X = \left(\frac{B^*}{2} - \frac{D_o}{2} \right) + \left(\frac{\frac{D_o}{2} - \frac{B^*}{2} + X_b}{Z_b} \right) Z \qquad (6.30)$$

where $D_o = \frac{2q}{u_i^2} d_o$

6.1.3 Effect of Air Flow on the Water Trajectories

It is now possible to substitute Equation (6.19) together with the appropriate value of X into Equation (6.11) to obtain the water trajectories. This is outlined below.

For case (i) with the air following the waterfall profile, combining Equations (6.26) and (6.19) gives:

$$F_z = \frac{2K}{X_b^2 / Z_b} \left[\log_e \left[1 - \left(\frac{X}{B^*/2} \right) \left(\frac{Z}{Z_b} \right)^{\frac{1}{2}} \right] \right] + \frac{\left(\frac{X_b}{B^*/2} \right) \left(\frac{Z}{Z_b} \right)^{\frac{1}{2}}}{1 - \left(\frac{X_b}{B^*/2} \right) \left(\frac{Z}{Z_b} \right)^{\frac{1}{2}}} \qquad (6.31)$$

Substituting Equation (6.31) into Equation (6.11) and arranging gives :

$$\eta = 2 \int_0^Y \frac{\frac{\lambda}{\eta_b^2}\, Y.dY}{\left[\frac{1 + K_1 \frac{\lambda}{\eta_b^2} Y^2}{1 + K_2 \frac{\lambda}{\eta_b^2} F(Y)^2} - 1\right]^{\frac{1}{2}}} \qquad (6.32)$$

where

$$Y = \left(\frac{X_b}{B^*/2}\right)\left(\frac{Z}{Z_b}\right)^{\frac{1}{2}} \qquad (6.33)$$

$$F(Y) = \log_e (1 - Y) + \frac{Y}{1 - Y} \qquad (6.34)$$

$$\eta = \frac{X}{B^*/2} = \frac{x}{B/2} \qquad (6.35)$$

$$\eta_b = \frac{X_b}{B^*/2} = \frac{x_b}{B/2} \qquad (6.36)$$

$$K_1 = B^*/2 \qquad (6.37)$$

$$K_2 = \frac{2K}{B^*/2} \qquad (6.38)$$

$$\lambda = \frac{Z_b}{B^*/2} = \frac{z_b}{B/2} \qquad (6.39)$$

$$= 1.843 \text{ for the present work}$$

Equation (6.32) was integrated numerically on a computer to yield dimensionless trajectories of the form Z versus X. A typical set of curves for a water inlet

velocity u_i = 0.475 m/s is shown in Figure 6.6. As might be expected, the horizontal travel of the water increases as the air flow increases. The corresponding values of the dimensionless pressure difference ΔP at the bottom of the test section, i.e., $Z = Z_b$, are also shown in Figure 6.6.

For Case (ii), with $\Delta P = \Delta P_b$, Equation (6.11) can be integrated analytically to give

$$X = \frac{1}{2\,\Delta P_b} \sin^{-1}\left(2\phi(R_b Z)\right) - \frac{1}{R_b}\phi(R_b Z) \qquad (6.40)$$

where the function ϕ is given by

$$\phi(R_b Z) = (R_b Z)^{\frac{1}{2}} (1 - R_b Z)^{\frac{1}{2}} \qquad (6.41)$$

and the ratio $R_b = \dfrac{\Delta P_b^2}{1 - 2\,\Delta P_b}$ (6.42)

It is possible to evaluate another family of trajectories of X versus Z, this time with a parameter ΔP_b, as shown in Figure 6.7.

It is useful from a conceptual point of view to simplify Equation (6.40) further. For the case of $\Delta P_b \ll \frac{1}{2}$ with $R_b Z \ll 1$, becomes:

$$X = 2 Z^{\frac{1}{2}} \left(1 + \frac{1}{3}\,\Delta P_b Z\right) \qquad (6.43)$$

a perturbation of Equation (6.13).

Equation (6.43) is also plotted in Figure 6.7, again a family of trajectories is obtained with the horizontal travel of the water increasing as the air flow (and hence ΔP_b) increases. The discrepancy between the approximation to Equation (6.40) by (6.43) is also shown in Figure 6.7. However, if the curves shown in Figure 6.7 are compared with those shown in Figure 6.6, the horizontal travel of the water is seen to be greater in the former case, as might be expected. Perhaps what is unexpected is the magnitude of this effect; in Figure 6.7, a value of $\Delta P_b \simeq 0.01$ is needed for $X_b \simeq 12$, compared with $\Delta P_b \simeq 0.04$ in Figure 6.6. Consequently, the two extreme assumptions embodied in the above analysis imply widely different air flowrates to give the same effect in the water trajectories.

For Case (iii), with linear varying air jet, combining Equations (6.30) and (6.19) with Equation (6.12) gives:

$$F_z = \int_0^z P\,dZ = \frac{KZ}{\frac{\bar{D}o}{2}\left[\frac{Do}{2} - \frac{Do/2 + X_b - B^*/2}{Z_b}\,z\right]} \quad (6.44)$$

Substituting Equation (6.44) into (6.11) and rearranging gives:

$$K_1\eta = \int_0^Z \frac{dZ}{\left[\frac{1+Z}{(1+F_z)^2} - 1\right]^{\frac{1}{2}}} \quad (6.45)$$

where

$$F_z = \frac{K_2 Z}{2\lambda_1 \left[K_1 \lambda_1 - \frac{\lambda_1 + \eta_b - 1}{\lambda} Z \right]} \qquad (6.46)$$

K_1, K_2, η_b and λ are defined by Equations (6.36) to (6.39) and

$$\lambda_1 = \frac{Do/2}{B^*/2} = \frac{do}{B} \qquad (6.47)$$

$$= 0.111 \quad \text{for the present geometry.}$$

Equation (6.45) can be evaluated in terms of eliptic functions of the first and second kind, but it is simpler to evaluate Equations (6.45) and (6.46) numerically on a computer.

These three numerical solutions are now exploited below.

6.1.4 The Condition for the Collapse of the Pair of Waterfalls

The condition for the collapse of the pair of waterfalls is similar for the three cases of air flow described above, but can be seen most readily from the simple case of $\Delta P = \Delta P_b$ with $\Delta P_b \ll \frac{1}{2}$ corresponding to Equation (6.43). At the bottom of the test section, the horizontal position of the trajectory X_b is given by Equation (6.43) with $Z = Z_b$, which can be reduced then to:

$$K_2 = \frac{6}{\lambda}(1 - \eta_b)^2 \left(\frac{\eta_b}{2\sqrt{\lambda/K_1}} - 1\right) \qquad (6.48)$$

Choosing a value of K_1, and remembering that for a given test section shape λ is fixed, a curve of η_b versus K_2, where K_2 is defined by Equation (6.38), can be plotted. The solution of Equation (6.48) with K_1 as a parameter is tabulated in Appendix O. It is also shown in Figure 6.8 as a family of curves for values of K_1 between 10 and 50. Each curve can be considered to represent the theoretical predictions of the horizontal position of the water jet at the bottom of the test section for a given water flowrate (M_w and u_i fixed) and a range of values of air flowrate M_A. For a given air flowrate M_A, two positions of the water jet are possible as indicated by η_b one corresponding to a low air velocity and low value of η_b, and the other corresponding to a high air velocity and a high value of η_b. Referring to Figure 6.8 for any "water-first" type test, i.e., (fixed K_1), it would be expected that the water trajectory would move from position (1) towards position (2) as the air flowrate is increased, i.e., (K_2 increased), causing the two water jets to come together. At the maximum (position 2) any further increase in air flow causes the water jets to collapse towards one another as shown in Figure 4.1b. The maximum such as that represented by position (2) corresponds to the maximum possible air flow and can be regarded as a kind of choked flow for water jet flow pattern.

The choked flow condition can be evaluated analytically for the simple case described by Equation (6.48). If the condition $\frac{dM_A}{dX_b} = 0$, or $\frac{dK_2}{d\eta} = 0$, is imposed, the maximum is found as

$$\eta_{b\ max} = \frac{1}{3}\left(1 + 4\sqrt{\lambda/K_1}\right) \qquad (6.49)$$

with

$$K_{2\ max} = \frac{4}{9\lambda} \cdot \frac{(1 - 2\sqrt{\lambda/K_1})^3}{\sqrt{\lambda/K_1}} \qquad (6.50)$$

It is also possible to plot similar curves to those shown in Figure 6.8 for Case (i), Case (ii) and Case (iii), using a digital computer. These are shown in Figures 6.9, 6.10 and 6.11 and have the same general form. The solution for the three cases is also tabulated in Appendices P ,Q and R.

6.1.5 Choking Conditions

It is worthwhile considering further the condition used above for the collapse of the pair of waterfalls, viz., $\frac{dM_A}{dX_b} = 0$. Consider the air flowing through cross section area A between the water jets. Then the conservation of mass gives:

$$\rho_A Au_A = M_A = \text{Constant} \qquad (6.51)$$

and the conservation of momentum:

$$-A\,dp - d(\rho_A u_A^2 A) = 0 \qquad (6.52)$$

if frictional and gravity effects for the air are neglected. As above, the variation of ρ_A can be neglected but, in the problem considered here, A varies with the pressure p as well as position z. Equation (6.52) then becomes:

$$\frac{dp}{dz} = \frac{\dfrac{M_A^2}{\rho_A A^3}\left|\dfrac{\partial A}{\partial z}\right|_p}{1 - \dfrac{M_A^2}{\rho_A A^3}\left|\dfrac{\partial A}{\partial p}\right|_z} \qquad (6.53)$$

where the denominator term

$$\frac{M_A^2}{\rho_A A^3} \cdot \left|\frac{\partial A}{\partial p}\right|_z = (\text{Mach Number})^2$$

Choking occurs when $\frac{dp}{dz} \longrightarrow \infty$, implying

$$\left[\frac{M_A}{\rho_A A}\right]^2 = \frac{A}{\rho_A \left|\dfrac{\partial A}{\partial p}\right|_z} = c_A^2 = (\text{"sonic" velocity})^2 \qquad (6.54)$$

In this equation it is assumed that the effect of pressure on the density of the air is small compared with its effect on the area between the waterfalls. In Equations (6.53) and (6.54) the Mach Number and sonic velocity terms are equivalent to those used in gas dynamics but with the gas compressibility effects small compared with area change effects.

Since $\Delta p = p_a - p = \frac{1}{2} \rho_A C_A^2$, Equation (6.54) can be rewritten as

$$\Delta p = -\frac{1}{2} \cdot \frac{A}{\left|\frac{\partial A}{\partial p}\right|_z} \qquad (6.55)$$

or

$$\frac{\partial (\Delta p^{\frac{1}{2}} A)}{\partial A} = 0 \qquad (6.56)$$

Now $\Delta p^{\frac{1}{2}} A \propto K_2^{\frac{1}{2}}$ and $dA \propto - d\eta_b$. Thus Equation (6.56) becomes

$$\frac{dK_2^{\frac{1}{2}}}{d\eta_b} = 0$$

or

$$\frac{dM_A}{dX_b} = 0$$

Thus the criterion used to give the collapsing of the pair or waterfalls is equivalent to that for choked flow in Equation (6.54). It can be shown (Appendix S) that the

corresponding "sonic" velocity given by Equation (6.54) is about 3 m/s, very much less than the velocity of sound in still air at the same temperature and pressure. This is probably due to the flexibility of the restraining water jets causing an area change and hence changing the $\frac{\partial A}{\partial p}$ term.

6.1.6. The Collapse Condition in Terms of J_s^* and J_w^*

Equations (6.20) and (6.48) can be written in a form suitable for making comparison with the experimental data by noting that

$$\frac{z_b}{B} = 2^{5/3} Fr_{wi}^{-2/3} Fr_{wb}^{-1/3} \frac{z_b}{B}$$

$$B^* = 2^{5/3} Fr_{wi}^{-2/3} Fr_{wb}^{-1/3} \qquad (6.57)$$

where

$$Fr_{wb} = \left[\frac{M_w}{\rho_w SB}\right]^2 / gB \qquad (6.58)$$

Thus

$$\left(\frac{M_A}{M_w}\right)^2 = \sqrt{\frac{2}{9}} \left(\frac{\rho_A}{\rho_w}\right) \left[Fr_{wb}^{-1/6} \frac{B}{z_b}^{1/2} - 2^{7/6} Fr_{wi}^{1/3}\right]^3 \qquad (6.59)$$

Alternatively, this can be written in terms of J_A^* and J_w^* where

$$J_A^* \simeq (Fr_{Ab})^{\frac{1}{2}} (\rho_A/\rho_w)^{\frac{1}{2}} \qquad (6.60)$$

$$Fr_{Ab} = \left[\frac{M_A}{\rho_A SB}\right]^2 / gB$$

and

$$J_w^* \simeq Fr_{wb}^{\frac{1}{2}} \qquad (6.61)$$

to give

$$\left[J_A^* . Fr_{wi}^{\frac{1}{2}}\right]^2 = \frac{\sqrt{2}}{9} (J_w^* . Fr_{wi})\left[\left(\frac{B}{z_b}\right)^{\frac{1}{2}} - 2^{7/6} (Fr_{wi} . J_w^*)^{1/3}\right]^3$$

(6.62)

A plot of $(J_A^* . Fr_{wi}^{\frac{1}{2}})$ versus $(J_w^* . Fr_{wi})$ for the test section geometry is shown in Figure 6.12. It is possible to transform the curves in Figure 6.8 directly.

In a similar manner, it is possible to transform the collapse condition shown in Figures 6.9 to 6.11 (also in tabulated forms in Appendix T) using Equations (6.57) to (6,61) to give curves of $J_A^* Fr_{wi}^{\frac{1}{2}}$ versus $J_w^* . Fr_{wi}$. These curves are also plotted in Figure 6.12. For Case (iii), a further refinement used was to take the two dimensional equivalent of the outlet hole to be given by:

$$\bar{d}_o = \sqrt{\frac{\pi}{4}}\, do \quad \text{i.e., area} = \bar{do}^{\,2} = \frac{\pi}{4} do^2$$

PAGE
MISSING
IN
ORIGINAL

6.1.7 Allowance for the Thickness of the Waterfalls

In the previous analysis, the effect of the thickness of the waterfall on the area available for the passage of air has been neglected. This is a good assumption near the top of the test section, but near the bottom, particularly when $\eta_b > 0.9$, a correction must be made. Details of this correction are shown in Appendix U. The calculations described previously were carried out with this correction factor and the results were also plotted in Figure 6.12 and tabulated in Appendix T.

6.2 COMPARISON BETWEEN THEORY AND EXPERIMENT

6.2.1 Water Trajectories with Zero Air Flow

Measurements were taken of the centre position of the water jet trajectories for zero air flow and various water flows and curves are shown in Figure 6.2 (also in Appendix M), as mentioned earlier. The three typical curves shown relate to water inlet conditions such that the Froude numbers, Fr_{wz}, measured just before the brink, were 1.49, 1.41, 1.375 and 1.118 and the flowrates per side (i.e., $M_w/2$) were 0.275, 0.395, 0.612 and 1.12 kg/s respectively.

According to the above theory, the trajectory is given by Equation (6.13), which can be rewritten as

$$x = \left(\frac{2}{g}\right) u_{iz}^{2\,\frac{1}{2}} \qquad (6.63)$$

or using Equation (6.14)a and eliminating H_{wm},

$$x = \left(\frac{2}{g}\right)^{\frac{1}{2}} k\left[\frac{g\, M_w Fr_{wz}}{2S\, \rho_w}\right]^{1/3} \left[1 + \frac{1}{k^2\, Fr_{wz}}\right]^{\frac{1}{2}} z^{\frac{1}{2}} \qquad (6.64)$$

A value of k = 0.819 was found to fit the experimental data for all the trajectories, giving $x = 11.6z^{\frac{1}{2}}$, $10.05z^{\frac{1}{2}}$ and $8.95z^{\frac{1}{2}}$ with x and z in mm. The agreement between theory and experiment is very good bearing in mind that only one adjustable parameter, k, was used, the complexity of the brink flow, and the fact that no allowance was made for drag on the walls of the test section.

6.2.2 Condition for the Collapse of the Pair of Waterfalls

The experimental values of the air flowrate M_A at which the two water jets collapse towards one another for a given water flow are plotted on Figure 6.3 with the corresponding values of J_A^*, J_w^* and Fr_{wz} listed in table 6.1, along with the parameters $Fr_{wi}^{\frac{1}{2}} J_A^*$ and $Fr_{wi} J_w^*$. These last two parameters are compared with the theoretical curves in Figure 6.12.

The first point to note from Figure 6.12 is that the theoretical curves and a line through the experimental points are qualitatively of the same shape, but that all the theories predict a higher value of air flow required for waterfall collapse. The theory, predicts

$J^*_A Fr_{wi}^{\frac{1}{2}} = 0$ for $J^*_w Fr_{wi} = 0$ and $J^*_w Fr_{wi} \simeq 0.1$; the former corresponds to the case of the waterfall thickness being infinitesimally thin for finite Fr_{wi}, and the latter to the two waterfalls meeting in the center of the test section without any assistance from the air. Unfortunately, experimental values below $J^*_w Fr_{wi} = 0.015$ could not be obtained, since, at these low values, the flow of air caused the sluggish waterfalls to part, giving a film flow as shown in Figure 4.1c.

The second point to note is how small a value of $J^*_A Fr_{wi}^{\frac{1}{2}}$ is required (even at the maximum) for the waterfalls collapse. The experimental data gives a maximum value of $J^*_A Fr_{wi}^{\frac{1}{2}} \simeq 0.007$ compared with the theoretical values of (i) 0.035 for the case of the air jet following the contours of the waterfall, (ii) 0.016 for the case of $\Delta P = \Delta P_b$, a constant, and (iii) 0.008 for the case of the linear jet with due allowance made for waterfall thickness. Clearly, the linear air jet theory gives the best agreement with experiment, at least when $J^*_w Fr_{wi} < 0.047$, i.e., where the outlet hole size $\overline{do}$ equals the waterfall gap $(B - 2x_b)$ at the bottom. For values of $J^*_w Fr_{wi} > 0.047$, i.e., high water flowrates, the theory with $\Delta P = \Delta P_b$ is closest to the experimental data, a not too surprising effect since the air jet will certainly separate from the waterfall and not follow the linear divergence to the outlet hole. The importance of the waterfall thickness is also evident in Figure 6.12 when $J^*_w Fr_{wi} > 0.047$.

The air flows at these higher values of water flows are very small, so much so that a mere shutting of the drain valve from the bottom tank, resulting in a small flow of displaced air, was enough to move point A to point B in Figure 6.12. The theory predicts this sensitivity in a satisfactory way.

Thus it is concluded that the linear air jet theory explains the theoretical data up to the water flowrates at which $\overline{do} = (B - 2x_b)$, whilst beyond that the $\Delta P = \Delta P_b$ theory gives the best fit. At the maximum, the theory exceeds the experiment by about 15%, reasonable agreement when the complexity of the flow and the simplifications of the theory is considered. It seems likely that, in water-first tests, (fixed k_1) as the air flow is increased (k_2 is increased), i.e., along the lower position of one of the curves in Figures 6.8 to 6.11, the possibility of jumping to the upper position of the curve will increase as the maximum k_2 value is reached. It is thus likely that the experimental values shown on Figure 6.12 were not true collapse points but somewhat less than the maximum value. Indeed, on occasions, a fluttering of the waterfall position was noted as the air passed between them.

Finally, it must be emphasised again, that the collapse condition analysed above occurs at air flowrates far below bypass conditions of interest in PWR refill problem.

6.3 NON-EQUILIBRIUM EFFECTS IN DIRECT CONDENSATION UNDER COUNTER CURRENT FLOW

During the refill stage of a LOCA, the effectiveness with which the emergency coolant traverses the PWR downcomer and reaches the lower plenum is of paramount importance. The comparison between the bypass characteristics obtained from the present air/water experiments and Campbell's steam/water data (35) -(Figures 5.1 to 5.4) - showed a completely different behaviour. The difference between the liquid/gas and liquid/vapour counter-current interaction is attributed to mass transfer, or condensation, effects which can be significant (and even overwhelming) depending on the temperature difference between the vapour(steam) and the liquid (water). Thus in order to correlate the flooding conditions for liquid/vapour combinations and hence define the hold-up process, the condensation effect must be separated and allowed for.

The main difficulty in isolating the amount of condensation lies in the lack of reliable information about the degree of thermal non-equilibrium which exists during the energy exchange between the liquid and the vapour. If thermal equilibrium conditions existed, then the amount of condensation could be determined from the energy (heat) transfer necessary

to raise the liquid temperature to that of the vapour. In fact, thermal non-equilibrium conditions exist i.e. the liquid temperature remains lower than that of the vapour and it is this degree of non-equilibrium which is unknown. However, recent experimental investigations (26-30) showed that the penetration curves for steam/water interactions with zero or near zero liquid subcooling were very close to those for air/water in the same vessel geometry. This enables the reduction of the data, obtained from bypass experiments carried out on a scaled model of a PWR reactor vessel, to isolate the non-equilibrium effects, usually in terms of a non-equilibrium factor.

Several empirical correlations (reviewed in Chapter 2) have been presented to predict the non-equilibrium factor, or condensation efficiency as it is sometimes called. These correlations were obtained using numerical best fits to test data. The confidence with which these correlations can be used to extrapolate to conditions outwith the test range is a function of the degree of physical basis supporting them.

In an attempt to understand the effects of condensation, heated walls, and counter-current flow on ECC penetrations, the non-equilibrium factor was isolated from Campbell's steam/water data using the

air/water correlation (equation (4.6) presented in section 4.4.2)as a base line (i.e. representing $\Delta T_{sub} = 0$). In addition, a physical model of the condensation effects, based on the simple flow pattern of a liquid film draining down a heated wall. was developed to predict and explain the behaviour of the non-equilibrium factor.

6.3.1 Isolation of Condensation Effects

If thermal equilibrium conditions existed during the direct contact heat exchange between the steam and water in the downcomer annulus, then the mass flowrate of steam required to be condensed in order to increase the water temperature to saturation would be

$$M_{s_c} = \frac{M_{w_i} \, c_{P_w} \, \Delta T_{sub}}{h_{fg}} = M_{w_i} \, Ja \qquad (6.65)$$

where

$$Ja = \text{Jakob number} = \frac{c_{P_w} \, \Delta T_{sub}}{h_{fg}} \qquad (6.66)$$

Thus the residual steam flowrate after condensation, $M_{s_{mod}}$ becomes

$$M_{s_{mod}} = M_s - M_w \, Ja \qquad (6.67)$$

and the increased water flowrate allowing for condensation is

$$M_{w_{mod}} = M_{w_i} + M_{w_i} Ja \tag{6.68}$$

If departure from thermal equilibrium conditions exists and the degree of non-equilibrium is represented by a non-equilibrium factor K_{ne} then equations (6.65), (6.67) and (6.68) become

$$M_{s_c} = K_{ne} Ja M_{w_i} \tag{6.69}$$

$$M_{s_{mod}} = M_s - K_{ne} Ja M_{w_i} \tag{6.70}$$

and

$$M_{w_{mod}} = M_{w_i} + K_{ne} Ja M_{w_i} \tag{6.71}$$

or in terms of Wallis dimensionless parameters

$$J^*_{sc} = K_{ne} Ja \left(\frac{\rho_w}{\rho_s} \right)^{\frac{1}{2}} J^*_w \tag{6.72}$$

$$J^*_{s_{mod}} = J^*_s - K_{ne} Ja \left(\frac{\rho_w}{\rho_s} \right)^{\frac{1}{2}} J^*_w \tag{6.73}$$

$$J^*_{w_{mod}} = J^*_w \quad (1 + K_{ne}\, Ja) \tag{6.74}$$

In equations (6.73) and (6.74), $J^*_{s_{mod}}$ and $J^*_{w_{mod}}$ are representative of the hold-up effect, since the effects of condensation have been allowed for, and can be correlated therefore by a Wallis type correlation to give

$$J^{*\frac{1}{2}}_{s_{mod}} + m\, J^{*\frac{1}{2}}_{w_{mod}} = c \tag{6.75}$$

Equations (6.73) and (6.74) together with equation (6.75) can be solved to isolate the non-equilibrium factor K_{ne} as

$$k_{ne} = \frac{-a_1 + \sqrt{a_1^2 - 4\, a_o a_2}}{2\, a_2} \tag{6.76}$$

where

$$a_o = \left[c^2 + m^2\, J^*_w - J^*_s\right]^2 - 4\, m^2 . c^2 . J^*_w \tag{6.77}$$

$$a_1 = 2J^*_w\, Ja \left[m^2 + \left(\frac{\rho_w}{\rho_s}\right)^{\frac{1}{2}}\right]\left[c^2 + m^2 . Jw^* - Js^*\right] - 4m^2 c^2 Jw^*\, Ja \tag{6.78}$$

$$a_2 = J^{*2}_w . Ja^2 . \left[m^2 + \left(\frac{\rho_w}{\rho_s}\right)^{\frac{1}{2}}\right]^2 \tag{6.79}$$

However, since the mass of steam condensed is small relative to the mass of water effecting the condensation, equation (6.74) can be approximated to

$$J^*_{w_{mod}} \simeq J^*_w \tag{6.80}$$

Thus, equations (6.73) and (6.80) together with equation (6.75) yield

$$K_{ne} = \frac{J^*_s - (c - m\, J^{*\frac{1}{2}}_w)^2}{\left(\frac{\rho_w}{\rho_s}\right)^{\frac{1}{2}} Ja\ \ J^*_w} \tag{6.81}$$

In this investigation, attention is focused on the Phase 2 geometry since it is a more realistic representation of the PWR than Phase 1. For this geometry,

$$m = 0.484 \tag{6.82}$$

and

$$c = 0.349 \tag{6.83}$$

The values of J^*_s and J^*_w required in equations (6.76) or (6.81) were obtained from Campbell's steam/water data shown in Figures 5.1 to 5.4. At this stage it is worthwhile stressing the following points.

(i) These data refer to steam first tests only since the reduction procedure adopted for isolating the effects of condensation could be applied more confidently to this type of test. The steam flowrate in the downcomer annulus (the area of interest as far as the direct contact condensation effect was concerned) is required whereas it was the inlet steam flowrate to the apparatus which was measured. In the water first tests, there was always the possibility of condensation in the lower plenum which could affect the isolation procedure.

(ii) The data points which lay below the air/water flooding line were disregarded since they would give negative non-equilibrium factors. This is possibly due to exceeding the limit of accuracy of the measurement instruments (turbine flowmeters) resulting in an experimental error. These data points lay in region 1 in figure 6.13 which shows a typical steam/water flooding behaviour as observed by many investigators (25,41). Region 1, in which the steam/water flooding line follows closely the air/water flooding line, extended from $J_w^* = o$ to a critical value = $Jw_{c,}^*$ near the interception of the air/water flooding line and the line of thermal equilibrium ($R_T = 1$) given by equation (6.65) which can be expressed in dimensionless terms as

$$J_s^* = Ja \cdot \left(\frac{\rho_w}{\rho_s}\right)^{\frac{1}{2}} \cdot J_w^* \qquad (6.84)$$

This interception point (point a in Figure 6.13) can be obtained by substituting equation (6.84) into equation (6.75) after replacing $J^*_{s_{mod}}$ and $J^*_{w_{mod}}$ with J_s^* and J_w^* respectively. Thus

$$J^{*\frac{1}{2}}_{w_c} = \frac{c}{\left[Ja^{\frac{1}{2}} \cdot \left(\frac{\rho_w}{\rho_s}\right)^{\frac{1}{4}} + m\right]} \qquad (6.85)$$

Thus the Campbell's steam/water data used in isolating the non-equilibrium factor corresponds to those of Region 2 in Figure 6.13.

(iii) Campbell's data were collected at the inception of bypass which means that the steam and water flow-rates were not independent.

The non-equilibrium factor K_{ne}, isolated and evaluated by the above mentioned method, is plotted in Figures 6.14 to 6.17 to a base of dimensionless inlet water flow J_w^* for a range of water subcoolings at a particular downcomer wall temperature, T_{wall}. In order to show the effect of downcomer wall temperature on the non-equilibrium factor, the data in Figures 6.14 to 6.17 were replotted for a range downcomer wall temperatures at a particular water subcooling in Figures 6.18 to 6.21.

As is evident from Figures 6.14 to 6.21, the non-equilibrium factor depends (in a complicated way) on the water flowrate, water subcooling and the downcomer wall temperature. In the following section a simple physical model is developed which incorporates the above factors and the physical dimensions of the downcomer annulus.

6.3.2 Condensation Model

In an attempt to understand the effects of condensation, heated walls, and countercurrent flow on the ECC penetration, a physical model based on the simple flow pattern shown in Figure 6.22 has been developed, assuming that a one dimensional presentation of this configuration represents the average chaotic phenomenon which occurs in the downcomer.

Figure 6.22 shows a water film draining down a heated wall, the temperature of which is uniform and constant at a temperature T_{wall}. The falling water film is assumed turbulent and both the velocity and temperature profiles are expected to be flatter than those of laminar flow. It is reasonable to assume that the temperature T, of the falling film is uniform across the film and is only changing in the flow direction. It is also assumed that the steam is saturated, and noncondensible gases are not present. The vapour shear stress at the liquid-vapour inter-

face is ignored.

Subcooled water at temperature T_{w_i} is injected at a rate M_{w_i} and the counter-current steam is injected at a rate M_{si} The mass balance for a differential section δx yields

$$\frac{dM_w}{dx}\,\delta x = -\frac{dM_s}{dx}\,\delta x \qquad (6.86)$$

This indicates that the mass exchange between steam and water is due to phase change. The energy balance for the same differential section can also be written as

$$\frac{d}{dx}\,(M_w c_p T)\,\delta x = -h_g \frac{d M_s}{dx}\delta x + h_w B\,(T_{wall}-T)\delta x \qquad (6.87)$$

where c_p is the specific heat at constant pressure, h_g is the specific enthalpy of the steam, B is the breadth of the test section and h_w is an average heat transfer coefficient between the downcomer wall and the water film.

Substituting equation (6.86) into equation (6.87), neglecting the change in c_p, and rearranging yields.

$$M_w c_p \frac{dT}{dx} = \left[h_{fg} + c_p (T_s - T)\right]\frac{dM_w}{dx} + h_w B\,(T_{wall}-T) \qquad (6.88)$$

where $h_{fg} = (h_g - c_p T_s)$ is the latent heat of evaporation and T_s is the saturation temperature. The heat transfer rate across the steam-water interface

of the differential section δx is given by

$$- h_{fg} \frac{dMs}{dx} \delta x = hB\ (Ts - T)\ \delta x \qquad (6.89)$$

where h is an average interfacial heat transfer coefficient. Substituting equation (6.86) into (6.89) yields

$$h_{fg} \frac{d\ M_w}{dx} = h\ B\ (T_s - T) \qquad (6.90)$$

Now, introducing the two dimensionless quantities,

$$\gamma = \frac{c_p\ (T_s - T_{wall})}{h_{fg}} \qquad (6.91)$$

and

$$\phi = \frac{T_{wall} - T}{T_s - T_{wall}} \qquad (6.92)$$

where γ is a Jakob number based on the temperature difference across the water film and ϕ is a dimensionless temperature difference. Usually $\gamma \ll 1$ and $Ja \ll 1$ and can be ignored in any comparison with unity. Substituting equations (6.91) and (6.92) into equations (6.88) and (6.90) and rearranging yields

$$-M_w \gamma \frac{d\phi}{dx} = \frac{d\ M_w}{dx} + \frac{h_w B \gamma}{c_p} \phi \qquad (6.93)$$

and

$$\frac{d\,M_w}{dx} = \frac{hB\gamma(1+\phi)}{c_p} \qquad (6.94)$$

Equation (6.94) can be written as

$$\phi = \left(\frac{c_p}{hB\gamma}\cdot\frac{dM_w}{dx}\right) - 1 \qquad (6.95)$$

Differentiating equation (6.95) with respect to x, substituting the resulting equation together with equation (6.95) into equation (6.93), noting that h is independent of x, and rearranging gives

$$M_w\,\frac{d^2M_w}{dx} + \frac{hB}{c_p}\left(1+\frac{h_w}{h}\right)\cdot\frac{d\,M_w}{dx} = \frac{hh_wB^2\gamma}{c_p^2} \qquad (6.96)$$

Equation (6.96) is a non-linear differential equation which cannot be solved analytically. However, the mass of steam condensed is usually very small compared with the injected water flowrate and this allows the following approximation to be made

$$M_w\,\frac{d^2M_w}{dx^2} \simeq M_{w_i}\,\frac{d^2\,M_w}{dx^2} \qquad (6.97)$$

Substituting equation (6.97) into equation (6.96) and arranging gives

$$\frac{d^2 M_w}{dx^2} + \alpha \frac{dM_w}{dx} = \psi \qquad (6.98)$$

where

$$\alpha = \frac{hB}{c_p M_{w_i}} \left(1 + \frac{h_w}{h} \right) \qquad (6.99)$$

and

$$\psi = \frac{hhw\ B^2 \gamma}{c_p^2\ M_{w_i}} \qquad (6.100)$$

Equation (6.98) is an ordinary differential equation which can be solved with the proper boundary conditions. The first boundary condition is

$$\text{at } x = 0 \quad , \quad M_w = M_{w_i} \quad \text{and} \quad T = T_{w_i} \qquad (6.101)$$

and the second boundary condition can be obtained from equation (6.94) at x = 0 to give

$$\left[\frac{dM_w}{dx} \right]_{x=0} = \frac{hB\gamma}{c_p} F \qquad (6.102)$$

where

$$F = \frac{T_s - T_{w_i}}{T_s - T_{wall}} \qquad (6.103)$$

Solving equation (6.98) with the boundary conditions given by equations (6.101) and (6.102) yields

$$\frac{Mw}{M_{w_i}} = 1 + Ja\left[\left(\frac{1}{\left(1+\frac{hw}{h}\right)} - \frac{h_w/h}{\left(1+\frac{hw}{h}\right)^2 F}\right)\left(1-e^{-\alpha x}\right) + \frac{(hw/h)\alpha x}{F\left(1+\frac{hw}{h}\right)^2}\right] \quad (6.104)$$

$$\text{Now, } M_w = M_{w_i} + M_{s_c} \quad (6.105)$$

where M_{s_c} is the mass of the condensed steam over the length x substituting equation (6.105) into equation (6.104) gives

$$\frac{M_{s_c}}{M_{w_i}} = Ja\left[\left(\frac{1}{\left(1+\frac{hw}{h}\right)} - \frac{(hw/h)}{F\left(1+\frac{hw}{h}\right)^2}\right)\left(1-e^{-\alpha x}\right) + \frac{(hw/h)\alpha x}{F\left(1+\frac{hw}{h}\right)^2}\right] \quad (6.106)$$

Equation (6.106) is of the same form as that for the condensed steam shown in equation (6.69) and hence the following expression for the non-equilibrium factor K_{ne}, over the length L of the downcomer, is

$$K_{ne} = \left[\frac{1}{\left(1+\frac{hw}{h}\right)} - \frac{hw/h}{F\left(1+\frac{hw}{h}\right)^2}\right]\left[1-e^{-\alpha L}\right] + \frac{(hw/h)\alpha L}{F\left(1+\frac{hw}{h}\right)^2} \quad (6.107)$$

where α and F are defined previously by equations (6.99) and (6.103) respectively,

Equation (6.107) gives an expression for the non-

equilibrium factor K_{ne} which incorporates the physical dimensions of the downcomer annulus, the water sub-cooling, the wall temperature, and the inlet water flow-rate.

At this stage it is worthwhile examining two extreme cases.

(i) Adiabatic Wall = i.e. no heat transfer to or from downcomer wall

In this case $h_w = o$, and equation (6.107) reduces to

$$K_{ne} = 1 - e^{-\frac{hBL}{c_p M_{w_i}}} \qquad (6.108)$$

which is the same expression as that derived by Liu et al (22) where heat transfer from the downcomer wall was neglected.

(ii) Saturated Wall Temperature

When $T_{wall} \rightarrow T_s$ i.e. $F \rightarrow \infty$ equation (6.107) reduces to

$$K_{ne} = \frac{1 - e^{-\alpha L}}{\left(1 + \frac{hw}{h}\right)} \qquad (6.109)$$

where α is previously defined by equation (6.99)

If an empirical correlation can be found for the interfacial heat transfer coefficient, equation (6.107) can then be used in conjuction with equations (6.73) to (6.75) to determine the bypass characteristics for subcooled water and steam. An attempt to find such an expression is presented in the following section.

6.3.3 Estimation of the Interfacial Heat Transfer Coefficient

The interfacial heat transfer coefficient which appeared in the expression for the non-equilibrium factor $K_{ne,}$ given by equation (6.107) is still unknown. Since detailed information on local interfacial heat transfer coefficients and local interfacial areas in counter current flooding flow of steam and water is not available at this time, average values of the interfacial heat transfer coefficient were determined from the experimental data (air-water data in conjuction with Campbell's steam/water data) and correlated against the dependent parameters. This was done using the method outlined in section 6.3.1 in conjunction with equation (6.107) making the following assumptions.

(i) The wall-film heat transfer coefficient h_w can be obtained from the Dittus-Boelter correlation given by

$$Nu_w = 0.023\ Re^{0.8}\ Pr^{0.4} \qquad (6.110)$$

where

$$Nu_w = \text{wall Nusselt Number} = \frac{h_w D_e}{k_w} \qquad (6.111)$$

$$Re = \text{film Reynolds Number} = \frac{4\ M_{w_i}}{B \mu_w} \qquad (6.112)$$

$$Pr = \text{film Prandtl Number} = \frac{c_p \mu_w}{k_w} \qquad (6.113)$$

$$D_e = \text{film hydraulic diameter} = 4\delta \qquad (6.114)$$

(ii) The film thickness δ, can be obtained from the Brötz empirical correlation, reported in reference (42), and given by

$$\left(\frac{g\delta^3}{\nu^2}\right)^{1/3} = 0.068\ Re^{2/3} \qquad (6.115)$$

(iii) The water properties in equations (6.110) to (6.115) were obtained from reference (40) at a mean bulk temperature T_b, given by

$$T_b = \frac{1}{2}\left[\left(\frac{T_{w_i} + T_s}{2}\right) + \left(\frac{T_{wall} + T_s}{2}\right)\right] \qquad (6.116)$$

where the term $(T_{w_i} + T_s)/2$ represents the mean temperature in the flow direction if the outlet water was saturated and the term $(T_{wall} + Ts)/2$ represents the mean temperature across the water film.

(iv) Due to the slightly superheated steam inlet conditions used during Campbell's experiments, the evaluation of Jakob numbers (defined by equation (6.66), was made using the enthalpy difference between the inlet steam condition and saturated liquid condition (in place of h_{fg}) where accuracy warranted this.

This allowed the interfacial heat transfer coefficient to be isolated and correlated in dimensionless form. In determining the dependent parameters, recourse was made to Bankoff (38) who argued that "except under highly transient or intense surface shear conditions, the principal resistance to condensation heat transfer, in absence of air, is on the liquid side". Figure 6.23 shows a plot of the interfacial Nusselt number Nu_i, versus $Pr^{1/3}\ Re^{0.8}$ and, as can be seen, both the slopes and the intersection with the x axis of the resulting straight lines are functions of the inlet subcooling. Several attempts were made to correlate this effect until that shown in Figure 6.24 was obtained with the resulting correlation being

given by

$$Nu_i = 0.011\ (Ja^{0.9}\ Pr^{1/3}\ Re^{0.8} - 700)\ /Ja^{1.25} \quad (6.117)$$

where

$$Nu_i = \frac{h\,D_e}{k_w} \quad (6.118)$$

Again, the water properties in equations (6.117) and (6.118) are calculated at the mean bulk temperature given by equation (6.116).

As mentioned earlier, the data points used are those corresponding to Region 2 in Figure 6.13 which roughly corresponds to the conditions prevailing at and beyond point "a" in Figure 6.13. The condition at point "a" can be represented, over the range of subcoolings tested by Campbell, by

$$Ja^{0.9}\ Pr^{1/3}\ Re^{0.8} = 700 \quad (6.119)$$

For the range $0 < Ja^{0.9}\ Pr^{1/3}\ Re^{0.8} \leq 700$ a different correlation is required to correllate the interfacial heat transfer coefficient in Region 1 in Figure 6.13. Unfortunately, no reliable data were available from Campbell's experiments in this region consequently

it was not possible to obtain a correlation for this Region using his data. However, the experimental work of Crowley (25) and Wallis (41) indicated that the amount of condensation in this Region is very small. Thus for the time being it is perhaps reasonable to assume that

$$\text{for } o < Ja^{0.9}\ Pr^{1/3}\ Re^{0.8} \leqslant 700 \quad , \quad Nu_i = O \qquad (6.120)$$

$$\text{for } \quad Ja^{0.9}\ Pr^{1/3}\ Re^{0.8} > 700 \quad , \quad Nu_i \text{ is given by equation (6.117)}$$

The author is aware, however, that Campbell's experiments (35) were not designed to isolate the non-equilibrium factor or the interfacial heat transfer coefficient and despite the care taken in using his steam first data some of the inlet steam could have condensed due to heat loss from the large steel tank (lower plenum) or due to contact with some of the water which penetrated to the lower plenum. Therefore equation (6.117) is not recommended for general use under conditions which differ from those prevailing in Campbell's experiments. However, it can be used here in the isolation of non-equilbrium factors.

6.3.4 Discussion of the Condensation Model

In this section an attempt is made to explain the behaviour of the non-equilibrium factors deduced from

Campbell's data and to show the qualitative and quantitative agreement between the theoretical model presented in section 6.3.2 and the experimental data.

Referring to Figures 6.18 to 6.21, it is clear that for any particular water flowrate and liquid subcooling, increasing the downcomer wall temperature decreases (in general) the non-equilibrium factor. The expression deduced from the condensation model predicts this behaviour. For any particular water flowrate and water subcooling equation (6.107) reduces to

$$K_{ne} = A_1 + \frac{A_2}{F} \qquad (6.121)a$$

or

$$K_{ne} = A_1 + A_3(T_s - T_{wall}) \qquad (6.121)b$$

Where $A_1, A_2, A_3,$ are constants. It is clear from equation (6.121) - b that increasing the wall temperature T_{wall} will reduce the non-equilibrium factor $K_{ne},$ which is the same effect as observed experimentally.

Referring to Figures 6.14 to 6.17, it is clear that for any particular water subcooling all the curves go through a maximum as the water flowrate (J^*_w) is

increased. This can be easily seem by examining the the special case of adiabatic wall given by equation (6.108) which can be rewritten as

$$K_{ne} = 1 - e^{-\alpha_i L} \qquad (6.122)$$

where

$$\alpha_i L = \frac{hBL}{c_p M_{w_i}} \qquad (6.123)$$

which can be expressed in terms of Re, Pr and Nu_i as

$$\alpha_i L = \frac{Nu_i}{Pr.Re} \quad \frac{L}{\delta} \qquad (6.124)$$

Substituting equations (6.115) into equation (6.124) yields

$$\alpha_i L = \frac{Nu_i}{0.068\ Pr\ \ Re^{5/3}} \left(\frac{g L^3}{\nu^2} \right)^{1/3} \qquad (6.125)$$

It is clear from equation (6.122) that increasing $\alpha_i L$ also increase K_{ne}. Referring to equation (6.125) it can be seen that increasing the water flowrate tends to reduce $\alpha_i L$ due to Re increasing but also tends to increase $\alpha_i L$ due to Nu_i increasing (equation 6.117) Thus the final behaviour of the non-equilibrium factor depends on the relative strength of these two opposing effects.

A maximum value of K_{ne} would exist only if

$$\frac{d\,K_{ne}}{d\,M_{w_i}} = 0 \qquad (6.126)$$

or alternatively

$$\frac{d\,K_{ne}}{dRe} = 0 \qquad (6.127)$$

Differentiating equation (6.122) with respect to Re gives

$$\frac{d\,K_{ne}}{d\,Re} = \frac{d\,(\alpha_i L)}{d\,Re}\, e^{-\alpha_i L} \qquad (6.128)$$

which indicates that

$$\frac{d\,K_{ne}}{d\,Re} = 0 \quad \text{if} \quad \frac{d\,(\alpha_i L)}{d\,Re} = 0$$

For the present work Nu_i was correlated by equation (6.117) Substituting equation (6.117) into equation (6.125) and rearranging gives.

$$\alpha_i L = \left(\frac{0.1618}{J_a^{0.35} Pr^{2/3}}\right)\left(\frac{g L^3}{\nu^2}\right)^{1/3}\left[\frac{Re^{0.8} - 700/Ja^{0.9} Pr^{1/3}}{Re^{5/3}}\right] \qquad (6.129)$$

Now, differentiating equation (6.129) with respect to Re and equating the resulting equation to zero gives

$$Re_{max}^{0.8} \simeq \frac{1350}{Ja^{0.9}\, Pr^{1/3}} \qquad (6.130)$$

which is the condition for maximum $\alpha_i L$ and hence maximum K_{ne}. A similar result can be obtained for the general case given by equation (6.107). Equation (6.130) indicates that as the subcooling decreases (Jakob number decreases), the value of Reynolds number required for maximum K_{ne} increases i.e. for lower subcoolings the maximum non-equilibrium factor occurs at higher water flowrates. Again this is confirmed by the experimental findings as shown in Figures 6.14 to 6.16. This maximum K_{ne}, however, does not seem to be sensitive to wall temperature and this is confirmed in Figure 6.18

Equation (6.117) can be written as

$$Nu_i = 0.011\, Re^{0.8} \left[\frac{Pr^{1/3}}{Ja^{0.35}} - \frac{700}{Ja^{1.25}\, Re^{0.8}} \right] \qquad (6.131)$$

over the range of subcoolings tested by Campbell (35) the variation in $\left(\frac{Pr^{1/3}}{Ja^{0.35}} \right)$ is small. Thus:

$$\left(\frac{Pr^{1/3}}{Ja^{0.35}} \right) \simeq \text{const.} \qquad (6.132)$$

Substituting equation (6.132) into equation (6.131) and rearranging gives

$$Nu_i \simeq a_1 \, Re^{0.8} - \frac{a_2}{Ja^{1.25}} \qquad (6.133)$$

where a_1 and a_2 are constants

Now, the effect of liquid subcooling on the non-equilibrium factor can be examined by considering two extreme cases.

Case (i) Small Water Flowrate

For any particular small water flowrate ($Re < Re_{max}$) equation (6.133) can be reduced to

$$Nu_i \simeq a_3 - \frac{a_2}{Ja^{1.25}} \qquad (6.134)$$

Equation (6.134) indicates that for a particular water flowrate, increasing Ja increases Nu_i which in turn increases α_L as indicated by equation (6.125). This will result in increasing K_{ne}. This is in agreement with the experimental findings as can be seen in Figures 6.14 to 6.16 at low water flowrates.

Case (ii) High Water Flowrates

For any particular high water flowrate ($Re \gg Re_{max}$)

the term $\frac{a_2}{Ja^{1.25}}$ will be small in comparison to

($a_1 \ Re^{0.8}$) in equation (6.133). Thus

$$Nu_i \simeq (a_1 \cdot Re^{0.8}) \qquad (6.135)$$

i.e. Nu_i can be considered a function of Re only.

Thus for a particular Reynolds number, equation (6.107) can be written as

$$K_{ne} = C_1 + \frac{C2}{F} \qquad (6.136)$$

or

$$K_{ne} = C_1 + C2 \ \frac{(T_s - T_{wall})}{\Delta T_{sub}} \qquad (6.137)$$

It is clear from equation (6.137) that at any particular wall temperature, increasing ΔT_{sub} reduces K_{ne}. Again this is in agreement with the experimental results as shown in Figures 6.14 to 6.16 at high water flows.

To summarise the above qualitative comparisons between the theoretical model and the experimental data, the behaviour of the non-equilibrium factor is idealised into three distinctive regions. These are shown in Figure 6.25 and are dealt with in turn.

Region I $0 < Ja^{0.9} Pr^{1/3} Re^{0.8} \leq 700$

The actual behaviour of the non-equilibrium factor in this region is unknown due to lack of reliable data. The author had to rely on other works (25,41) to idealise the condition in this region which indicated indicated that K_{ne} is very small and could be approximated to zero i.e. k_{ne} is represented by the line O A in Figure 6.25. The range of flowrates covered by this region increases as Ja decreases.

Region II $700 < Ja^{0.9} Pr^{1/3} Re^{0.8} \leq 1350$ (at least for unheated wall)

In this region, the non-equilibrium factor rises from zero (point A) to a maximum (point B). In the simple case of adiabatic wall this maximum is given by equation (6.130). Since the flowrates in this region are not very high, increasing the liquid subcooling increases the non-equilibrium factor due to the increase in the interfacial heat transfer coefficient as indicated in Case (i) above.

Region III $Re > Re_{max}$

In this region the non-equilibrium factor falls from a maximum value along the line B-C in Figure 6.25. As the water flowrate is increased beyond point B, $\alpha_l L$ decreases (for the general case the effect of increasing Re is more complicated) and hence K_{ne} decreases. At high flowrates in this region the interfacial heat

transfer can be considered independent of Ja. Thus increasing Ja will decrease K_{ne} as indicated in case (ii) above.

For all the three regions for any particular water flowrate and subcooling, increasing the wall temperature reduces K_{ne} as indicated from equation (6.121)

The above discussion has indicated the qualitative agreement between the model and the experimental data. In order to show the quantitative comparison between theory and experiment, equation (6.117) was used together with equations (6.110) to (6.115) into equation (6.107) to calculate K_{ne} which was then used in equations (6.73) to (6.75) to estimate J_s^* for any particular J_w^*. Figures 6.26 to 6.28 show a comparison between the experimental and predicted flooding steam flowrates and, as can be seen, the agreement is very good except perhaps in Figures 6.28, where the downcomer wall temperature approached the saturation temperature (T_{wall} = 100 $\mathring{c}$). At these high wall temperatures where the pressure fluctuations could cause film boiling, a different correlation for wall/film heat transfer coefficient h_w, may have to be used.

In order to compare the applicability of the above

analysis relative to the "best fit" correlation available, the latest BCL correlation presented by Collier et al (39) was used to calculate the steam dimensionless flux at flooding and compared with Campbell's experimental values. The BCL correlation is given by

$$K_{ne} = \frac{1.84}{1 + 47.78 \quad J^*_{w_i}} \qquad (6.138)$$

and the comparisons are shown in Figures 6.29 to 6.31. It is clear from the figures, that the BCL correlation tends to give "horizontal" predictions with errors up to $\pm$ 100%, It goes without saying that the effects of water subcoolings are not represented at all in equation (6.138) and this is evident in Figures 6.29 to 6.31.

Finally, the author does not claim that this theoretical model is the last word in the solution of this complicated problem. Further experiments are clearly needed to examine in more detail the different effects emerging from the above analysis. It is hoped, however, that the simple condensation model presented in this Chapter, will be another step forward.

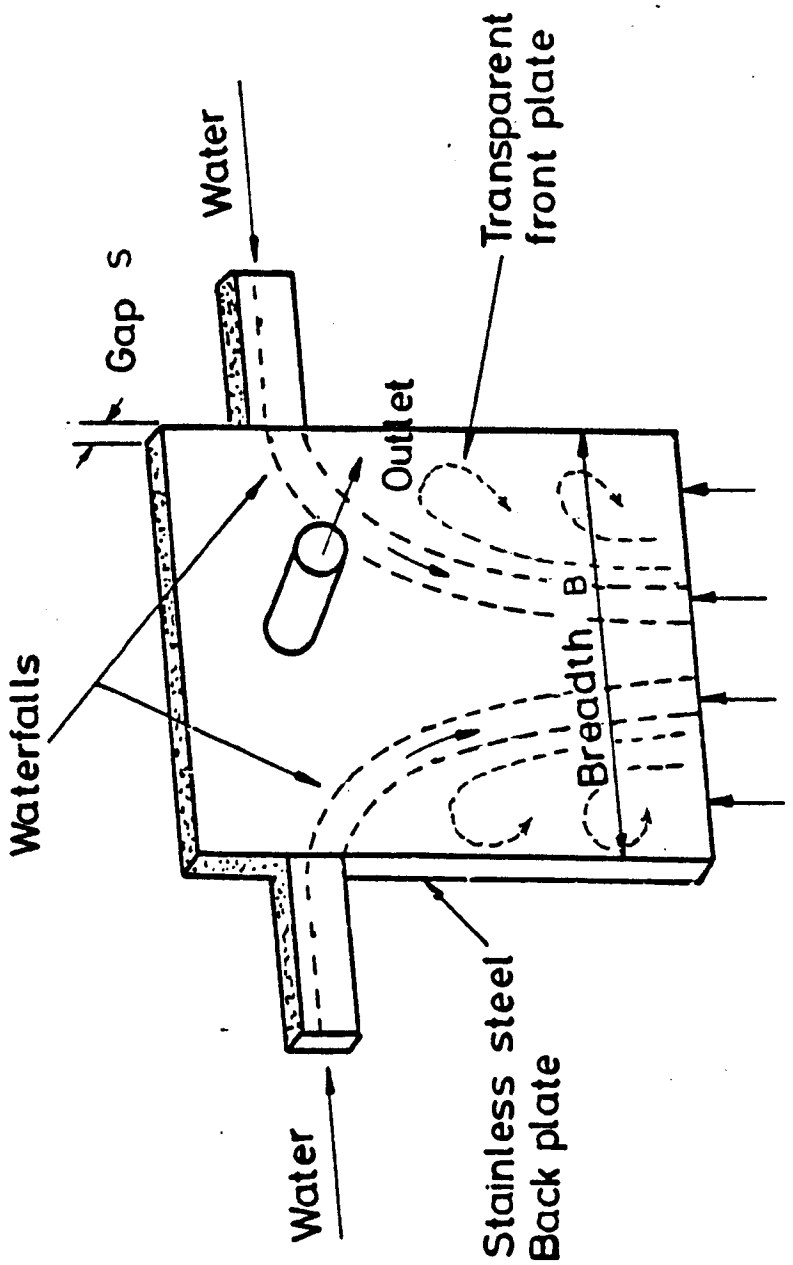

Fig 6.1 TEST SECTION FOR PHASE 1 TESTS – TANGENTIAL ENTRY.

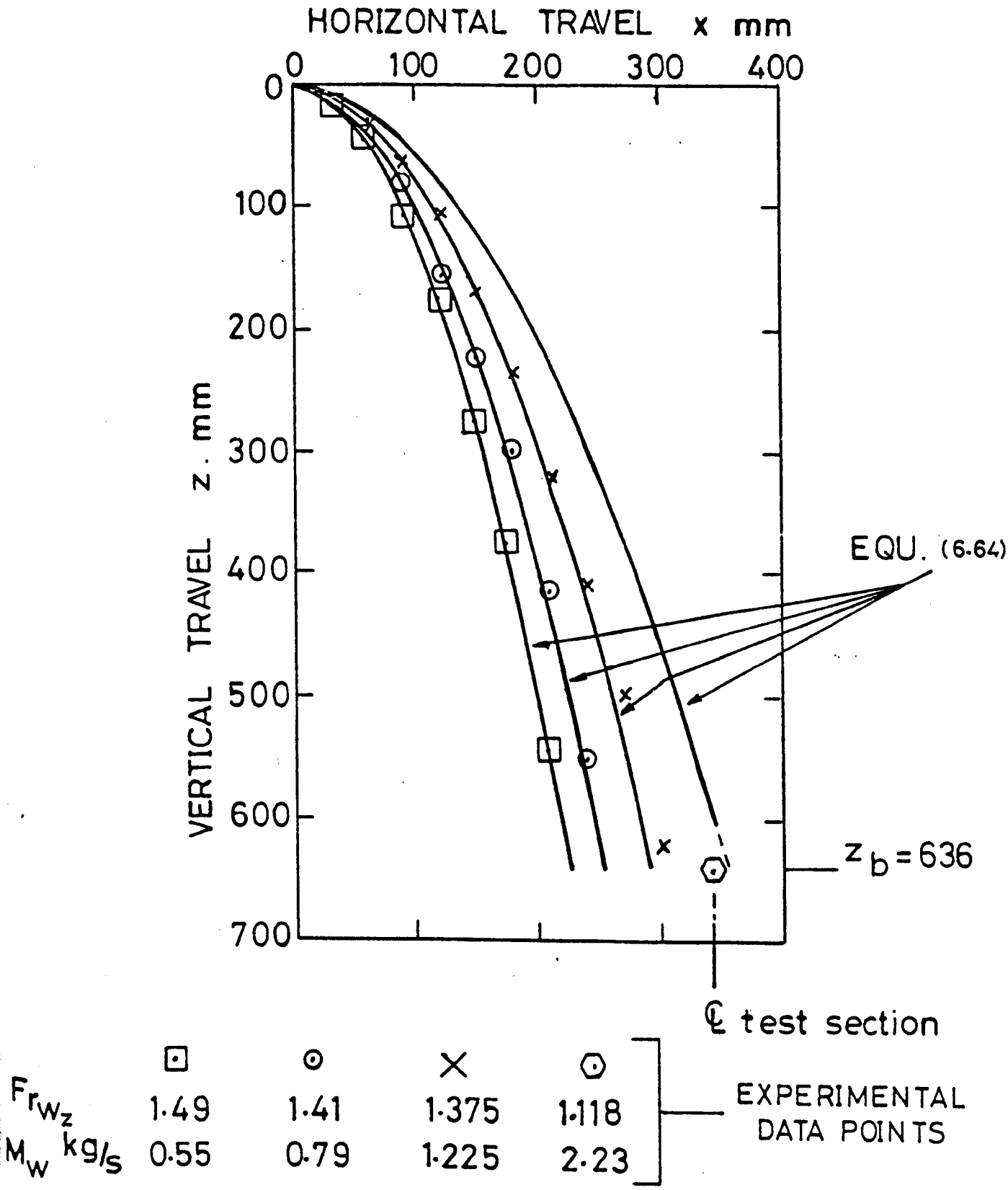

FIG 6.2 TYPICAL WATERFALL TRAJECTORIES-ZERO AIR FLOW

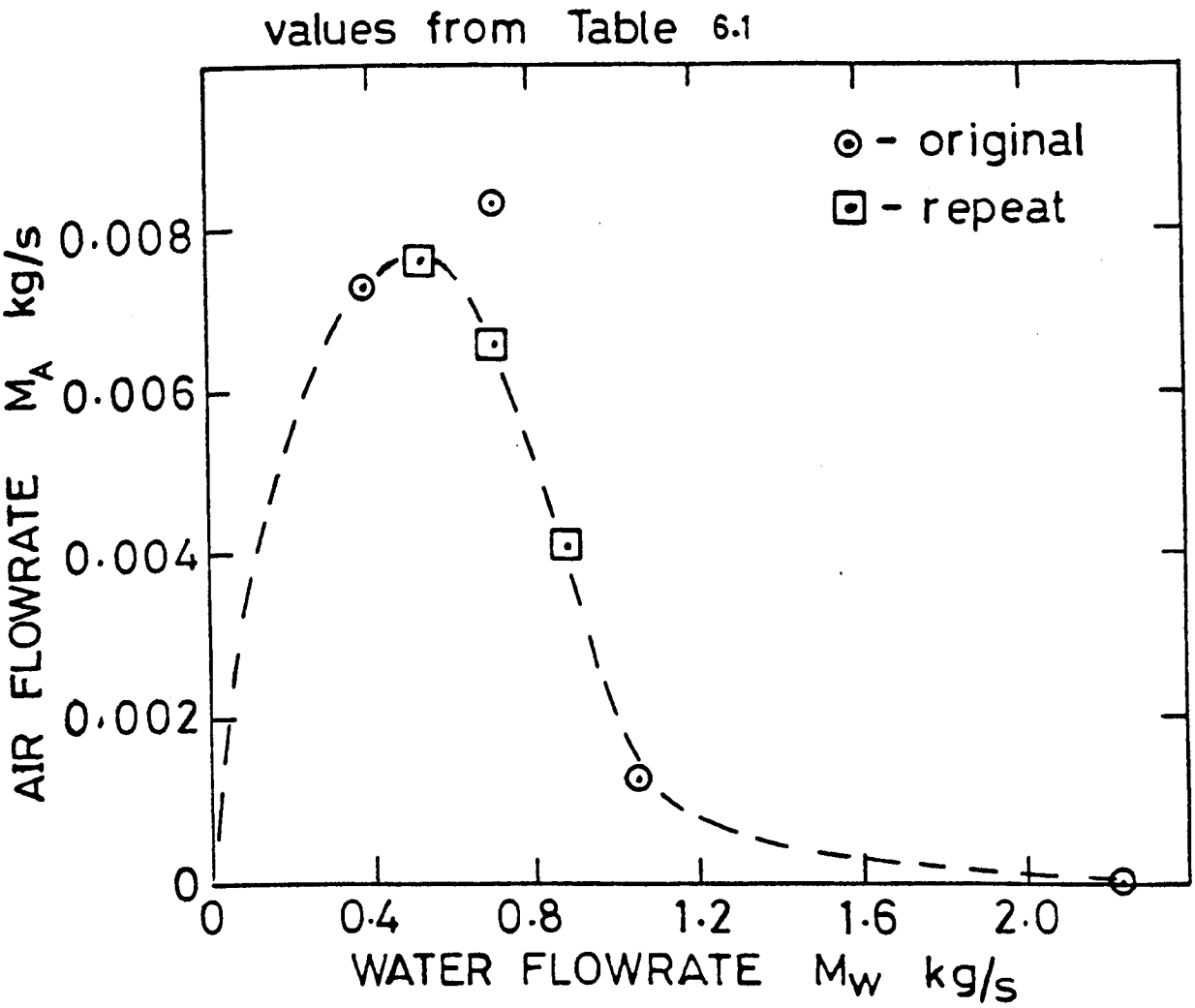

Fig 6.3 EXPERIMENTAL DATA FOR WATERFALL COLLAPSE.

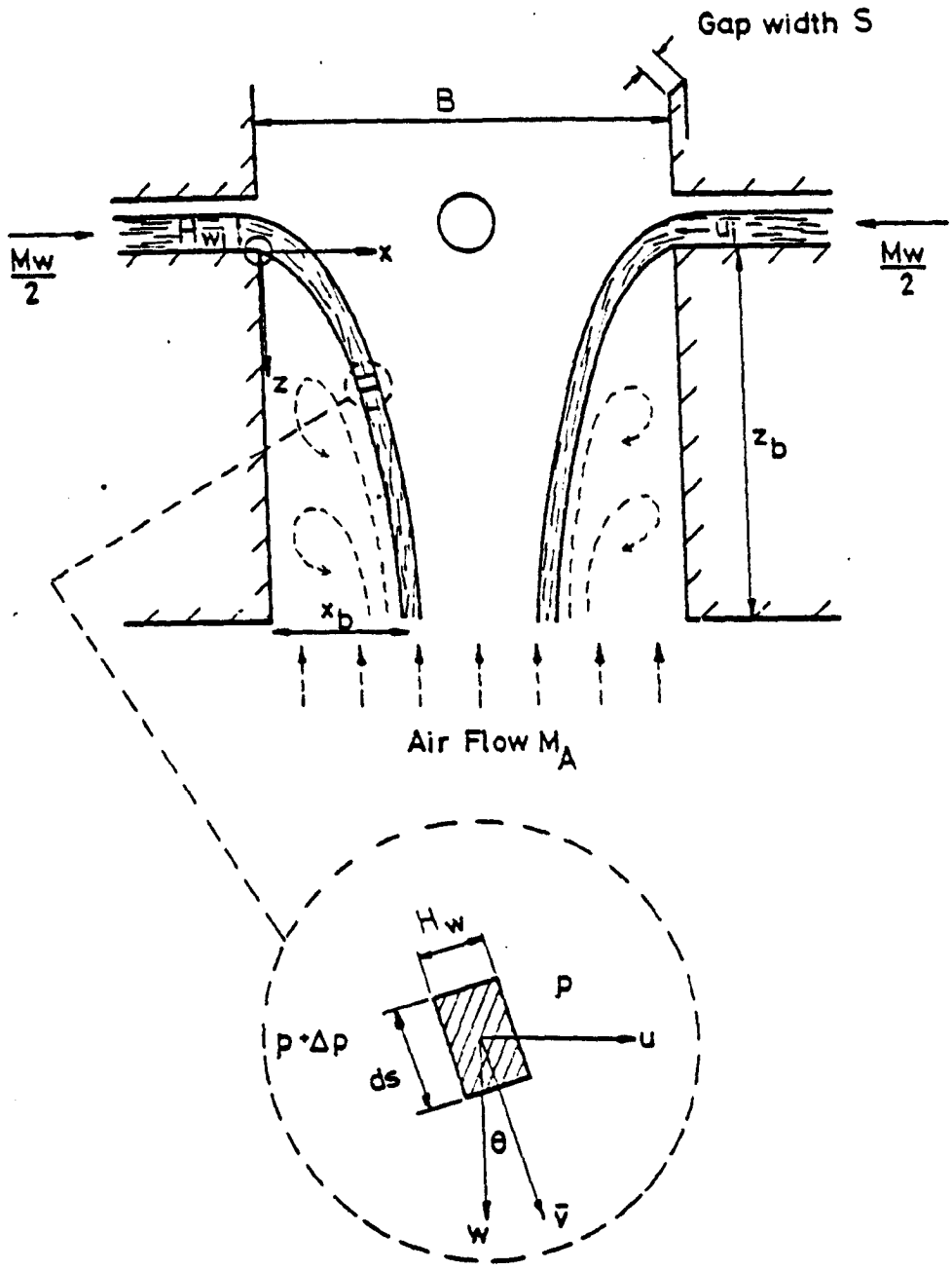

DETAIL OF WATERFALL ELEMENT

Fig 6.4 CO-ORDINATE SYSTEM FOR WATERFALL ANALYSIS

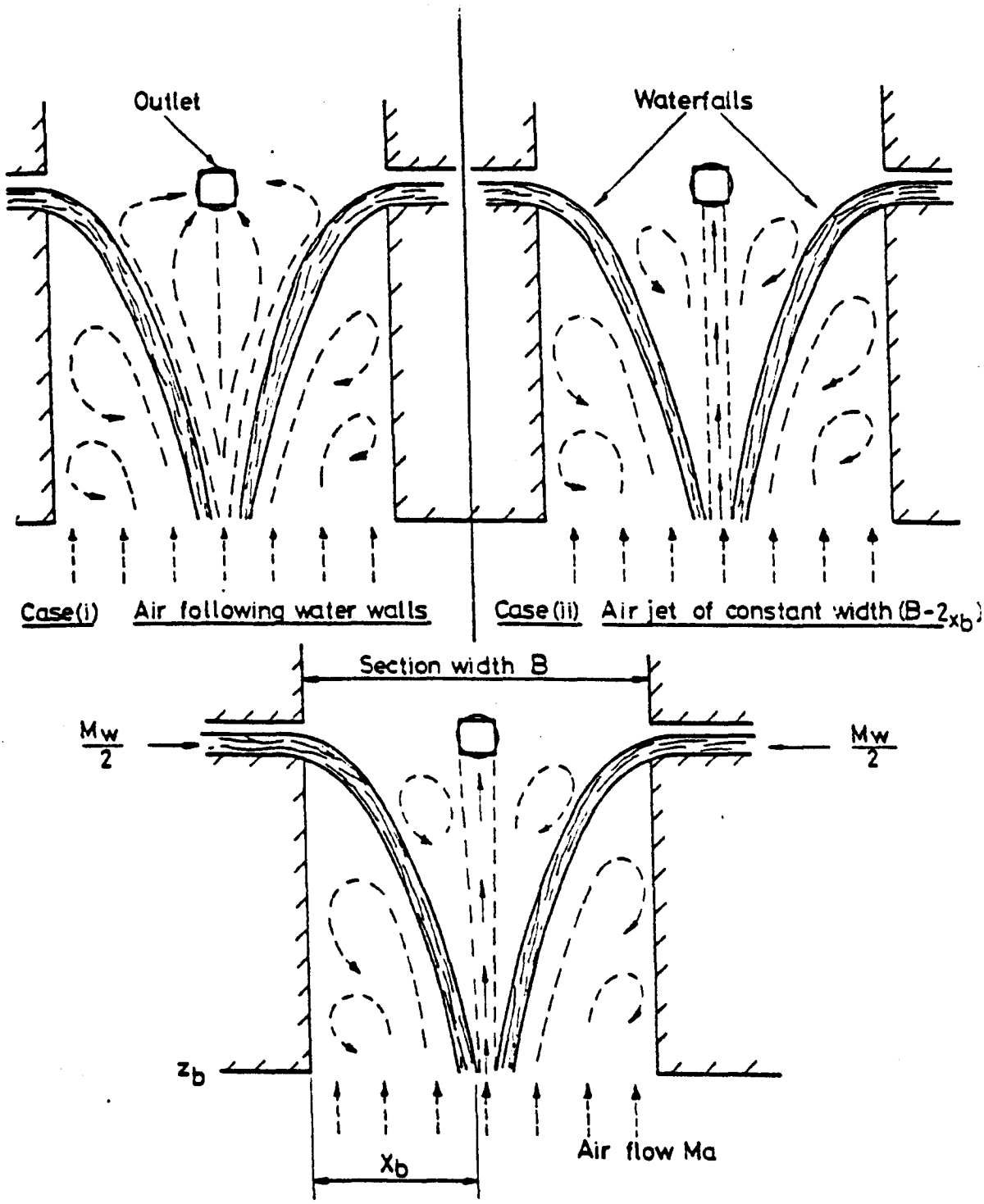

Fig 6.5 POSSIBLE AIR FLOW PATTERNS

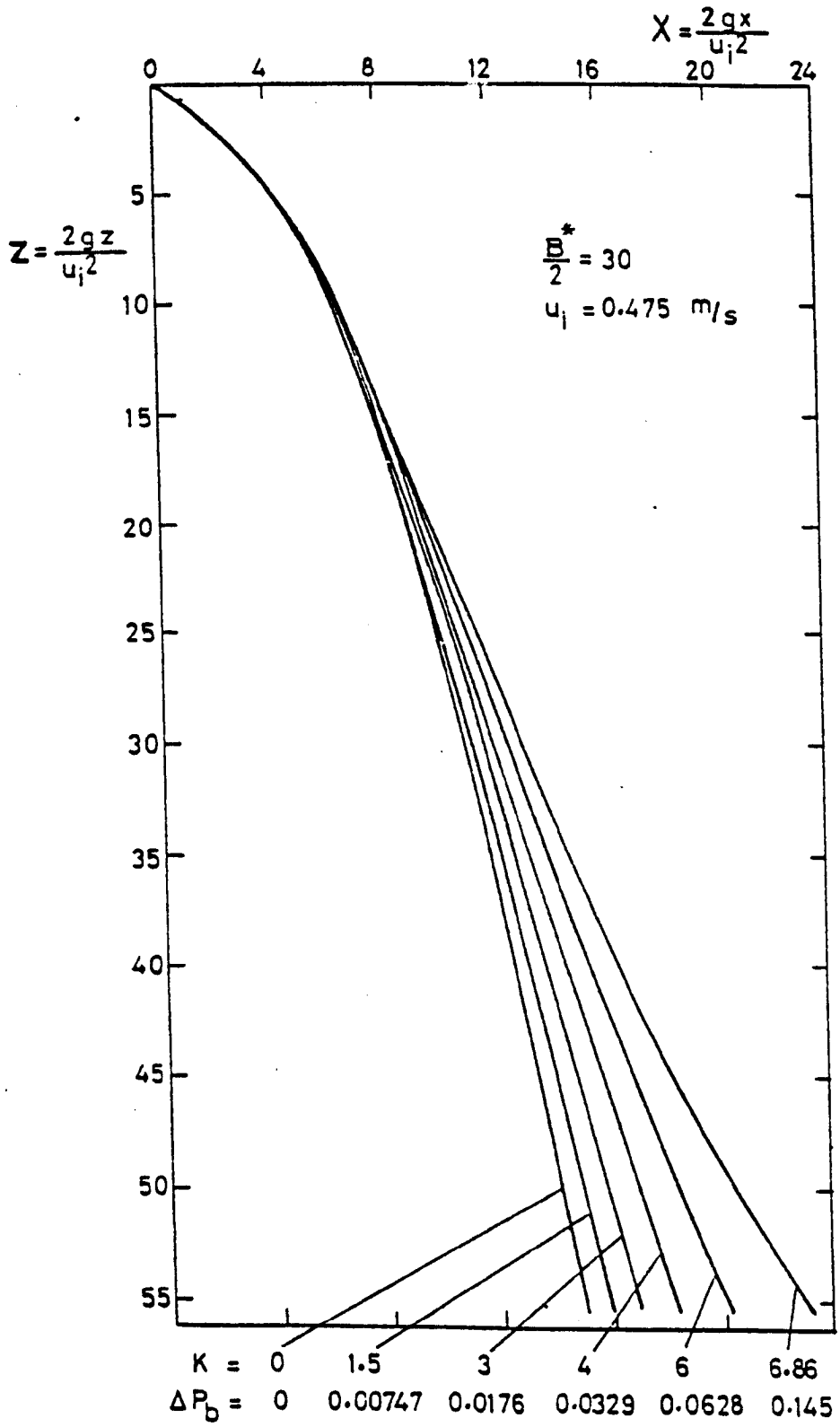

Fig 6.6 DIMENSIONLESS WATER TRAJECTORIES - CASE (i).

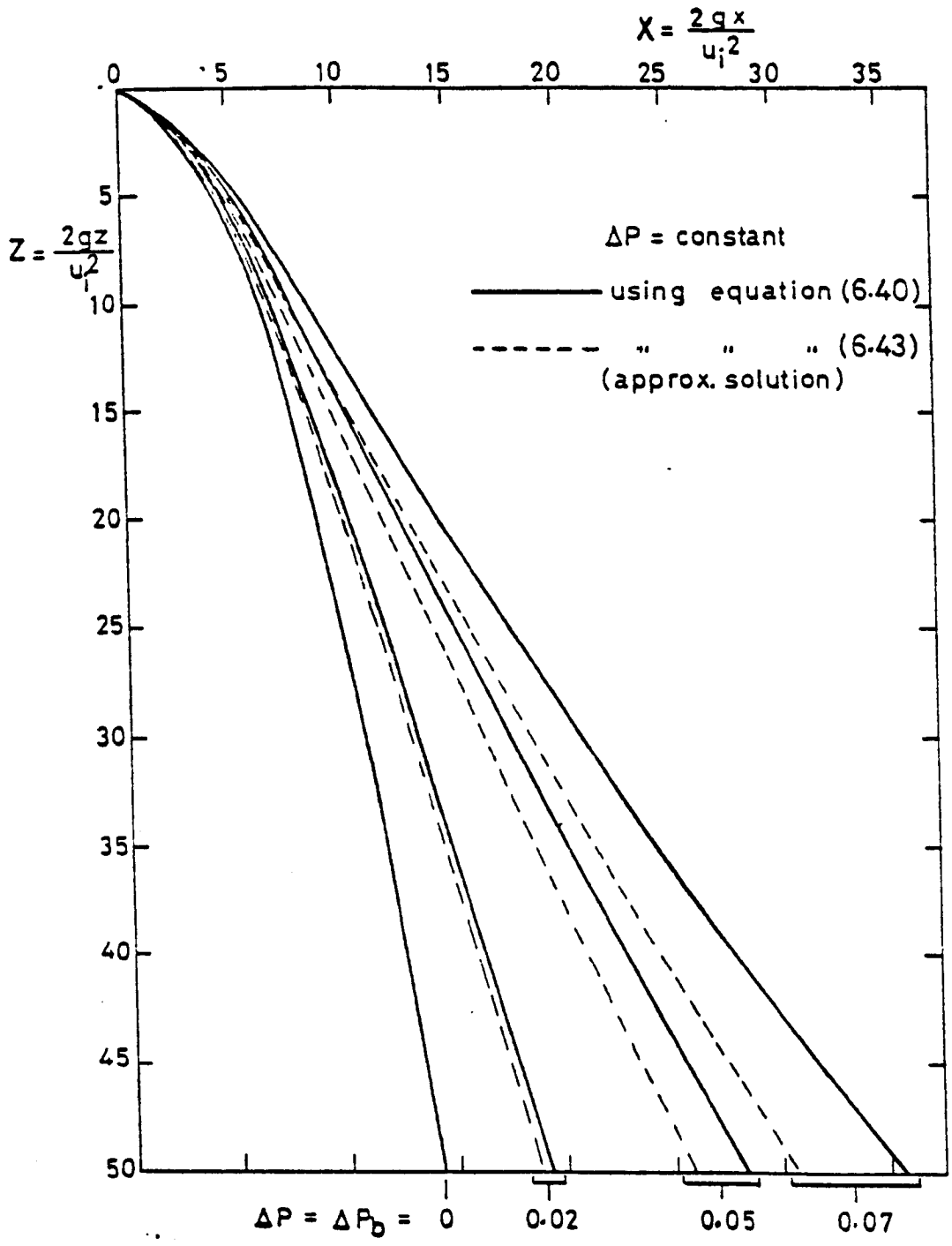

Fig 6.7 DIMENSIONLESS WATER TRAJECTORIES — CASE (ii)

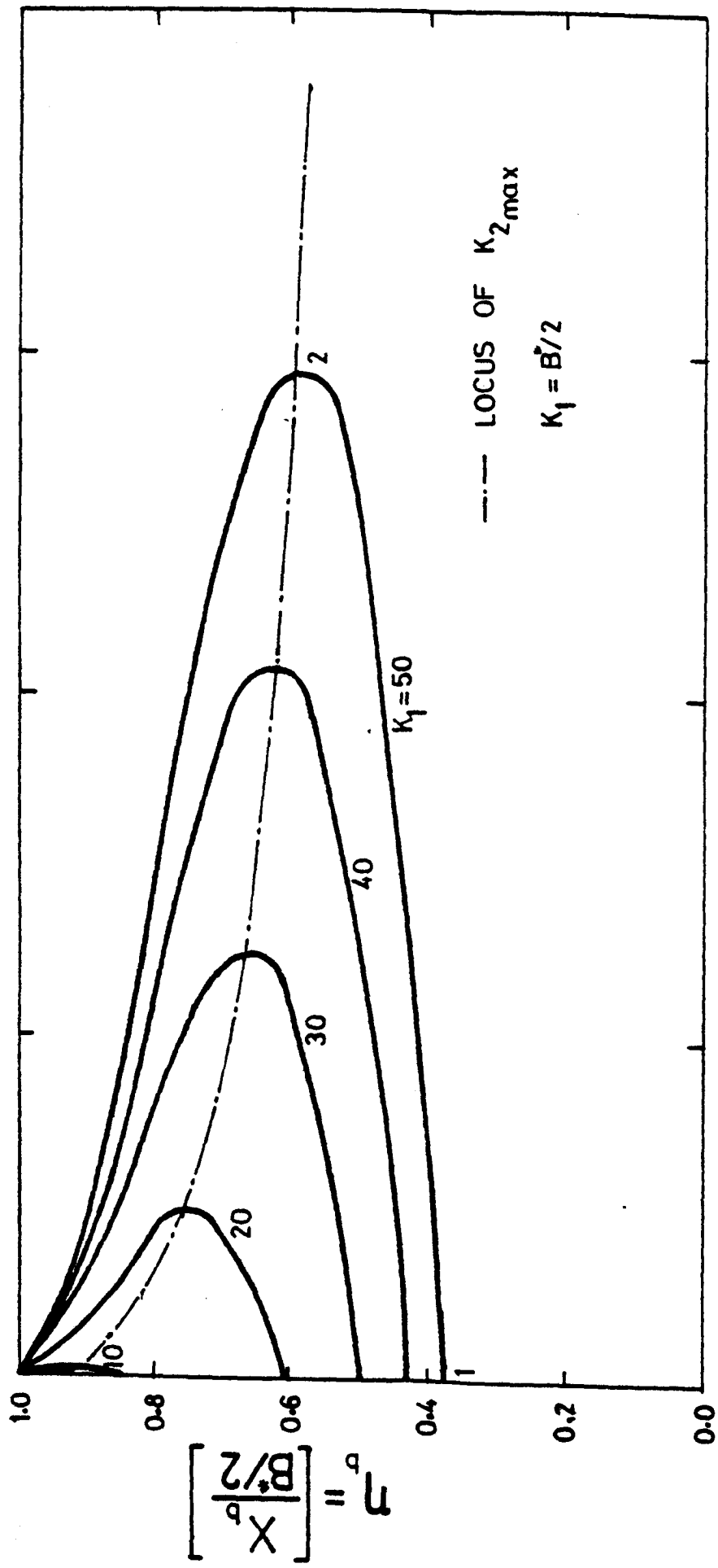

Fig 6.8 Position Of Waterfalls At Bottom Of Test Section For Case Of Constant ΔP - (Approximate Solution)

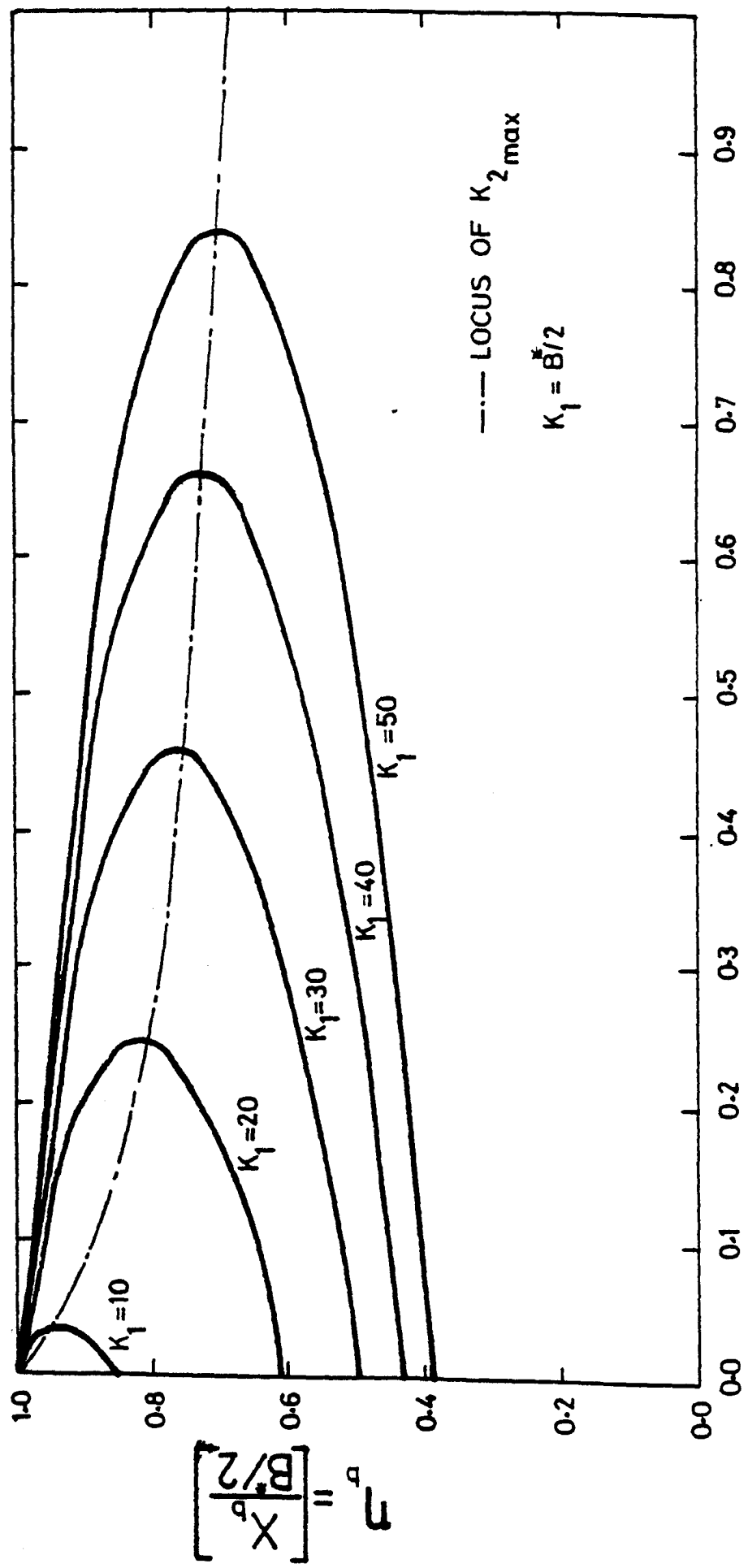

Fig 6.9 Position Of Waterfalls At Bottom Of Test Section For The Case Of Air Following Water Walls

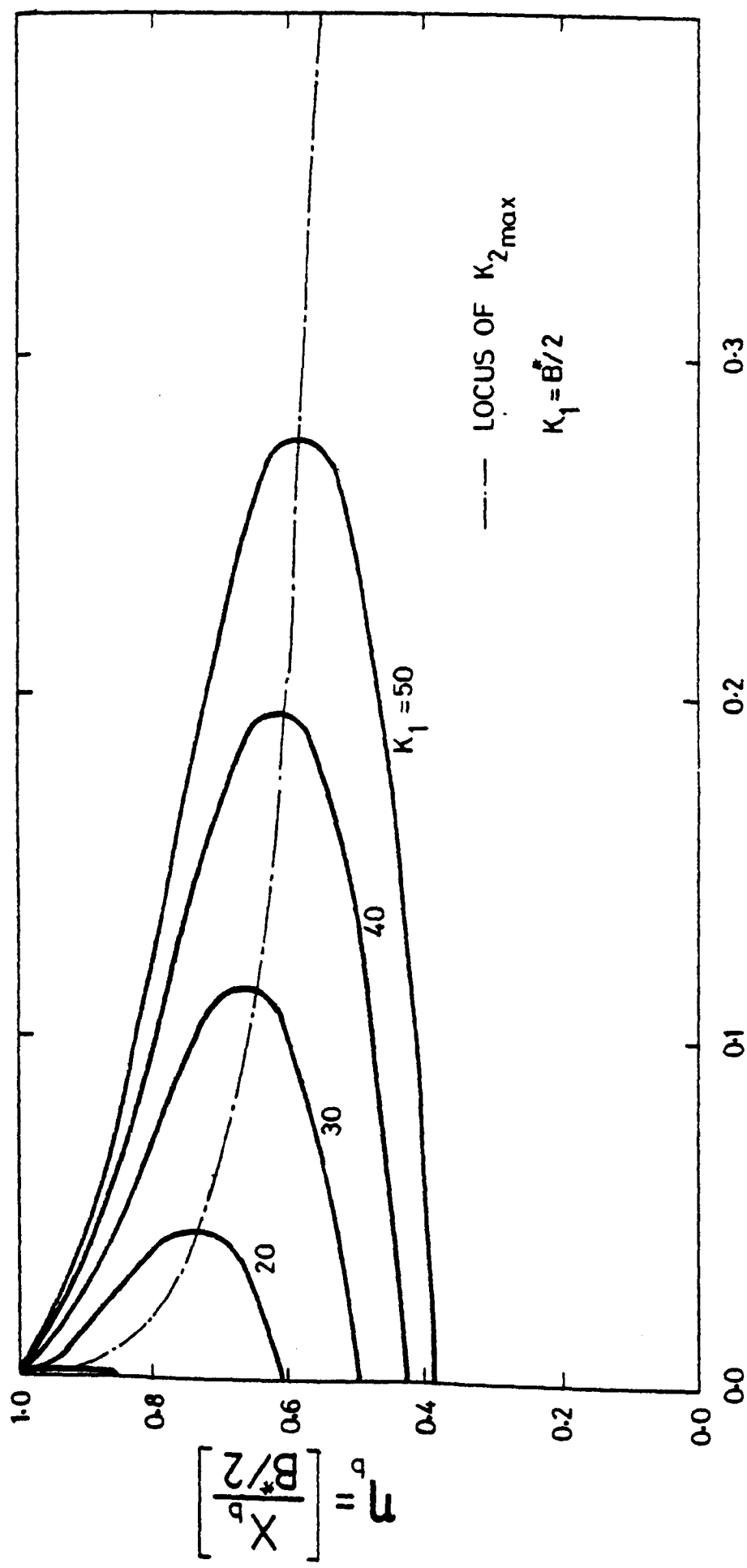

Fig 6.10 Position Of Waterfalls At Bottom Of Test Section For The Case Of Constant ΔP - (Exact Solution)

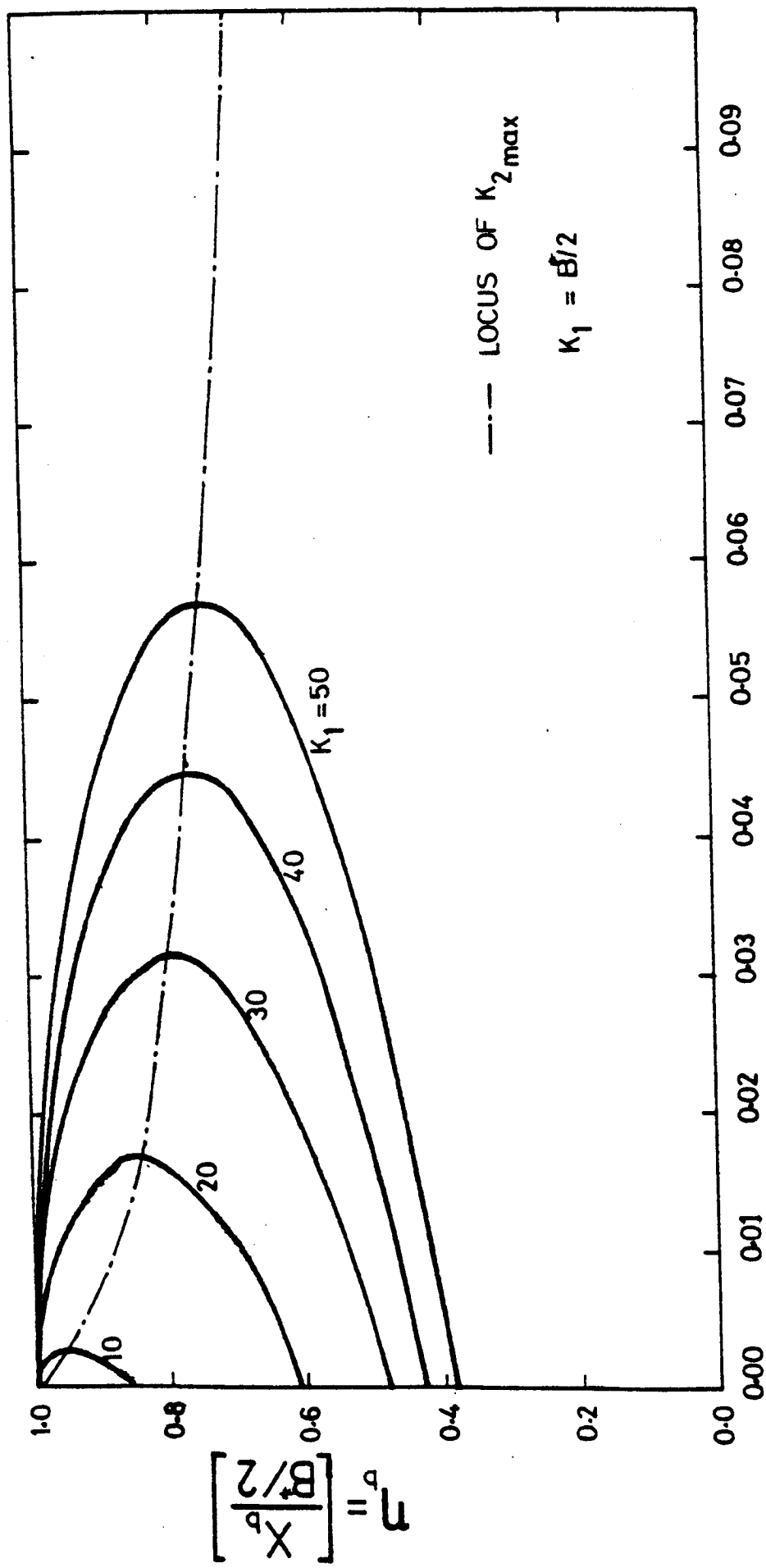

Fig 6.11 Position Of Waterfalls At Bottom Of Test Section For The Case Of Linear Varying Air Jet

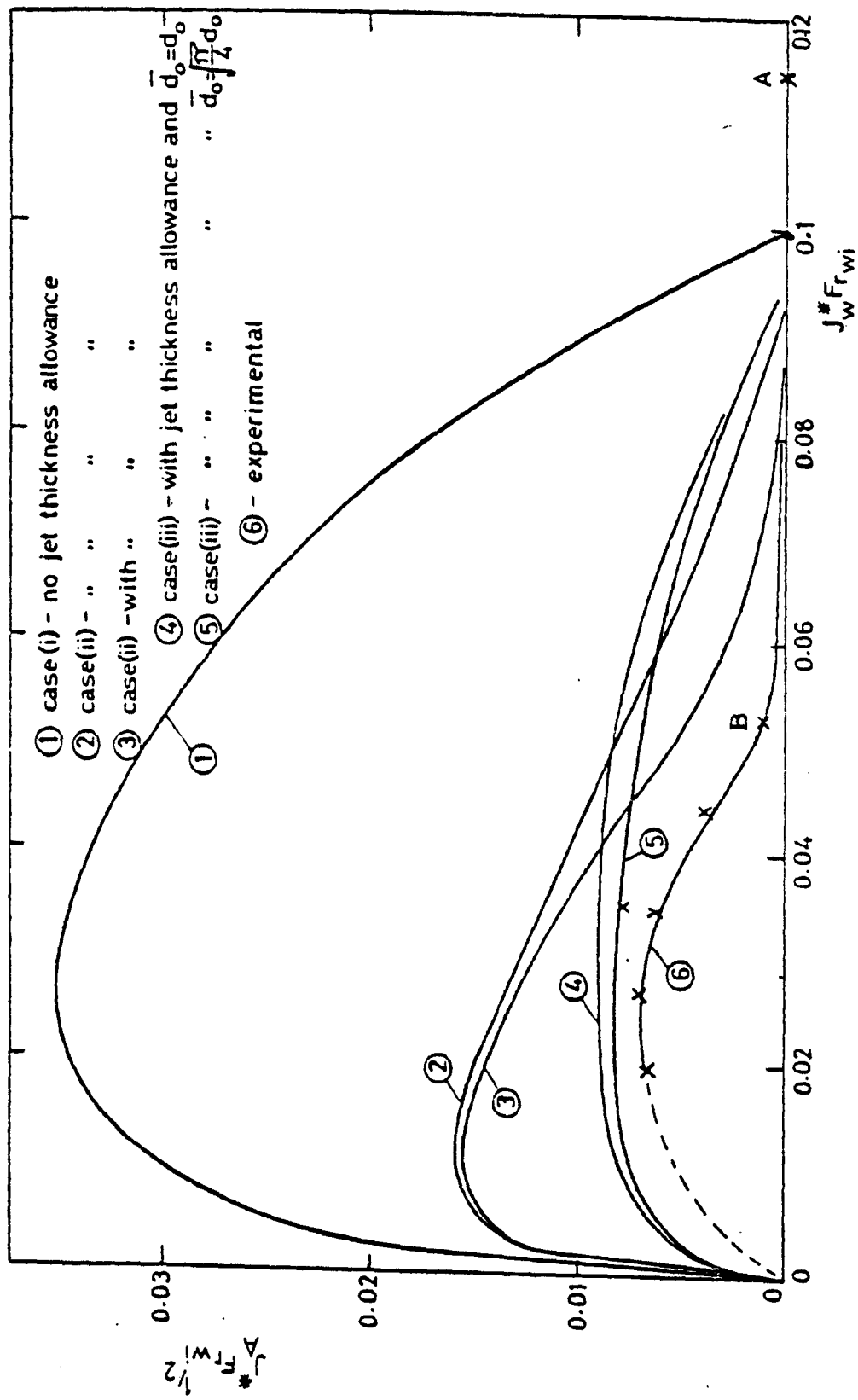

Fig 6.12 COMPARISON BETWEEN THEORY AND EXPERIMENT - COLLAPSE CONDITION FOR WATERFALL PAIR

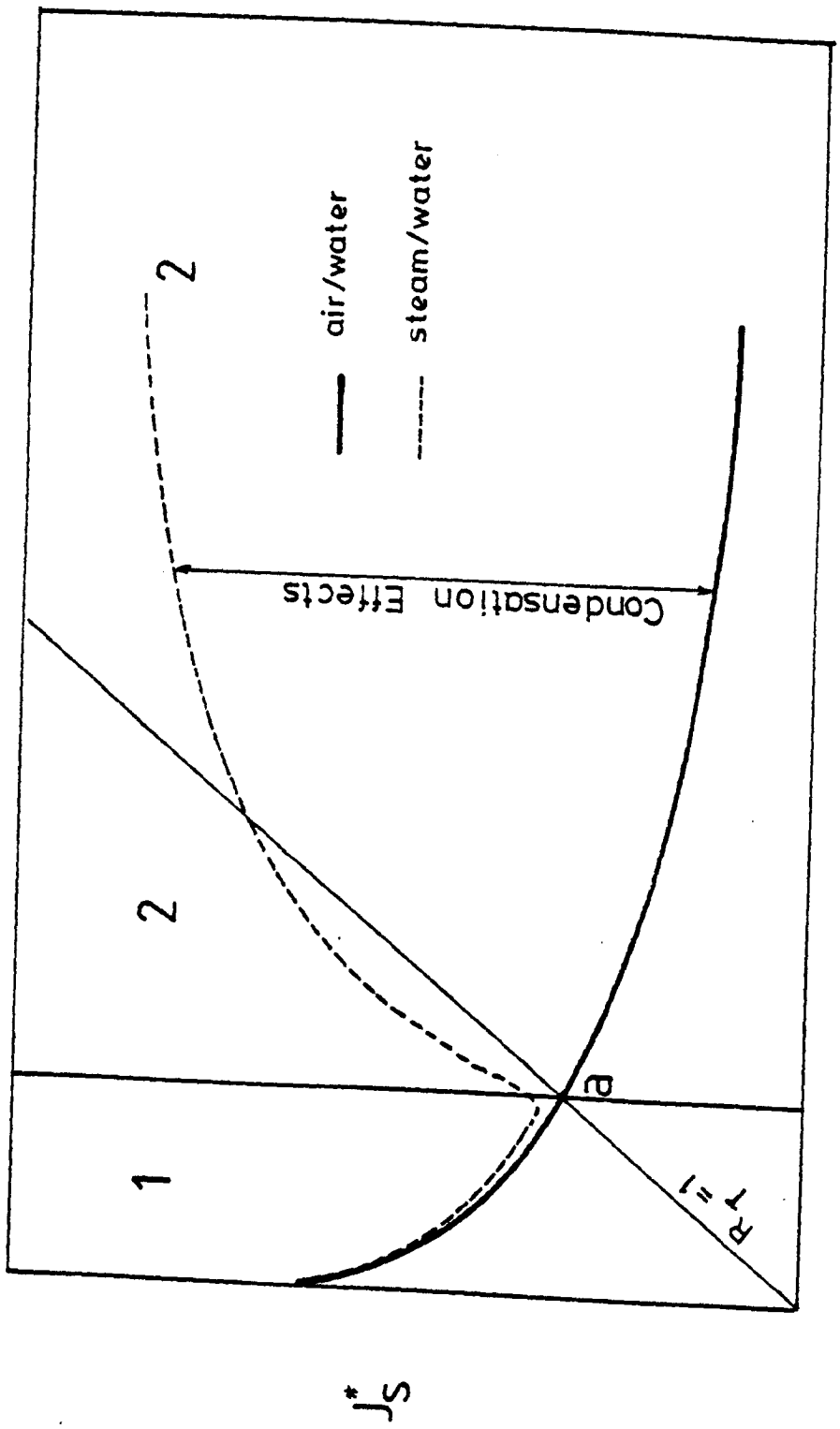

Fig 6.13 Sketch Of Typical Flooding Behaviour

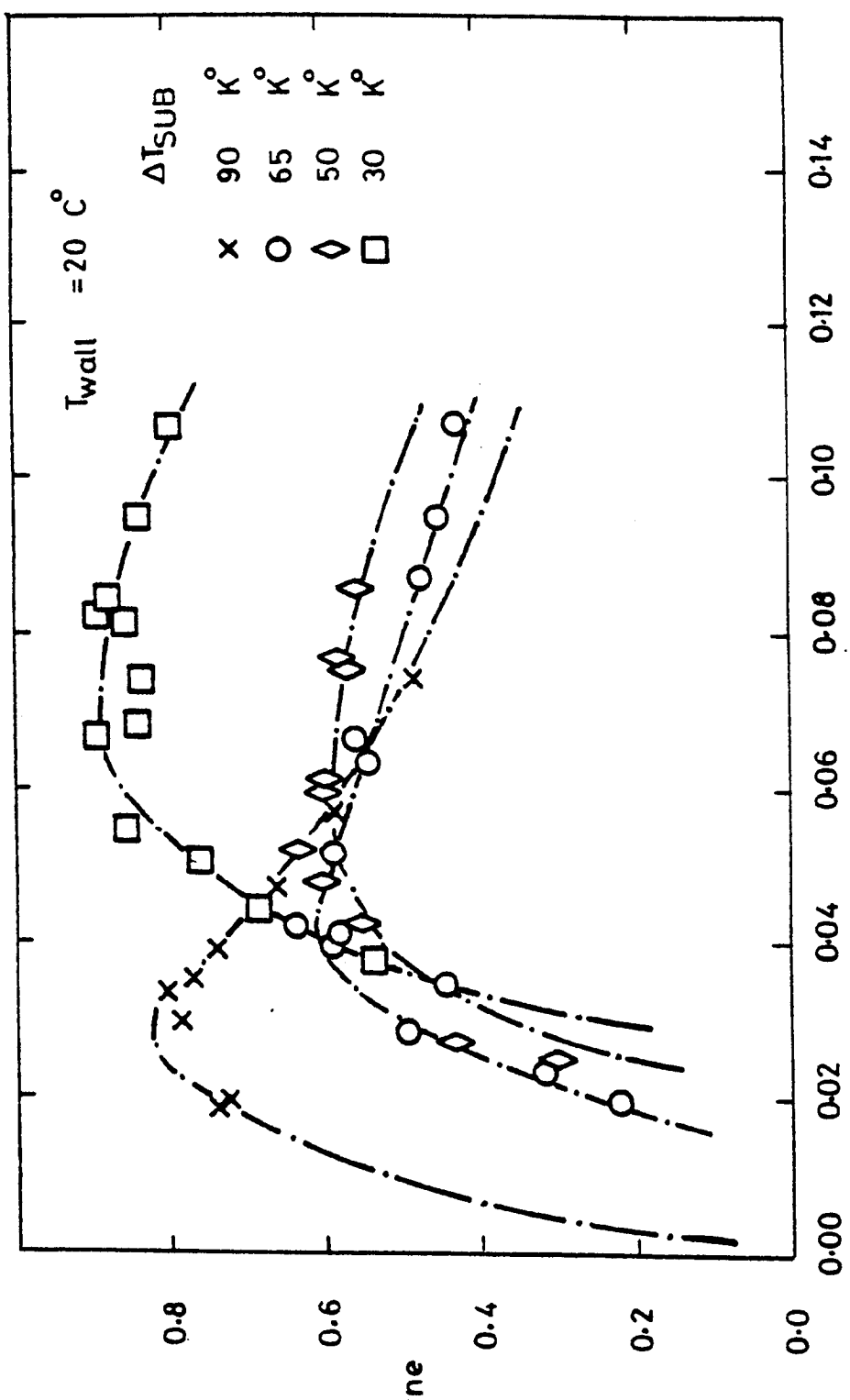

Fig 6.14 VARIATION OF NON-EQUILIBRIUM FACTOR, K_{ne}, WITH DIMENSIONLESS WATER FLUX, j^*_w

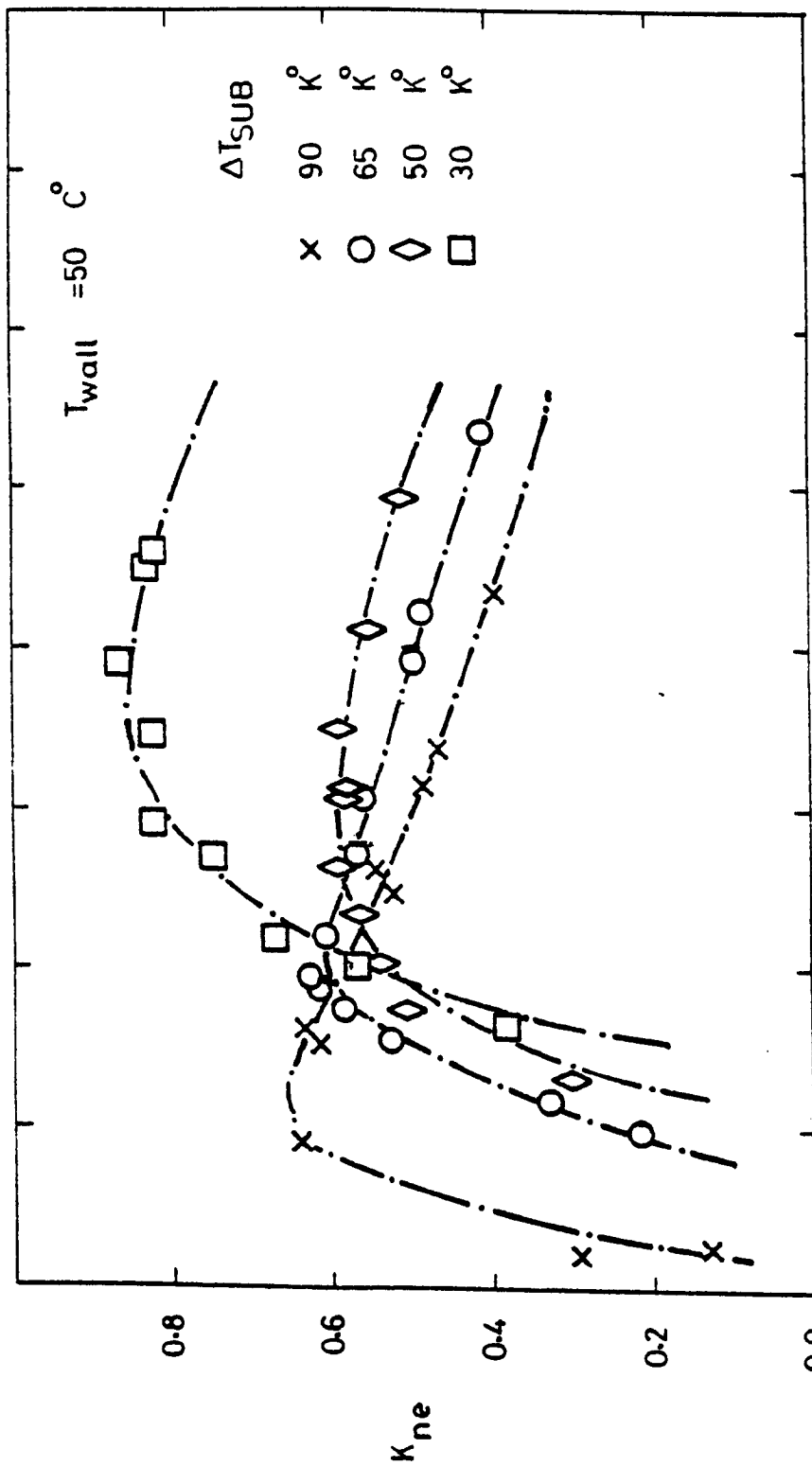

Fig 6.15 VARIATION OF NON-EQUILIBRIUM FACTOR, K_{ne}, WITH DIMENSIONLESS WATER FLUX, j^*_w

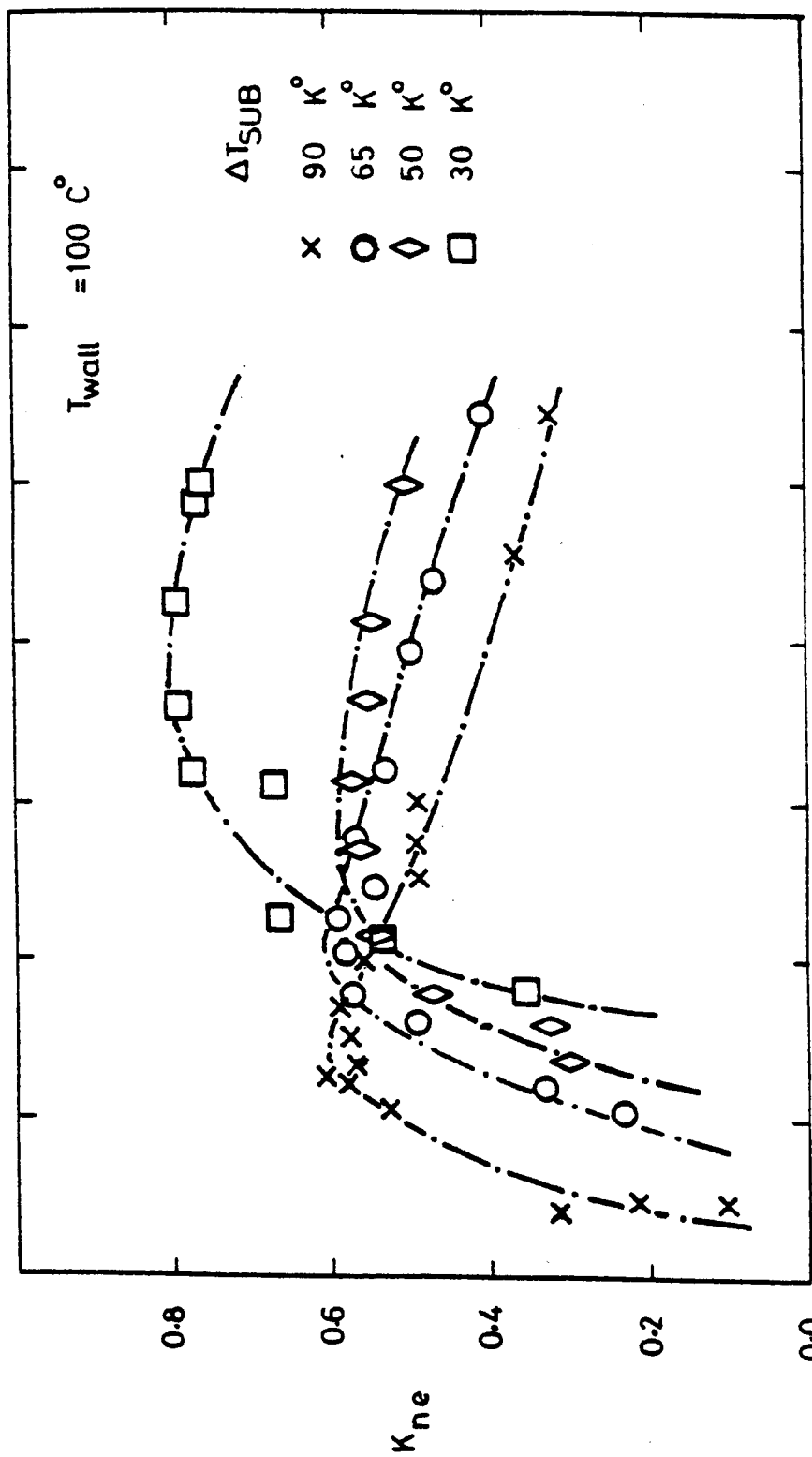

Fig 6.16 VARIATION OF NON-EQUILIBRIUM FACTOR, K_{ne}, WITH DIMENSIONLESS WATER FLUX, j_w^*

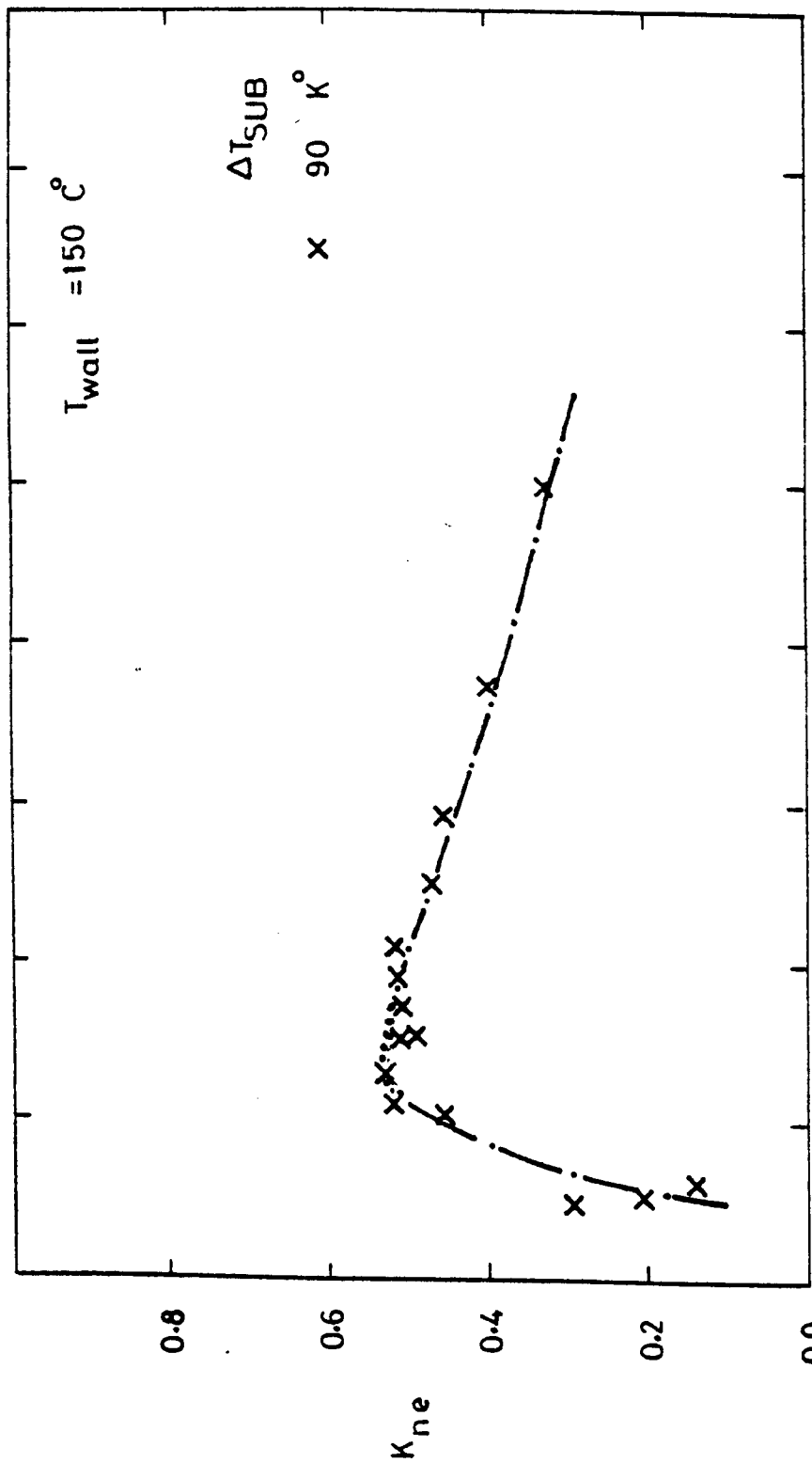

Fig 6.17 VARIATION OF NON-EQUILIBRIUM FACTOR, K_{ne}, WITH DIMENSIONLESS WATER FLUX, J_w^*

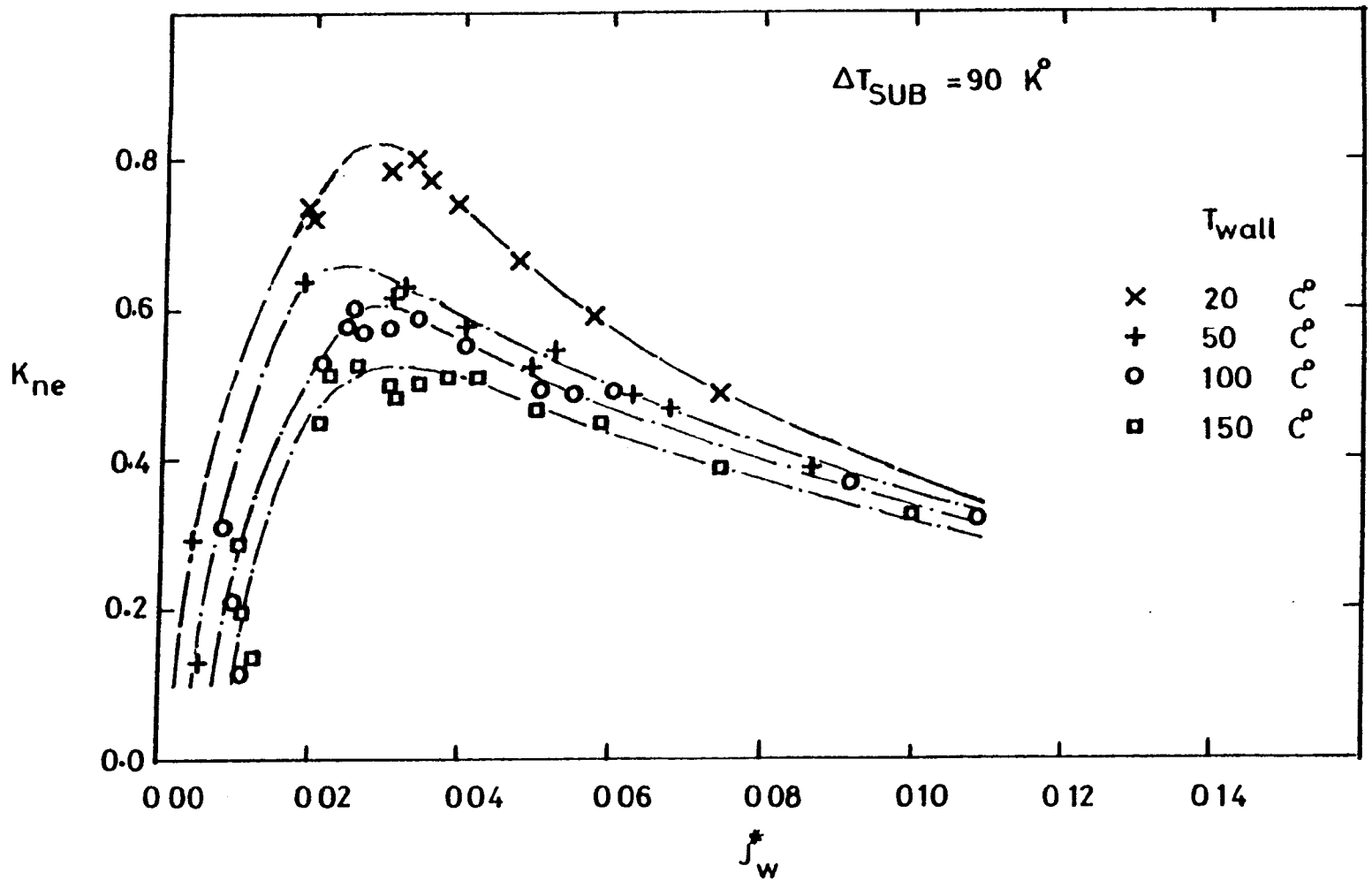

Fig 6·18 EFFECT OF WALL TEMPERATURE ON THE NON-EQUILIBRIUM FACTOR

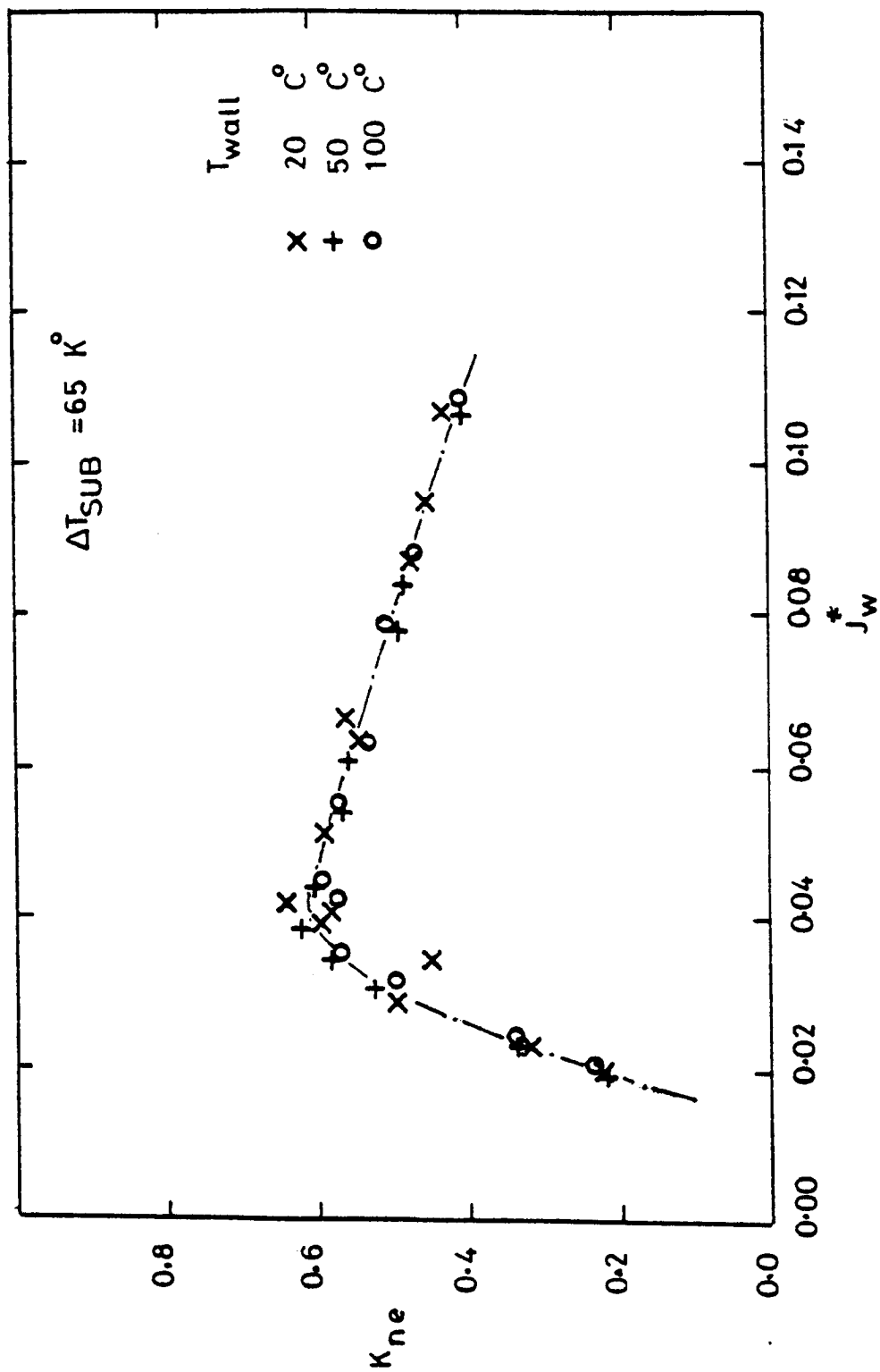

Fig 6.19 EFFECT OF WALL TEMPERATURE ON THE NON-EQUILIBRIUM FACTOR

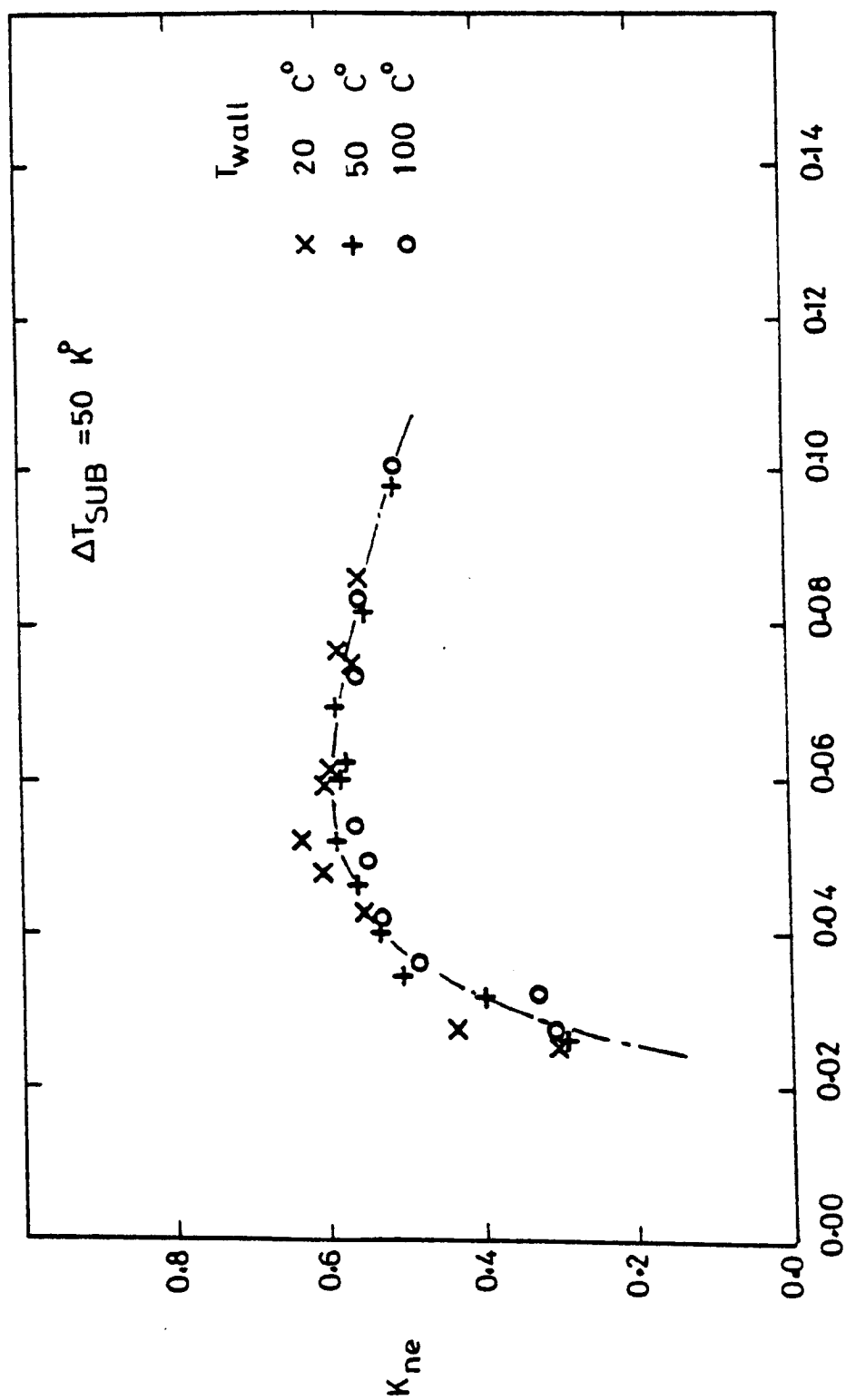

Fig 6.20 EFFECT OF WALL TEMPERATURE ON THE NON-EQUILIBRIUM FACTOR

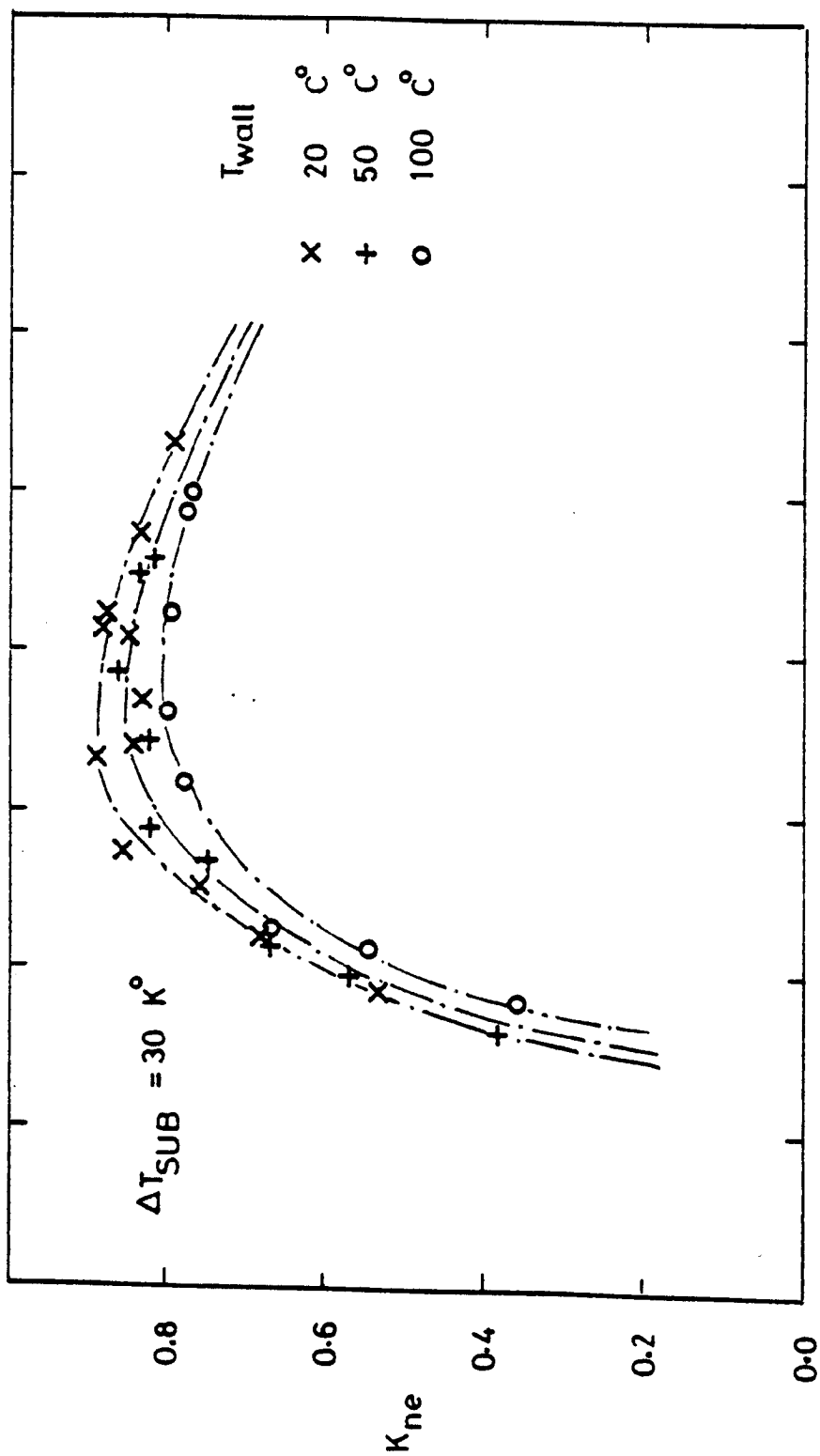

Fig 6.21 EFFECT OF WALL TEMPERATURE ON THE NON-EQUILIBRIUM FACTOR

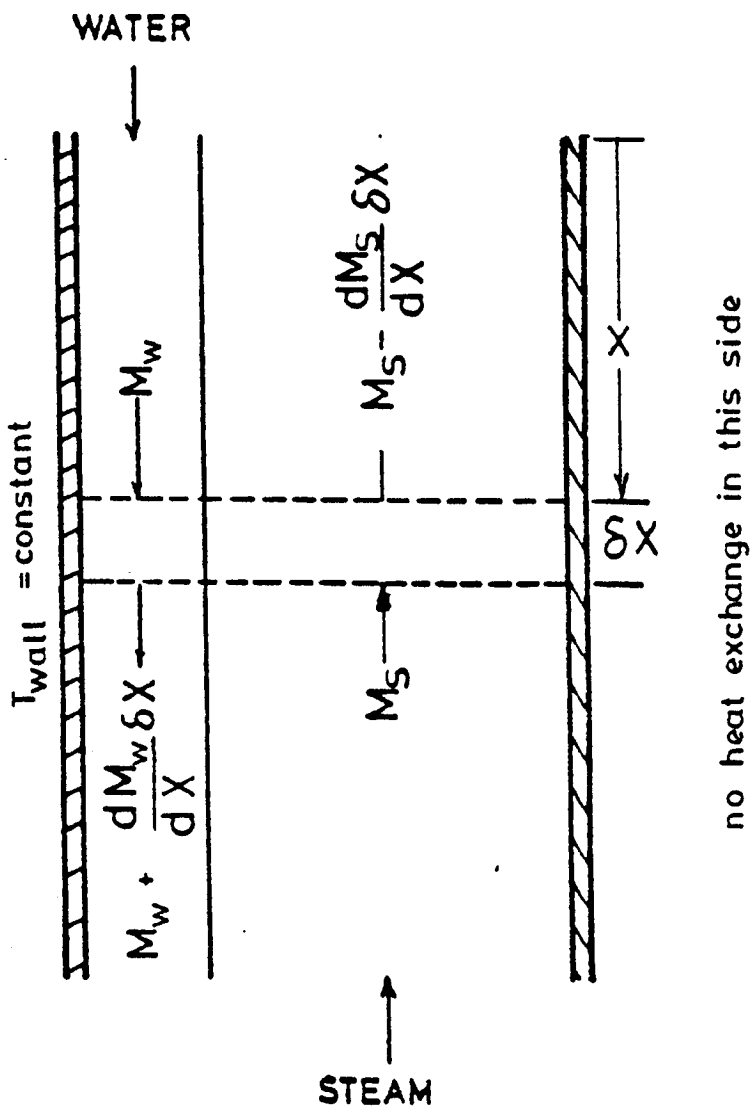

Fig 6.22 Counter-current Annular Flow

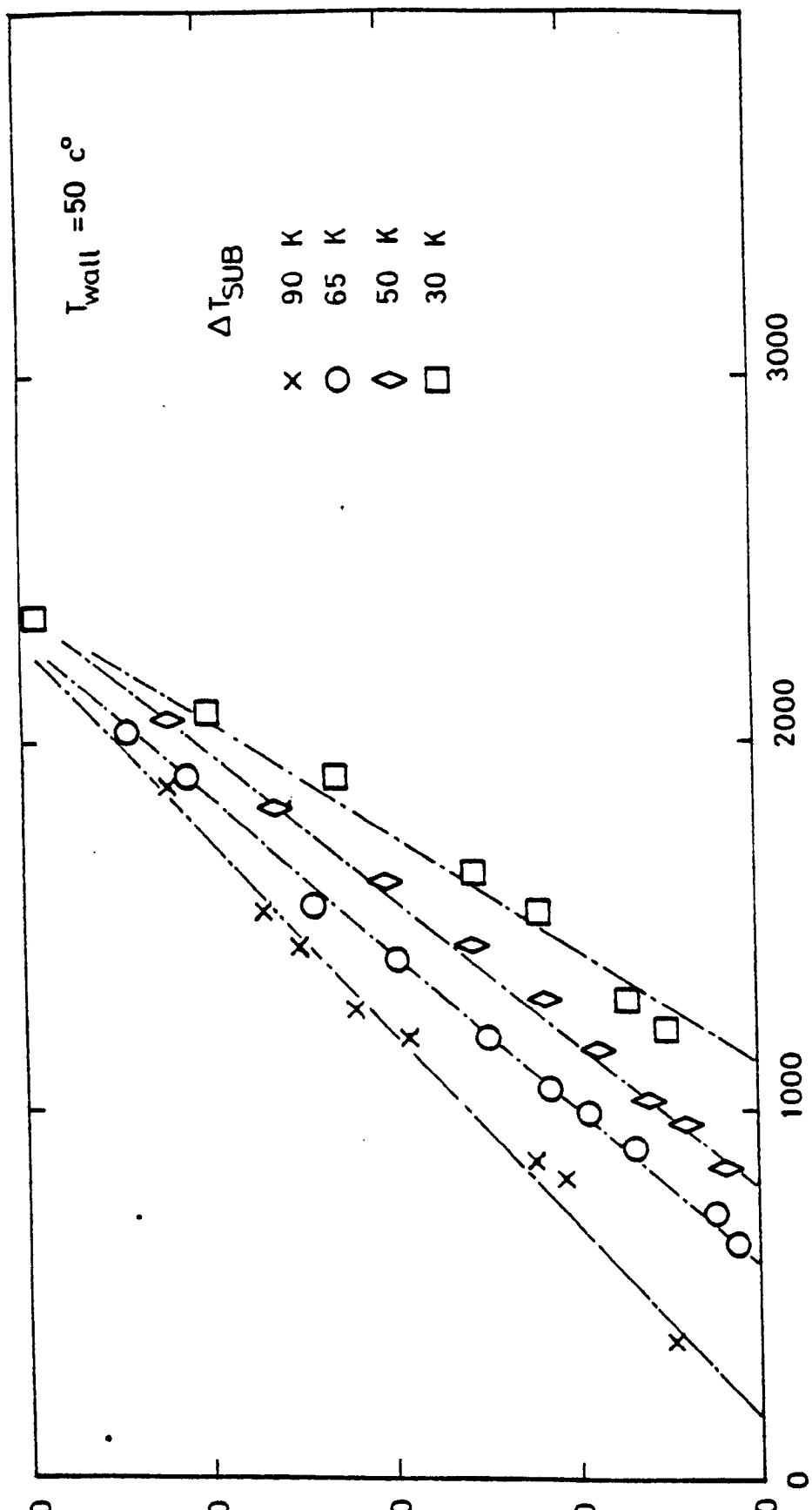

Fig 6.23 CORRELATION OF INTERFACIAL NUSSELT NUMBER AS A FUNCTION OF WATER PRANDTL AND REYNOLDS NUMBERS

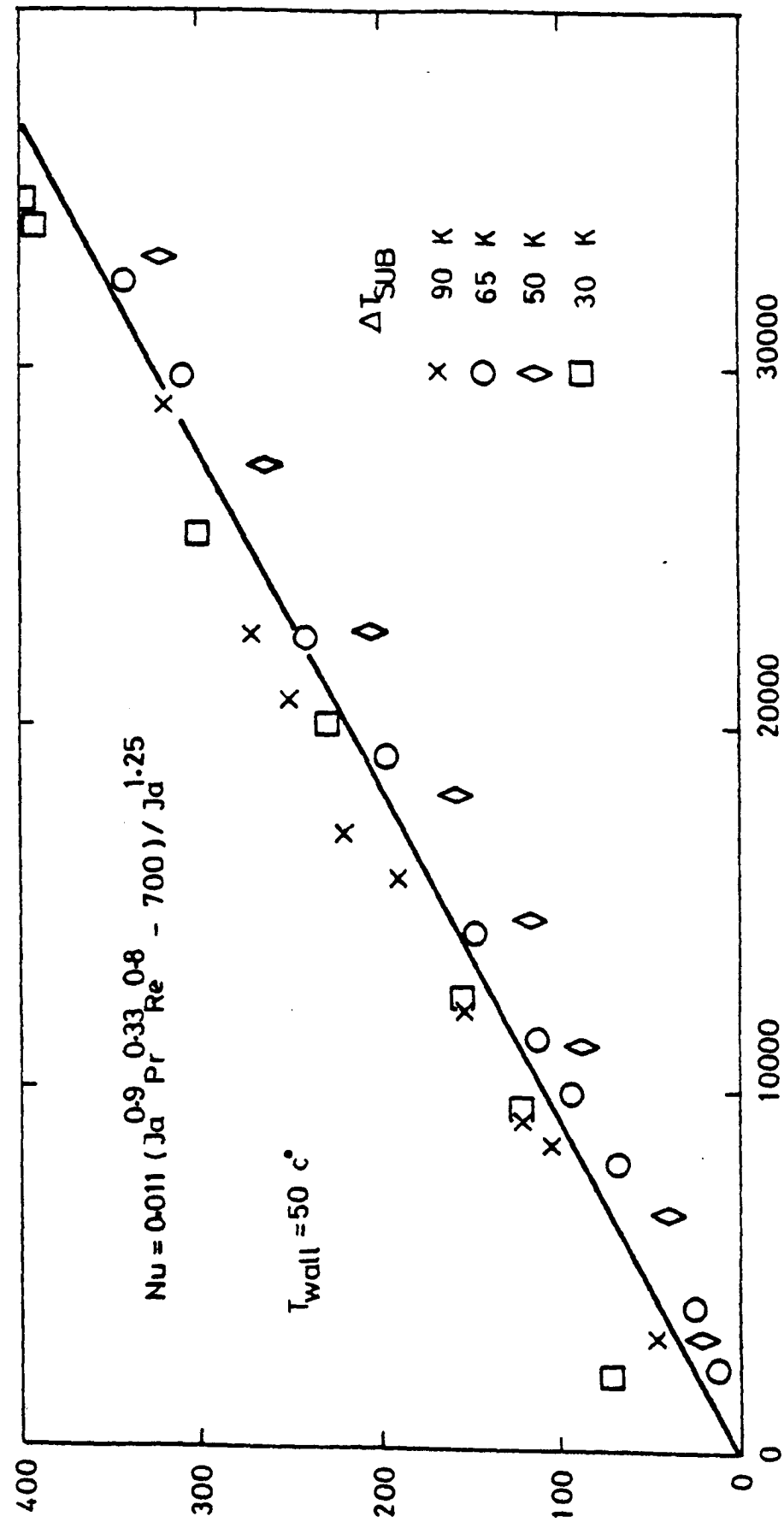

Fig 6.24 CORRELATION OF INTERFACIAL NUSSELT NUMBER

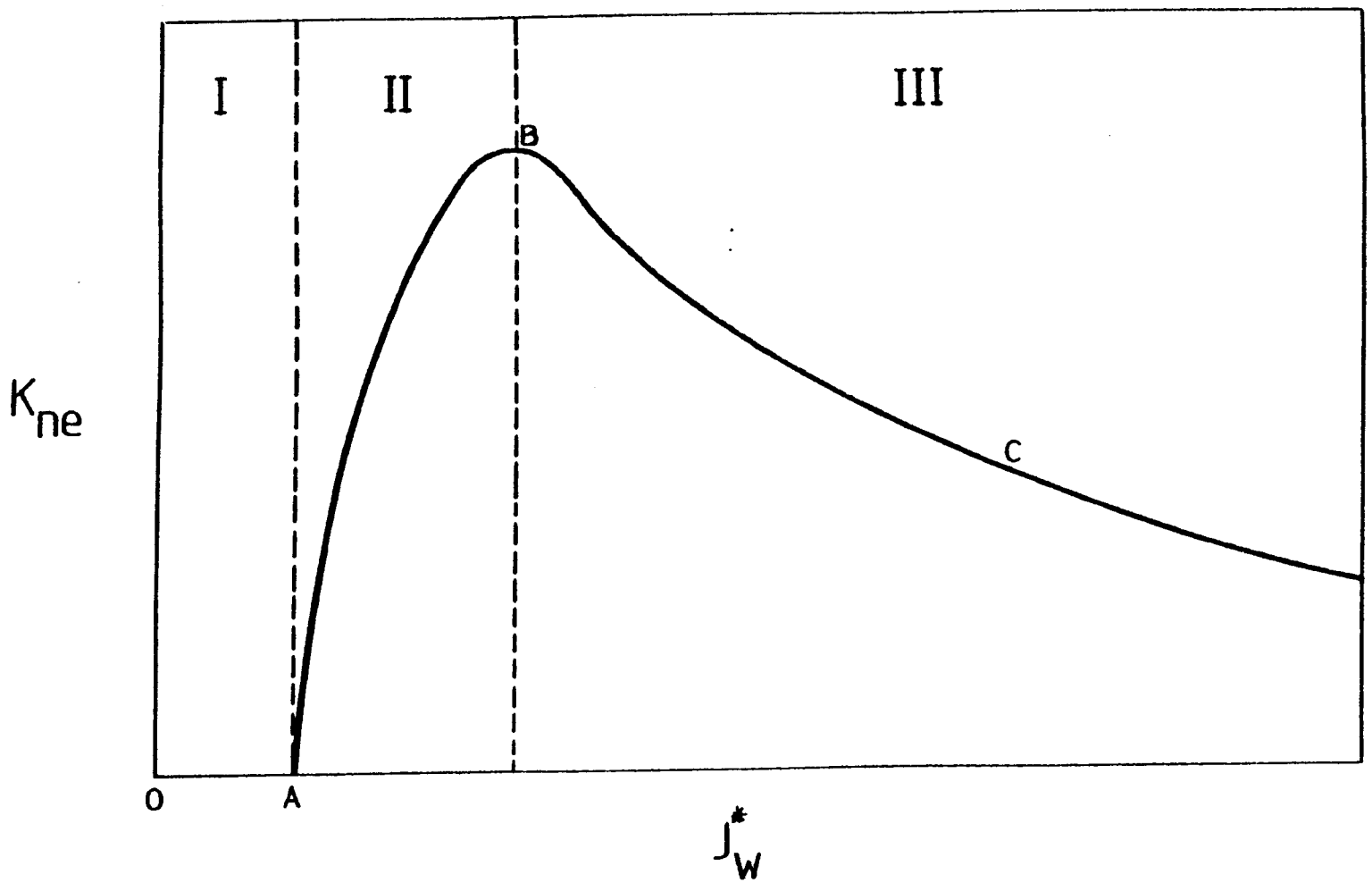

Fig 6.25 Sketch Of Typical Non-equilibrium Behaviour

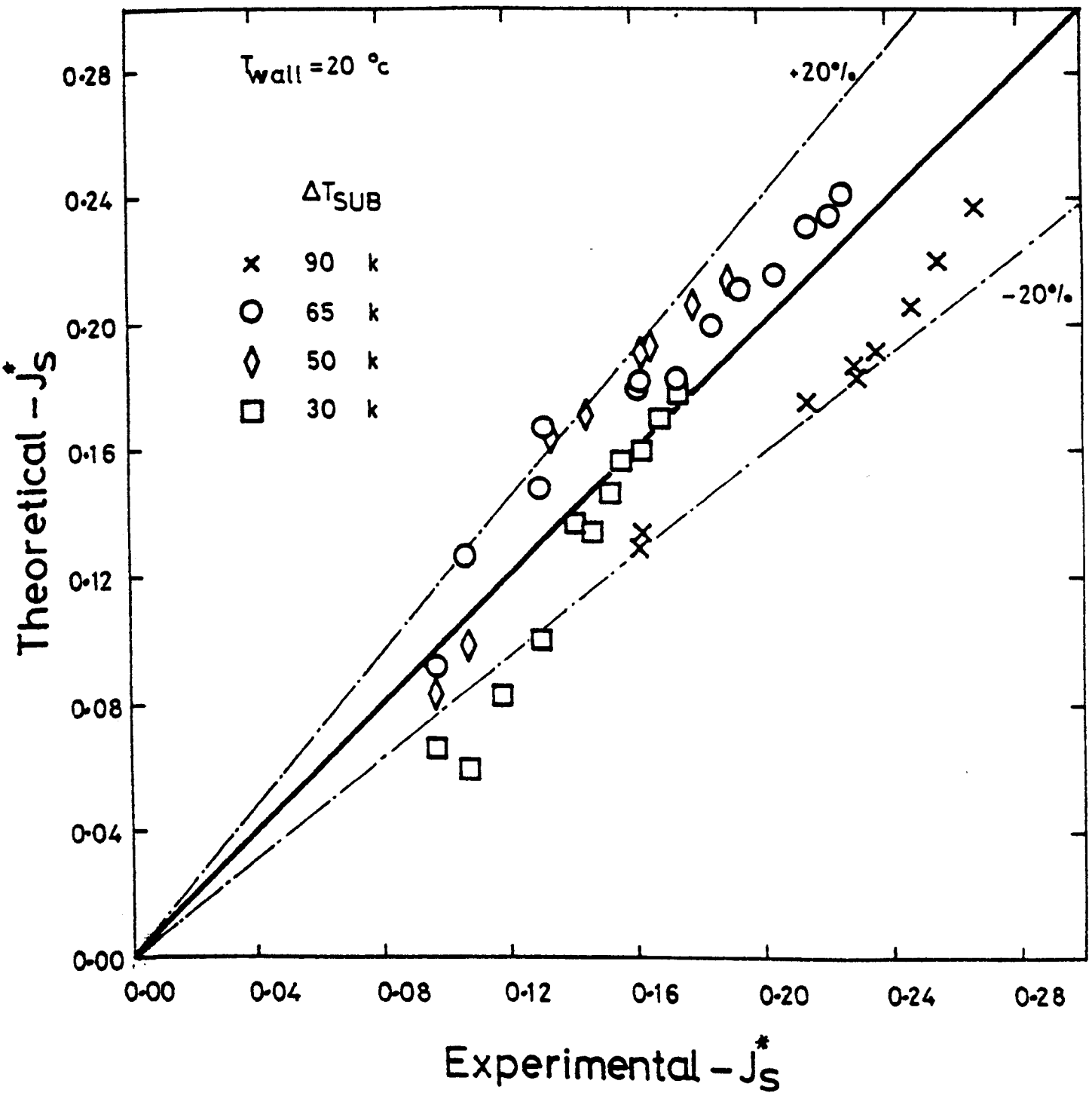

Fig 6.26 Comparison Between Calculated And Experimental J_S^*

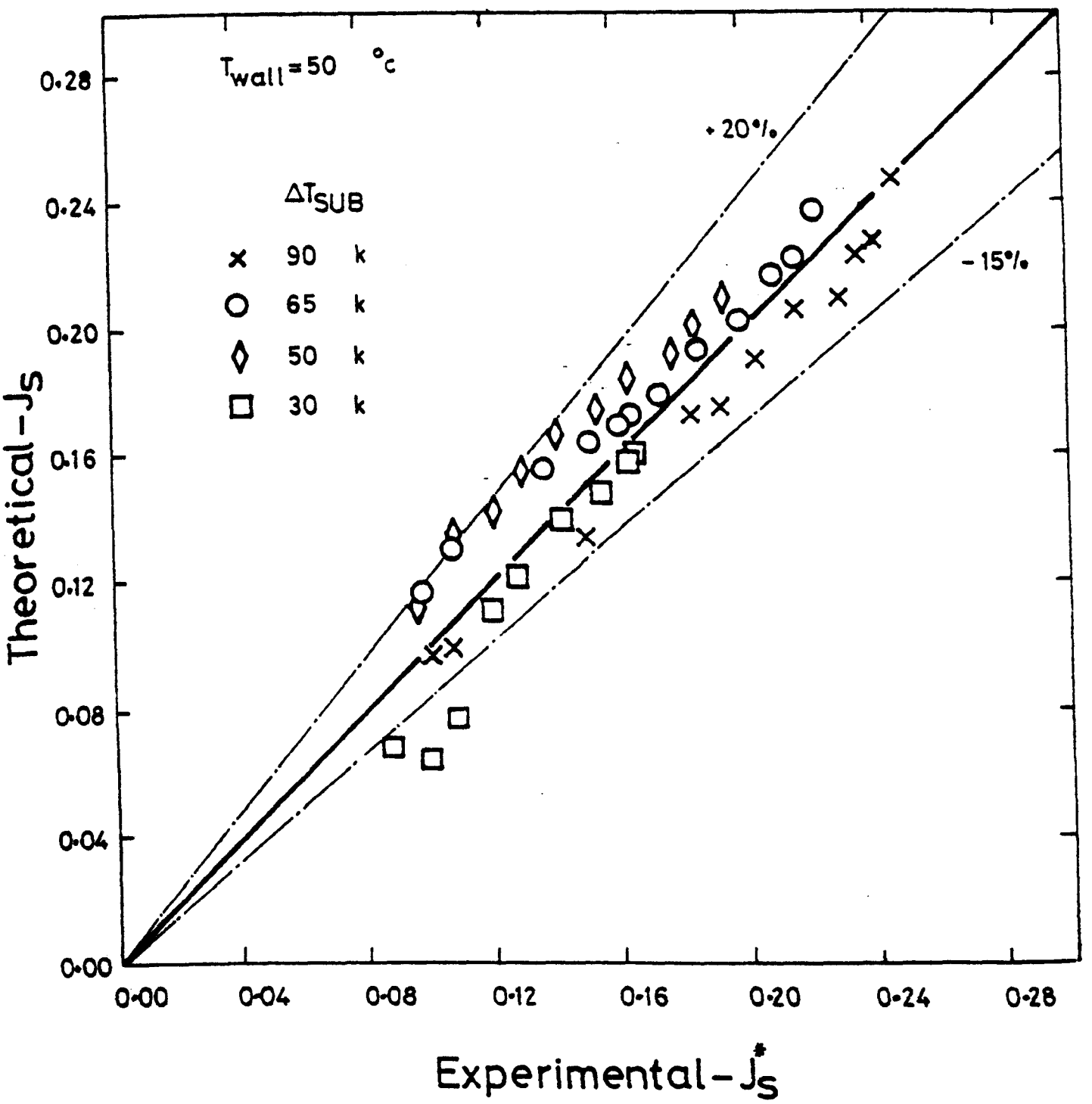

Fig 6.27 Comparison Between Calculated And Experimental J_s^*

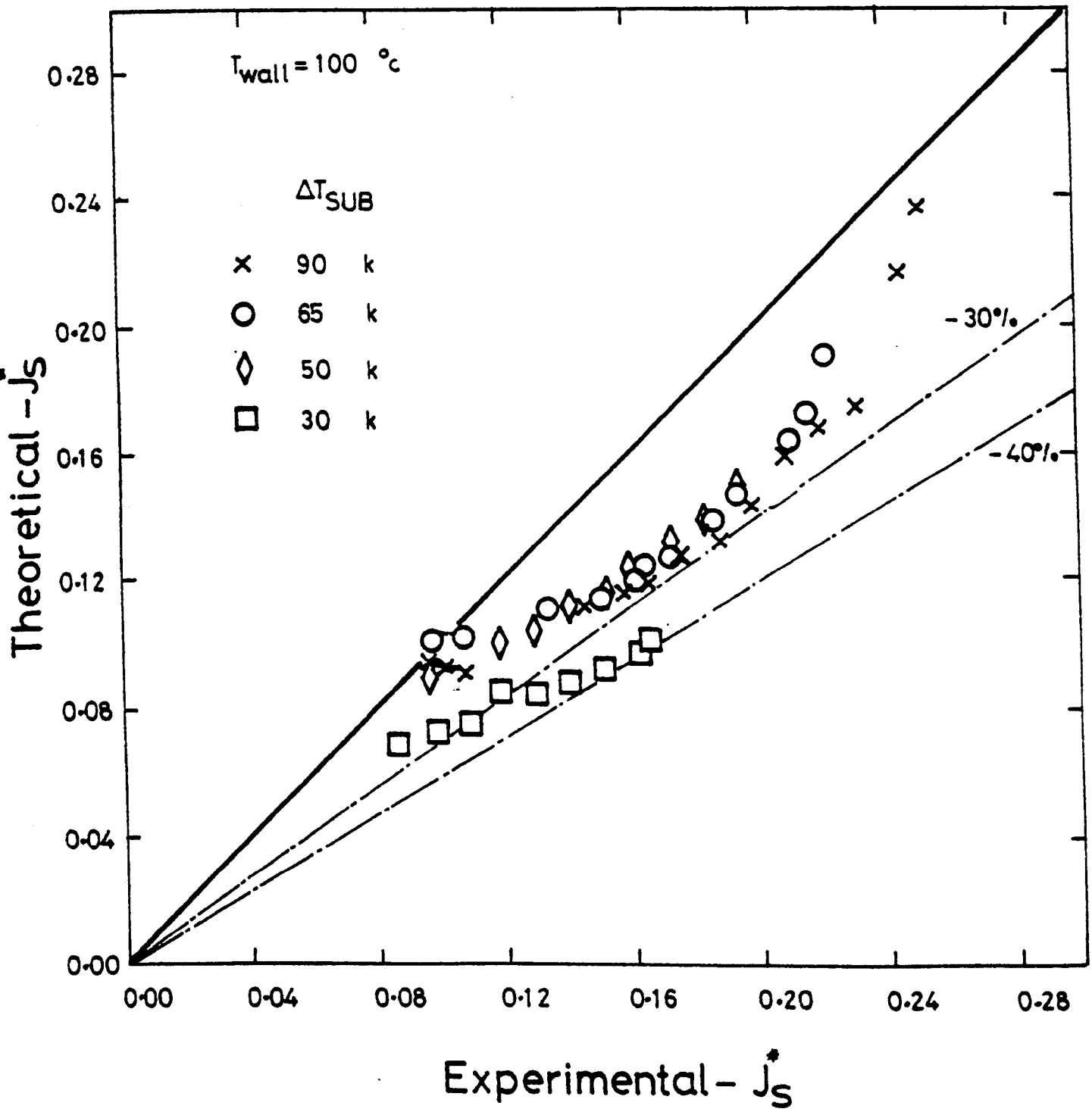

Fig 6.28 Comparison Between Calculated And Experimental J_S^*

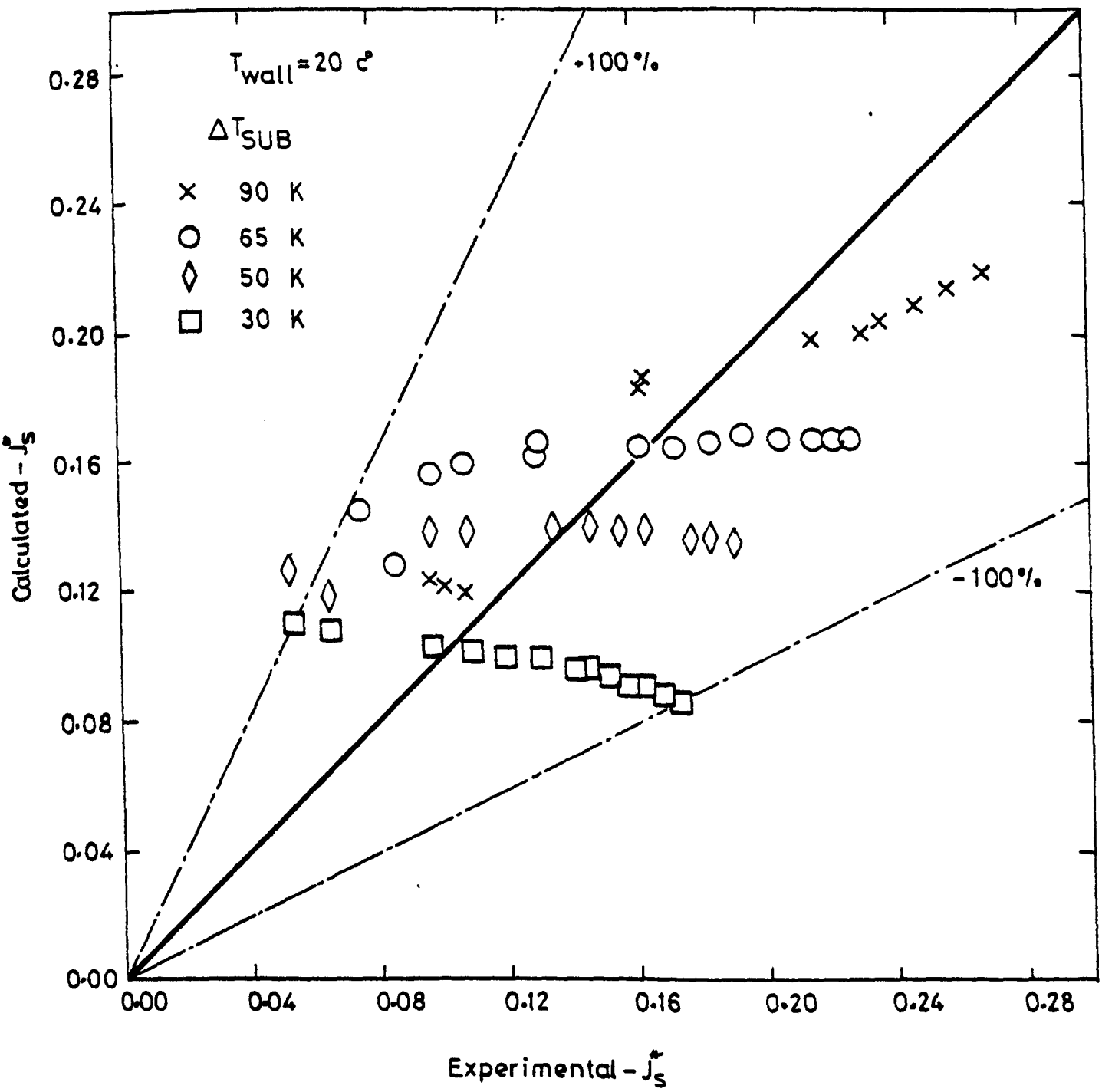

Fig 6.29 Comparison Between Experiment And Predicted Values Using BCL Correlation (39)

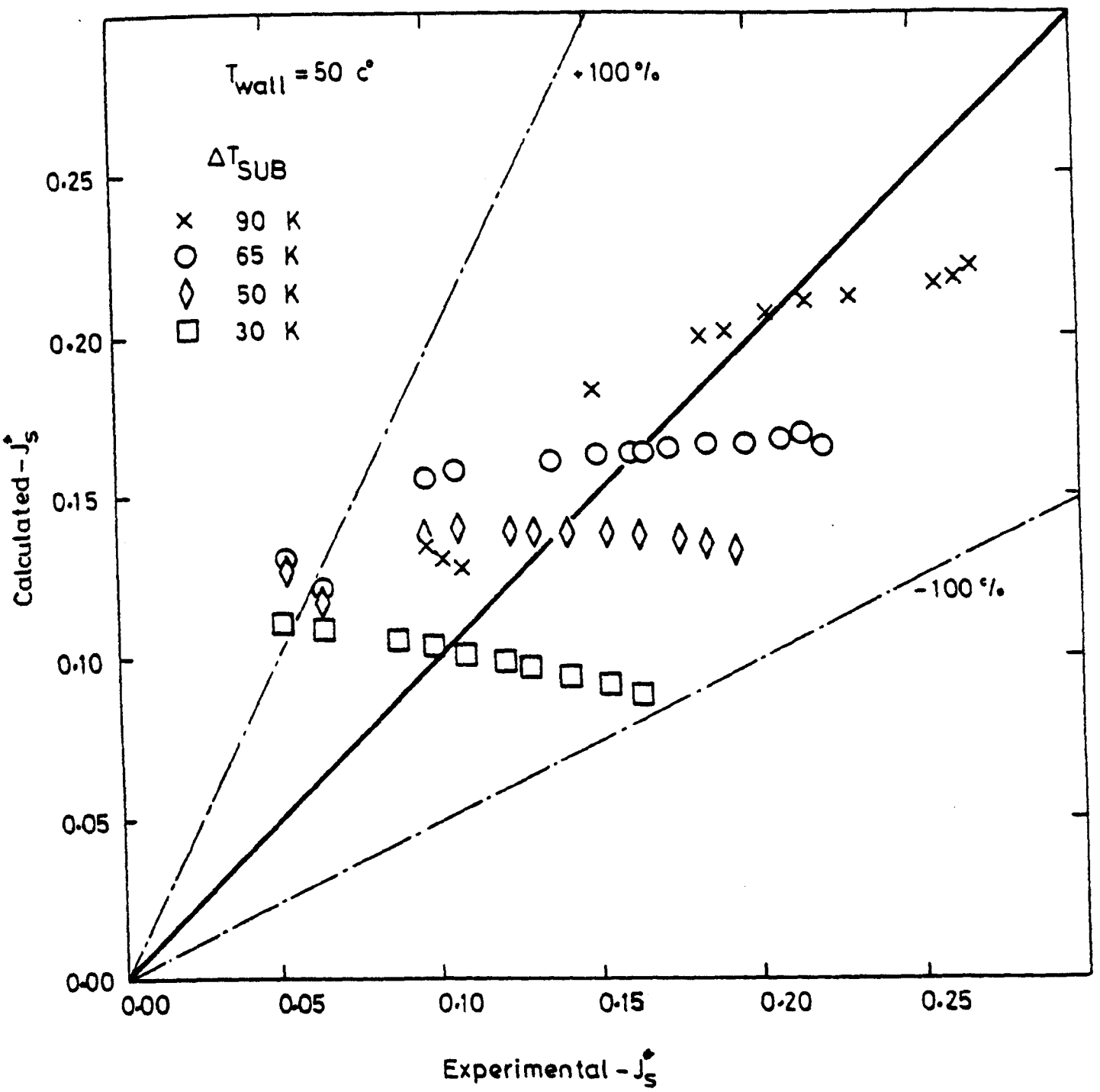

Fig 6.30 Comparison Between Experiment And Predicted Values Using BCL Correlation (39)

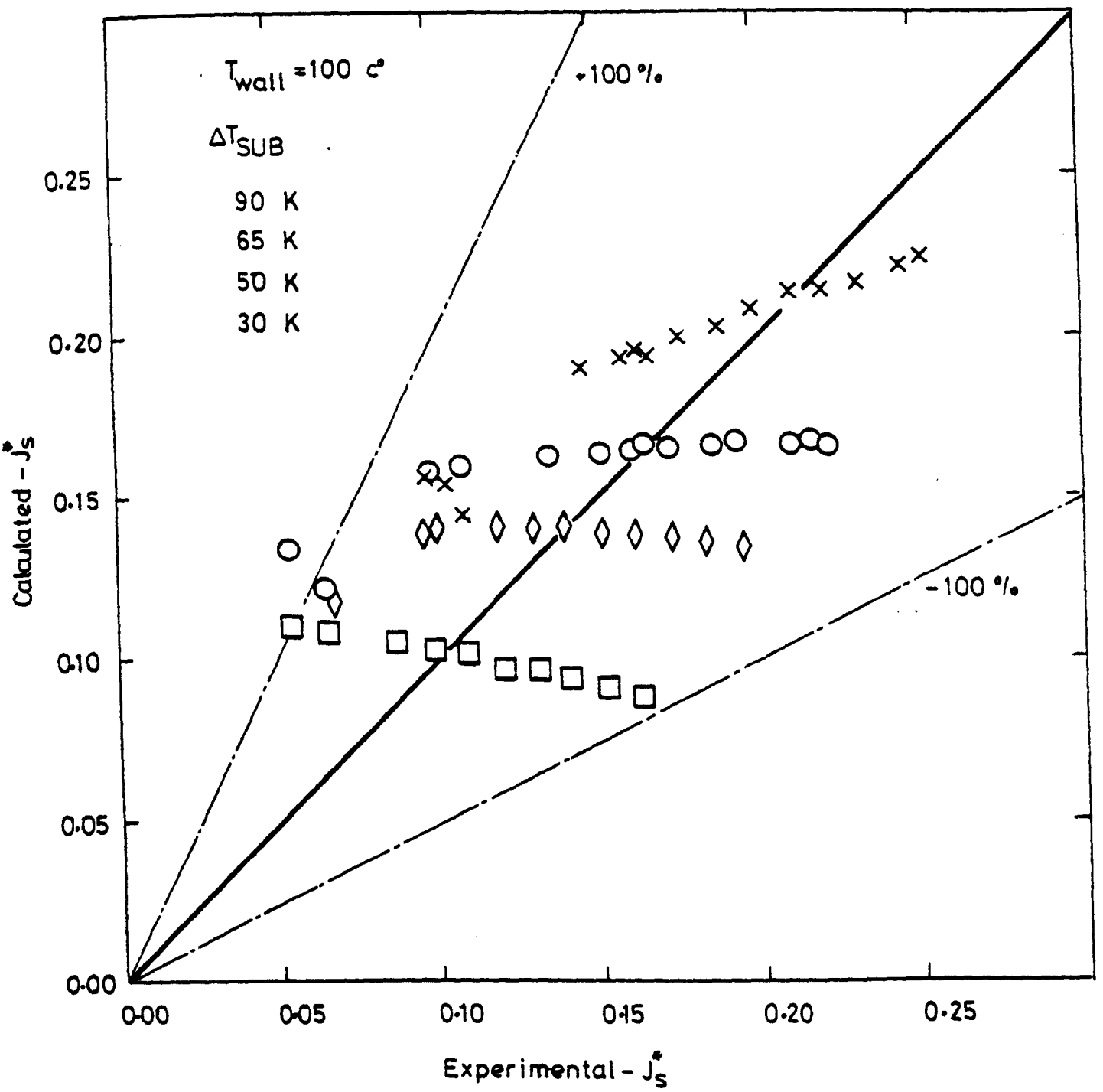

Fig 6.31 Comparison Between Experiment And Predicted Values Using BCL Correlation (39)

CHAPTER 7

CONCLUSIONS AND RECOMMENDATIONS

CHAPTER 7: CONCLUSIONS AND RECOMMENDATIONS

7.1 CONCLUSIONS

(i) An experimental and theoretical programme of work has been carried out for the countercurrent flow of air/water in two 1/10 - scaled PWR planar test sections, namely Phase 1 and Phase 2 Test Sections.

(ii) The experimental observations revealed that the flow regimes in the Phase 1 test series were characterised by air flowing between two waterfalls and in the Phase 2 Tests by annular countercurrent flow, i.e. water film on the downcomer wall.

(iii) The Phase 1 air-water test data were correlated by the expression

$$J_A^{*\frac{1}{2}} + 1.26\, J_{w_i}^{*\frac{1}{2}} = 0.43 \qquad (4.4)$$

for the inception of bypass. Equation (4.4) was also found to correlate the partial penetration data if $J^*_{w_i}$ was replaced by $J^*_{w_{LP}}$

(iv) The corresponding data relating to the inception of bypass for the Phase 2 test series were correlated using the equation

$$J_A^{*\frac{1}{2}} + 0.484\, J_{w_i}^{*\frac{1}{2}} = 0.349 \qquad (4.6)$$

(v) The effect of mode of injection on flooding was established by comparing "air first" and "water first". The data for the two cases was almost identical, i.e. the mode of injection had no effect on bypass characteristcs.

(vi) The effect of the angle of water injection into the test section was examined by comparing the Phase 1 and Phase 2 test series. The Phase 2 data was found to give better penetration characteristics from a LOCA point of view.

(vii) The comparison between the present data and the theoretical work in the literature indicated that none of the correlations gave satisfactory predictions.

(viii) The data supported the experimental findings in Creare regarding the condition for complete bypass which could be approximated to

$$J_A^{*\frac{1}{2}} \simeq 0.4$$

(ix) A comparison between the present air/water data and Campbell's steam/water data revealed that the bypass characteristics for the two cases were completely different. This was attributed to condensation effects which were found to play a stabi-

lising role on the bypass characteristics as far as a LOCA is concerned.

(x) The non-equilibrium effects existing during countercurrent steam/water situations were isolated and were found to depend on the water flowrate, the degree of inlet subcooling and the downcomer wall temperature.

(xi) A simple theoretical model was presented for countercurrent steam/water systems which yielded an expression for the non-equilibrium factor given by

$$K_{ne}=\left(\frac{1}{\left(1+\frac{hw}{h}\right)}-\frac{(hw/h)}{F\left(1+\frac{hw}{h}\right)^2}\right)\left(1-e^{-\alpha L}\right)+\frac{(hw/h)\,\alpha L}{F\left(1+\frac{hw}{h}\right)^2} \qquad (6.107)$$

This was shown to give superior representation of the data to the predictions of a recent BCL empirical correlation

(xii) The experimental work in the Phase 1 tests also gave rise to a theoretical study which provided a satisfactory explanation of a collapse of the pair of waterfalls when air flowed between them.

7.2 RECOMMENDATION

7.2.1 Application To Reactor System

The condensation model and associated work presented in this thesis can be used to determine the upward steam flow in the annulus which is necessary for the inception of bypass provided the following information is known.

(i) Inlet water flowrate (ECC flow) and temperature.

(ii) Steam pressure and temperature (from history of depressurisation).

(iii) Downcomer wall temperature (from history of depressurisation).

(iv) Bypass (or flodding) characteristic in absence of condensation, e.g. Equation (6.75).

The procedure is as follows:

(a) Evaluate the mass flowrate of steam $M_{s_{nc}}$ necessary to start bypass in the absence of condensation - from equation (6.75).

(b) Evaluate Ja, Re, Pr, D_e from the known information using Equations (6.66), (6.112), (6.113), and (6.114).

(c) Estimate h_w and h using equation (6.110) and (6.117) or (6.120).

(d) Evaluate K_{ne} from Equation (6.107).

(e) Determine the steam condensation rate M_{s_c} using Equation (6.69).

(f) The upward steam flowrate M_s in the annulus which is necessary for the inception of bypass is then given by $$M_s = M_{s_{nc}} + M_{s_c}$$

7.2.2 Recommendations For Future Work

Future work should include studies of:

(i) Further scaled PWR geometries (larger and smaller, if possible).

(ii) The characteristic dimension to be used in Wallis correlation - by using different geometries and varying the physical dimensions of the model i.e. gap size, downcomer circumference and downcomer length.

(iii) Better simulations of PWR geometries including hot leg projections through the annulus and a scaled lower plenum.

(iv) The effect of impinging jets on liquid film thickness.

(v) The effect of impinging jets over hot walls on the wall/film heat transfer coefficient.

(vi) A more controlled range of liquid subcoolings, particularly at low ΔT_{sub} values.

(vii) Experimental work to isolate the interfacial heat transfer coefficient.

(viii) The effects of air inlet pressure loss and shear stress on the water wall for the Phase 1 geometry theory; also the possible effects of water droplet entrainment in the air at entry to the test section.

REFERENCES

REFERENCES

1. SCHUTT, J.B.

"A Theoretical Study of the Phenomenon of Bridging in Wetted Wall Columns", Ph.D. Thesis, University of Rochester, New York (1959)

2. CETINBUDAKLAR, A.G. and JAMESON, G.J.

"The Mechanism of Flooding in Vertical Counter-Current Two-Phase Flow", Chem. Eng. Sci., Vol 24, pp 1669 (1969)

3. CLIFT, R., RITCHARD, C.L. and NEDDERMAN, R.M.

"The Effect of Viscosity on the Flooding Conditions in Wetted Wall Columns", Chem. Eng. Sci., Vol 21, pp 87 (1966)

4. SHEARER, C.J. and DAVIDSON, J.F.

"The investigation of Standing Wave Due to Gas Blowing Upward over a Liquid Film; Its Relations to Flooding in Wetted Wall Columns", J. Fluid Mech., Vol 22, Part 2, pp 321 (1965)

5. UEDA, T. and SUZUKI, S.

"Behaviour of Liquid Films and Flooding in Counter-Current Two-Phase Flow - Part 2 : Flow in Annuli and Rod Bundles", Int. J. Multiphase Flow, Vol 4, pp 157, (1978)

6. DUKLER, A.E., CHOPRA, A., MOALIAM MARON, D. and SEMIAT,R.

"Two-Phase Interaction in Counter-Current Flow",

Annual Report, Univ. Houston, Texas, Dept. Chem. Eng. (Dec. 1978)

7. GROLMES, M.A., LAMBERT, G.A. and FAUSKE, H.K.

"Flooding in Vertical Tubes", Inst. Chem. Engrs., Symposium on Multiphase Flow Systems, Ser. 38, Part I, Paper A4, (1974)

8. TOBILEVICH, N.Yu., SAGAN, I.I. and PORZHEZINSKII, YU.G. Translated from Inzhenesno-Fizicheskii Zhurnal, Vol. 15, 855-861 (1968)

9. WALLIS, G.B. and KUO, J.T.

"The Behaviour of Gas-Liquid Interfaces in Vertical Tubes", Int. J. Multiphase Flow, Vol 2, pp521 (1976)

10. BANKOFF, S.G.

"Entrapment of Gas in the Spreading of Liquid over a Rough Surface", AIChE Journal, Vol 4, pp 24 (1958)

11. KUTATELADZE, S.S.

"Elements of the Hydrodynamics of Gas-Liquid Systems", Fluid Mech. Soviet Research, Vol 1, No. 4, pp29-50 (1972)

12. WALLIS, G.B.

"One Dimensional Two-Phase Flow", McGraw Hill Book Co., New York (1969)

13. WALLIS, G.B.

"Annular Two-Phase Flow - Part 1, Simple Theory", J. Basic Engineering, pp 59-72 (March 1970)

14. WALLIS, G.B.,

"Annular Two-Phase Flow - Part 2, Additional Effects", J. Basic Engineering, pp73-82 (March 1970)

15. WALLIS, G.B. and MAKKENCHERY, S.

"The Hanging Film Phenomenon in Vertical Annular Two-Phase Flow", J. Fluid Engineering, pp 297 (1974)

16. IMURA, H., KUSUDA, H and FUNATSU, S.

"Flooding Velocity in a Counter-Current Annular Two-Phase Flow", Chemical Engineering Science, Vol. 32, pp 79-87 (1977)

17. CHUNG, K.S.

"Flooding Phenomenon in Counter-Current Two-Phase Flow Systems", Ph.D. Thesis, University of California, Berkeley, 1978

18. TIEN,C.L., CHUNG, K.S. and LIU, C.P.

"Flooding in Two-Phase Counter-Current Flows", EPRI No. 1283, Topical Report (Dec. 1979)

19. DUKLER, A.E. and SMITH, L.

"Two-Phase Interactions in Counter-Current Flow - Studies of the Flooding Mechanism", Summary Report No. 2, USNRC, Contract AT(49-24)0194 (Dec. 1977)

20. HINZE, J.O.

"Fundamentals of the Hydro-dynamic Mechanism of Splitting in Dispersion Process", AIChE J., Vol 1, pp289 (1955)

21. TIEN, C.L.

"A Simple Analytical Model for Counter-Current Flow Limiting Phenomena with Vapour Condensation", Letter in Heat and Mass Transfer, Vol 4, pp 231 (1977)

22. LIU, J.S.K., COLLIER, R.A. and CUDNIK, R.A.

"Flooding of Counter-Current Steam-Water Flow in an Annulus", ASME Meeting, San Francisco, California, 10-15 December 1978.

23. AKERS, W.W. and ROSSON, H.F.

"Condensation Inside a Horizontal Tube", Chemical Engineering Progress Symposium Serios, No. 30, Vol 56 (1960)

24. WALLIS., G.B., BLOCK, J.A. and CROWLEY, C.J.

"Flow Regimes in a Simulated PWR Downcomer Annulus", AEC Report COO-2294-1, January 1974

25. CROWLEY, C.J., WALLIS, G.B. and LUDWIG, D.L.

"Steam/Water Interaction in a Scaled Pressurized Water Reactor Downcomer Annulus", AEC Report COO-2294-4, September 1974.

26. BLOCK, J.A. and CROWLEY, C.J.

"Effect of Steam Upflow and Superheated Walls on ECC Delivery in a Simulated Multiloop PWR Geometry", Creare Quarterly Progress Report TN-210. May 1975.

27. BLOCK, J.A., ROTHE, P.H., FANNING, M.W., CROWLEY, C.J. and WALLIS, G.B.

"Analysis of ECC Delivery", Creare Topical Report TN-231, April 1976.

28. CROWLEY, C.J., BLOCK, J.A. and ROTHE, P.H.

"An Evaluation of ECC Penetration Data Using Two Scaling Parameters", Creare Topical Report TN-233, September 1976.

29. CUDNIK, R.A., FLANIGAN, L.J., CARBIENER, W.A., WOOTON, R.O. and DENNING, R.S.

"Penetration Behaviour in a 1/15 Scale Model of a Four-Loop Pressurized Water Reactor", BCL Topical Report, BMI-NUREG - 1973, June 1977

30. ROTHE, P.H. and CROWLEY, C.J.

"Scaling of Pressure and Sub-Cooling for Counter-Current Flow", Creare Quarterly Progress Report, TN-285, October 1978

31. ALB, G.P. and CHAMBRE, L.

"Correlations for the Penetration of ECC Water in a Model of a PWR Downcomer Annulus", Nuclear Engineering and Design, Vol 53, pp 237-248 (1979)

32. RICHTER, H.J. and MURPHY, S.L.

"Effect of Scale in Two-Phase Counter-Current Flow Flooding in Annuli", Final Report, NUREG/CR-0822, May 1979

33. RICHTER, H.J. and WALLIS, G.B.

"ECC Bypass Scaling", NUREG/CR-0850, June 1979

34. RICHTER, H.J.

"Flooding in Tubes and Annuli", Permagon Press, MF-25, 1981

35. CAMPBELL, T.

"Nuclear Reactor Safety - PWR Refill Studies", Ph.D. Thesis, University of Strathclyde, Glasgow, U.K. (1979)

36. SIMPSON, H.C., ROONEY, D.H. and CAMPBELL, T.

"Some Experimental and Theoretical Aspects of

PWR Refill", Paper E1, European Two-Phase Flow Group Meeting, Stockholm, May 1978.

37. MARKLAND, E.

"Calculations of Flow at A Free Overfall by Relaxation Method", Proc. Inst. Civil Engrs., Vol 31, 71-78 (1965)

38. BANKOFF, S.G.

"Some Condensation Studies Pertinent to LWR Safety", Pergamon Press, MF 237, 1979.

39. COLLIER, R.P., FLANIGAN, L.J., BISHOP, T.A. and LIU, S.K.

"Status Report on ECC Penetration Scaling Research", NUREG/CR-0651, BMI-2019, February 1979

40. MAYHEW, Y.R. and ROGERS, G.F.C.

"Thermodynamics and Transport Properties of Fluids - SI Units", Second Edition, Oxford, Basil Blackwell, 1976.

41. WALLIS, G.B., de SIEYES, D.C., ROSSELLI, R.J., and LACOMBE, J

"Counter Current Annular Flow Regimes for Steam and Subcooled Water in a Vertical Tube", EPRI NP - 1336. Topical Report, January 1980.

42. FULFORD, G.D.

"The Flow of Liquids in Thin Films", Advances in Chem. Eng., Vol. 5, pp 151 -236, 1964

43. SOLOV'EV. A.V., PREOBRAZHENSKII, E.I., and SEMENOV, P.A.

"Hydraulic Resistance in Two-Phase Flow", International Chemical Engineering, Vol. 7, N° 1, pp 59-63, January 1967.

ACKNOWLEDGEMENT

ACKNOWLEDGEMENT

The author wishes to express his sincere gratitude to the following people:

Professor H.C. Simpson, BSc, SM, ScD, FIMechE, FInstP, FRSE, Dean of School of Mechanical and Chemical Engineering and Naval Architecture, for his helpful criticisms, suggestions and collaboration in this investigation.

Dr. D.H. Rooney, BSc, ARCST, PhD, CEng, FIMechE, MIED, who supervised the project and to whom the author is greatly indebted for his invaluable help and guidance throughout the research.

The staff of the Heat Engines Laboratory for their help in the construction of the experimental rig.

Miss Jeanette Smith, who typed the final version of this thesis.

The author also gratefully acknowledges the financial and other assistance received from the U.K. Nuclear Installations Inspectorate.

APPENDICES

APPENDIX A

CALIBRATION OF ORIFICE PLATE FOR AIR FLOWRATE MEASUREMENTS

APPENDIX A

CALIBRATION OF ORIFICE PLATE FOR AIR FLOWRATE MEASUREMENTS

The orifice plate was designed, manufactured, constructed and calibrated in accordance with British Standards BS1042-Part I, 1964.

The mean diameter was calculated using six diameter measurements taken on a NIKON Profile Projector at x50 MAG. The diameter measurements were as follows:

Degree	Diameters, mm
0	41.351
30	41.353
60	41.338
90	41.342
120	41.343
150	41.357

The mean diamter, d, = 41.347mm (1.6278 inches).

Referring to BS 1042, the following results were derived on the basis of the 50.8mm (2 inch) diameter air pipeline:

$d/D = 0.814$

$m = (d/D)^2 = 0.6625$

$m^2 = 0.4389$

$E = 1/(1 - m^2)^{\frac{1}{2}} = 1.335$

From Figure 38-a, Page 120, in BS 1042, C = 0.6117

From Figure 38-c, Page 121 for Case B (steel, cold drawn), $Z_D = 1.014$

From Appendix A, Page 159

$$W = 3.478 \times 10^{-6} CZ \epsilon E d^2 \sqrt{h\rho} \quad kg/s \qquad (A-1)$$

$$R_d = \frac{4000}{\pi} W/\mu d \qquad (A-2)$$

where

$Z = Z_D \cdot Z_{RD}$ = correction factor

W = mass flowrate, kg/s

μ = dynamic viscosity, kg/m.s

ρ = density of air, kg/m^3

h = head drop across the orofice, mm H_2O

R_d = Reynold's number

d = mean diameter of orifice, mm

For dry air

$$\frac{P \times 100}{\rho T} = 0.287 \quad kJ/kgK \qquad (A-3)$$

where

P = absolute pressure upstream of orifice, bars

T = absolute temperature, K

From (A-3)

$$\rho = 348.43205 \frac{P}{T} \qquad (A-4)$$

From (A-1), (A-4) and using the values of d,c, and Z_d calculated above, we get

$$W = 0.0919 \times Z_{RD} \times \epsilon \times \sqrt{\frac{hP}{T}} \quad kg/s \qquad (A-5)$$

also equation (A-2) can be written as

$$Rd = 30.794\ W/\mu \qquad (A-6)$$

From Figure 38-b, Page 120, the following values can be obtained

Rd	Z_{RD}
500,000	1.006
200,000	1.014
100,000	1.021
50,000	1.029

The above values were curve fitted using an ICL-1904S computer to give

$$Z_{RD} = 1.2061 - 0.02138\ (\ell nRd) + 0.000462\ (\ell nRd)^2 \qquad (A-7)$$

From Figure 39, Page 122 , taking $\gamma = 1.4$ and $m = 0.6625$, the following values were obtained:

ϵ	h/P mm/bara
1.000	0.0
0.986	368.3
0.971	736.6
0.957	1104.9
0.942	1473.2

ϵ	h/P mm/bara
0.928	1841.5
0.914	2209.8

The above values were also curve fitted to give

$$\epsilon = 1.0 - 0.0000393\ (h/P) \qquad \text{(A-8)}$$

From Thermodynamics and Transport Properties of Fluids by Mayhew and Rogers, 1972, the values of μ for air were obtained as:

T (K)	$\mu \times 10^5$ kg/m.s
275	1.725
300	1.846
325	1.962
350	2.075
375	2.181

$$\mu \times 10^5 = 0.4745 + 0.004568\ T \qquad \text{(A-9)}$$

How the Equations Were Used

The following steps were carried out:

1. The values of Z_{RD} were assumed to be equal to unity and ϵ calculated from equation (A-8)
2. Using Equation (A-5), the mass flowrate was calculated using measured values of h, P and T.
3. Reynold's number was calculated from equation (A-6) combined with equation (A-9) and the uncorrected value of the mass flowrate.
4. Z_{RD} was calculated from equation (A-7).

5. The correct value of mass flowrate was calculated using equation (A-5) with proper value of Z_{RD}.

Equations (A-5), (A-7), (A-8) and (A-9) are shown on the following graphs.

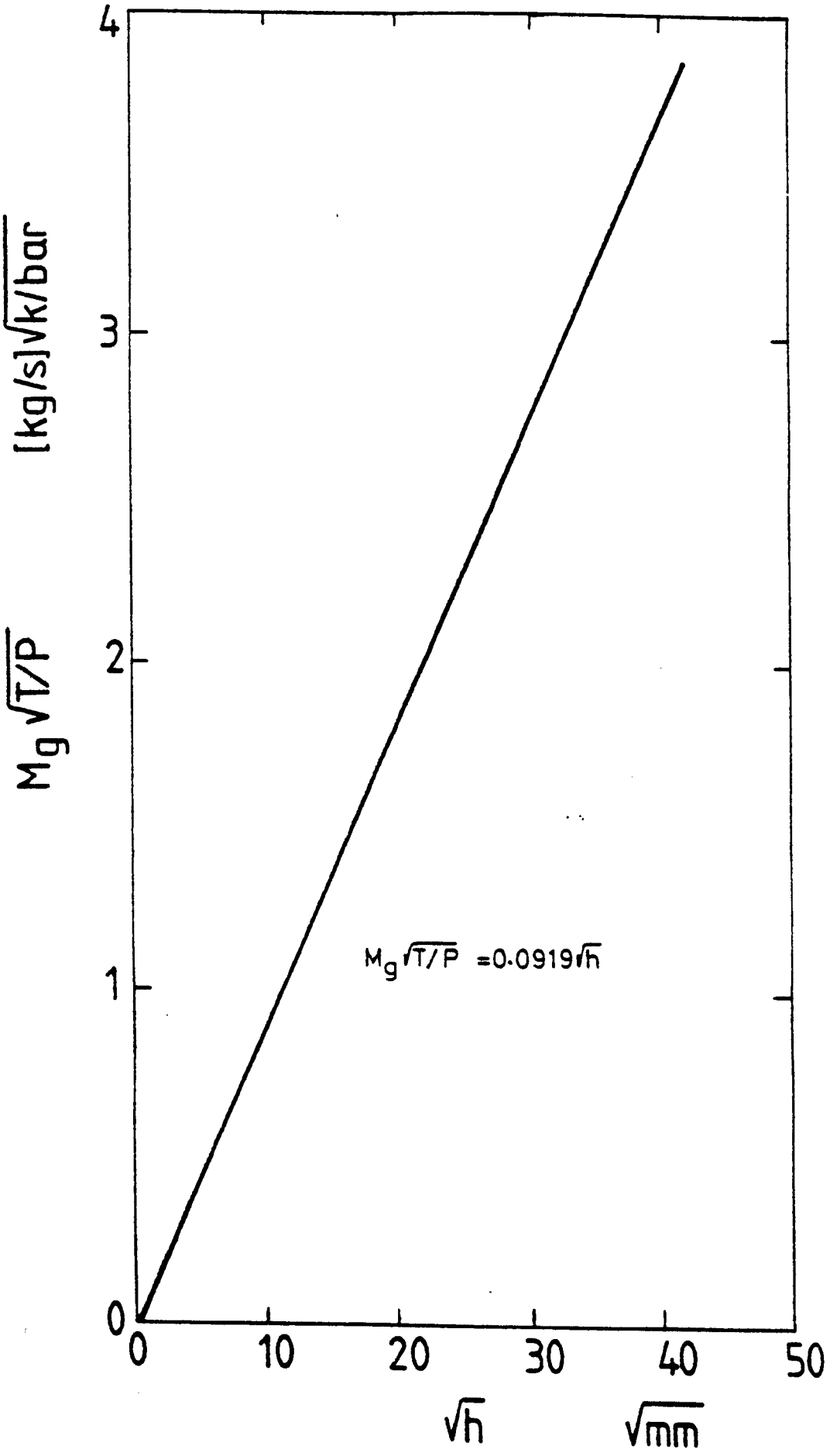

Fig A-1 Characteristics Of Air Flow Orifice [BS 1042]

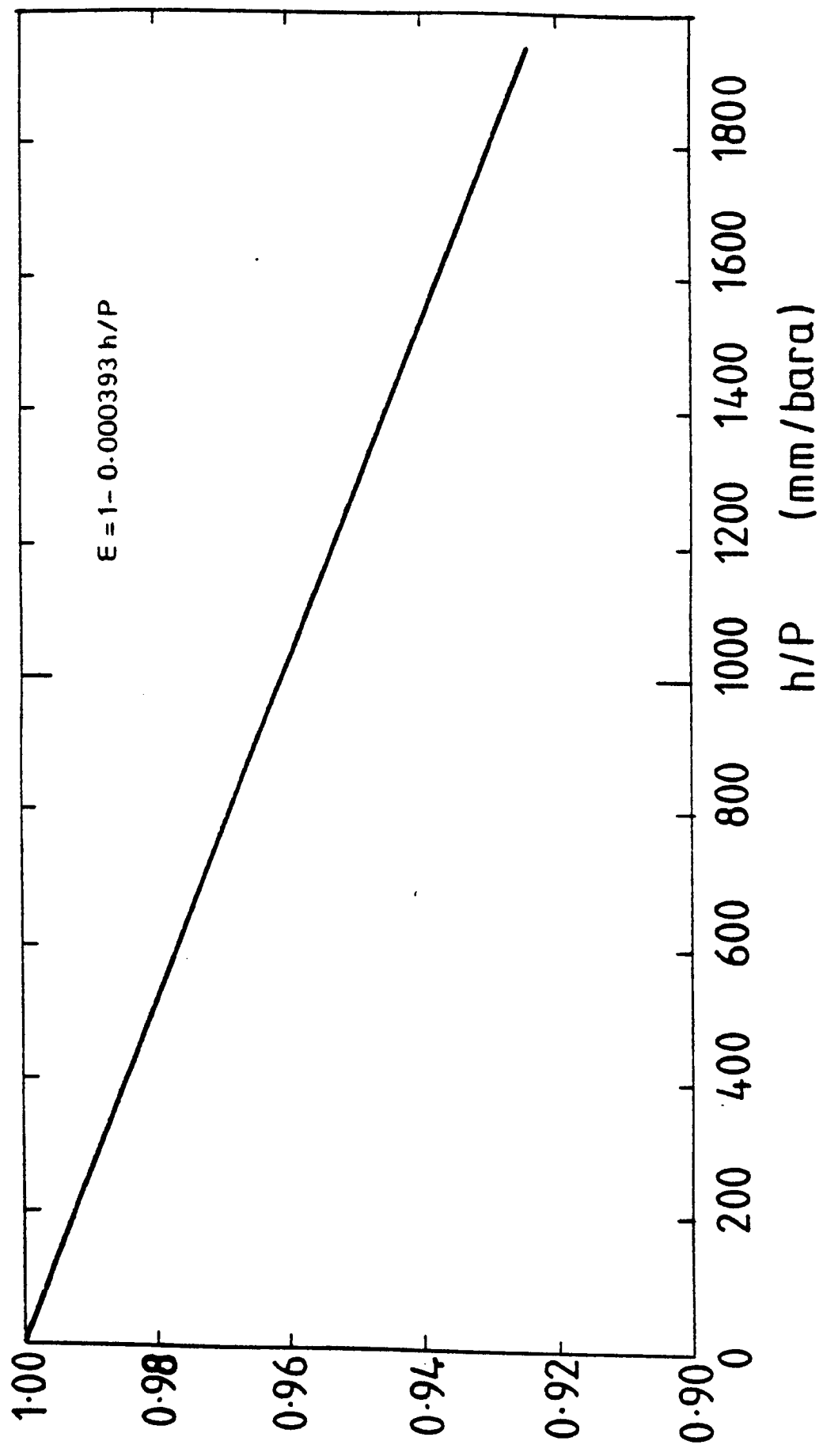

Fig A-2 Variation Of ε With h/P

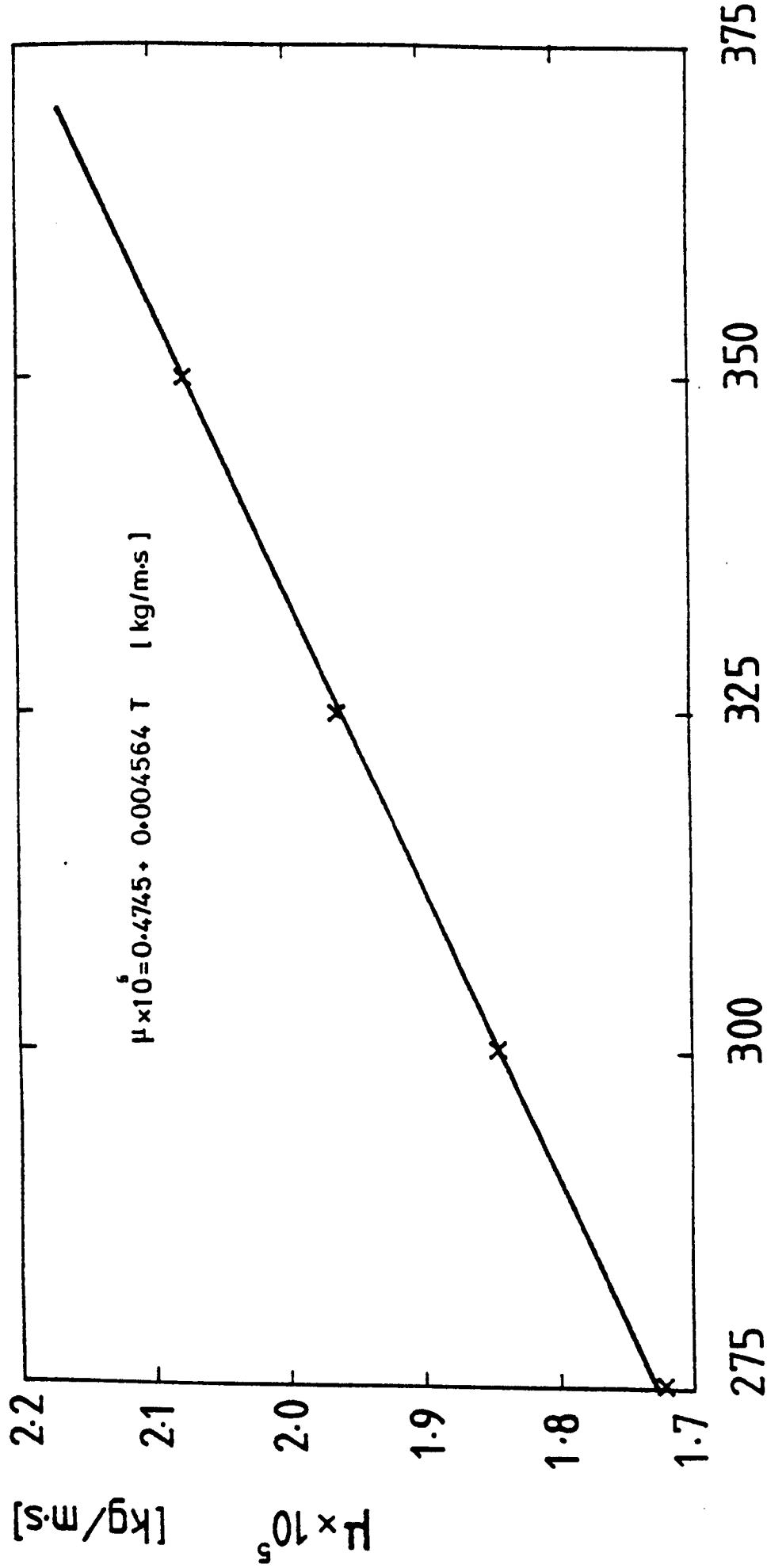

Fig A-3 Variation Of Air Dynamic Visosity With Temperature

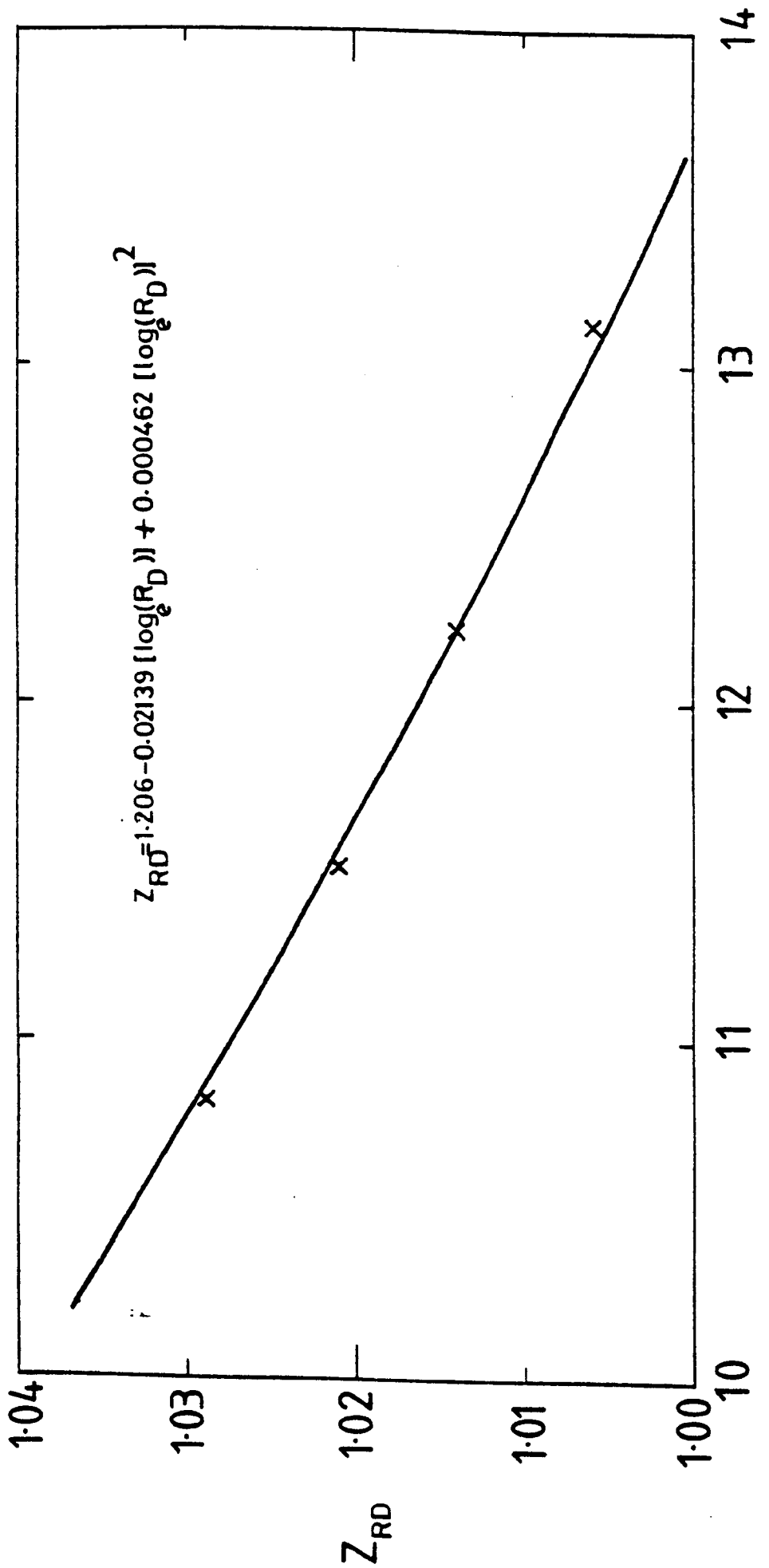

Fig A-4 Variation Of Z_{RD} With Reynolds Number, R_D

APPENDIX B

CALIBRATION OF ROTAMETERS FOR AIR FLOWRATE MEASUREMENTS

APPENDIX B

CALIBRATION OF ROTAMETERS FOR AIR FLOWRATE MEASUREMENTS

The rotameters used for air flowrate measurements were calibrated in accordance with "Calibration Data for 'Metric' Series Rotameters", provided by Rotameter Manufacturing Company. The rotameters have the following characteristics:

Tube size 47

Duralumin Float (Metric type A)

INSTRUCTIONS

1. Symbols and Units

ω = weight of float in grams

σ = mean density of float in g/cm^3

ρ = density of fluid at working temperature and pressure in g/cm^3

ν = kinematic viscosity of fluid at working conditions in Stokes

F_T = "theoretical" capacity in liters/min (based on no change in Reynold's number)

F = actual flow in liters/min at any selected reading

$f = \frac{F}{F_T}$

K_1, K_2 are instrument constants which vary with tube sizes, and are given.

2. Formulae

$$I = \log \left[K_1 \times \nu \times \sqrt{\frac{\sigma \times \rho}{\omega (\sigma - \rho)}} \times 10^4 \right] \quad \text{(B-1)}$$

$$F_T = K_2 \times \sqrt{\frac{\omega (\sigma - \rho)}{\sigma \times \rho}} \quad \text{(B-2)}$$

3. Evaluation

From the appropriate tables in Calibration Data for "Metric" Series Rotameters":

ω = 62.15 grams

σ = 2.80 grams/cm^3

K_1 = 2.30

K_2 = 4.355

From Air Tables, the properties of air at standard conditions are

ρ = 1.2505 x 10^{-3} grams/cm^3

ν = 0.1430 cm^2/sec

From (B-1),

I = 1.169

From (B-2),

F_T = 970.67

$$F = 970.67 \times f \text{ liters/min} \quad \text{(B-3)}$$

From the dynamic characteristics of metric series

rotameters size 47, combined with equation (B-3), the following table was constructed:

TABLE B-1

Calibration of Rotameters

(P = 1 bar and T = 288K)

Scale Reading, cm	Flowrate, Lit/min
0.125	97.067
3.500	194.134
6.688	291.201
9.625	388.268
12.563	485.335
15.375	582.402
18.125	679.469
20.750	776.536
23.188	873.603
25.563	970.670

The results tabulated above are also plotted in Figure B-1 together with the calibration curve provided by the manufacturers. It is clear that the manufacturer's calibration curve would give higher flowrate than that calculated from the charts. The two curves will coincide if K_2 is multiplied by a factor of 1.03, i.e., K_2 should be taken as 4.486 instead of 4.355.

In the working range the change in absolute

temperature is very small, i.e., T ≃ constant and μ = constant, also $\sigma \gg \delta$. This will reduce equation (B-1) to

$$I = \log(K_3/\sqrt{\rho}) \qquad \text{(B-4)}$$

where

$$K_3 = \frac{K_1 \times \mu \times 10^4}{\sqrt{\omega}} \qquad \text{(B-5)}$$

at $T = T_o$ and $P = P_o$

$$I_o = \log (K_3/\sqrt{\rho_o}) \qquad \text{(B-6)}$$

at $T = T_1$ and $P = P_1$

$$I_1 = \log(K_3/\sqrt{\rho_1}) \qquad \text{(B-7)}$$

From (B-6) and (B-7) we get:

$$I_1 = I_o - \frac{1}{2} \log \left(\frac{\rho_1}{\rho_o}\right) \qquad \text{(B-8)}$$

or

$$I_1 = I_o - \frac{1}{2} \log \left(\frac{P_1}{P_o}\right) \qquad \text{(B-9)}$$

For small changes in pressure, I can be taken as constant since the working pressure ranged from 0.8 to 1.2 bars the calibration curve was calculated at 1.0 bar using the same method as above. The results were curve fitted using an ICL-1904S computer to give

$$M_a = 10.422 + 3.032\ R_A + 0.026\ R_A^2 \quad \text{kg/h} \qquad \text{(B-10)}$$

Equation (B-10) is shown on Figure B-2.

Very few tests were carried out at P = 0.5 bar. The calibration curve was

$$M_a = 8.676 + 2.685\ R_A + 0.019\ R_A^2 \quad kg/h \qquad (B\text{-}11)$$

Equation (B-11) is shown on Figure B-3.

To allow for small variation in pressure (P_o) in calculating the flowrate the following equation was deduced from equation (B-2):

$$M_{actual} = M_o \times \sqrt{\rho_1 / \rho_o} \qquad (B\text{-}12)$$

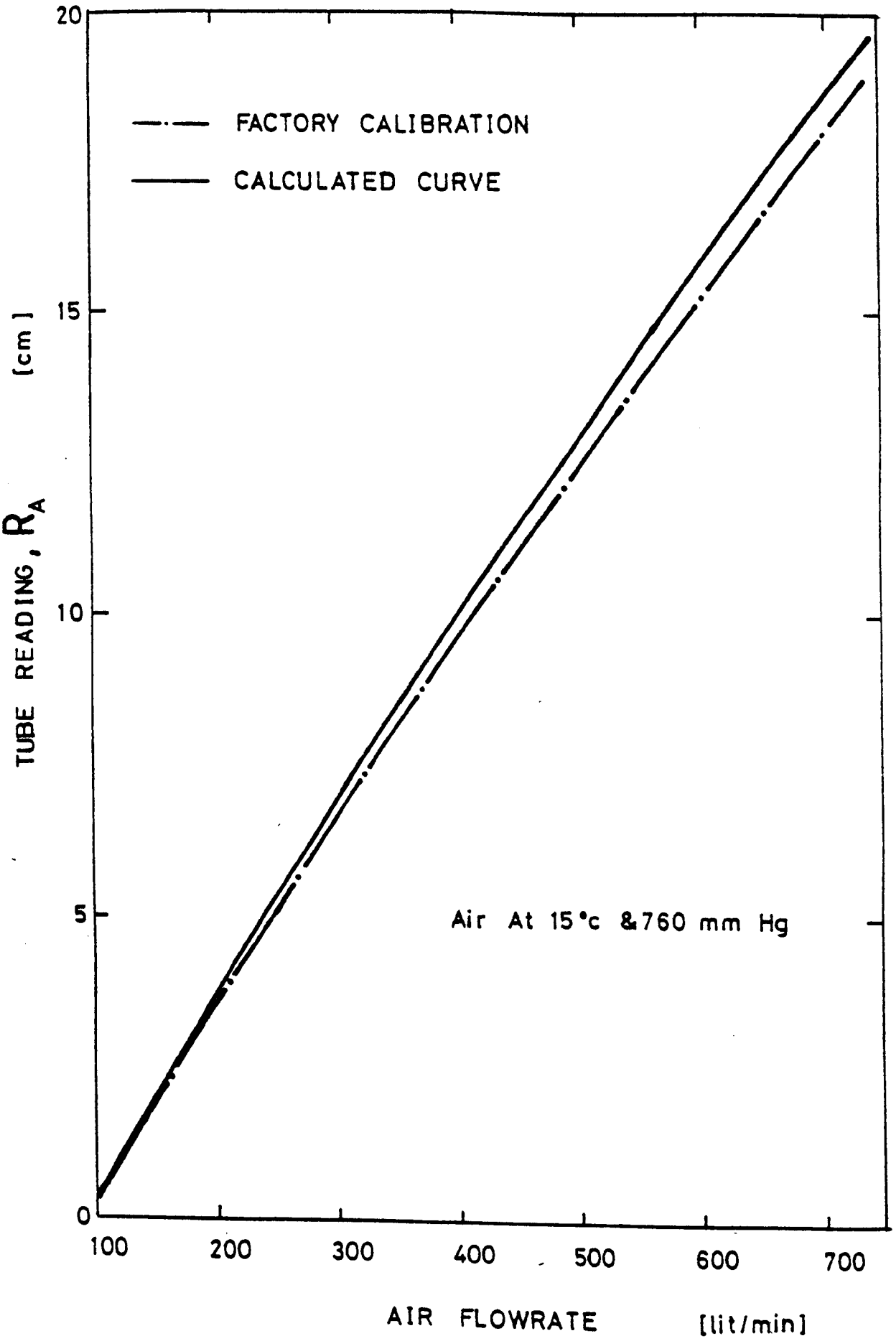

Fig B-1 Calibration Of The Rotameters

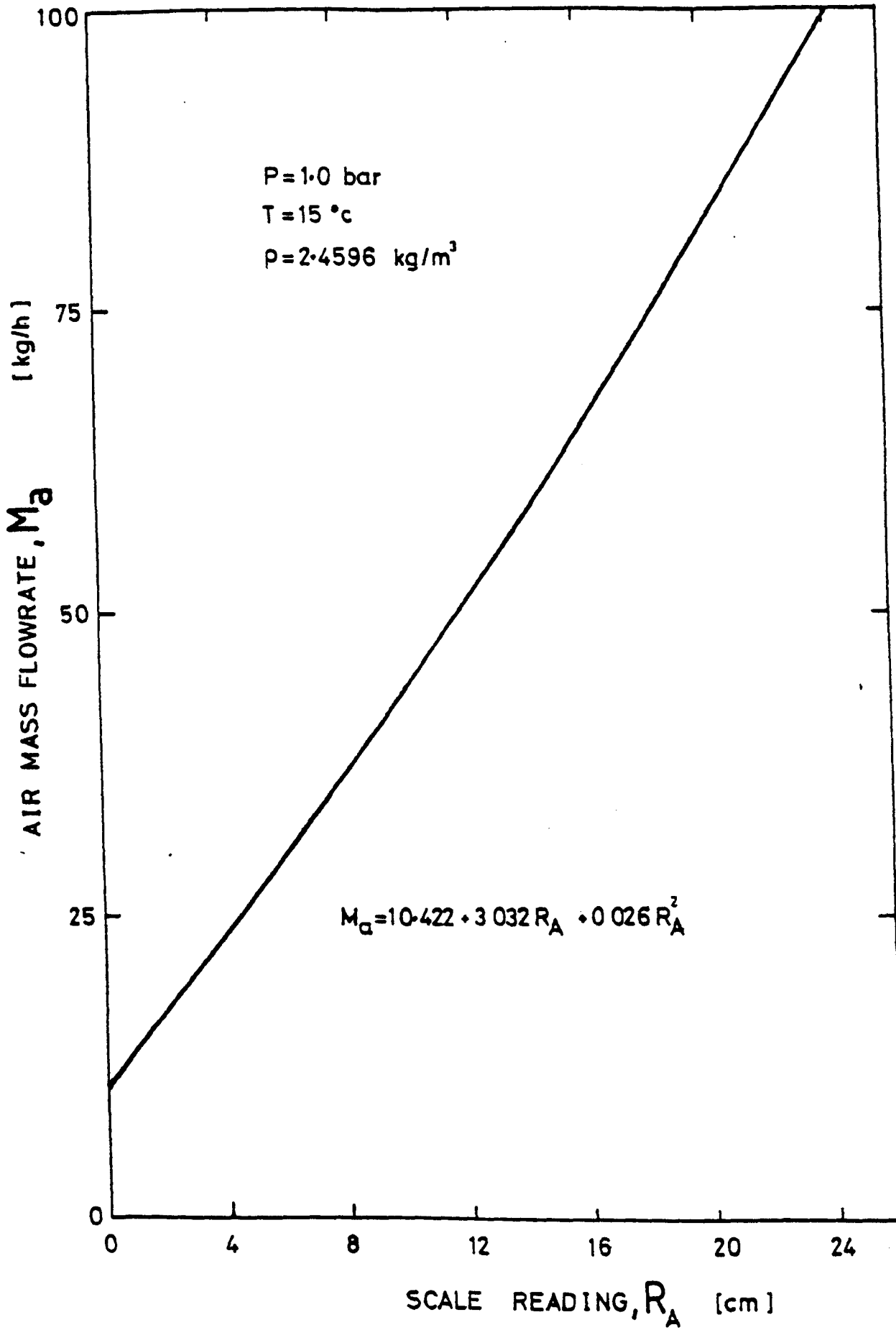

Fig B-2 Calibration Of The Rotameters

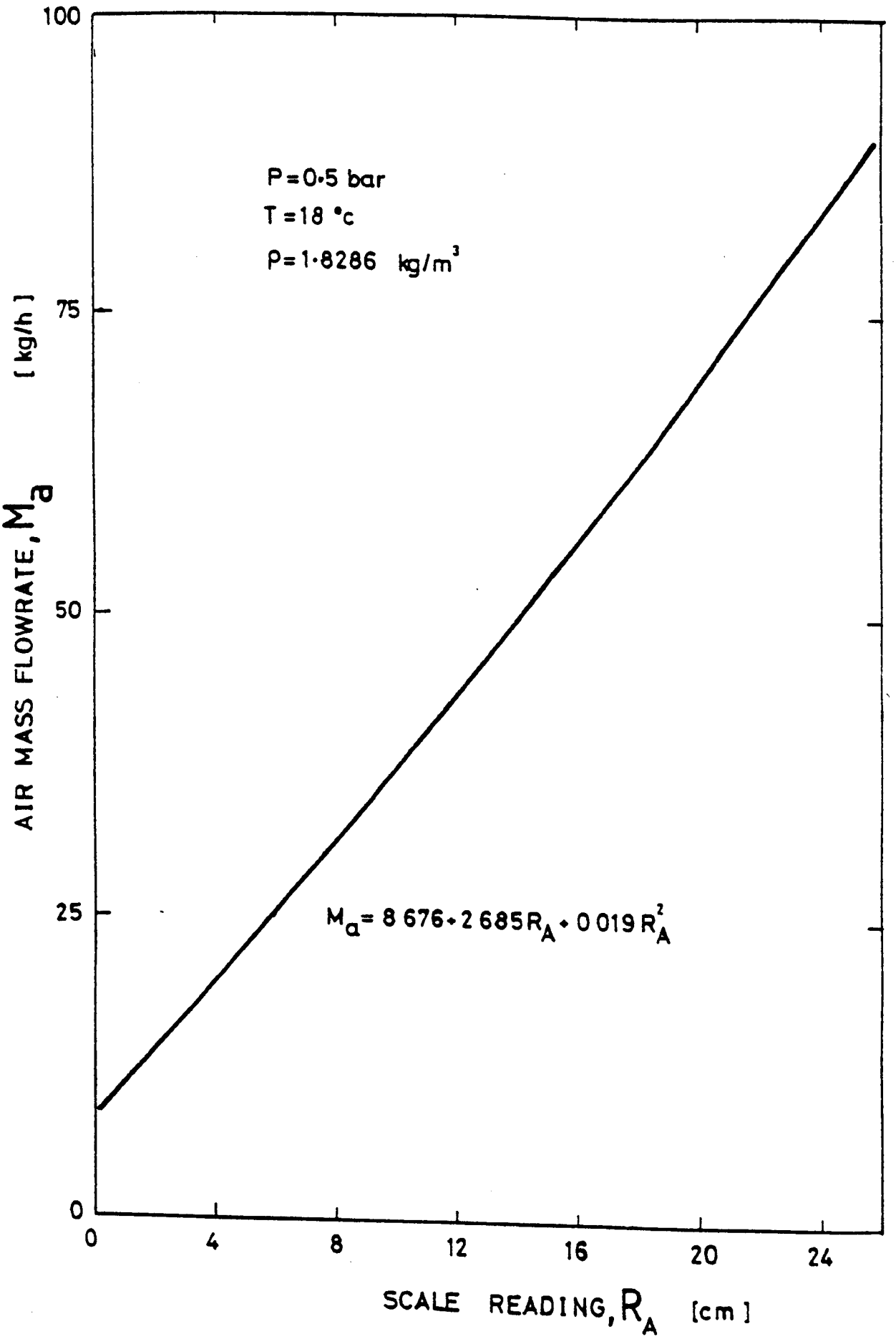

Fig B-3 Calibration Of The Rotameters

APPENDIX C

CALIBRATION OF TURBINE FLOWMETERS FOR WATER FLOWRATES

APPENDIX C

CALIBRATION OF TURBINE FLOWMETERS FOR WATER FLOWRATES

The turbine flowmeters, manufactured by Meter-Flow Ltd., were used in measuring the inlet water flowrate to the test sections. Due to space consideration, the meters were installed vertically, contrary to the manufacturer's recommendation. In situ calibration was carried out and compared with the manufacturer's calibration.

The calibration was carried out by allowing the water to flow into a tank mounted on a weighing machine. For each amount of water passed into the tank in a given time, the meter reading was recorded. This process was repeated three times for each meter reading and the mean taken to correspond to that particular reading. This procedure was repeated for a range of flowrates and the results were fed into a computer programme to find the best fitting curve.

The results of calibration before Phase 1 tests, which were checked after the end of Phase 1 test series, are shown in Tables C-1 and C-2. At the beginning of Phase 2 tests, the two meters were sent to the manufacturer for overhaul. On return to the laboratory, they were calibrated using the method mentioned above. The results of this calibration are tabulated in Tables C-3 and C-4. A graphical representation of all four calibrations is shown in Figures C-1, C-2, C-3 and C-4.

TABLE C-1

In-situ Calibration of Meter No. 18021/75

For Phase 1 Tests

Meter Reading R_{w1}%	Volume Flowrate - Q m^3/hr
10	1.775
20	3.711
30	5.377
40	7.089
50	8.709
60	10.474

The equation to give best fit was found to be:

$$Q = 0.0346 + 0.1736R_{w1} \quad m^3/hr$$

TABLE C-2

In-situ Calibration of Meter No. 18022/75

For Phase 1 Tests

Meter Reading R_{w2}%	Volume Flowrate - Q m^3/hr
10.0	1.664
20.0	3.320
30.0	4.941
40.0	6.533
50.0	8.403
60.0	10.411
70.0	12.477
74.5	13.608

The equation to give best fit was found to be:

$$Q = 0.09139 + 0.14475R_{w2} + 0.00046R_{w2}^2 \quad m^3/hr$$

TABLE C-3

In-situ Calibration of Meter No. 18021/75

For Phase 2 Tests

Meter Reading R_{w1} %	Volume Flowrate - Q m^3/hr
2	0.440
4	0.802
6	1.122
8	1.493
10	1.859
16	2.956
22	4.099
28	5.269
34	6.383
40	7.391
46	8.474
52	9.594
62	11.351

The equation to give best fit was found to be:

$$Q = 0.0488 + 0.1835\ R_{w1} \quad m^3/hr$$

TABLE C-4

In-situ Calibration of Meter No. 18022/75

For Phase 2 Tests

Meter Reading R_{w2}%	Volume Flowrate - Q m^3/hr
2	0.335
4	0.646
6	0.950
8	1.401
10	1.719
16	2.858
22	4.031
28	5.126
34	6.156
40	7.249
46	8.312
52	9.406
73.5	13.964

The equation to give best fit was found to be:

$$Q = -0.1255 + 0.1871\ R_{w2} \quad m^3/hr$$

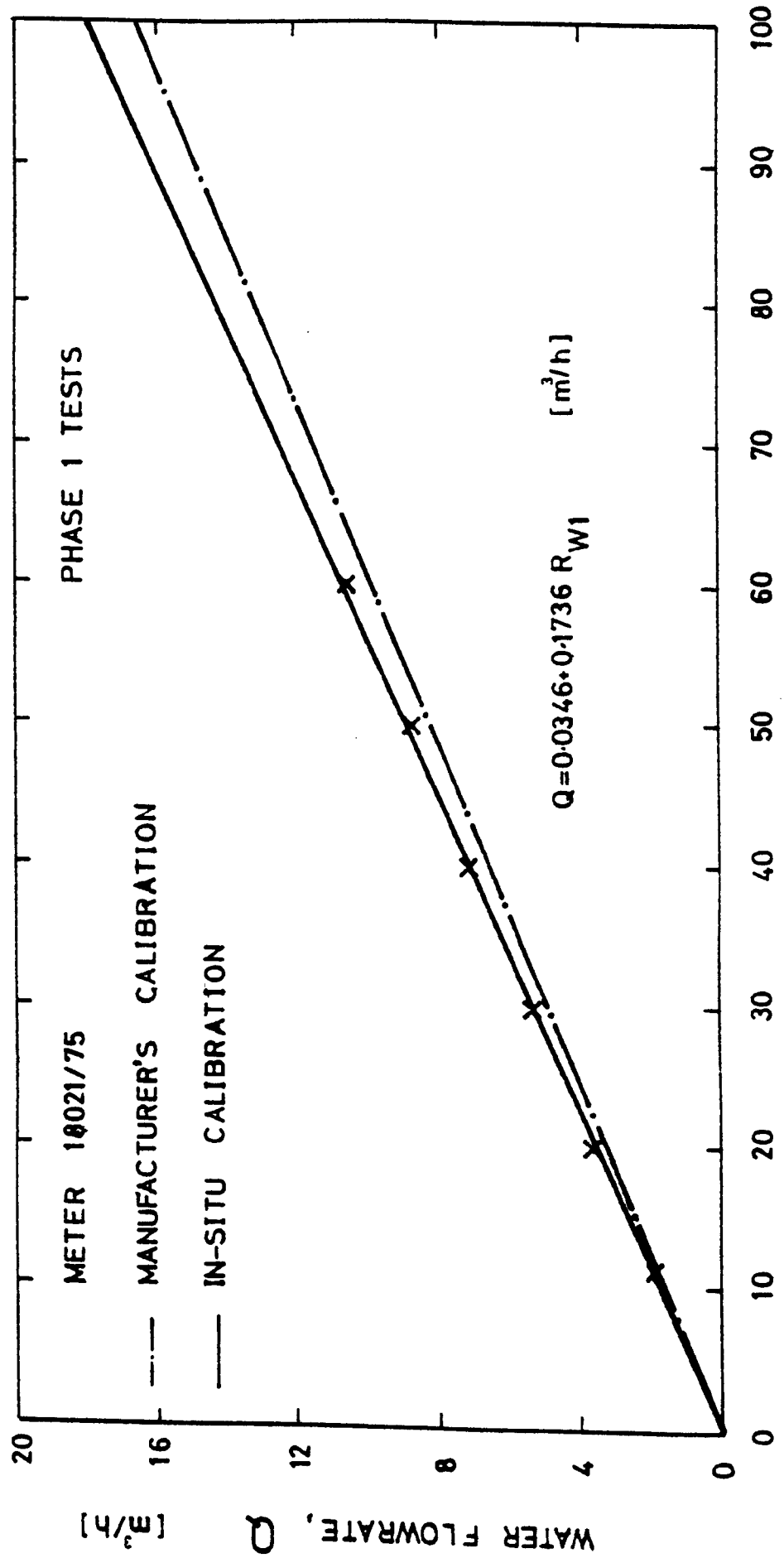

Fig C-1 Calibration Of Turbine Flowmeter

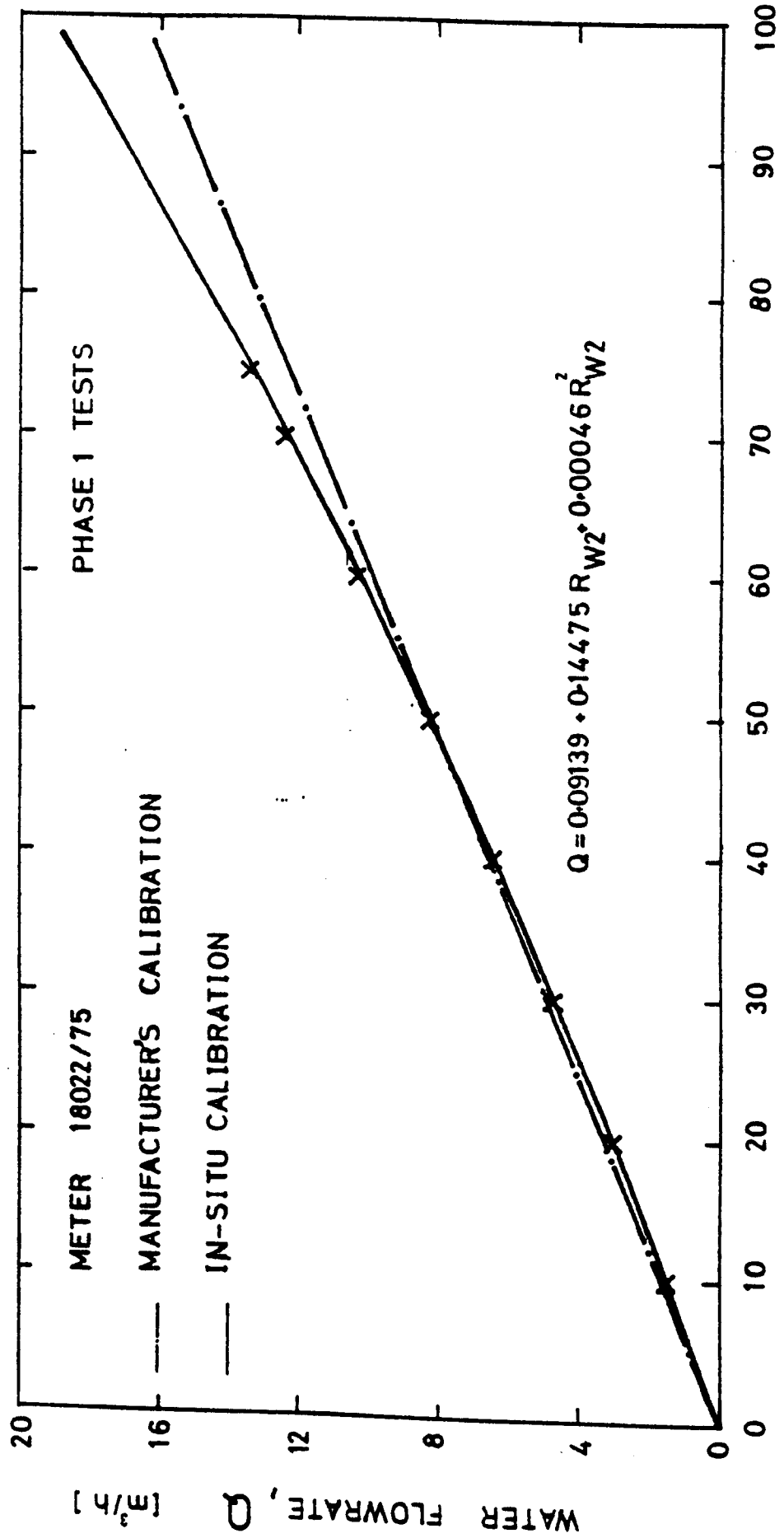

Fig C-2 Calibration Of Turbine Flowmeter

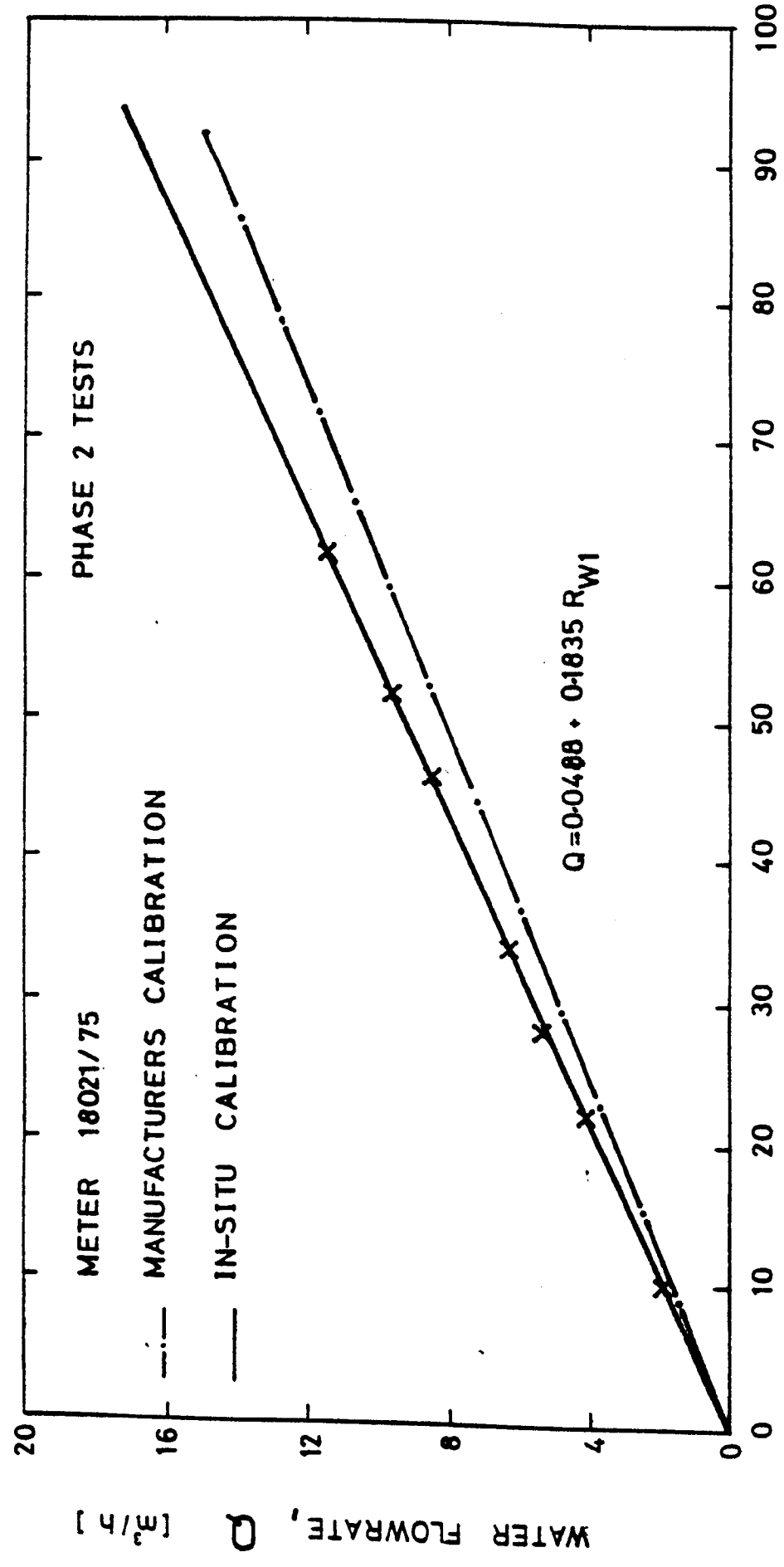

Fig C-3 Calibration Of Turbine Flowmeter

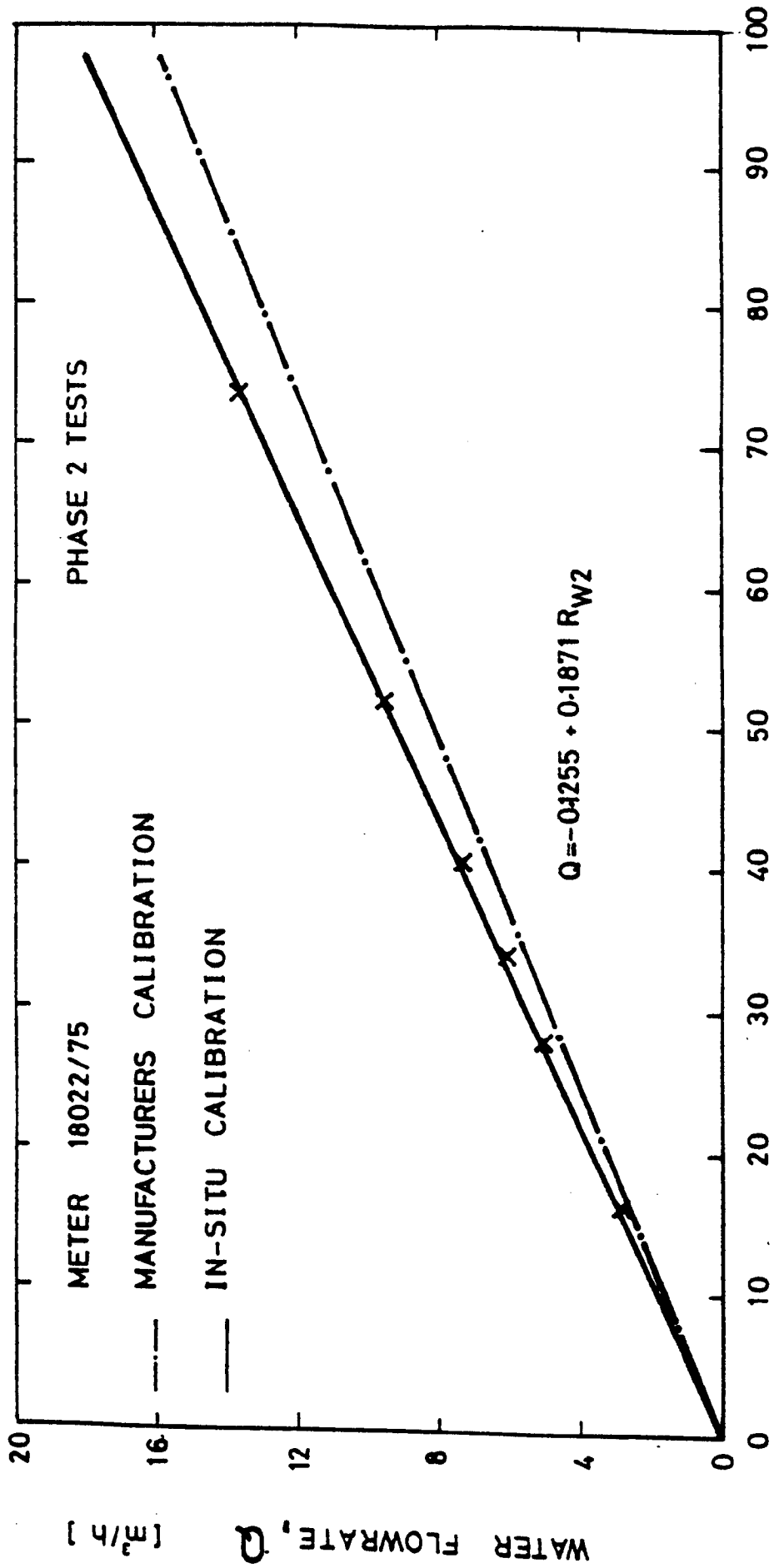

Fig C-4 Calibration Of Turbine Flowmeter

APPENDIX D

EXPERIMENTAL MEASUREMENTS

(UNPROCESSED)

PHASE 1 TESTS

TEST NO. 02057901

R_{A1} cm	R_{A2} cm	H_A (mm_{H_2O})	p_A bar	T_A °C	H_{LP} (mm_{H_2O})	T_{LP} °C	R_{W1} %	R_{W2} %	M_{W_O} lb	t sec	Z_1 mm	Z_2 mm
0.00	0.00	100.00	1.02	17.80	35.00	15.70	4.00	4.30	0.28	62.70	18.00	18.00
0.00	0.00	150.00	1.05	17.10	65.00	14.70	4.00	4.30	0.66	63.10	18.00	18.00
0.00	0.00	220.00	1.03	16.20	80.00	13.60	4.00	4.30	1.54	63.10	18.00	18.00
0.00	0.00	335.00	1.05	14.20	140.00	11.10	4.00	4.30	30.00	156.70	18.00	18.00
0.00	0.00	470.00	1.05	13.70	230.00	8.60	4.00	4.30	100.00	235.70	18.00	18.00
0.00	0.00	620.00	1.05	16.80	316.00	12.90	4.00	4.30	100.00	176.00	18.00	18.00
0.00	0.00	708.00	1.05	13.40	400.00	8.50	4.00	4.30	100.00	140.30	18.00	18.00
0.00	0.00	990.00	1.03	10.90	540.00	7.20	4.00	4.30	100.00	114.10	18.00	18.00
0.00	0.00	1095.00	1.01	9.20	590.00	4.60	4.00	4.30	100.00	114.70	18.00	18.00
0.00	0.00	1470.00	1.06	17.70	700.00	12.20	4.00	4.30	100.00	114.70	18.00	18.00
0.00	0.00	1610.00	1.05	17.80	760.00	12.60	4.00	4.30	100.00	113.70	18.00	18.00

TABLE D-1 Experimental Measurements

PHASE 1 TESTS

TEST NO. 05047902

R_{A1} cm	R_{A2} cm	H_A ($mm\ H_2O$)	p_A bar	T_A °C	H_{LP} ($mm\ H_2O$)	T_{LP} °C	R_{W1} %	R_{W2} %	M_{WO} lb	t sec	Z_1 mm	Z_2 mm
0.00	0.00	50.00	1.15	17.60	27.00	16.20	6.00	6.00	0.11	75.20	21.00	21.00
0.00	0.00	85.00	1.15	17.50	30.00	15.50	6.00	6.00	0.17	76.90	21.00	21.00
0.00	0.00	110.00	1.04	17.20	44.00	15.60	6.00	6.00	0.44	81.30	21.00	21.00
0.00	0.00	150.00	1.07	16.70	62.00	14.70	6.00	6.00	0.85	69.80	21.00	21.00
0.00	0.00	195.00	1.09	15.80	83.00	13.70	6.00	6.00	1.79	68.90	21.00	21.00
0.00	0.00	260.00	1.10	14.90	126.00	12.30	6.00	6.00	30.00	135.50	21.00	21.00
0.00	0.00	380.00	1.10	13.30	234.00	8.00	6.00	6.00	100.00	179.30	21.00	21.00
0.00	0.00	555.00	1.10	11.40	285.00	6.80	6.00	6.00	100.00	141.80	21.00	21.00
0.00	0.00	635.00	1.08	10.20	410.00	6.90	6.00	6.00	100.00	104.70	21.00	21.00
0.00	0.00	750.00	0.80	8.70	350.00	7.90	6.00	6.00	100.00	100.80	21.00	21.00
0.00	0.00	905.00	0.71	17.40	330.00	12.20	6.00	6.00	100.00	124.70	21.00	21.00
0.00	0.00	1175.00	0.71	15.10	445.00	11.10	6.00	6.00	100.00	101.40	21.00	21.00
0.00	0.00	1330.00	0.80	11.90	515.00	9.70	6.00	6.00	100.00	94.00	21.00	21.00

TABLE D-2 Experimental Measurements

PHASE 1 TESTS

TEST NO 02057903

R_{A1} cm	R_{A2} cm	H_A ($mm\ H_2O$)	p_A bar	T_A °C	H_{LP} ($mm\ H_2O$)	T_{LP} °C	R_{W1} %	R_{W2} %	M_{WO} lb	t sec	Z_1 mm	Z_2 mm
5.20	0.00	0.00	0.99	17.60	3.00	15.10	7.00	8.00	0.00	62.70	24.00	24.00
0.00	0.00	45.00	0.99	17.40	21.00	15.10	7.00	8.00	0.00	63.10	24.00	24.00
0.00	0.00	110.00	1.00	17.00	45.00	15.20	7.00	8.00	0.72	63.50	24.00	24.00
0.00	0.00	165.00	1.01	17.10	65.00	11.50	7.00	8.00	10.00	297.20	24.00	24.00
0.00	0.00	275.00	1.01	17.00	105.00	10.50	7.00	8.00	20.00	98.20	24.00	24.00
0.00	0.00	290.00	1.03	15.90	165.00	11.60	7.00	8.00	100.00	219.70	24.00	24.00
0.00	0.00	440.00	1.03	15.10	260.00	11.00	7.00	8.00	100.00	126.50	24.00	24.00
0.00	0.00	645.00	1.02	14.30	400.00	10.90	7.00	8.00	100.00	92.30	24.00	24.00
0.00	0.00	770.00	0.99	12.90	520.00	10.40	7.00	8.00	100.00	78.20	24.00	24.00
0.00	0.00	1018.00	0.96	11.70	640.00	9.60	7.00	8.00	100.00	73.00	24.00	24.00
0.00	0.00	1530.00	1.03	17.20	966.00	9.90	7.00	8.00	100.00	64.70	24.00	24.00

TABLE D-3 Experimental Measurements

PHASE 1 TESTS

TEST NO. 06047904

R_{A1} cm	R_{A2} cm	H_A (mm_{H_2O})	p_A bar	T_A °C	H_{LP} (mm_{H_2O})	T_{LP} °C	R_{W1} %	R_{W2} %	M_{WO} lb	t sec	Z_1 mm	Z_2 mm
0.00	0.00	64.00	0.80	19.00	28.00	16.20	10.80	12.00	1.05	58.30	29.00	29.00
0.00	0.00	125.00	0.91	18.10	78.00	13.40	10.80	12.00	20.00	53.90	29.00	29.00
0.00	0.00	184.00	0.91	17.80	120.00	13.80	10.80	12.00	100.00	133.80	29.00	29.00
0.00	0.00	325.00	0.91	17.00	270.00	12.90	10.80	12.00	100.00	80.10	29.00	29.00
0.00	0.00	490.00	0.91	15.50	395.00	12.20	10.80	12.00	100.00	63.50	29.00	29.00
0.00	0.00	700.00	0.91	13.50	530.00	11.20	10.80	12.00	100.00	53.80	29.00	29.00
0.00	0.00	930.00	0.91	11.30	657.00	9.90	10.80	12.00	200.00	97.60	29.00	29.00
0.00	0.00	1130.00	0.91	8.60	767.00	8.10	10.80	12.00	200.00	94.00	29.00	29.00
0.00	0.00	1290.00	0.85	8.20	885.00	8.60	10.80	12.00	200.00	92.10	29.00	29.00

TABLE D-4 Experimental Measurements

PHASE 1 TESTS

TEST NO. 09047905

R_{A1} cm	R_{A2} cm	H_A ($mm H_2O$)	p_A bar	T_A °C	H_{LP} ($mm H_2O$)	T_{LP} °C	R_{W1} %	R_{W2} %	M_{WO} lb	t sec	Z_1 mm	Z_2 mm
0.00	0.00	43.00	0.91	18.30	23.00	12.90	16.80	18.00	1.95	57.00	40.00	40.00
0.00	0.00	65.00	0.95	18.20	68.00	14.40	16.80	18.00	50.00	70.80	40.00	40.00
0.00	0.00	180.00	0.73	18.10	180.00	13.60	16.80	18.00	100.00	71.40	40.00	40.00
0.00	0.00	275.00	0.94	16.40	330.00	8.60	16.80	18.00	100.00	52.80	40.00	40.00
0.00	0.00	327.00	0.78	17.10	345.00	10.50	16.80	18.00	100.00	51.60	40.00	40.00
0.00	0.00	430.00	0.94	14.80	600.00	8.40	16.80	18.00	200.00	68.70	40.00	40.00
0.00	0.00	700.00	0.93	13.20	910.00	7.50	16.80	18.00	200.00	62.10	40.00	40.00
0.00	0.00	935.00	0.92	10.80	1129.00	7.00	16.80	18.00	200.00	58.70	40.00	40.00
0.00	0.00	1130.00	0.91	8.90	1278.00	6.30	16.80	18.00	200.00	57.80	40.00	40.00
0.00	0.00	1210.00	0.89	14.70	1278.00	8.10	16.80	18.00	200.00	58.00	40.00	40.00
0.00	0.00	1270.00	0.85	15.40	1469.00	8.20	16.80	18.00	200.00	56.90	40.00	40.00

TABLE D-5 Experimental Measurements

PHASE 1 TESTS

TEST NO. 10047906

R_{A1} cm	R_{A2} cm	H_A (mm H_2O)	p_A bar	T_A °C	H_{LP} (mm H_2O)	T_{LP} °C	R_{W1} %	R_{W2} %	M_{WO} lb	t sec	Z_1 mm	Z_2 mm
0.00	0.00	24.00	0.86	19.00	40.00	15.40	22.00	24.00	10.00	40.70	65.00	65.00
0.00	0.00	51.00	0.85	18.10	86.00	11.80	22.00	24.00	40.00	36.80	65.00	65.00
0.00	0.00	150.00	0.90	17.60	260.00	11.70	22.00	24.00	100.00	43.90	65.00	65.00
0.00	0.00	325.00	0.80	16.90	550.00	13.40	22.00	24.00	200.00	59.40	65.00	65.00
0.00	0.00	475.00	0.71	14.80	802.40	9.90	22.00	24.00	300.00	75.90	65.00	65.00
0.00	0.00	693.00	0.76	12.60	1088.00	11.80	22.00	24.00	300.00	66.10	65.00	65.00
0.00	0.00	980.00	0.80	9.90	1536.80	7.60	22.00	24.00	400.00	87.00	65.00	65.00
0.00	0.00	1060.00	0.73	15.40	1251.20	10.60	22.00	24.00	400.00	89.40	65.00	65.00
0.00	0.00	1080.00	0.71	14.70	1305.60	9.70	22.00	24.00	400.00	89.60	65.00	65.00
0.00	0.00	1320.00	0.90	14.40	1591.20	10.90	22.00	24.00	400.00	86.40	65.00	65.00
0.00	0.00	1450.00	1.00	13.80	1795.20	10.10	22.00	24.00	400.00	85.10	65.00	65.00

TABLE D-6 Experimental Measurements

PHASE 1 TESTS

TEST NO. 17047907

R_{A1} cm	R_{A2} cm	H_A (mm_{H_2O})	p_A bar	T_A °C	H_{LP} (mm_{H_2O})	T_{LP} °C	R_{W1} %	R_{W2} %	M_{WO} lb	t sec	Z_1 mm	Z_2 mm
6.20	0.00	0.00	0.46	16.30	10.00	13.20	28.00	30.00	0.18	61.50	71.00	71.00
16.50	0.00	0.00	0.38	16.00	20.00	13.00	28.00	30.00	20.00	87.90	71.00	71.00
0.00	0.00	24.00	0.23	16.60	60.00	13.00	29.00	30.00	50.00	52.40	71.00	71.00
0.00	0.00	72.00	0.40	16.30	150.00	12.70	28.00	30.00	100.00	47.40	71.00	71.00
0.00	0.00	190.00	0.52	16.20	400.00	12.60	28.00	30.00	200.00	53.90	71.00	71.00
0.00	0.00	305.00	0.48	15.80	550.00	11.40	28.00	30.00	200.00	44.80	71.00	71.00
0.00	0.00	440.00	0.82	14.70	1060.80	9.20	28.00	30.00	300.00	56.80	71.00	71.00
0.00	0.00	627.00	0.83	17.00	1523.20	11.50	28.00	30.00	300.00	71.70	71.00	71.00
0.00	0.00	860.00	0.93	16.60	1700.00	9.60	28.00	30.00	400.00	69.30	71.00	71.00
0.00	0.00	1070.00	0.90	13.40	1890.40	8.10	28.00	30.00	400.00	68.50	71.00	71.00
0.00	0.00	1220.00	0.97	9.30	2053.60	6.60	28.00	30.00	400.00	68.00	71.00	71.00

TABLE D-7 Experimental Measurements

PHASE 1 TESTS

TEST NO. 18047908

R_{A1} cm	R_{A2} cm	H_A ($mm H_2O$)	p_A bar	T_A °C	H_{LP} ($mm H_2O$)	T_{LP} °C	R_{W1} %	R_{W2} %	M_{W_O} lb	t sec	Z_1 mm	Z_2 mm
7.00	0.00	0.00	0.57	18.80	22.00	15.00	34.70	37.00	20.00	27.00	71.00	71.00
20.00	0.00	0.00	0.55	18.80	60.00	13.90	34.70	37.00	30.00	21.70	71.00	71.00
28.00	0.00	0.00	0.51	18.70	83.00	13.60	34.70	37.00	100.00	52.40	71.00	71.00
0.00	0.00	45.00	0.32	18.30	165.00	13.00	34.70	37.00	100.00	31.80	71.00	71.00
0.00	0.00	75.00	0.41	18.00	255.00	13.20	34.70	37.00	200.00	51.10	71.00	71.00
0.00	0.00	185.00	0.68	17.60	605.00	13.10	34.70	37.00	300.00	53.80	71.00	71.00
0.00	0.00	315.00	0.53	17.40	980.00	12.60	34.70	37.00	300.00	49.40	71.00	71.00
0.00	0.00	450.00	0.73	16.60	1319.20	11.20	34.70	37.00	400.00	61.40	71.00	71.00
0.00	0.00	650.00	0.72	15.70	1645.60	10.20	34.70	37.00	500.00	72.00	71.00	71.00
0.00	0.00	930.00	0.72	14.50	1727.20	9.30	34.70	37.00	500.00	71.80	71.00	71.00
0.00	0.00	1040.00	0.80	12.40	2080.00	8.90	34.70	37.00	500.00	70.00	71.00	71.00
0.00	0.00	1235.00	0.92	10.10	2203.20	8.10	34.70	37.00	500.00	69.20	71.00	71.00

TABLE D-8 Experimental Measurements

PHASE 1 TESTS

TEST NO. 19047909

R_{A1} cm	R_{A2} cm	H_A (mm_{H_2O})	p_A bar	T_A °C	H_{LP} (mm_{H_2O})	T_{LP} °C	R_{W1} %	R_{W2} %	M_{W_O} lb	t sec	Z_1 mm	Z_2 mm
0.00	0.00	30.00	1.00	18.30	160.00	12.70	40.20	42.00	100.00	29.00	71.00	71.00
0.00	0.00	60.00	0.98	17.50	530.00	11.50	40.20	42.00	200.00	32.50	71.00	71.00
0.00	0.00	200.00	0.98	17.30	952.00	10.50	40.20	42.00	400.00	56.30	71.00	71.00
0.00	0.00	370.00	0.98	17.00	1428.00	9.30	40.20	42.00	500.00	64.60	71.00	71.00
0.00	0.00	460.00	1.00	15.40	1496.00	8.30	40.20	42.00	500.00	64.10	71.00	71.00
0.00	0.00	700.00	0.99	14.00	1836.00	7.80	40.20	42.00	500.00	62.10	71.00	71.00
0.00	0.00	810.00	1.00	11.50	2516.00	7.90	40.20	42.00	600.00	75.00	71.00	71.00
0.00	0.00	970.00	1.10	11.90	2312.00	7.60	40.20	42.00	600.00	71.60	71.00	71.00
0.00	0.00	1100.00	0.97	10.80	2312.00	7.60	40.20	42.00	600.00	72.40	71.00	71.00

TABLE D-9 Experimental Measurements

PHASE 1 TESTS

TEST NO. 23047910

R_{A1} cm	R_{A2} cm	H_A ($mm H_2O$)	p_A bar	T_A °C	H_{LP} ($mm H_2O$)	T_{LP} °C	R_{W1} %	R_{W2} %	M_{W_O} lb	t sec	Z_1 mm	Z_2 mm
0.00	0.00	24.00	0.94	14.10	500.00	8.90	47.50	49.00	200.00	39.30	71.00	71.00
0.00	0.00	34.00	0.93	18.80	320.00	13.00	47.50	49.00	300.00	61.20	71.00	71.00
0.00	0.00	60.00	0.94	14.50	748.00	9.50	47.50	49.00	300.00	51.10	71.00	71.00
0.00	0.00	220.00	0.91	14.10	1292.00	8.80	47.50	49.00	400.00	55.40	71.00	71.00
0.00	0.00	280.00	0.96	17.40	1496.00	10.00	47.50	49.00	200.00	26.40	71.00	71.00
0.00	0.00	475.00	0.96	15.70	2094.40	9.20	47.50	49.00	400.00	44.90	71.00	71.00
0.00	0.00	690.00	0.93	13.90	2624.80	8.60	47.50	49.00	400.00	42.90	71.00	71.00
0.00	0.00	1000.00	0.97	7.90	3128.00	6.50	47.50	49.00	500.00	52.80	71.00	71.00
0.00	0.00	1170.00	0.96	12.50	2516.00	7.20	47.50	49.00	500.00	54.60	71.00	71.00
0.00	0.00	1285.00	0.95	16.00	2040.00	8.70	47.50	49.00	500.00	55.40	71.00	71.00

TABLE D-10 Experimental Measurements

PHASE 1 TESTS

TEST NO. 12077911

R_{A1} cm	R_{A2} cm	H_A (mm H_2O)	p_A bar	T_A °C	H_{LP} (mm H_2O)	T_{LP} °C	R_{W1} %	R_{W2} %	M_{WO} lb	t sec	Z_1 mm	Z_2 mm
6.00	0.00	0.00	1.00	19.90	3.00	19.50	5.40	6.00	0.00	10.00	22.00	22.00
6.00	0.00	0.00	1.00	19.90	4.00	19.60	9.00	10.00	0.00	10.00	30.00	30.00
6.00	0.00	0.00	1.00	19.80	38.00	17.10	30.00	31.00	10.00	56.10	69.00	69.00
6.00	0.00	0.00	1.00	19.80	44.00	16.90	32.50	34.50	20.00	61.40	71.00	71.00
6.00	0.00	0.00	1.00	19.80	52.00	16.60	35.50	36.50	30.00	43.90	71.00	71.00
6.00	0.00	0.00	1.00	19.90	60.00	16.60	40.50	42.50	60.00	57.50	71.00	71.00
6.00	0.00	0.00	1.00	20.00	70.00	16.70	45.00	48.00	100.00	69.40	71.00	71.00
6.00	0.00	0.00	1.00	20.00	70.00	16.70	50.00	50.00	100.00	71.00	71.00	71.00
6.00	0.00	0.00	1.00	20.10	72.00	17.10	54.00	55.00	100.00	60.00	71.00	71.00
6.00	0.00	0.00	1.00	20.10	75.00	17.60	59.00	58.50	100.00	53.20	71.00	71.00

TABLE D-11 Experimental Measurements

PHASE 1 TESTS

TEST NO. 12077912

R_{A1} cm	R_{A2} cm	H_A (mm_{H_2O})	p_A bar	T_A °C	H_{LP} (mm_{H_2O})	T_{LP} °C	R_{W1} %	R_{W2} %	M_{W_O} lb	t sec	Z_1 mm	Z_2 mm
25.00	0.00	0.00	1.00	21.00	7.00	17.80	6.00	5.40	0.00	60.00	20.00	21.00
25.00	0.00	0.00	1.00	20.70	40.00	18.00	23.00	25.00	10.00	54.10	65.00	66.00
25.00	0.00	0.00	1.00	20.60	56.00	18.00	26.00	28.00	20.00	28.00	70.00	70.00
25.00	0.00	0.00	1.00	20.60	70.00	19.70	28.80	30.80	140.00	129.00	70.00	70.00
25.00	0.00	0.00	1.00	20.60	85.00	19.90	31.00	33.00	200.00	130.80	70.00	70.00
25.00	0.00	0.00	1.00	20.60	105.00	19.50	34.00	36.00	200.00	97.00	70.00	71.00
25.00	0.00	0.00	1.00	20.60	210.00	18.60	42.00	42.00	300.00	88.00	71.00	71.00
25.00	0.00	0.00	1.00	20.60	315.00	19.00	45.50	47.50	300.00	67.40	71.00	71.00
25.00	0.00	0.00	1.00	20.90	465.00	18.60	49.00	49.50	600.00	119.40	71.00	71.00
25.00	0.00	0.00	1.00	20.90	490.00	19.00	59.00	59.50	500.00	88.00	71.00	71.00

TABLE D-12 Experimental Measurements

PHASE 1 TESTS

TEST NO. 17077913

R_{A1} cm	R_{A2} cm	H_A ($mm\ H_2O$)	p_A bar	T_A °C	H_{LP} ($mm\ H_2O$)	T_{LP} °C	R_{W1} %	R_{W2} %	M_{W_O} lb	t sec	Z_1 mm	Z_2 mm
0.00	0.00	90.00	1.00	17.40	50.00	15.40	12.50	14.00	10.00	51.50	36.00	37.00
0.00	0.00	90.00	1.00	17.60	92.00	14.90	19.00	21.00	100.00	118.20	50.00	50.00
0.00	0.00	90.00	1.00	17.70	45.00	14.70	24.00	26.00	100.00	56.00	70.00	70.00
0.00	0.00	90.00	1.00	17.70	225.00	14.90	29.90	31.80	200.00	70.40	71.00	71.00
0.00	0.00	90.00	1.00	17.70	290.00	14.00	34.00	36.00	200.00	48.10	71.00	71.00
0.00	0.00	90.00	1.00	17.70	380.00	13.80	38.00	40.00	300.00	61.50	71.00	71.00
0.00	0.00	90.00	1.00	17.70	450.00	13.20	41.00	43.00	400.00	64.40	75.00	75.00
0.00	0.00	90.00	1.00	17.70	761.60	12.80	44.00	46.00	400.00	61.70	75.00	75.00
0.00	0.00	90.00	1.00	17.80	924.80	12.10	49.50	50.50	400.00	58.60	75.00	75.00

TABLE D-13 Experimental Measurements

PHASE 1 TESTS

TEST NO. 13087914

R_{A1} cm	R_{A2} cm	H_A ($mm\ H_2O$)	p_A bar	T_A °C	H_{LP} ($mm\ H_2O$)	T_{LP} °C	R_{W1} %	R_{W2} %	M_{W_O} lb	t sec	Z_1 mm	Z_2 mm
0.00	0.00	180.00	1.00	18.10	50.00	17.90	4.00	6.00	1.37	95.80	20.00	21.00
0.00	0.00	180.00	1.00	17.60	95.00	18.40	9.00	10.00	30.00	63.00	29.00	29.00
0.00	0.00	180.00	1.00	17.50	160.00	18.70	11.00	13.00	100.00	103.70	35.00	36.00
0.00	0.00	180.00	1.00	17.40	170.00	18.20	12.00	14.50	100.00	91.20	40.00	40.00
0.00	0.00	180.00	1.00	20.20	275.00	19.70	17.50	21.00	200.00	105.80	63.00	68.00
0.00	0.00	180.00	1.00	20.40	375.00	18.00	22.00	24.00	200.00	71.50	70.00	70.00
0.00	0.00	180.00	1.00	20.50	470.00	18.60	26.00	27.50	300.00	75.70	71.00	71.00
0.00	0.00	180.00	1.00	20.30	660.00	18.60	30.50	32.00	400.00	78.10	71.00	71.00
0.00	0.00	180.00	1.00	19.90	898.00	19.00	36.00	39.50	400.00	60.00	71.00	71.00
0.00	0.00	180.00	1.00	19.00	1088.00	18.30	40.00	40.00	500.00	74.10	71.00	71.00
0.00	0.00	180.00	1.00	18.60	1360.00	19.20	48.00	49.00	500.00	70.00	71.00	71.00

TABLE D-14 Experimental Measurements

PHASE 1 TESTS

TEST NO. 14087915

R_{A1} cm	R_{A2} cm	H_A ($mm H_2O$)	p_A bar	T_A °C	H_{LP} ($mm H_2O$)	T_{LP} °C	R_{W1} %	R_{W2} %	M_{WO} lb	t sec	Z_1 mm	Z_2 mm
0.00	0.00	330.00	1.04	18.60	160.00	16.70	5.00	6.00	50.00	145.00	21.00	21.00
0.00	0.00	330.00	1.04	18.10	270.00	16.80	9.00	10.00	100.00	91.50	32.00	32.00
0.00	0.00	330.00	1.04	17.10	445.00	16.90	14.00	18.00	300.00	128.00	55.00	60.00
0.00	0.00	330.00	1.04	15.60	485.00	16.70	17.50	19.50	400.00	142.10	62.00	64.00
0.00	0.00	330.00	1.04	14.70	700.00	16.50	24.00	26.00	500.00	120.70	71.00	71.00
0.00	0.00	330.00	1.04	14.40	952.00	16.00	30.00	32.50	500.00	87.60	71.00	71.00
0.00	0.00	330.00	1.04	18.80	1170.00	17.00	36.00	38.00	600.00	85.50	71.00	71.00
0.00	0.00	330.00	1.04	18.80	1360.00	16.20	42.00	44.00	600.00	84.00	71.00	71.00
0.00	0.00	330.00	1.04	18.00	1605.00	14.20	49.00	49.00	600.00	76.20	71.00	71.00

TABLE D-15 Experimental Measurements

PHASE 1 TESTS

TEST NO. 15087916

R_{A1} cm	R_{A2} cm	H_A ($mm\ H_2O$)	p_A bar	T_A °C	H_{LP} ($mm\ H_2O$)	T_{LP} °C	R_{W1} %	R_{W2} %	M_{WO} lb	t sec	Z_1 mm	Z_2 mm
0.00	0.00	500.00	1.00	18.30	310.00	17.10	5.40	6.00	100.00	120.20	24.00	24.00
0.00	0.00	500.00	1.00	17.90	420.00	15.80	9.00	10.00	200.00	136.80	33.00	34.00
0.00	0.00	500.00	1.00	16.60	465.00	13.90	13.50	15.50	200.00	89.00	46.00	47.00
0.00	0.00	500.00	1.00	14.70	680.00	12.30	18.50	21.00	300.00	87.20	68.00	69.00
0.00	0.00	500.00	1.00	13.80	1061.00	9.70	24.00	26.00	400.00	83.40	71.00	71.00
0.00	0.00	500.00	1.00	13.00	1115.00	8.90	30.00	32.00	500.00	85.00	71.00	71.00
0.00	0.00	500.00	1.00	12.60	1482.00	8.70	36.00	37.50	500.00	69.20	71.00	71.00
0.00	0.00	500.00	1.00	12.40	1578.00	8.90	42.00	42.00	600.00	76.20	71.00	71.00

TABLE D-16 Experimental Measurements

PHASE 1 TESTS

TEST NO. 21087917

R_{A1} cm	R_{A2} cm	H_A (mm_{H_2O})	p_A bar	T_A °C	H_{LP} (mm_{H_2O})	T_{LP} °C	R_{W1} %	R_{W2} %	M_{W_O} lb	t sec	Z_1 mm	Z_2 mm
0.00	0.00	1000.00	1.00	18.00	555.00	12.70	5.00	5.00	60.00	62.20	22.00	22.00
0.00	0.00	1000.00	1.00	18.30	700.00	12.60	8.50	9.50	100.00	58.60	35.00	35.00
0.00	0.00	1000.00	1.00	18.30	911.20	12.80	14.50	16.50	200.00	67.50	60.00	60.00
0.00	0.00	1000.00	1.00	18.00	1346.40	13.10	23.00	25.50	300.00	63.30	70.00	70.00
0.00	0.00	1000.00	1.00	17.70	1917.60	16.50	30.00	32.00	400.00	63.20	70.00	70.00
0.00	0.00	1000.00	1.00	17.70	2108.00	15.50	36.00	38.00	500.00	69.00	70.00	70.00
0.00	0.00	1000.00	1.00	17.60	2475.20	14.20	42.00	44.00	500.00	59.00	70.00	70.00
0.00	0.00	1000.00	1.00	17.10	2652.00	13.40	50.00	50.00	600.00	59.50	70.00	70.00
0.00	0.00	1000.00	1.00	14.70	3400.00	16.10	59.00	60.00	600.00	52.80	70.00	70.00

TABLE D-17 Experimental Measurements

PHASE 2 TESTS

TEST NO. 22098018

R_{A1} cm	R_{A2} cm	H_A ($mm H_2O$)	p_A bar	T_A °C	H_{LP} ($mm H_2O$)	T_{LP} °C	R_{W1} %	R_{W2} %	M_{WO} lb	t sec	Z_1 mm	Z_2 mm
0.00	0.00	290.00	1.14	19.00	95.00	15.00	5.30	6.20	2.00	48.10	21.00	21.00
0.00	0.00	340.00	1.14	18.00	126.00	12.00	5.30	6.20	3.00	66.00	21.00	21.00
0.00	0.00	385.00	1.14	17.00	220.00	12.00	5.30	6.20	10.00	48.00	21.00	21.00
0.00	0.00	455.00	1.15	16.00	205.00	10.00	5.30	6.20	2.00	36.60	21.00	21.00
0.00	0.00	520.00	1.02	16.00	310.00	11.00	5.30	6.20	30.00	54.60	21.00	21.00
0.00	0.00	645.00	1.03	16.00	380.00	11.00	5.30	6.20	50.00	78.80	21.00	21.00
0.00	0.00	790.00	1.04	16.00	500.00	11.00	5.30	6.20	100.00	118.40	21.00	21.00
0.00	0.00	925.00	1.06	15.00	600.00	11.00	5.30	6.20	100.00	108.90	21.00	21.00
0.00	0.00	1050.00	1.08	13.00	600.00	8.00	5.30	6.20	100.00	151.60	21.00	21.00
0.00	0.00	1100.00	1.08	12.00	640.00	7.00	5.30	6.20	100.00	149.20	21.00	21.00
0.00	0.00	1380.00	1.02	11.00	720.00	7.00	5.30	6.20	100.00	130.90	21.00	21.00

TABLE D-18 Experimental Measurements

PHASE 2 TESTS

TEST NO. 23098019

R_{A1} cm	R_{A2} cm	H_A ($mm H_2O$)	p_A bar	T_A °C	H_{LP} ($mm H_2O$)	T_{LP} °C	R_{W1} %	R_{W2} %	M_{WO} lb	t sec	Z_1 mm	Z_2 mm
0.00	0.00	277.00	1.04	19.00	92.00	11.00	6.60	7.40	2.00	60.40	23.00	23.00
0.00	0.00	365.00	1.04	19.00	200.00	12.00	6.60	7.40	20.00	64.80	23.00	23.00
0.00	0.00	435.00	1.04	19.00	290.00	12.00	6.60	7.40	30.00	71.30	23.00	23.00
0.00	0.00	570.00	1.04	18.00	310.00	12.00	6.60	7.40	50.00	85.70	23.00	23.00
0.00	0.00	635.00	1.04	19.00	390.00	12.00	6.60	7.40	50.00	75.60	23.00	23.00
0.00	0.00	755.00	1.05	17.00	480.00	12.00	6.60	7.40	50.00	61.40	23.00	23.00
0.00	0.00	920.00	1.05	17.00	590.00	11.00	6.60	7.40	100.00	111.00	23.00	23.00
0.00	0.00	1045.00	1.05	15.00	640.00	11.00	6.60	7.40	100.00	112.40	23.00	23.00
0.00	0.00	1150.00	1.05	14.00	750.00	11.00	6.60	7.40	100.00	96.80	23.00	23.00
0.00	0.00	1185.00	1.05	13.00	760.00	100.00	6.60	7.40	100.00	95.60	23.00	23.00
0.00	0.00	1360.00	1.02	12.00	830.00	10.00	6.60	7.40	100.00	92.70	23.00	23.00

TABLE D-19 Experimental Measurements

PHASE 2 TESTS

TEST NO. 24098020

R_{A1} cm	R_{A2} cm	H_A ($mm H_2O$)	p_A bar	T_A °C	H_{LP} ($mm H_2O$)	T_{LP} °C	R_{W1} %	R_{W2} %	M_{WO} lb	t sec	Z_1 mm	Z_2 mm
0.00	0.00	240.00	1.05	18.00	65.00	16.00	10.10	10.80	2.00	76.60	32.00	32.00
0.00	0.00	290.00	1.05	17.00	270.00	10.00	10.10	10.80	30.00	53.30	32.00	32.00
0.00	0.00	395.00	1.04	17.00	380.00	11.00	10.10	10.80	100.00	82.80	32.00	32.00
0.00	0.00	500.00	1.05	16.00	480.00	11.00	10.10	10.80	100.00	70.10	32.00	32.00
0.00	0.00	575.00	1.06	15.00	560.00	11.00	10.10	10.80	100.00	66.20	32.00	32.00
0.00	0.00	770.00	1.06	14.00	720.00	11.00	10.10	10.80	100.00	60.90	32.00	32.00
0.00	0.00	865.00	1.07	13.00	800.00	10.00	10.10	10.80	100.00	56.10	32.00	32.00
0.00	0.00	950.00	1.08	12.00	870.00	10.00	10.10	10.80	100.00	57.00	32.00	32.00
0.00	0.00	1010.00	1.08	11.00	898.00	10.00	10.10	10.80	100.00	55.20	32.00	32.00
0.00	0.00	1110.00	1.05	10.00	979.00	9.00	10.10	10.80	100.00	54.40	32.00	32.00
0.00	0.00	1340.00	1.02	9.00	1156.00	9.00	10.10	10.80	100.00	51.30	32.00	32.00

TABLE D-20 Experimental Measurements

PHASE 2 TESTS

TEST NO. 24098021

R_{A1} cm	R_{A2} cm	H_A ($mm H_2O$)	p_A bar	T_A °C	H_{LP} ($mm H_2O$)	T_{LP} °C	R_{W1} %	R_{W2} %	M_{W_O} lb	t sec	Z_1 mm	Z_2 mm
0.00	0.00	200.00	1.07	18.00	70.00	11.00	15.50	16.10	2.00	96.10	50.00	50.00
0.00	0.00	240.00	1.07	18.00	300.00	10.00	15.50	16.10	70.00	59.80	50.00	50.00
0.00	0.00	315.00	1.07	17.00	450.00	10.00	15.50	16.10	100.00	52.10	50.00	50.00
0.00	0.00	440.00	1.07	17.00	600.00	10.00	15.50	16.10	200.00	86.70	50.00	50.00
0.00	0.00	505.00	1.07	16.00	700.00	10.00	15.50	16.10	200.00	76.70	50.00	50.00
0.00	0.00	580.00	1.08	16.00	810.00	11.00	15.50	16.10	200.00	73.60	50.00	50.00
0.00	0.00	718.00	1.08	14.00	952.00	11.00	15.50	16.10	200.00	72.40	50.00	50.00
0.00	0.00	865.00	1.07	13.00	1129.00	11.00	15.50	16.10	200.00	70.80	50.00	50.00
0.00	0.00	965.00	1.08	11.00	1197.00	10.00	15.50	16.10	200.00	70.60	50.00	50.00
0.00	0.00	1080.00	1.06	11.00	1333.00	10.00	15.50	16.10	200.00	67.90	50.00	50.00
0.00	0.00	1320.00	1.03	10.00	1496.00	8.00	15.50	16.10	200.00	71.80	50.00	50.00

TABLE D-21 Experimental Measurements

PHASE 2 TESTS

TEST NO. 25098022

R_{A1} cm	R_{A2} cm	H_A ($mm\ H_2O$)	p_A bar	T_A °C	H_{LP} ($mm\ H_2O$)	T_{LP} °C	R_{W1} %	R_{W2} %	M_{W_O} lb	t sec	Z_1 mm	Z_2 mm
0.00	0.00	155.00	1.09	19.00	70.00	12.00	20.70	21.20	2.00	67.70	59.00	59.00
0.00	0.00	190.00	1.09	19.00	280.00	11.00	20.70	21.20	50.00	34.90	59.00	59.00
0.00	0.00	260.00	1.09	18.00	475.00	11.00	20.70	21.20	200.00	82.40	59.00	59.00
0.00	0.00	355.00	1.09	18.00	650.00	11.00	20.70	21.20	200.00	64.80	59.00	59.00
0.00	0.00	455.00	1.10	17.00	830.00	11.00	20.70	21.20	300.00	88.70	59.00	59.00
0.00	0.00	565.00	1.10	16.00	1034.00	11.00	20.70	21.20	300.00	82.50	59.00	59.00
0.00	0.00	710.00	1.10	15.00	1224.00	11.00	20.70	21.20	300.00	80.90	59.00	59.00
0.00	0.00	880.00	1.10	14.00	1401.00	11.00	20.70	21.20	300.00	81.50	59.00	59.00
0.00	0.00	990.00	1.08	12.00	1496.00	11.00	20.70	21.20	300.00	79.30	59.00	59.00
0.00	0.00	1120.00	1.06	11.00	1686.00	10.00	20.70	21.20	300.00	81.30	59.00	59.00
0.00	0.00	1260.00	1.03	10.00	1795.00	10.00	20.70	21.20	300.00	77.50	59.00	59.00

TABLE D-22 Experimental Measurements

PHASE 2 TESTS

TEST NO. 26098023

R_{A1} cm	R_{A2} cm	H_A ($mm H_2O$)	p_A bar	T_A °C	H_{LP} ($mm H_2O$)	T_{LP} °C	R_{W1} %	R_{W2} %	M_{WO} lb	t sec	Z_1 mm	Z_2 mm
0.00	0.00	75.00	1.08	19.00	32.00	10.00	26.30	26.70	0.50	49.90	76.00	76.00
0.00	0.00	112.00	1.08	19.00	70.00	10.00	26.30	26.70	2.00	52.10	76.00	76.00
0.00	0.00	160.00	1.08	19.00	400.00	9.00	26.30	26.70	100.00	39.00	76.00	76.00
0.00	0.00	225.00	1.08	18.00	590.00	10.00	26.30	26.70	200.00	55.70	76.00	76.00
0.00	0.00	340.00	1.07	18.00	870.00	11.00	26.30	26.70	300.00	66.60	76.00	76.00
0.00	0.00	410.00	1.03	15.00	1061.00	11.00	26.30	26.70	300.00	63.50	76.00	76.00
0.00	0.00	500.00	1.04	14.00	1278.00	10.00	26.30	26.70	300.00	60.50	76.00	76.00
0.00	0.00	650.00	1.03	14.00	1632.00	10.00	26.30	26.70	300.00	57.90	76.00	76.00
0.00	0.00	880.00	1.04	14.00	1887.00	10.00	26.30	26.70	400.00	75.50	76.00	76.00
0.00	0.00	1080.00	1.03	12.00	2135.00	10.00	26.30	26.70	400.00	74.10	76.00	76.00
0.00	0.00	1245.00	1.03	11.00	2298.00	9.00	26.30	26.70	400.00	73.50	76.00	76.00

TABLE D-23 Experimental Measurements

PHASE 2 TESTS

TEST NO. 30098024

R_{A1} cm	R_{A2} cm	H_A ($mm\ H_2O$)	p_A bar	T_A °C	H_{LP} ($mm\ H_2O$)	T_{LP} °C	R_{W1} %	R_{W2} %	M_{W_O} lb	t sec	Z_1 mm	Z_2 mm
0.00	0.00	45.00	1.18	13.00	27.00	9.00	32.80	33.10	0.50	40.70	76.00	76.00
0.00	0.00	94.00	1.17	13.00	260.00	8.00	32.80	33.10	100.00	46.50	76.00	76.00
0.00	0.00	155.00	1.18	13.00	550.00	9.00	32.80	33.10	300.00	75.80	76.00	76.00
0.00	0.00	330.00	1.14	12.00	1170.00	9.00	32.80	33.10	300.00	53.50	76.00	76.00
0.00	0.00	450.00	1.15	12.00	1523.00	11.00	32.80	33.10	400.00	64.60	76.00	76.00
0.00	0.00	580.00	1.13	12.00	1936.00	11.00	32.80	33.10	400.00	61.50	76.00	76.00
0.00	0.00	670.00	1.01	16.00	1931.00	11.00	32.80	33.10	400.00	60.80	76.00	76.00
0.00	0.00	810.00	1.01	15.00	2203.00	11.00	32.80	33.10	400.00	59.70	76.00	76.00
0.00	0.00	900.00	1.02	15.00	2339.00	10.00	32.80	33.10	400.00	59.40	76.00	76.00
0.00	0.00	1000.00	1.03	14.00	2475.00	10.00	32.80	33.10	400.00	59.20	76.00	76.00
0.00	0.00	1200.00	1.03	12.00	2706.00	9.00	32.80	33.10	400.00	58.10	76.00	76.00

TABLE D-24 Experimental Measurements

PHASE 2 TESTS

TEST NO. 30098025

R_{A1} cm	R_{A2} cm	H_A (mm H_2O)	p_A bar	T_A °C	H_{LP} (mm H_2O)	T_{LP} °C	R_{W1} %	R_{W2} %	M_{W_O} lb	t sec	Z_1 mm	Z_2 mm
0.00	0.00	70.00	1.17	13.00	50.00	8.00	37.90	38.00	2.00	12.20	76.00	76.00
0.00	0.00	102.00	1.17	13.00	340.00	8.00	37.90	38.00	200.00	59.50	76.00	76.00
0.00	0.00	270.00	1.12	13.00	1115.00	10.00	37.90	38.00	300.00	48.30	76.00	76.00
0.00	0.00	360.00	1.12	13.00	1523.00	10.00	37.90	38.00	400.00	57.60	76.00	76.00
0.00	0.00	485.00	1.12	12.00	1904.00	11.00	37.90	38.00	400.00	55.40	76.00	76.00
0.00	0.00	562.00	1.11	12.00	2298.00	10.00	37.90	38.00	400.00	53.20	76.00	76.00
0.00	0.00	810.00	1.10	11.00	2380.00	8.00	37.90	38.00	400.00	50.50	76.00	76.00
0.00	0.00	900.00	1.01	15.00	2598.00	10.00	37.90	38.00	500.00	63.90	76.00	76.00
0.00	0.00	985.00	1.01	14.00	2720.00	10.00	37.90	38.00	500.00	65.30	76.00	76.00
0.00	0.00	1055.00	1.02	14.00	2802.00	10.00	37.90	38.00	500.00	65.60	76.00	76.00
0.00	0.00	1180.00	1.03	12.00	2956.00	8.00	37.90	38.00	600.00	80.50	76.00	76.00

TABLE D-25 Experimental Measurements

PHASE 2 TESTS

TEST NO. 01108026

R_{A1} cm	R_{A2} cm	H_A ($mm H_2O$)	p_A bar	T_A °C	H_{LP} ($mm H_2O$)	T_{LP} °C	R_{W1} %	R_{W2} %	M_{WO} lb	t sec	Z_1 mm	Z_2 mm
0.00	0.00	75.00	1.10	16.00	45.00	11.00	44.90	44.90	2.00	16.60	76.00	76.00
0.00	0.00	90.00	1.10	16.00	260.00	10.00	44.90	44.90	100.00	40.00	76.00	76.00
0.00	0.00	130.00	1.09	16.00	320.00	9.00	44.90	44.90	300.00	54.20	76.00	76.00
0.00	0.00	275.00	1.08	15.00	1401.00	9.00	44.90	44.90	400.00	53.50	76.00	76.00
0.00	0.00	355.00	1.08	15.00	1605.00	11.00	44.90	44.90	500.00	61.90	76.00	76.00
0.00	0.00	490.00	1.08	15.00	1727.00	9.00	44.90	44.90	600.00	75.80	76.00	76.00
0.00	0.00	635.00	1.07	13.00	2108.00	9.00	44.90	44.90	600.00	69.00	76.00	76.00
0.00	0.00	860.00	1.08	11.00	2543.00	7.00	44.90	44.90	600.00	69.60	76.00	76.00
0.00	0.00	910.00	1.08	10.00	2720.00	7.00	44.90	44.90	600.00	66.70	76.00	76.00
0.00	0.00	940.00	1.08	8.00	2992.00	6.00	44.90	44.90	600.00	68.90	76.00	76.00
0.00	0.00	1130.00	1.06	7.00	3332.00	6.00	44.90	44.90	600.00	67.90	76.00	76.00

TABLE D-26 Experimental Measurements

PHASE 2 TESTS

TEST NO. 10108027

R_{A1} cm	R_{A2} cm	H_A ($mm\ H_2O$)	p_A bar	T_A °C	H_{LP} ($mm\ H_2O$)	T_{LP} °C	R_{W1} %	R_{W2} %	M_{WO} lb	t sec	Z_1 mm	Z_2 mm
0.00	0.00	220.00	1.08	16.00	65.00	13.00	6.60	7.40	1.00	39.60	24.00	24.00
0.00	0.00	365.00	1.07	15.00	210.00	12.00	6.60	7.40	30.00	79.60	24.00	24.00
0.00	0.00	435.00	1.09	13.00	285.00	10.00	6.60	7.40	40.00	77.50	24.00	24.00
0.00	0.00	480.00	1.11	11.00	310.00	10.00	6.60	7.40	50.00	91.70	24.00	24.00
0.00	0.00	590.00	1.07	16.00	330.00	13.00	6.60	7.40	40.00	77.10	24.00	24.00
0.00	0.00	800.00	1.08	14.00	430.00	17.00	6.60	7.40	100.00	185.50	24.00	24.00
0.00	0.00	890.00	1.09	10.00	650.00	17.00	6.60	7.40	100.00	109.20	24.00	24.00
0.00	0.00	960.00	1.08	9.00	685.00	17.00	6.60	7.40	100.00	105.80	24.00	24.00
0.00	0.00	990.00	1.00	12.00	680.00	17.00	6.60	7.40	100.00	90.80	24.00	24.00
0.00	0.00	1120.00	1.00	14.00	748.00	16.00	6.60	7.40	100.00	101.30	24.00	24.00
0.00	0.00	1325.00	0.99	16.00	884.00	16.00	6.60	7.40	100.00	106.40	24.00	24.00

TABLE D-27 Experimental Measurements

PHASE 2 TESTS

TEST NO. 13108028

R_{A1} cm	R_{A2} cm	H_A (mm_{H_2O})	p_A bar	T_A °C	H_{LP} (mm_{H_2O})	T_{LP} °C	R_{W1} %	R_{W2} %	M_{W_O} lb	t sec	Z_1 mm	Z_2 mm
0.00	0.00	295.00	1.06	15.00	105.00	12.00	6.60	7.40	2.00	53.70	24.00	24.00
0.00	0.00	390.00	1.08	14.00	150.00	11.00	6.60	7.40	2.00	47.50	24.00	24.00
0.00	0.00	390.00	1.09	13.00	250.00	14.00	6.60	7.40	30.00	75.10	24.00	24.00
0.00	0.00	485.00	1.10	12.00	290.00	13.00	6.60	7.40	50.00	60.00	24.00	24.00
0.00	0.00	595.00	1.10	10.00	340.00	12.00	6.60	7.40	100.00	118.50	24.00	24.00
0.00	0.00	770.00	1.04	15.00	550.00	14.00	6.60	7.40	100.00	106.30	24.00	24.00
0.00	0.00	925.00	1.08	11.00	600.00	13.00	6.60	7.40	100.00	117.50	24.00	24.00
0.00	0.00	1005.00	1.08	9.00	680.00	12.00	6.60	7.40	100.00	102.70	24.00	24.00
0.00	0.00	1035.00	1.03	8.00	694.00	12.00	6.60	7.40	100.00	101.90	24.00	24.00

TABLE D-28 Experimental Measurements

PHASE 2 TESTS

TEST NO. 16108029

R_{A1} cm	R_{A2} cm	H_A ($mm H_2O$)	p_A bar	T_A °C	H_{LP} ($mm H_2O$)	T_{LP} °C	R_{W1} %	R_{W2} %	M_{WO} lb	t sec	Z_1 mm	Z_2 mm
0.00	0.00	230.00	1.07	17.00	80.00	13.00	10.10	10.80	2.00	80.20	34.00	34.00
0.00	0.00	320.00	1.08	16.00	350.00	13.00	10.10	10.80	60.00	60.10	34.00	34.00
0.00	0.00	380.00	1.09	14.00	350.00	11.00	10.10	10.80	100.00	97.80	34.00	34.00
0.00	0.00	485.00	1.10	13.00	460.00	11.00	10.10	10.80	100.00	75.90	34.00	34.00
0.00	0.00	550.00	1.11	12.00	530.00	10.00	10.10	10.80	100.00	74.20	34.00	34.00
0.00	0.00	665.00	1.11	11.00	620.00	7.00	10.10	10.80	100.00	74.00	34.00	34.00
0.00	0.00	790.00	1.11	9.00	694.00	7.00	10.10	10.80	100.00	68.60	34.00	34.00
0.00	0.00	825.00	1.06	8.00	721.00	6.00	10.10	10.80	100.00	68.50	34.00	34.00
0.00	0.00	950.00	1.01	14.00	802.00	13.00	10.10	10.80	100.00	60.40	34.00	34.00
0.00	0.00	1060.00	1.00	15.00	898.00	12.00	10.10	10.80	100.00	61.10	34.00	34.00
0.00	0.00	1295.00	0.98	16.00	1061.00	12.00	10.10	10.80	100.00	59.70	34.00	34.00

TABLE D-29 Experimental Measurements

PHASE 2 TESTS

TEST NO. 16108030

R_{A1} cm	R_{A2} cm	H_A ($mm H_2O$)	p_A bar	T_A °C	H_{LP} ($mm H_2O$)	T_{LP} °C	R_{W1} %	R_{W2} %	M_{WO} lb	t sec	Z_1 mm	Z_2 mm
0.00	0.00	170.00	1.09	18.00	55.00	16.00	15.50	16.10	1.00	54.10	45.00	45.00
0.00	0.00	220.00	1.09	18.00	270.00	15.00	15.50	16.10	100.00	75.80	45.00	45.00
0.00	0.00	300.00	1.09	17.00	480.00	14.00	15.50	16.10	100.00	48.40	45.00	45.00
0.00	0.00	370.00	1.09	15.00	610.00	18.00	15.50	16.10	100.00	41.80	45.00	45.00
0.00	0.00	540.00	1.09	14.00	830.00	18.00	15.50	16.10	200.00	72.90	45.00	45.00
0.00	0.00	685.00	1.10	12.00	1020.00	16.00	15.50	16.10	200.00	71.20	45.00	45.00
0.00	0.00	800.00	1.09	10.00	1170.00	14.00	15.50	16.10	200.00	71.10	45.00	45.00
0.00	0.00	920.00	1.00	16.00	938.00	12.00	15.50	16.10	200.00	79.40	45.00	45.00
0.00	0.00	1050.00	1.02	16.00	1061.00	11.00	15.50	16.10	200.00	78.40	45.00	45.00
0.00	0.00	1115.00	1.06	14.00	1115.00	11.00	15.50	16.10	200.00	76.80	45.00	45.00
0.00	0.00	1310.00	1.03	11.00	1306.00	10.00	15.50	16.10	200.00	73.40	45.00	45.00

TABLE D-30 Experimental Measurements

PHASE 2 TESTS

TEST NO. 17108031

R_{A1} cm	R_{A2} cm	H_A ($mm H_2O$)	p_A bar	T_A °C	H_{LP} ($mm H_2O$)	T_{LP} °C	R_{W1} %	R_{W2} %	M_{WO} lb	t sec	Z_1 mm	Z_2 mm
0.00	0.00	140.00	1.08	17.00	80.00	13.00	20.70	21.20	1.00	35.70	60.00	60.00
0.00	0.00	180.00	1.08	17.00	300.00	13.00	20.70	21.20	100.00	51.90	60.00	60.00
0.00	0.00	245.00	1.09	16.00	480.00	12.00	20.70	21.20	200.00	71.70	60.00	60.00
0.00	0.00	330.00	1.10	16.00	600.00	12.00	20.70	21.20	200.00	66.30	60.00	60.00
0.00	0.00	480.00	1.12	15.00	884.00	12.00	20.70	21.20	200.00	57.50	60.00	60.00
0.00	0.00	590.00	1.12	13.00	1074.00	12.00	20.70	21.20	300.00	83.50	60.00	60.00
0.00	0.00	690.00	1.10	12.00	1224.00	9.00	20.70	21.20	300.00	84.20	60.00	60.00
0.00	0.00	835.00	1.10	10.00	1442.00	8.00	20.70	21.20	300.00	81.90	60.00	60.00
0.00	0.00	940.00	1.08	9.00	1564.00	9.00	20.70	21.20	300.00	78.20	60.00	60.00
0.00	0.00	1070.00	1.00	14.00	1632.00	11.00	20.70	21.20	300.00	75.60	60.00	60.00
0.00	0.00	1240.00	1.00	15.00	1809.00	10.00	20.70	21.20	300.00	79.60	60.00	60.00

TABLE D-31 Experimental Measurements

PHASE 2 TESTS

TEST NO. 17108032

R_{A1} cm	R_{A2} cm	H_A ($mm\ H_2O$)	p_A bar	T_A °C	H_{LP} ($mm\ H_2O$)	T_{LP} °C	R_{W1} %	R_{W2} %	M_{WO} lb	t sec	Z_1 mm	Z_2 mm
0.00	0.00	95.00	1.15	18.00	42.00	11.00	26.30	26.70	0.50	26.30	76.00	76.00
0.00	0.00	125.00	1.15	18.00	325.00	11.00	26.30	26.70	100.00	46.70	76.00	76.00
0.00	0.00	220.00	1.14	18.00	610.00	11.00	26.30	26.70	200.00	55.20	76.00	76.00
0.00	0.00	295.00	1.14	17.00	748.00	11.00	26.30	26.70	300.00	74.40	76.00	76.00
0.00	0.00	400.00	1.15	16.00	1115.00	10.00	26.30	26.70	300.00	65.30	76.00	76.00
0.00	0.00	490.00	1.15	15.00	1278.00	10.00	26.30	26.70	300.00	64.90	76.00	76.00
0.00	0.00	610.00	1.12	13.00	1537.00	10.00	26.30	26.70	300.00	61.60	76.00	76.00
0.00	0.00	770.00	1.01	16.00	1727.00	12.00	26.30	26.70	300.00	57.80	76.00	76.00
0.00	0.00	940.00	1.03	16.00	1931.00	11.00	26.30	26.70	400.00	77.60	76.00	76.00
0.00	0.00	1050.00	1.04	14.00	2026.00	9.00	26.30	26.70	400.00	79.90	76.00	76.00
0.00	0.00	1235.00	1.05	12.00	2244.00	8.00	26.30	26.70	400.00	79.20	76.00	76.00

TABLE D-32 Experimental Measurements

PHASE 2 TESTS

TEST NO. 2010 8033

R_{A1} cm	R_{A2} cm	H_A ($mm H_2O$)	p_A bar	T_A °C	H_{LP} ($mm H_2O$)	T_{LP} °C	R_{W1} %	R_{W2} %	M_{W_O} lb	t sec	Z_1 mm	Z_2 mm
0.00	0.00	110.00	1.13	17.00	45.00	10.00	32.80	33.10	1.00	24.80	76.00	76.00
0.00	0.00	125.00	1.13	16.00	270.00	12.00	32.80	33.10	100.00	44.00	76.00	76.00
0.00	0.00	170.00	1.12	16.00	565.00	8.00	32.80	33.10	200.00	47.90	76.00	76.00
0.00	0.00	240.00	1.11	15.00	735.00	8.00	32.80	33.10	300.00	59.20	76.00	76.00
0.00	0.00	340.00	1.11	14.00	993.00	8.00	32.80	33.10	400.00	75.70	76.00	76.00
0.00	0.00	460.00	1.12	12.00	1455.00	8.00	32.80	33.10	400.00	65.60	76.00	76.00
0.00	0.00	585.00	1.12	11.00	1714.00	7.00	32.80	33.10	400.00	65.70	76.00	76.00
0.00	0.00	700.00	1.11	9.00	1931.00	7.00	32.80	33.10	400.00	64.80	76.00	76.00
0.00	0.00	860.00	1.00	14.00	2122.00	9.00	32.80	33.10	400.00	60.90	76.00	76.00
0.00	0.00	1015.00	0.99	13.00	2122.00	7.00	32.80	33.10	400.00	64.10	76.00	76.00
0.00	0.00	1110.00	0.98	13.00	2421.00	7.00	32.80	33.10	400.00	62.20	76.00	76.00

TABLE D-33 Experimental Measurements

PHASE 2 TESTS

TEST NO. 20108034

R_{A1} cm	R_{A2} cm	H_A ($mm H_2O$)	p_A bar	T_A °C	H_{LP} ($mm H_2O$)	T_{LP} °C	R_{W1} %	R_{W2} %	M_{W_O} lb	t sec	Z_1 mm	Z_2 mm
0.00	0.00	95.00	1.11	17.00	215.00	10.00	37.90	38.00	100.00	62.00	76.00	76.00
0.00	0.00	110.00	1.10	17.00	435.00	10.00	37.90	38.00	100.00	29.20	76.00	76.00
0.00	0.00	205.00	1.10	17.00	780.00	9.00	37.90	38.00	200.00	35.10	76.00	76.00
0.00	0.00	255.00	1.09	16.00	1020.00	9.00	37.90	38.00	400.00	68.20	76.00	76.00
0.00	0.00	345.00	1.09	15.00	1346.00	9.00	37.90	38.00	400.00	60.80	76.00	76.00
0.00	0.00	435.00	1.10	15.00	1578.00	9.00	37.90	38.00	400.00	60.20	76.00	76.00
0.00	0.00	575.00	1.10	13.00	1945.00	8.00	37.90	38.00	400.00	56.50	76.00	76.00
0.00	0.00	700.00	1.10	11.00	2162.00	7.00	37.90	38.00	400.00	55.10	76.00	76.00
0.00	0.00	780.00	1.11	10.00	2380.00	7.00	37.90	38.00	400.00	54.50	76.00	76.00
0.00	0.00	950.00	1.08	9.00	2625.00	6.00	37.90	38.00	400.00	54.20	76.00	76.00
0.00	0.00	1160.00	1.02	8.00	2910.00	6.00	37.90	38.00	400.00	52.90	76.00	76.00

TABLE D-34 Experimental Measurements

PHASE 2 TESTS

TEST NO. 21108035

R_{A1} cm	R_{A2} cm	H_A ($mm H_2O$)	p_A bar	T_A °C	H_{LP} ($mm H_2O$)	T_{LP} °C	R_{W1} %	R_{W2} %	M_{WO} lb	t sec	Z_1 mm	Z_2 mm
0.00	0.00	340.00	1.06	16.00	115.00	13.00	5.80	7.40	5.00	112.00	22.00	25.00
0.00	0.00	330.00	1.08	16.00	120.00	8.00	7.00	7.80	5.00	112.80	25.00	25.00
0.00	0.00	335.00	1.11	15.00	330.00	8.00	10.10	10.80	100.00	103.70	32.00	32.00
0.00	0.00	330.00	1.15	14.00	500.00	9.00	15.50	16.10	100.00	45.60	50.00	50.00
0.00	0.00	340.00	1.15	14.00	680.00	10.00	20.70	21.20	300.00	82.50	76.00	76.00
0.00	0.00	330.00	1.16	13.00	966.00	9.00	26.30	26.70	300.00	66.30	76.00	76.00
0.00	0.00	330.00	1.16	13.00	1142.00	9.00	32.80	33.10	300.00	53.10	76.00	76.00
0.00	0.00	330.00	1.15	13.00	1523.00	9.00	37.90	38.00	400.00	62.50	76.00	76.00
0.00	0.00	325.00	1.13	13.00	1673.00	9.00	44.90	44.90	500.00	62.10	76.00	76.00

TABLE D-35 Experimental Measurements

PHASE 2 TESTS

TEST NO. 27108036

R_{A1} cm	R_{A2} cm	H_A ($mm H_2O$)	p_A bar	T_A °C	H_{LP} ($mm H_2O$)	T_{LP} °C	R_{W1} %	R_{W2} %	M_{WO} lb	t sec	Z_1 mm	Z_2 mm
0.00	0.00	55.00	1.10	19.00	62.00	12.00	44.90	44.90	5.00	28.70	76.00	76.00
0.00	0.00	65.00	1.10	19.00	300.00	11.00	44.90	44.90	100.00	30.70	76.00	76.00
0.00	0.00	100.00	1.10	18.00	525.00	11.00	44.90	44.90	400.00	81.10	76.00	76.00
0.00	0.00	145.00	1.10	18.00	725.00	10.00	44.90	44.90	400.00	65.80	76.00	76.00
0.00	0.00	205.00	1.11	17.00	1034.00	10.00	44.90	44.90	400.00	57.90	76.00	76.00
0.00	0.00	280.00	1.11	16.00	1374.00	10.00	44.90	44.90	400.00	53.90	76.00	76.00
0.00	0.00	465.00	1.10	15.00	1958.00	10.00	44.90	44.90	400.00	49.70	76.00	76.00
0.00	0.00	625.00	1.10	13.00	2516.00	9.00	44.90	44.90	500.00	57.50	76.00	76.00
0.00	0.00	775.00	1.10	12.00	2856.00	8.00	44.90	44.90	500.00	56.00	76.00	76.00
0.00	0.00	870.00	1.03	11.00	2938.00	7.00	44.90	44.90	500.00	55.50	76.00	76.00
0.00	0.00	1060.00	1.01	10.00	2182.00	7.00	44.90	44.90	500.00	55.10	76.00	76.00

TABLE D-36 Experimental Measurements

APPENDIX E

AIR/WATER DATA (PHASE 1 TESTS)

STRATHCLYDE DATA

PHASE 1 TESTS

Water First Tests

TABLE E-1 Liquid Bridging

M_{wi} =0.4031 kg/s J^*_w = 0.0088 Fr_{w_z} = 1.1008

TEST NO. 02057901

M_A kg/s	J^*_A	M_{WO} kg/s	$M_{W_{LP}}$ kg/s
0.0784	0.0487	0.0020	0.4012
0.0966	0.0597	0.0048	0.3984
0.1162	0.0717	0.0111	0.3921
0.1440	0.0881	0.0868	0.3163
0.1700	0.1031	0.1924	0.2107
0.1934	0.1178	0.2577	0.1455
0.2074	0.1248	0.3232	0.0799
0.2433	0.1452	0.3975	0.0057
0.2547	0.1509	0.3954	0.0078
0.2920	0.1745	0.3954	0.0078
0.3039	0.1812	0.3989	0.0043

M_{wi} =0.5702 kg/s J^*_w = 0.0125 Fr_{w_z} = 1.3900

TEST NO. 05047902

M_A kg/s	J^*_A	M_{WO} kg/s	$M_{W_{LP}}$ kg/s
0.0575	0.0357	0.0007	0.5695
0.0747	0.0463	0.0010	0.5692
0.0827	0.0513	0.0025	0.5677
0.0971	0.0601	0.0056	0.5646
0.1112	0.0686	0.0118	0.5584
0.1285	0.0789	0.1004	0.4698
0.1552	0.0941	0.2529	0.3172
0.1872	0.1130	0.3198	0.2504
0.1993	0.1195	0.4332	0.1370
0.2013	0.1213	0.4499	0.1203
0.2114	0.1285	0.3637	0.2065
0.2400	0.1448	0.4473	0.1229
0.2626	0.1575	0.4825	0.0877

STRATHCLYDE DATA PHASE 1 TESTS

Water First Tests

TABLE E-2 Liquid Bridging

M_{wi} = 0.7024 kg/s J^*_w = 0.0154 Fr_{w_z} = 1.4099

TEST NO. 02057903

M_A kg/s	J^*_A	M_{WO} kg/s	$M_{W_{LP}}$ kg/s
0.0074	0.0046	0.0000	0.7024
0.0525	0.0326	0.0000	0.7024
0.0819	0.0507	0.0051	0.6973
0.1003	0.0616	0.0153	0.6871
0.1288	0.0789	0.0924	0.6100
0.1331	0.0815	0.2064	0.4960
0.1634	0.0994	0.3585	0.3439
0.1965	0.1188	0.4913	0.2111
0.2129	0.1279	0.5799	0.1225
0.2419	0.1443	0.6213	0.0812
0.2955	0.1738	0.7010	0.0015

M_{wi} = 1.0567 kg/s J^*_w = 0.0232 Fr_{w_z} = 1.8085

TEST NO. 06047904

M_A kg/s	J^*_A	M_{WO} kg/s	$M_{W_{LP}}$ kg/s
0.0594	0.0369	0.0081	1.0486
0.0852	0.0525	0.1683	0.8884
0.1030	0.0634	0.3389	0.7178
0.1363	0.0832	0.5662	0.4905
0.1669	0.1012	0.7142	0.3425
0.1990	0.1196	0.8430	0.2137
0.2289	0.1365	0.9293	0.1274
0.2522	0.1492	0.9649	0.0918
0.2642	0.1556	0.9848	0.0719

STRATHCLYDE DATA PHASE 1 TESTS

Water First Tests

TABLE E-3 Liquid Bridging

M_{wi} = 1.6103 kg/s J^*_w = 0.0353 Fr_{w_z} = 1.6010

TEST NO. 09047905

M_A kg/s	J^*_A	M_{WO} kg/s	$M_{W_{LP}}$ kg/s
0.0503	0.0311	0.0155	1.5948
0.0623	0.0385	0.3203	1.2900
0.0971	0.0596	0.6352	0.9751
0.1269	0.0767	0.8589	0.7514
0.1321	0.0800	0.8789	0.7314
0.1581	0.0943	1.3203	0.2900
0.2002	0.1175	1.4606	0.1497
0.2302	0.1338	1.5452	0.0651
0.2520	0.1453	1.5693	0.0411
0.2563	0.1482	1.5638	0.0465
0.2591	0.1486	1.5941	0.0162

M_{wi} = 2.1345 kg/s J^*_w = 0.0468 Fr_{w_z} = 0.6553

TEST NO. 10047906

M_A kg/s	J^*_A	M_{WO} kg/s	$M_{W_{LP}}$ kg/s
0.0372	0.0230	0.1114	2.0231
0.0538	0.0331	0.4930	1.6416
0.0930	0.0567	1.0331	1.1015
0.1324	0.0799	1.5270	0.6075
0.1558	0.0923	1.7925	0.3420
0.1904	0.1117	2.0583	0.0762
0.2282	0.1304	2.0851	0.0494
0.2299	0.1337	2.0291	0.1054
0.2309	0.1337	2.0246	0.1099
0.2679	0.1536	2.0996	0.0349
0.2877	0.1634	2.1317	0.0028

STRATHCLYDE DATA

PHASE 1 TESTS

Water First Tests

TABLE E-4 Liquid Bridging

M_{wi} = 2.7065 kg/s J^*_w = 0.0594 Fr_{w_z} = 0.8085

TEST NO. 17047907

M_A kg/s	J^*_A	M_{WO} kg/s	$M_{W_{LP}}$ kg/s
0.0072	0.0044	0.0013	2.7052
0.0156	0.0096	0.1032	2.6033
0.0305	0.0188	0.4327	2.2738
0.0559	0.0343	0.9568	1.7497
0.0939	0.0569	1.6828	1.0237
0.1168	0.0702	2.0246	0.6819
0.1549	0.0906	2.3953	0.3112
0.1836	0.1057	1.8976	0.8090
0.2138	0.1218	2.6177	0.0888
0.2365	0.1333	2.6483	0.0583
0.2583	0.1442	2.6677	0.0388

M_{wi} = 3.3710 kg/s J^*_w = 0.0739 Fr_{w_z} = 1.2542

TEST NO. 18047908

M_A kg/s	J^*_A	M_{WO} kg/s	$M_{W_{LP}}$ kg/s
0.0081	0.0050	0.3359	3.0351
0.0198	0.0122	0.6270	2.7441
0.0278	0.0172	0.8655	2.5055
0.0430	0.0264	1.4261	1.9449
0.0571	0.0349	1.7750	1.5960
0.0971	0.0583	2.5289	0.8421
0.1203	0.0714	2.7541	0.6169
0.1522	0.0884	2.9545	0.4165
0.1816	0.1038	3.1494	0.2216
0.2045	0.1163	3.1582	0.2129
0.2337	0.1309	3.2394	0.1316
0.2630	0.1464	3.2768	0.0942

STRATHCLYDE DATA

PHASE 1 TESTS

Water First Tests

TABLE E-5 Liquid Bridging

M_{wi} = 3.8878 kg/s J^*_w = 0.0853 Fr_{w_z} = 1.6682

TEST NO. 19047909

M_A kg/s	J^*_A	M_{WO} kg/s	$M_{W_{LP}}$ kg/s
0.0431	0.0264	1.5638	2.3240
0.0604	0.0363	2.7909	1.0969
0.1094	0.0644	3.2221	0.6657
0.1479	0.0851	3.5102	0.3776
0.1657	0.0950	3.5376	0.3502
0.2030	0.1146	3.6515	0.2363
0.2192	0.1205	3.6281	0.2597
0.2447	0.1355	3.8004	0.0874
0.2520	0.1395	3.7584	0.1294

M_{wi} = 4.6027 kg/s J^*_w = 0.1009 Fr_{w_z} = 2.3381

TEST NO. 23047910

M_A kg/s	J^*_A	M_{WO} kg/s	$M_{W_{LP}}$ kg/s
0.0383	0.0229	2.3080	2.2947
0.0450	0.0274	2.2231	2.3796
0.0601	0.0357	2.6625	1.9402
0.1132	0.0655	3.2745	1.3282
0.1283	0.0738	3.4357	1.1670
0.1665	0.0933	4.0402	0.5625
0.1985	0.1088	4.2286	0.3741
0.2421	0.1296	4.2946	0.3081
0.2580	0.1416	4.1531	0.4496
0.2673	0.1499	4.0931	0.5096

STRATHCLYDE DATA

PHASE 1 TESTS

Air First Tests

TABLE E-6 LIQUID BRIDGING

M_A = 0.0081 kg/s

J_A^* = 0.0051

TEST NO. 12077911

M_{wi} kg/s	M_{wo} kg/s	$M_{W_{LP}}$ kg/s	J_W^*	Fr_{w_z}
0.5413	0.0000	0.5413	0.0119	1.0868
0.8839	0.0000	0.8839	0.0194	1.1429
2.8510	0.0808	2.7701	0.0625	0.9778
3.1416	0.1477	2.9939	0.0689	1.0893
3.3848	0.3099	3.0749	0.0742	1.2648
3.9278	0.4732	3.4545	0.0861	1.7026
4.4778	0.6535	3.8243	0.0982	2.2129
4.7761	0.6388	4.1374	0.1047	2.5180
5.2372	0.7559	4.4813	0.1149	3.0271
5.6216	0.8525	4.7691	0.1233	3.4878

M_A = 0.0282 kg/s

J_A^* = 0.0174

TEST NO. 12077912

M_{wi} kg/s	M_{wo} kg/s	$M_{W_{LP}}$ kg/s	J_W^*	Fr_{w_z}
0.5452	0.0000	0.5452	0.0120	1.3998
2.2292	0.0838	2.1454	0.0489	0.6989
2.5148	0.3239	2.1909	0.0552	0.7284
2.7835	0.4922	2.2913	0.0610	0.8923
2.9960	0.6934	2.3025	0.0657	1.0337
3.2877	0.9351	2.3527	0.0721	1.2191
3.9746	1.5461	2.4285	0.0872	1.7445
4.4274	2.0186	2.4088	0.0971	2.1634
4.7014	2.2790	2.4225	0.1031	2.4397
5.7251	2.5768	3.1483	0.1256	3.6174

STRATHCLYDE DATA PHASE 1 TESTS

Air First Tests

TABLE E-7 LIQUID BRIDGING

M_A = 0.0741 kg/s J_A^* = 0.0451

TEST NO. 17077913

M_{wi} kg/s	M_{wo} kg/s	$M_{W_{LP}}$ kg/s	J_W^*	Fr_{w_z}
1.2258	0.0881	1.1377	0.0269	1.2218
1.8520	0.3837	1.4683	0.0406	1.0838
2.3242	0.8098	1.5143	0.0510	0.6221
2.8848	1.2884	1.5964	0.0633	0.9185
3.2877	1.8857	1.4020	0.0721	1.1930
3.6803	2.2123	1.4681	0.0807	1.4949
3.9774	2.8169	1.1606	0.0872	1.4813
4.2769	2.9401	1.3367	0.0938	1.7127
4.7785	3.0957	1.6829	0.1048	2.1380

M_A = 0.1041 kg/s J_A^* = 0.0636

TEST NO. 13087914

M_{wi} kg/s	M_{wo} kg/s	$M_{W_{LP}}$ kg/s	J_W^*	Fr_{w_z}
0.4737	0.0065	0.4672	0.0104	1.0325
0.8839	0.2160	0.6679	0.0194	1.2653
1.1098	0.4373	0.6724	0.0243	1.0870
1.2236	0.4973	0.7263	0.0268	0.9254
1.7796	0.8573	0.9223	0.0390	0.4457
2.1345	1.2686	0.8660	0.0468	0.5247
2.4912	1.7973	0.6939	0.0546	0.6851
2.9234	2.3227	0.6006	0.0641	0.9433
3.5587	3.0234	0.5353	0.0780	1.3982
3.7768	3.0602	0.7166	0.0828	1.5753
4.6268	3.2394	1.3874	0.1015	2.3627

STRATHCLYDE DATA

PHASE 1 TESTS

Air First Tests

TABLE E-8 LIQUID BRIDGING

$M_A = 0.1419$ kg/s

$J_A^* = 0.0851$

TEST NO. 14087915

M_{wi} kg/s	M_{wo} kg/s	$M_{W_{LP}}$ kg/s	J_W^*	Fr_{w_z}
0.9220	0.1564	0.3656	0.0114	1.1638
0.8839	0.4956	0.3882	0.0194	0.9417
1.4753	1.0629	0.4124	0.0324	0.4512
1.7116	1.2766	0.4350	0.0375	0.4634
2.3242	1.8787	0.4455	0.0510	0.5962
2.9235	2.5886	0.3349	0.0641	0.9433
3.4835	3.1826	0.3010	0.0764	1.3393
4.0770	3.2394	0.8376	0.0894	1.8345
4.6750	3.5710	1.1041	0.1025	2.4127

$M_A = 0.1737$ kg/s

$J_A^* = 0.1023$

TEST NO. 15087916

M_{wi} kg/s	M_{wo} kg/s	$M_{W_{LP}}$ kg/s	J_W^*	Fr_{w_z}
0.5413	0.3773	0.1640	0.0119	0.8371
0.8839	0.6630	0.2208	0.0194	0.8222
1.3399	1.0191	0.3208	0.0294	0.7054
1.8279	1.5603	0.2676	0.0401	0.4106
2.3242	2.1751	0.1490	0.0510	0.5962
2.8992	2.6677	0.2315	0.0636	0.9277
3.4586	3.2768	0.1818	0.0758	1.3203
3.9746	3.5710	0.4036	0.0872	1.7445

STRATHCLYDE DATA PHASE 1 TESTS

Air First Tests

TABLE E-9 LIQUID BRIDGING

M_A =0.2399 kg/s J_A^* =0.1379

TEST NO. 21087917

M_{wi} kg/s	M_{wo} kg/s	$M_{W_{LP}}$ kg/s	J_W^*	Fr_{w_z}
0.4803	0.4375	0.0429	0.0105	0.8576
0.8384	0.7739	0.0645	0.0184	0.6476
1.4325	1.3437	0.0887	0.0314	0.3753
2.2526	2.1494	0.1032	0.0494	0.5844
2.8992	2.8703	0.0289	0.0636	0.9680
3.4835	3.3347	0.1489	0.0764	1.3975
4.0770	3.9096	0.1674	0.0894	1.9142
4.7761	4.5733	0.2029	0.1047	2.6275
5.7528	5.1536	0.5993	0.1262	3.8115

APPENDIX F

AIR/WATER DATA (PHASE 2 TESTS)

STRATHCLYDE DATA

PHASE 2 TESTS

Water First Tests

TABLE F-1 Liquid Bridging

M_{wi} = 0.5711 kg/s J^*_w = 0.0125 Fr_{w_z} = 1.5198

TEST NO. 22098018

M_A kg/s	J^*_A	M_{WO} kg/s	$M_{W_{LP}}$ kg/s
0.1359	0.0840	0.0189	0.5523
0.1472	0.0903	0.0206	0.5505
0.1567	0.0957	0.0945	0.4767
0.1706	0.1039	0.0248	0.5464
0.1765	0.1072	0.2492	0.3220
0.1964	0.1189	0.2878	0.2834
0.2171	0.1306	0.3830	0.1881
0.2357	0.1412	0.4165	0.1547
0.2524	0.1504	0.2992	0.2720
0.2585	0.1535	0.3040	0.2672
0.2839	0.1679	0.3465	0.2247

M_{wi} = 0.6998 kg/s J^*_w = 0.0153 Fr_{w_z} = 1.6169

TEST NO. 23098019

M_A kg/s	J^*_A	M_{WO} kg/s	$M_{W_{LP}}$ kg/s
0.1298	0.0796	0.0150	0.6848
0.1488	0.0910	0.1400	0.5598
0.1621	0.0987	0.1908	0.5090
0.1848	0.1124	0.2646	0.4352
0.1948	0.1180	0.2999	0.3998
0.2126	0.1283	0.3693	0.3305
0.2337	0.1401	0.4086	0.2912
0.2492	0.1490	0.4035	0.2963
0.2612	0.1554	0.4685	0.2313
0.2654	0.1808	0.4744	0.2254
0.2815	0.1666	0.4892	0.2106

STRATHCLYDE DATA PHASE 2 TESTS

Water First Tests

TABLE F-2 Liquid Bridging

M_{wi} = 1.0549 kg/s J^*_w = 0.0231 Fr_{w_z} = 1.0772

TEST NO. 24098020

M_A kg/s	J^*_A	M_{WO} kg/s	$M_{W_{LP}}$ kg/s
0.1215	0.0753	0.0118	1.0431
0.1335	0.0811	0.2553	0.7997
0.1549	0.0938	0.5477	0.5072
0.1745	0.1051	0.6470	0.4080
0.1875	0.1125	0.6851	0.3699
0.2162	0.1288	0.7447	0.3102
0.2296	0.1360	0.8084	0.2465
0.2411	0.1424	0.7956	0.2593
0.2487	0.1467	0.8216	0.2333
0.2586	0.1518	0.8337	0.2213
0.2810	0.1636	0.8840	0.1709

M_{wi} = 1.6057 kg/s J^*_w = 0.0352 Fr_{w_z} = 0.5248

TEST NO. 24098021

M_A kg/s	J^*_A	M_{WO} kg/s	$M_{W_{LP}}$ kg/s
0.1116	0.0686	0.0094	1.5962
0.1221	0.0740	0.5309	1.0748
0.1397	0.0841	0.8705	0.7352
0.1645	0.0983	1.0462	0.5595
0.1762	0.1049	1.1826	0.4231
0.1888	0.1121	1.2324	0.3733
0.2101	0.1239	1.2528	0.3529
0.2296	0.1343	1.2811	0.3246
0.2433	0.1417	1.2847	0.3209
0.2555	0.1479	1.3358	0.2698
0.2792	0.1600	1.2633	0.3424

STRATHCLYDE DATA

PHASE 2 TESTS

Water First Tests

TABLE F-3 Liquid Bridging

M_{wi} = 2.1358 kg/s J^*_w = 0.0468 Fr_{w_z} = 0.5520

TEST NO. 25098022

M_A kg/s	J^*_A	M_{WO} kg/s	$M_{W_{LP}}$ kg/s
0.0988	0.0608	0.0134	2.1224
0.1094	0.0665	0.6497	1.4861
0.1276	0.0769	1.1008	1.0351
0.1486	0.0888	1.3997	0.7361
0.1684	0.0998	1.5339	0.6020
0.1874	0.1101	1.6491	0.4867
0.2096	0.1221	1.6818	0.4541
0.2328	0.1346	1.6694	0.4665
0.2459	0.1416	1.7157	0.4201
0.2599	0.1482	1.6735	0.4623
0.2732	0.1551	1.7555	0.3803

M_{wi} = 2.7072 kg/s J^*_w = 0.0594 Fr_{w_z} = 0.4777

TEST NO. 26098023

M_A kg/s	J^*_A	M_{WO} kg/s	$M_{W_{LP}}$ kg/s
0.0690	0.0424	0.0045	2.7026
0.0841	0.0516	0.0174	2.6898
0.1003	0.0604	1.1629	1.5443
0.1186	0.0709	1.6284	1.0788
0.1448	0.0857	2.0429	0.6643
0.1579	0.0927	2.1426	0.5646
0.1746	0.1013	2.2488	0.4583
0.1978	0.1131	2.3498	0.3574
0.2294	0.1297	2.4027	0.3045
0.2531	0.1417	2.4481	0.2591
0.2712	0.1506	2.4681	0.2391

STRATHCLYDE DATA PHASE 2 TESTS

Water First Tests

TABLE F-4 Liquid Bridging

M_{wi} = 3.3712 kg/s J^*_w = 0.0739 Fr_{w_z} = 0.7407

TEST NO. 30098024

M_A kg/s	J^*_A	M_{WO} kg/s	$M_{W_{LP}}$ kg/s
0.0553	0.0339	0.0056	3.3656
0.0794	0.0481	0.9753	2.3959
0.1019	0.0609	1.7949	1.5763
0.1465	0.0853	2.5431	0.8281
0.1709	0.0983	2.8081	0.5630
0.1924	0.1092	2.9497	0.4215
0.1991	0.1126	2.9836	0.3875
0.2184	0.1222	3.0386	0.3326
0.2303	0.1279	3.0540	0.3172
0.2432	0.1344	3.0643	0.3069
0.2661	0.1454	3.1223	0.2489

M_{wi} = 3.8858 kg/s J^*_w = 0.0852 Fr_{w_z} = 0.9841

TEST NO. 30098025

M_A kg/s	J^*_A	M_{WO} kg/s	$M_{W_{LP}}$ kg/s
0.0687	0.0420	0.0743	3.8115
0.0827	0.0499	1.5244	2.3614
0.1320	0.0771	2.8169	1.0690
0.1519	0.0872	3.1494	0.7364
0.1760	0.0996	3.2745	0.6114
0.2042	0.1136	3.4099	0.4760
0.2248	0.1242	3.5922	0.2937
0.2297	0.1263	3.5486	0.3372
0.2402	0.1315	3.4725	0.4133
0.2488	0.1358	3.4567	0.4292
0.2640	0.1432	3.3802	0.5056

STRATHCLYDE DATA PHASE 2 TESTS

Water First Tests

TABLE F-5 Liquid Bridging

M_{wi} = 4.6013 kg/s J^*_w = 0.1009 Fr_{w_z} = 1.3799

TEST NO. 01108026

M_A kg/s	J^*_A	M_{WO} kg/s	$M_{W_{LP}}$ kg/s
0.0696	0.0428	0.0546	4.5467
0.0761	0.0463	1.1338	3.4675
0.0910	0.0551	2.5102	2.0911
0.1315	0.0758	3.3908	1.2106
0.1490	0.0854	3.6633	0.9380
0.1743	0.0991	3.5898	1.0115
0.1978	0.1107	3.9436	0.6577
0.2303	0.1262	3.9096	0.6917
0.2370	0.1290	4.0796	0.5217
0.2415	0.1299	3.9493	0.6520
0.2628	0.1396	4.0075	0.5938

STRATHCLYDE DATA PHASE 2 TESTS

Air First Tests

TABLE F-6 Liquid Bridging

M_{wi} = 0.6998 kg/s J^*_w = 0.0153 Fr_{w_z} = 1.3774

TEST NO. 10108027

M_A kg/s	J^*_A	M_{WO} kg/s	$M_{W_{LP}}$ kg/s
0.1177	0.0725	0.0115	0.6883
0.1507	0.0921	0.1709	0.5289
0.1655	0.1004	0.2341	0.4657
0.1750	0.1061	0.2473	0.4525
0.1900	0.1156	0.2353	0.4645
0.2213	0.1350	0.2445	0.4553
0.2351	0.1420	0.4153	0.2845
0.2435	0.1469	0.4287	0.2711
0.2410	0.1454	0.4995	0.2003
0.2547	0.1529	0.4477	0.2521
0.2741	0.1635	0.4262	0.2735

M_{wi} = 0.6998 kg/s J^*_w = 0.0153 Fr_{w_z} = 1.3774

TEST NO. 13108028

M_A kg/s	J^*_A	M_{WO} kg/s	$M_{W_{LP}}$ kg/s
0.1354	0.0832	0.0169	0.6829
0.1562	0.0956	0.0191	0.6807
0.1569	0.0960	0.1812	0.5186
0.1752	0.1068	0.3779	0.3219
0.1941	0.1179	0.3827	0.3171
0.2148	0.1296	0.4266	0.2731
0.2384	0.1433	0.3860	0.3138
0.2489	0.1488	0.4416	0.2582
0.2498	0.1492	0.4451	0.2547

STRATHCLYDE DATA PHASE 2 TESTS

Air First Tests

TABLE F-7 Liquid Bridging

M_{wi} = 1.0549 kg/s J^*_w = 0.0231 Fr_{w_z} = 0.8643

TEST NO. 16108029

M_A kg/s	J^*_A	M_{WO} kg/s	$M_{W_{LP}}$ kg/s
0.1198	0.0738	0.0113	1.0436
0.1414	0.0860	0.4528	0.6022
0.1546	0.0937	0.4637	0.5912
0.1749	0.1054	0.5975	0.4574
0.1866	0.1120	0.6112	0.4437
0.2049	0.1218	0.6129	0.4421
0.2235	0.1323	0.6611	0.3938
0.2258	0.1333	0.6621	0.3929
0.2361	0.1407	0.7509	0.3041
0.2477	0.1467	0.7422	0.3127
0.2704	0.1590	0.7597	0.2953

M_{wi} = 1.6057 kg/s J^*_w = 0.0352 Fr_{w_z} = 0.7464

TEST NO. 16108030

M_A kg/s	J^*_A	M_{WO} kg/s	$M_{W_{LP}}$ kg/s
0.1035	0.0642	0.0084	1.5973
0.1175	0.0720	0.5983	1.0074
0.1371	0.0830	0.9370	0.6687
0.1524	0.0924	1.0850	0.5207
0.1835	0.1101	1.2442	0.3615
0.2071	0.1228	1.2739	0.3318
0.2233	0.1311	1.2757	0.3300
0.2312	0.1366	1.1424	0.4633
0.2474	0.1452	1.1569	0.4487
0.2580	0.1510	1.1810	0.4246
0.2778	0.1610	1.2357	0.3699

STRATHCLYDE DATA PHASE 2 TESTS

Air First Tests

TABLE F-8 Liquid Bridging

M_{wi} = 2.1358 kg/s J^*_w = 0.0468 Fr_{w_z} = 0.5252

TEST NO. 17108031

M_A kg/s	J^*_A	M_{WO} kg/s	$M_{W_{LP}}$ kg/s
0.0941	0.0579	0.0127	2.1231
0.1064	0.0649	0.8738	1.2620
0.1243	0.0750	1.2650	0.8708
0.1442	0.0865	1.3681	0.7678
0.1742	0.1032	1.5774	0.5584
0.1932	0.1135	1.6294	0.5064
0.2078	0.1206	1.6158	0.5200
0.2285	0.1312	1.6612	0.4746
0.2411	0.1380	1.7398	0.3960
0.2493	0.1427	1.7997	0.3362
0.2668	0.1514	1.7092	0.4266

M_{wi} = 2.7072 kg/s J^*_w = 0.0594 Fr_{w_z} = 0.4777

TEST NO. 17108032

M_A kg/s	J^*_A	M_{WO} kg/s	$M_{W_{LP}}$ kg/s
0.0788	0.0485	0.0086	2.6986
0.0902	0.0548	0.9711	1.7361
0.1189	0.0712	1.6432	1.0640
0.1375	0.0818	1.8287	0.8785
0.1602	0.0936	2.0835	0.6236
0.1772	0.1028	2.0964	0.6108
0.1964	0.1127	2.2087	0.4985
0.2128	0.1216	2.3539	0.3533
0.2353	0.1331	2.3377	0.3695
0.2495	0.1401	2.2704	0.4368
0.2710	0.1506	2.2905	0.4167

STRATHCLYDE DATA PHASE 2 TESTS

Air First Tests

TABLE F-9 Liquid Bridging

M_{wi} = 3.3712 kg/s J^*_w = 0.0739 Fr_{w_z} = 0.7407

TEST NO. 2010 8033

M_A kg/s	J^*_A	M_{WO} kg/s	$M_{W_{LP}}$ kg/s
0.0845	0.0519	0.0183	3.3529
0.0901	0.0549	1.0307	2.3405
0.1046	0.0624	1.8936	1.4776
0.1239	0.0734	2.2982	1.0730
0.1472	0.0861	2.3964	0.9748
0.1715	0.0984	2.7653	0.6058
0.1931	0.1094	2.7611	0.6101
0.2108	0.1184	2.7995	0.5717
0.2246	0.1256	2.9788	0.3924
0.2429	0.1354	2.8300	0.5411
0.2528	0.1392	2.9165	0.4547

M_{wi} = 3.8858 kg/s J^*_w = 0.0852 Fr_{w_z} = 0.9841

TEST NO. 20108034

M_A kg/s	J^*_A	M_{WO} kg/s	$M_{W_{LP}}$ kg/s
0.0782	0.0476	0.7315	3.1544
0.0839	0.0506	1.6082	2.2776
0.1140	0.0675	2.5125	1.3733
0.1268	0.0743	2.6599	1.2259
0.1473	0.0850	2.9836	0.9022
0.1653	0.0945	3.0134	0.8725
0.1899	0.1068	3.2107	0.6751
0.2096	0.1166	3.2923	0.5935
0.2217	0.1223	3.3285	0.5573
0.2423	0.1322	3.3470	0.5389
0.2630	0.1419	3.4292	0.4566

STRATHCLYDE DATA

PHASE 2 TESTS

Air First Tests

TABLE F-10 Liquid Bridging

M_{wi} = 4.6013 kg/s J^*_w = 0.1009 Fr_{w_z} = 1.3799

TEST NO. 21108035

M_A kg/s	J^*_A	M_{WO} kg/s	$M_{W_{LP}}$ kg/s
0.0394	0.0366	0.0790	4.5223
0.0645	0.0392	1.4772	3.1241
0.0799	0.0480	2.2368	2.3645
0.0960	0.0571	2.7569	1.8444
0.1143	0.0670	3.1331	1.4682
0.1334	0.0771	3.3656	1.2357
0.1707	0.0963	3.6500	0.9513
0.1977	0.1089	3.9436	0.6577
0.2197	0.1192	4.0492	0.5521
0.2287	0.1235	4.0857	0.5156
0.2505	0.1393	4.1154	0.4859

M_A = 0.1461 J^*_A = 0.0866

TEST NO. 27108036

M_{wi} kg/s	M_{wo} kg/s	$M_{W_{LP}}$ kg/s	J^*_W	Fr_{w_z}
0.6590	0.0202	0.6388	0.0145	1.3374
0.7410	0.0201	0.7209	0.0162	1.3249
1.0549	0.4373	0.6176	0.0231	1.0772
1.6057	0.9945	0.6111	0.0352	0.5248
2.1358	1.6491	0.4867	0.0468	0.2973
2.7072	2.0521	0.6551	0.0594	0.4777
3.3712	2.5622	0.8089	0.0739	0.7407
3.8858	2.9025	0.9834	0.0852	0.9841
4.6013	3.6515	0.9498	0.1009	1.3799

APPENDIX G

PENETRATION CHARACTERISTICS

FOR PHASE 1 DATA

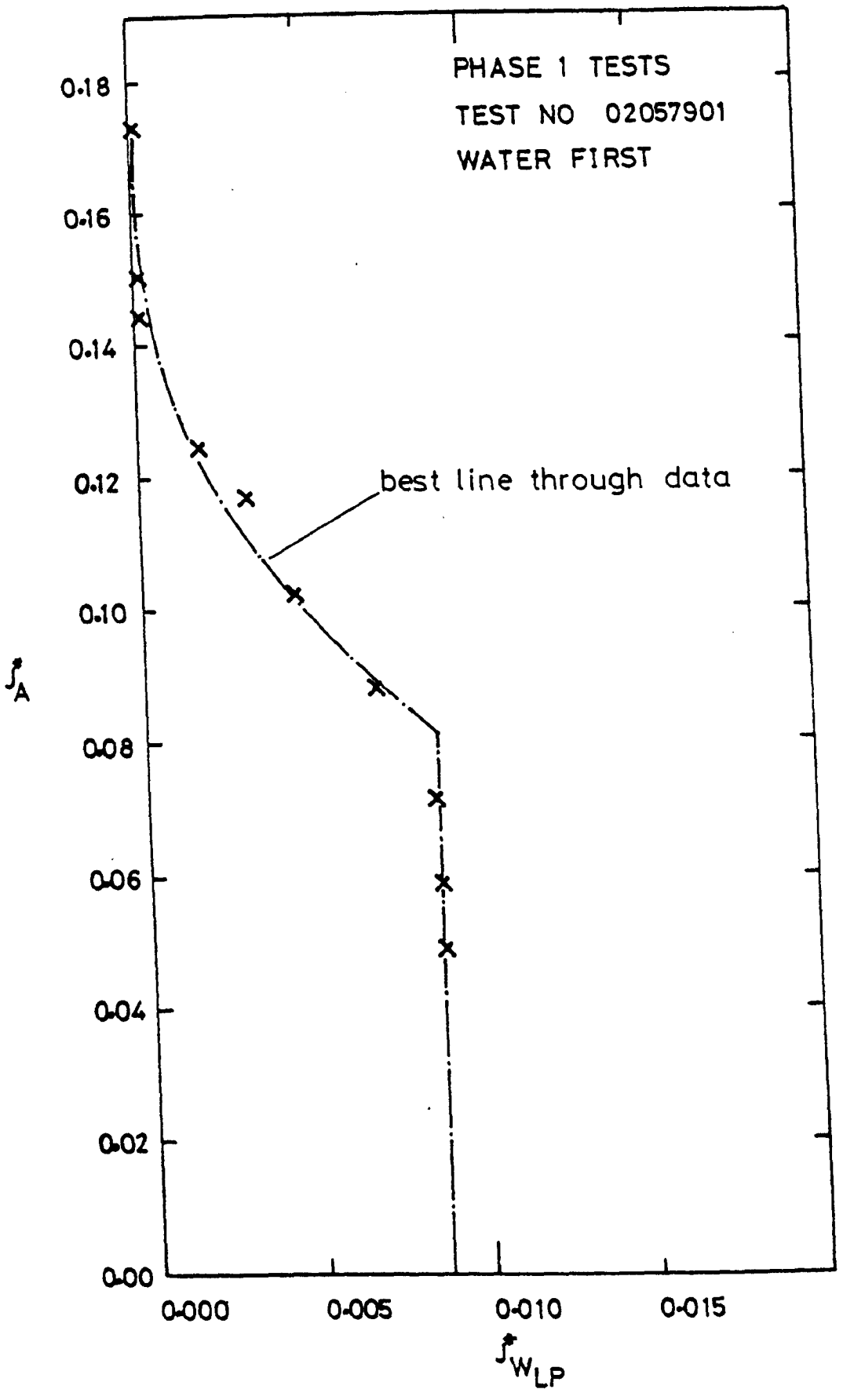

Fig G-1 Penetration Characteristics From Air-Water Tests

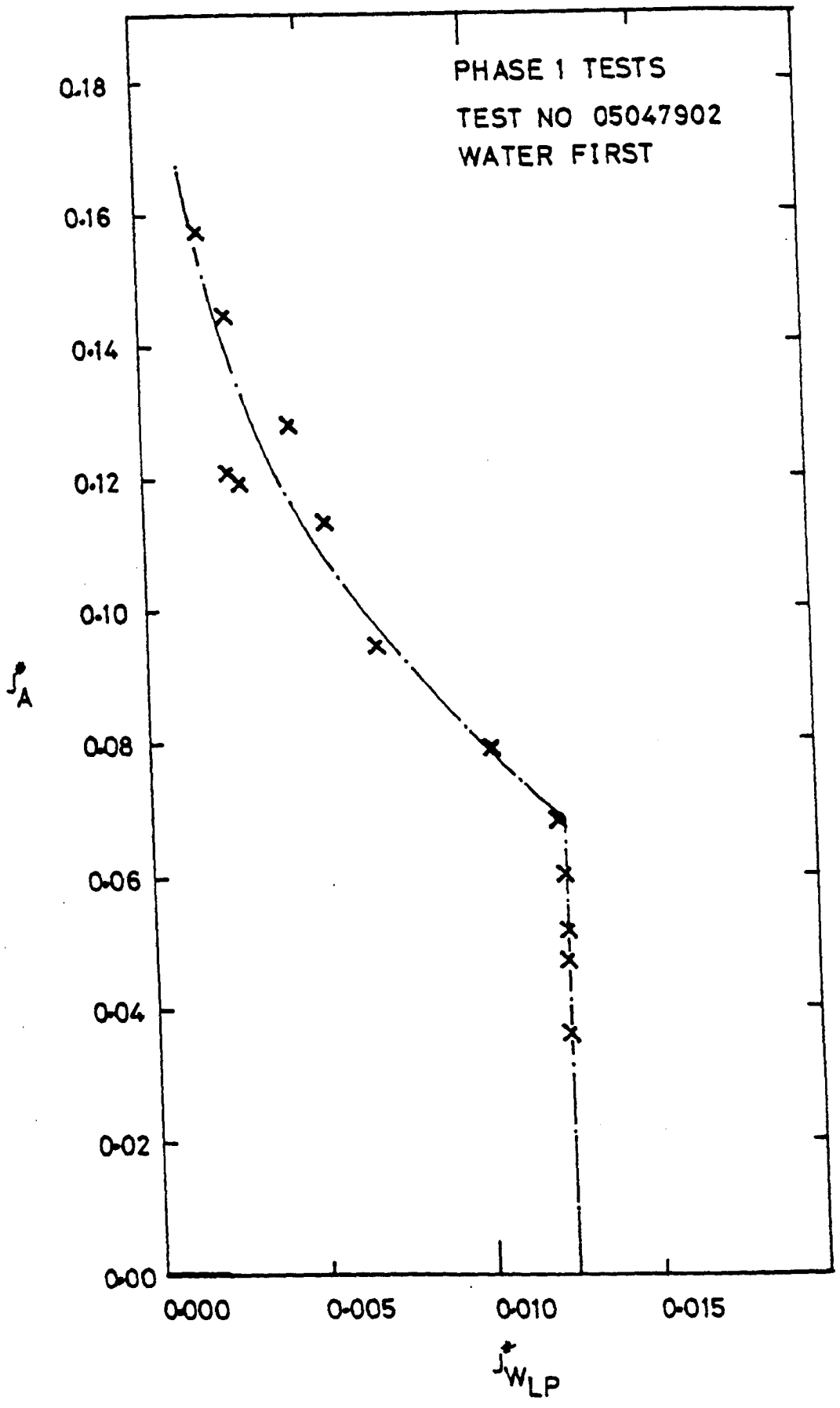

Fig G-2 Penetration Characteristics From Air-Water Tests

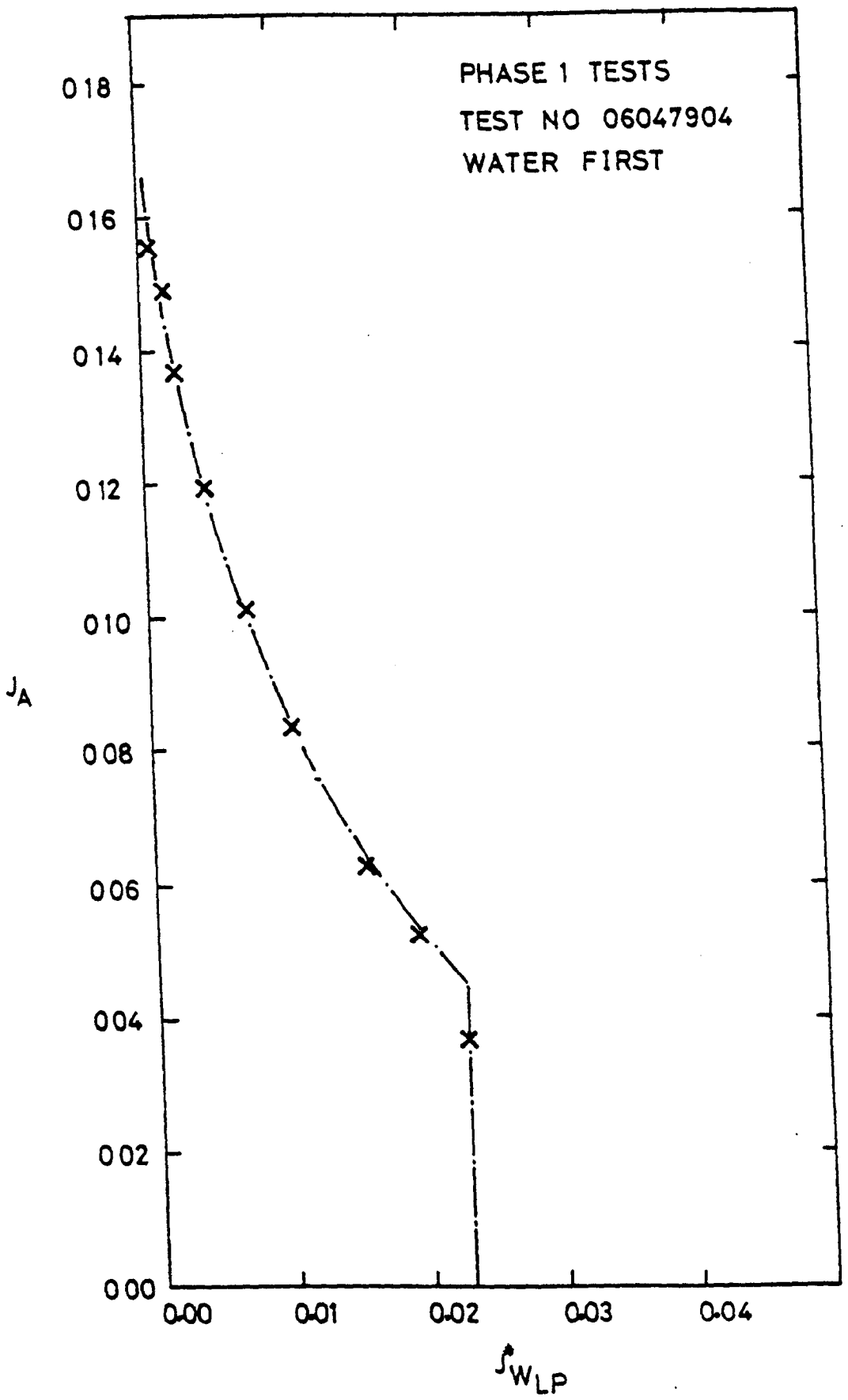

Fig G-3 Penetration Characteristics From Air-Water Tests

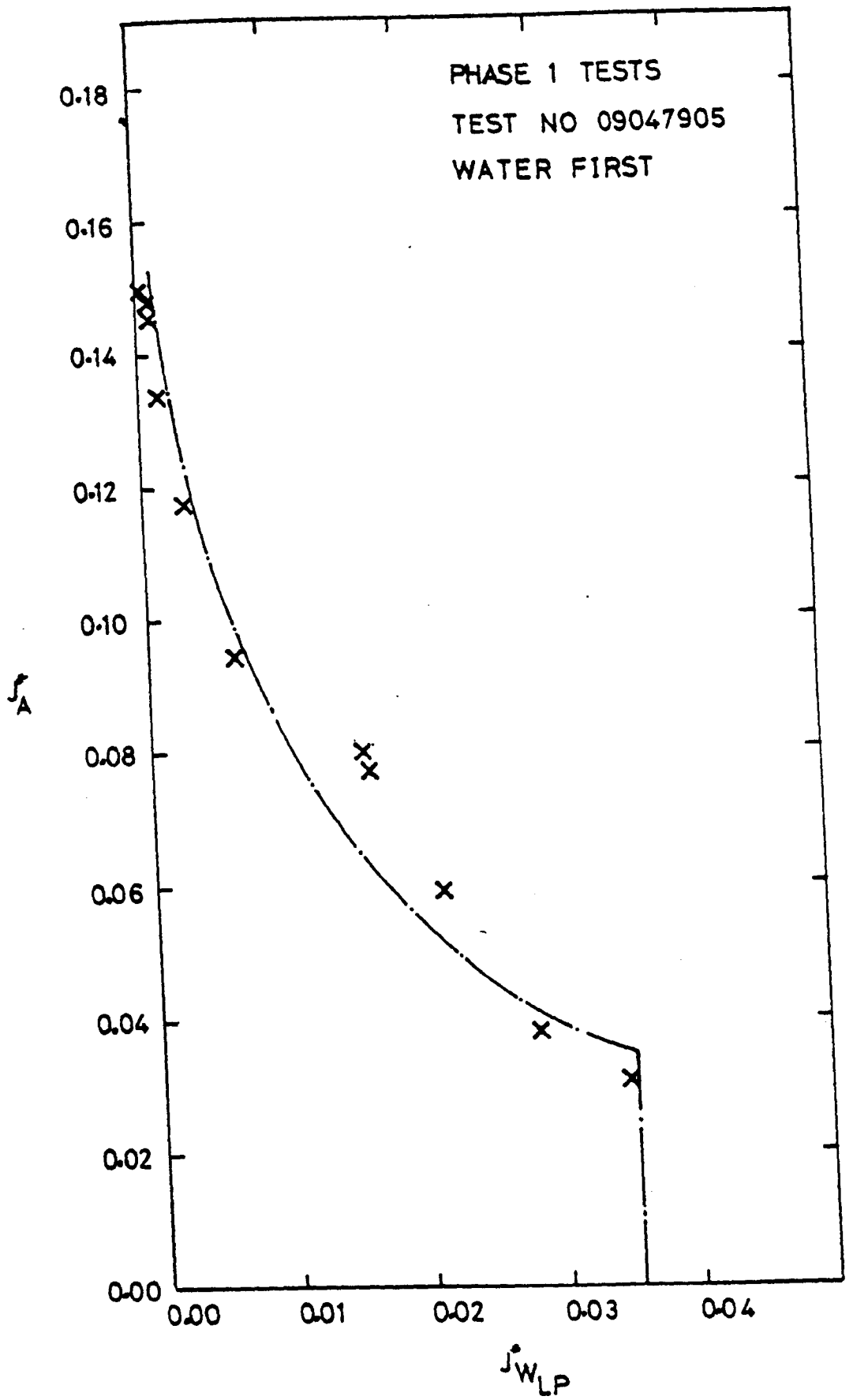

Fig G-4 Penetration Characteristics From Air-Water Tests

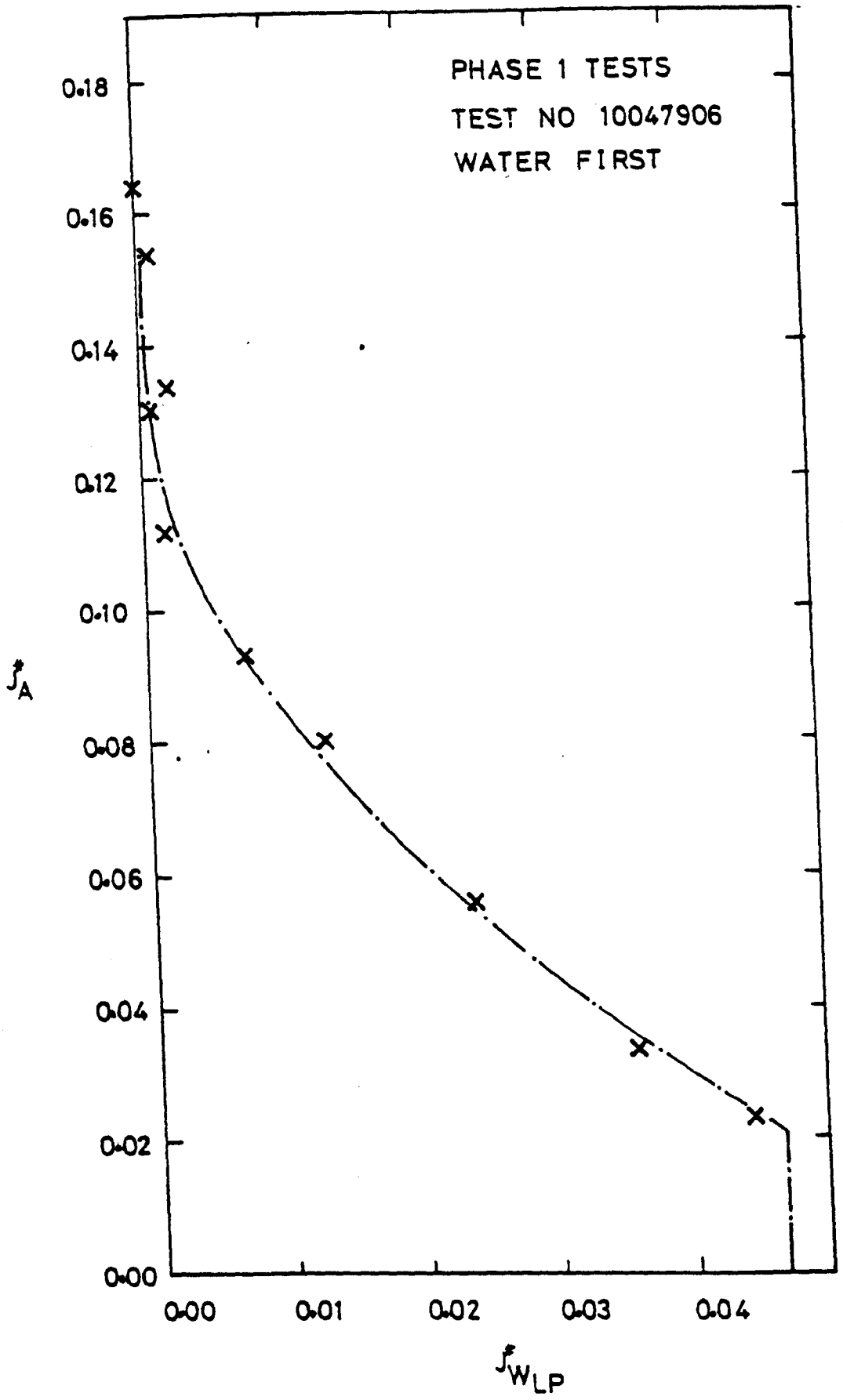

Fig G-5 Penetration Characteristics From Air-Water Tests

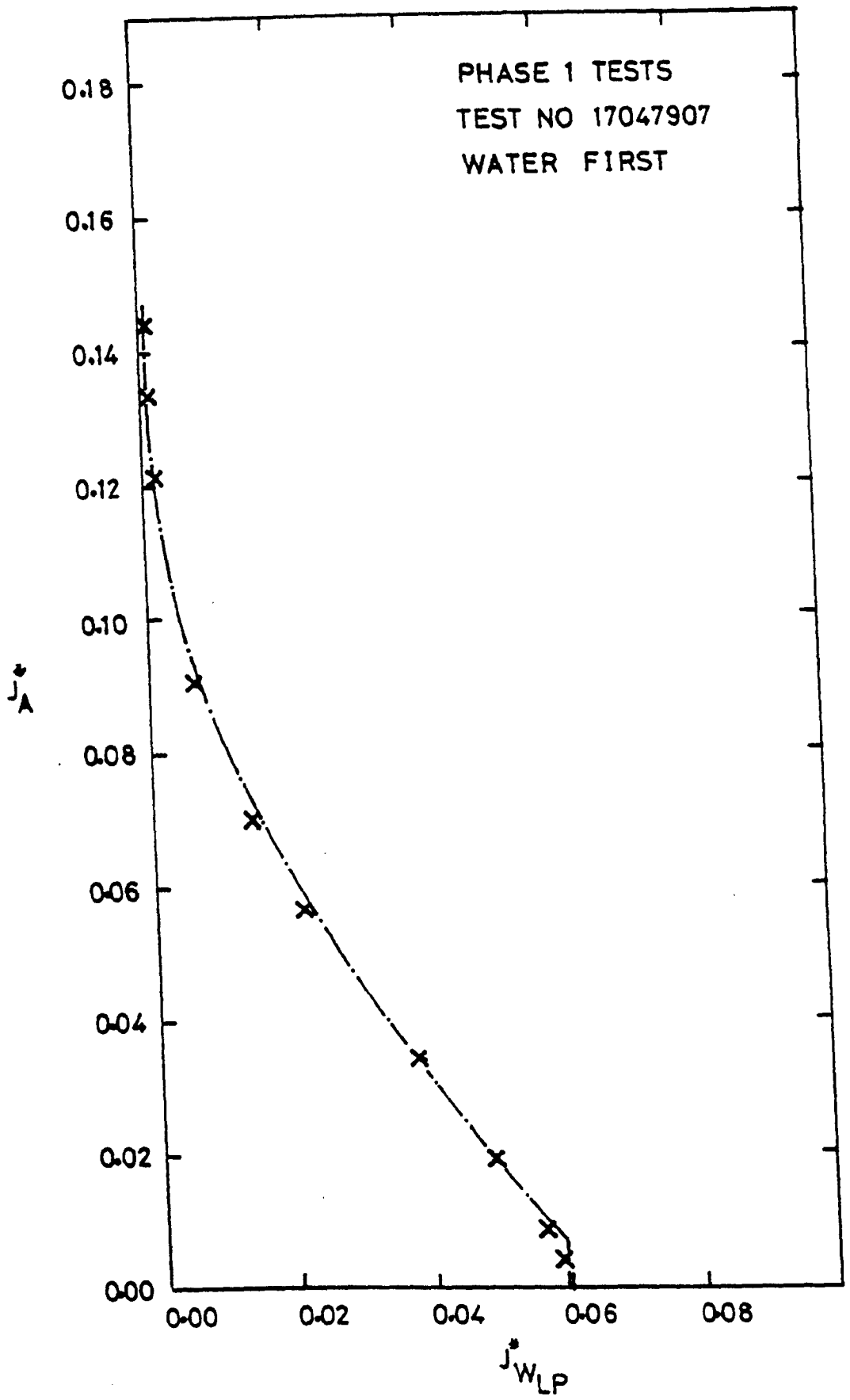

Fig G-6 Penetration Characteristics From Air-Water Tests

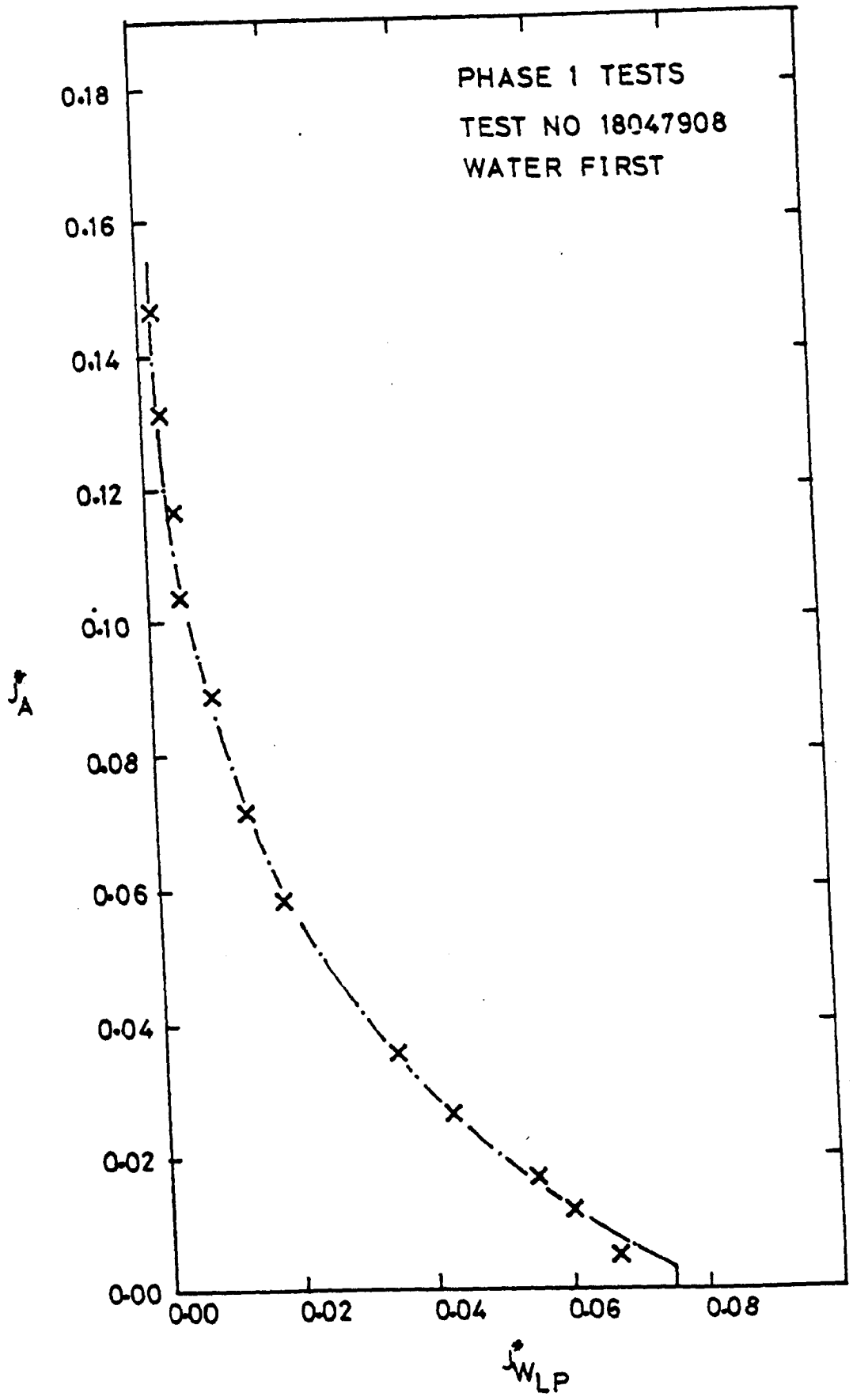

Fig G-7 Penetration Characteristics From Air-Water Tests

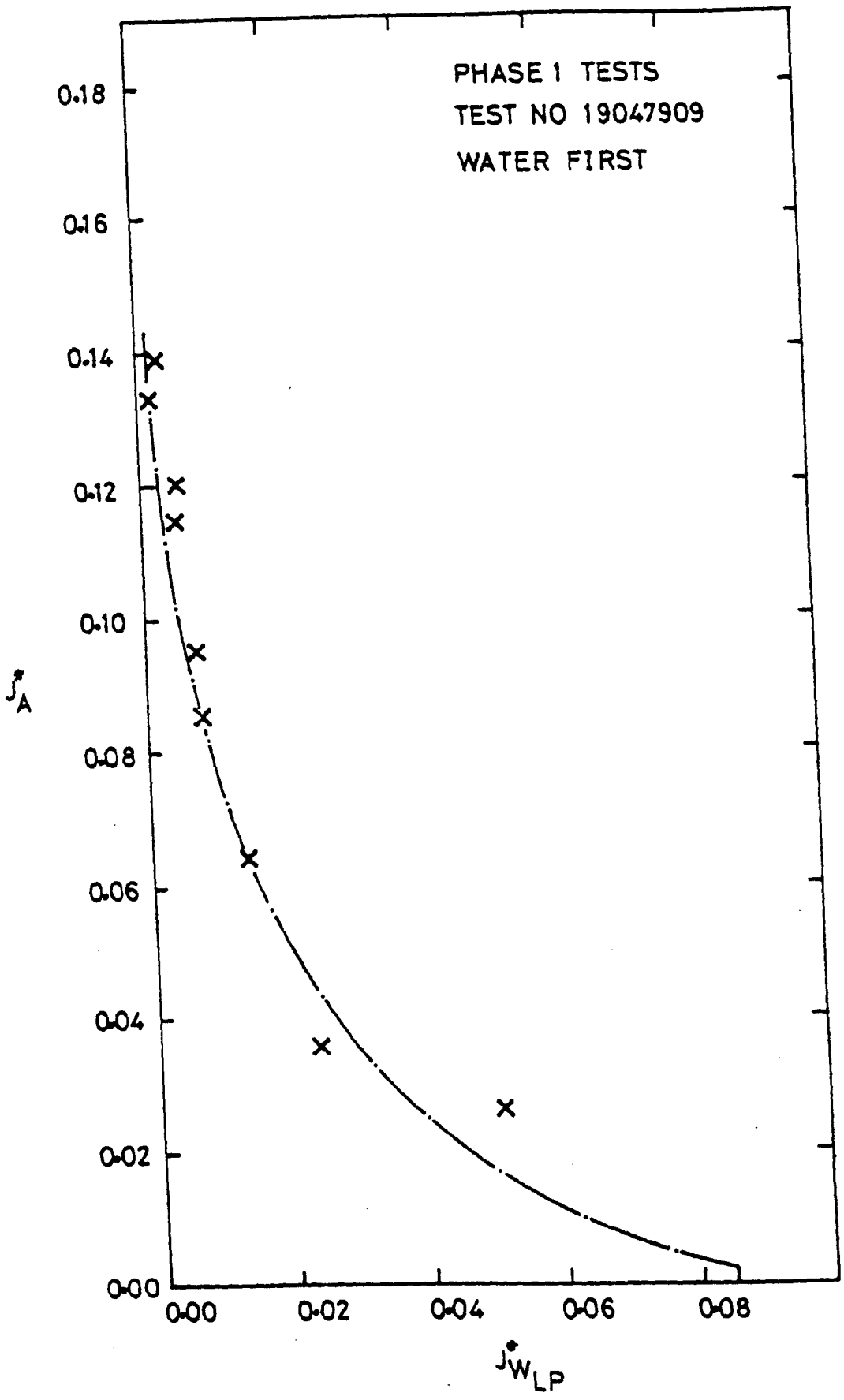

Fig G-8 Penetration Characteristics From Air-Water Tests

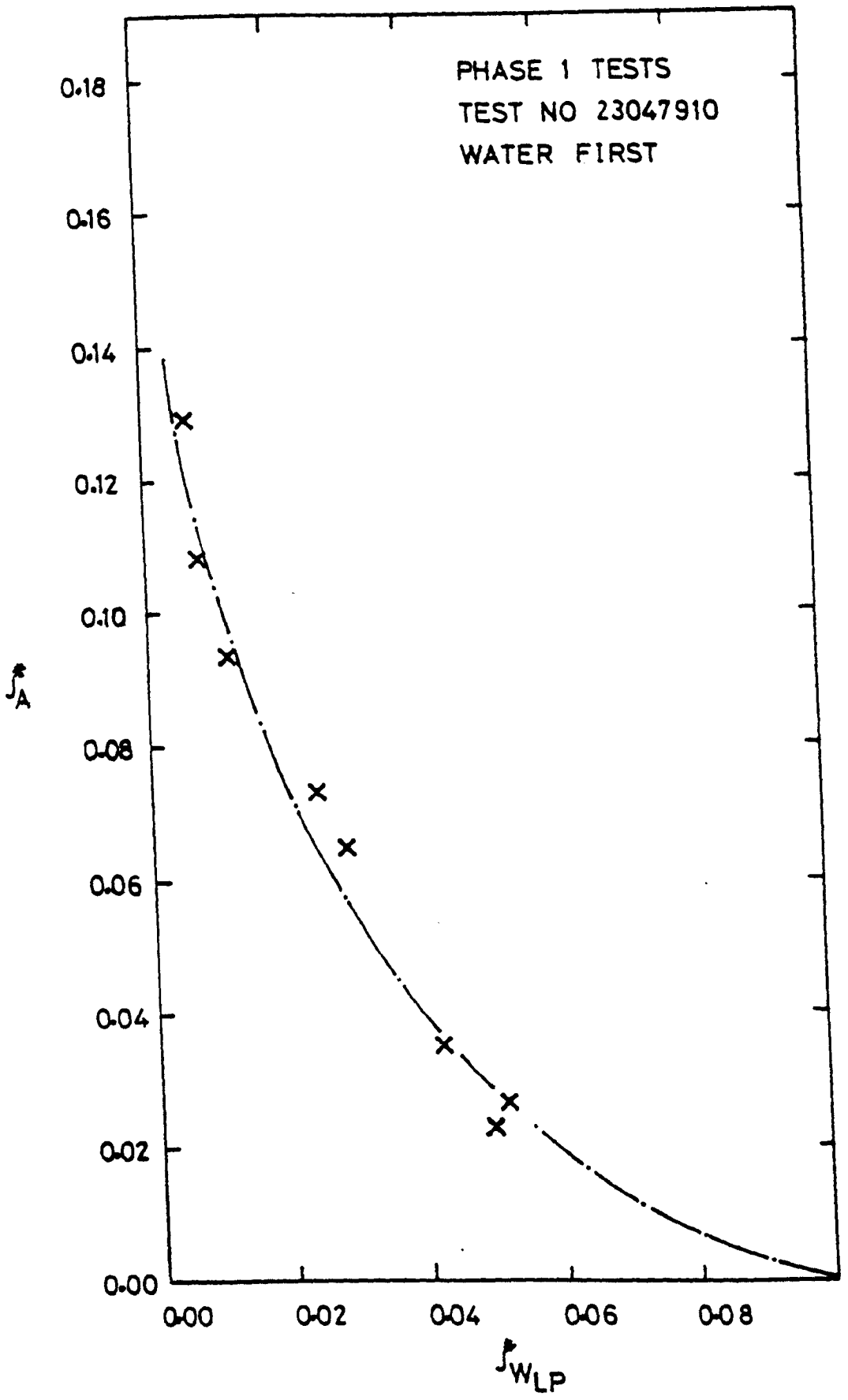

Fig G-9 Penetration Characteristics From Air-Water Tests

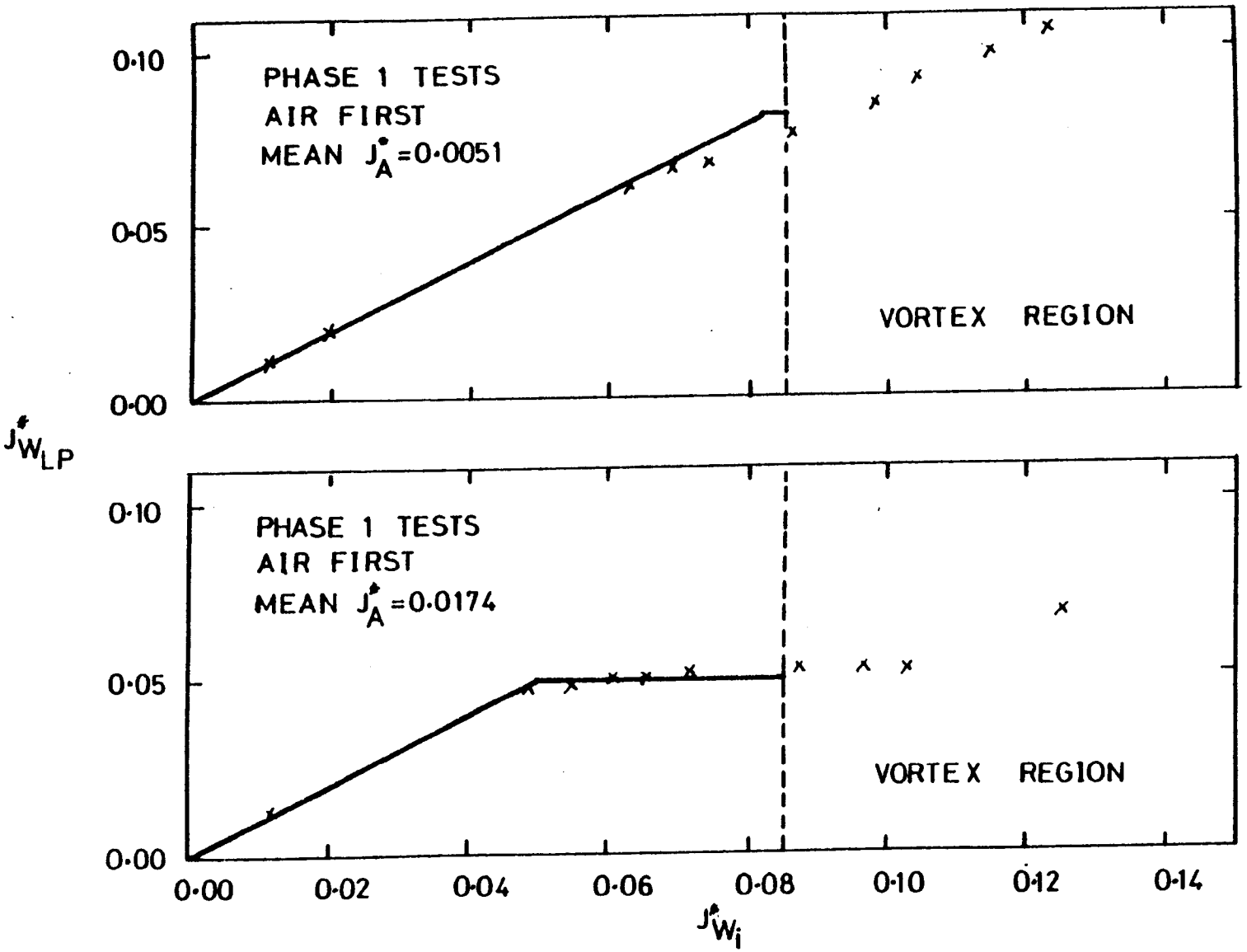

Fig G-10 Degree of Penetration to Lower Plenum of Inlet Water for Particular Air Flowrates

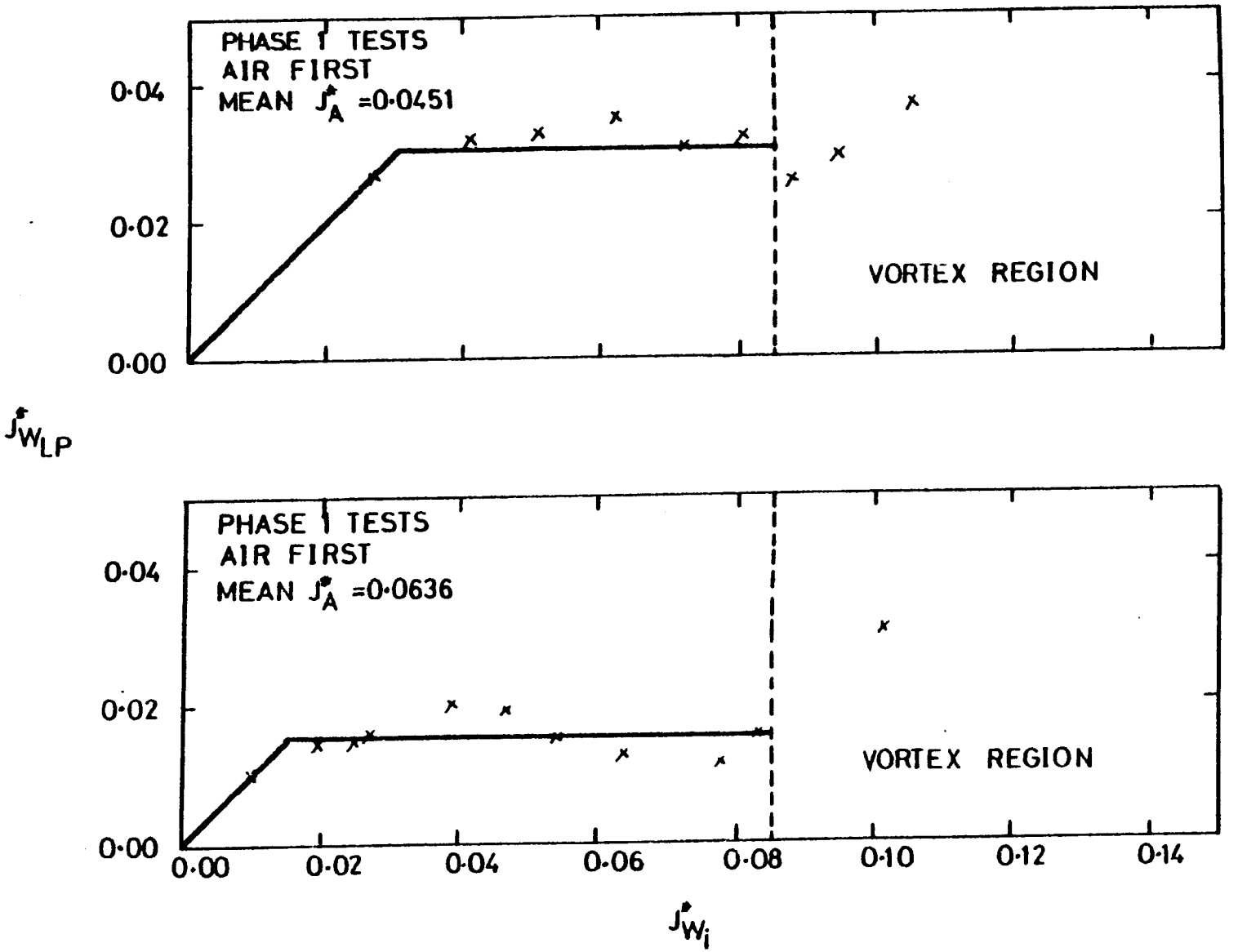

Fig G-11 Degree of Penetration to Lower Plenum of Inlet Water for Particular Air Flowrates

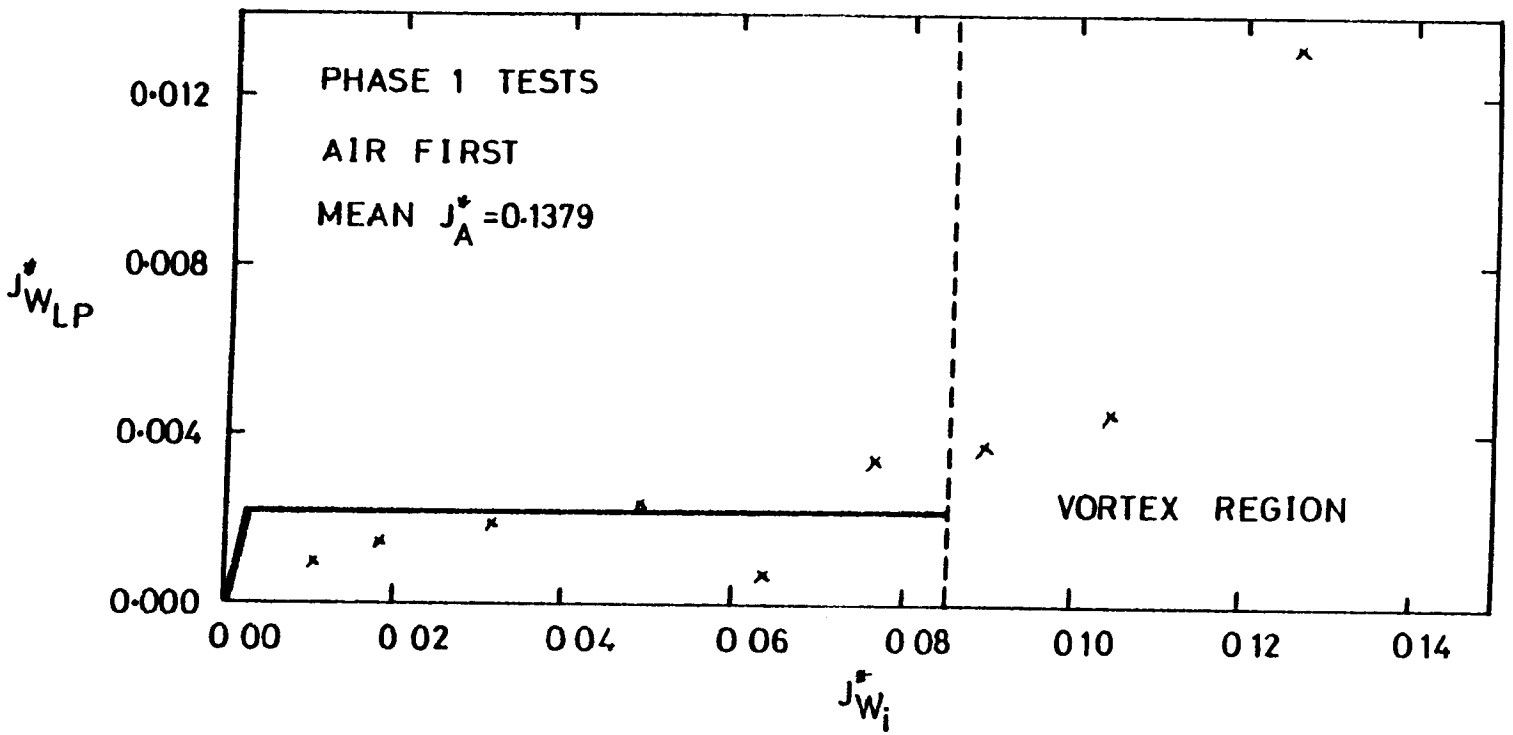

Fig G-12 Degree of Penetration to Lower Plenum of Inlet Water for Particular Air Flowrates

APPENDIX H

PENETRATION CHARACTERISTICS FOR PHASE 2 DATA

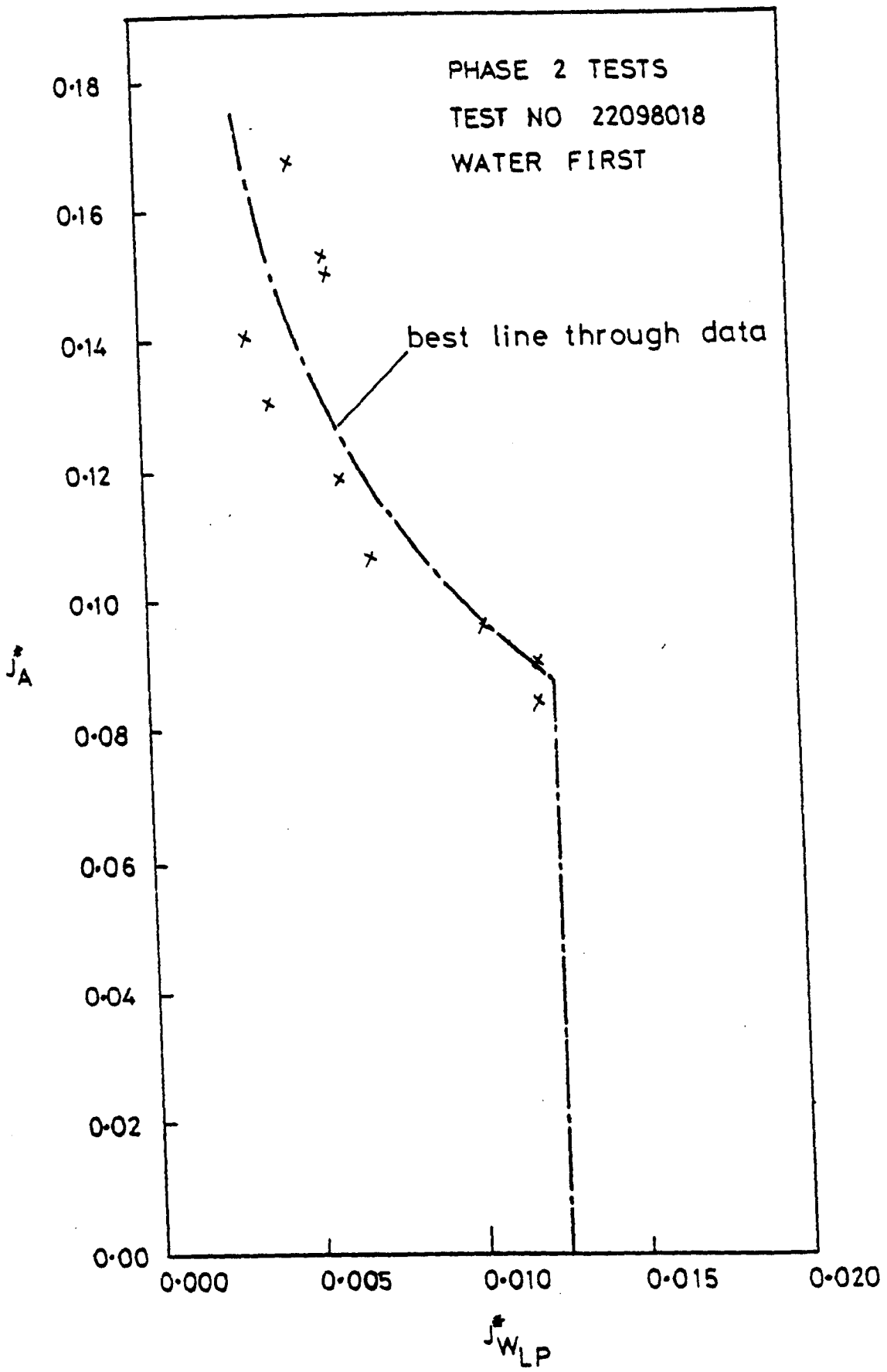

Fig H-1 Penetration Characteristics From Air-Water Tests

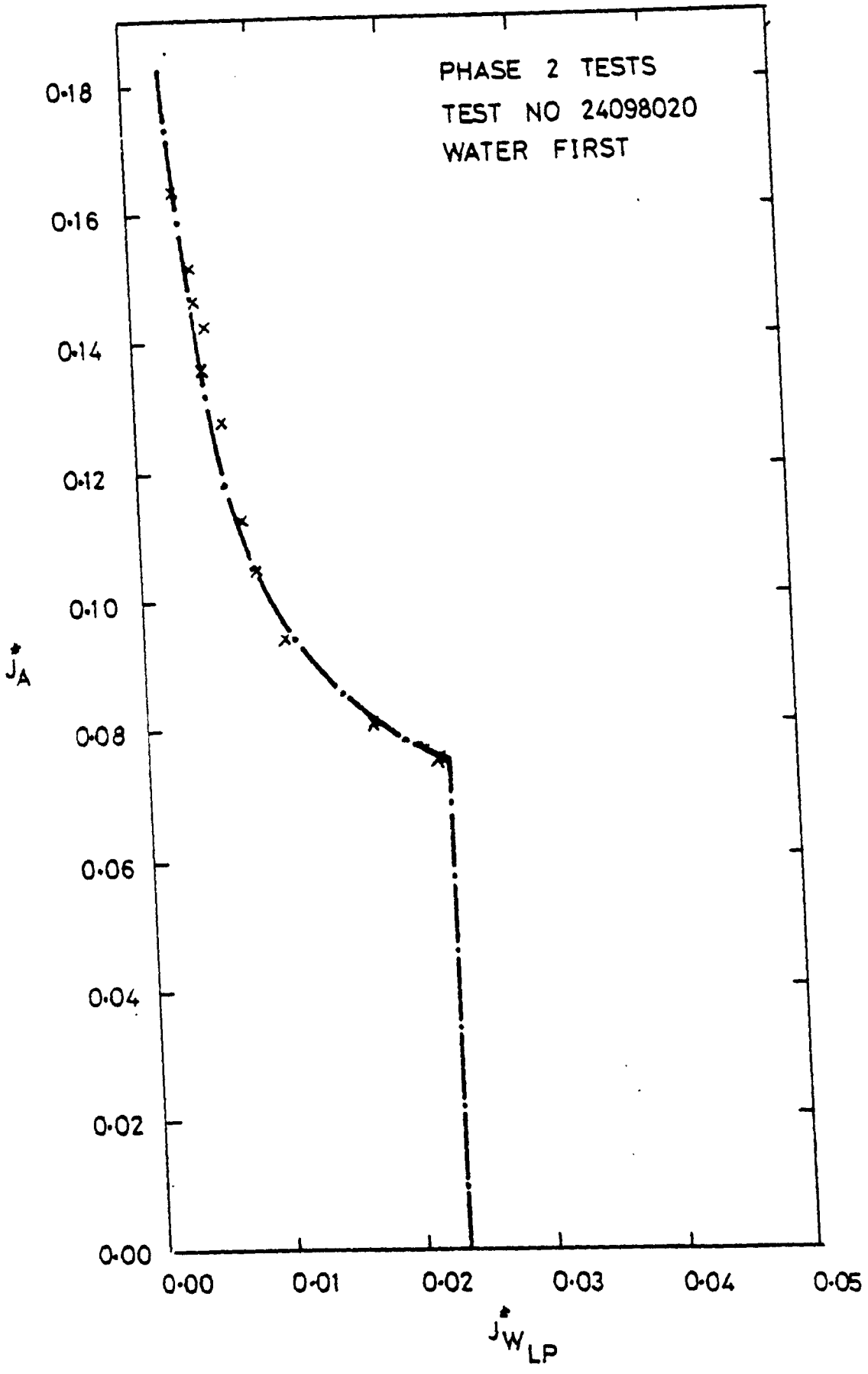

Fig H-2 Penetration Characteristics From Air-Water Tests

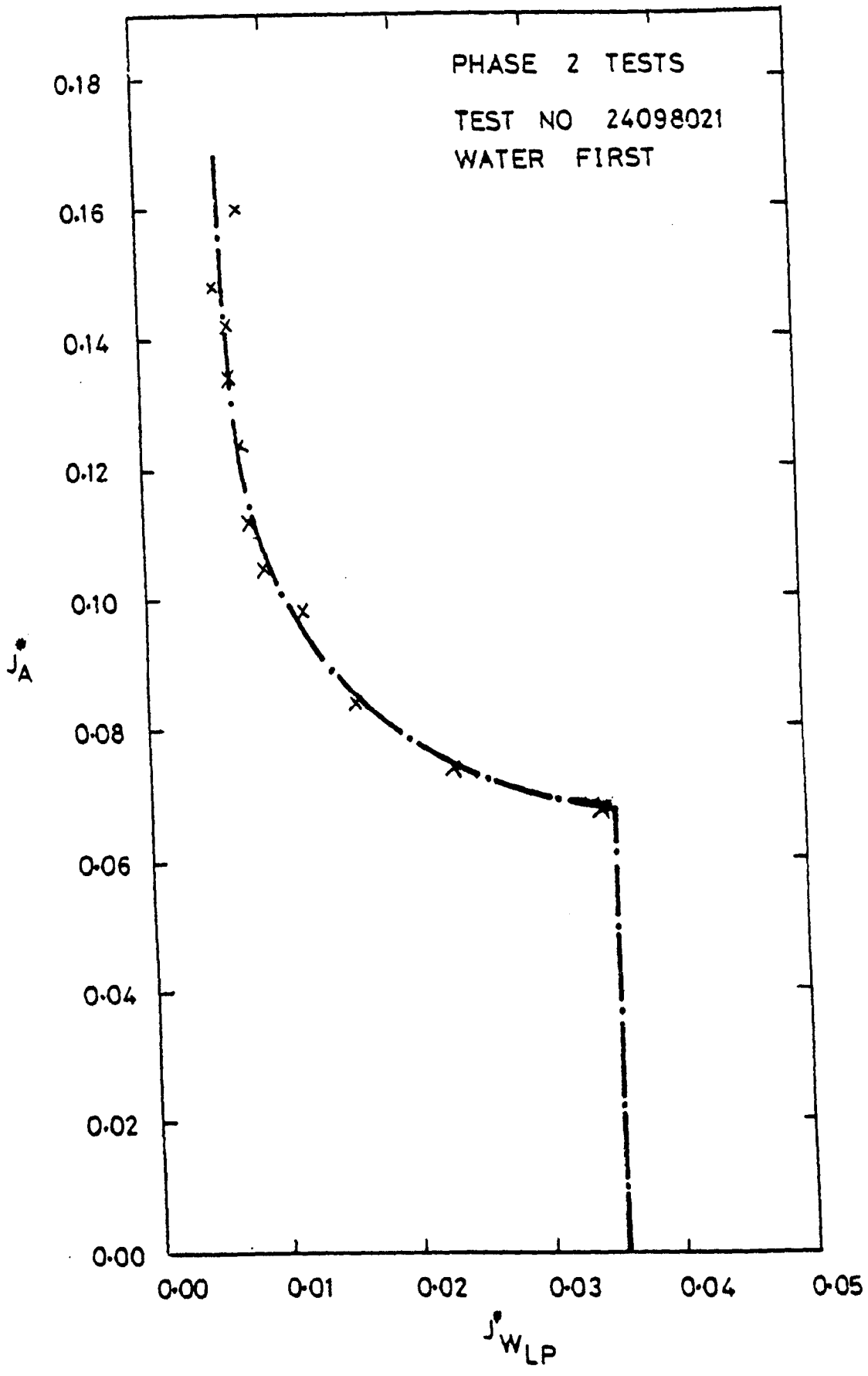

Fig H-3 Penetration Characteristics From Air-Water Tests

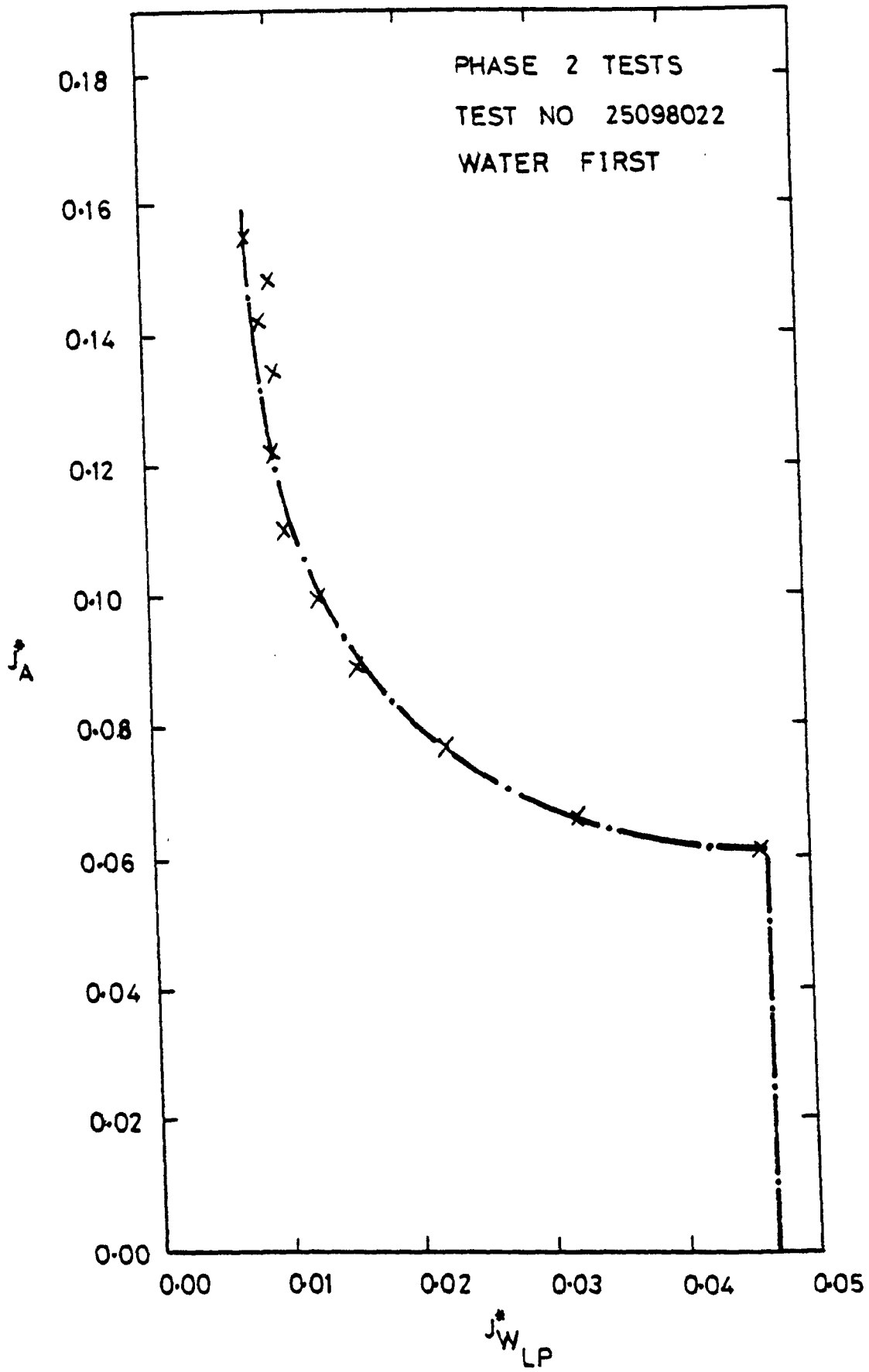

Fig H-4 PENETRATION CHARCTERISTICS FROM AIR-WATER TESTS

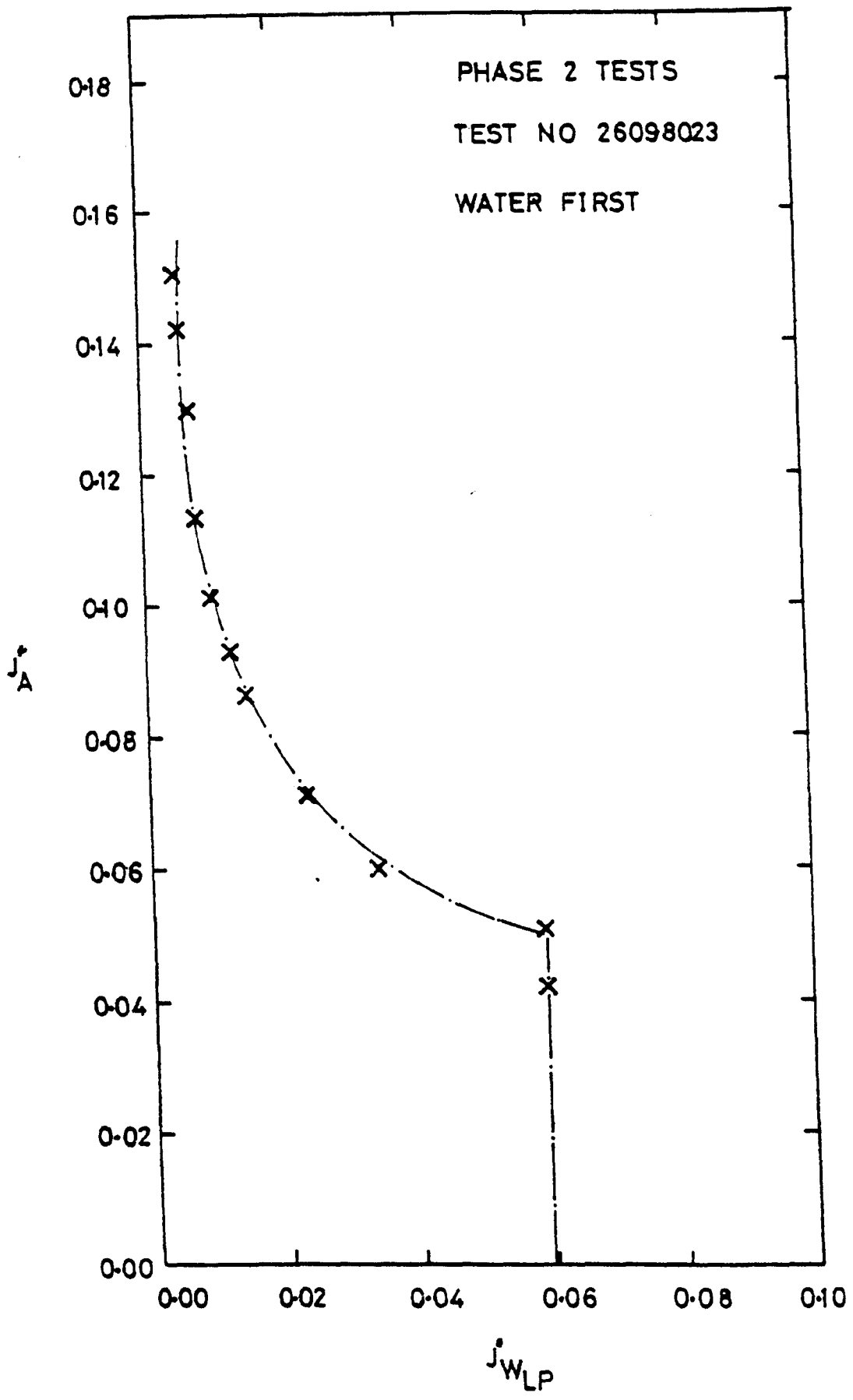

Fig H-5 PENETRATION CHARACTERISTICS FROM AIR-WATER TESTS

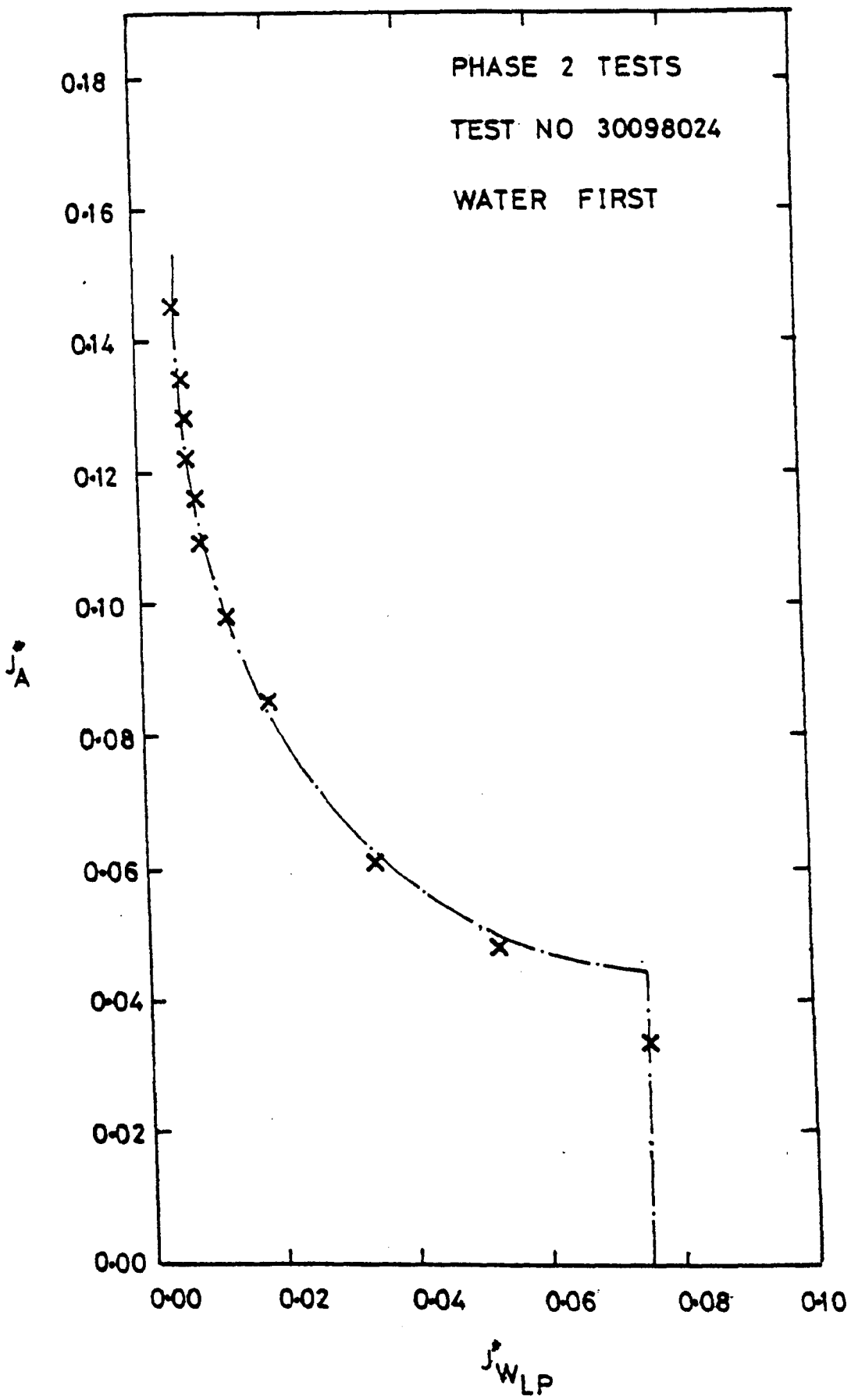

Fig H-6 PENETRATION CHARACTERISTICS FROM AIR-WATER TESTS

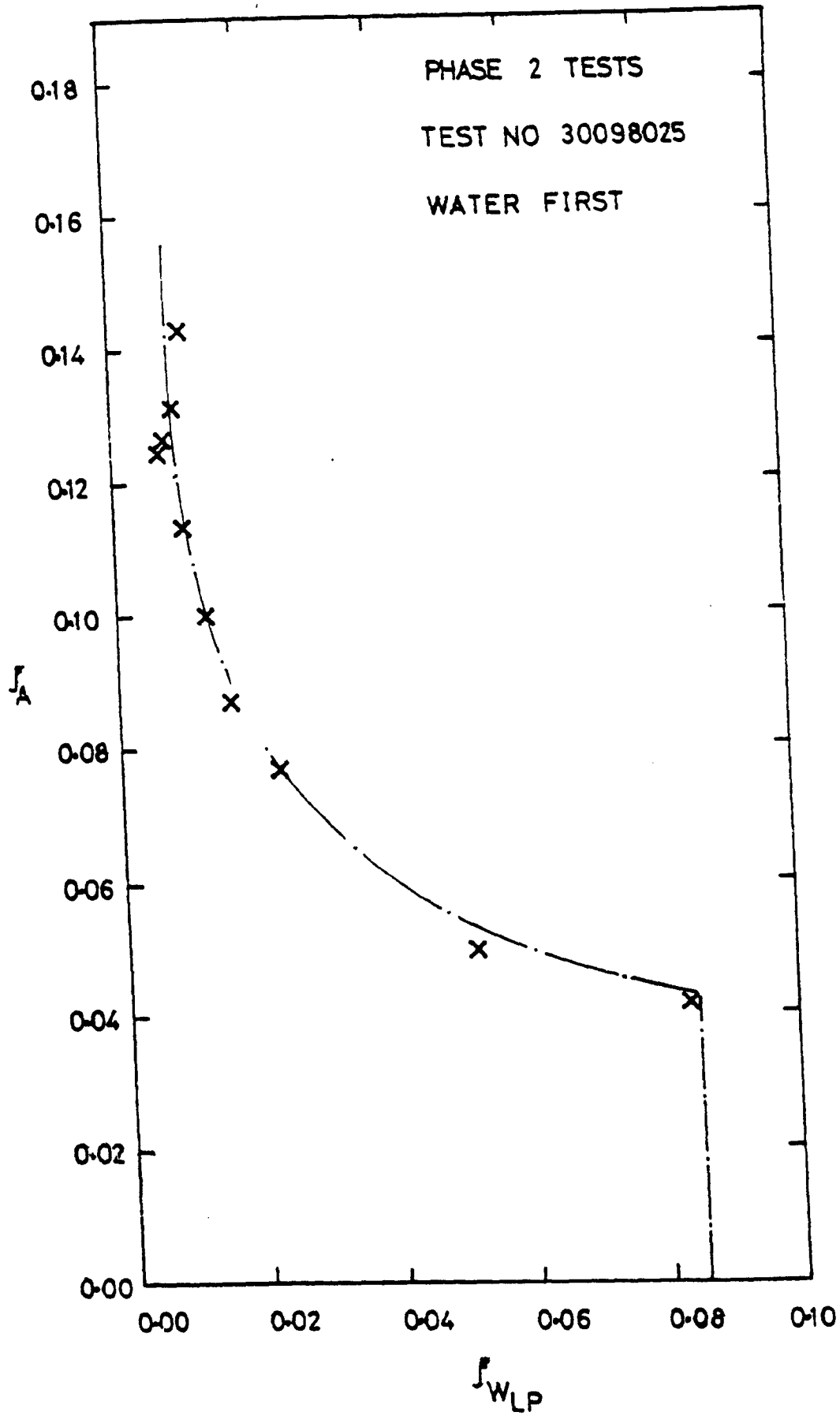

Fig H-7 PENETRATION CHARACTERISTICS FROM AIR-WATER TESTS

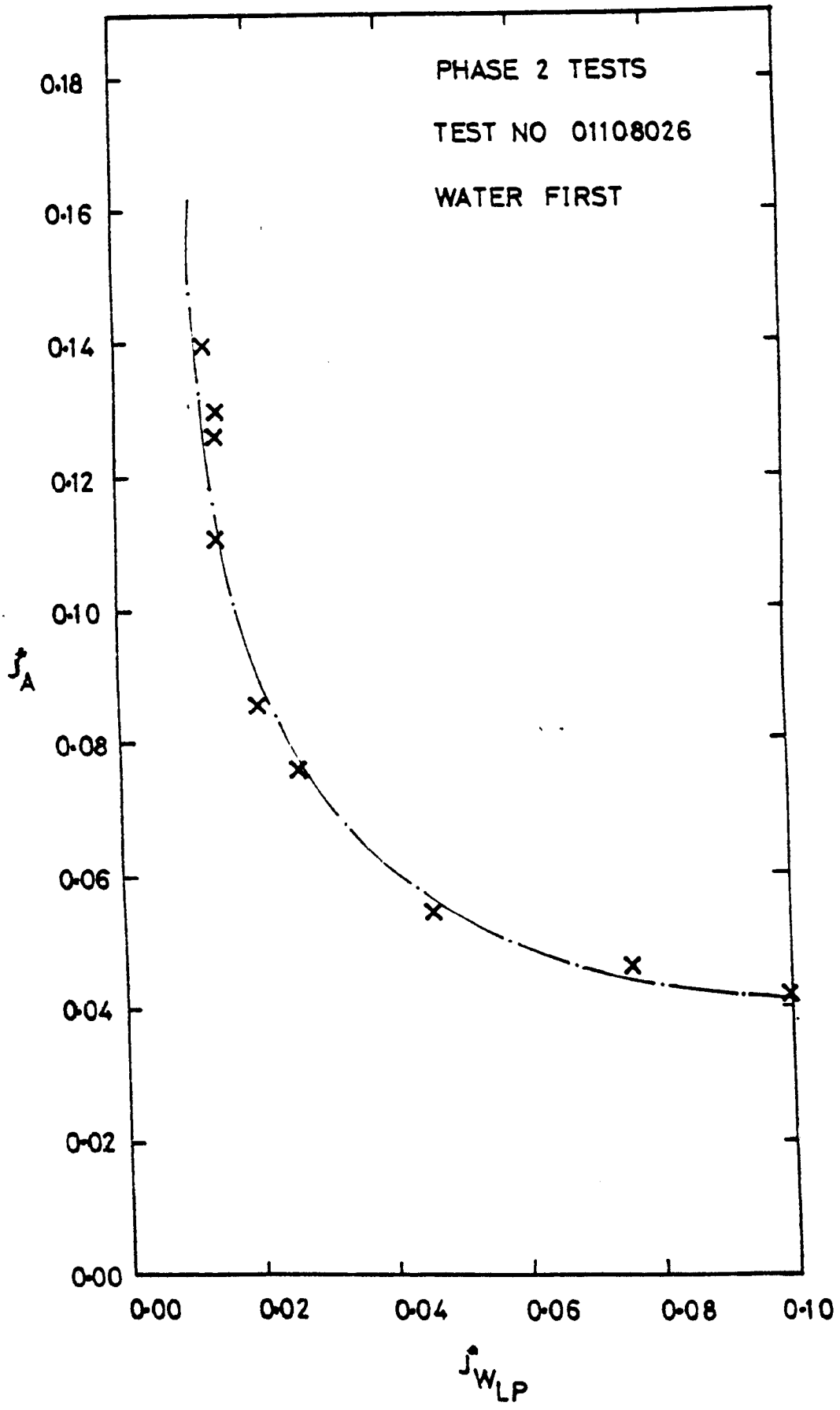

Fig H-8 PENETRATION CHARACTERISTICS FROM AIR-WATER TESTS

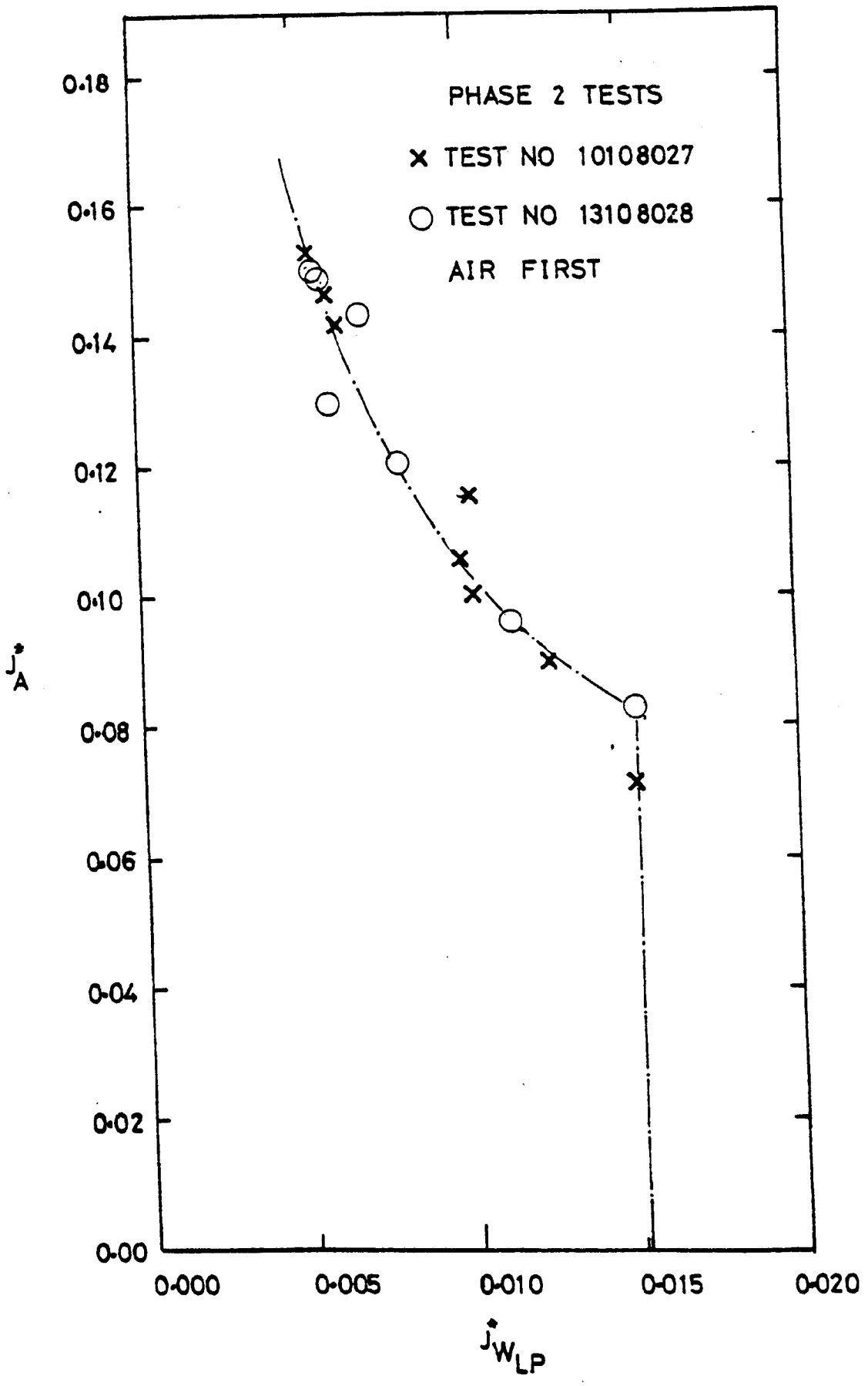

Fig H-9 PENETRATION CHARACTERISTICS FROM AIR-WATER TESTS

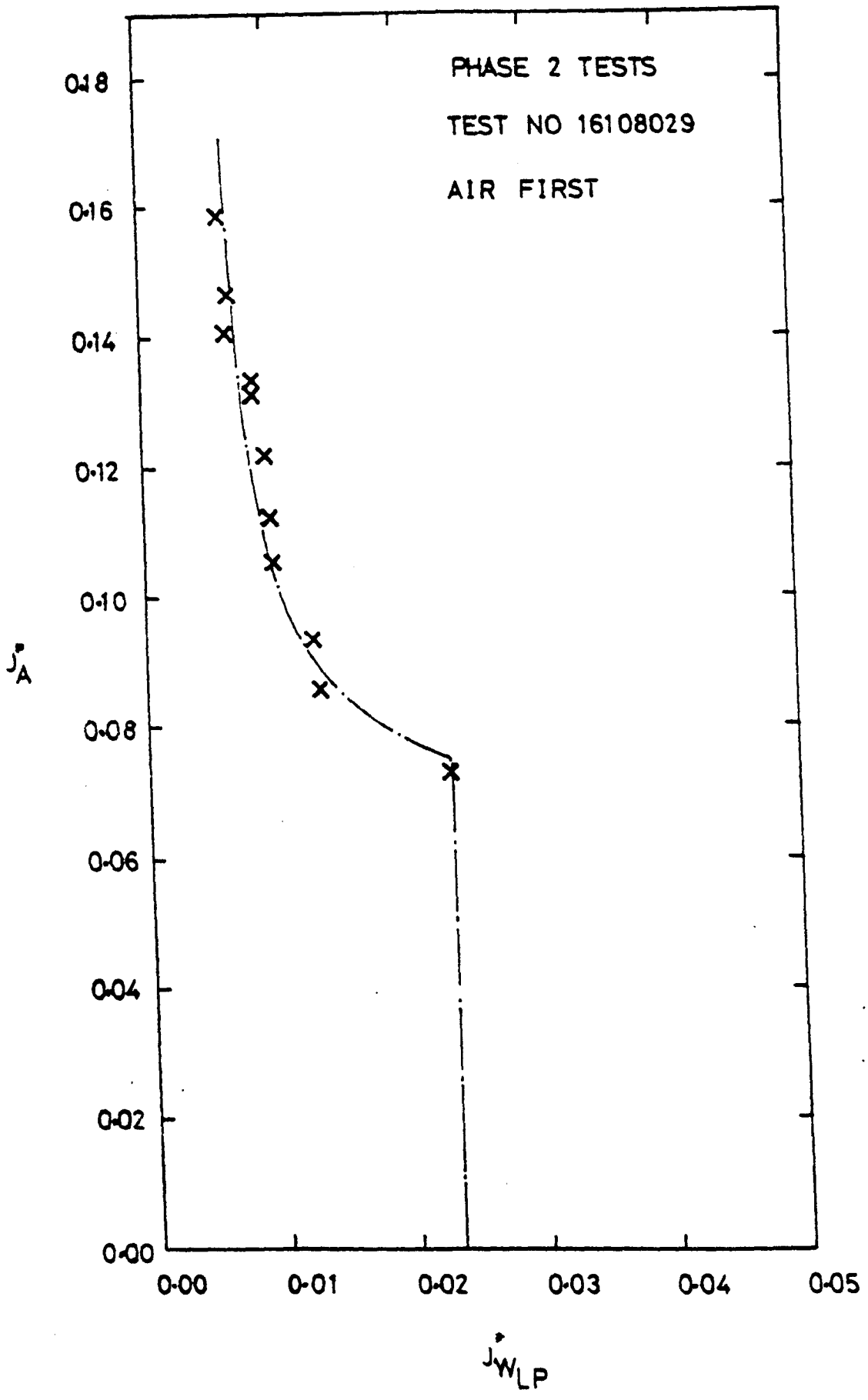

Fig H-10 PENETRATION CHARACTERISTICS FROM AIR-WATER TESTS

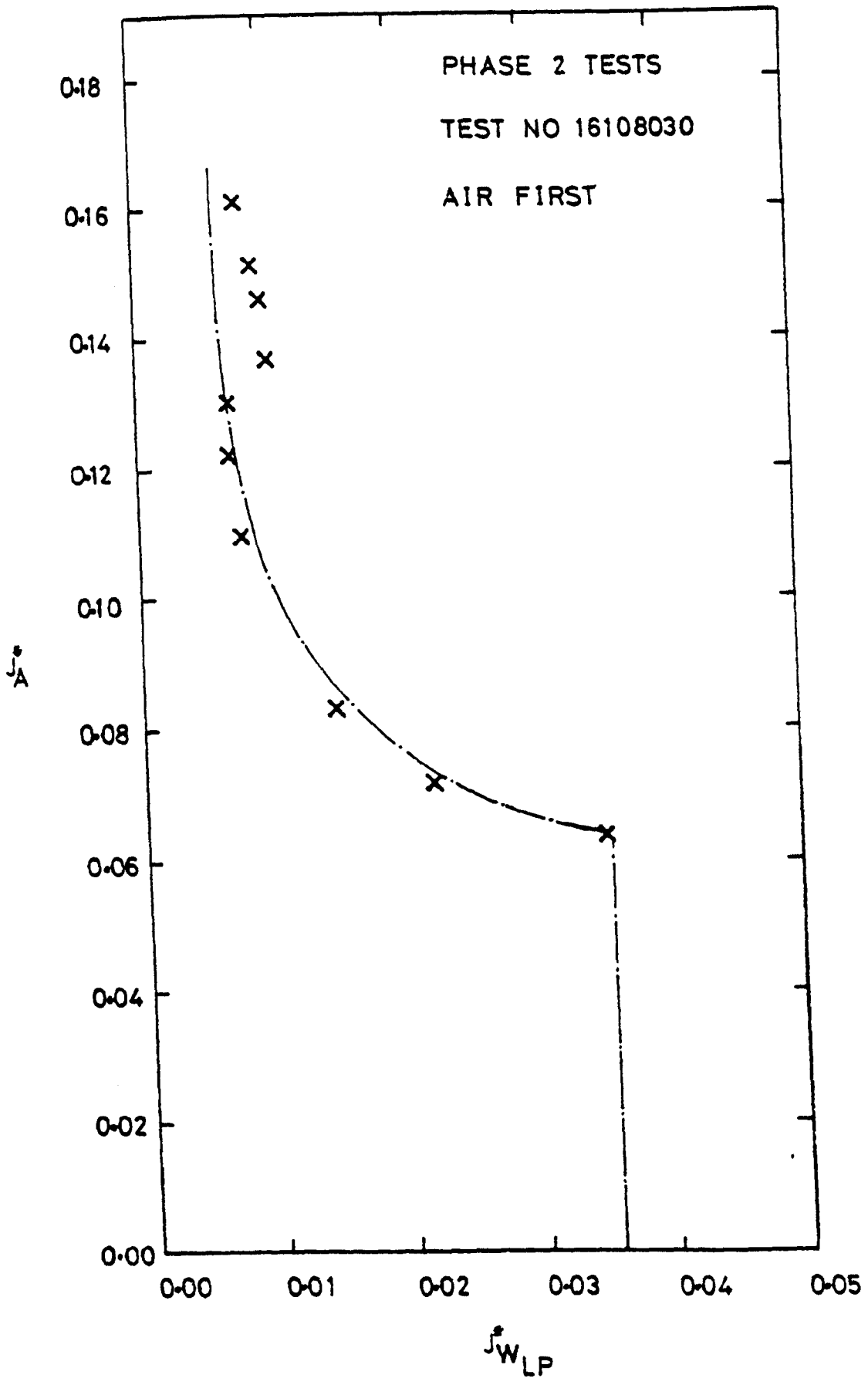

Fig H-11 PENETRATION CHARACTERISTICS FROM AIR-WATER TESTS

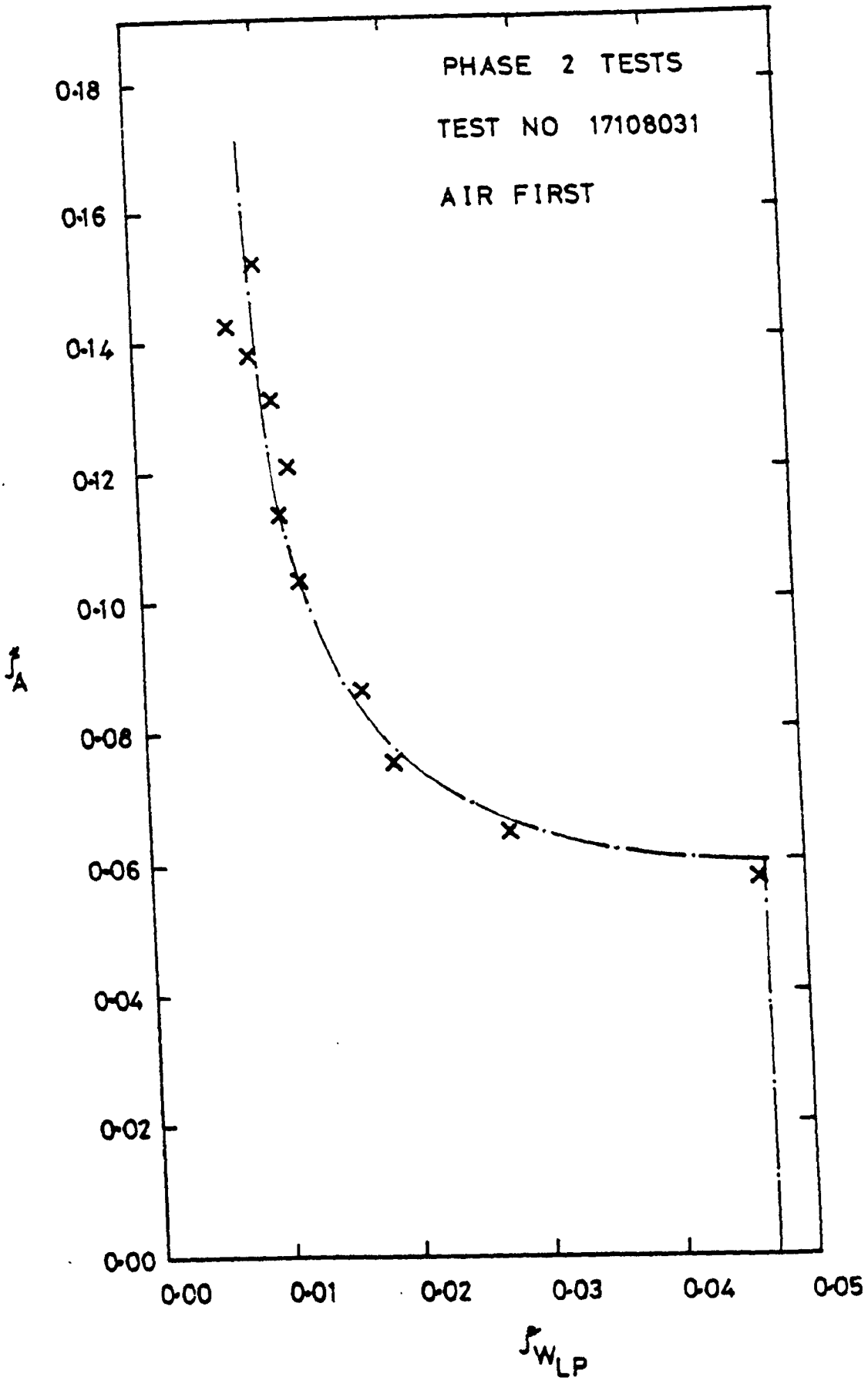

Fig H-12 PENETRATIOT CHARACTERISTICS FROM AIR-WATER TESTS

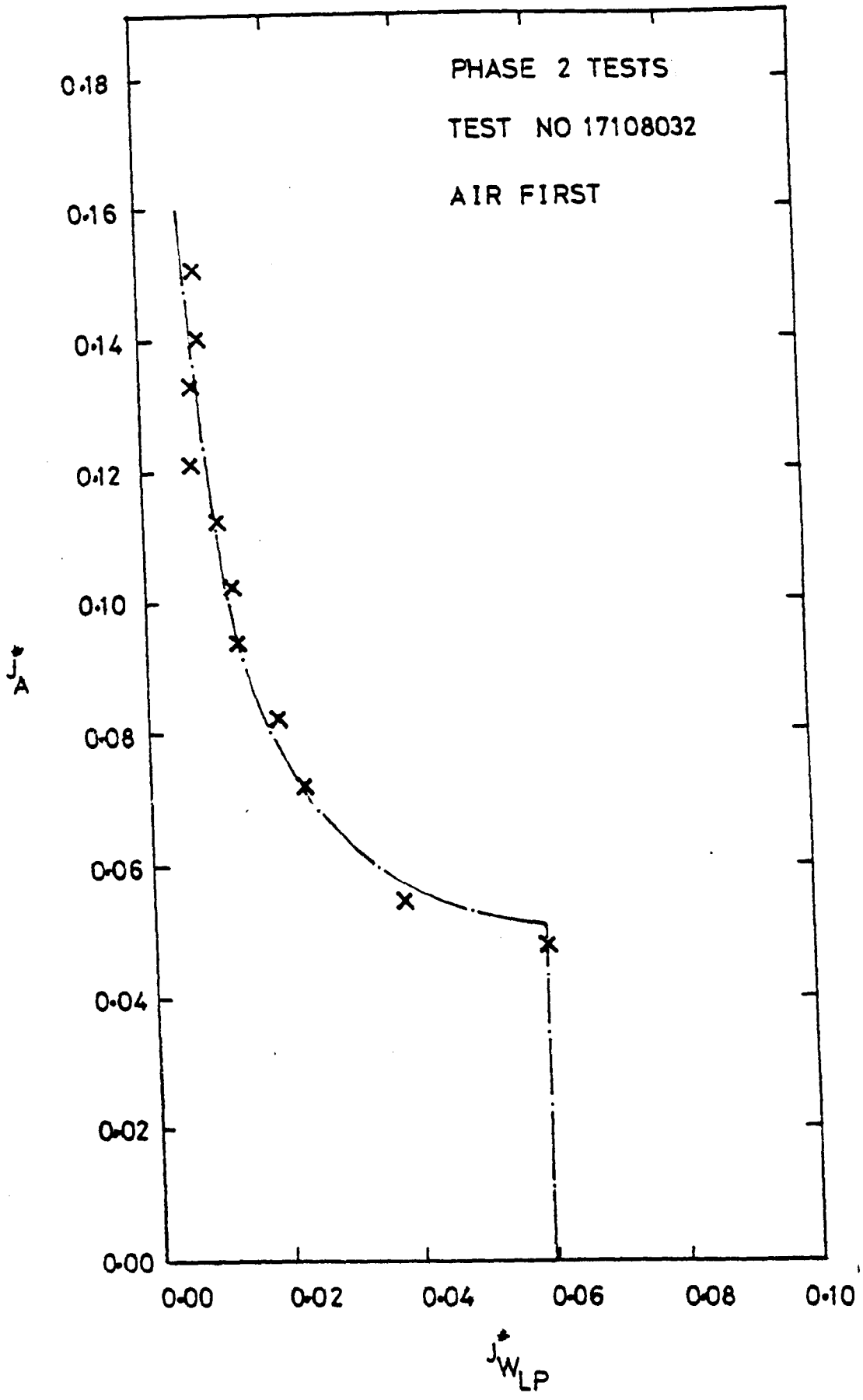

Fig H-13 PENETRATION CHARACTERISTICS FROM AIR-WATER TESTS

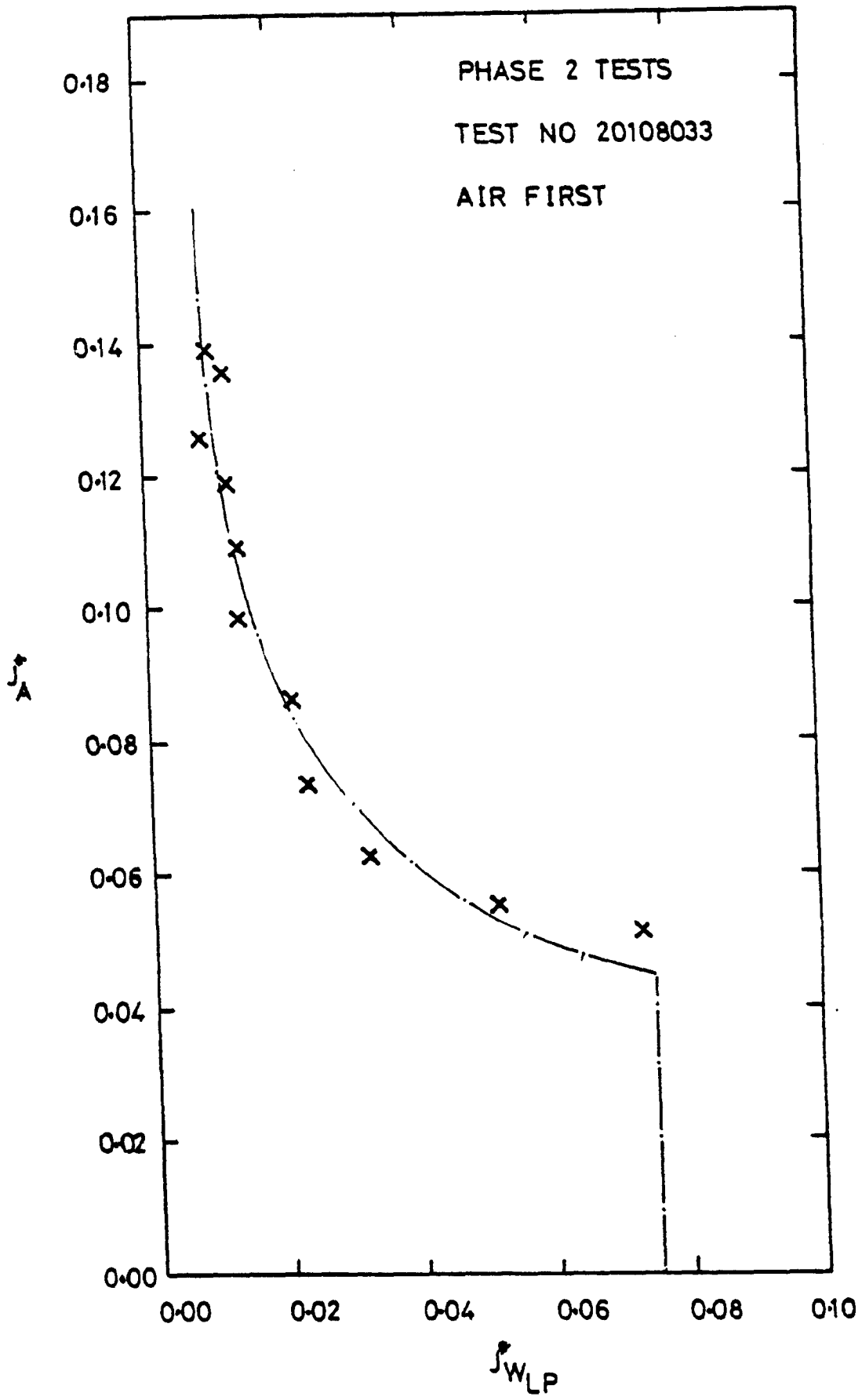

Fig H-14 PENETRATION CHARACTERISTICS FROM AIR-WATER TESTS

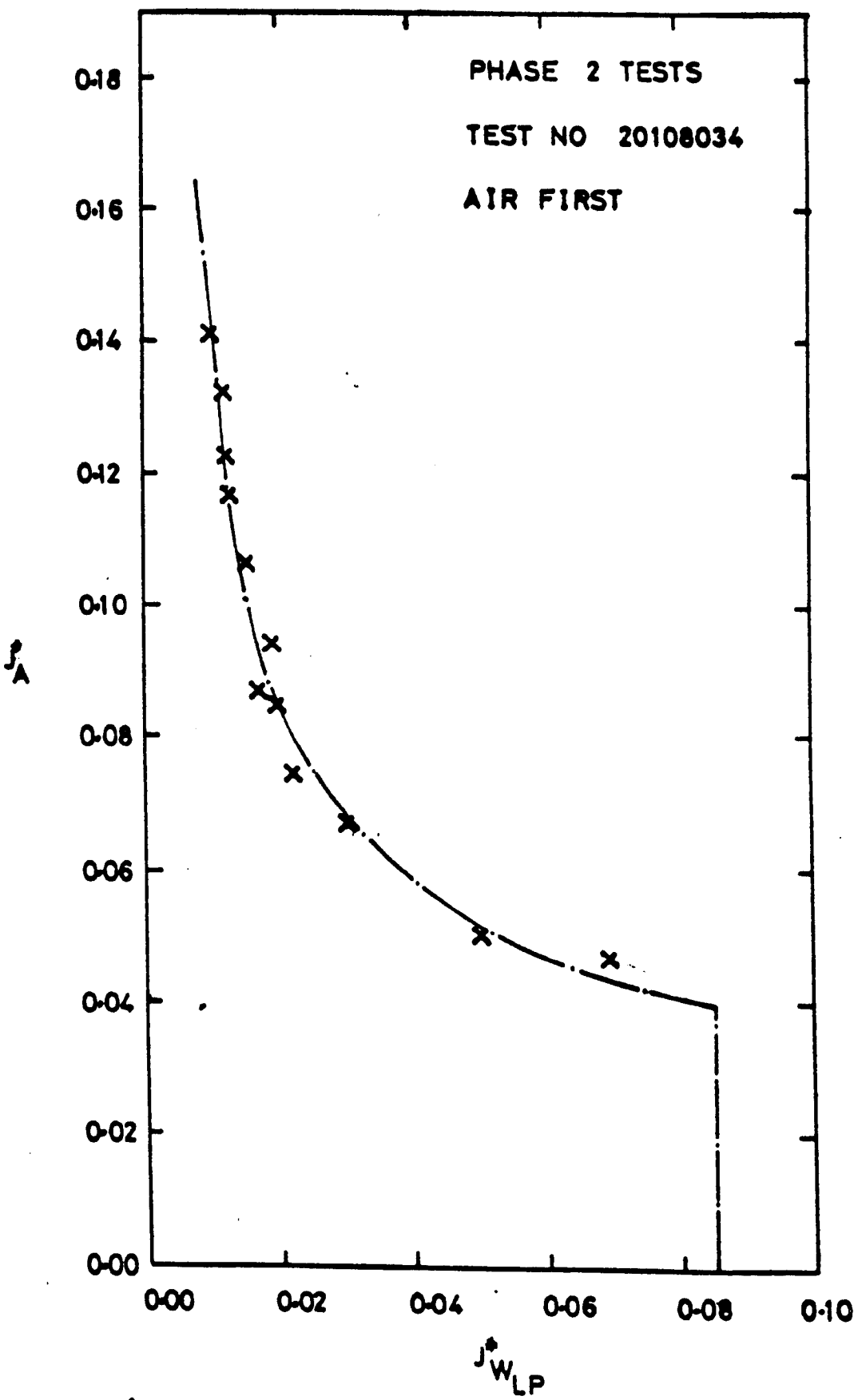

Fig H-15 PENETRATION CHARACTERISTICS FROM AIR-WATER TESTS

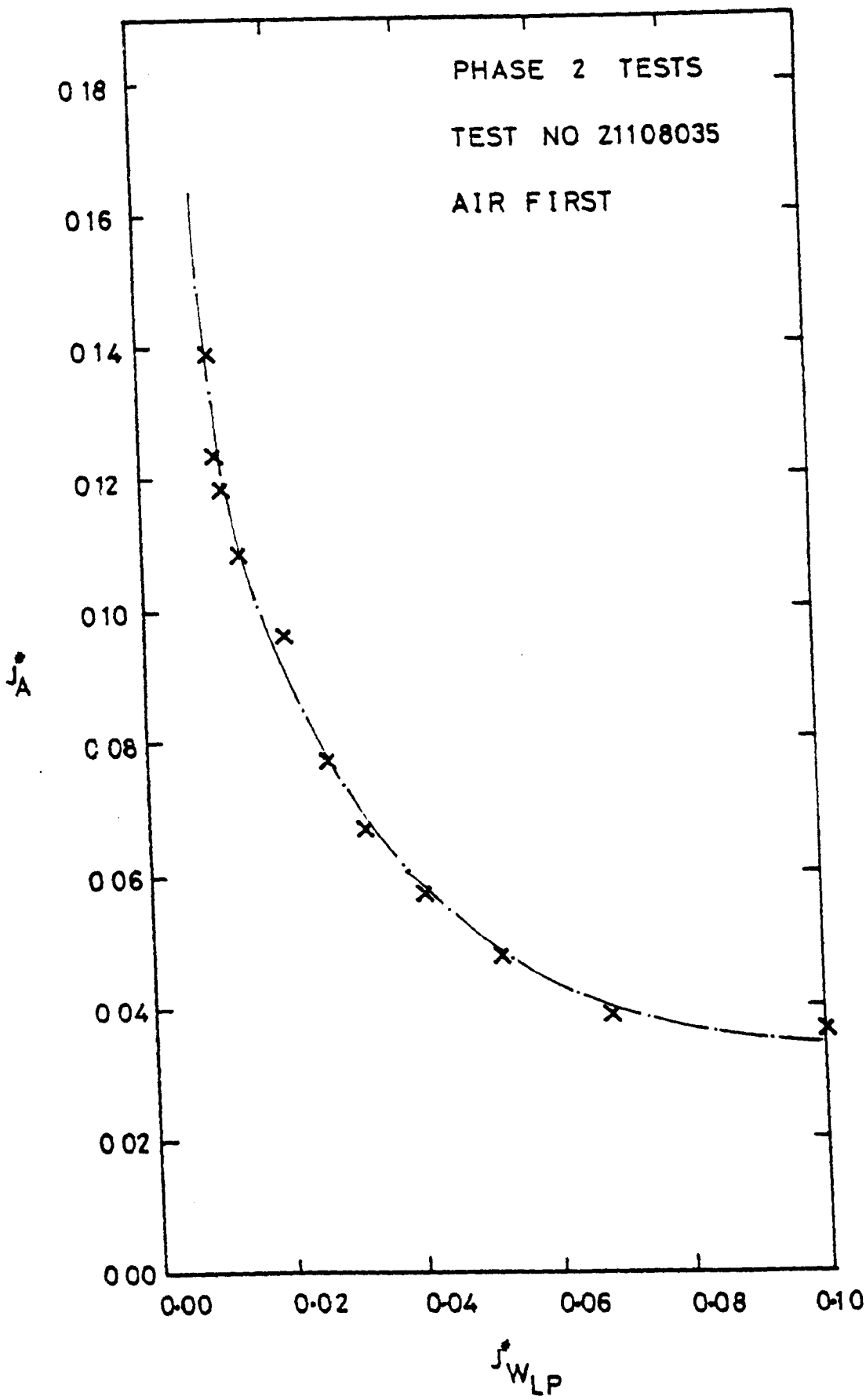

Fig H-16 PENETRATION CHARACTERISTICS FROM AIR-WATER TESTS

APPENDIX I

COMPARISON BETWEEN PARTIAL PENETRATION DATA FOR PHASE 1 TESTS AND EQUATION (4.4)

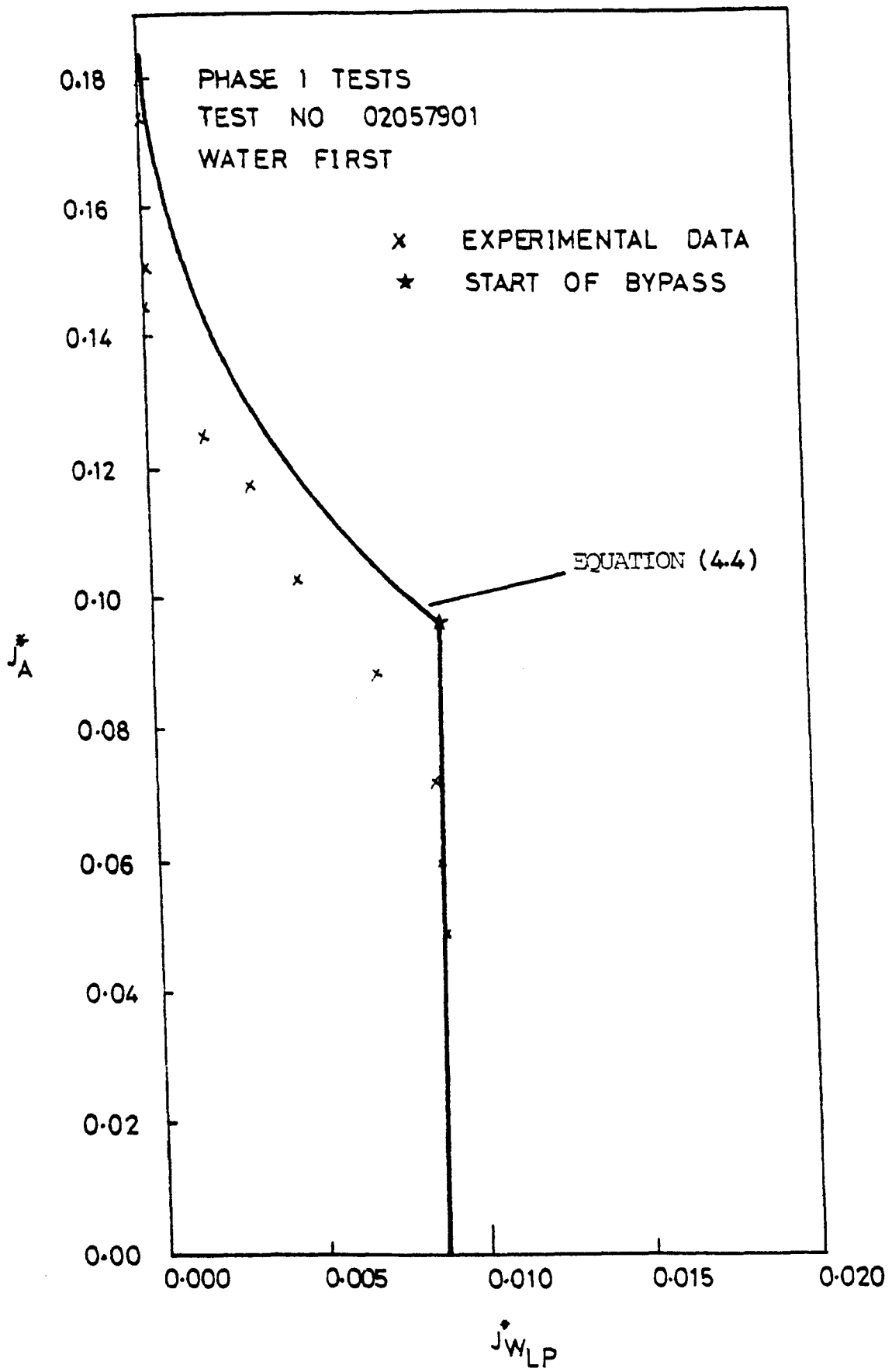

Fig I-1 Comparison of Experimental Data with Equation (44)

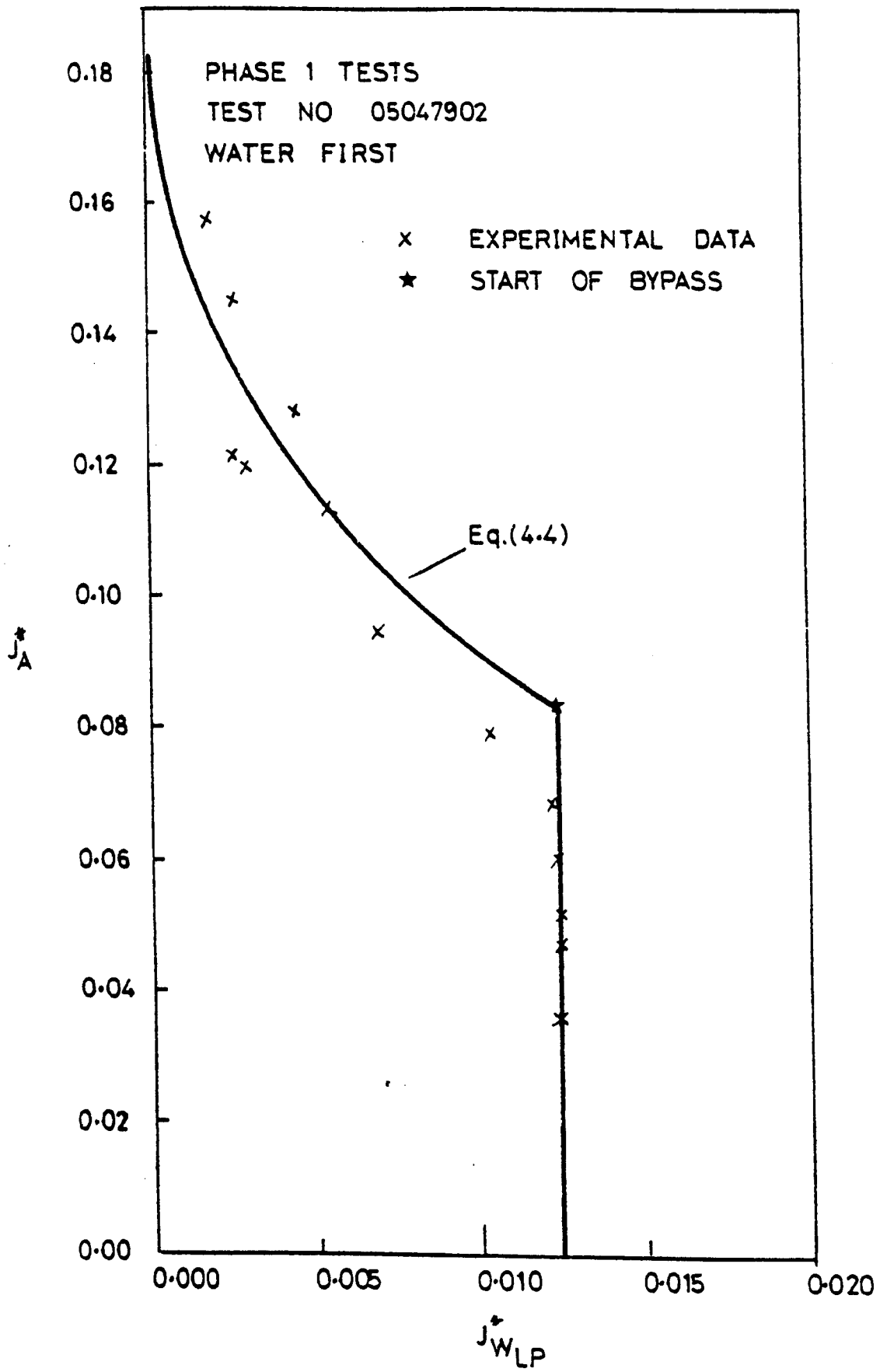

Fig I-2 Comparison of Experimental Data with Equation (4.4)

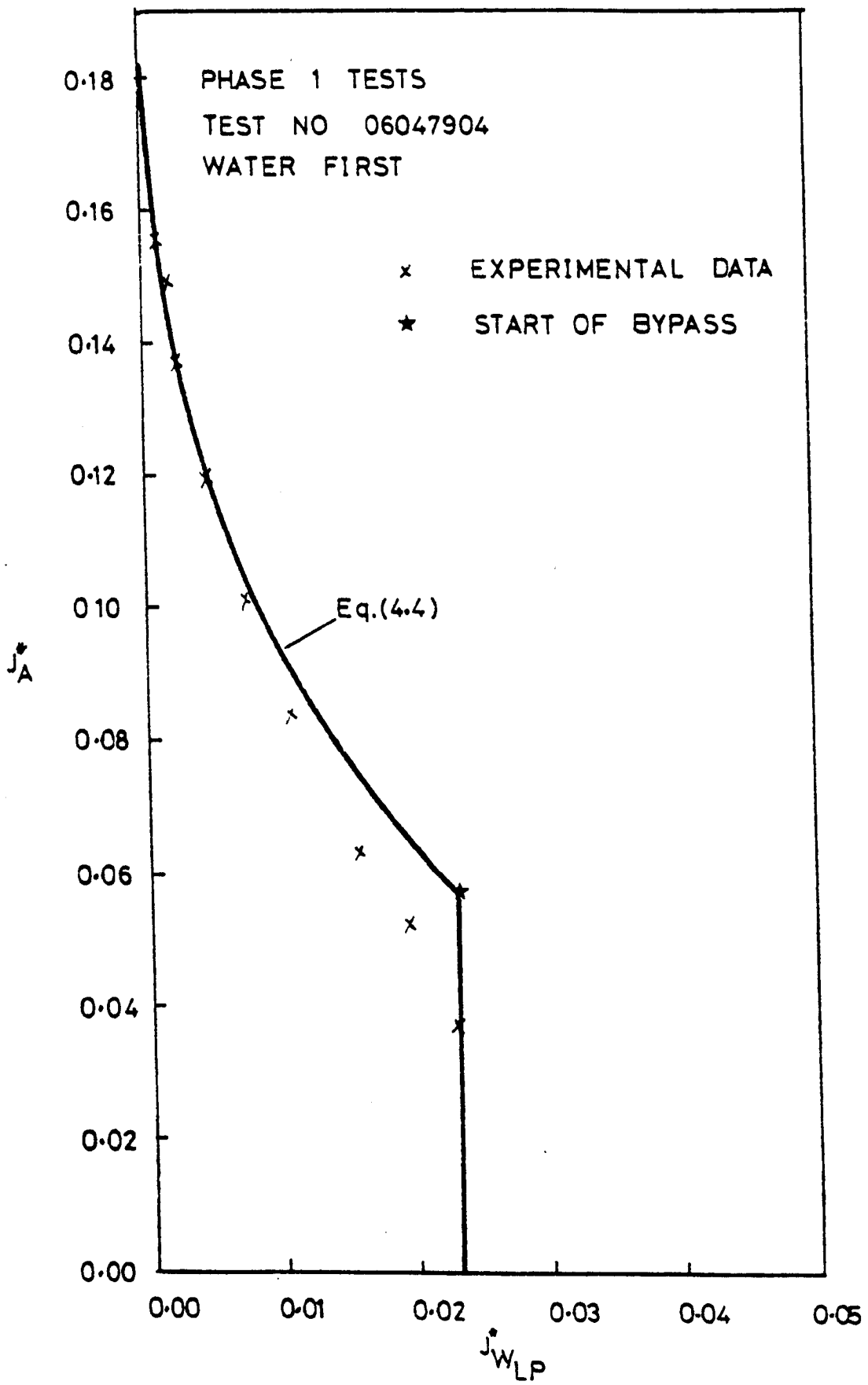

Fig I-3 Comparison of Experimental Data with Equation (4.4)

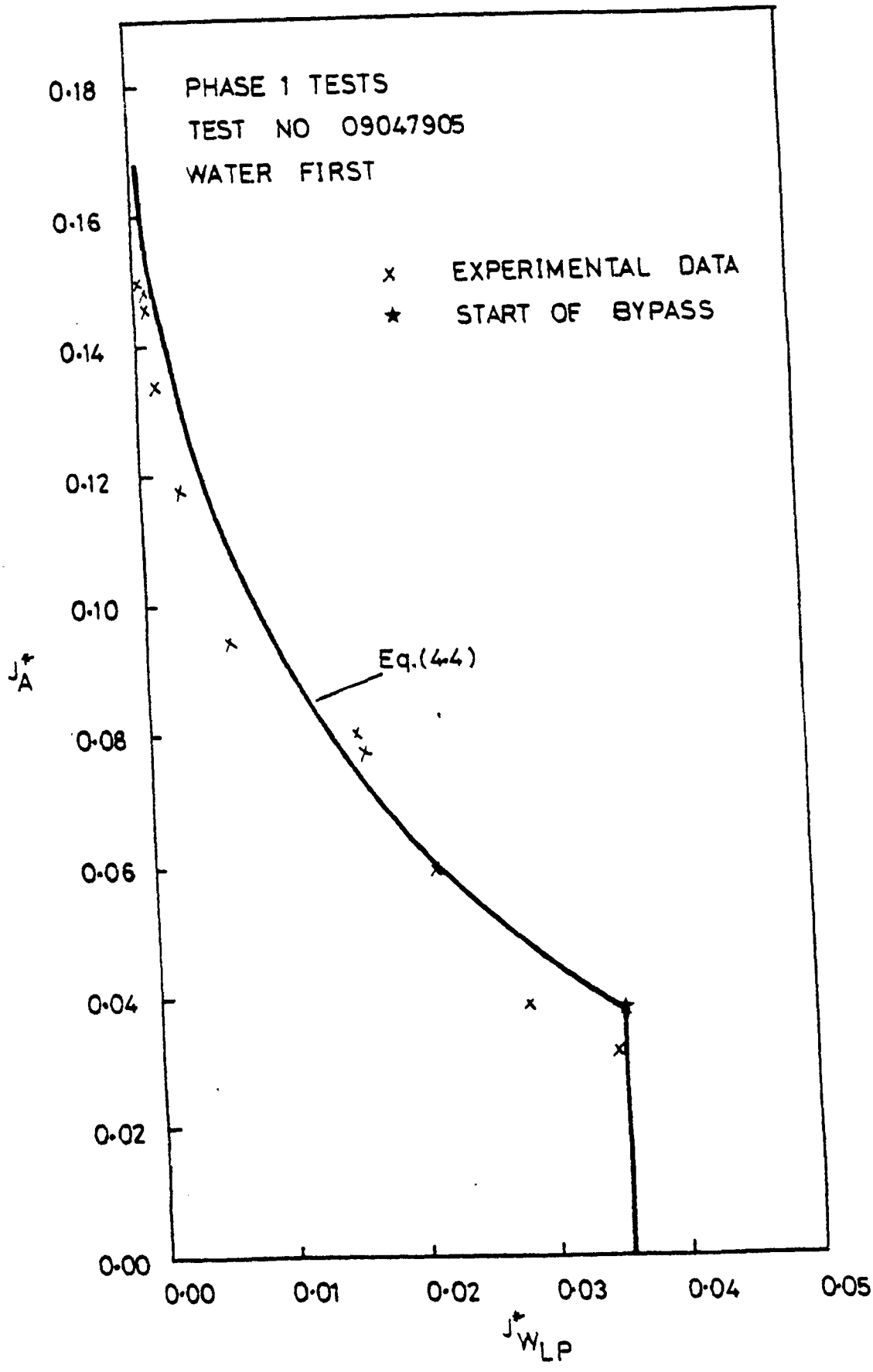

Fig 1-4 Comparison of Experimental Data with Equation (44)

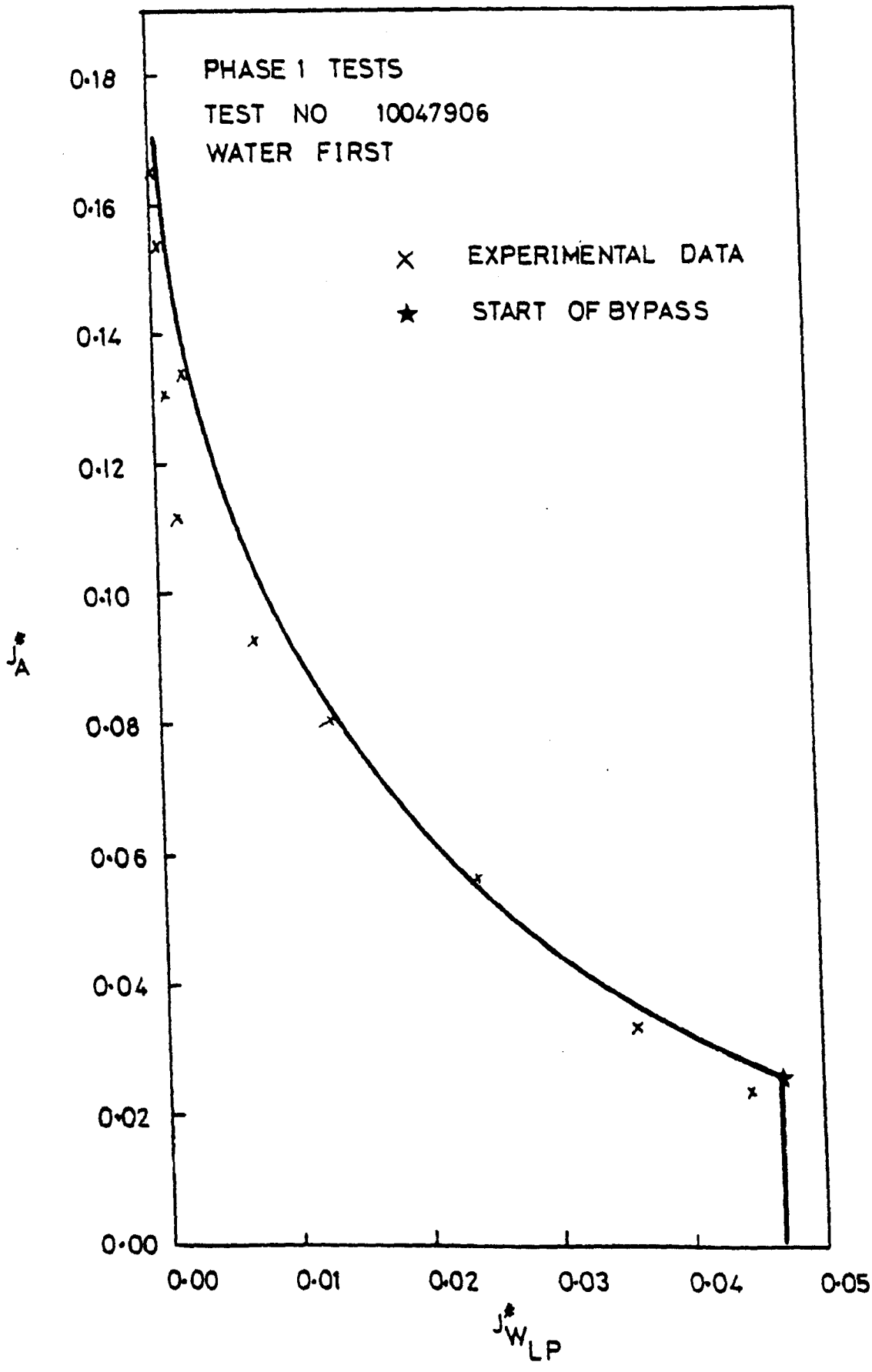

Fig 1-5 Comparison of Experimental Data with Equation (4.4)

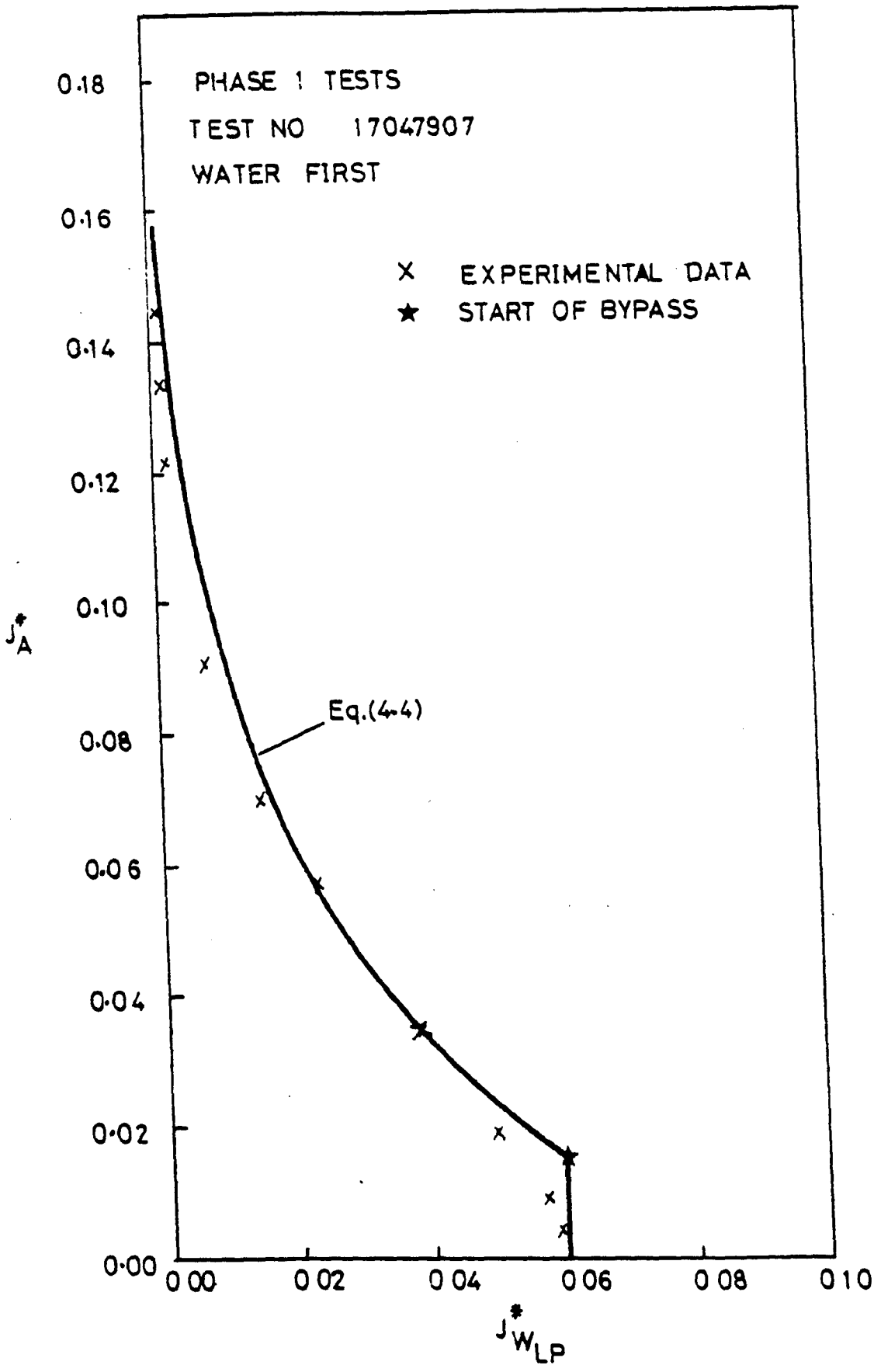

Fig 1-6 Comparison of Experimental Data with Equation (4-4)

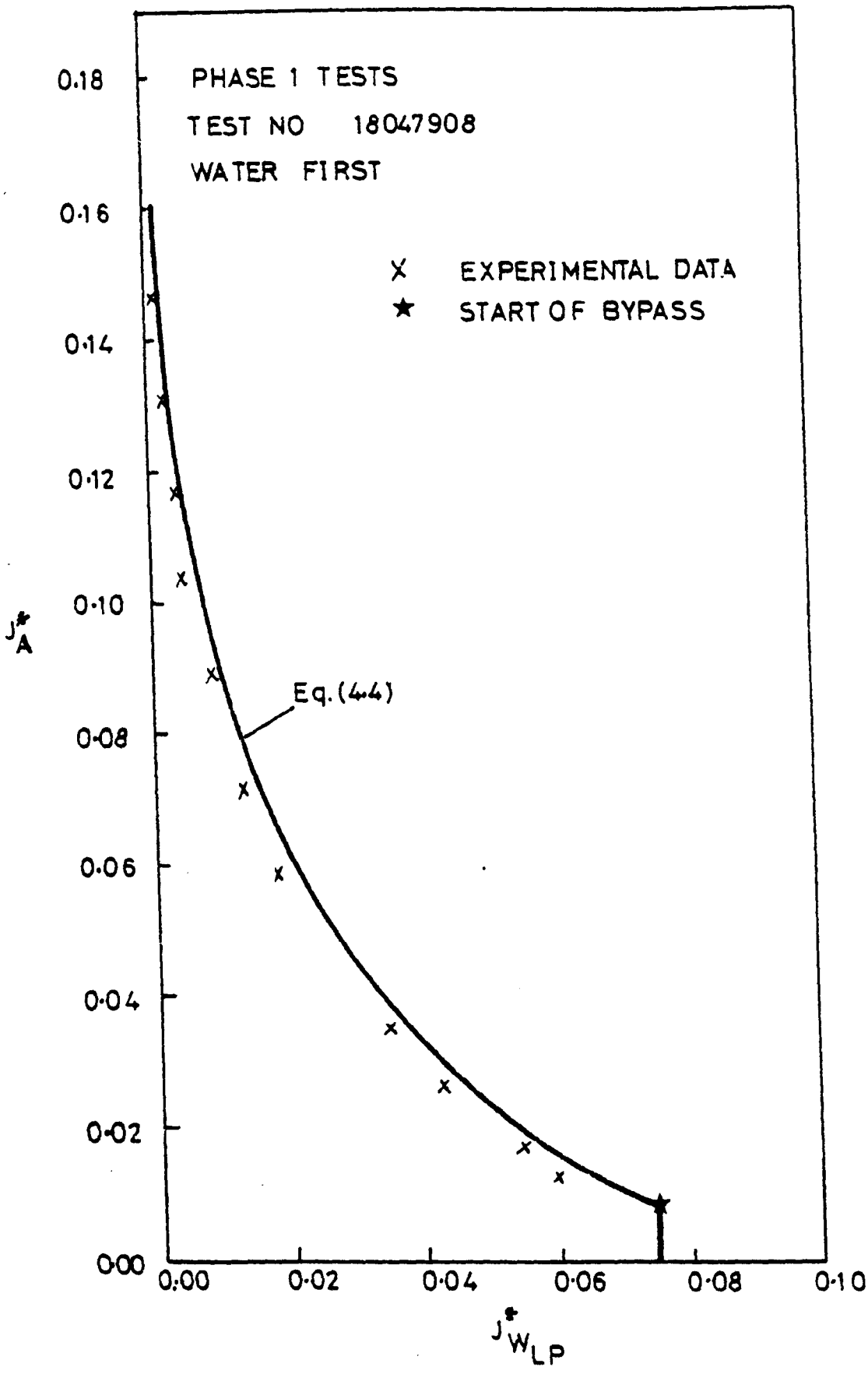

Fig 1-7 Comparison of Experimental Data with Equation (44)

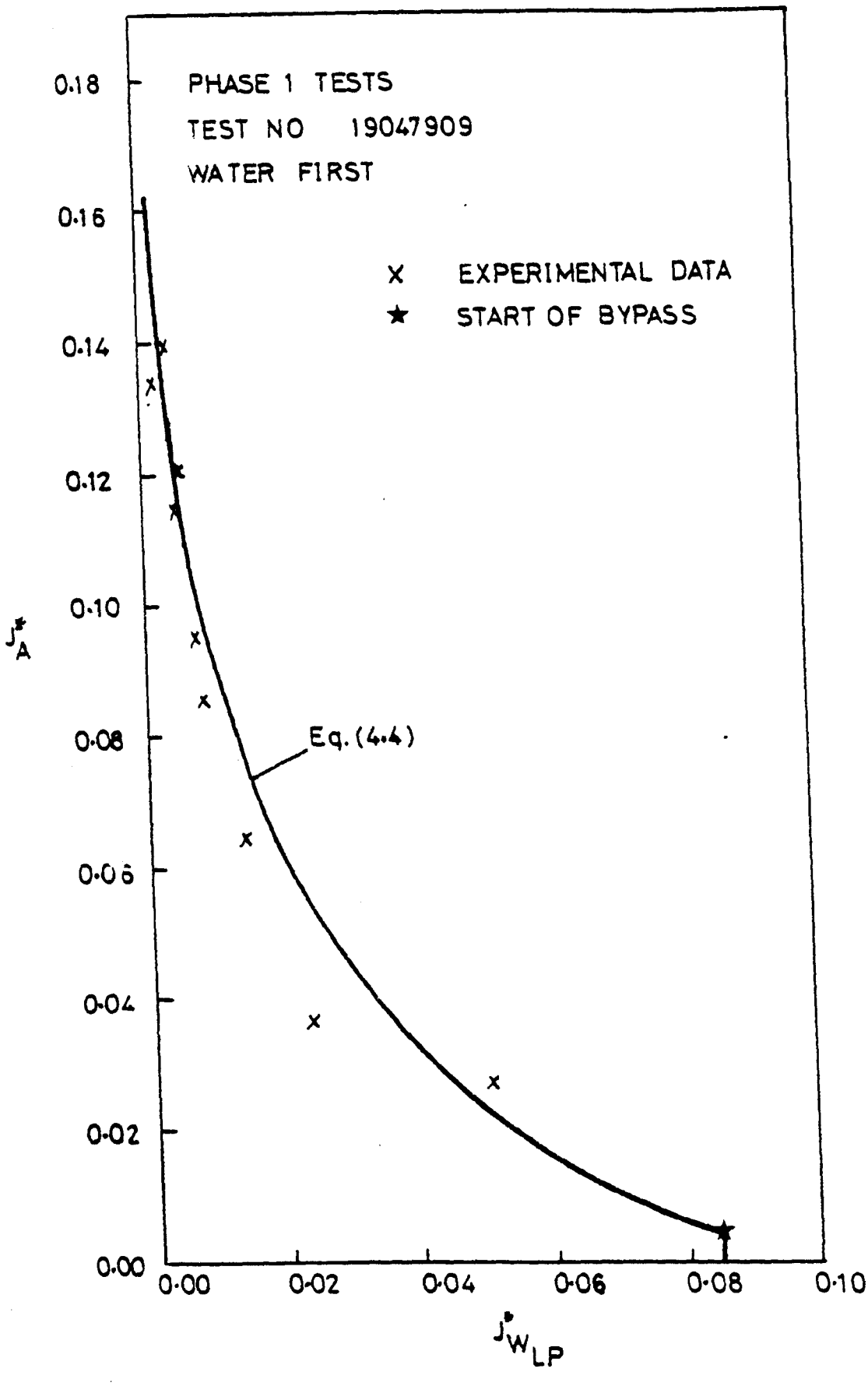

Fig I-8 Comparison of Experimental Data with Equation (4.4)

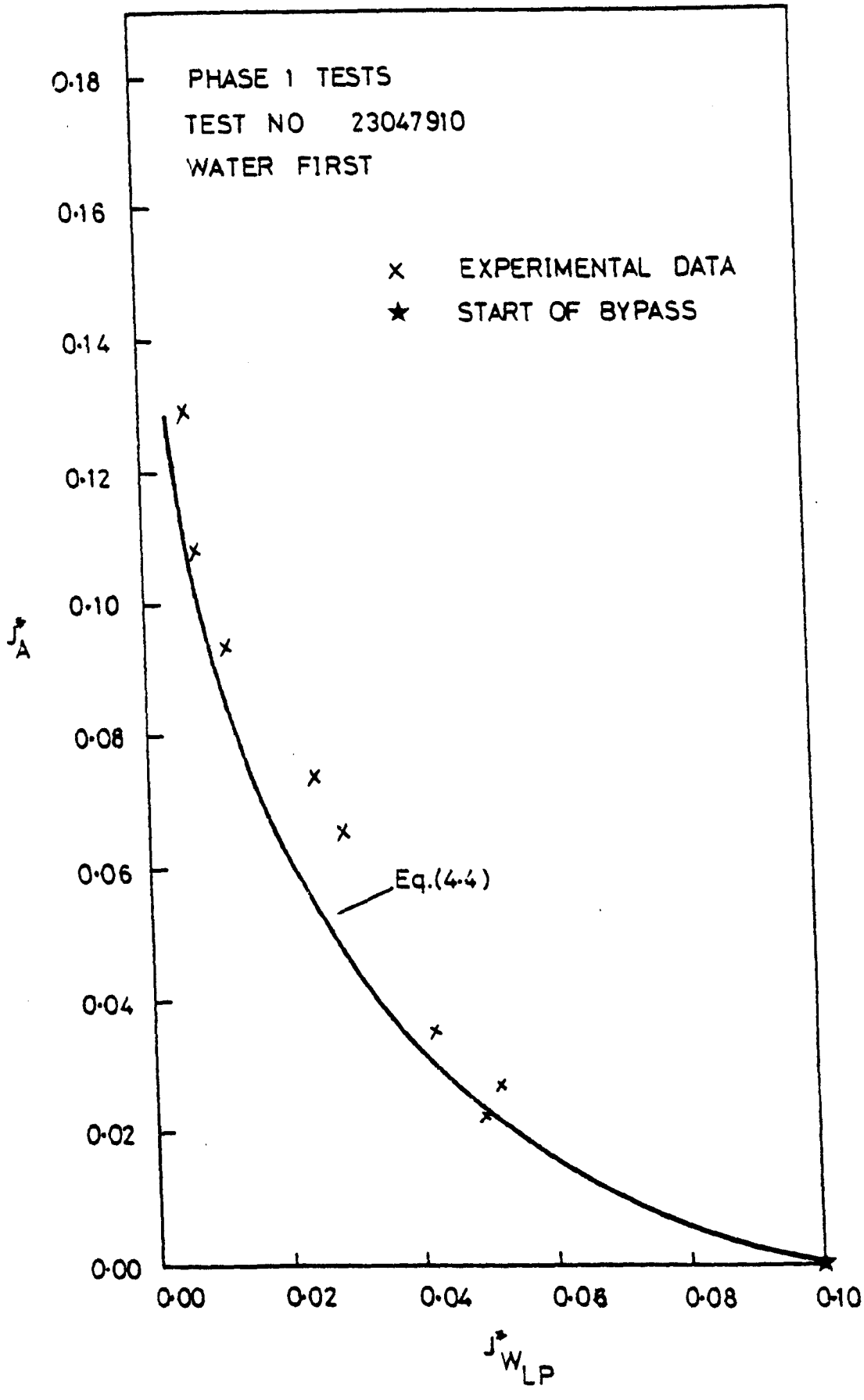

Fig 1-9 Comparison of Experimental Data with Equation (4.4)

APPENDIX J

COMPARISON OF "WATER-FIRST" WITH "AIR-FIRST" TEST DATA (Phase 2 Tests)

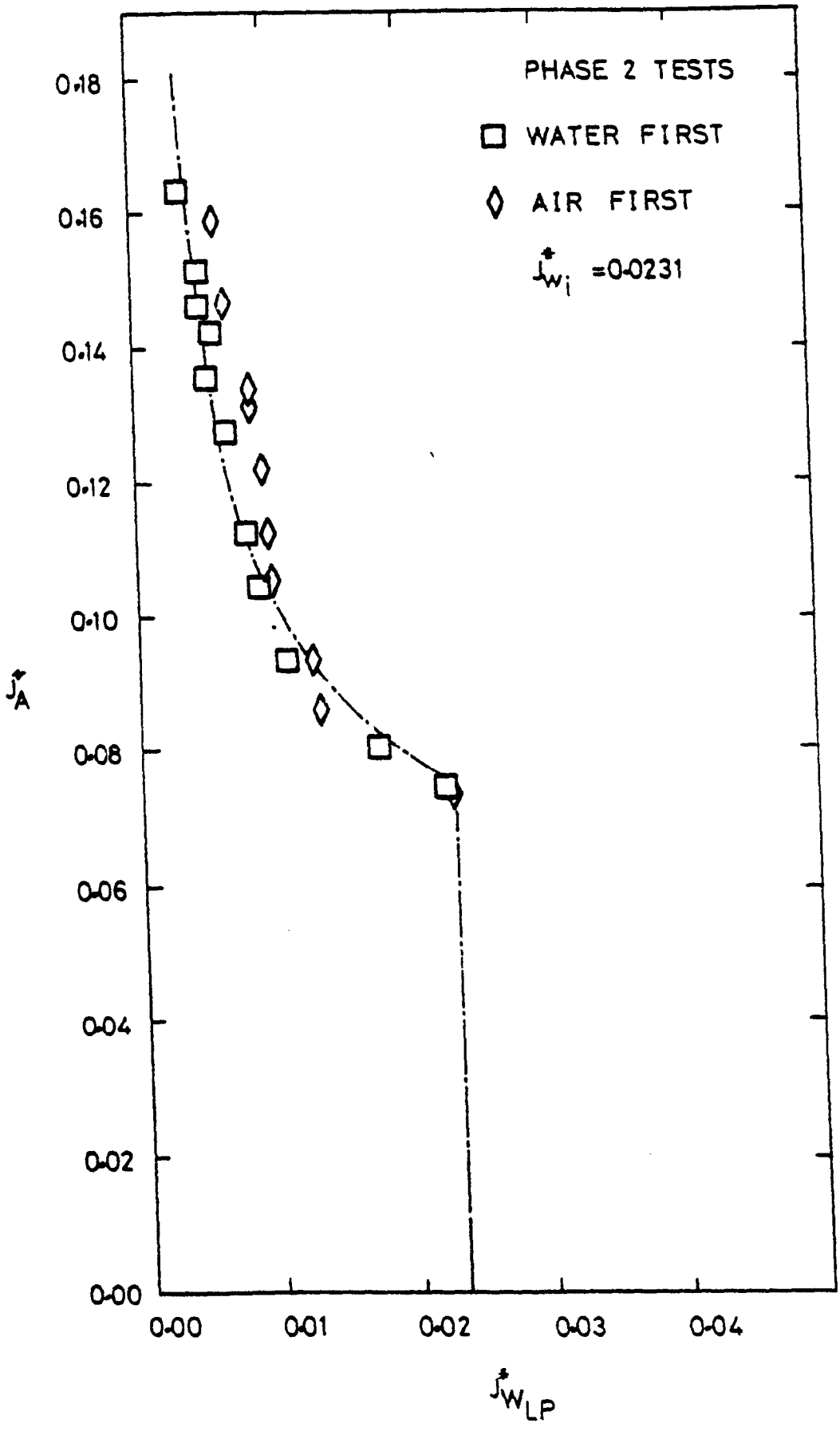

Fig J-1 Comparison Of "Water First" With "Air First" Test Data

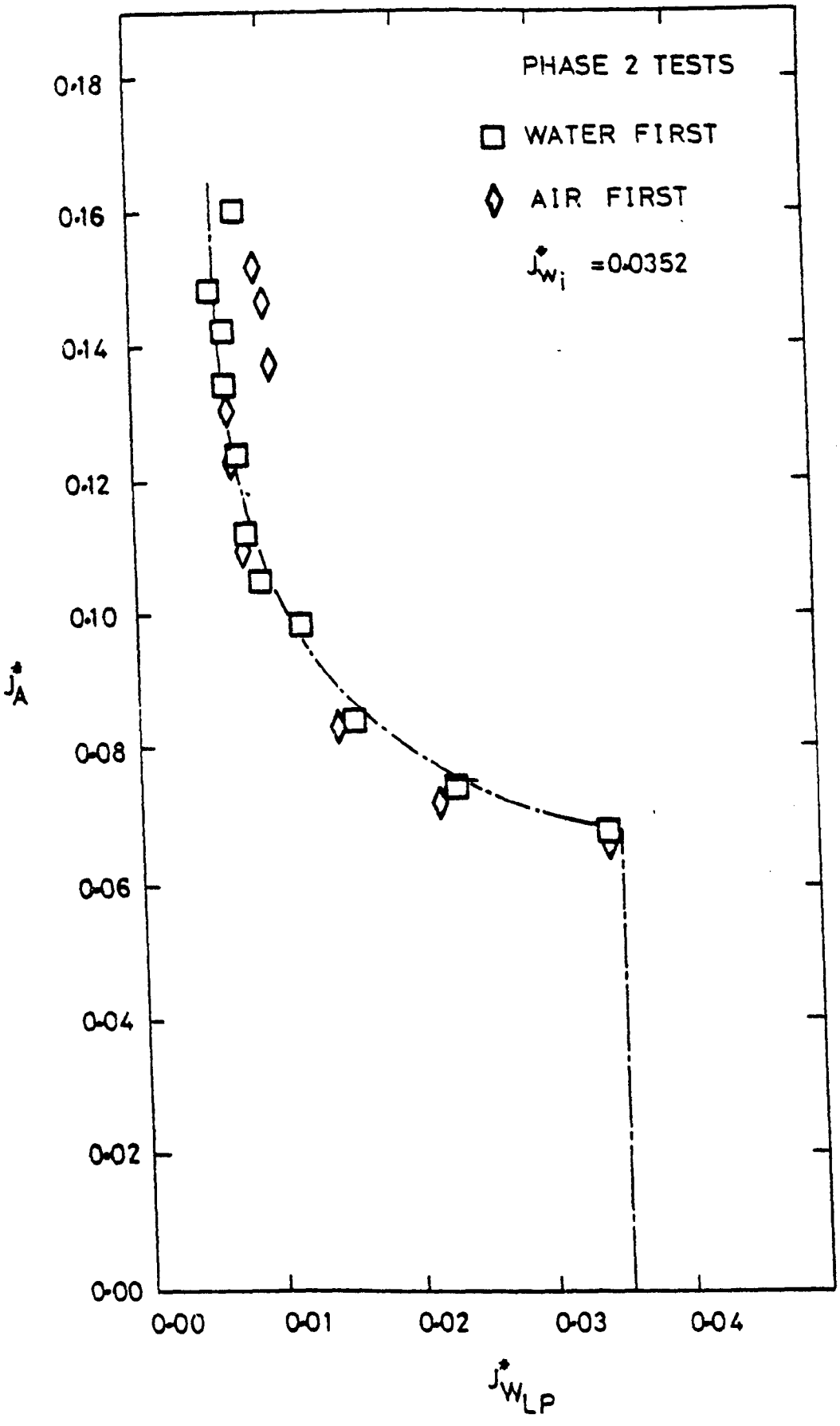

Fig J-2 Comparison Of "Water First" With "Air First" Test Data

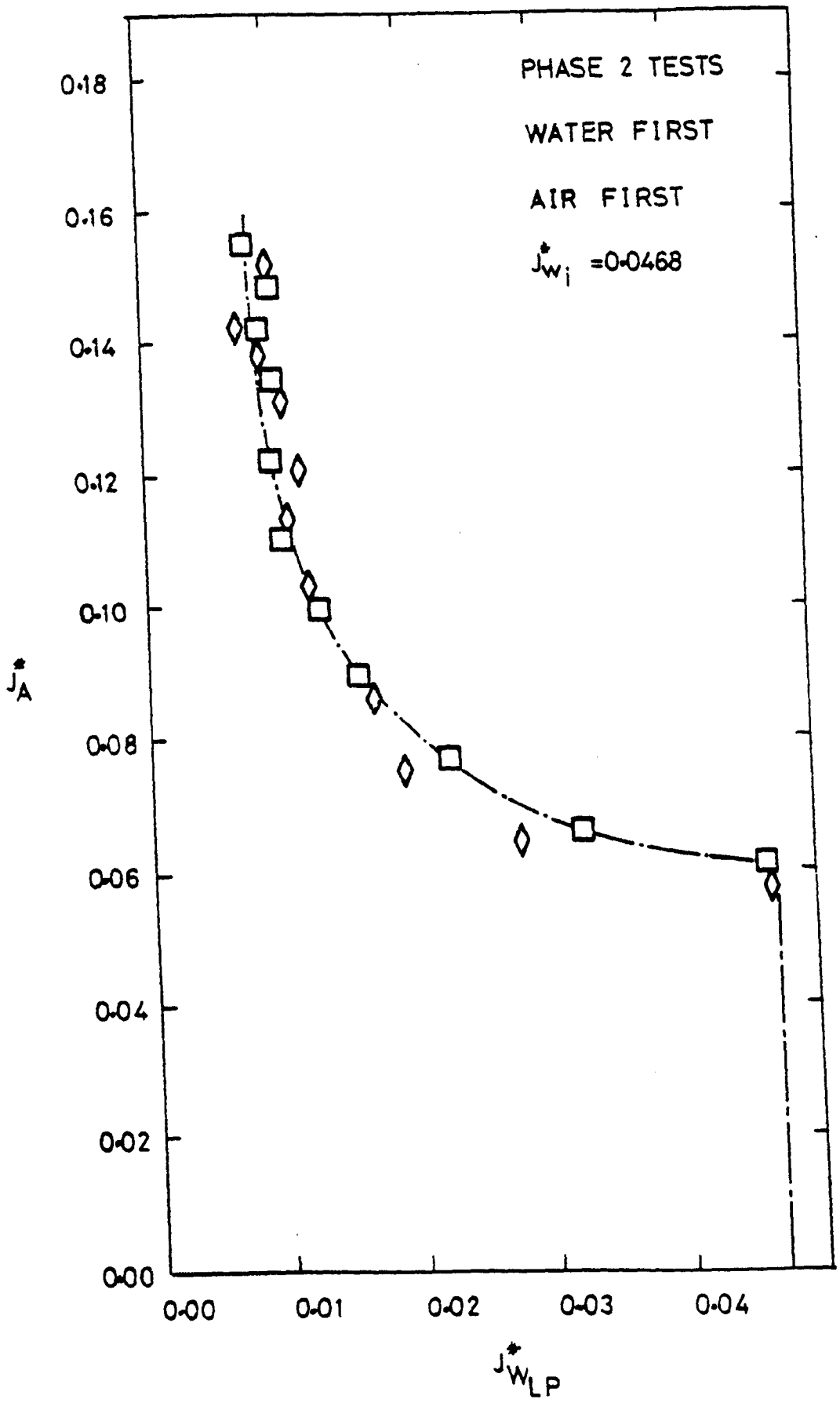

Fig J-3 Comparison Of "Water First" With "Air First" Test Data

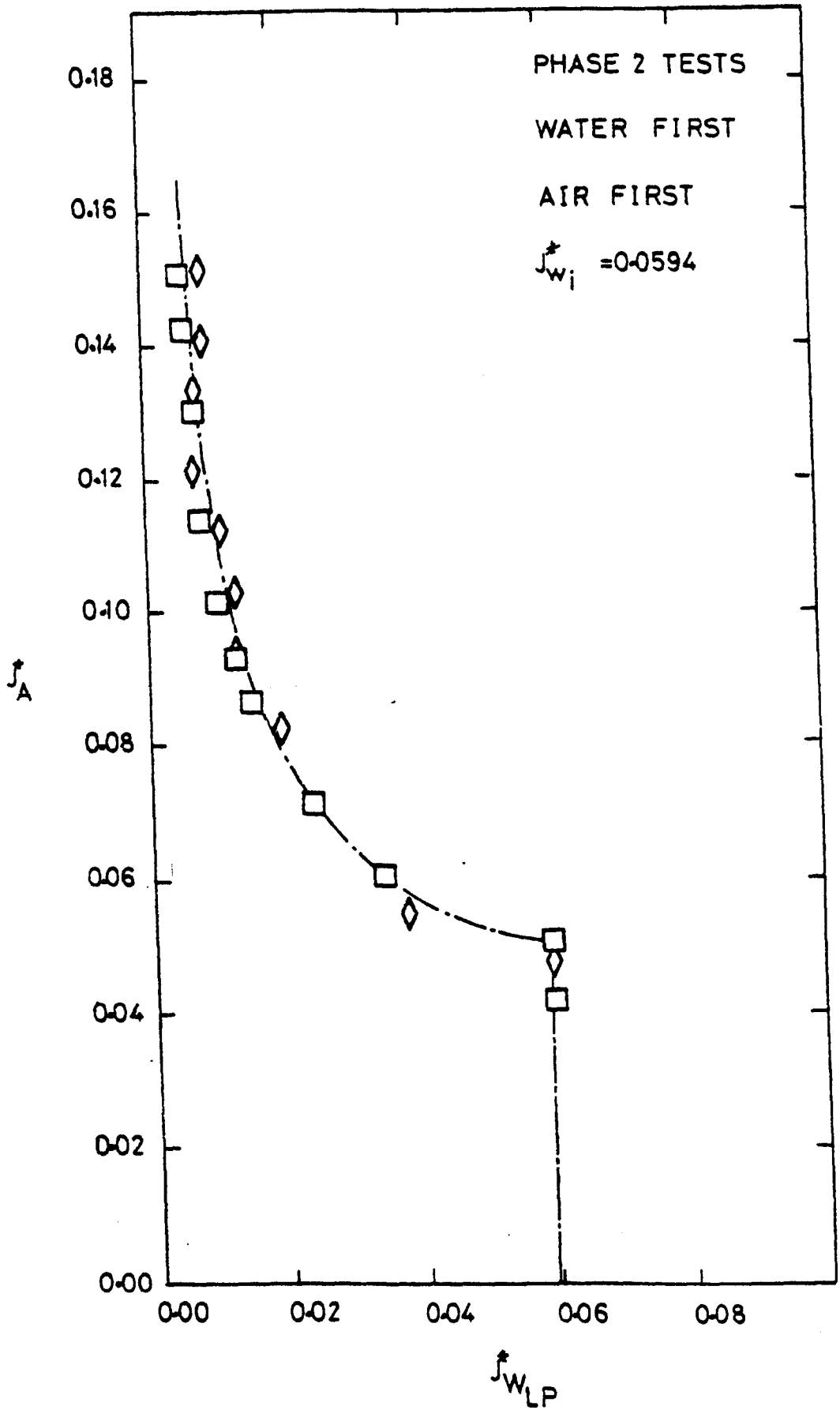

Fig J-4 Comparison Of "Water First" With "Air First" Test Data

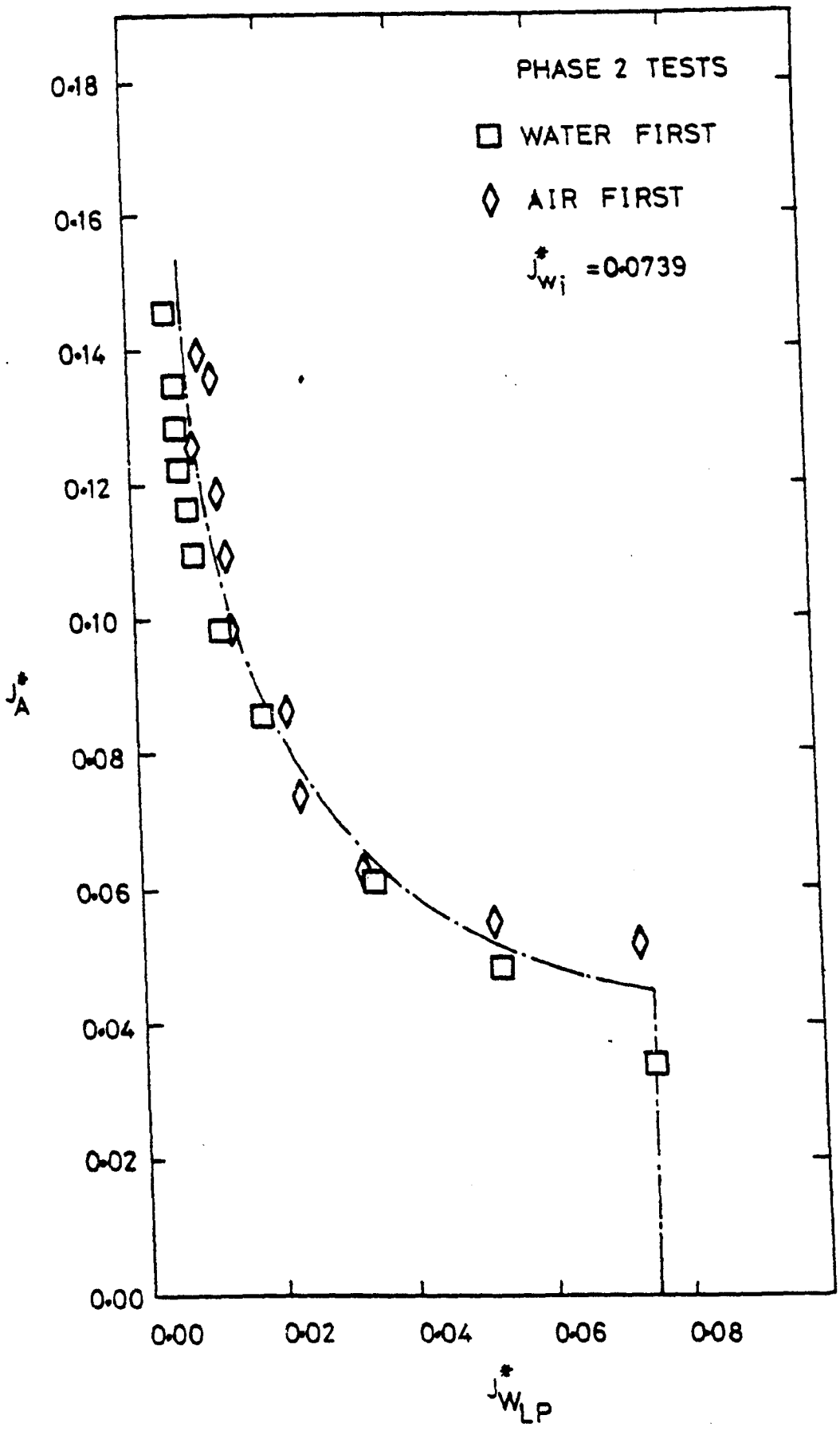

Fig J-5 Comparison Of "Water First" With "Air First" Test Data

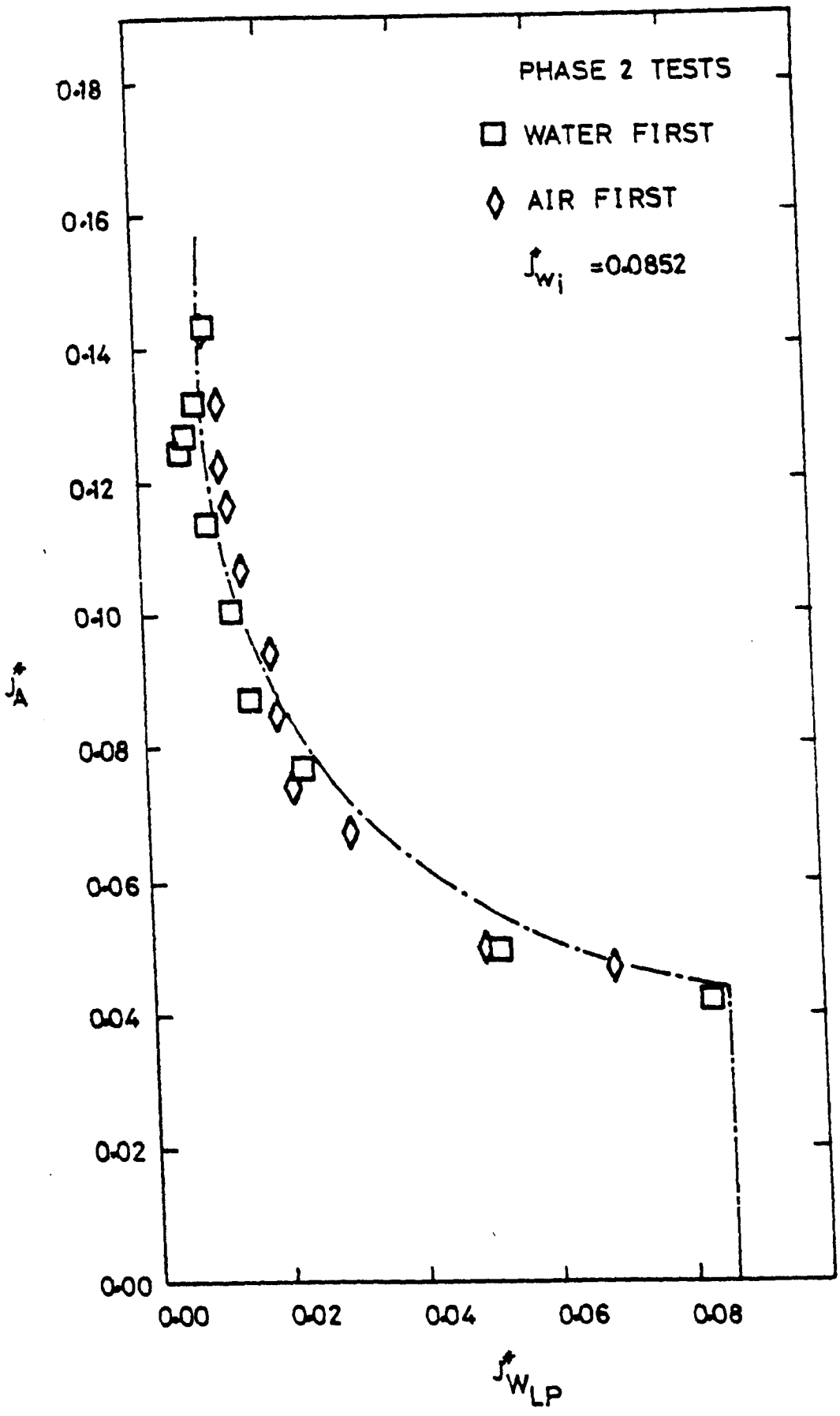

Fig J-6 Comparison Of "Water First" With "Air First" Test Data

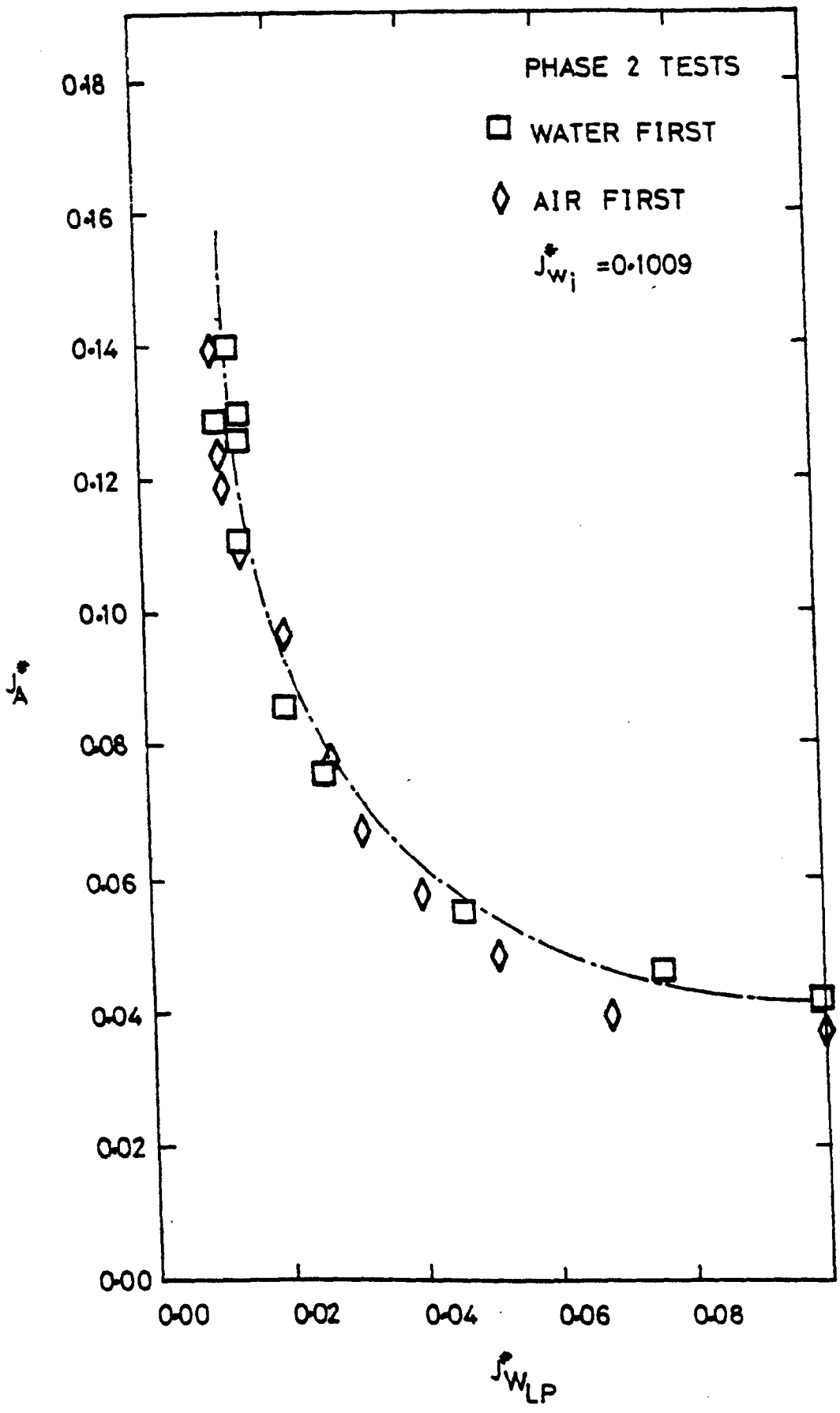

Fig J-7 Comparison Of "Water First" With "Air First" Test Data

APPENDIX K

COMPARISON OF PHASE 1 AND PHASE 2 TEST DATA

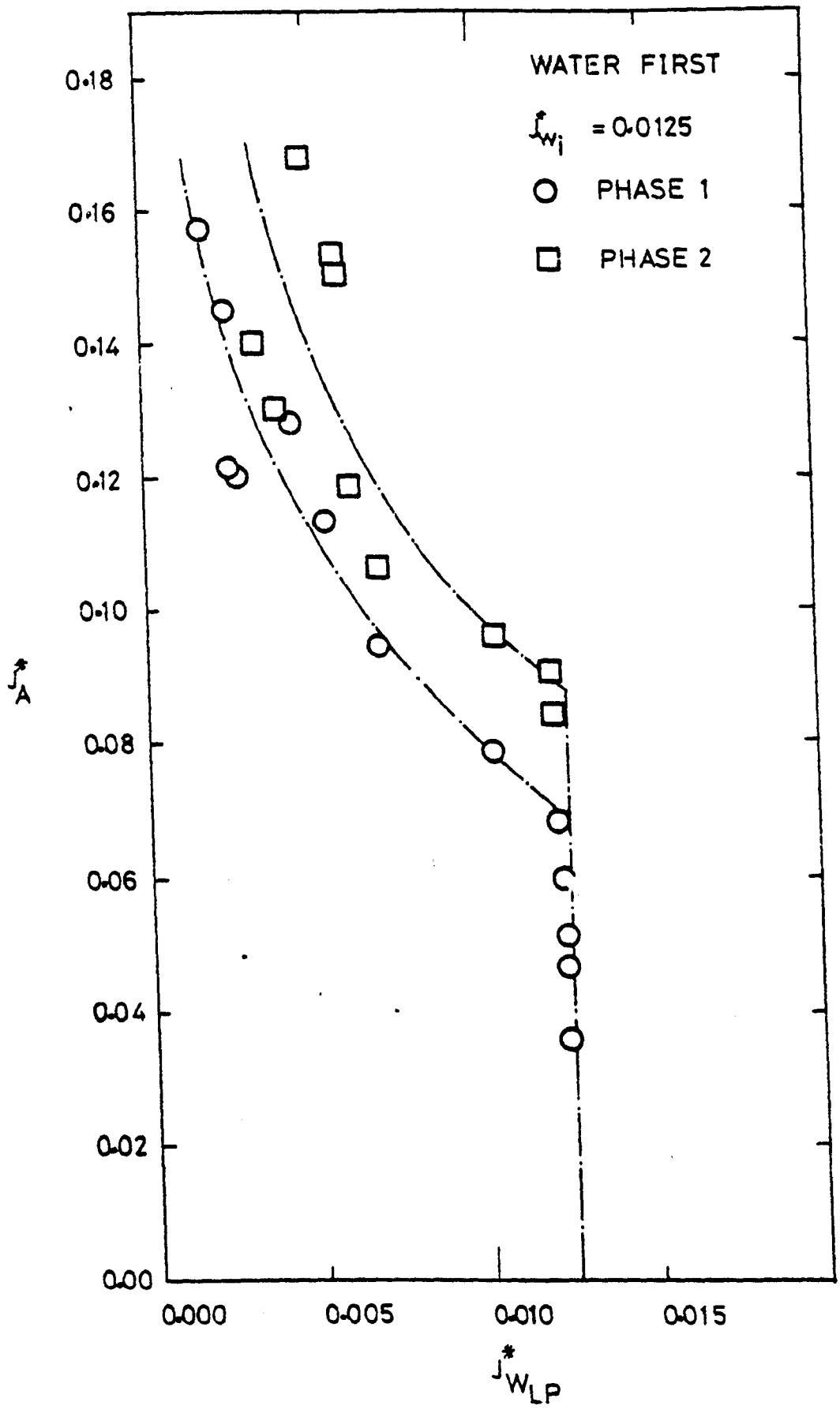

Fig K-1 Comparison Of Phase 1 & Phase 2 Test Data

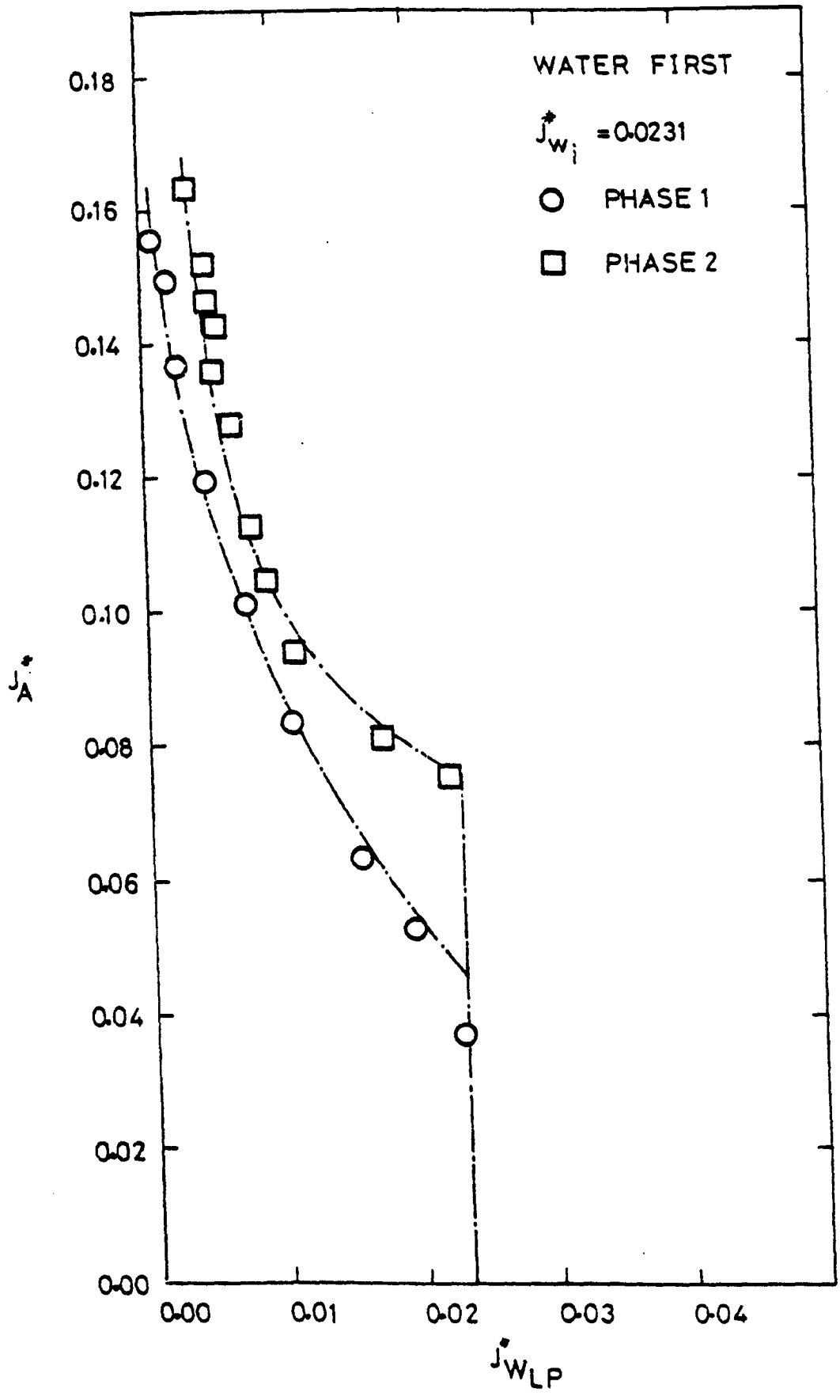

Fig K-2 Comparison Of Phase 1 & Phase 2 Test Data

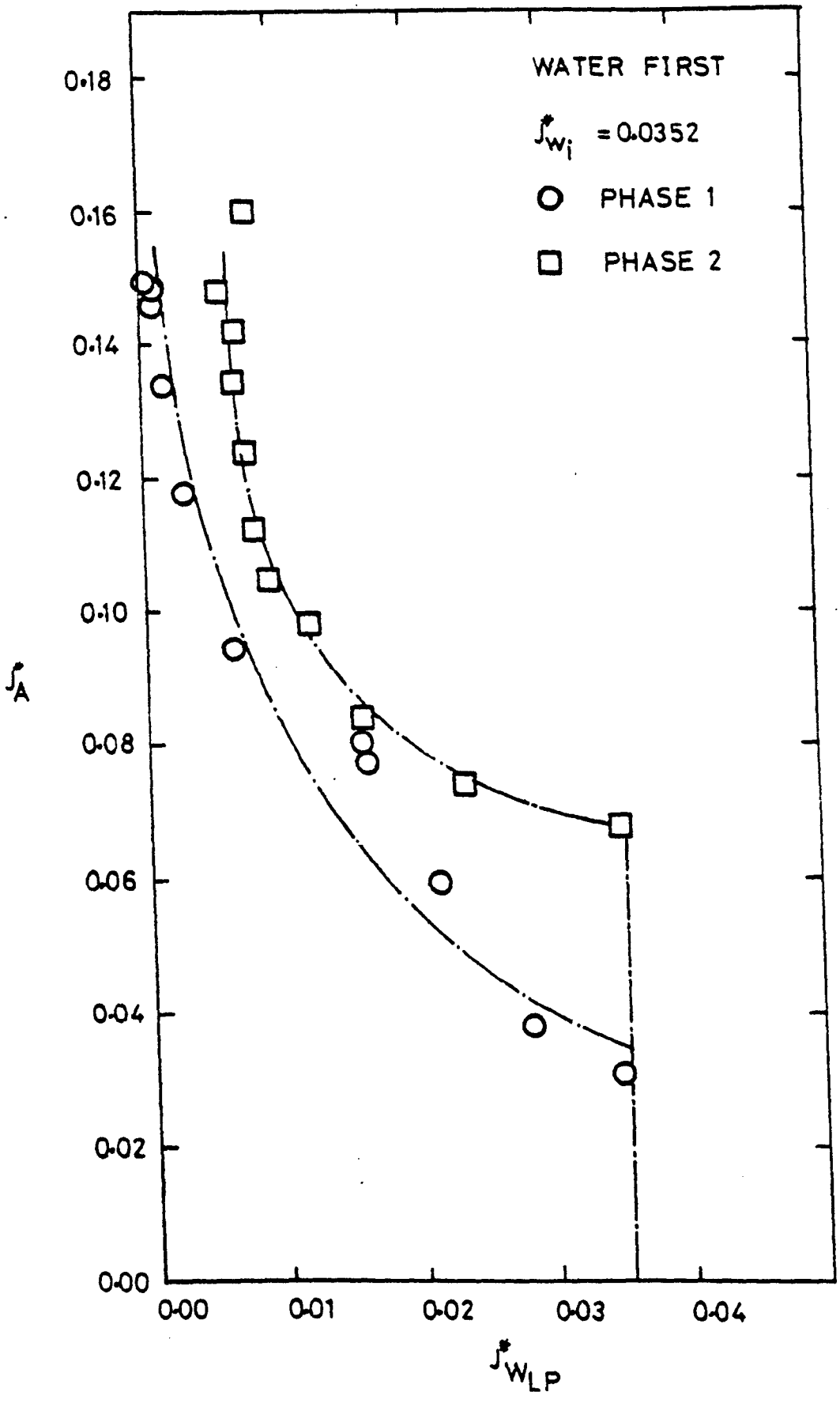

Fig. K-3 Comparison Of Phase 1 & Phase 2 Test Data

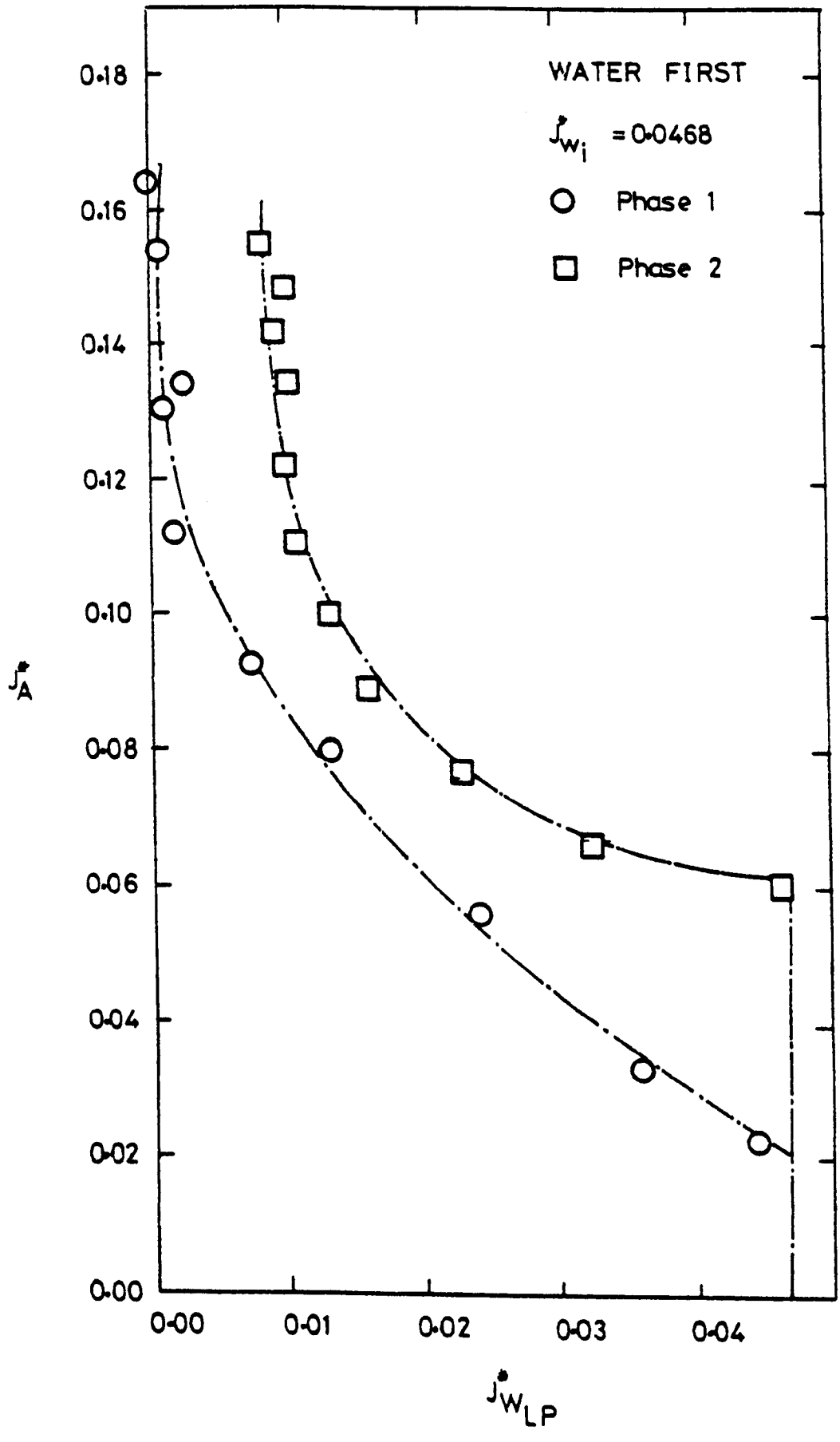

Fig K-4 Comparison Of Phase 1 & Phase 2 Test Data

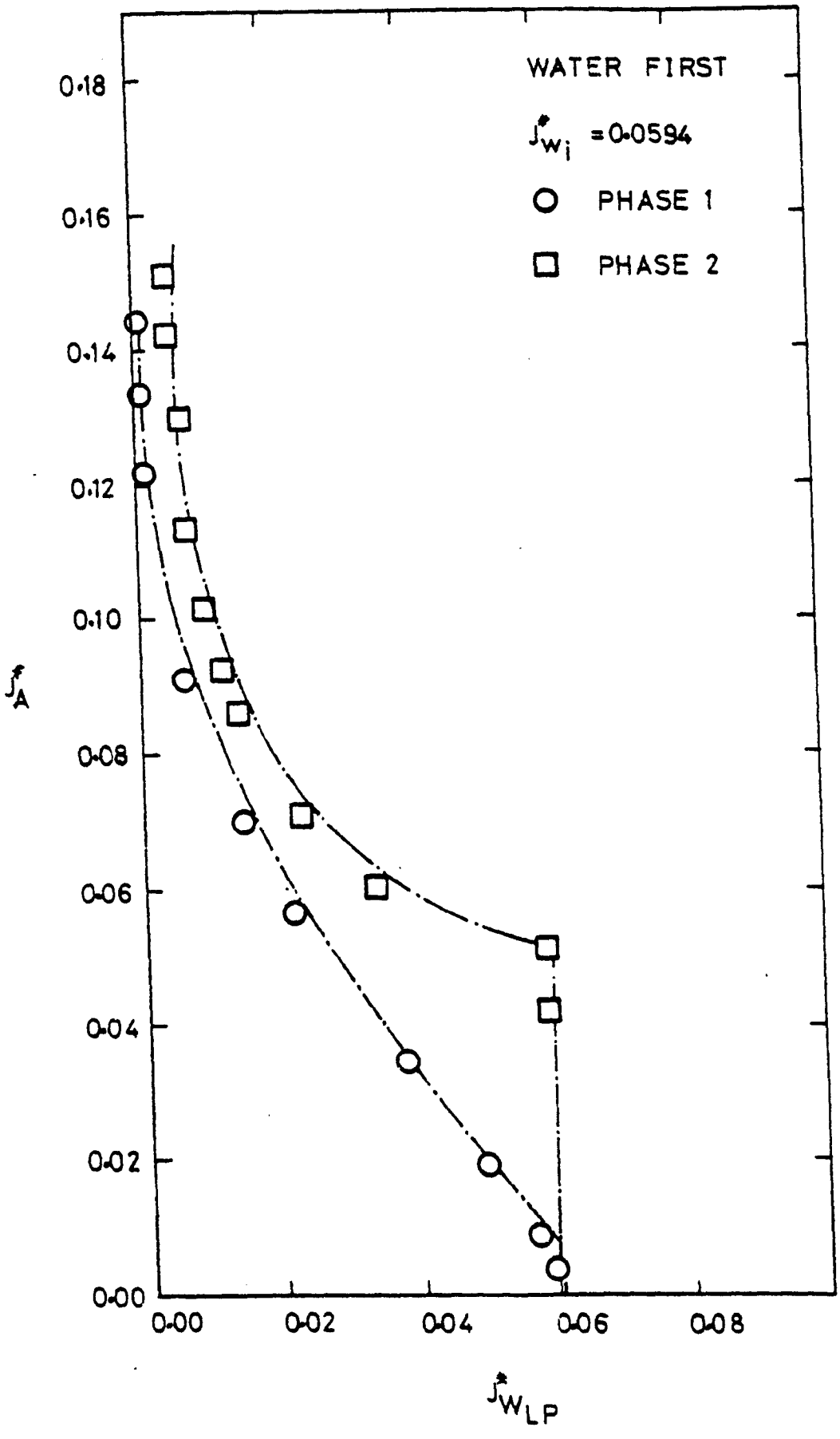

Fig K-5 Comparison Of Phase 1 & Phase 2 Test Data

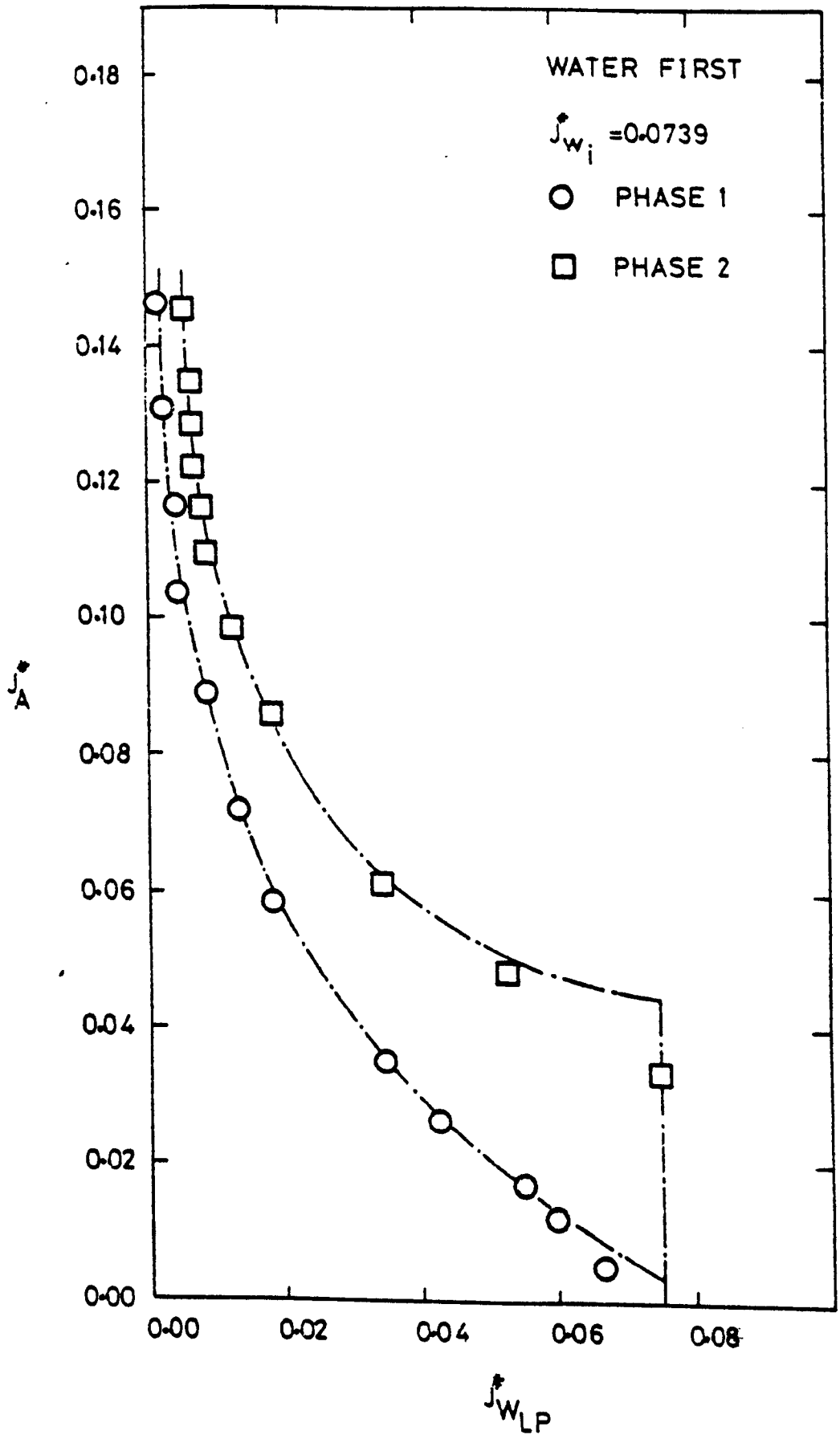

Fig K-6 Comparison Of Phase 1 & Phase 2 Test Data

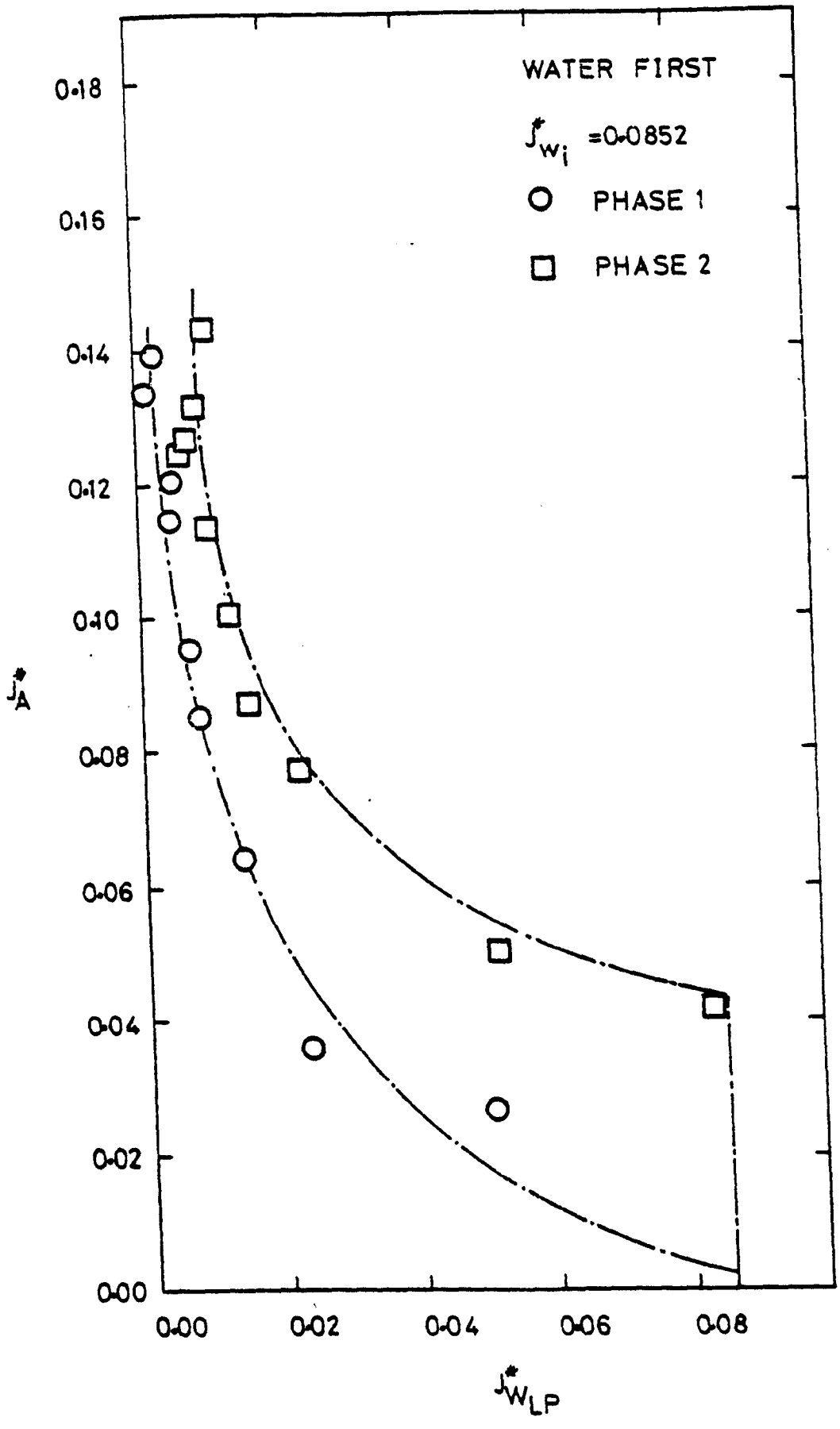

Fig K-7 Comparison Of Phase 1 & Phase 2 Test Data

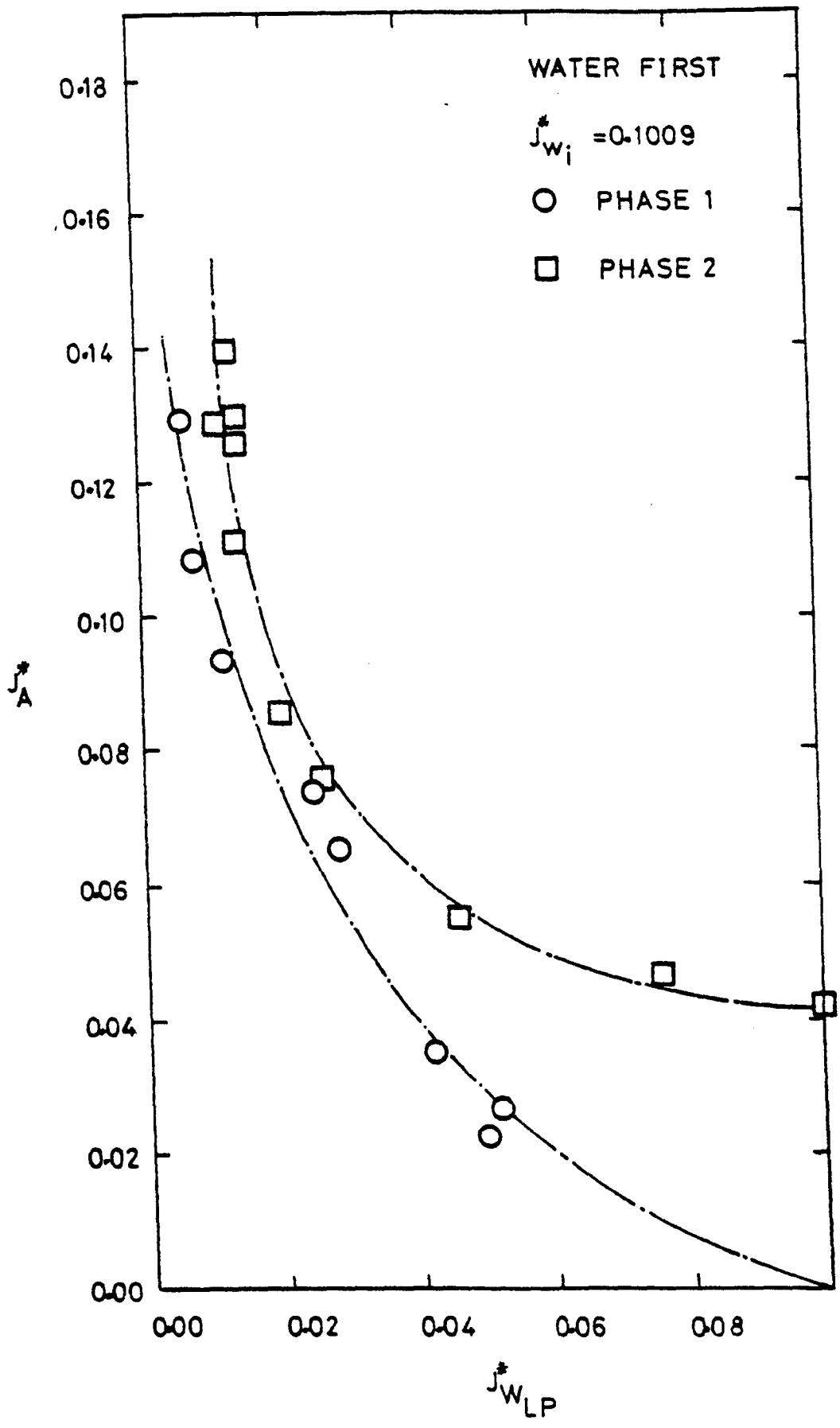

Fig K-8 Comparison Of Phase 1 & Phase 2 Test Data

APPENDIX L

CONVERSION OF THEORETICAL WORK TO WALLIS PARAMETERS

APPENDIX L

CONVERSION OF THEORETICAL WORK TO WALLIS PARAMETERS

The results obtained in the present experimental programme are presented in terms of Wallis parameters, defined as

$$J_L^* = \frac{M_L}{BS\,\rho_L}\left[\frac{\rho_L}{gB(\rho_L - \rho_g)}\right]^{\frac{1}{2}} \simeq \frac{Q_m}{S}\frac{1}{\sqrt{gB}} \qquad \text{(L-1)}$$

and

$$J_g^* = \frac{M_g}{BS\,\rho_g}\left[\frac{\rho_g}{gB(\rho_L - \rho_g)}\right]^{\frac{1}{2}} \simeq j_g\frac{1}{\sqrt{gB}}\left(\frac{\rho_g}{\rho_L}\right)^{\frac{1}{2}} \qquad \text{(L-2)}$$

where

Q_m = volume flowrate per unit width

j_g = superficial gas velocity

The different theoretical equation used for comparison with the present data are dealt with in turn.

L.1 SCHUTT'S THEORY

Schutt's analysis yielded equations (2.1) through (2.9) to define the flooding conditions. The equations are very complicated in their present form; a major difficulty being the finding of an expression for n_{tr}. Schutt presented graphs to help in estimating n_{tr} and these graphs were used to construct Figure L-1, which

shows the variation of n_{tr} with Re. It can be seen in Figure L-1 that n_{tr} can be approximated to unity for values of R_e exceeding 3500 for tube diameters of 1½" and 3". Most of the present data have the value of inlet water Reynolds number greater than 3500, also the hydraulic diameter = 2". Taking n_{tr} = 1 and ignoring δ in comparison with D/2, reduces Equation (2.1) to:

$$U_g\left(\frac{\rho_g}{\rho_L}\right)^{\frac{1}{2}} = U_L\left[\left(\frac{Dg}{4U_L^2} - \frac{8}{Re}\right) \cdot \frac{2\tan\epsilon \cdot r}{2\tan\epsilon \cdot r - 1}\right]^{\frac{1}{2}} \qquad \text{(L-3)}$$

where

$$r = \frac{\left[1 + \exp\left(\frac{8\pi\delta}{D}\right)\right]^2}{\left[1 - \exp\left(\frac{8\pi\delta}{D}\right)\right]} + 1 \qquad \text{(L-4)}$$

$$Re = \frac{4Q_m}{\nu} \qquad \text{(L-5)}$$

From Equations (L-1) and (L-5),

$$J_L^* = Re \cdot \frac{\nu}{4S\sqrt{gB}} \qquad \text{(L-6)}$$

From Equations (L-6) and (2.6)

$$\delta = 3.425 \times 10^{-5} \times \left(\frac{4S}{\nu}\sqrt{gB}\right)^{0.375} J_L^{*0.375} \qquad \text{(L-7)}$$

From Equations (2.8) and (L-7),

$$U_L = \frac{q}{4\nu}(3.425 \times 10^{-5})^2\left(\frac{4S}{\nu}\sqrt{gB}\right)^{0.75} J_L^{*0.75} \qquad \text{(L-8)}$$

Since the film thickness is small compared to the gap size, the gas velocity U_g can be taken as equal to the superfacial velocity, j_g, i.e.,

$$U_g \simeq j_g \tag{L-9}$$

From (L-2) and (L-9), we get

$$U_g \left(\frac{\rho_g}{\rho_L}\right)^{\frac{1}{2}} = J_g^* \cdot \sqrt{gB} \tag{L-10}$$

The following values were used for the calculations :

$$B = 0.686 \text{ m} \tag{L-11}$$

$$S = 0.0254 \text{ m} \tag{L-12}$$

$$\mu = 0.0011 \text{ Kg/m.s} \tag{L-13}$$

$$\rho_L = 1000 \text{ Kg/m}^3 \tag{L-14}$$

$$\rho_g = 1.25 \text{ Kg/m}^3 \tag{L-15}$$

$$D_H = 2S = 0.0508 \text{ m} \tag{L-16}$$

From Equations (L-11) to (L-15), together with Equation (L-8),

$$\frac{U_L}{\sqrt{gB}} = \frac{g}{4\nu\sqrt{gB}} (3.425 \times 10^{-5})^2 \left(\frac{4S}{\nu}\sqrt{gB}\right)^{0.75} J_L^{*0.75} \tag{L-17}$$

OR

$$\frac{U_L}{\sqrt{gB}} = 10.92\, J_L^{*0.75} \tag{L-18}$$

Similarly,

$$\frac{qD}{4U_L^2} = \frac{1.55 \times 10^{-4}}{J_L^{*0.75}} \qquad \text{(L-19)}$$

Substituting Equations (L-11) through (L-14) into (L-6) gives

$$Re = 2.396 \times 10^{5} J_L^* \qquad \text{(L-20)}$$

OR

$$\frac{8}{Re} = \frac{3.34 \times 10^{-5}}{J_L^*} \qquad \text{(L-21)}$$

Equation (L-7) can be made dimensionless by dividing both sides of the equation by D_H. This gives

$$\frac{\delta}{D_H} = 0.07\, J_L^{*0.375} \qquad \text{(L-22)}$$

Substituting Equation (L-22) into (L-4) leads to

$$\Gamma = \frac{\left[1 + \exp\left(1.763\, J_L^{*0.375}\right)\right]^2}{\left[1 - \exp\left(1.763\, J_L^{*0.375}\right)\right]} + 1 \qquad \text{(L-23)}$$

and from (L-13), (L-14) and (2.9)

$$\sqrt{\tan\epsilon} = 0.1581 \qquad \text{(L-24)}$$

$$2\tan\epsilon = 0.05 \qquad \text{(L-25)}$$

Substituting Equations (L-18), (L-19), (L-21), (L-25) and (L-10) into (L-3) and arranging gives

$$J_g^* = 0.063 \left[(4.64\ J_L^{*0.75} - J_L^{*0.5}) \frac{\Gamma}{\Gamma - 20} \right]^{\frac{1}{2}} \qquad \text{(L-26)}$$

Equation (L-26) is compared with the experimental data in Figure 5.10.

L.2 GROLMES et al

The following equation was derived by Grolmes et al (7) to describe flooding conditions:

$$U_g = 1.15 \left(\frac{\rho_L}{\rho_g} \right)^{\frac{1}{2}} \left(\frac{g \delta}{f_{2\phi}} \right)^{\frac{1}{2}} \qquad \text{(L-27)}$$

where

$$f_{2\phi} = 0.006 + 2 \times 10^6 \delta^2 \quad \text{(for air/water)} \qquad \text{(L-28)}$$

and

$$\delta = \left[\frac{3 \mu_L Q_m}{\rho_L g} \right]^{1/3} \qquad \text{(L-29)}$$

Equation (L-29) can be expressed as

$$\delta = \left(\frac{3 \mu^2}{4 \rho^2 g} \right)^{1/3} Re^{1/3} \qquad \text{(L-30)}$$

From Equation (L-10) and (L-26)

$$J_g^* = 1.15 \left(\frac{\delta}{B}\right)^{\frac{1}{2}} \frac{1}{\sqrt{f_{2\phi}}} \qquad \text{(L-31)}$$

Dividing both sides of Equation (L-30) by B gives

$$\left(\frac{\delta}{B}\right) = \left(\frac{3\mu^2}{4g\rho^2 B^3}\right)^{1/3} Re^{1/3} \qquad \text{(L-32)}$$

From (L-11) to (L-14) and (L-20) into (L-30) and (L-32)

$$\delta = 0.0028\, J_L^{*1/3} \qquad \text{(L-33)}$$

$$\left(\frac{\delta}{B}\right) = 0.0041\, J_L^{*1/3} \qquad \text{(L-34)}$$

From Equations (L-28), (L-33) and (L-34) into (L-31),

$$J_g^* = \frac{0.074\, J_L^{*1/6}}{(0.006 + 15.68\, J_L^{*2/3})^{\frac{1}{2}}} \qquad \text{(L-35)}$$

Equation (L-35) is compared with the experimental data in Figure 5.11.

L-3 IMURA et al

Equation (2.65) was derived by Imura et al (16) for counter-current two-phase flow in an annulus. For a planar test section, Equation (2.65) is reduced to:

$$\frac{G}{L} + \left(\frac{\rho_g}{\rho_L}\right)\left(\frac{A_g}{A_L}\right) = \left(\frac{A_g}{A}\right)\left(\frac{1}{L}\right)\sqrt{\frac{\xi \rho_g \sigma}{\delta}} \qquad \text{(L-36)}$$

where

$$A = BS \qquad \text{(L-37)}$$

$$A_g = BS\left(1 - \frac{\delta}{S}\right) \qquad \text{(L-38)}$$

$$A_L = BS\left(\frac{\delta}{S}\right) \qquad \text{(L-39)}$$

For $\frac{\delta}{S} \ll 1$

$$A_g \simeq A \qquad \text{(L-40)}$$

and

$$\frac{A_g}{A_L} \simeq \frac{1}{\left(\frac{\delta}{S}\right)} \qquad \text{(L-41)}$$

Equations (L-1) and (L-2) can be written as

$$J_L^* = \frac{L}{\rho_L} \cdot \frac{1}{\sqrt{gB}} \qquad \text{(L-42)}$$

and

$$J_g^* = \frac{G}{\rho_g} \cdot \frac{1}{\sqrt{gB}} \cdot \left(\frac{\rho_g}{\rho_L}\right)^{\frac{1}{2}} \qquad \text{(L-43)}$$

Substituting Equations (L-40) to (L-43) into Equation (L-36) gives:

$$\frac{J_g^*}{J_L^*}\left(\frac{\rho_g}{\rho_L}\right)^{1/2} + \left(\frac{\rho_g}{\rho_L}\right)\frac{1}{\left(\frac{\delta}{S}\right)} = \frac{1}{J_L^*}\sqrt{\frac{\xi\rho_g\sigma}{\rho_L^2 gBS\left(\frac{\delta}{S}\right)}} \qquad \text{(L-44)}$$

The film thickness was obtained from the following equations:

$$\delta = 0.369\left[\frac{3\,\mu_L^2}{\rho_L^2 g}\right]^{1/3} \cdot Re^{1/3} \qquad Re > 400 \qquad \text{(L-45)}$$

$$\delta = \left[\frac{3\,\mu_L^2}{\rho_L^2 g}\right]^{1/3} \cdot Re^{1/3} \qquad Re \leqslant 400 \qquad \text{(L-46)}$$

where

$$Re = \frac{M_L}{B\mu} = \frac{\rho_L S}{\mu_L} \cdot \sqrt{gB} \cdot J_L^* \qquad \text{(L-47)}$$

Substituting Equations (L-11) to (L-14) into Equations (L-45) to (L-47) and dividing Equations (L-45) and (L-46) gives:

$$\frac{\delta}{S} = 0.1106\, J_L^{*1/3} \qquad J_L^* \leqslant 0.0067 \qquad \text{(L-48)}$$

and

$$\frac{\delta}{S} = 0.2553\, J_L^{*1/2} \qquad J_L^* > 0.0067 \qquad \text{(L-49)}$$

From Thermodynamics and Transport Properties of Fluids (40)

$$\mu_g = 1.8 \times 10^{-5} \text{ Kg/m.s} \quad \text{for air at temperature } t = 20^0\text{C} \qquad \text{(L-50)}$$

Substituting Equations (L-11) to (L-16) and (L-50) together with a value for $\sigma = 0.072$ N/m into (2.66) gives:

$$\xi = 1.413 \qquad \text{(L-51)}$$

Substituting Equations (L-11) to (L-15) together with (L-48) or (L-49) into (L-44) and arranging, then

for $J_L^* \leqslant 0.0067$

$$J_g^* = \frac{0.0733}{J_L^{*1/6}} - 0.3197\, J_L^{*2/3} \qquad \text{(L-52)}$$

and for $J_L^* > 0.0067$

$$J_g^* = \frac{0.0483}{J_L^{*\frac{1}{4}}} - 0.1385\, J_L^{\frac{1}{2}} \qquad \text{(L-53)}$$

Equations (L-52) and (L-53) were used to plot the curve shown in Figure 5.12.

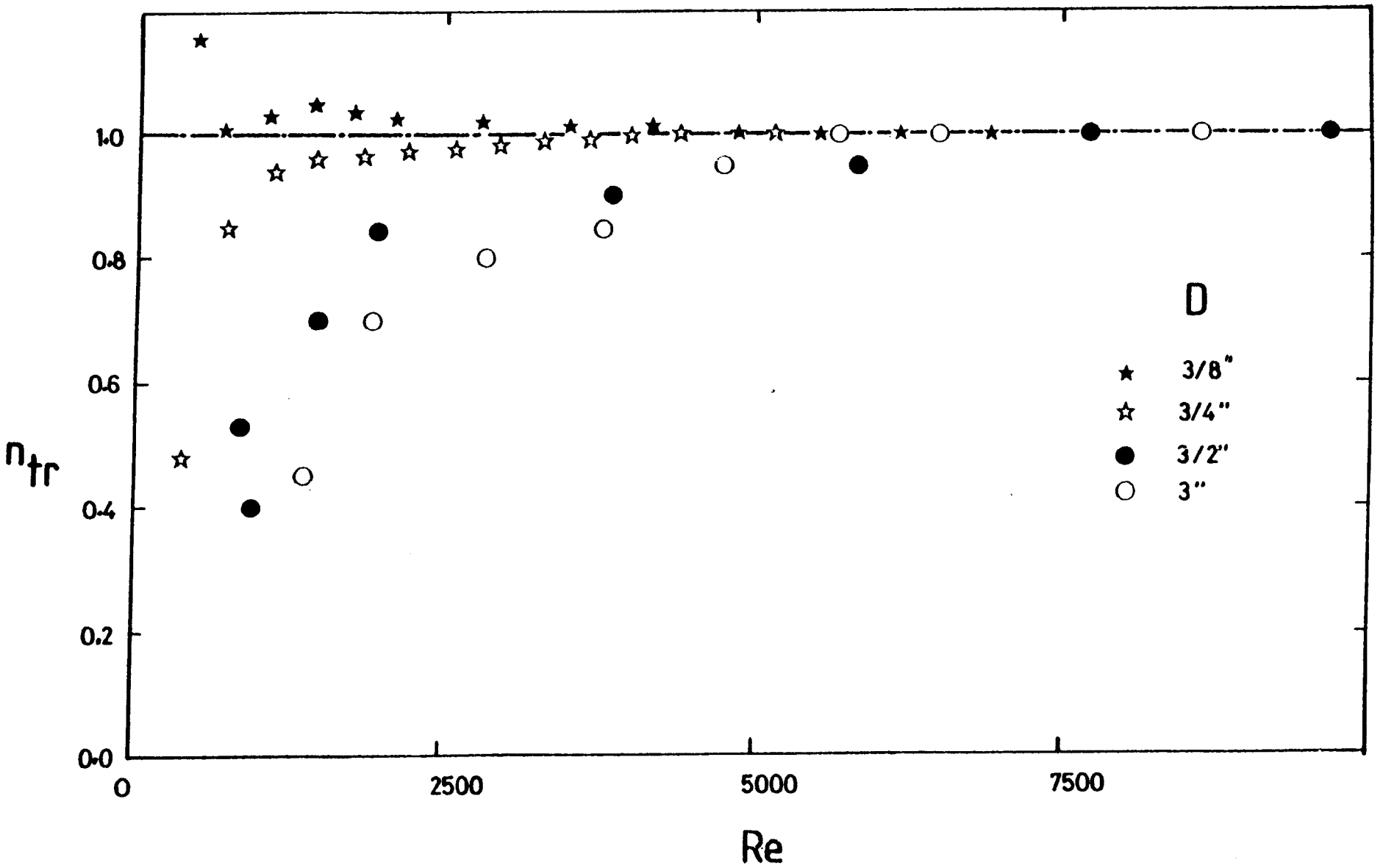

Fig L-1 Variation Of Profile Factor, n_{tr} With Reynolds Number, Re For Counter-Current Air/Water System

APPENDIX M

MEASUREMENTS OF THE WATERFALL TRAJECTORIES

TABLE M-1 MEASUREMENTS OF THE WATERFALL TRAJECTORIES

$\frac{M_w}{2}$ = 0.275 kg/s H_{w_i} = 20 mm

X	0	30	60	90	120	150	180	210	240	270	300
Y_t	20	35	65	130	205	305	403	272	-	-	-
Y_b	40	55	85	145	205	305	403	272	-	-	-
Y_m	30	45	75	138	205	305	403	272	-	-	-
Y	0	15	45	108	175	275	373	542	-	-	-

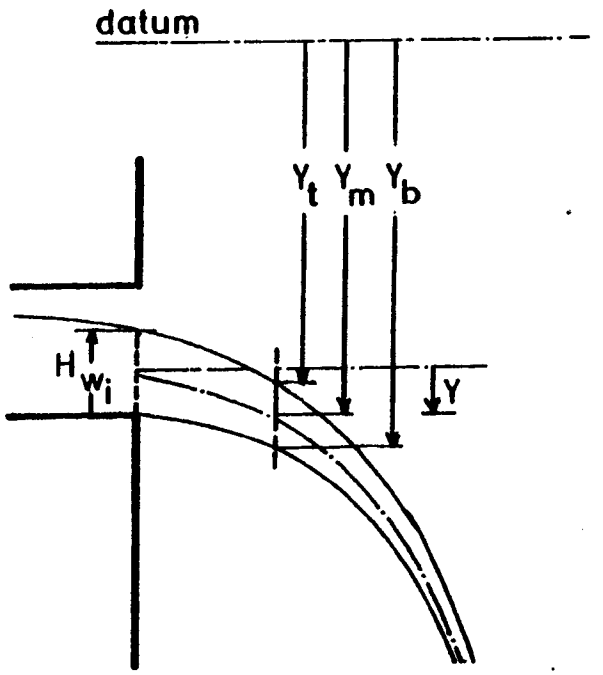

☆ ALL DIMENSIONS ARE IN MILLIMETRES

TABLE M-2 MEASUREMENTS OF THE WATERFALL TRAJECTORIES

$\frac{M_w}{2}$ = 0.395 kg/s H_{w_i} = 26 mm

X	0	30	60	90	120	150	180	210	240	270	300
Y_t	14	27	53	95	185	250	325	440	575	-	-
Y_b	40	49	73	120	185	250	325	440	575	-	-
Y_m	27	38	63	108	185	250	325	440	575	-	-
Y	0	11	36	81	158	223	298	413	548	-	-

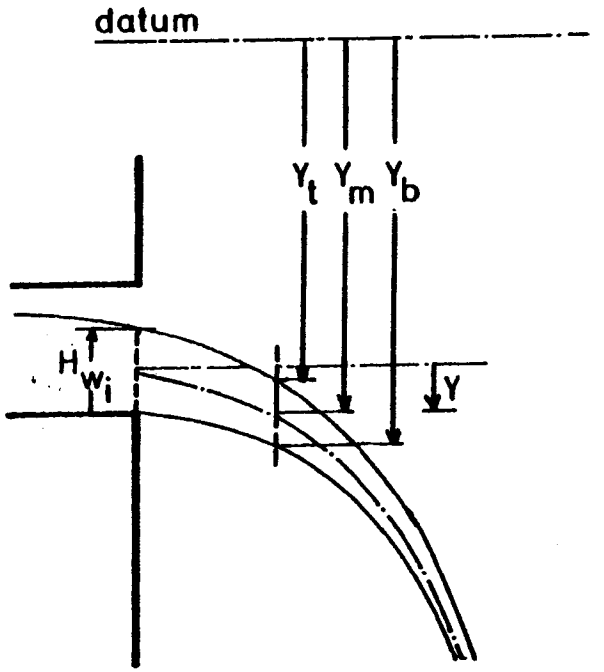

☆ ALL DIMENSIONS ARE IN MILLIMETRES

TABLE M-3 MEASUREMENTS OF THE WATERFALL TRAJECTORIES

$\frac{M_w}{2}$ = 0.612 kg/s H_{w_i} = 33.3mm

X	0	30	60	90	120	150	180	210	240	270	300
Y_t	7.50	20.50	35.85	72.95	106.95	149.75	216.60	326.50	-	-	-
Y_b	40.80	46.80	67.40	99.20	143.45	204.15	233.05	347.95	-	-	-
Y_m	24.15	33.65	51.62	86.08	125.20	176.95	224.83	337.23	-	-	-
Y	0.00	9.50	27.00	61.90	101.05	152.80	200.70	313.10	-	-	-

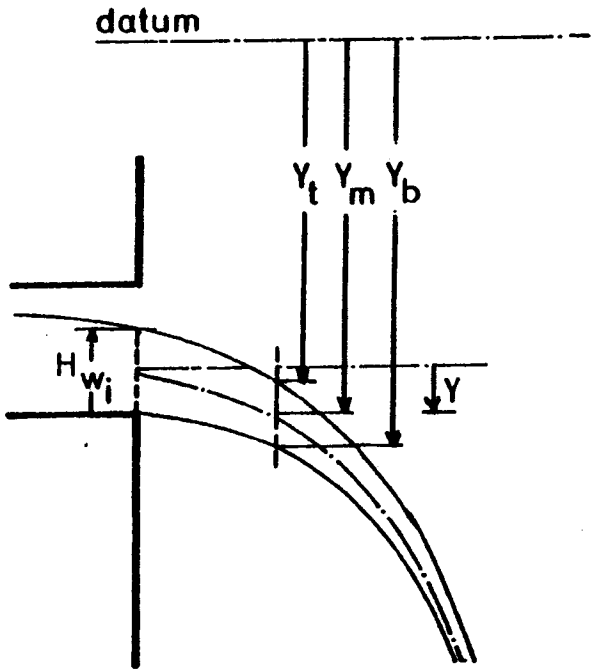

☆ ALL DIMENSIONS ARE IN MILLIMETRES

TABLE M-4 MEASUREMENTS OF THE WATERFALL TRAJECTORIES

$\frac{M_w}{2}$ = 0.612 kg/s H_{w_i} = 35 mm

X	0	30	60	90	120	150	180	210	240	270	300
Y_t	5	20	40	70	110	180	250	330	420	510	630
Y_b	40	47	70	100	140	200	260	350	440	530	650
Y_m	22.5	33.5	55	85	125	190	255	340	430	520	640
Y	0	11	32.5	62.5	62.5	167.5	232.5	317.5	407.5	497.5	617.5

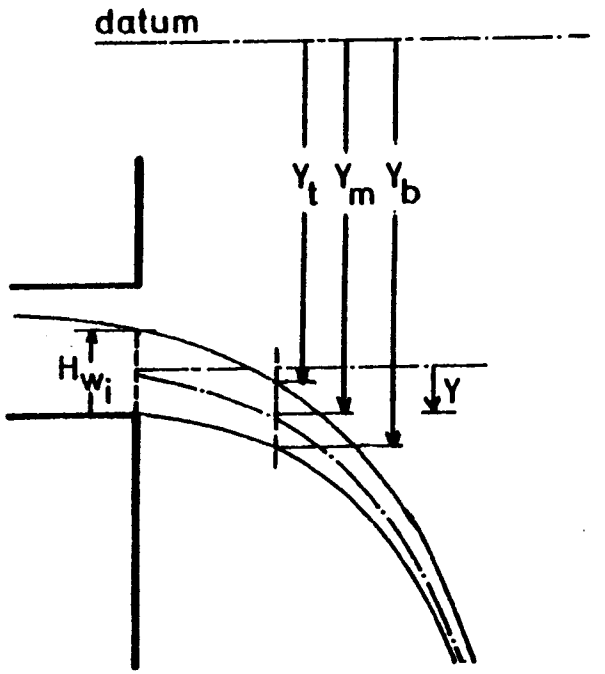

☆ ALL DIMENSIONS ARE IN MILLIMETRES

TABLE M-5 MEASUREMENTS OF THE WATERFALL TRAJECTORIES

$\frac{M_w}{2}$ = 0.612 kg/s H_{w_i} = 35 mm

X	0	30	60	90	120	150	180	210	240	270	300
Y_t	5	15	36	70	105	150	190	260	320	370	410
Y_b	40	45	66	95	125	170	220	270	330	380	430
Y_m	22.5	30	51	82.5	115	160	205	265	325	375	420
Y	0	7.5	28.5	60	92.5	137.5	182.5	242.5	302.5	352.5	397.5

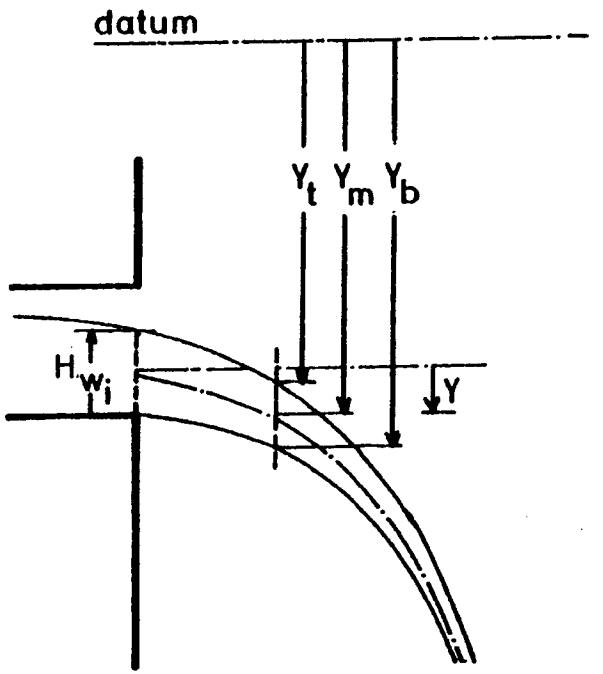

☆ ALL DIMENSIONS ARE IN MILLIMETRES

VALVE CLOSED

APPENDIX N

FLOW OVER THE BRINK INTO THE TEST SECTION

APPENDIX N

FLOW OVER THE BRINK INTO THE TEST SECTION

As the water in the inlet pipe approaches the entrance to the test section, the hydrostatic head has to adjust such that, after the water flows over the brink, the pressure on the underside of the jet becomes uniform and atmospheric. This is a complex problem which has been studied extensively by civil engineers and normally requires numerical integration of the fluid flow equations for the water jet. This integration has been done by Markland (37), who studied the ideal problem of flow of a stream initially with uniform velocity, u, over the brink. The velocity, pressure and energy profiles at three stations (upstream, brink and downstream), are indicated in Figure N-1. It can be seen that as the water at section 1 approaches the brink at section 2, it accelerates and thus, by continuity, the surface height decreases. At section 1, the velocity profile is flat and the pressure and energy increase linearly from top to bottom of the water jet. At section 2, the pressure at the bottom of the channel has dropped to atmospheric, leaving a pressure maximum inside the water jet, and the velocity distribution increases in a non-linear manner from top to bottom, although the energy distribution is still linear. At section 3, the velocity distribution is again flat and the pressure uniformly atmospheric.

The effect of the hydrostatic head at section 1 therefore is to accelerate the fluid at section 2. There is, however, a residual pressure potential which can accelerate the water further.

In the actual experiments, the flow patterns were more complex. The water was fed to the side arms down a vertical pipe resulting in an undulating surface, initially as shown in Figure N-2. The actual measurements are shown in Tables 1 - 5 in this Appendix. As it can be seen from Figure N-2, the decrease in water depth (and hence the increase in Froude number) is apparent as the brink is approached. Because of the complexity of the real flow and the non-linear aspects of the above theory, a simplified analysis was made to estimate the effective water jet velocity just after the brink, based on the measured total mass flow, M_w, of the inlet water and the measured water depth, H_{w2}, at section 2.

At section 2, the energy varies linearly from u_2^2 to $(u_2^2 + 2gH_{w2})$ and the square of the velocity varies in a non-linear manner between these two limits. Thus the mean energy at section2, $\bar{E}_2$, is given by :

$$\bar{E}_2 = u_2^2 + g H_{w2} \qquad (N-1)$$

The term u_2^2 will be somewhat less than the corresponding mean velocity term $\bar{u}_2^2$, but this will be taken care of in

a conversion factor k^2. Thus, writing an energy balance on the fluid between section 2 and section 3 (section 3 close to section 2), where the velocity u_3 is assumed uniform at constant atmospheric pressure and channel height H_{w3}, gives:

$$\bar{u}_2 \, H_{w2} \left[k^2 \, \bar{u}_2^2 + g \, H_{w2} \right] = \bar{u}_3 \, H_{w3} . \bar{u}_3^2 \qquad \text{(N-2)}$$

By continuity

$$\bar{u}_2 \, H_{w2} = \bar{u}_3 \, H_{w3} \qquad \text{(N-3)}$$

Thus

$$\bar{u}_3^2 = k^2 \, \bar{u}_2^2 + g \, H_{w2} \qquad \text{(N-4)}$$

giving

$$\bar{u}_3^2 = k^2 \, \bar{u}_2^2 \left[1 + \frac{1}{k^2 \, Fr_{w2}} \right]$$

where

$$Fr_{w_2} = \frac{\bar{u}_2^2}{g H_w^2} \quad \text{and} \quad k^2 = \left(\frac{u_2}{\bar{u}_2} \right)^2 \qquad \text{(N-5)}$$

It is also possible to estimate the channel height, H_{w3}, as

$$H_{w3} = \frac{\bar{u}_2 H_{w2}}{\bar{u}_3} = \frac{\bar{u}_2 H_{w2}}{k \bar{u}_2 \left[1 + \frac{1}{k^2 Fr_{w2}}\right]^{\frac{1}{2}}}$$

$$= \frac{H_{w2}}{k \left[1 + \frac{1}{k^2 Fr_{w2}}\right]^{\frac{1}{2}}} \qquad \text{(N-6)}$$

Thus,

$$Fr_{w3} = \frac{\bar{u}_3^2}{g H_{w3}} = k^3 Fr_{w2} \left[1 + \frac{1}{k^2 Fr_{w2}}\right]^{3/2} \qquad \text{(N-7)}$$

Using the nomenclature of the main part of the thesis, the effective u_i and Fr_{wi}, just after the brink is given by:

$$u_i = k \left[\frac{M_w/2}{\rho_w H_{wz} S}\right] \left[1 + \frac{1}{k^2 Fr_{wz}}\right]^{\frac{1}{2}} \qquad \text{(6.14)a}$$

and

$$Fr_{wi} = k^3 Fr_{wz} \left[1 + \frac{1}{k^2 Fr_{wz}}\right]^{3/2} \qquad \text{(6.14)b}$$

From the experimental data, k was found to be 0.819.

TABLE N-1

EXPERIMENTAL VALUES OF WATER DEPTH APPROACHING BRINK OF TEST SECTION

$\frac{M_w}{2} = 0.275$ kg/s $\qquad H_{w_i} =$ 20 mm

DISTANCE FROM BRINK	0	55	110	165	220	275	330	385	440	495	550
WATER DEPTH	20	——	29	30	31	33	34	35	37	38	39

☆ ALL DIMENSIONS ARE IN MILLIMETRES

TABLE N-2

EXPERIMENTAL VALUES OF WATER DEPTH APPROACHING BRINK OF TEST SECTION

$\frac{M_w}{2} = 0.395$ kg/s $\qquad H_{w_i} =$ 26 mm

DISTANCE FROM BRINK	0	55	110	165	220	275	330	385	440	495	550
WATER DEPTH	26	—	35	37	39	40	41	43	45	45	55

☆ ALL DIMENSIONS ARE IN MILLIMETRES

TABLE N-3

EXPERIMENTAL VALUES OF WATER DEPTH APPROACHING BRINK OF TEST SECTION

$\frac{M_w}{2} = 0.612$ kg/s $\qquad H_{w_i} = 33.3$mm

DISTANCE FROM BRINK	0	55	110	165	220	275	330	385	440	495	550
WATER DEPTH	33.3	——	46.2	47.1	49.7	52.7	52.7	52.7	57.2	51.3	60.6

☆ ALL DIMENSIONS ARE IN MILLIMETRES

TABLE N-4

EXPERIMENTAL VALUES OF WATER DEPTH APPROACHING BRINK OF TEST SECTION

$\frac{M_w}{2} = 0.612 kg/s$ $\qquad$ $H_{w_i} =$ 35 mm

DISTANCE FROM BRINK	0	55	110	165	220	275	330	385	440	495	550
WATER DEPTH	35	——	46	48	50	53	55	56	60	55	65

☆ ALL DIMENSIONS ARE IN MILLIMETRES

TABLE N-5

EXPERIMENTAL VALUES OF WATER DEPTH APPROACHING BRINK OF TEST SECTION

$\frac{M_w}{2} = 0.612$ kg/s $\qquad H_{w_i} = 35$ mm

DISTANCE FROM BRINK	0	55	110	165	220	275	330	385	440	495	550
WATER DEPTH	35	—	46	48	50	53	55	56	60	55	65

☆ ALL DIMENSIONS ARE IN MILLIMETRES

VALVE CLOSED

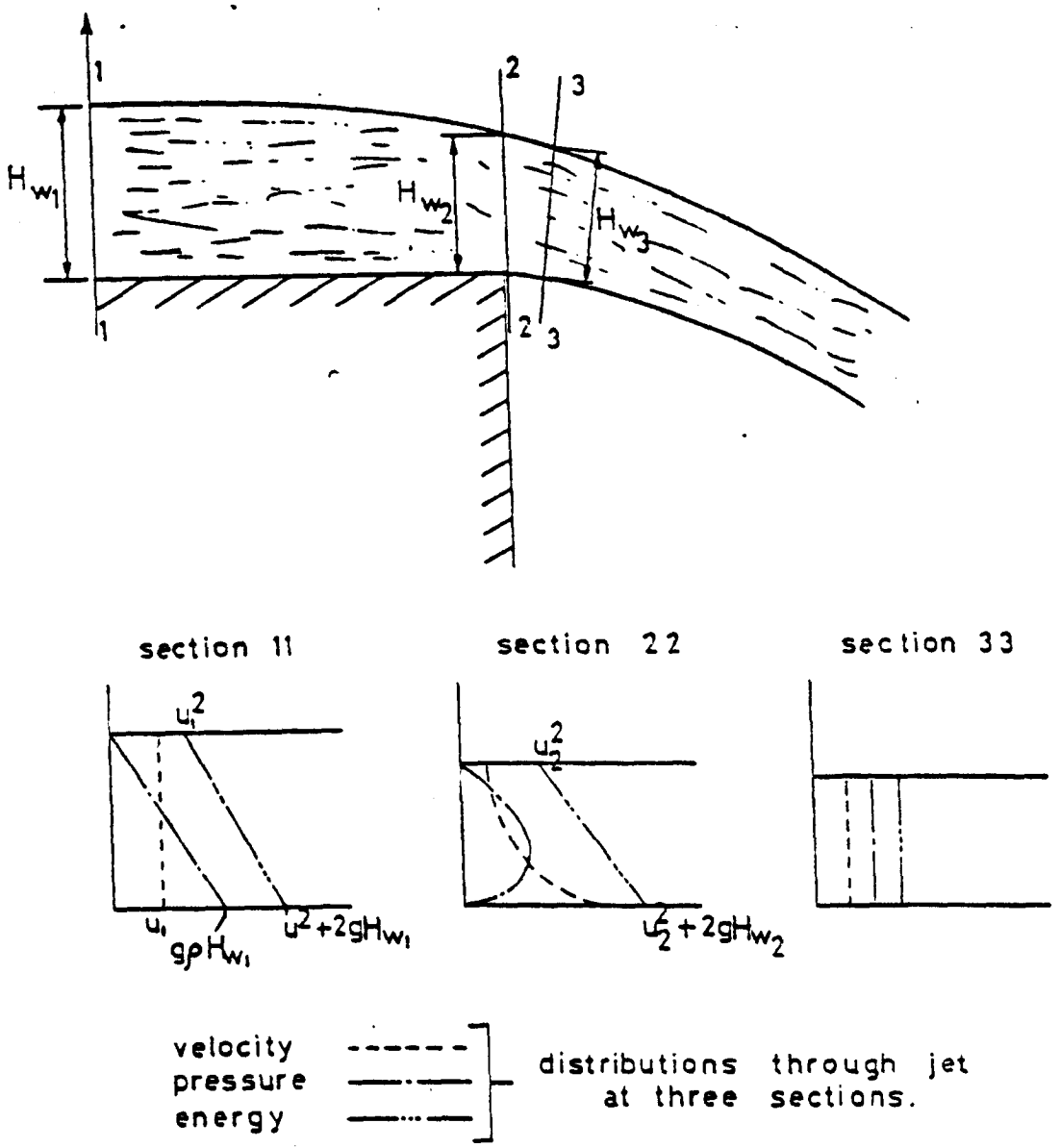

Fig N-1 REPRESENTATION OF IDEALISED FLOW OVER A BRINK.

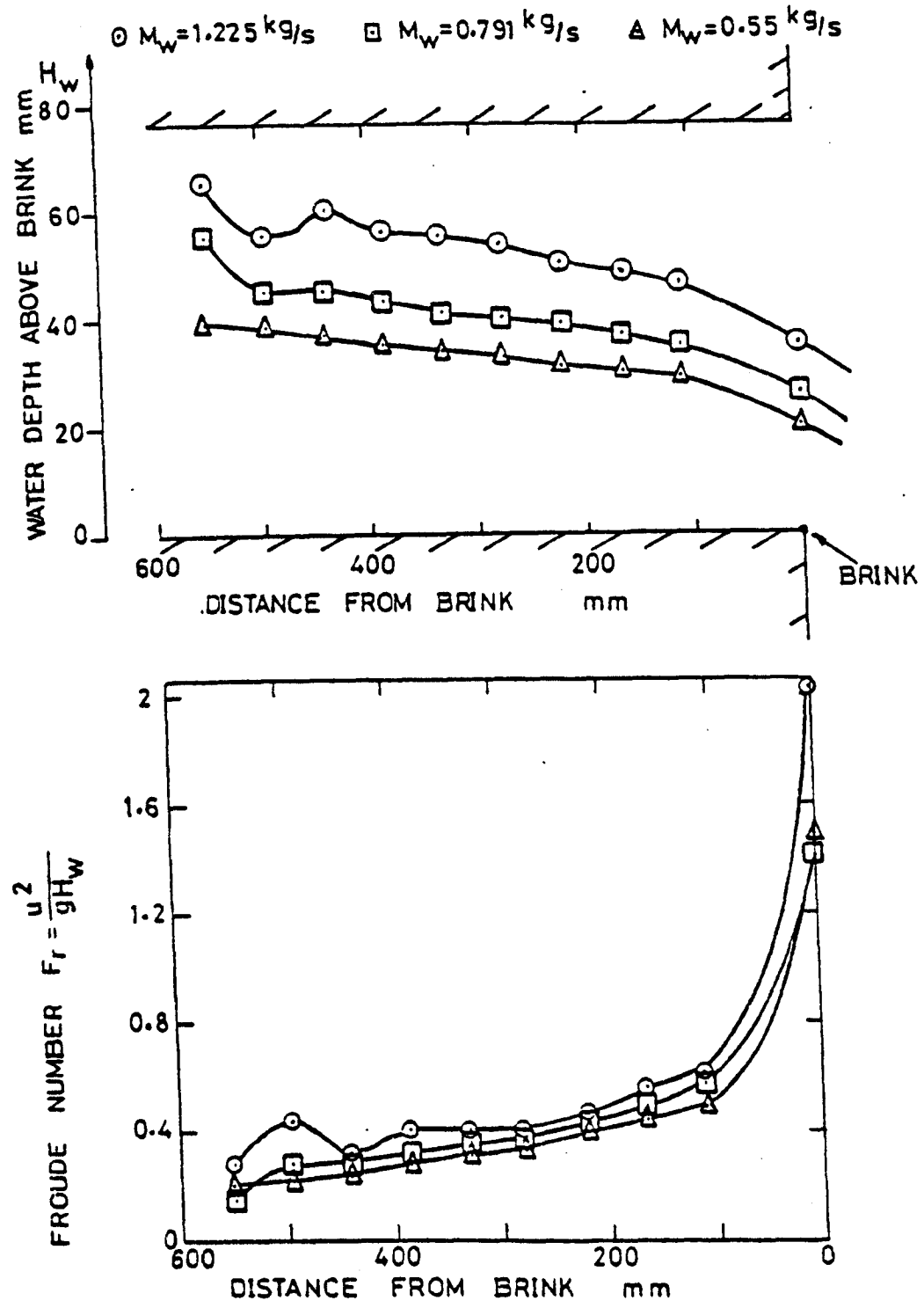

Fig N-2 EXPERIMENTAL VALUES OF WATER DEPTH AND FROUDE NUMBER APPROACHING BRINK OF TEST SECTION.

APPENDIX O

POSITION OF WATERFALLS AT BOTTOM OF TEST SECTION FOR CASE OF CONSTANT ΔP

(APPROXIMATE SOLUTION)

Table 0-1

K_1 = 10.0

K_2	Lower η_b	Higher η_b
0.	0.858684	1.000000
0.000100	0.859948	0.985589
0.000200	0.861347	0.979376
0.000300	0.862800	0.973792
0.000400	0.864335	0.969100
0.000500	0.865940	0.964755
0.000600	0.867625	0.960615
0.000700	0.869432	0.956596
0.000800	0.871351	0.952631
0.000900	0.873417	0.948662
0.001000	0.875663	0.944638
0.001100	0.878139	0.940474
0.001200	0.880923	0.936093
0.001300	0.884148	0.931348
0.001400	0.888079	0.925965
0.001500	0.893440	0.919286

Table 0-2

K_1 = 20.0

K_2	Lower η_b	Higher η_b
0.	0.687124	1.000000
0.000200	0.689571	0.967845
0.000400	0.692381	0.953648
0.000600	0.694667	0.942215
0.000800	0.697311	0.932768
0.001000	0.699848	0.923186
0.001200	0.702857	0.914783
0.001400	0.705766	0.906635
0.001600	0.708776	0.898869
0.001800	0.711897	0.891386
0.002000	0.715142	0.883919
0.002200	0.718503	0.876615
0.002400	0.722057	0.869257
0.002600	0.725764	0.861101
0.002800	0.729678	0.854822
0.003000	0.733823	0.847412
0.003200	0.738237	0.839878
0.003400	0.742932	0.832133
0.003600	0.748051	0.824897
0.003800	0.753670	0.815655
0.004000	0.759946	0.806641
0.004200	0.767148	0.796781
0.004400	0.775798	0.785555
0.004600	0.787153	0.771675
0.004800	0.799895	0.747200

Table 0-3

K_1 = 30.0

K_2	Lower η_b	Higher η_b
0.	0.495715	1.000000
0.010000	0.501851	0.941559
0.020000	0.508312	0.914750
0.030000	0.515146	0.892735
0.040000	0.522418	0.872921
0.050000	0.530211	0.854286
0.060000	0.538635	
0.070000	0.547856	0.818189
0.080000	0.558093	0.799892
0.090000	0.569741	0.780714
0.100000	0.583483	0.759932
0.110000	0.600838	
0.120000	0.627156	

Table 0-4

K_1 = 40.0

K_2	Lower η_b	Higher η_b
0.	0.429360	1.000000
0.010000	0.433469	0.949650
0.020000	0.437041	0.927218
0.030000	0.442007	0.909296
0.040000	0.446522	0.893386
0.050000	0.451192	0.878890
0.060000	0.456041	0.865284
0.070000	0.461084	0.852263
0.080000	0.466344	0.839061
0.090000	0.471846	0.827312
0.100000	0.477627	0.815122
0.110000	0.483722	0.802973
0.120000	0.490184	0.790759
0.130000	0.497077	0.778391
0.140000	0.504492	0.765749
0.150000	0.512547	0.752672
0.160000	0.521419	
0.170000	0.531383	0.724354
0.180000	0.542906	0.708332
0.190000	0.556928	
0.200000	0.576089	

Table O-5

K_1 = 50.0

K_2	Lower η_b	Higher η_b
0.	0.383979	1.000000
0.020000	0.390325	0.934543
0.040000	0.396951	0.904819
0.060000	0.403894	0.883698
0.080000	0.411195	0.859870
0.100000	0.418908	0.838994
0.120000	0.427102	0.819784
0.140000	0.435864	0.801385
0.160000	0.445313	0.782342
0.180000	0.455617	0.763468
0.200000	0.467018	0.744033
0.220000	0.479905	0.723571
0.240000	0.494956	0.701339
0.260000	0.513594	
0.280000	0.540156	0.642753

Table O-6

K_1 = 60.0

K_2	Lower η_b	Higher η_b
0.	0.350583	1.000000
0.020000	0.355710	0.939508
0.040000	0.361073	0.912451
0.060000	0.366627	0.890624
0.080000	0.372391	0.871422
0.100000	0.378387	0.853714
0.120000	0.384644	0.837034
0.140000	0.391191	0.820998
0.160000	0.398072	0.805387
0.180000	0.405326	0.789995
0.200000	0.413023	0.774076
0.220000	0.421239	0.759257
0.240000	0.430079	0.743594
0.260000	0.439691	0.727481
0.280000	0.450288	0.710667
0.300000	0.462282	0.692795
0.320000	0.476008	0.673254
0.340000	0.492856	0.650876
0.360000	0.515957	0.622433

Table 0-7

$K_1 = 70.2$		
K_2	Lower η_b	Higher η_b
0.	0.324522	1.000000
0.020000	0.328948	0.943230
0.040000	0.333497	0.918634
0.060000	0.338176	0.897859
0.080000	0.342996	0.880273
0.100000	0.347968	0.864274
0.120000	0.353125	0.848969
0.140000	0.358425	0.834589
0.160000	0.363944	0.820710
0.180000	0.369683	0.807185
0.200000	0.375668	0.793960
0.220000	0.381928	0.780749
0.240000	0.388500	0.767641
0.260000	0.395430	0.754475
0.280000	0.402773	0.741175
0.300000	0.410606	0.727619
0.320000	0.419026	0.713703
0.340000	0.428169	0.699259
0.360000	0.438234	0.684072
0.380000	0.449526	0.667814
0.400000	0.462570	0.649970
0.420000	0.478411	0.629454
0.440000	0.499871	0.603453

Table 0-8

$K_1 = 80.2$		
K_2	Lower η_b	Higher η_b
0.	0.383562	1.000000
0.020000	0.387450	0.946124
0.040000	0.391429	0.922363
0.060000	0.395503	0.903423
0.080000	0.399678	0.886912
0.100000	0.403965	0.871912
0.120000	0.408367	0.857926
0.140000	0.412895	0.844671
0.160000	0.417562	0.831968
0.180000	0.422371	0.819662
0.200000	0.427342	0.807654
0.220000	0.432489	0.795861
0.240000	0.437828	0.784224
0.260000	0.443386	0.772660
0.280000	0.449169	0.761117
0.300000	0.455224	0.749553
0.320000	0.461582	0.737884
0.340000	0.468285	0.726070
0.360000	0.475389	0.714015
0.380000	0.482967	0.701654
0.400000	0.491114	0.688868
0.420000	0.499964	0.675513
0.440000	0.509710	0.661379
0.460000	0.520657	0.646158
0.480000	0.533324	0.629327
0.500000	0.548704	0.609828
0.526200	0.589918	0.584708

Table 0-9

$K_1 = 90.0$

K_2	Lower η_b	Higher η_b
0.	0.286281	1.000000
0.020000	0.289686	0.948473
0.040000	0.29321	0.925845
0.060000	0.296870	0.907887
0.080000	0.300577	0.892273
0.100000	0.304368	0.878123
0.120000	0.308247	0.864992
0.140000	0.312219	0.852585
0.160000	0.316290	0.840729
0.180000	0.320473	0.829296
0.200000	0.324763	0.818203
0.220000	0.329179	0.807354
0.240000	0.333730	0.796696
0.260000	0.338423	0.786177
0.280000	0.343274	0.775765

Table 0-9 (cont.)

$K_1 = 90.0$

K_2	Lower η_b	Higher η_b
0.320000	0.348298	0.765395
0.330000	0.353509	0.755035
0.340000	0.358938	0.744668
0.360000	0.364586	0.734288
0.380000	0.370503	0.723653
0.400000	0.376719	0.712933
0.420000	0.383278	0.721996
0.440000	0.390233	0.693793
0.460000	0.397661	0.679227
0.480000	0.405658	0.667185
0.500000	0.414362	0.654543
0.520000	0.423974	0.641091
0.540000	0.434813	0.626484
0.560000	0.447442	0.610168
0.580000	0.463052	0.590960
0.600000	0.485336	0.565124

Table 0-10

K_1 = 100.0

K_2	Lower η_b	Higher η_b
0.	0.271514	1.000000
0.020000	0.274685	0.950432
0.040000	0.277911	0.928748
0.060000	0.281199	0.911579
0.080000	0.284549	0.896691
0.100000	0.287963	0.883230
0.120000	0.291449	0.870767
0.140000	0.295006	0.859024
0.160000	0.298641	0.847833
0.180000	0.302358	0.837072
0.200000	0.306162	0.826652
0.220000	0.310059	0.816515
0.240000	0.314054	0.806585
0.260000	0.318154	0.796824
0.280000	0.322370	0.787192
0.300000	0.326706	0.777664
0.320000	0.331175	0.768192
0.340000	0.335787	0.758753
0.360000	0.340556	0.749317
0.380000	0.345495	0.739868

Table 0-10 (cont.)

K_1 = 100.0

K_2	Lower η_b	Higher η_b
0.400000	0.350625	0.730356
0.420000	0.355962	0.720759
0.440000	0.361535	0.711054
0.460000	0.367371	0.701183
0.480000	0.373509	0.691121
0.500000	0.379991	0.680798
0.520000	0.386880	0.670167
0.540000	0.394250	0.659127
0.560000	0.402207	0.647588
0.580000	0.410897	0.635387
0.600000	0.420545	0.622296
0.620000	0.431512	0.607958
0.640000	0.444465	0.591698
0.660000	0.460933	0.571975
0.680000	0.487864	0.542616

APPENDIX P

POSITION OF WATERFALLS AT BOTTOM OF TEST SECTION FOR THE CASE OF AIR FOLLOWING WATER FALLS

Table P-1

K_1 = 10.00

K_2	Lower γ_b	Higher γ_b
0.	0.858451	
0.002000	0.861316	
0.004000	0.864263	0.997073
0.006000	0.867408	0.995543
0.008000	0.870556	0.993953
0.010000	0.873814	0.992304
0.012000	0.877195	0.990554
0.014000	0.880824	0.988714
0.016000	0.884525	0.986744
0.018000	0.888413	0.984615
0.020000	0.892641	0.982295
0.022000	0.897052	0.979715
0.024000	0.901932	0.976796
0.026000	0.907298	0.973406
0.028000	0.913368	0.969287
0.030000	0.920710	0.963897
0.032000	0.931161	0.955189

Table P-2

K_1 = 20.00

K_2	Lower γ_b	Higher γ_b
0.	0.606960	
0.010000	0.611613	
0.020000	0.616466	
0.030000	0.621334	
0.040000	0.626317	0.985359
0.050000	0.631422	0.981730
0.060000	0.636658	0.978090
0.070000	0.642035	0.974411
0.080000	0.647675	0.970691
0.090000	0.653388	0.966902
0.100000	0.659286	0.963032
0.110000	0.665386	0.959043
0.120000	0.671825	0.954923
0.130000	0.678423	0.950614
0.140000	0.685306	0.946074
0.150000	0.692637	0.941255
0.160000	0.700250	0.936076
0.170000	0.708433	0.930437
0.180000	0.717169	0.924207
0.190000	0.726501	0.917228
0.200000	0.736934	0.909219
0.210000	0.748498	0.899781
0.220000	0.761985	0.888122
0.230000	0.778867	0.872344
0.240000	0.805226	0.839509

Table P-3

K_1 = 30.0		
K_2	Lower γ_b	Higher γ_b
0.	0.495605	
0.020000	0.501676	
0.040000	0.507888	
0.060000	0.514250	0.983192
0.080000	0.520774	0.977743
0.100000	0.527577	0.972333
0.120000	0.534479	0.966924
0.140000	0.541587	0.961495
0.160000	0.548922	0.956016
0.180000	0.556609	0.950456
0.200000	0.564485	0.944787
0.220000	0.572668	0.938938
0.240000	0.581304	0.932859
0.260000	0.590249	0.926489
0.280000	0.599750	0.919720
0.300000	0.609708	0.912431
0.320000	0.620411	0.904472
0.340000	0.631809	0.895644
0.360000	0.644321	0.885665
0.380000	0.658267	0.874106
0.400000	0.673995	0.860308
0.420000	0.692906	0.842891
0.440000	0.718028	0.817764

Table P-4

K_1 = 40.0		
K_2	Lower γ_b	Higher γ_b
0.	0.429142	
0.020000	0.433794	
0.040000	0.438520	
0.060000	0.443428	
0.080000	0.448323	0.981207
0.100000	0.453303	0.976668
0.120000	0.458374	0.972179
0.140000	0.463540	0.967699
0.160000	0.468807	0.963250
0.180000	0.474180	0.958800
0.200000	0.479778	0.954341
0.220000	0.485398	0.949872
0.240000	0.491148	0.945372
0.260000	0.497036	0.940833
0.280000	0.503074	0.936233
0.300000	0.509385	0.931554
0.320000	0.515772	0.926775
0.340000	0.522349	0.921865
0.360000	0.529237	0.916816
0.380000	0.536267	0.911567
0.400000	0.543552	0.906097
0.420000	0.551225	0.900338
0.440000	0.559133	0.894259
0.460000	0.567405	0.887770
0.480000	0.576218	0.880791
0.500000	0.585529	0.873232

Table P-4 (cont.)

K_1 = 40.0		
K_2	Lower γ_b	Higher γ_b
0.520000	0.595346	0.864963
0.540000	0.606005	0.855814
0.560000	0.617597	0.845545
0.580000	0.630528	0.833787
0.600000	0.645209	0.819919
0.620000	0.662757	0.802591
0.640000	0.686101	0.777544

Table P-5

K_1 = 50.0		
K_2	Lower γ_b	Higher γ_b
0.	0.383857	
0.020000	0.387716	
0.040000	0.391622	
0.060000	0.395577	
0.080000	0.399583	
0.100000	0.403642	0.979422
0.120000	0.407757	0.975462
0.140000	0.412033	0.971543
0.160000	0.416273	0.967644
0.180000	0.420576	0.963774
0.200000	0.424944	0.959915
0.220000	0.429381	0.956065
0.240000	0.433890	0.952216
0.260000	0.438474	0.948366
0.280000	0.443240	0.944507
0.300000	0.447996	0.940637
0.320000	0.452841	0.936748
0.340000	0.457779	0.932828
0.360000	0.462816	0.928869
0.380000	0.467958	0.924859
0.400000	0.473317	0.920790
0.420000	0.478701	0.916650
0.440000	0.484213	0.912421
0.460000	0.489863	0.908091
0.480000	0.495762	0.903642
0.500000	0.501733	0.899053

Table P-5 (cont.)

K_1 = 50.0		
K_2	Lower γ_b	Higher γ_b
0.520000	0.507878	0.894293
0.540000	0.514214	0.889344
0.560000	0.520871	0.884165
0.580000	0.527663	0.878735
0.600000	0.534814	0.873006
0.620000	0.542173	0.866937
0.640000	0.549861	0.860468
0.660000	0.558047	0.853539
0.680000	0.566680	0.846052
0.700000	0.575754	0.837933
0.720000	0.585586	0.829024
0.740000	0.596237	0.819126
0.760000	0.608063	0.807947
0.780000	0.621366	0.794959
0.800000	0.637022	0.779121
0.820000	0.656979	0.757494
0.840000	0.692135	0.719300

Table P-6

K_1 = 60.0		
K_2	Lower γ_b	Higher γ_b
0.	0.350331	
0.020000	0.353769	
0.040000	0.357144	
0.060000	0.360554	
0.080000	0.364000	
0.100000	0.367484	
0.120000	0.371006	
0.140000	0.374567	
0.160000	0.378170	
0.180000	0.381814	
0.200000	0.385503	
0.220000	0.389341	
0.240000	0.393130	
0.260000	0.396968	
0.280000	0.400857	
0.300000	0.404800	
0.320000	0.408798	
0.340000	0.412854	
0.360000	0.416970	
0.380000	0.421254	
0.400000	0.425508	
0.420000	0.429832	
0.440000	0.434228	
0.460000	0.438701	
0.480000	0.443255	
0.500000	0.447997	
0.520000	0.452737	

Table P-6 (cont.)

K_1 = 60.0		
K_2	Lower η_b	Higher η_b
0.540000	0.457572	
0.560000	0.462509	
0.580000	0.467555	
0.600000	0.472820	
0.620000	0.478118	
0.640000	0.483549	
0.660000	0.489125	
0.680000	0.494963	
0.700000	0.500880	
0.720000	0.506982	
0.740000	0.513397	
0.760000	0.519949	
0.780000	0.526855	
0.800000	0.533967	
0.820000	0.541506	
0.840000	0.549342	
0.860000	0.557731	
0.880000	0.566665	
0.900000	0.576271	
0.920000	0.586725	
0.940000	0.598403	
0.960000	0.611680	
0.980000	0.627698	
1.000000	0.649245	

Table P-7

K_1 = 70.0		
K_2	Lower η_b	Higher η_b
0.	0.324368	
0.020000	0.327337	
0.040000	0.330332	
0.060000	0.333352	
0.080000	0.336400	
0.100000	0.339580	
0.120000	0.342691	
0.140000	0.345831	
0.160000	0.349002	
0.180000	0.352204	
0.200000	0.355439	
0.220000	0.358706	
0.240000	0.362008	
0.260000	0.365346	
0.280000	0.368719	
0.300000	0.372234	
0.320000	0.375691	
0.340000	0.379189	
0.360000	0.382729	
0.380000	0.386313	
0.400000	0.389941	
0.420000	0.393617	
0.440000	0.397341	
0.460000	0.401215	
0.480000	0.405050	
0.500000	0.408941	

Table P-7 (cont.)

K_1 = 70.0		
K_2	Lower γ_b	Higher γ_b
0.520000	0.412889	
0.540000	0.416897	
0.560000	0.420968	
0.580000	0.425105	
0.600000	0.429413	
0.620000	0.433701	
0.640000	0.438066	
0.660000	0.442512	
0.680000	0.447044	
0.700000	0.451667	
0.720000	0.456495	
0.740000	0.461328	
0.760000	0.466271	
0.780000	0.471331	
0.800000	0.476625	
0.820000	0.481961	
0.840000	0.487445	
0.860000	0.493192	
0.880000	0.499027	
0.900000	0.505056	
0.920000	0.511407	
0.940000	0.517907	
0.960000	0.524781	
0.980000	0.531875	
1.000000	0.539433	
1.020000	0.547415	

Table P-7 (cont.)

K_1 = 70.0		
K_2	Lower γ_b	Higher γ_b
1.040000	0.555907	
1.060000	0.565023	
1.080000	0.574923	
1.100000	0.585949	
1.120000	0.598425	
1.140000	0.613243	
1.160000	0.632865	

Table P-8

K_1 = 80.0		
K_2	Lower η_b	Higher η_b
0.	0.303439	
0.020000	0.306132	
0.040000	0.308846	
0.060000	0.311580	
0.080000	0.314337	
0.100000	0.317115	
0.120000	0.319916	
0.140000	0.322740	
0.160000	0.325588	
0.180000	0.328565	
0.200000	0.331469	
0.220000	0.334398	
0.240000	0.337353	
0.260000	0.340336	
0.280000	0.343346	
0.300000	0.346386	
0.320000	0.349455	
0.340000	0.352554	
0.360000	0.355684	
0.380000	0.358949	
0.400000	0.362152	
0.420000	0.365389	
0.440000	0.368662	
0.460000	0.371971	
0.480000	0.375319	
0.500000	0.378706	

Table P-8 (cont.)

K_1 = 80.0		
K_2	Lower η_b	Higher η_b
0.520000	0.382134	
0.540000	0.385604	
0.560000	0.389222	
0.580000	0.392788	
0.600000	0.396403	
0.620000	0.400067	
0.640000	0.403783	
0.660000	0.407552	
0.680000	0.411378	
0.700000	0.415363	
0.720000	0.419317	
0.740000	0.423336	
0.760000	0.427422	
0.780000	0.431580	
0.800000	0.435812	
0.820000	0.440229	
0.840000	0.444634	
0.860000	0.449130	
0.880000	0.453719	
0.900000	0.458410	
0.920000	0.463318	
0.940000	0.468244	
0.960000	0.473294	
0.980000	0.478581	
1.000000	0.483925	
1.020000	0.489428	

Table P-8 (cont.)

K_1 = 80.0		
K_2	Lower γ_b	Higher γ_b
1.040000	0.495209	
1.060000	0.501093	
1.080000	0.507190	
1.100000	0.513640	
1.120000	0.520261	
1.140000	0.527307	
1.160000	0.534717	
1.180000	0.542558	
1.200000	0.550919	
1.220000	0.559921	
1.240000	0.569736	
1.260000	0.580738	
1.280000	0.593401	
1.300000	0.608704	
1.320000	0.630030	

Table P-9

K_1 = 90.0		
K_2	Lower γ_b	Higher γ_b
0.	0.286101	
0.020000	0.288578	
0.040000	0.291072	
0.060000	0.293584	
0.080000	0.296113	
0.100000	0.298660	
0.120000	0.301226	
0.140000	0.303811	
0.160000	0.306415	
0.180000	0.309039	
0.200000	0.311683	
0.220000	0.314347	
0.240000	0.317134	
0.260000	0.319847	
0.280000	0.322582	
0.300000	0.325341	
0.320000	0.328123	
0.340000	0.330929	
0.360000	0.333759	
0.380000	0.336616	
0.400000	0.339498	
0.420000	0.342407	
0.440000	0.345343	
0.460000	0.348409	
0.480000	0.351409	
0.500000	0.354439	

Table P-9 (cont.)

K_1 = 90.0		
K_2	Lower η_b	Higher η_b
0.520000	0.357500	
0.540000	0.360593	
0.560000	0.363720	
0.580000	0.366880	
0.600000	0.370076	
0.620000	0.373308	
0.640000	0.376677	
0.660000	0.379993	
0.680000	0.383349	
0.700000	0.386747	
0.720000	0.390189	
0.740000	0.393676	
0.760000	0.397210	
0.780000	0.400794	
0.800000	0.404532	
0.820000	0.408228	
0.840000	0.411980	
0.860000	0.415791	
0.880000	0.419664	
0.900000	0.423601	
0.920000	0.427708	
0.940000	0.431793	
0.960000	0.435953	
0.980000	0.440194	
1.000000	0.444519	
1.020000	0.449038	

Table P-9 (cont.)

K_1 = 90.0		
K_2	Lower η_b	Higher η_b
1.040000	0.453559	
1.060000	0.458182	
1.080000	0.462914	
1.100000	0.467870	
1.120000	0.472859	
1.140000	0.477986	
1.160000	0.483365	
1.180000	0.488818	
1.200000	0.494451	
1.220000	0.500395	
1.240000	0.506464	
1.260000	0.512894	
1.280000	0.519514	
1.300000	0.526580	
1.320000	0.534038	
1.340000	0.541969	
1.360000	0.550475	
1.380000	0.559704	
1.400000	0.569987	
1.420000	0.581696	
1.440000	0.595462	
1.460000	0.613612	

Table P-10

K_1 = 100.0		
K_2	Lower η_b	Higher η_b
0.	0.271352	
0.020000	0.273650	
0.040000	0.275961	
0.060000	0.278287	
0.080000	0.280730	
0.100000	0.283091	
0.120000	0.285469	
0.140000	0.287862	
0.160000	0.290271	
0.180000	0.292697	
0.200000	0.295140	
0.220000	0.297599	
0.240000	0.300077	
0.260000	0.302572	
0.280000	0.305086	
0.300000	0.307618	
0.320000	0.310271	
0.340000	0.312848	
0.360000	0.315445	
0.380000	0.318063	
0.400000	0.320702	
0.420000	0.323362	
0.440000	0.326045	
0.460000	0.328750	
0.480000	0.331479	
0.500000	0.334232	
0.520000	0.337010	

Table P-10 (cont.)

K_1 = 100.0		
K_2	Lower η_b	Higher η_b
0.540000	0.339913	
0.560000	0.342748	
0.580000	0.345609	
0.600000	0.348498	
0.620000	0.351416	
0.640000	0.354363	
0.660000	0.357340	
0.680000	0.360348	
0.700000	0.363388	
0.720000	0.366461	
0.740000	0.369672	
0.760000	0.372821	
0.780000	0.376007	
0.800000	0.379231	
0.820000	0.382495	
0.840000	0.385799	
0.860000	0.389145	
0.880000	0.392536	
0.900000	0.396077	
0.920000	0.399569	
0.940000	0.403111	
0.960000	0.406704	
0.980000	0.410352	
1.000000	0.414057	
1.020000	0.417924	
1.040000	0.421759	
1.060000	0.425661	

Table P-10 (cont.)

K_1 = 100.0		
K_2	Lower η_b	Higher η_b
1.080000	0.429632	
1.100000	0.433677	
1.120000	0.437899	
1.140000	0.442113	
1.160000	0.446414	
1.180000	0.450808	
1.200000	0.455301	
1.220000	0.460011	
1.240000	0.464736	
1.260000	0.469584	
1.280000	0.474672	
1.300000	0.479812	
1.320000	0.485109	
1.340000	0.490694	
1.360000	0.496374	
1.380000	0.502380	
1.400000	0.508534	
1.420000	0.515078	
1.440000	0.521948	
1.460000	0.529203	
1.480000	0.536918	
1.500000	0.545195	
1.520000	0.554175	
1.540000	0.564179	
1.560000	0.575472	
1.580000	0.588965	
1.600000	0.606634	

Table

K_1 =		
K_2	Lower η_b	Higher η_b

APPENDIX Q

POSITION OF WATERFALLS AT BOTTOM OF TEST SECTION FOR CASE OF CONSTANT ΔP

(EXACT SOLUTION)

Table Q-1

$K_1 = 10.$

K_2	Lower η_b	Higher η_b
0.	0.858604	
0.002100	0.860162	
0.003200	0.861815	
0.000300	0.863552	
0.000400	0.865377	
0.000500	0.867331	
0.000600	0.869424	
0.000700	0.871684	0.951305
0.000800	0.874155	0.946605
0.000900	0.876898	0.941786
0.001000	0.880017	0.936716
0.001100	0.883698	0.931207
0.001200	0.888331	0.924828
0.001300	0.895312	0.916179

Table Q-2

$K_1 = 20$

K_2	Lower η_b	Higher η_b
0.	0.607124	
0.002000	0.609773	
0.004000	0.612498	0.949493
0.006000	0.615311	0.937096
0.008000	0.618216	0.926247
0.010000	0.621215	0.916343
0.012000	0.624326	0.907066
0.014000	0.627555	0.898225
0.016000	0.630917	0.889692
0.018000	0.634428	0.881363
0.020000	0.638102	0.873168
0.022000	0.641964	0.865037
0.024000	0.646045	0.856908
0.026000	0.650378	0.848717
0.028000	0.655007	0.840397
0.030000	0.659997	0.831867
0.032000	0.665434	0.823025
0.034000	0.671444	0.813731
0.036000	0.678229	0.803773
0.038000	0.686142	0.792791
0.040000	0.695917	0.780038
0.042000	0.709780	0.763279

Table Q-3

K_1 = 30		
K_2	Lower η_b	Higher η_b
0.	0.495715	
0.010000	0.502194	
0.020000	0.509061	
0.030000	0.516363	
0.040000	0.524206	0.862477
0.050000	0.532688	0.842226
0.060000	0.541964	0.822459
0.070000	0.552295	0.802615
0.080000	0.564055	0.782102
0.090000	0.577955	0.760073
0.100000	0.595532	0.734878
0.110000	0.622223	0.700997

Table Q-4

K_1 = 40		
K_2	Lower η_b	Higher η_b
0.	0.429302	
0.010000	0.433580	
0.020000	0.437994	
0.030000	0.442576	
0.040000	0.447314	
0.050000	0.452237	0.869382
0.060000	0.457376	0.854755
0.070000	0.462737	0.840761
0.080000	0.468362	0.827186
0.090000	0.474277	0.813869
0.100000	0.480530	0.800674
0.110000	0.487190	0.787472
0.120000	0.494313	0.774136
0.130000	0.502022	0.760520
0.140000	0.510447	0.746446
0.150000	0.519804	0.731670
0.160000	0.530442	0.715820
0.170000	0.542993	0.698249
0.180000	0.558865	0.677531
0.190000	0.583128	0.648560

Table Q-5

$K_1 = 50$

K_2	Lower η_b	Higher η_b
0.	0.383979	
0.020000	0.390547	
0.040000	0.397415	
0.060000	0.404645	
0.080000	0.412287	0.848375
0.100000	0.420398	0.826899
0.120000	0.429079	0.806318
0.140000	0.438429	0.786157
0.160000	0.448630	0.766019
0.180000	0.459908	0.745505
0.200000	0.472637	0.724123
0.220000	0.487472	0.701138
0.240000	0.505736	0.675144
0.260000	0.531301	0.642224

Table Q-6

$K_1 = 60$

K_2	Lower η_b	Higher η_b
0.	0.350523	
0.020000	0.355857	
0.040000	0.361379	
0.060000	0.367122	
0.080000	0.373090	
0.100000	0.379328	
0.120000	0.385854	
0.140000	0.392712	
0.160000	0.399963	
0.180000	0.407651	
0.200000	0.415874	
0.220000	0.424724	
0.240000	0.434371	
0.260000	0.445027	
0.280000	0.457037	
0.300000	0.471016	
0.320000	0.488199	
0.340000	0.512169	

Table Q-7

$K_1 = 70.$

K_2	Lower η_b	Higher η_b
0.	0.324522	
0.020000	0.329053	
0.040000	0.333718	
0.060000	0.338521	
0.080000	0.343492	
0.100000	0.348621	
0.120000	0.353941	
0.140000	0.359460	
0.160000	0.365202	
0.180000	0.371203	
0.200000	0.377480	
0.220000	0.384077	
0.240000	0.391051	
0.260000	0.398446	
0.280000	0.406359	
0.300000	0.414875	
0.320000	0.424165	
0.340000	0.434433	
0.360000	0.446033	
0.380000	0.459550	
0.400000	0.476274	
0.420000	0.500076	

Table Q-8

$K_1 = 80.$

K_2	Lower η_b	Higher η_b
0.	0.303562	
0.020000	0.307513	
0.040000	0.311597	
0.060000	0.315763	
0.080000	0.320052	
0.100000	0.324453	
0.120000	0.328980	
0.140000	0.333654	
0.160000	0.338473	
0.180000	0.343456	
0.200000	0.348618	
0.220000	0.353988	
0.240000	0.359571	
0.260000	0.365399	
0.280000	0.371513	
0.300000	0.377934	
0.320000	0.384727	
0.340000	0.391936	
0.360000	0.399657	
0.380000	0.407981	
0.400000	0.417078	
0.420000	0.427164	
0.440000	0.438611	
0.460000	0.452067	
0.480000	0.468992	
0.500000	0.494490	

Table Q-9

$K_1 = 90.$

K_2	Lower η_b	Higher η_b
0.	0.286201	
0.020000	0.289754	
0.040000	0.293376	
0.060000	0.297276	
0.080000	0.300861	
0.100000	0.304749	
0.120000	0.308723	
0.140000	0.312798	
0.160000	0.316983	
0.180000	0.321295	
0.200000	0.325727	
0.220000	0.330295	
0.240000	0.335010	
0.260000	0.339900	
0.280000	0.344960	
0.300000	0.350216	
0.320000	0.355702	
0.340000	0.361425	
0.360000	0.367423	
0.380000	0.373750	
0.400000	0.380433	
0.420000	0.387556	
0.440000	0.395181	
0.460000	0.403447	
0.480000	0.412503	
0.500000	0.422599	

Table Q-9 (cont.)

$K_1 = 90.$

K_2	Lower η_b	Higher η_b
0.520000	0.434160	
0.540000	0.447966	
0.560000	0.465928	
0.580000	0.497941	

Table Q-10

K_1 = 100

K_2	Lower η_b	Higher η_b
0.	0.271514	
0.020000	0.274723	
0.040000	0.278016	
0.060000	0.281367	
0.080000	0.284776	
0.100000	0.288272	
0.120000	0.291831	
0.140000	0.295470	
0.160000	0.299194	
0.180000	0.303003	
0.200000	0.306920	
0.220000	0.310932	
0.240000	0.315052	
0.260000	0.319288	
0.280000	0.323659	
0.300000	0.328163	
0.320000	0.332815	
0.340000	0.337630	
0.360000	0.342634	
0.380000	0.347832	
0.400000	0.353249	
0.420000	0.358926	
0.440000	0.364879	
0.460000	0.371164	
0.480000	0.377820	
0.500000	0.384930	

Table Q-10 (cont.)

K_1 = 100.

K_2	Lower η_b	Higher η_b
0.520000	0.392570	
0.540000	0.400885	
0.560000	0.410053	
0.580000	0.420377	
0.600000	0.432358	
0.620000	0.447055	
0.640000	0.467590	

APPENDIX R

POSITION OF WATERFALLS AT BOTTOM OF TEST SECTION FOR THE CASE OF LINEAR VARYING JET - ($\bar{d}_o = d_o$)

Table R-1

K_1 = 10.		
K_2	Lower η_b	Higher η_b
0.	0.858604	
0.000200	0.863022	
0.000400	0.867740	
0.000600	0.872604	
0.000800	0.877691	0.996694
0.001000	0.883232	0.995454
0.001200	0.889035	0.993874
0.001400	0.895411	0.991785
0.001600	0.902337	0.988935
0.001800	0.910283	0.984955
0.002000	0.919722	0.979156
0.002200	0.932661	0.969488

Table R-2

K_1 = 20		
K_2	Lower η_b	Higher η_b
0.	0.607124	
0.001000	0.614602	
0.002000	0.622403	
0.003000	0.630409	
0.004000	0.638686	
0.005000	0.647364	0.990281
0.006000	0.656351	0.987611
0.007000	0.665742	0.984331
0.008000	0.675592	0.980212
0.009000	0.686124	0.975063
0.010000	0.697234	0.968774
0.011000	0.709257	0.961235
0.012000	0.722262	0.952286
0.013000	0.736773	0.941617
0.014000	0.753330	0.928639
0.015000	0.773336	0.912011
0.016000	0.800825	0.887504

Table R-3

K_1 = 30		
K_2	Lower η_b	Higher η_b
0.	0.495715	
0.002000	0.505600	
0.004000	0.515921	
0.006000	0.526556	
0.008000	0.537592	
0.010000	0.549202	
0.012000	0.561285	
0.014000	0.573981	0.974696
0.016000	0.587508	0.967517
0.018000	0.601852	0.958758
0.020000	0.617360	0.948329
0.022000	0.634205	0.936061
0.024000	0.653011	0.921543
0.026000	0.674545	0.903955
0.028000	0.700675	0.881528
0.030000	0.737087	0.848453

Table R-4

K_1 = 40		
K_2	Lower η_b	Higher η_b
0.	0.429302	
0.002000	0.436945	
0.004000	0.444717	
0.006000	0.452843	
0.008000	0.461076	
0.010000	0.469523	
0.012000	0.478200	
0.014000	0.487243	
0.016000	0.496503	
0.018000	0.506078	
0.020000	0.516001	
0.022000	0.526309	0.963823
0.024000	0.537206	0.957174
0.026000	0.548516	0.949685
0.028000	0.560414	0.941306
0.030000	0.573143	0.931977
0.032000	0.586636	0.921579
0.034000	0.601297	0.909920
0.036000	0.617244	0.896702
0.038000	0.635189	0.881424
0.040000	0.656030	0.863167
0.042000	0.681731	0.839810
0.044000	0.720451	0.803174

Table R-5

$K_1 = 50$

K_2	Lower η_b	Higher η_b
0.	0.383979	
0.002000	0.390346	
0.004000	0.396800	
0.006000	0.403467	
0.008000	0.410207	
0.010000	0.417080	
0.012000	0.424092	
0.014000	0.431251	
0.016000	0.438566	
0.018000	0.446163	
0.020000	0.453871	
0.022000	0.461782	
0.024000	0.469911	
0.026000	0.478276	0.964860
0.028000	0.486898	0.959761

Table R-5 (cont.)

$K_1 = 50$

K_2	Lower η_b	Higher η_b
0.030000	0.495937	0.954112
0.032000	0.505205	0.947923
0.034000	0.514831	0.941183
0.036000	0.524859	0.933854
0.038000	0.535474	0.925915
0.040000	0.546540	0.917297
0.042000	0.558233	0.907918
0.044000	0.570818	0.897649
0.046000	0.584241	0.886311
0.048000	0.598994	0.873662
0.050000	0.615369	0.859264
0.052000	0.634094	0.842396
0.054000	0.656777	0.821489
0.056000	0.688182	0.791713

Table R-6

$K_1 = 60$

K_2	Lower η_b	Higher η_b
0.	0.350523	
0.002000	0.356055	
0.004000	0.361651	
0.006000	0.367313	
0.008000	0.373186	
0.010000	0.379074	
0.012000	0.385059	
0.014000	0.391144	
0.016000	0.397336	
0.018000	0.403637	
0.020000	0.410055	
0.022000	0.416714	
0.024000	0.423426	
0.026000	0.430283	
0.028000	0.437297	
0.030000	0.444476	
0.032000	0.451834	
0.034000	0.459381	

Table R-6 (cont.)

$K_1 = 60$

K_2	Lower η_b	Higher η_b
0.036000	0.467267	
0.038000	0.475288	
0.040000	0.483562	
0.042000	0.492115	
0.044000	0.500974	
0.046000	0.510312	
0.048000	0.519949	
0.050000	0.530034	
0.052000	0.540758	
0.054000	0.552020	
0.056000	0.564126	
0.058000	0.577092	
0.060000	0.591356	
0.062000	0.607256	
0.064000	0.625548	
0.066000	0.648077	
0.068000	0.680461	

Table R-7

$K_1 = 70$		
K_2	Lower γ_b	Higher γ_b
0.	0.324522	
0.002000	0.329457	
0.004000	0.334444	
0.006000	0.339482	
0.008000	0.344573	
0.010000	0.349877	
0.012000	0.355155	
0.014000	0.360508	
0.016000	0.365940	
0.018000	0.371452	
0.020000	0.377049	
0.022000	0.382734	
0.024000	0.388510	
0.026000	0.394507	
0.028000	0.400517	
0.030000	0.406642	
0.032000	0.412885	
0.034000	0.419256	
0.036000	0.425760	
0.038000	0.432406	

Table R-7 (cont.)

$K_1 = 70$		
K_2	Lower γ_b	Higher γ_b
0.040000	0.439307	
0.042000	0.446298	
0.044000	0.453471	
0.046000	0.460838	
0.048000	0.468417	
0.050000	0.476226	
0.052000	0.484399	
0.054000	0.492774	
0.056000	0.501465	
0.058000	0.510510	
0.060000	0.520071	
0.062000	0.530020	
0.064000	0.540511	
0.066000	0.551777	
0.068000	0.563745	
0.070000	0.576845	
0.072000	0.591283	
0.074000	0.607603	
0.076000	0.626954	
0.078000	0.652103	

Table R-8

$K_1 = 80$		
K_2	Lower γ_b	Higher γ_b
0.	0.303562	
0.002000	0.308048	
0.004000	0.312576	
0.006000	0.317146	
0.008000	0.321759	
0.010000	0.326531	
0.012000	0.331289	
0.014000	0.336105	
0.016000	0.340983	
0.018000	0.345924	
0.020000	0.350930	
0.022000	0.356004	
0.024000	0.361148	
0.026000	0.366364	
0.028000	0.371757	
0.030000	0.377157	
0.032000	0.382644	
0.034000	0.388224	
0.036000	0.393900	
0.038000	0.399678	
0.040000	0.405563	
0.042000	0.411560	
0.044000	0.417676	

Table R-8 (cont.)

$K_1 = 80$		
K_2	Lower γ_b	Higher γ_b
0.046000	0.424029	
0.048000	0.430434	
0.050000	0.436988	
0.052000	0.443701	
0.054000	0.450584	
0.056000	0.457651	
0.058000	0.465017	
0.060000	0.472529	
0.062000	0.480285	
0.064000	0.488308	
0.066000	0.496626	
0.068000	0.505397	
0.070000	0.514462	
0.072000	0.523964	
0.074000	0.534092	
0.076000	0.544742	
0.078000	0.556240	
0.080000	0.568580	
0.082000	0.582254	
0.084000	0.597618	
0.086000	0.615665	
0.088000	0.638570	
0.090000	0.676940	

Table R-9

K_1 = 90		
K_2	Lower η_b	Higher η_b
0.	0.286201	
0.004000	0.294502	
0.008000	0.302944	
0.012000	0.311664	
0.016000	0.320521	
0.020000	0.329582	
0.024000	0.338861	
0.028000	0.348373	
0.032000	0.358240	
0.036000	0.368326	
0.040000	0.378721	
0.044000	0.389455	
0.048000	0.400560	
0.052000	0.412197	
0.056000	0.424233	
0.060000	0.436808	
0.064000	0.449996	
0.068000	0.464051	
0.072000	0.478874	
0.076000	0.494866	
0.080000	0.512109	
0.084000	0.531228	
0.088000	0.552813	
0.092000	0.578316	
0.096000	0.611106	
0.100000	0.674555	

Table R-10

K_1 = 100		
K_2	Lower η_b	Higher η_b
0.	0.271514	
0.004000	0.279237	
0.008000	0.287082	
0.012000	0.295154	
0.016000	0.303345	
0.020000	0.311706	
0.024000	0.320247	
0.028000	0.328980	
0.032000	0.337915	
0.036000	0.347183	
0.040000	0.356623	
0.044000	0.366329	
0.048000	0.376325	
0.052000	0.386636	
0.056000	0.397402	
0.060000	0.408492	
0.064000	0.420024	
0.068000	0.432053	
0.072000	0.444766	
0.076000	0.458074	
0.080000	0.472167	
0.084000	0.487344	
0.088000	0.503614	
0.092000	0.521555	
0.096000	0.541609	
0.100000	0.564896	
0.104000	0.593609	

APPENDIX S

EVALUATION OF AIR VELOCITY AT CHOKING CONDITION

APPENDIX S

EVALUATION OF AIR VELOCITY AT CHOKING CONDITION

At choking:

$$u_A = \frac{M_A}{\rho_A S(B-2x_b)} = \frac{M_A}{\rho_A S} \cdot \frac{2g}{u_i^2} \cdot \frac{1}{B^*(1 - \eta_b)} \qquad (S-1)$$

where $$\eta_b = \frac{2X_b}{B^*}$$

Now

$$K = \left[\frac{M_A}{M_w}\right]^2 \cdot \left[\frac{\rho_w}{\rho_A}\right] Fr_{wi}^{-1}$$ from Equation (6.20)

with

$$u_i^2 = gH_{wi}Fr_{wi}\left[\frac{M_w}{2S\,\rho_w u_i}\right] = g\,Fr_{wi}^{2/3} \times \left[\left(\frac{M_w}{2\,\rho_w S}\right)^2 \times \frac{1}{g}\right]^{1/3} \qquad (S-2)$$

hence from (S-1)

$$u_A = \frac{M_w K^{\frac{1}{2}} \left(\frac{\rho_A}{\rho_w}\right)^{\frac{1}{2}} Fr_{wi}^{\frac{1}{2}}}{\rho_A S} \times \frac{2g}{gFr_{wi}^{2/3}\left[\left(\frac{M_w}{2\,\rho_w S}\right)^2 \frac{1}{g}\right]^{1/3}} \times$$

$$\frac{1}{B^*(1 - \eta_b)} \qquad \text{(S-3)}$$

Now

$$Fr_{wb} = \left[\frac{M_w}{\rho_w SB}\right]^2 \cdot \frac{1}{gB}$$

giving

$$\left[\frac{M_w}{2\ \rho_w S}\right]^2 = \frac{B^3 Fr_{wb}}{4} \qquad \text{(S-4)}$$

and from (6.57)

$$Fr_{wb}^{1/3} = \frac{2^{5/3}}{B^* Fr_{wi}^{2/3}} \qquad \text{(S-5)}$$

hence from (S-3)

$$u_A = 2 \left[\frac{K}{B^*/2}\right]^{\frac{1}{2}} \left[\frac{1}{1 - \eta_b}\right] \left[\frac{\rho_w}{\rho_A}\right]^{\frac{1}{2}} \left[\frac{gB}{Fr_{wi}}\right]^{\frac{1}{2}} \left[\frac{1}{B^*/2}\right] \qquad \text{(S-6)}$$

For this work

$$\sqrt{gB} = \sqrt{9.81 \times 0.69} = 2.602 \text{ m/s}$$

$\rho_w = 1000 \text{ kg/m}^3$

$\rho_A = 1.308 \text{ kg/m}^3$

$Fr_{wi} = 2.2$

hence,

$$u_A \simeq 97\left[\frac{K}{B^*/2}\right]^{\frac{1}{2}} \left[\frac{1}{1 - \eta_b}\right]\left[\frac{1}{B^*/2}\right]$$

A typical value of $B^*/2$ during the tests was 20 and, from Figure 6.11, this gives corresponding values of $\left(\frac{K}{B^*/2}\right) \simeq 0.0085$ and $\left(\frac{X_b}{B^*/2}\right) \simeq 0.84$,

hence

$$u_A \simeq (97)(0.0085)^{\frac{1}{2}}\left(\frac{1}{0.16}\right)\left(\frac{1}{20}\right) \simeq 2.8 \text{ m/s}$$

APPENDIX T

TABLES OF THE COLLAPSE CONDITIONS

TABLE T-1

COLLAPSE CONDITIONS FOR CASE (i)

WITH NO JET THICKNESS ALLOWANCE

K_1	K_{2max}	γ_{bmax}
7.372	0.000000	1.000000
8.000	0.003898	0.982952
10.000	0.032952	0.943902
15.000	0.133471	0.874346
20.000	0.242921	0.828267
30.000	0.457294	0.770663
40.000	0.657205	0.734846
50.000	0.842856	0.710216
60.000	1.016242	0.691898
70.000	1.179249	0.677613
80.000	1.333420	0.665840
90.000	1.479990	0.656359
100.000	1.619945	0.648078

TABLE T-2

COLLAPSE CONDITIONS FOR CASE (ii)

WITH NO JET THICKNESS ALLOWANCE

K_1	K_{2max}	η_{bmax}
7.372	0.000000	1.000000
8.000	0.000026	0.970454
9.000	0.000384	0.935811
10.000	0.001352	0.904189
13.000	0.001352	0.904188
17.000	0.026001	0.769726
20.000	0.043413	0.735120
30.000	0.114892	0.659730
40.000	0.194533	0.614467
50.000	0.275559	0.583909
60.000	0.355582	0.561068
70.000	0.433535	0.543387
80.000	0.509475	0.529145
90.000	0.583195	0.517414
100.000	0.654754	0.507423

TABLE T-3

COLLAPSE CONDITIONS FOR CASE (ii) - (APPROX.)

WITH NO JET THICKNESS ALLOWANCE

K_1	K_{2max}	η_{bmax}
7.843	0.000000	1.000000
10.000	0.001588	0.905736
20.000	0.048174	0.738083
30.000	0.124773	0.663810
40.000	0.208824	0.619534
50.000	0.293631	0.589319
60.000	0.376962	0.567015
70.000	0.458052	0.549681
80.000	0.536689	0.535708
90.000	0.612887	0.524134
100.000	0.686742	0.514343

TABLE T-4

COLLAPSE CONDITIONS FOR CASE (iii)*

WITH NO JET THICKNESS ALLOWANCE

K_1	K_{2max}	η_{bmax}
7.843	0.000000	1.000000
10.00	0.002322	0.950757
20.000	0.016635	0.844161
30.000	0.031211	0.792908
40.000	0.044757	0.761064
50.000	0.057307	0.739940
60.000	0.069006	0.723621
70.000	0.079989	0.710894
80.000	0.090365	0.700765
90.000	0.100220	0.692391
100.000	0.109623	0.685671
200.000	0.187345	0.646555

* $\bar{do} = do$

TABLE T-5

COLLAPSE CONDITIONS FOR CASE (ii)

WITH JET THICKNESS ALLOWANCE

K_1	K_{2max}	η_{bmax}
8.000	0.000000	0.990688
9.000	0.000088	0.947704
10.000	0.000234	0.890225
13.000	0.006092	0.839794
17.000	0.02203	0.774580
20.000	0.038545	0.738644
30.000	0.108363	0.661798
40.000	0.187348	0.616124
50.000	0.268125	0.584632
60.000	0.348088	0.561984
70.000	0.426266	0.544112
80.000	0.502304	0.529849
90.000	0.576150	0.517877
100.000	0.647846	0.507761

TABLE T-6

COLLPASE CONDITIONS FOR CASE (iii)*

WITH JET THICKNESS ALLOWANCE

K_1	K_{2max}	η_{bmax}
10.000	0.001605	0.956803
20.000	0.015357	0.848476
30.000	0.029821	0.794924
40.000	0.043355	0.763324
50.000	0.055923	0.741890
60.000	0.067651	0.725009
70.000	0.078666	0.711616
80.000	0.089075	0.701497
90.000	0.098962	0.693149
100.000	0.108395	0.685783

* $\bar{d}o$ = do

TABLE T-7

COLLAPSE CONDITIONS FOR CASE (iii)*

WITH JET THICKNESS ALLOWANCE

K_1	K_{2max}	η_{bmax}
10.00	0.001585	0.963854
20.000	0.014015	0.853569
30.000	0.026930	0.801677
40.000	0.038965	0.769671
50.000	0.050121	0.746839
60.000	0.060521	0.731286
70.000	0.070283	0.718042
80.000	0.079504	0.707816
90.000	0.088260	0.699121
100.000	0.096613	0.692208

* $\bar{d}o = \sqrt{\frac{\pi}{4}}\, do$

APPENDIX U

ALLOWANCE FOR THE THICKNESS OF THE WATERFALLS

APPENDIX U

ALLOWANCE FOR THE THICKNESS OF THE WATERFALLS

The waterfall thickness has two effects, (a) it increases z_b by $\frac{H_{wi}}{2}$, (b) it decreases the air passage width by $H'_w = \frac{H_w}{\cos\theta}$ or in dimensionless form, by

$$H^{*'}_w = \left[\frac{2gH_w}{u_i^2}\right] \frac{1}{\cos\theta} \quad .$$

From Equations (6.3) and (6.6):

$$H^{*'}_w = \left[\frac{2g}{u_i^2}\right] \frac{H_{wi} u_i}{\bar{v}} \quad \frac{\bar{v}}{u_i\left[\left(1 + \frac{2gz}{u_i^2}\right) - \left(1 + \frac{1}{\rho_w H_w u_i^2}\int_0^z p\,dz\right)^2\right]^{\frac{1}{2}}}$$

Now consider the value of $H^*_w = H^*_{wb}$ where $z = z_b$ (where the correction is important) and for the simplicity assume there that $\cos\theta \simeq 1$

$$H^*_{wb} = \frac{2g}{u_i^2} \frac{H_{wi}\, u_i}{[2gz_b + u_i^2]^{\frac{1}{2}}} = \frac{2}{Fr_{wi}} \cdot \frac{1}{(1 + Z_b)^{\frac{1}{2}}} \qquad (U\text{-}1)$$

This correction was applied to the whole of the waterfall.

This in the previous calculations Z_b was replaced by Z'_b and $\frac{B^*}{2}$ by $\frac{B^{*'}}{2}$ where

$$Z_b' = Z_b + \frac{2q}{u_i^2} H_{wi} = Z_b + \frac{2}{Fr_{wi}} \qquad \text{(U-2)}$$

and

$$\frac{B^{*'}}{2} = \frac{B^*}{2} - \frac{1}{Fr_{wi}\ (1 + Z_b)^{\frac{1}{2}}} \qquad \text{(U-3)}$$